

**Memorias del Congreso Anual
de la Sociedad Nuclear Mexicana**

**XXXV Congreso Anual
Empowering the Energy Transition**



Sociedad Nuclear Mexicana

Enero - Diciembre 2024

Publicación Anual

ISSN: 3061-7472

Editores de la publicación:
Alejandría Denisse Pérez Valseca
Roberto Carlos Lopez Solis

MEMORIAS DEL CONGRESO ANUAL DE LA SOCIEDAD NUCLEAR MEXICANA. Volumen 3, Congreso número 35, enero-diciembre 2024, es una publicación anual de la Sociedad Nuclear Mexicana A. C., Avenida Mariano Escobedo No. Ext. 510, No. Int. 801, Colonia Anzures, Alcaldía Miguel Hidalgo, C.P. 11590, Ciudad de México, México. Página electrónica de la revista <https://www.sociedadnuclear.mx/memorias/> y dirección electrónica comite.editorial@sociedadnuclear.mx Editor Responsable: Alejandría Denisse Pérez Valseca. Certificado de Reserva de Derechos al Uso Exclusivo del Título 04-2024-080812220500-102, ISSN: 3061-7472, ambos otorgados por el Instituto Nacional del derecho de Autor. Responsables de la última actualización de este número: Alejandría Denisse Pérez Valseca y Roberto Carlos Lopez Solis. Avenida Mariano Escobedo No. Ext. 510, No. Int. 801, Colonia Anzures, Alcaldía Miguel Hidalgo, C.P. 11590, Ciudad de México, México. Fecha de la última modificación: diciembre 2024. Tamaño del archivo 26 MB.

Las opiniones expresadas por los autores no necesariamente reflejan la postura del editor de la publicación.

Queda estrictamente prohibida la reproducción total o parcial de los contenidos e imágenes de la publicación sin previa autorización de la Sociedad Nuclear Mexicana.

35th SNM Annual Congress
31st WIn Global Annual Conference
1st WIn ARCAL Regional Congress

October 28th - 30th, 2024

Mexico City, Mexico.

“Empowering the Energy Transition”

Conference Proceedings

Welcome

On behalf of the Mexican Nuclear Society and the different branches of the Women in Nuclear Association, we are pleased to welcome you to the 31st WiN Global / 35th SNM / 1st WiN ARCAL Annual Conference. Being the first time that these organizations work all together in a single conference, the Mexican Nuclear Society is very proud to host it in Mexico City.

Women empowerment is fundamental to the progress of the nation and society, and for this reason, it is the focus of this year's conference, having the theme "emPowering the Energy Transition".

In this conference the subjects to be covered are separated into nine tracks: 1. Energy Transition; 2. Reactor Physics, Fuel Cycle, and Non-Proliferation; 3. Nuclear Reactor Thermal-hydraulics and Safety; 4. Operation, Maintenance, Materials, and New Designs; 5. Environment and Non-Electric Applications; 6. Energy Planning; 7. Radiological Protection and Safety; 8. Gender Equality Diversity, and Inclusion; and 9. emPowering the Next Generation.

The plenary speakers are a diverse selection of distinguished professionals that include representatives from non-profitable international organizations, private industry, research centers, academia, and more; from all around the world.

Regarding the venue, Mexico City is in the heart of the country with close connection from different touristic and cultural attractions; just to mention one, less than one-hour distance from the city it is placed the archeological complex of Teotihuacan, where the Temple of Quetzalcoatl, the Pyramid of the Moon and the Pyramid of the Sun are located.

Finally, we would like to thank to our different sponsors "TFV Mexico Operations", "KOCEN Co, Ltd.", "State Atomic Energy Corporation Rosatom", "World Nuclear Association" and "Vertek Industrial Supply Inc.", without them this conference would not have been possible.

We hope you all enjoy your stay here in Mexico and have a fruitful conference through the many plenary and technical sessions and have the opportunity to exchange ideas by the contact with new and old friends.

With Warm Regards,

Dr. Alejandro Nuñez Carrera
President of the Mexican Nuclear Society

Mesa Directiva

Sociedad Nuclear Mexicana

2024-2026

Presidente

Alejandro Núñez Carrera

Vicepresidente

Fabian Barrios Eufrasio

Secretario

María de Lourdes Zúñiga Ramírez

Tesorero

Roberto Carlos López Solís

Vocal de socios

Consuelo Letechipía de León

Vocal de prensa y difusión

Brian Oliva Ambrosi

Vocal de acción social, capacitación y desarrollo profesional

Oziel Rojas Ávila

Vocal de acción técnica, científica e industrial

Lina Celis del Ángel Centeno

Vocal de legislación

Alma Georgina Martínez López

ORGANIZING INSTITUTIONS



Sociedad Nuclear Mexicana



SPONSORS



ROSATOM



**WORLD NUCLEAR
ASSOCIATION**



Content by Authors

**SELECT THE LETTER WHICH CORRESPONDS TO THE FIRST LETTER OF THE
LASTNAME OF THE AUTHOR YOU ARE LOOKING FOR**

THEN GO TO THE TRACK OF INTEREST

A	B	C	D
E	F	G	H
I	J	K	L
M	N	O	P
Q	R	S	T
U	V	W	X
Y	Z		

A

Ahmad, Tanveer	Neutron Activation Analysis and Atomic Absorption Spectrometry of Watermelon Rind as Potential Bioadsorbent for Toxic Metals Decontamination of Water (Track 5)
Amador García, Rodolfo	Development of a Reactor Building model of a BWR5 for the calculation of on-site and off-site fission product masses with the MAAP5 code (Track 3)
Ambruster Sánchez, Liz	Safety Analysis Methodology Development for Multipurpose Nuclear Microreactors (Track 4)
Arreola Ramírez, Jesus Andrés	Investigating the relationship between soil properties and natural gamma emitter activity in Zacatecas using linear models and neural networks (Track 5)
Arroyo García, Daniela Alejandra	Burnup Analysis of Fuel Assemblies from the Last Operating Cycles of a BWR (Track 2)
Ayala, Carolina Natalia	Plan for the Decommissioning of Nuclear Facilities (Track 7)

C

Campos Muñoz, Alejandro	Solution of the neutronics benchmark of the NuScale-like core using the AZTRAN code (Track 2)
Castillo Hernández, Orestes	Risk-Informed Design: A New Approach in the Nuclear Industry (Track 4)
Castillo Méndez, José Alejandro	Analysis of Plutonium Production in a BWR Reactor (Track 2) Burnup Analysis of Fuel Assemblies from the Last Operating Cycles of a BWR (Track 2)
Castillo Salinas, Daniel Tonalli	Analysis of Plutonium Production in a BWR Reactor (Track 2)
Chukwurah, Chinelo Jennifer	Women Educating Nations: The Role of Grassroot Women's Nuclear Education in National Nuclear Strategy (Track 8)
Cruz Lopez, Carlos Antonio	Two Alternative Proofs to an Inequality Related to a Periodic Power Variation in a Nuclear Reactor (Track 2)
Cruz Vázquez, Karina	Preliminary Neutronic Design of a Multipurpose Nuclear Microreactor (Track 2)

D

- Davila Rangel, Ignacio
Qualitative Characterization of Uranium Samples, Oriented to Investigation in Nuclear Forensics (Track 2)
- Del Valle Gallegos, Edmundo
AZIMUTAL, a Tool for the Visualization of Group Constants and Automation in the Generation of NEMTAB Files (Track 2)
Development, Verification, and Validation of an Advanced Nodal Version of the AZKIND Code (Track 2)
Graphical Interface for Generating SERPENT Input for Light-Water Nuclear Reactors (Track 2)
Mexican Results on the Refined Phase of the NEA Lead-cooled Fast Reactor Benchmark (Track 2)
Results of Mexico's Participation in the Extension Phase of Neutronics Benchmark of the CEFR Reactor Start-Up Test (Track 2)
Solution of the neutronics benchmark of the NuScale-like core using the AZTRAN code (Track 2)
- Dominguez Alfaro, Jesus Jorge
Helium Fraction Reactivity Effects in a Thermal Molten Salt Nuclear Reactor (Track 2)
- Duran Gonzalez, Julian Arturo
Solution of the neutronics benchmark of the NuScale-like core using the AZTRAN code (Track 2)

E

- Elkomey, Heba F.
Advocacy Driving Women's Impact in Non-Proliferation (Track 8)
- Escareño Juárez, Edmundo
Investigating the relationship between soil properties and natural gamma emitter activity in Zacatecas using linear models and neural networks (Track 5)
- Espinosa Paredes, Gilberto
Helium Fraction Reactivity Effects in a Thermal Molten Salt Nuclear Reactor (Track 2)
Multiphysics and multiscale analysis of HTR-10 reactor (Track 3)
Two Alternative Proofs to an Inequality Related to a Periodic Power Variation in a Nuclear Reactor (Track 2)

F

- Faiz, Yasir
Neutron Activation Analysis and Atomic Absorption Spectrometry of Watermelon Rind as Potential Bioadsorbent for Toxic Metals Decontamination of Water (Track 5)
- François Lacouture Juan Luis
Hot channel analysis of the NuScale core with ATFs using Computational Fluid Dynamics (Track 3)
- Implementation of the DWSIM process simulator for thermodynamic analysis of supercritical N2 Brayton cycle for advanced nuclear power plants (Track 1)
- Neutronic Evaluation of Two Different Types of Fuel Material on the Performance of a Fast Nuclear Microreactor: First Approach to Mizton (Track 2)
- Preliminary Neutronic Design of a Multipurpose Nuclear Microreactor (Track 2)
- Two Alternative Proofs to an Inequality Related to a Periodic Power Variation in a Nuclear Reactor (Track 2)

G

- Galicia Aragon, Juan
Results of Mexico's Participation in the Extension Phase of Neutronics Benchmark of the CEFR Reactor Start-Up Test (Track 2)
- Gálvez Gonzalez, Brian
The reactivation of the AJENM (A Mexican Young Association in Nuclear) (Track 9)
- Gómez Torres, Armando Miguel
AZIMUTAL, a Tool for the Visualization of Group Constants and Automation in the Generation of NEMTAB Files (Track 2)
- Development, Verification, and Validation of an Advanced Nodal Version of the AZKIND Code (Track 2)
- Graphical Interface for Generating SERPENT Input for Light-Water Nuclear Reactors (Track 2)
- Mexican Results on the Refined Phase of the NEA Lead-cooled Fast Reactor Benchmark (Track 2)
- Results of Mexico's Participation in the Extension Phase of Neutronics Benchmark of the CEFR Reactor Start-Up Test (Track 2)
- Solution of the neutronics benchmark of the NuScale-like core using the AZTRAN code (Track 2)

Gyane, Eva

Nuclear Technology Innovations and Export Controls (Track 2)

H

Hernández Flores, Juan
Enrique

Analysis of Plutonium Production in a BWR Reactor (Track 2)

Hernandez Galeana,
Jaime

Potential use of the TRIGA Mark III Reactor for Neutrographies (Track 5)

Hernández Ramírez,
Daniel

Investigating the relationship between soil properties and natural gamma emitter activity in Zacatecas using linear models and neural networks (Track 5)

Herrera García, Cintya
Fabiola

Qualitative Characterization of Uranium Samples, Oriented to Investigation in Nuclear Forensics (Track 7)

Huaccho Zavala,
Gianfranco

Solution of the neutronics benchmark of the NuScale-like core using the AZTRAN code (Track 2)

Huang, Guofang

Nuclear Heating Empowering the Energy Transition (Track 1)

I

Indauliya, Gunjan

Technical Expertise and Innovations in the Defuelling Program for Advanced Gas-cooled Reactor: Strategies for Optimization, Reliability, and Safety (Track 1)

J

Jelassi, Haikel

Performance and Degradation pathways of Erythrosine by Ionizing Radiation in Aqueous Solutions (Track 5)

Juárez Martínez, Luis
Carlos

Implementation of the DWSIM process simulator for thermodynamic analysis of supercritical N₂ Brayton cycle for advanced nuclear power plants (Track 1)

K

Kanwal, Sadia	Neutron Activation Analysis and Atomic Absorption Spectrometry of Watermelon Rind as Potential Bioadsorbent for Toxic Metals Decontamination of Water (Track 5)
Kniznik, Laura	Plan for the Decommissioning of Nuclear Facilities (Track 7)
Krizan, Sofia Elias	Plan for the Decommissioning of Nuclear Facilities (Track 7)

L

Lara Almazán, Nancy	Qualitative Characterization of Uranium Samples, Oriented to Investigation in Nuclear Forensics (Track 7)
Leon Aboyte, Ana Paulina	The reactivation of the AJENM (A Mexican Young Association in Nuclear) (Track 9)
Lopez Solis, Roberto	First Steps on the Designing and Modeling of a High Temperature Gas Cooled Microreactor (Track 2) Helium Fraction Reactivity Effects in a Thermal Molten Salt Nuclear Reactor (Track 2) Mexican Results on the Refined Phase of the NEA Lead-cooled Fast Reactor Benchmark (Track 2) Results of Mexico's Participation in the Extension Phase of Neutronics Benchmark of the CEFR Reactor Start-Up Test (Track 2)

M

Martín del Campo Márquez, Cecilia	Energy Transition Scenario with Nuclear Energy Deployment (Track 1)
Martínez Caballero, Eduardo	BWR Fuel Lattices with Minor Actinides (Track 2) Development of a Reactor Building model of a BWR5 for the calculation of on-site and off-site fission product masses with the MAAP5 code (Track 3)
Medina Almazán, Aida Liliana	Integration of the Equipment Reliability Process and Ageing Management for the Safe and Reliable Long Term Operation of NPPs (Track 4)
Mena de la Noval, Fabián Luis	Hot channel analysis of the NuScale core with ATFs using Computational Fluid Dynamics (Track 3)

- Montaño Acevedo, Celeste Jeanette
First Steps on the Designing and Modeling of a High Temperature Gas Cooled Microreactor (Track 2)
Potential use of the TRIGA Mark III Reactor for Neutrographies (Track 5)
- Montes Tadeo, José Luis
BWR Fuel Lattices with Minor Actinides (Track 2)
- Morones García, Emiliano
Neutronic Evaluation of Two Different Types of Fuel Material on the Performance of a Fast Nuclear Microreactor: First Approach to Mizton (Track 2)
Preliminary Neutronic Design of a Multipurpose Nuclear Microreactor (Track 2)

N

- Nelson Edelstein, Pamela Fran
Energy Transition Scenario with Nuclear Energy Deployment (Track 1)
Probabilistic Risk Assessment of the HVAC Extraction Hoods of a Radioisotope Plant (Track 4)
Risk-Informed Design: A New Approach in the Nuclear Industry (Track 4)
Safety Analysis Methodology Development for Multipurpose Nuclear Microreactors (Track 4)
- Noomen, Ahlem
Performance and Degradation pathways of Erythrosine by Ionizing Radiation in Aqueous Solutions (Track 5)

O

- Okoye, Geraldine Nneka
Advocacy Driving Women's Impact in Non-Proliferation (Track 8)
Women Educating Nations: The Role of Grassroot Women's Nuclear Education in National Nuclear Strategy (Track 8)
- Olguín Rodríguez, Itzel Adriana
Potential use of the TRIGA Mark III Reactor for Neutrographies (Track 5)
- Ortega Chagoyan, Blanca Jessica
Development of a BWR5 Reactor Building model for on-site and off-site dose calculations with MAAP5-DOSE (Track 3)
Development of a Reactor Building model of a BWR5 for the calculation of on-site and off-site fission product masses with the MAAP5 code (Track 3)
- Ortiz Servín, Juan José
Analysis of Plutonium Production in a BWR Reactor (Track 2)

- Ortiz Villafuerte, Javier
Ortiz Villafuerte, Javier (cont)
- Burnup Analysis of Fuel Assemblies from the Last Operating Cycles of a BWR (Track 2)
- Development of a BWR5 Reactor Building model for on-site and off-site dose calculations with MAAP5-DOSE (Track 3)
- Development of a Reactor Building model of a BWR5 for the calculation of on-site and off-site fission product masses with the MAAP5 code (Track 3)

P

- Perez González, Yosvany
Pérez Parrazal, Omar
Perez Valseca, Alejandria Denisse
- Hot channel analysis of the NuScale core with ATFs using Computational Fluid Dynamics (Track 3)
- Probabilistic Risk Assessment of the HVAC Extraction Hoods of a Radioisotope Plant (Track 4)
- Implementation of the DWSIM process simulator for thermodynamic analysis of supercritical N2 Brayton cycle for advanced nuclear power plants (Track 1)
- Helium Fraction Reactivity Effects in a Thermal Molten Salt Nuclear Reactor (Track 2)
- Multiphysics and multiscale analysis of HTR-10 reactor (Track 3)
- Unprotected Transients Simulations of a Liquid Metal-cooled Fast Reactor (Track 3)

R

- Ramírez Sánchez, José Ramon
Ríos Martínez, Carlos
Robles Nuñez, Ambar Gissel
- BWR Fuel Lattices with Minor Actinides (Track 2)
- Investigating the relationship between soil properties and natural gamma emitter activity in Zacatecas using linear models and neural networks (Track 5)
- Social and Environmental Justice: Pillars of the Energy Transition (Track 1)

S

Sanchez Espinoza, Victor Hugo	Solution of the neutronics benchmark of the NuScale-like core using the AZTRAN code (Track 2)
Serrano Bentancour, Agostina	Nuclear Technology Innovations and Export Controls (Track 2)
Serrano Hernandez, Edmundo Leonardo	Development, Verification, and Validation of an Advanced Nodal Version of the AZKIND Code (Track 2)
Sharma, Diksha	Technical Expertise and Innovations in the Defuelling Program for Advanced Gas-cooled Reactor: Strategies for Optimization, Reliability, and Safety (Track 1)
Shehzadi, Samreen	Neutron Activation Analysis and Atomic Absorption Spectrometry of Watermelon Rind as Potential Bioadsorbent for Toxic Metals Decontamination of Water (Track 5)

V

Vázquez Rodríguez, Rodolfo	Unprotected Transients Simulations of a Liquid Metal-cooled Fast Reactor (Track 3)
Velazquez C. Saul Ricardo	AZIMUTAL, a Tool for the Visualization of Group Constants and Automation in the Generation of NEMTAB Files (Track 2)
Viáis Juárez, Jorge	Development of a BWR5 Reactor Building model for on-site and off-site dose calculations with MAAP5-DOSE (Track 3) Development of a Reactor Building model of a BWR5 for the calculation of on-site and off-site fission product masses with the MAAP5 code (Track 3)
Villamil Clavijo, Sergio Andrés	Graphical Interface for Generating SERPENT Input for Light-Water Nuclear Reactors (Track 2)

X

Xolocostli Munguia, Jose Vicente	Solution of the neutronics benchmark of the NuScale-like core using the AZTRAN code (Track 2)
----------------------------------	---

Y

Yartey , Miriam Naa	Advocacy Driving Women's Impact in Non-Proliferation (Track 8)
Yescas Pozos, Erick Josue	Multiphysics and multiscale analysis of HTR-10 reactor (Track 3)
Yuego N, Adeline	Advocacy Driving Women's Impact in Non-Proliferation (Track 8)

Z

Zaouak, Amira	Performance and Degradation pathways of Erythrosine by Ionizing Radiation in Aqueous Solutions (Track 5)
Zarazua Ortega, Graciela	Qualitative Characterization of Uranium Samples, Oriented to Investigation in Nuclear Forensics (Track 7)
Zhou, Jun	Nuclear Heating Empowering the Energy Transition (Track 1)

Content by Track

SELECT THE TRACK OF YOUR INTEREST

THEN SELECT THE PAPER TO OPEN IT

- Track 1 Energy Transition**
- Track 2 Reactor Physics, Fuel Cycle, and Non-Proliferation**
- Track 3 Nuclear Reactor Thermal-hydraulics and Safety**
- Track 4 Operation, Maintenance, Materials, and New Designs**
- Track 5 Environment and Non-Electric Applications**
- Track 6 Energy Planning**
- Track 7 Radiological Protection and Safety**
- Track 8 Gender Equality Diversity, and Inclusion**
- Track 9 emPowering the Next Generation**

Track 1: Energy Transition

Nuclear Heating Empowering the Energy Transition

Guofang Huang and Jun Zhou

Social and Environmental Justice: Pillars of the Energy Transition

Ambar Gissel Robles Nuñez

Implementation of the DWSIM process simulator for thermodynamic analysis of supercritical N₂ Brayton cycle for advanced nuclear power plants

Luis Carlos Juárez Martínez, Alejandría Denisse Pérez Valseca and Juan Luis François Lacouture

Technical Expertise and Innovations in the Defuelling Program for Advanced Gas-cooled Reactor: Strategies for Optimization, Reliability, and Safety

Diksha Sharma and Gunjan Indauliya

Energy Transition Scenario with Nuclear Energy Deployment

Cecilia Martín del Campo Márquez, Pamela F. Nelson

Track 2: Reactor Physics, Fuel Cycle, and Non-Proliferation

BWR Fuel Lattices with Minor Actinides

Jose-Luis Montes-Tadeo, Eduardo Martínez Caballero and José Ramón Ramírez Sánchez

Analysis of Plutonium Production in a BWR Reactor

Hernández Flores Juan Enrique, Ortiz Servin Juan José and Castillo Méndez José Alejandro

Burnup Analysis of Fuel Assemblies from the Last Operating Cycles of a BWR

Daniela Alejandra Arroyo García, Juan José Ortiz-Servin, Alejandro Castillo and Daniel Tonalli Castillo Salinas

Development, Verification, and Validation of an Advanced Nodal Version of the AZKIND Code

Edmundo Leonardo Serrano Hernández, Edmundo del Valle Gallegos and Armando Miguel Gómez Torres

Preliminary Neutronic Design of a Multipurpose Nuclear Microreactor

Karina Cruz Vázquez, Juan Luis François and Emiliano Morones García

Neutronic Evaluation of Two Different Types of Fuel Material on the Performance of a Fast Nuclear Microreactor: First Approach to Mizton

Emiliano Morones-García and Juan-Luis François

Helium Fraction Reactivity Effects in a Thermal Molten Salt Nuclear Reactor

Jesús Jorge Domínguez Alfaro, Gilberto Espinosa-Paredes, Alejandría Denisse Pérez-Valseca and Roberto Lopez-Solis

AZIMUTAL, a Tool for the Visualization of Group Constants and Automation in the Generation of NEMTAB Files

Velazquez C. Saul Ricardo, del Valle G. Edmundo and Gomez T. Armando Miguel

Graphical Interface for Generating SERPENT Input for Light-Water Nuclear Reactors

Sergio Andrés Villamil Clavijo, Edmundo del Valle Gallegos and Armando Miguel Gómez Torres

First Steps on the Designing and Modeling of a High Temperature Gas Cooled Microreactor

Roberto Lopez-Solis and Celeste Montaña-Acevedo

Nuclear Technology Innovations and Export Controls

Eva Gyane and Agostina Serrano Bentancour

Two Alternative Proofs to an Inequality Related to a Periodic Power Variation in a Nuclear Reactor

Carlos Antonio Cruz López, Gilberto Espinosa Paredes and Juan Luis François Lacouture

Solution of the neutronics benchmark of the NuScale-like core using the AZTRAN code

J. Vicente Xolocostli Munguía, Armando M. Gómez Torres, Julián A. Durán González, Gianfranco Huaccho Zavala, Alejandro Campos Muñoz, Víctor H. Sánchez Espinoza and Edmundo del Valle Gallegos

Mexican Results on the Refined Phase of the NEA Lead-cooled Fast Reactor Benchmark

Roberto Lopez-Solis, Armando Gomez-Torres and Edmundo del Valle-Gallegos

Results of Mexico's Participation in the Extension Phase of Neutronics Benchmark of the CEFR Reactor Start-Up Test

Roberto Lopez-Solis, Armando Gomez-Torres, Juan Galicia-Aragon and Edmundo del Valle-Gallegos

Track 3: Nuclear Reactor Thermal-hydraulics and Safety

Hot channel analysis of the NuScale core with ATFs using Computational Fluid Dynamics

Yosvany Pérez González, Juan Luis François Lacouture and Fabián Luis Mena de la Noval

Development of a Reactor Building model of a BWR5 for the calculation of on-site and off-site fission product masses with the MAAP5 code

Blanca Jessica Ortega Chagoyan, Javier Ortiz Villafuerte, Jorge Viais Juárez, Eduardo Martinez Caballero and Rodolfo Amador García

Multiphysics and multiscale analysis of HTR-10 reactor

Erick Josue Yescas Pozos, Gilberto Espinosa Paredes and Alejandría Denisse Pérez-Valseca

Development of a BWR5 Reactor Building model for on-site and off-site dose calculations with MAAP5-DOSE

Blanca Jessica Ortega Chagoyan, Javier Ortiz Villafuerte and Jorge Viais Juárez

Unprotected Transients Simulations of a Liquid Metal-cooled Fast Reactor

Alejandría Denisse Pérez-Valseca and Rodolfo Vázquez-Rodríguez

Track 4: Operation, Maintenance, Materials, and New Designs

Probabilistic Risk Assessment of the HVAC Extraction Hoods of a Radioisotope Plant

Omar Pérez Parrazal and Pamela F. Nelson

Safety Analysis Methodology Development for Multipurpose Nuclear Microreactors

Liz A. Ambruster Sánchez and Pamela F. Nelson

Risk-Informed Design: A New Approach in the Nuclear Industry

Orestes Castillo Hernández and Pamela F. Nelson

Integration of the Equipment Reliability Process and Ageing Management for the Safe and Reliable Long Term Operation of NPPs

Aida Liliana Medina Almazán

Track 5: Environment and Non-Electric Applications

Performance and Degradation pathways of Erythrosine by Ionizing Radiation in Aqueous Solutions

Amira Zaouak, Ahlem Noomen and Haikel Jelassi

Neutron Activation Analysis and Atomic Absorption Spectrometry of Watermelon Rind as Potential Bioadsorbent for Toxic Metals Decontamination of Water

Samreen Shehzadi, Sadia Kanwal, Tanveer Ahmad and Yasir Faiz

Potential use of the TRIGA Mark III Reactor for Neutrographies

Hernandez Galeana, Jaime, Montaña-Acevedo Celeste and Olguín-Rodríguez Itzel

Investigating the relationship between soil properties and natural gamma emitter activity in Zacatecas using linear models and neural networks

Arreola-Ramírez Jesús Andrés, Ríos-Martínez Carlos and Escareño-Juárez Edmundo Hernández-Ramírez Daniel

Track 6: Energy Planning

No technical papers presented

Track 7: Radiological Protection and Safety

Plan for the Decommissioning of Nuclear Facilities

M Carolina Natalia Ayala and Laura Kniznik and Sofia Elias Krizan

Qualitative Characterization of Uranium Samples, Oriented to Investigation in Nuclear Forensics

Cintya Fabiola Herrera García, Graciela Zarazúa Ortega, Ignacio Dávila Rangel and Nancy Lara Almazán

Track 8: Gender Equality Diversity, and Inclusion

Women Educating Nations: The Role of Grassroot Women's Nuclear Education in National Nuclear Strategy

Geraldine Nneka Okoye and Chinelo Jennifer Chukwurah

Advocacy Driving Women's Impact in Non-Proliferation

Adeline Yuego N., Miriam Naa Yartey Y, Geraldine Nneka Okoye and Heba F. Elkomey

Track 9: emPowering the Next Generation

The reactivation of the AJENM (A Mexican Young Association in Nuclear)

Gálvez González Brian, Ana Paulina León Aboyte

Track 1

Energy Transition

Nuclear Heating Empowering the Energy Transition

Guofang Huang^{1} and Jun Zhou^{2*}*

State Power Investment Corporation

huangguofang@spic.com.cn;zhoujun@snerdi.com.cn

Abstract

Under the "dual carbon goal"-carbon emission peaking and carbon neutrality, the decarbonization of China's energy system is becoming increasingly urgent. As a zero-carbon emission clean energy source, nuclear power possesses unparalleled advantages in terms of stability, economic viability and safety. Particularly in the heating sector, there exists significant market space. The comprehensive utilization of nuclear power plays a crucial role in China's energy transition. Nuclear heating stands out as a key breakthrough point.

1. INTRODUCTION

The "dual carbon goal" is a significant commitment made by China to tackle climate change and promote sustainable development. It refers to achieving peak carbon emissions by 2030 and achieving carbon neutrality by 2060. During the inaugural Nuclear Energy Summit held in March 2024, Chinese Vice Premier Guoqing Zhang emphasized that nuclear power holds unique advantages when it comes to addressing climate change and ensuring energy security. As a clean, efficient, and reliable source of energy with substantial environmental benefits and economic advantages compared to other forms of heating such as coal-fired power plants or gas boilers, nuclear power plays a pivotal role in driving China's energy transition.

2. GLOBAL NUCLEAR HEATING STATUS

2.1. Current Situation of Nuclear Heating Worldwide

There are 59 commercial nuclear power units worldwide generating electricity while producing hot water or steam for heating. Notably distributed across cold Nordic countries where they have been proven safe over approximately 1000 reactor years. Countries like Switzerland, Bulgaria, Czech Republic & Russia have successfully implemented regional projects utilizing nuclear energy for district heating purposes.

^{1*} Guofang Huang, WiN China President, State Power Investment Corporation.

^{2*} Jun Zhou, WiN China member, State Power Investment Corporation.

The two nuclear power units at the Beznau Nuclear Power Station in Switzerland supply heat to 11 surrounding cities through the REFUNA district heating system, serving approximately 20,000 individual, industrial, and agricultural users. Each unit has a peak district heating load of about 80MWt, and its electrical power output is reduced to 10MWe during district heating operations. Currently, Russia operates 11 nuclear power plants with a total of 37 units, seven of which provide heat externally. In May 2020, Russia's first floating nuclear power plant "Akademik Lomonosov" commenced full operation in the Chukotka region, marking the world's inaugural operational floating nuclear power plant and becoming the primary source of electricity and heat energy in that area. The Czech Republic is constructing a 42-kilometer network of heating pipes for the Dukovani nuclear power plant scheduled for commissioning in 2027. The Dukovani Nuclear Power Plant currently houses four VVER-440 units operational from 1985 to 1987. This initiative will assist Brno, the second largest city in the Czech Republic, in reducing its reliance on natural gas by potentially meeting up to half of its heating requirements.

2.2. Current Situation of Nuclear Heating in China

Haiyang Nuclear Power Heating Project of Shandong province stands out as the landmark initiative being the first in China to implement large-scale nuclear steam extraction for district-heating purposes. Its successful completion has resulted in zero emissions attributed to Haiyang Nuclear Power. Additionally, the long-distance nuclear district-heating system spanning 56.7 kilometers between Haiyang & Rushan was put into operation in November 2023, promising a transformation era of nuclear district-heating systems. The design flow is 1370t/h, the heat capacity is 900MWt. After subsequent phases are completed, this extended pipeline network will cover thirty million m² while achieving increased unit thermal efficiency from 36.69% to 55.9%.

CAP1400 is the world's largest third generation passive PWR NPP, it stands for China Advanced Passive nuclear safety design concept, the output power is 1534MWe and each unit's annual power generation reaches 11.4 billion kilowatt-hour. This advanced PWR nuclear power plant not only fills technological gaps within China's nuclear power industry but also promotes overall industry advancement. CAP1400 applies passive system, i.e., under station blackout condition, the reactors can realize safe shutdown automatically without operator's action within 72 hours. The main equipment are designed for 60 year's life and convenient for operation and maintenance. The serious accident probability one hundred times lower than the second generation units, the annual emission of greenhouse gases such as carbon dioxide can be reduced by more than 9 million tons. The initial phase National Nuclear Demonstration Project constructing two CAP1400 units. The feasibility study report indicates that unit provide steam extraction capacities sufficient enough(maximum pumping capacity 800tons/h)for district heating schemes encompassing 13.5 million m² according to Weihai city's future plans.

3. Characteristics and Market Analysis of Nuclear Heating Technology

3.1. Characteristics of nuclear heating technology

Nuclear heating encompasses nuclear cogeneration heating and small reactor heating. Cogeneration heating utilizes steam from the thermal system of a nuclear power plant to heat circulating water in the network, which is then transferred to end users through multiple levels of thermal exchange stations. Small reactor heating employs heat energy released by nuclear fission to warm the primary working medium, which subsequently heats the circulating water in the network. Both processes involve surface heat exchangers for safe and efficient heat transfer without mass transfer or environmental emissions. Characteristics of nuclear heating technology are concluded as below.

Safety: Nuclear heating technology has been proven safe and reliable internationally, utilizing surface heat exchangers with multistage physical isolation.

Economy: The heat price of cogeneration project of nuclear power unit is about 30-40 RMB/GJ, The cost advantage of nuclear heating becomes evident when compared to cogeneration thermal coal prices exceeding 1000 RMB/ton, especially considering potential carbon tax costs and technical improvements.

Stability: With large energy density and minimal reliance on natural conditions, nuclear power offers stable fuel supply for long-term sustainable development. The energy released from the complete fission of 1kg of U-235 exceeds that released by the combustion of 2700 tons of coal. The annual fuel requirements of the mega kilowatt nuclear power plant and the coal power plant are 20-30 tons and 3-4 million tons respectively.

Clean and low-carbon: Nuclear fission releases substantial energy without traditional energy carbon involvement or harmful gas emissions.

3.2. Spatial analysis of the Nuclear Heating market for the "15th Five-Year Plan"

Currently dominated by coal-fired central heating, China's northern cities face significant pollution challenges due to high carbon emissions(CO₂/SO₂/NO_x)and air pollution from coal combustion. District heating presents comprehensive benefits such as energy conservation, environmental improvement, and enhanced quality but requires clean alternatives to replace coal.

China encourages district-based central heating where feasible due to its comprehensive benefits including improved air quality control and enhanced energy utilization rates. In line with China's "dual carbon" target, finding clean alternative energies is crucial; thus, nuclear-based solutions are expected to play a pivotal role in future clean-energy developments.

By the end of 2023, northern China's total heated area reached 24.5 billion m² (17.5 billion urban & 7 billion rural). Considering negative population growth since 2022. It is conservatively estimated that urban heated areas after 2025 will be based on town sizes of 2025. Operational projects have introduced a capacity for providing nuclear-based district-heating covering an area of approximately 160 million m² With ongoing construction projects coming online, it is anticipated that by 2030 this capacity will increase up to about 320 million m². Considering city-specific circumstances around these plants along with feasibility studies into alternative options. As illustrated in Figure 1, it is projected that China's overall nuclear-heated area could reach approximately 150 million and 1.5 billion m² by 2030 and 2060 respectively.

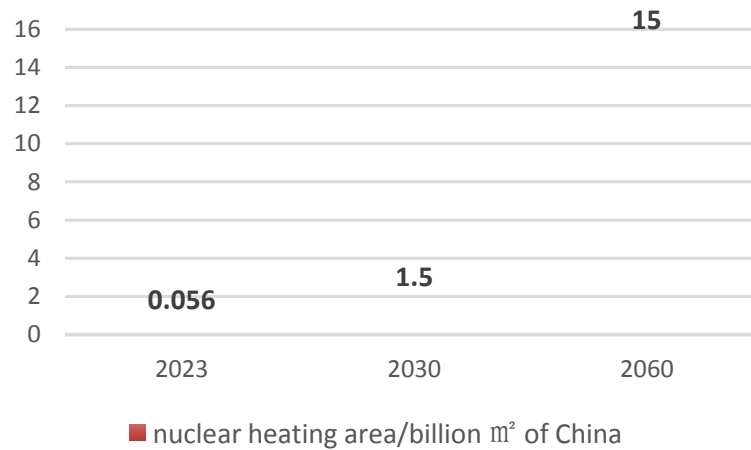


Figure 1. Nuclear Heating Area Prediction of China

4. Development Trend of Nuclear Heating Technology

The development of nuclear heating technology involves two major aspects: the heat source side and the heat network side. Currently, there are two main methods of nuclear heating on the heat source side worldwide, namely combined heat and power generation, and small nuclear reactor heating. On the heat network side, technologies mainly focus on large temperature difference and long-distance heating, both of which have been demonstrated and applied.

4.1. Nuclear Power Units Cogeneration

At a nuclear power plant, steam from the steam turbine generator set is extracted to heat the circulating water in the heat network. The first heating station is established within the nuclear power plant, where high-temperature circulating water is transported to an external thermal company's heat exchange station to transfer nuclear energy into an external heating system. In this process, the two-circuit system serves as the heat source while the long-distance heat transmission network functions as a three-circuit system; meanwhile, on the user end for heating purposes generally operates with four or five circuits within their own systems.

4.2. Small Reactor Heating

Currently there are two mainstream types for small reactor heating technology in China's: pool-type heating reactors and shell-type heating reactors.

① Shell-Type Nuclear Heating Reactor: Tsinghua University initiated research and development of low-temperature nuclear heating reactor technology in 1980s which has been continuously invested for over 30 years. From 1991 to 1995, Tsinghua University's Nuclear Research Institute completed research on a commercial NHR200-I reactor with a capacity of 200MWt; further research was conducted on comprehensive utilization technologies such as cogeneration and nuclear desalination of seawater. Tsinghua University has further developed NHR200-II low temperature nuclear heating reactor with higher operating parameters, improved the design

parameters, and has the ability to provide saturated steam, which can be used for nuclear heating, industrial steam, steam, combined heat and power supply, seawater desalination, etc.

Haiyang Nuclear Power Plant of SPIC plans to build an integrated heating reactor with a thermal power of 200 MWt and a maximum steam supply capacity of 205 t/h. It is mainly to supply industrial steam to external sources. At the same time, it will carry out the thermal demonstration, and serve as a backup heat source for Haiyang heating in winter. Haiyang integrated heating reactor adopts the full natural cycle design, at the same time, the regulator, one and two loop heat exchange components and control rod drive mechanism are built into the reactor pressure vessel, the reactor pressure vessel is placed in the small containment, the whole small containment is immersed in the reactor pool.

② Pool-Type Nuclear Heating Reactor: In November 2017, CNNC completed the demonstration of nuclear heating for 49-2 reactors, and officially released the model scheme of "Yanlong" swimming pool type low temperature heating reactor. The designed thermal power of "Yanlong" reactor is 400MW, and the heating area can be 10 million to 20 million m². Pool nuclear heating reactor's main advantage is running under atmospheric pressure and low temperature, with the characteristic of inherent security, high reliability, mature technology, simple system, stable operation, small area, more suitable for close to urban residential areas. Take a 400MW pool low-temperature heating reactor as an example, which can replace 320,000 tons of coal or 160 million m³ per year of natural gas, can reduce carbon dioxide 640,000 tons, sulfur dioxide 5000 tons per year, which has significant environmental benefits.

4.3. Large temperature difference and long distance heating technology

China's NPPs are mainly distributed in coastal areas, and are faced with the problems of distance heating and high cost. Nuclear energy heating distance often reaches more than 100 kilometers, and using conventional heating parameters and system processes is no longer economical. The large temperature difference and long distance heating technology proposed by Tsinghua University provides a solution. This technology has been applied in the long distance heating project of Taiyuan Gujiao Power Plant, and has achieved good economic benefits, and its heating cost can be equal to the cost of coal heating.

The large temperature difference and long distance heating system is a two-pipe system, and the circulation medium is the softening water. Due to the long heating distance, return water temperature need to be reduced as low as possible. The system adopts three heat network, two levels of cooling mode, as illustrated in Figure 2, through the terminal temperature difference, greatly reduce the heat network water temperature to about 15°C, back to the plant after heating to 125°C, heating temperature difference of 110°C, compared with the conventional heating system, can greatly improve the heat network transmission capacity to more than 80%.

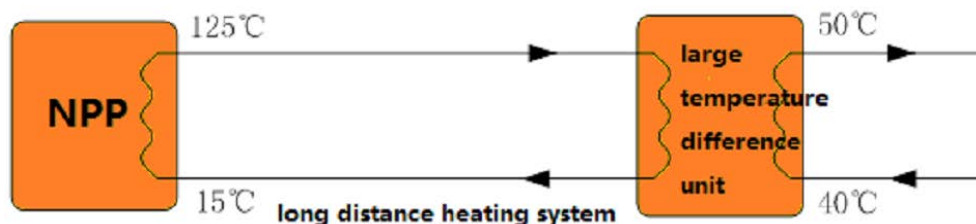


Figure 2. The large temperature difference and long distance heating system graphic

5. CONCLUSIONS

Nuclear heating represents the most crucial way for the comprehensive utilization of nuclear energy in China, offering significant market potential in light of “dual carbon” goal. Characterized by cleanliness, low-carbon emissions, safety, and reliability, nuclear heating has undergone preliminary economic validation. It currently stands as a rare and relatively mature alternative to fossil fuels and serves as a means to fulfill large-scale central heating demands, plays a pivotal role in driving China’s energy transition. The successful implementation of Haiyang Nuclear Power Plant has enabled cross-regional long-distance nuclear heating across a vast area, with a coverage area spanning 13 million m². Projections indicate that by 2030 and 2060, China's nuclear heating coverage will expand to encompass 150 million and 1.5 billion m² respectively. Breakthroughs are anticipated in SMR technology for localized heating applications as well as long large temperature difference and long distance heating technology—offering valuable insights for global efforts in comprehensively utilizing and development of nuclear energy.

REFERENCES

1. China Nuclear Energy Industry Association, China Nuclear Energy Development Report, Social Sciences Academic Press, BeiJing, China(2023)

Social and Environmental Justice: Pillars of the Energy Transition

Ambar Gissel Robles Nuñez

Comisión Federal de Electricidad

ambar.robles@cfe.mx

Abstract

Throughout its existence, humanity has faced various energy transitions driven by changes in paradigms of generation and consumption. In the 19th century, the use of internal combustion engines and the shift from a local to a global economy led to the industrialization of the primary sector. The current energy transition arises from the need to decarbonize the energy sector through an orderly and planned shift in electricity generation, moving from conventional sources to clean, sustainable energy.

The energy transition is a commitment made by Mexico; it is part of the 2030 Agenda, which is aligned with the fulfillment of the 17 Sustainable Development Goals. Among which are "End Poverty", "Quality Education", "Gender Equality", "Affordable and Clean Energy" and "Reduction of inequalities", all these objectives are transversal to each other, that is, to achieve an end to poverty we must ensure that electricity is affordable and universal, and at the same time establish policies and programs that favor the education of girls and women, historically marginalized. By improving women's educational level, they will be able to access more and better jobs. By having paid jobs, they will have economic independence, which will allow them to access political and social power, if they so wish.

The electric service has two ways of affecting girls and women, the first is through lighting. The perception of security of a woman who lives in a house with light is greater than another who lacks it, in addition, public lighting causes gender violence to decrease (OXFAM, 2024).

The second way is by generating jobs with a gender perspective; this fact alone allows women to access different types of power, but it also implies a paradigm shift with gender roles, respect for children's rights that allow them to have well-being and complete training in STEM areas that few women still achieve.

The triple planetary crisis, caused by climate change, call on decision-makers to include the nuclear energy as the base load for electricity generation, accompanying by energies such as geothermal, hydroelectric, and wind power.

This article aims to raise two of the pillars of the energy transition through a new model of electricity generation transversal to gender equity policies, Mexico's economic growth, and the achievement of climate goals.

1. INTRODUCTION

The fulfilment of the 2030 Agenda for Sustainable Development: a plan of action for people, the planet, prosperity, and universal peace; encompasses the 17 Sustainable Development Goals (SDGs). Goal 7, which focuses on access to affordable and clean energy, is one of the precursors to the new idea of changing how electricity has been generated and incorporate principles that ensure social and environmental justice.

Access to safe and continuous energy greatly influences the possibilities for human development and economic development. The neoliberal economic model continues to promote consumerism, creating technologies with scheduled lifespans, single-use plastics and clothing, electric vehicles, smart TVs, etc., which increase energy demand. Although this economic model does not align at all with the SDGs, it is essential to provide electricity service to all populations, prioritizing those that, due to their geographical conditions, have not been provided with service.

According to the first National Survey on Energy Consumption in Private Homes (ENCEVI), 99% of inhabited homes in Mexico has electricity (INEGI, 2018). This means that there are 1.3 million inhabited homes in our country without electrical service. In other words, these homes lack lighting, household appliances, heating... etc. Putting them in a highly vulnerable position for adapting to the effects of climate change (frost, droughts, extreme temperatures, hurricanes, torrential rains, among others).

It is important to note that many of these homes without electricity are in the five states with the highest percentage of the population living in poverty in our country: Chiapas with 67.4%, Guerrero with 60.4%, Oaxaca with 58.4%, Puebla with 54%, and Tlaxcala with 52.5% (CONEVAL, 2023). Poverty, according to the general guidelines and criteria for defining, identifying, and measuring poverty, refers to people who experience at least one deprivation in their social rights and have a monthly income per person that is insufficient to acquire a basic food basket, as well as other goods and services. In 2022, 36 out of 100 people were living in poverty, meaning that 46.75 million people are unable to afford services like electricity.

Despite efforts to electrify all country and make it affordable for everyone, there are still populations without service or who cannot afford it; the absence of electricity and/or unequal access changes the opportunities available for girls, boys, women, and men in areas such as health,

education, security, jobs, mobility, hours of productivity, and more. Therefore, this new energy transition must achieve the following objectives:

- Fulfill the SDGs.
- Achieve climate goals (financing, reducing greenhouse gas emissions, strengthening resilience, and decreasing vulnerability).
- Ensure a stable and affordable energy supply.
- Universal access to energy.
- Enable robust economic growth.

To achieve the goals of a just energy transition, it is essential to include a gender perspective (defence of personal liberties) as a principle in work plans that allow women to escape multidimensional poverty, which already poses a risk to their lives. Unfortunately, another social factor that contributes to poverty must also be addressed: gender violence.

The National Electricity System (NES) is responsible for generating, transmitting, distributing, and commercializing electricity throughout Mexico, but as highlighted in this brief introduction, millions of people still lack access to this service. Among these people, almost all are women who do not have basic services in their homes, such as lighting.

Lighting helps people feel safer and has benefits that go beyond security. The lack of lighting makes people feel unsafe, especially when they arrive at a new place for the first time.

Lighting changes the way women inhabit public spaces. A well-lit area creates a greater sense of security. Lighting can:

- Reduce the risk of gender violence and other threats to personal safety;
- Improve the ability to avoid physical dangers at night;
- Ensure safe and dignified access to basic services; and
- Support family and community relationships and contribute to the effectiveness of police and emergency services (OXFAM, 2024).

2. 1st PILLAR. GENDER PERSPECTIVE

The first step in proposing an energy model that counters the effects of the planetary crisis with a gender perspective is to apply human rights to girls and women, recognizing the clear differences (caregiving, motherhood, exclusion from all sectors, vulnerability due to being single mothers, divorced, etc.) between men and women.

The differences between women and men go beyond physical traits; they relate how they participate in social structures. Gender roles, often reinforced in family settings and schools from a young age, shape beliefs through workshops, sports, and extracurricular activities. For example, women are often directed towards sewing, volleyball, and arts, while men are offered options like electrical work, carpentry, soccer, and basketball. Although these distinctions do not outright prohibit individuals from joining groups that do not align with their gender, they often lead to bullying, discrimination, and questioning of one's sexuality if they do not conform to patriarchal norms. Therefore, it is essential to deconstruct the states and social institutions that have historically given power (a legacy of patriarchy, created by men and for men) solely to men, not based on meritocracy, but on an imposed expectation of strength and provision.

As part of a just energy transition, it must reduce inequality between women and men (SDGs 5 and 10). To achieve this, there must be a shift in power from men to women. This transition can be accomplished if, from childhood, girls' rights are applied in the same way as boys' rights, ensuring equal access to education, health, life, identity, and family living, as outlined in Article 13 of the General Law on the Rights of Children and Adolescents. If boys and girls are educated in non-sexist environments, the differential treatment between them will diminish, and it will be possible to reduce the teachings that program women to be the sole caregivers, house administrators, fit only for certain professions, behaviours, places deemed appropriate for women, and even the level of education allowed by families.

As a result of neglect by civil society and the state, female childhoods in Mexico experience multiple adverse conditions that hinder their full development due to discrimination, prejudice, biases, and gender norms. These inequalities are reflected in professional, labour, and occupational spheres. For example, women are underrepresented in science, technology, engineering, and mathematics (STEM). Only 3 out of 10 women choose a STEM-related career (IMCO, 2022), and just 29.8% of engineering, manufacturing, and construction enrolments are women (INEGI, 2021). Furthermore, only 6% of global leadership positions in the technology sector are held by women (UNESCO, 2019).

In Mexico, the rate of economically inactive women is 71.8%, compared to 28.1% for men, making it one of the lowest among OECD countries (INEGI, ENOE, 2024). Additionally, of the 4.4 million people aged 15 and older who are illiterate, nearly 66% are women (2.9 million). This leaves women vulnerable in the labour market, with wage gaps that reach up to 35% (INEGI, Literacy Status, 2020).

Gender equity remains one of the greatest challenges in human rights and is far from being achieved, largely due to the alarming lack of funding for measures aimed at this goal. This lack of funding represents a global annual deficit of \$360 million for initiatives aimed at achieving gender equality. Additionally, 75% of countries are expected to implement public spending cuts by 2025 (UN Women, 2022), attributed to conflicts and rising fuel and food prices. Reducing investment in essential services, care policies, and social protection would significantly affect women.

On average, the next generation of women will spend 2.3 more hours per day on unpaid domestic and care work than men (UN Women, 2022). In Mexico, this translates to a gap of over 12 hours per week that women devote to these tasks compared to men. Studies show that closing gender employment gaps could increase per capita GDP by 20% in all regions of the world. In Mexico, one concrete example is the promotion of Comprehensive Care Systems, which, in addition to freeing up time for women by reducing work burdens, stimulate job creation and generate returns on investment.

A new transversal Mexican energy model is essential, one that aligns with other state secretariats to strengthen and create more educational institutions, mentoring programs in STEM fields, a safe childcare system, and companies that guarantee gender-responsive jobs. This means considering the hours dedicated to home care, gestation and lactation periods, and socio-cultural backgrounds (respecting traditions, clothing, oral language) without these factors being reasons to avoid hiring or promoting a woman. Additionally, work must be done to create a justice system that prevents impunity in cases of femicide and gender-based violence, ensuring the safety of women regardless of the decisions they make about their bodies, education, work, civil status, romantic relationships, and any other.

An energy matrix that fulfils a just energy transition must empower women by giving them the same opportunities to access economic, political, and social power as men, thereby beginning to build a world with equal rights and gender equity.

3. 2nd PILLAR. ENVIRONMENTAL

The rising global temperature has rooted in several factors. The first is the loss of natural water bodies (rivers, lakes, lagoons, glaciers, seas, etc.); the second is changes in the composition of the troposphere due the increase of the concentration of O₃ and greenhouse gases (CO₂, CH₄, N₂O, fluorinated gases like HFCs, SF₆, and NF₃) [GHG]; and finally, for the loss of forest cover.

Before the Industrial Revolution, mobility relied on animals and electricity generation was powered by water and windmills. However, the invention of the steam engine (1769) brought drastic changes in the way goods and services were consumed and produced. One of the most significant changes was the industrialization of electricity, a sector that over several centuries, has accumulated tons of CO₂ equivalents in the world, causing deaths because of respiratory diseases and the climate change.

The electricity sector is not the only contributor to this phenomenon, but it is one of the largest contributors to the factors driving global warming. This is due to use of water in power plants to

produce steam and for cooling systems, the generation of GHG emissions from burning fossil fuels, and land-use changes for the construction of reservoirs for hydroelectric plants or concrete slabs for the installation of equipment such as substations, aeroderivative turbines, solar panels, and more.

Deforestation is not usually associated with electricity generation. However, all conventional and renewable power plants require an exemption permit (Article 117 of the General Law on Sustainable Forestry Development) to remove forest vegetation. This authorization is conditioned on a series of activities to minimize negative environmental impacts and requires an economic contribution to the Mexican Forestry Fund. Unfortunately, these resources are rarely delivered due to the lack of reforestation projects in communities affected by desertification. To put the impact of the electricity industry on forest land loss into perspective, the Puerto Peñasco Photovoltaic Plant covers 2,000 hectares, from which forest vegetation was removed, wildlife was displaced, and the soil was compacted for site levelling (CFE, 2024).

Centuries of fossil fuel combustion, exploitation of water bodies and biotic elements, meteorological phenomena, seasonal changes, etc., have led civil society and the scientific community to change their relationship with the natural environment. This gave rise to environmental sciences, which began to permeate planning instruments, laws, and knowledge so that primary sector activities would no longer degrade the ecological balance. One of the first paradigms to shift was the notion that "pollution is global, not local." This phrase had such an impact that it led to the first international environmental meetings to agree on global action to prevent an environmental catastrophe that would affect human quality of life and economic growth.

Many years have passed since the 1st Earth Summit (1972), since which they have been celebrated countless conventions, agreements, treaties, and protocols have been held with the aim of conserving, preserving, and reversing the effects of anthropogenic activities unleashed by the Industrial Revolution, the Information Age, and now, Artificial Intelligence. Despite all the voices raised in response to the planet's deterioration, world economies continue to allocate financial resources to flora, fauna, and biotic and abiotic elements to determine the growth of each country's Gross Domestic Product (GDP).

Today, by the clear disinterest of politicians and leaders in changing the globalized economic model, the Earth is facing a triple planetary crisis.

3.1. Climate Crisis

The climate crisis encompasses the effects of thermal inversion phenomena, the greenhouse effect, and the increase global temperature, causing changes on the biogeochemical and meteorological cycles. These effects place people in specific locations at risk due to their geographical and economic characteristics.

The impacts of climate change on the planet have become one of the main reasons why millions of people around the world migrate to less affected areas within their own country or choose to emigrate to other countries (UNAM, 2024). For example, El Bosque, a community in the municipality of Centla, Tabasco, has been swallowed by the sea, which has taken away dozens of houses and schools. Essentially the entire territory that was home to approximately 200 people from 60 families.

Hurricane OTIS, which made landfall on Mexico's Pacific coast in 2023, affected 848,647 people in Acapulco and 79,605 in Coyuca de Benítez, according to the latest report from the United Nations (UN).

3.2. Hydric Crisis

The United Nations considers that when water is scarce, contaminated, or when people have unequal or no access to this vital resource, tensions between communities and countries can increase.

Water and wealth are closely linked. Wealthier people not only have better access to safe and public water, but they can also afford to pay for expensive water from private sources. In contrast, those living in poverty, who often do not have access to government-supplied water, must allocate a significant portion of their income to purchasing water (OXFAM, 2024).

Changes in the chemical and biochemical oxygen demand, as well as the temperature of rivers and seas—major regulators of the planet's temperature—affect the water cycle. This cycle enables the recharge of aquifers, the birth of runoff, and the preservation of primary producers, which are responsible for photosynthesis and, consequently, the formation of the atmosphere that allows life as we know it.

3.3. Loss of Biodiversity

This crisis is driven by the two previous factors—climate change and water scarcity—along with the excessive exploitation of ecosystems and land-use changes in forested areas. The loss of biodiversity leads to the decline of species, particularly flora, which we rely on for essential processes such as nutrient fixation in the soil through the phosphorus and nitrogen cycles.

Conventional power plants discharge water into natural bodies of water at higher temperatures than when it was initially drawn, causing disruptions in the reproductive cycles of certain fish species that are sensitive to temperature changes.

Some renewable energy sources, such as solar and wind, also affect the population size of certain species of flying fauna and reptiles. Several experts worldwide have called for the removal of wind turbines due to their impact on the decline of migratory birds, such as Canadian ducks and bats. Solar panels covering large desert areas prevent reptiles from thermoregulating, a vital function that allows them to maintain an appropriate body temperature without entering a state of torpor.

4. ENERGY MIX FOR ACHIEVING THE ENERGY TRANSITION GOALS

After addressing some aspects of social justice that the energy transition should accommodate, it becomes relatively straightforward to describe the technologies that should be used in Mexico to achieve climate goals, align with the SDGs, and ensure an affordable and stable electricity system.

Currently, Mexico's energy mix consists of a base load of fossil fuels, generating 29,764 MW through natural gas, diesel, and coal (Figure 1). Additionally, 12,357 MW of installed renewable energy capacity is generated primarily by hydroelectric plants. Nuclear energy, classified as clean energy under the Electricity Industry Law, contributes 1,608 MW (Figure 1).

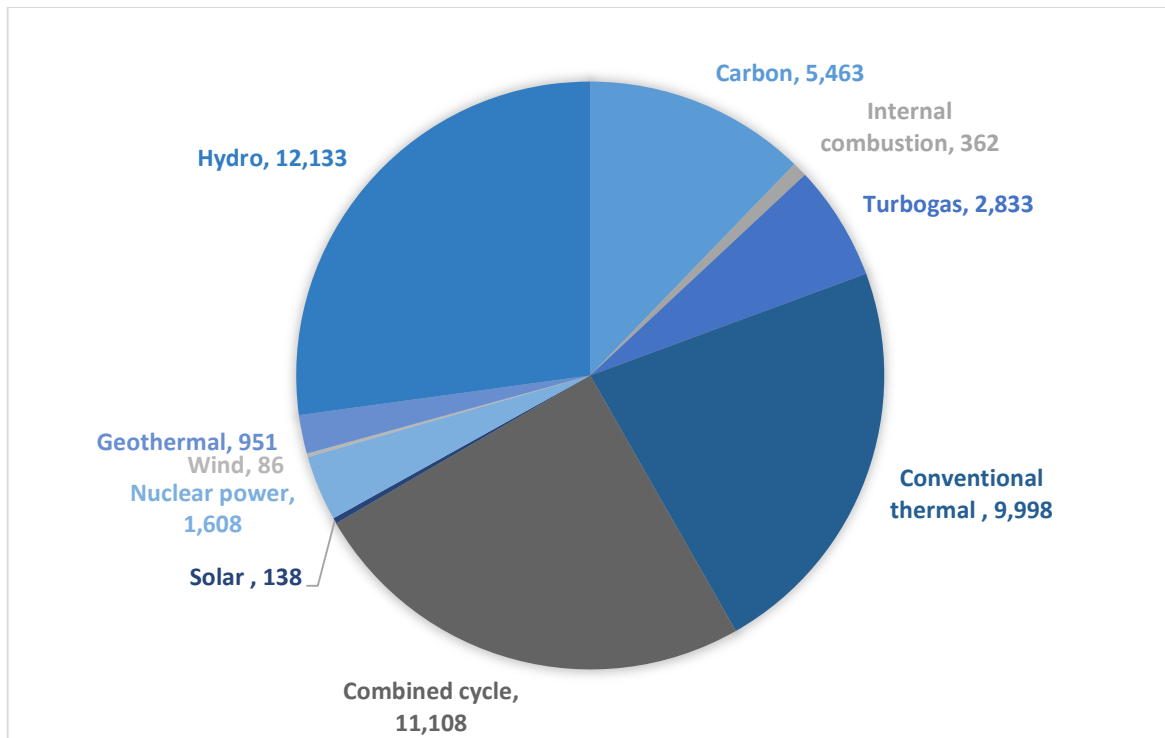
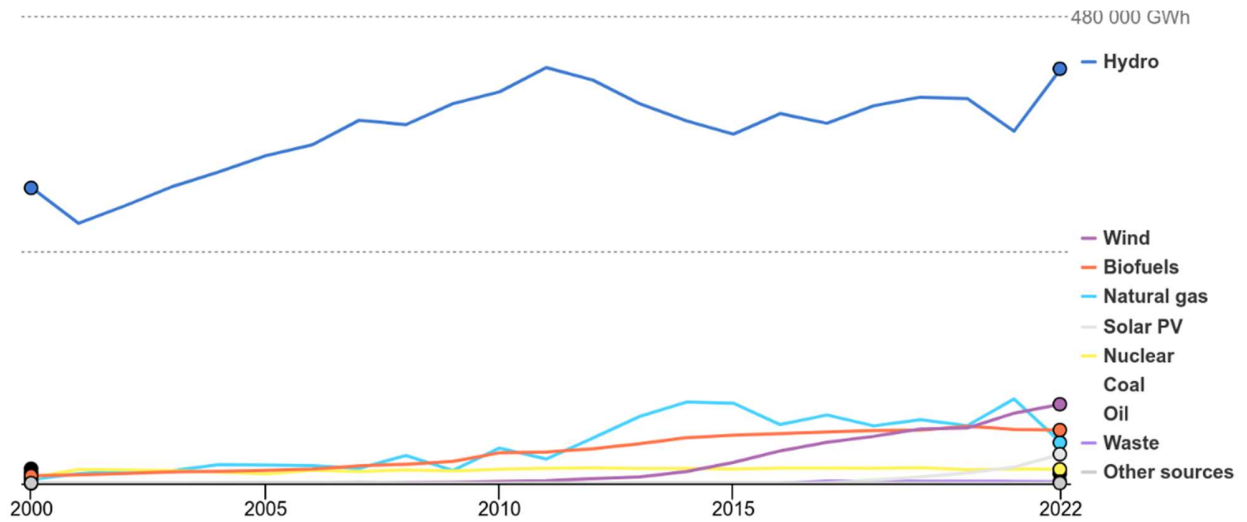


Figure 1 Installed capacity of Federal Electricity Commission (CFE by its acronym in Spanish) as of December 31, 2023 (MW) (SENER S. d., 2018)

The carbon dioxide (CO₂) intensity is a representation of the GHG footprint of 1 kWh consumed within a specific area. This footprint is measured in grams of CO₂ equivalent (gCO₂-eq) and accounts for each GHG, converting them to their CO₂ equivalent in terms of global warming potential over 100 years (e.g., 1 gram of methane emitted has the same impact on global warming over 100 years as ~34 grams of CO₂ during the same period).

In terms of CO₂ intensity, Brazil is the only country in Latin America with low CO₂ intensity, mainly due to the increase in its installed capacity of hydroelectric plants between 2001 and 2015, rising from 267,876 GWh to 359,743 GWh. By 2022, Brazil achieved 63% hydroelectric generation. Although the use of nuclear energy has remained stable, without any increase since 2000, Brazil still has 14,599 GWh of installed capacity. The rest of the technologies have seen little growth; however, gas and biofuel have been the fuels with the most significant growth prospects (Figure 2).



Source: International Energy Agency. Licence: CC BY 4.0

Figure 2. Evolution of the electric power generation in Brazil since 2000

Globally, the regions and in some cases countries with the lowest greenhouse gas emissions base their electricity generation on nuclear energy (France) and hydropower (Sweden, Iceland, Norway, and Quebec), as shown in Table 1. Additionally, when it comes to renewable energy use, wind power plants generally have a larger share compared to solar plants. It is also important to note the significant contribution of geothermal energy to Iceland's energy matrix.

Table I CO₂ Intensity and Emission Factors by Regions of the World

Zone	CO ₂ Intensity	Hydro (%)	Nuclear (%)	Wind (%)	Solar (%)	Geothermal (%)	Biomass (%)	Gas (%)	Coal (%)
France	22	14.2	65.3	9.5	6.3	0	1.3	1.4	0
Sweden	25	44	29.8	18.7	2.4	0	0.2	0.1	0.3
Iceland	28	69.8	0	0	0	30.2	0	0	0
Norway	33	83.3	1.4	11.1	1.1	0	0.4	1.4	0.1
Quebec	36	86.8	2	6.6	0	0	3.3	1.2	0
Brazil	72	68.4	2.4	12.9	9.3	0	0	0	0

Despite not committing to the goal of achieving net-zero GHG emissions by 2030, Mexico pledged in 2022 to increase its Nationally Determined Contributions (NDCs) under the Paris Agreement from 22% to 35% by 2030. Additionally, Mexico reaffirmed its goal to reduce black carbon emissions by 51% unconditionally by 2030 and by 70% conditionally.

A 35% reduction in emissions by 2030 would prevent 347 MtCO_{2e} in that year, while fulfilling the conditional commitments would raise this to 397 MtCO_{2e}. The NDC implementation period spans from 2020 to 2030 and considers policies implemented since 2013 following the publication of Mexico's General Climate Change Law. This target would help reduce emission intensity per unit of GDP by around 40% between 2013 and 2030 (INECC, Nationally Determined Contribution, 2022).

Nuclear energy is a low-carbon energy source. In 2018, it produced about 10% of the world's electricity. Along with increasingly numerous renewable energy sources and the shift from coal to gas as a fuel, the increase in nuclear energy production helped stabilize global CO₂ emissions at 33 GtCO_{2e} in 2019 (IAEA, 2023).

If Mexico increases its installed capacity of nuclear energy as a baseload and combines it with renewable energies in the same proportion as shown in PRODESEN by 2030. Fossil fuels could be left out; in this way, there is a first option for GHG reduction, as shown in the following Figure 3.

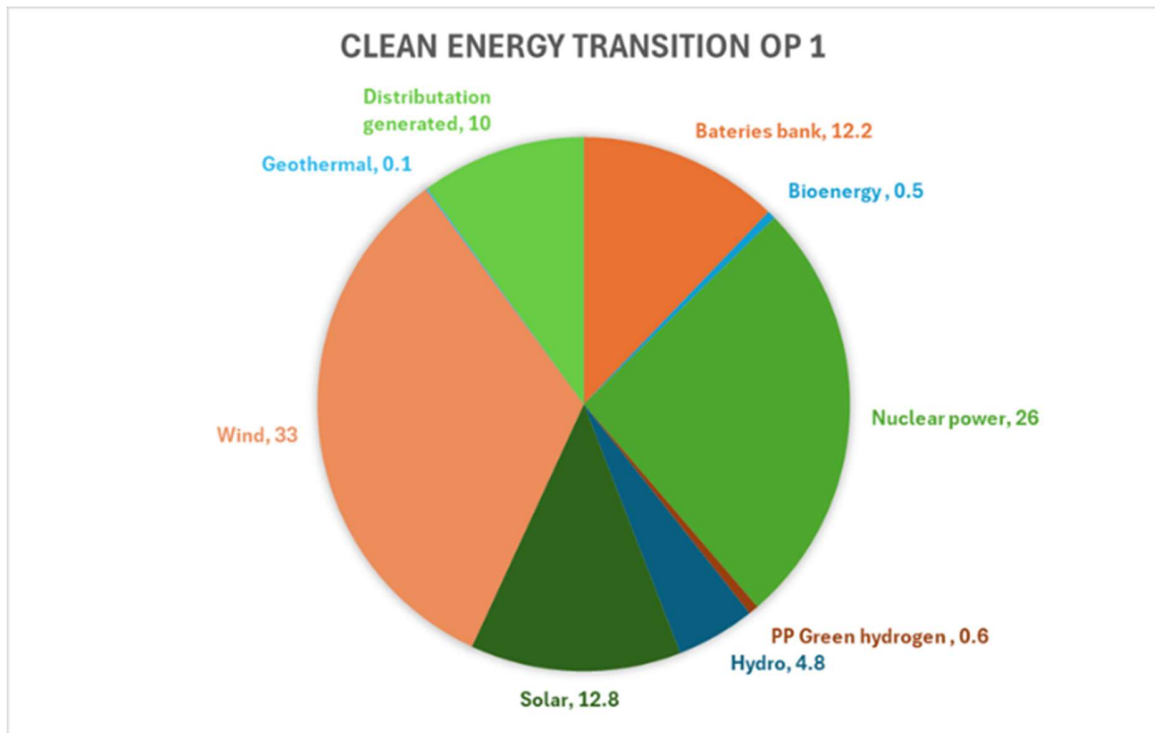


Figure 3 Clean energy transition, option 1

If hydropower plants will be considered as the baseload of the NES, as a Brazil, and the rest of the clean technologies as indicated in the same program of the same year, then the energy matrix would be as follows (Figure 4).

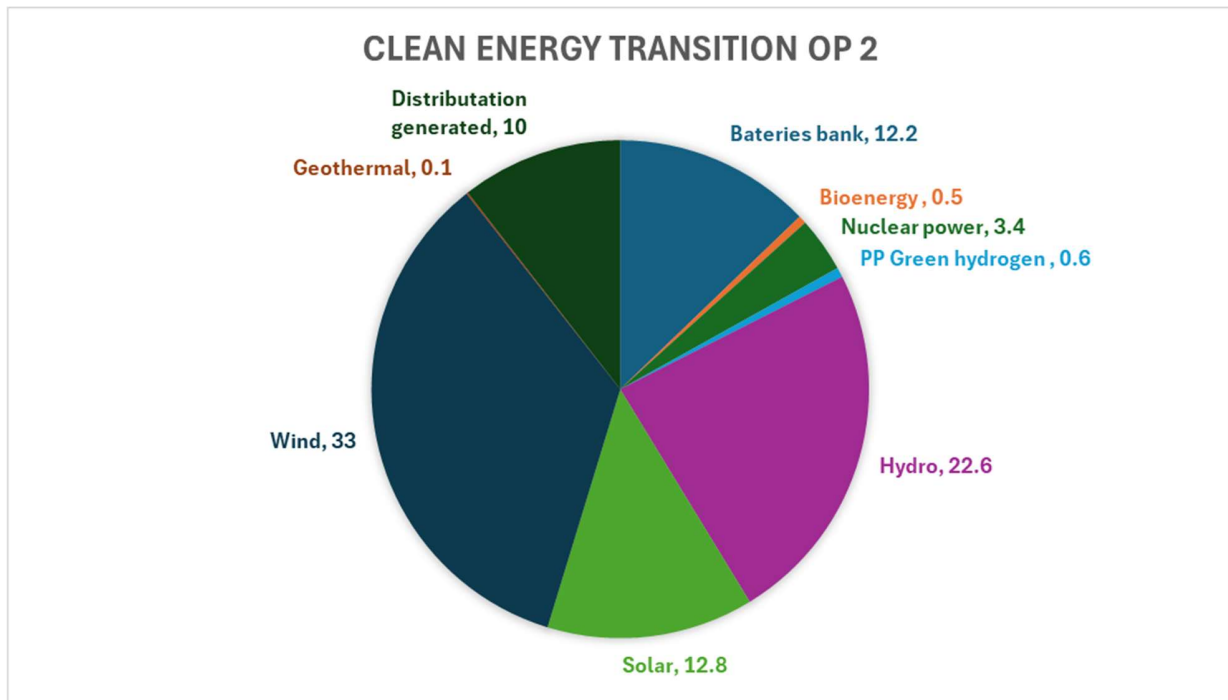


Figure 4 Clean energy transition, option 2

Nuclear energy can play a key role for Mexico in transitioning to a clean energy future and, consequently, in meeting the 35% emission reduction target. In addition to reducing GHG emissions, nuclear energy contributes to other mitigation components considered in Mexico's NDC, such as:

- **Reducing land use in forest areas.** According to the national emissions inventory, absorption from the permanence of forest lands, grasslands, and agricultural lands was -172,997.6 GgCO₂e, making forest soil conservation a key component for carbon sequestration (INECC, 2015).
- **Electricity generation.** The electricity sector reports emissions of CO₂, CH₄, and N₂O from fossil fuel use in power plants operated by CFE and Independent Power Producers. In 2013, this sector contributed 126,607.66 GgCO₂e, which accounts for 19% of the total emissions in the national inventory (INECC, 2015).

According to the National Electricity System Development Program 2018-2032 (PRODESEN), nuclear energy capacity is projected to triple between 2029 and 2031, adding 1,360 MW each year. Increasing this technology in the energy matrix would ensure

Mexico's contribution to slowing global temperature rise and reducing the effects of climate change on vulnerable areas in the country.

- **Industry.** If Mexico's electricity industry charts a decarbonization route for the National Electricity System (NES) by using nuclear energy as a base load alongside hydroelectric and geothermal plants, it could help reduce the 220 MtCO₂ emitted globally in 2022. Electricity generation accounts for more than 90% of global emissions (IEA, 2023).
- **Oil and gas.** One of the emission sources accounted for in Mexico is fugitive emissions from gas, mining, and oil extraction, although these represent only 6% of the 638 MtCO₂e of GHGs in the 2015 national inventory. By using radioactive material for electricity generation, this source of GHGs could be mitigated.

5. CONCLUSIONS

Nuclear energy can play a key role for Mexico in transitioning to clean energy future and, consequently, in meeting the 35% emission reduction target. In addition to reducing GHG emissions, nuclear energy contributes to other mitigation components considered in Mexico's NDC, such as:

- Reducing land use in forest areas.
- Electricity generation.
- Industry.
- Oil and gas.

The use of nuclear energy for electricity generation is fundamental to ensuring service continuity, stability system, low-cost tariffs, universal access, the country's economic growth, decrease the effect of the climate change over the global temperature.

The transition to low-emission electricity generation technologies presents an opportunity for Mexico to reduce its reliance on gas purchases for the operation of combined-cycle plants.

The nuclear sciences represent opportunities for the women, represent for the effort of organizations as Woman in Nuclear (WiN), International Youth Nuclear Congress (IYNC), North American Young Generation in Nuclear (NAYGN), Nuclear for Climate (N4C) and the internships and scholarship programs offered by IAEA like Mire Sklodowska- Curie and Lise Meitner.

The increase in women's participation in STEM areas is determined by the respect and application of non-discriminatory laws and a Government and its Institutions that eliminate gender roles.

Even though STEM areas are dominated by men, the CFE makes efforts to reduce the gender gap in the electricity sector, which is why it created the Gender and Inclusion Unit. Who has carried out different strategies to make the work of women workers visible, empower them, recognize them, provide spaces to exercise motherhood, in addition to guaranteeing that they carry out their activities in workspaces free of violence.

We are not only facing an environmental crisis but also a political and financial crisis that continues to fail to prioritize the climate crisis, despite it being an existential threat.

6. REFERENCES

CFE. (2024). *El futuro de la energía solar. Desafíos de la red de transmisión de la CFV Puerto Peñasco*. Mexico: Comisión Federal de Electricidad.

CONEVAL. (2023, Agosto 10). pp. 1-10.

CONEVAL. (2024, Julio 02). Retrieved from <https://www.coneval.org.mx/Medicion/Paginas/Mujeres.aspx#:~:text=47.2%20millones%20de%20mexicanos%20viven,pero%20tiene%20un%20ingreso%20bajo>.

IAE. (2023, julio 11). *IEA*. Retrieved from <https://www.iea.org/energy-system/electricity>

IMCO. (2022). *Programa de las Naciones Unidas para el Desarrollo*. Retrieved from <https://www.undp.org/es/mexico/proyectos/redes-ctim>

INECC. (2015). Retrieved from <https://www.gob.mx/inecc/acciones-y-programas/inventario-nacional-de-emisiones-de-gases-y-compuestos-de-efecto-invernadero>

INECC. (2022). *Contribución Determinada a nivel Nacional*. México: SEMARNAT.

INEGI. (2018, Noviembre 7). pp. 1, 2.

INEGI. (2020). *Condición de Alfabetismo*. Retrieved from https://www.inegi.org.mx/app/tabulados/interactivos/?pxq=Educacion_Educacion_02_fa5c35ea-9385-41f0-86df-bf2bbfc929e3&idrt=15&opc=t

INEGI. (2021). Retrieved from <https://www.undp.org/es/mexico/proyectos/redes-ctim>

- INEGI. (2024). *ENOE*. Retrieved from Encuesta Nacional de Ocupación y Empleo:
https://www.inegi.org.mx/sistemas/olap/consulta/general_ver4/MDXQueryDatos_Colores.asp?proy=enoe_pe_ed15_pnea
- Mundial, P. (2024, Julio 02). Retrieved from <https://www.pactomundial.org/ods/5-igualdad-de-genero/>
- OIEA. (2023). *IAEA*. Retrieved from <https://www.iaea.org/es/temas/energia-nucleoelectrica-y-cambio-climatico-descarbonizacion#ftn1>
- ONU, M. (2019, Diciembre 30). *Programa Segunda Oportunidad*. Retrieved from <https://mexico.unwomen.org/es/noticias-y-eventos/articulos/2019/12/segunda-oportunidad>
- ONU, M. I. (2022). *Plan Estratégico*. Retrieved from Un Women Strategic Plan:
<https://www.unwomen.org/sites/default/files/2022-10/UN-Women-Strategic-Plan-2022-2025-brochure-es.pdf>
- OXFAM. (2024, Marzo 21). Retrieved from <https://www.oxfam.org/es/notas-prensa/crisis-mundial-de-agua-pesar-de-la-amenaza-tan-solo-una-de-cada-cuatro-de-las-mayores#:~:text=Seg%C3%BAn%20las%20Naciones%20Unidas%2C%202000,menos%20un%20mes%20al%20a%C3%B1o.>
- OXFAM. (2024, julio 03). Retrieved from <https://oxfamilibrary.openrepository.com/bitstream/handle/10546/621101/gd-lighting-gender-safety-emergencias-public-171120-es.pdf;jsessionid=DC36B4055797D0DC3203BF0CE4ABAFDF?sequence=5>
- SENER. (2024). *CENACE*. Retrieved from PRODESEN Infraestructura del Sistema Eléctrico Nacional:
https://www.cenace.gob.mx/Docs/16_MARCOREGULATORIO/Prodecen//19%202024-2038%20Anexos.pdf
- SENER, S. d. (2018, 10 12). *Gobierno de México*. Retrieved from https://base.energia.gob.mx/prodesen/PRODESEN2018/RESUMEN_EJECUTIVO_PRODESEN_2018-2032.pdf
- UNAM. (2024, junio 24). *Gaceta UNAM*. Retrieved from Gaceta UNAM:
<https://www.gaceta.unam.mx/desplazados-climaticos-en-aumento-advierte-la-onu/>
- UNESCO. (2019). *PNUD*. Retrieved from <https://www.undp.org/es/mexico/proyectos/redes-ctim>

Implementation of the DWSIM process simulator for thermodynamic analysis of supercritical N₂ Brayton cycle for advanced nuclear power plants

Luis Carlos Juárez Martínez

Universidad Autónoma de Chihuahua

Circuito Universitario S/N, Campus UACH II, 31125 Chihuahua, Chih.

ljuarezm@uach.mx

Alejandría Denisse Pérez Valseca

Universidad Autónoma Metropolitana, Unidad Iztapalapa

Av. San Rafael Atlixco 186, Leyes de Reforma 1ra Secc, Iztapalapa, 09340 Ciudad de México, CDMX

alepv@xanum.uam.mx

Juan Luis François Lacouture

Universidad Nacional Autónoma de México

Paseo Cuauhnáhuac 8532, Col. Progreso, 62550 Jiutepec, Morelos, México

juan.luis.francois@gmail.com

Abstract

Given the worldwide efforts for low-carbon energy sources, nuclear power, and particularly Generation IV reactors, are seen as sustainable options to improve efficiency in power generation. Current reactors utilize steam Rankine cycles, which are less efficient compared to gas turbines and combined cycles. This study explores the thermodynamic analysis of a supercritical nitrogen (N₂) Brayton cycle for advanced nuclear power plants using the open-source simulation tool DWSIM. This work compares the thermodynamic performance of the nitrogen Brayton cycle with reference design. The analysis showed minimal temperature differences, with a maximum variation of 0.96%, with no pressure differences. Power generation and consumption calculations showed small percentage differences (0.93% for turbine power, 1.92% for the low-pressure compressor, and 2.35% for the high-pressure compressor). The cycle efficiency calculated with DWSIM was 37.86%, which closely matches the reported 38.26%. This study demonstrates that DWSIM can effectively model and verify the performance of advanced power cycles in nuclear reactors, offering a cost-effective and flexible alternative to commercial simulation tools.

1. INTRODUCTION

The importance of research and development of low-carbon energy sources is a global goal, due to the increasing global warming and climate change. To achieve this goal, nuclear power is a promising and sustainable option. Currently, there are 440 power reactors in the world, which provide about 10% of global electricity, and over 30 countries utilize nuclear energy [1].

For decades, several countries have promoted research on Generation IV reactors, because they are a promising reactor types that are called to be more sustainable, safer, more economically competitive, and more proliferation resistance than previous generations [2].

Current nuclear power plants (NPPs) are way behind in thermal efficiency (30–42%) using a Rankine cycle for power generation [3]. Comparatively, gas turbines with turbine inlet temperatures up to and greater than 1400 °C have cycle efficiencies of around 40% that can be boosted to around 60% in a combined cycle. The ability of the combined cycle or Brayton cycle with a heat recuperator, drastically improve net plant efficiency that is an especially appealing feature to employ with a nuclear power source but has previously been technically infeasible given the high operating temperature requirements of the combined cycle. Nowadays, with the new nuclear reactor technologies the use of Brayton cycle is possible [4].

Prototype Generation IV nuclear reactors under development use a steam Rankine cycle for power conversion, as in the case of the Supercritical water-cooled reactor (SCWR) and the Very high-temperature gas reactor (VHTR) [2]. For Molten Salt Reactors (MSR), the use of a supercritical CO₂ Brayton recompression cycle has been also explored [5]. In the case of Lead-cooled fast reactors (LFR), the use of the supercritical CO₂ Brayton cycle, the traditional steam Rankine cycle, and the helium (He) Brayton cycle have been presented and studied for several researchers as [6]. Gas-cooled fast reactors (GFR) designs have been studied coupled with a direct closed Brayton cycles [7]. In the case of Sodium-cooled fast reactors (SFR), the reaction between sodium and water presents a major safety issue in its development, limiting the use of the Rankine cycle for power conversion. As an alternative, the use of supercritical Nitrogen Brayton cycle has been explored.

In the work of Park *et al.*, (2018) [5], the use of the nitrogen Brayton cycle as a power conversion system for a sodium-cooled fast reactor was developed and optimized, increasing the efficiency of the cycle to 38.26%. The use of the nitrogen Brayton cycle coupled with SFR has been explored to eliminate the intermediate sodium loop, obtaining an optimization of the system by Bi *et al.*, (2016) [8]. The thermodynamic N₂ Brayton cycle for SFR has been designed, applying material and energy balance calculations, considering different working fluids and cycle configurations [9,10].

To design and simulate the thermodynamic performance of nuclear power plants, the use of commercial software has been widely explored. as the case of: Aspen-HYSYS® developed by AspenTech® that used to mathematically model chemical processes, from unit operations to full chemical plants and refineries [11]; CHEMCAD®, which is an integrated suite of intuitive chemical process simulation software that fits into the chemical engineering workflow [12]; Thermoflow® that is a set of engineering software tools designed for the design, simulation, and

performance analysis of thermal power plants, including combined cycle, gas turbine, steam turbine, and cogeneration plants. It is extensively used in the energy sector by engineers and designers to model the thermodynamic and operational behavior of power plants under various scenarios. These software tools are highly developed, allowing the simulation of a wide range of processes, with many unit operations and thermofluids. However, the cost of the license could be a limitation for more widespread use.

On the other hand, open-source process simulators are now available that allow the design, coupling, and simulation chemical process and power cycles for the most common fluids. Additionally, the use of open-source codes generates greater flexibility in programming and reduces operating costs make them available for any user.

In this work, we present a thermodynamic analysis and verification of a supercritical N₂ Brayton Cycle for advanced nuclear power plants, using the process simulation tool named as Daniel Wegner Simulator (DWSIM) which is an open-source, CAPE-OPEN compliant chemical process simulator tailored to the needs of both academic and industrial users [14].

2. SYSTEM DESCRIPTION

The supercritical nitrogen Brayton cycle selected in this work was proposed by Park et.al, in 2018 [5]. In the study, the authors performed a thermodynamic analysis and optimization of a N₂ Brayton cycle coupled to a sodium-cooled fast reactor. The study presents the cycle configuration with all the operational parameters such as: mass flow rate, temperatures, pressures, work generated and consumed, and heat exchanger loads. In the study, optimal values for the mentioned parameters were calculated through a sensitivity analysis evaluating different operating conditions along with thermal cycle efficiencies [5].

The cycle description and characteristics are listed below:

- At first, the supercritical N₂ is heated from 367.04 °C and 18.1 MPa up to 503.1 °C and 18.0 MPa in a sodium to gas heat exchanger (SGHX). The hot sodium comes from nuclear reactor, and it exchanges 764.5 MW of heat. The pressure drop in the SGHX is 0.1 MPa.
- Second, when N₂ exits the SGHX passes through a gas turbine where it is expanded from 18.0 to 9.73 MPa with an isentropic efficiency of 93%.
- Third, after turbine the expanded fluid enters the recuperator where 1730.95 MW of heat are exchanged. Nitrogen enters the recuperator at 392.42 °C and exits at 77.06 °C. The inlet pressure is 9.68 MPa with a pressure drop of 0.05 MPa.
- Fourth, before the Low-Pressure Compressor (LPC), nitrogen is cooled up to 27 °C that is the reference ambient temperature. The cooling process takes place in a Precooler where 288.25 MW of heat are transferred to the surroundings. The pressure dropped in LPC is about 0.059 MPa.
- Fifth, nitrogen is compressed in a Low-Pressure Compressor from 9.68 MPa up to 12.97 MPa. The compression process is performed with an isentropic efficiency of 89%.
- Sixth, due to the compression process, the nitrogen temperature is also increased from 27 °C to 57 °C. Then the working fluid is cooled down to reach the ambient temperature once

again at 27 °C. Afterwards, nitrogen enters the High-pressure Compressor (HPC) where it is compressed to 18.15 MPa with an isentropic efficiency of 88 %.

- Seventh, after the HPC nitrogen is directed to the recuperator to be heated from 62.06 °C to 367.04 °C before restarting the cycle. The pressure drop in the recuperator is 0.05 MPa.

The cycle described above is presented in Figure 1, with all the operational conditions.

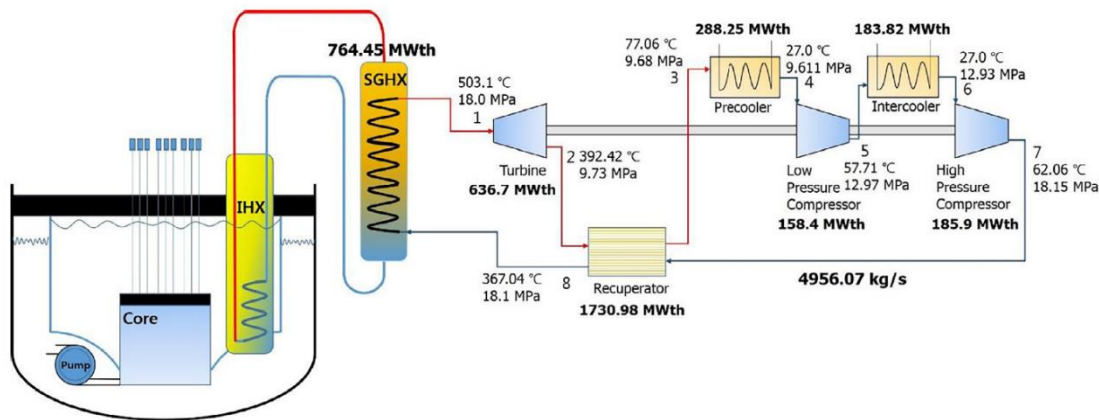


Figure 1. Super critical nitrogen Brayton cycle sketch [5]

It is important to highlight that supercritical critical state of a substance is reached at a certain pressure and temperature above the critical point. In this respect, the critical point of nitrogen is about 3.3978 MPa and -146.96 °C [15]. Considering this, nitrogen keeps supercritical at every stage of the cycle since the lowest pressure value in the cycle is 9.73 MPa at turbine exhausts.

3. SOFTWARE DESCRIPTION

The cycle described above was simulated using the Daniel Wegner Simulator (DWSIM). DWSIM is an open-source, CAPE-OPEN compliant chemical process simulator designed to meet the requirements of both academic and industrial users. It provides a comprehensive set of features and functionalities, making it a versatile tool for various applications in process engineering, including process design and optimization, process safety and environmental analysis, industrial applications, power conversion systems, and academic research [14].

DWSIM is characterized by a user-friendly interface featuring an intuitive graphical user interface (GUI) that allows users to easily create and manage simulations. It offers an extensive library of thermodynamic models and property packages, such as Peng-Robinson, Soave-Redlich-Kwong, and Raoult's Law, and supports electrolyte and solid-phase modeling, enhancing its applicability to a wide array of chemical processes research [14].

The simulator supports a broad range of unit operations, including chemical reactors, distillation columns, heat exchangers, pumps and compressors, and allows users to create and integrate custom unit operations when necessary. DWSIM includes tools for performing energy and material balance

calculations, sensitivity analysis, parameter estimation, and optimization, along with advanced features for process control and dynamic simulation [14].

Additionally, users can utilize scripting and automation capabilities with Python and IronPython. The simulator supports plugins to extend functionalities and integrates with other software and databases via CAPE-OPEN standards. DWSIM offers detailed graphical representation of flowsheets and unit operations, plotting and charting tools for visualizing simulation results, and comprehensive reporting features for documenting and sharing simulation studies. The software is available for Windows, Linux, and macOS, and supports cloud-based simulation capabilities [14].

Table I. Key design parameters [5]

Parameter	Process Unit	Value
Pressure ratio	Turbine	1.85
	Low-pressure Compressor	1.35
	High-pressure Compressor	1.404
Power (MW)	Turbine	636.7
	Low-pressure Compressor	158.4
	High-pressure Compressor	185.9
Heat load (MW)	SGHX	764.45
	Recuperator	1730.98
	Precooler	288.25
	Intercooler	183.82
Isentropic Efficiency (%)	Turbine	93
	Low-pressure Compressor	89
	High-pressure Compressor	88
Cycle	Mass flow rate (kg/s)	4956.07
	Ambient temperature (°C)	27
	Cycle efficiency (%)	38.26

4. METHODOLOGY

In this section the mathematical models that describe the material and energy balance equations are presented.

4.1. Material balance

The material balance equation derivation of a system is as follows:

$$\frac{dM}{dt} = (\dot{m}_{in}) - (\dot{m}_{out}) + (\dot{G}) - (\dot{C}) \quad (1)$$

Where, $\frac{dM}{dt}$ is the rate of mass accumulation in the system, \dot{m}_{in} and \dot{m}_{out} are the inlet and outlet mass flow rate through the system, and \dot{G} and \dot{C} are the generation and depletion of chemical species due to chemical reactions in the system.

Assuming steady state condition and no chemical reaction in the system, the derivative term along with the rate of mass generation/depletion are canceled, and equation (1) can be rewritten in the following form:

$$(\dot{m}_{in}) = (\dot{m}_{out}) \quad (2)$$

Equation (2) accounts all the inlet mass flow rate in a unit process and sum be equal the outlet mass flow rate. As it was presented in Table I, the nominal mass flow rate of N₂ in the cycle is 4956.07 kg/s.

4.2. Energy balance

The energy balance equation derivation of a system is presented in equation (3).

$$\frac{dE}{dt} = (\dot{E}_{in}) - (\dot{E}_{out}) + (\dot{E}_G) - (\dot{E}_C) \quad (3)$$

Where, derivative term $\frac{dE}{dt}$ means the energy accumulation in the system, second and third terms (\dot{E}_{in} and \dot{E}_{out}) are the energy entering and exiting the systems, and fourth and fifth terms (\dot{E}_G and \dot{E}_C) are energy generation and depletion due to chemical reactions in the system. Under steady-state conditions with no chemical reaction, equation (4) can be rewritten in the following form:

$$(\dot{E}_{in}) = (\dot{E}_{out}) \quad (4)$$

Based on the first law of thermodynamics, when kinetic and potential energies are negligible, the energy exchange between a thermodynamic open system with the surroundings is achieved in the form of work (\dot{W}), heat (\dot{Q}) and mass flow rate (\dot{m}) [19]. These assumptions were applied to each process unit in the power cycle. All the material and energy balance equations that are solved in DWSIM are presented in Table II.

Based on reference [5], the process flowsheet of the nuclear power plant developed in DWSIM is shown in Figure 2.

Table II. Mass and energy balance equations of the nuclear system.

Name of the component	Mass balance equations	Energy balance equations
Turbine	$\dot{m}_1 = \dot{m}_2$	$\dot{m}_1 h_1 = \dot{W}_T + \dot{m}_2 h_2$
Recuperator	$\dot{m}_2 + \dot{m}_7 = \dot{m}_3 + \dot{m}_8$	$\dot{m}_2 h_2 + \dot{m}_7 h_7 = \dot{m}_3 h_3 + \dot{m}_8 h_8$
Precooler	$\dot{m}_3 = \dot{m}_4$	$\dot{m}_3 h_3 = \dot{Q}_{PC} + \dot{m}_4 h_4$
Low-pressure Compressor	$\dot{m}_4 = \dot{m}_5$	$\dot{m}_4 h_4 + \dot{W}_{LPC} = \dot{m}_5 h_5$
Intercooler	$\dot{m}_5 = \dot{m}_6$	$\dot{m}_5 h_5 = \dot{Q}_{IC} + \dot{m}_6 h_6$
High-pressure Compressor	$\dot{m}_6 = \dot{m}_7$	$\dot{m}_6 h_6 + \dot{W}_{HPC} = \dot{m}_7 h_7$
SGHX	$\dot{m}_8 = \dot{m}_1$	$\dot{m}_8 h_8 + \dot{Q}_{SGHX} = \dot{m}_1 h_1$

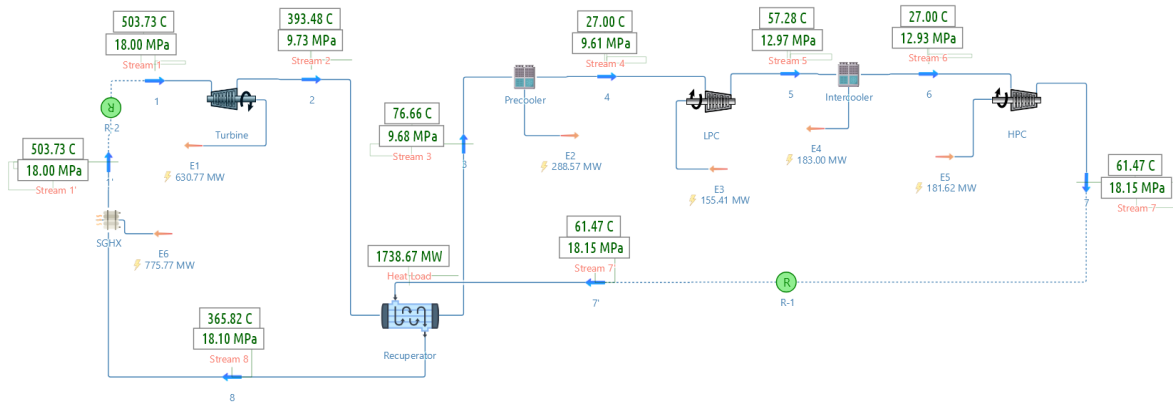


Figure 2. DWSIM process flowsheet of the supercritical nitrogen Brayton cycle

5. VERIFICATION AND RESULTS

To verify the results obtained with DWSIM, some parameters such as pressure and temperature at every stage, turbine power generation, compressors power consumption, heat exchanger loads and thermal efficiency of the cycle, were calculated and compared with the reference study [5].

Regarding thermal efficiency of a power cycle is a measure of how effectively the cycle converts heat energy into work. It is defined as the ratio of the net-work output of the cycle to the heat input [16].

Hence, to compute the thermal efficiency (η_{TH}) of the power cycle, equation (5) can be used.

$$\eta_{TH} = \frac{\text{Net work}}{\text{Heat input}} = \frac{\dot{W}_{Turbine} - \dot{W}_{LPC} - \dot{W}_{HPC}}{\dot{Q}_{SGHX}} \quad (5)$$

The steady-state simulation results obtained with DWSIM showed that pressures and temperatures at every stage of the cycle are the same as those reported by Park et.al., (2018) [5]. The biggest temperature difference was found at stream 7 with a percentage difference around 0.96%, that is 0.59 °C lower than the reported value.

Concerning pressures, no significant differences were found between calculated and reference. These results can be seen in Table III.

The comparison in terms of turbine power generation, compressor power intake, and heat exchanger loads are shown in Table IV.

The analysis indicates that the largest difference between the evaluated parameters occurs at HPC power intake, where DWSIM-calculated value was about 181.62 MW, compared to the reported value of 185.90 MW, that is 4.28 MW lower than the optimal value reported.

The discrepancies found can be attributed to different thermodynamic property packages used: specifically, the Peng-Robinson equation of state employed in this study compared to the NIST reference thermodynamic property package, which explains the small differences observed. Additionally, the convergence of the numerical methods used in both studies (reference vs DWSIM) can also lead to the small differences found in the results.

With respect to thermal efficiency of the cycle, the calculated efficiency using DWSIM was around 37.86%, meanwhile the reported efficiency was 38.26%. Therefore, it can be said that the thermal performance obtained with DWSIM is in a good agreement to the reference with small differences.

Table III. Pressure and Temperature comparison

Stream	Temperature (°C) DWSIM	Temperature (°C) Reference	% Difference	Pressure (MPa) DWSIM	Pressure (MPa) Reference	% Difference
1	503.73	503.1	0.1250	18.00	18.00	0.0
2	393.48	392.42	0.2693	9.73	9.73	0.0
3	76.66	77.06	0.5217	9.68	9.68	0.0
4	27.00	27.0	0	9.611	9.611	0.0
5	57.28	57.71	0.7506	12.97	12.97	0.0
6	27.00	27.0	0	12.93	12.93	0.0
7	61.47	62.06	0.9598	18.15	18.15	0.0
8	365.82	367.04	0.3334	18.10	18.10	0.0

Table IV. Power and heat load comparison

Process Unit	DWSIM		Reference	
	Power (MW) / Heat Load (MW)		Power (MW) / Heat Load (MW)	
Turbine	630.77	/ -----	636.70	/ -----
LPC	155.41	/ -----	158.40	/ -----
HPC	181.62	/ -----	185.90	/ -----
SGHX	-----	/ 775.77	-----	/ 764.45
Precooler	-----	/ 288.57	-----	/ 288.25
Intercooler	-----	/ 183.00	-----	/ 183.82
Recuperator	-----	/ 1738.67	-----	/ 1730.98

6. CONCLUSIONS

In this study, the implementation of DWSIM for thermodynamic analysis of a supercritical nitrogen Brayton cycle coupled to a sodium-cooled fast reactor was performed and compared to the reference design.

The comparison of temperatures showed small differences compared to reference. The highest temperature differences were found at stream 7 with a percentage difference of 0.96%. In respect to pressures, no difference was found.

The turbine power generation and compressor power consumption were calculated considering their respective isentropic efficiencies, yielding percentage differences of 0.93% for the turbine, 1.92% for the LPC, and 2.30% for the HPC, respectively.

Finally, the evaluation of cycle efficiency using DWSIM yielded a value of 37.86%, which falls within the reported range of 38.26%.

Therefore, it can be concluded that DWSIM is a suitable tool for the thermodynamic analysis of “supercritical nitrogen nuclear power plants”. Consequently, this tool can be effectively used for modeling and simulation of advanced nuclear power plants, taking advantage of its open-source nature.

NOMENCLATURE

Table V. Nomenclature

Letters	<i>kPa; kilopascal</i>
<i>h; specific enthalpy</i>	<i>MW; megawatt</i>
<i>ṁ; mass flow rate</i>	Subscripts
<i>η; efficiency</i>	<i>HPC; high – pressure compressor</i>
<i>Q̇; heat flow</i>	<i>IC; intercooler</i>
<i>Ẇ; rate of work</i>	<i>LPC; low – pressure compressor</i>
Units	<i>numbers; stream number</i>
<i>°C; celsius</i>	<i>PC; precooler</i>
<i>kg/s; kilogram per second</i>	<i>SGHX; sodium to gas heat exchanger</i>

REFERENCES

1. “International Atomic Energy Agency (IAEA), Nuclear Power Reactors Website” <https://www.iaea.org/topics/nuclear-power-reactors> (2024).
2. “Generation IV systems (GENIV) Website” https://www.gen-4.org/gif/jcms/c_59461/generation-iv-systems (2024).
3. Dragunov, A., Saltanov, E., Piore, I., Kirillov, P., Duffey, R., “Power cycles of generation III and III+ nuclear power plants”, *Journal of Nuclear Engineering and Radiation Science*, **Volume 1**, p. 021006-1/021006-10, (2015).
4. Zohuri, B., *Combined Cycle Driven Efficiency for Next Generation Nuclear Power Plants: An Innovative Design Approach*, Springer, Switzerland, (2015).
5. J. H. Park, J. Yoon, J. Eoh, H. Kim, M. H. Kim., “Optimization and sensitivity analysis of the nitrogen Brayton cycle as a power conversion system for a sodium-cooled fast reactor”, *Nuclear Engineering and Design*, **Volume 340**, p. 325-334, (2018).
6. Ming-Jia L., Yan-Jun J., Han-Hui Z., Guo-Jia Q., Meng-Jie L., “The thermodynamic and cost-benefit-analysis of miniaturized lead-cooled fast reactor with supercritical CO₂ power cycle in the commercial market”, *Progress in Nuclear Energy*, **Volume 103**, p. 135-150, (2018).
7. Herranz, L. E., J. I. Linares, and B. Y. Moratilla., “Power cycle assessment of nuclear high temperature gas-cooled reactors”, *Applied Thermal Engineering*, **Volume 29**, p. 1759–1765, (2009).
8. S. Bi. Seo, H. Seo, I. C. Bang, “Adoption of nitrogen power conversion system for small scale ultra-long cycle fast reactor eliminating intermediate sodium loop”, *Annals of Nuclear Energy*, **Volume 87**, Part 2, p. 621-629, (2016).
9. Yoon, J., Eoh, J., Kim, H., Kim, D. E., Kim M. (2018), “Design Characteristics of N₂ Brayton Cycle Power Conversion System coupled with an SFR in terms of Thermal Balance and Cycle Efficiency”, *Proceedings of the KNS 2018 Spring Meeting*, (p. v), Korea, Republic of: KNS, (2018).
10. Olumayegun, O., Wang, M. and Kelsall, G. (2017), “Thermodynamic analysis and preliminary design of closed Brayton cycle using nitrogen as working fluid and coupled to small modular Sodium-cooled fast reactor (SM-SFR)”. *Applied Energy*, **Volume 191**. pp. 436-453. <https://doi.org/10.1016/j.apenergy.2017.01.099>
11. “Aspen-HYSYS Chemical process simulator Website” <https://www.aspentech.com/en/products/engineering/aspens-hysys> (2024).
12. “CHESTATIONS™ Website” <https://www.chemstations.com/CHEMCAD/> (2024).
13. “Thermoflow Website” <https://www.thermoflow.com/> (2024).
14. “DWSIM open-source process simulator Website” <https://dwsim.org/> (2024).
15. “National Institute of Standards and Technology Website” <https://webbook.nist.gov/chemistry/fluid/> (2024).
16. Dincer, I., & Bicer, Y., *Integrated Energy systems for multigeneration*. Elsevier Science (2019).

Technical Expertise and Innovations in the Defuelling Program for Advanced Gas-cooled Reactor: Strategies for Optimization, Reliability, and Safety

Diksha Sharma *

*AtkinsRéalis, The Hub 500 Park Avenue Aztec West, Bristol, United Kingdom, BS32 4RZ,
sdiksha375@gmail.com*

Gunjan Indauliya

*AtkinsRéalis, The Hub 500 Park Avenue Aztec West, Bristol, United Kingdom, BS32 4RZ,
Gunjan.indauliya@gmail.com*

Abstract

The defuelling process for Advanced Gas-cooled Reactors (AGRs) in the UK is managed by EDF and involves the careful removal of irradiated nuclear fuel from the reactors. This critical operation is necessary to maintain nuclear safety and prevent potential accidents and hazards. As the AGR approaches the end of its operational life, defuelling becomes crucial for risk reduction and decommissioning. Safe and timely handling procedures are necessary to prevent accidents and radioactive releases, reduce risks, and ensure responsible management of nuclear power plants.

To ensure the safe transportation and storage of nuclear fuel, procedures need to be incorporated to reduce the impact on the environment and reduce risks to workers, identify potential hazards that may cause hazards, and propose As Low as Reasonably Practicable (ALARP) alternatives and safety case justifications. The abovementioned activities enhance the comprehensive safety and sustainability of the UK's nuclear energy strategy.

Several crucial areas help optimize and ensure the reliability of the defuelling process, such as:

ALARP Assessment: ALARP assessments should be carried out to determine risks associated with defuelling and identify the best steps to reduce them to as low as reasonably practicable.

Human Factor Assessment: HF consideration should be given to defuelling to assess the potential impact of human errors and interventions and the possible measures to improve safety and human performance at this stage.

Probabilistic Safety Assessment: PSA methods can also be used while defuelling to quantitatively estimate the possibility of accidents and their consequences, support decision-making by horizontal risk comparison, etc.

Maintenance, Inspection, and Testing: adopting preventive maintenance, inspection, and testing procedures to maintain the quality and credibility of the defuelling equipment and systems, and minimize the possibility of equipment unreliability and unplanned downtime or failure.

Worker Risk Assessment: conducting a thorough assessment of the potential hazards and human exposure during defuelling and taking the necessary measures to protect the workers' safety and health.

* Footer if necessary, in 9-point Times New Roman font.

Engineering Changes and Modifications: after completing the first defuelling cycle, the engineering should be revised to get a comprehensive idea about the feasibility of making changes or modifications to optimize the defuelling process and whether there is a potential for new operations or conditions.

With these important work areas on track and well addressed, the safety of the defuelling operations can be improved so that the nuclear plants can be decommissioned successfully with minimal risks to workers, the environment, and the public. In conclusion, the defuelling process is an extremely complicated and very intricate undertaking, it should be carefully designed to ensure the safety of the plant, personnel, and environment. This conference abstract introduces a framework to improve the operation, reliability, and safety of an advanced reactor with several strategies and technologies to secure the safe, reliable, and sustainable use of the AGR nuclear energy system for a clean and secure energy future.

1. INTRODUCTION

The nuclear power plants in the United Kingdom have played a significant role in generating a substantial portion of the country's nuclear energy. As these reactors approach the end of their operational lifespan, defuelling is crucial to ensure safety and prepare for the decommissioning process. The defuelling operation involves removing irradiated nuclear fuel from the reactors, a complex and risky endeavor that requires careful planning and execution.

This technical paper aims to emphasize the crucial significance of refining the defuelling process for advanced gas-cooled reactors (AGRs). As these reactors approach their decommissioning phase, it becomes crucial to prioritize strategies that improve the efficiency, reliability, and safety of defuelling operations. The objective is to offer valuable insights and share knowledge on the most recent technical advancements and innovations that can be utilized to address the inherent challenges associated with defuelling.

By discussing this topic, we aim to emphasize the importance of implementing cutting-edge methodologies and technologies that not only expedite the defuelling process but also guarantee its utmost safety. This is essential not only for the safety of the individuals involved and the preservation of the environment but also for the smooth progression to the subsequent stages of reactor decommissioning.

The paper begins by examining the current state of defuelling operations, highlighting the main challenges faced, and analyzing the conventional approaches used. It then explores cutting-edge methods and advancements that have been created to improve the process.

2. MAIN CONTENT

2.1 History and Development

AGRs, which were developed in the 1960s and 1970s, are a distinctive reactor design that is exclusively used in the UK. They employ carbon dioxide as a coolant and graphite as a moderator, operating at elevated temperatures to attain high thermal efficiency. AGRs have played a crucial role in the UK's energy infrastructure, serving as a dependable source of low-

carbon electricity. Nevertheless, as these reactors grow older, their efficiency declines, and the expenses for upkeep rise, ultimately resulting in their scheduled decommissioning.

2.2. Challenges during Defuelling

Technical challenges: The intricate design of AGRs, which includes a large graphite core and complex fuel assembly, makes defuelling a technically demanding task. The fuel elements, having been subjected to high levels of radiation, necessitate cautious handling to prevent any harm and maintain secure containment.

Safety concerns: The main worry during defuelling is the risk of radiation exposure to both workers and the surrounding environment. To ensure safety and proper waste management, it is crucial to adhere to strict safety protocols.

Coordinating logistics for defuelling operations requires collaboration between various teams and facilities, encompassing the transportation of spent fuel to reprocessing or storage sites. Efficiently managing these logistics is crucial to reducing downtime and expenses.

Safe and timely defuelling processes are essential to prevent accidents and radioactive releases, mitigate risks, and to ensure responsible management of nuclear energy facilities.

The approach and methodology mentioned in the paper ensures a conscientious defuelling process that guarantees safe nuclear fuel handling and storage. This approach includes identifying methods to minimize environmental impacts and reduce the risk posed to operators, determining the likelihood of hazards that might lead to severe radiological release, and proposing ALARP alternatives and safety case justifications.



Figure 1 : DEFUELLING WORK AREAS AND

The abovementioned activities in Figure 1 enhance the comprehensive safety and sustainability of the UK's nuclear energy.

2.1.1. ALARP Assessment

An ALARP assessment is a crucial component of the defuelling process. This assessment aims to identify and evaluate the risks associated with defuelling and implement measures to reduce these risks to the lowest practicable level. The ALARP principle is central to ensuring that all potential hazards are managed effectively. It involves a systematic approach to identifying potential hazards, evaluating the likelihood and consequences of these hazards, and implementing measures to mitigate them.

Process of ALARP Assessment

- **Hazard Identification:** The first step involves identifying all potential hazards related to the defuelling process. This includes mechanical failures, human errors, and environmental factors.
- **Risk Evaluation:** Once hazards are identified, the next step is to evaluate the risks associated with each hazard. This involves assessing the likelihood of occurrence and the potential consequences.
- **Implementation of Controls:** Based on the risk evaluation, appropriate controls are implemented to mitigate the risks. These controls can be engineering solutions, procedural changes, or administrative controls.
- **Continuous Monitoring:** After implementing controls, continuous monitoring is necessary to ensure that the risks remain at an acceptable level. This involves regular inspections, audits, and reviews.

By adopting the ALARP approach, the defuelling process can be optimized to enhance safety and sustainability. This involves a continuous cycle of risk assessment and mitigation, ensuring that all risks are reduced to levels that are as low as reasonably practicable. This approach not only ensures compliance with regulatory requirements but also enhances the overall safety culture within the organization.

2.1.2. Human Factor Assessment

Human Factors (HF) play a significant role in the defuelling process. A HF assessment is essential to evaluate the potential impact of human errors and interventions during defuelling. The HF assessment focuses on understanding how human performance can be affected by various factors, including environmental conditions, equipment design, and procedural complexity.

Components of Human Factor Assessment

- **Environmental Conditions:** Assessing how factors like lighting, temperature, and noise levels affect human performance.
- **Equipment Design:** Ensuring that equipment is designed to be user-friendly and reduce the likelihood of errors.
- **Procedural Complexity:** Simplifying procedures to make them easier to follow and less prone to errors.

- **Human Performance Optimization:** Implementing training programs and ergonomic improvements to enhance human performance.

By identifying areas where human performance can be improved, the HF assessment helps to reduce the likelihood of accidents caused by human error. This involves analyzing past incidents, conducting simulations, and implementing measures to enhance training, communication, and ergonomics. The goal is to create an environment where human performance is optimized, and the risk of errors is minimized.

2.1.3. Probabilistic Safety Assessment

Probabilistic Safety Assessment (PSA) methods are used to quantitatively estimate the probability of accidents and their potential consequences during defuelling. PSA involves the use of mathematical models to analyze various scenarios and assess their associated risks. This approach allows for a comprehensive evaluation of the potential hazards and the implementation of measures to mitigate these risks.

Process of Probabilistic Safety Assessment

- **Scenario Development:** Identifying and developing possible scenarios that could lead to accidents.
- **Event Tree Analysis:** Using event trees to map out the sequence of events leading to each scenario.
- **Fault Tree Analysis:** Using fault trees to identify the root causes of each scenario.
- **Risk Calculation:** Quantifying the risk associated with each scenario using mathematical models.
- **Comparison and Decision-Making:** Comparing the risks of different scenarios and making informed decisions to mitigate them.

By analyzing different scenarios, PSA supports decision-making by comparing horizontal risks and identifying areas where improvements can be made. This quantitative approach provides a robust framework for assessing the safety of the defuelling process and identifying areas for improvement. By incorporating PSA into the defuelling strategy, organizations can ensure that all potential risks are identified and managed effectively.

2.1.3. Maintenance, Inspection, and Testing

Preventive maintenance, inspection, and testing are critical to maintaining the quality and reliability of defuelling equipment and systems. Regular maintenance and inspection ensure that equipment is in good working condition, reducing the likelihood of unplanned downtime or failure. By implementing a comprehensive maintenance program, the reliability of the defuelling process can be significantly enhanced.

Components of Maintenance Program

- **Regular Inspections:** Conducting regular inspections to identify any potential issues.

- **Testing of Critical Components:** Testing key components to ensure they are functioning properly.
- **Timely Replacement of Parts:** Replacing worn or outdated parts before they fail.
- **Documentation and Record-Keeping:** Maintaining detailed records of all maintenance activities.

The maintenance program should include regular inspections, testing of critical components, and timely replacement of worn or outdated parts. This proactive approach helps to identify and address potential issues before they lead to equipment failure. By maintaining the reliability of defuelling equipment, organizations can ensure that operations proceed smoothly and safely.

2.1.4. Worker Risk Assessment

The safety and health of workers involved in the defuelling process are paramount. A thorough worker risk assessment is necessary to identify potential hazards and human exposure during defuelling. This assessment involves evaluating the working conditions, identifying potential hazards, and implementing measures to protect workers.

Components of Worker Risk Assessment

- **Hazard Identification:** Identifying all potential hazards that workers may be exposed to during defuelling.
- **Exposure Assessment:** Assessing the level of exposure to each hazard.
- **Control Measures:** Implementing control measures to reduce exposure to acceptable levels.
- **Health Monitoring:** Monitoring the health of workers to identify any adverse effects.

Key components of the worker risk assessment include providing appropriate personal protective equipment (PPE), ensuring proper training, and establishing safety protocols. By prioritizing worker safety, organizations can reduce the overall risk associated with the defuelling process. This involves not only protecting workers from immediate hazards but also ensuring their long-term health and well-being.

2.1.5. Engineering Changes and Modifications

After completing the initial defuelling cycle, it is important to review and revise the engineering aspects of the process. This review provides insights into the feasibility of making changes or modifications to optimize the defuelling process. Engineering changes and modifications may involve updating procedures, enhancing equipment design, or implementing new technologies.

Process of Engineering Changes and Modifications

- **Review of Initial Cycle:** Analyzing the data from the initial defuelling cycle to identify areas for improvement.
- **Feasibility Analysis:** Evaluating the feasibility of potential changes or modifications.
- **Implementation of Changes:** Implementing the changes and modifications identified.
- **Monitoring and Evaluation:** Continuously monitoring the effects of the changes and evaluating their effectiveness.

The goal of these changes is to improve the efficiency and safety of the defuelling process. By continuously evaluating and updating engineering practices, organizations can ensure that the defuelling process is optimized to reduce risks and enhance safety. This iterative approach allows for continuous improvement and adaptation to changing conditions and requirements.

3. APPLICATION OF THE DEFUELLING WORK AREAS

The various work areas in the defuelling process provide valuable insights into optimizing operations, helping to reduce time, costs, and manpower. Given that defuelling is often a complex and challenging task, applying these focused strategies can streamline the process and improve efficiency. Below are the specific applications of these approaches.

3.1 Application of ALARP Assessment

The ALARP assessment is applied in the defuelling process to systematically identify hazards and evaluate their associated risks, ensuring that risks are reduced to the lowest reasonable level. By examining both the likelihood and consequences of potential hazards such as fuel damage or equipment failures, mitigation measures like safety protocols or equipment upgrades are implemented. Continuous monitoring ensures that the risk remains minimized, promoting a safer working environment and ensuring compliance with regulatory standards.

3.2 Application of Human Factor Assessment

The Human Factor (HF) assessment is used to minimize human errors and optimize operator performance during the defuelling process. It evaluates how environmental conditions, equipment design, and procedural complexity influence human behavior. For example, ensuring user-friendly equipment interfaces and providing clear, simplified procedures can help reduce operational mistakes. This assessment also highlights areas where training or ergonomic improvements are needed, leading to enhanced operator performance and lower chances of human error.

3.3 Application of Probabilistic Safety Assessment

Probabilistic Safety Assessment (PSA) is employed to provide a quantitative estimation of the risks associated with different defuelling scenarios. Through techniques such as event tree and fault tree analysis, it helps in mapping out possible sequences of events that could lead to accidents. By calculating the probability of these events, PSA enables decision-makers to prioritize risk mitigation measures, such as adding redundant safety systems or improving procedural responses, thereby improving overall safety and operational planning.

3.4 Application of Maintenance, Inspection, and Testing

Maintenance, inspection, and testing are critical applications in the defuelling process to ensure the continued functionality and reliability of equipment. Regular inspections help identify potential issues, while the testing of critical components ensures they are operating as expected. A proactive maintenance schedule, which includes timely part replacement, helps prevent unexpected breakdowns or failures. These practices significantly reduce downtime and enhance

operational safety, ensuring that defuelling can proceed smoothly without unplanned interruptions.

3.5 Application of Worker Risk Assessment

Worker risk assessment is used to evaluate and control the risks faced by personnel involved in the defuelling process. By identifying potential hazards like fuel exposure, slips, or burns, and assessing the level of risk to workers, this assessment helps implement protective measures such as proper use of personal protective equipment (PPE), comprehensive training, and emergency protocols. It also includes monitoring the health of workers, ensuring that long-term exposure to hazards does not affect their well-being, thus promoting a safer work environment.

3.6 Application of Engineering Changes and Modifications

The application of engineering changes and modifications after an initial defuelling cycle allows for continuous process optimization. By reviewing data from the first cycle, inefficiencies and potential improvements in equipment or procedures are identified. Feasibility studies are then conducted to assess the practicality of implementing these changes, such as upgrading equipment or modifying fuel handling procedures. Continuous monitoring post-implementation ensures that these changes effectively enhance the safety and efficiency of future defuelling operations.

4. Benefits of Adapting Key Work Areas During Defuelling

Adapting specific work areas during the defuelling process is essential for enhancing safety, efficiency, and reliability. By focusing on critical aspects such as risk management, human factors, safety assessments, and equipment maintenance, organizations can significantly minimize risks while optimizing operations. Below are the key benefits of adapting these essential work areas during defuelling.

- Ensures risks are minimized to the lowest practicable level, enhancing safety during the defuelling process.
- Promotes compliance with safety regulations, preventing potential legal or operational issues.
- Reduces human errors by addressing environmental conditions, simplifying procedures, and improving equipment design.
- Enhances operator performance through training and ergonomic improvements, leading to more efficient and safer operations.
- Provides a data-driven, quantitative approach to risk management, allowing for better decision-making on safety measures and resource allocation.
- Identifies and prioritizes critical risks, leading to targeted safety improvements and accident prevention.
- Increases equipment reliability through regular maintenance, inspections, and testing, reducing the likelihood of mechanical failures.
- Prevents unplanned downtime by identifying potential issues early, improving operational efficiency.

- Safeguards workers by identifying hazards, assessing exposure, and implementing safety measures such as PPE and health monitoring.
- Reduces the risk of workplace accidents and long-term health issues, fostering a safer work environment.
- Improves the defuelling process by applying lessons learned, optimizing equipment design, and updating procedures.
- Allows for continuous improvements and adaptations, ensuring the process remains efficient, safe, and up-to-date with technological advancements.

5. ADDITIONAL INFORMATION

5.1 Abbreviations and Acronyms

The abbreviations used throughout the paper are mentioned below.

AGR: Advanced Gas-cooled Reactor

ALARP: As Low as Reasonably Practicable

EDF: Électricité de France

HF: Human Factor

IAEA: International Atomic Energy Agency

NDA: Nuclear Decommissioning Authority

ONR: Office for Nuclear Regulation

PPE: Personal Protective Equipment

PSA: Probabilistic Safety Assessment

5.2 Units

The units used throughout the paper are mentioned below:

kW: kilowatt

MW: megawatt

kWh: kilowatt-hour

mSv: millisievert (used for radiation dose)

Bq: becquerel (used for radioactivity)

5.3 Equations

Probabilistic Safety Assessment involves using mathematical models to estimate accident probabilities and consequences. One key equation used in PSA is the risk equation:

This equation helps quantify the risk associated with various scenarios in the defuelling process.

Eq. 1

$$\text{Risk} = \text{Probability of Event} \times \text{Consequence of Event}$$

6. CONCLUSIONS

The defueling process for AGRs is a highly complex and intricate operation that demands meticulous planning and precise execution. Incorporating ALARP assessments, Human Factor evaluations, Probabilistic Safety Assessments, and robust maintenance, inspection, and testing protocols significantly enhances the safety and reliability of the defueling process. Furthermore, comprehensive worker risk assessments, along with continuous engineering reviews and modifications, play a critical role in optimizing the process and maintaining high safety standards.

The strategies and innovations outlined in this paper provide a solid framework for refining the defueling process, ensuring the safe, reliable, and sustainable management of AGRs. By addressing these critical areas, defueling operations can be executed effectively, minimizing risks to workers, the environment, and the public. Continued emphasis on safety, reliability, and innovation will ensure that AGR defueling operations support a clean and secure energy future. These efforts yield cost and time savings, improve efficiency, and enhance maintenance and inspection practices. In addition, fostering collaboration empowers personnel and strengthens stakeholder confidence, paving the way for a safer and more sustainable future for nuclear energy.

REFERENCES

1. EDF Energy. (2023). Advanced Gas-cooled Reactor (AGR) Defuelling. Retrieved from [EDF Energy](<https://www.edfenergy.com/>)
2. Office for Nuclear Regulation. (2022). Safety Assessment Principles for Nuclear Facilities. Retrieved from [ONR](<https://www.onr.org.uk/saps/>)
3. International Atomic Energy Agency. (2021). Probabilistic Safety Assessment. Retrieved from [IAEA](<https://www.iaea.org/>)
4. Health and Safety Executive. (2020). ALARP in Nuclear Safety. Retrieved from [HSE](<https://www.hse.gov.uk/>)
5. Nuclear Decommissioning Authority. (2019).

Exercise in Planning an Energy Transition Scenario with Implementation of Nuclear Energy

Cecilia Martín del Campo, Pamela F. Nelson

*Faculty of Engineering, National Autonomous University of Mexico
Circuito Escolar s/n, Ciudad Universitaria, 04510 CDMX, Mexico
cecilia.martin.del.campo@gmail.com; pnelson_007@yahoo.com*

Abstract

Many countries worldwide use nuclear science and technology to contribute to their sustainable development goals in energy, human health, food production, water management and environmental protection. A brief review of the advantages of nuclear energy over other energies is presented. The convenience of using the small modular reactors in Mexico in the future was described, and a list of publications from the International Atomic Energy Agency with relevant information concerning the deployment of these reactors is also presented. Two long-term energy transition scenarios for Mexico with a large deployment of renewables were analyzed. The first scenario does not consider new nuclear plants for the future, and the second does. A simplified model of the national electrical system is used. Nine nodes represent the electrical system, seven are interconnected to share electricity. The generating technologies are generic plants of each main technology used in Mexico. Several sustainable advantages were observed in the nuclear scenario versus the non-nuclear scenario. To generate the same energy by 2050, in the transition scenario without nuclear, 2,440 MW of additional capacity must be installed, compared to the scenario with nuclear. In the scenario with nuclear the share of clean energy is 84% versus 78% in the non-nuclear scenario. The annual GHG emissions are 29% lower, the consumption of natural gas is 28% lower, emissions of air pollutants are 28% lower, the capacity of batteries is 6% lower, and the transmission losses are 32% lower. These results can serve as a basis for further studies to evaluate scenarios where solar and wind can participate greatly in the mix of generating technologies grace to enough nuclear contribution in the power system. The added capacity of nuclear energy in the electrical system of Mexico can provide the opportunity to have an energy transition friendlier to climate change, with better air quality, and lower dependence on natural gas consumption which is a commodity imported in large amounts in México.

1. INTRODUCTION

It has been proven that the cleanest energies are also the safest energies, and this is the case for nuclear power, which has a low mortality rate due to accidents and air pollution and the lowest rate of carbon emissions of all technologies [1]. Another reason to move to a greater proportion of nuclear energy in the electricity mix is to comply with the United Nations Sustainable Development Goal (SDG) 7, which seeks to “Ensure access to affordable, reliable, sustainable and modern energy for all” [2]. There are 415 reactors in operation with 373,735 MW, and 62 reactors under construction which will contribute 64,971 GW to global clean energy [3].

One of the strengths of the Federal Electricity Commission (CFE) is that it is the only power company with the right to build and operate nuclear power plants in Mexico. CFE successfully operates a nuclear power plant with two generating units that add up to 1,608 MW. However, Mexico should define a nuclear roadmap so that CFE can install more nuclear plants and comply with the State policy that guarantees energy self-sufficiency and the Energy Transition of Mexico (TEM). The TEM involves replacing, over the next decades, most of the primary energy of fossil origin in the Mexican energy system, to build a new energy system based on renewable and nuclear.

2. IAEA'S ROLE IN DEVELOPING NUCLEAR PLANS FOR MEMBER COUNTRIES

Through the diversity of its programs and projects, the International Atomic Energy Agency (IAEA) works with member countries to promote the use of nuclear technology in different practical fields, under safe conditions and for peaceful purposes. Mexico is a member of the IAEA through the Latin America and the Caribbean division with 31 countries. Within this division, the Regional Cooperation Agreement for the Promotion of Nuclear Science and Technology in Latin America and the Caribbean (ARCAL) has been formed, whose purpose is to promote the use of nuclear technology in matters related to food, health, environment, energy, industry, and radiation safety. The Faculty of Engineering at UNAM is currently participating in an ARCAL project called Support for the Development of Comprehensive Energy Plans that consider Climate, Land, Energy and Water (CLEW) in Latin America and the Caribbean. In this context, we are incorporating new modelling tools to consider CLEW in the transition planning.

In nuclear energy planning, the IAEA has the International Project on Fuel Cycles and Innovative Reactors (INPRO), which supports members in nuclear systems planning, fuel cycles and collaborative activities to promote the sustainable development of nuclear energy. Such assistance can generate human resource development, technological support, operation, and energy security. In energy planning, through its programs and projects, the IAEA helps member countries meet the growing demand for energy for development while improving energy security, reducing environmental and health effects and mitigating climate change. Mexico is a member of INPRO [4].

International publications appear daily that can be consulted to delve deeper into transition scenarios in which nuclear energy, in combination with renewable energies, is considered a currently mature technological option. The IAEA's energy planning and modelling instruments are used by more than 135 countries and 20 international organisms, allowing countries to consider all

aspects of energy supply and demand focused on the SDGs. Recent documents and their link to the website from which they can be downloaded are listed below:

- INTERNATIONAL ATOMIC ENERGY AGENCY, Nuclear Cogeneration for Climate Change Mitigation and Sustainable Development Goals, IAEA-TECDOC-2056, IAEA, Vienna (2024). <https://www.iaea.org/publications/15488/nuclear-cogeneration-for-climate-change-mitigation-and-sustainable-development-goals>
- INTERNATIONAL ATOMIC ENERGY AGENCY, From Knowledge to Action: IAEA Toolkit for Sustainable Energy Planning, Outlooks, IAEA, Vienna (2024). <https://www.iaea.org/publications/15667/from-knowledge-to-action-iaea-toolkit-for-sustainable-energy-planning>
- INTERNATIONAL ATOMIC ENERGY AGENCY, Milestones in the Development of a National Infrastructure for Nuclear Power, IAEA Nuclear Energy Series No. NG-G-3.1 (Rev. 2), IAEA, Vienna (2024). <https://www.iaea.org/publications/15516/milestones-in-the-development-of-a-national-infrastructure-for-nuclear-power>.
- INTERNATIONAL ATOMIC ENERGY AGENCY, The Climate, Land, Energy and Water Framework, IAEA-TECDOC-2065, IAEA, Vienna (2024). <https://www.iaea.org/publications/15686/the-climate-land-energy-and-water-framework>

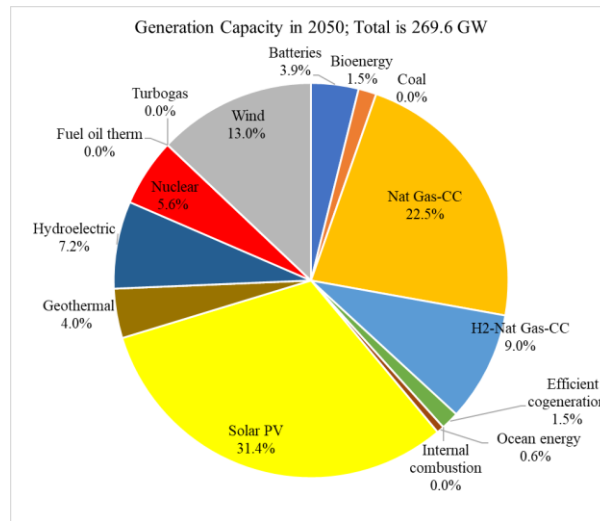
Small Modular Reactors (SMR) are based on a compact nuclear reactor design. The interest in this type of design – aimed at producing electricity and industrial process steam in cogeneration – lies in the desire to reduce direct investment costs, simplify the licensing process, shorten construction periods and make it possible for plants to be located as the main source of microgrids far from large electricity transmission networks, or in places that are difficult to access. Due to the small unit and their modular nature, it is possible to produce these reactors in a factory with advantages in terms of manufacturing quality, ease of approval and standardization, with shipment to the site already complete and ready to achieve the desired power by adding modular units in the site. SMRs have ready-made refurbishments that are easy to transport and manufacture, arrive on time and put the reactor into operation. For modern reactors, including SMRs, the availability factor is greater than 95%, due to the flexibility to carry out the refueling in a staggered manner in the modules that make up a plant. Nuclear power plants with large or small reactors are long-term investments, and can operate for 80 years. All these characteristics of SMRs justify their use in Mexico's long-term energy outlook.

3. ENERGY TRANSITION SCENARIOS FOR MEXICO BY 2050

3.1. Background

The Ministry of Energy (SENER, by its acronym in Spanish) in the latest Development Program of the National Electrical System (PRODESEN 2023-2037), in the Indicative Program for the Addition and Retirement of Power Plants (PIRCE by its acronym in Spanish) the addition of 150 MW of nuclear capacity appears. No major details have been reported in the PIRCE, but an SMR is assumed to be installed [5]. However, in 2021 the Mexican electricity system operator, the National Center for Energy Control (CENACE by its acronym in Spanish) published three long-term scenarios [6] in which a nuclear energy capacity of 11,509 MW is assumed to be installed in 2050. In scenario 3, which considers 932 TWh of annual electricity demand by 2050, the installed

capacity required is 273,206 MW where nuclear contributes 4.2%. Figure 1 shows the share of energy technologies in the installed capacity according to that reference scenario. The contribution of solar PV includes 7.7% of PV distributed generation. This case considers the contribution of combined cycle plants fueled by 70% natural gas (NG) and 30% hydrogen (H₂) as a transition cleaner fuel. However, this technology requires additional solar plants to provide the electricity for the electrolysis needed to produce hydrogen from clean energy. Each molecule of water (H₂O) splits into two hydrogen atoms and one oxygen atom, so you need a fair amount of water to get that 1 kg of hydrogen. Producing 1 kg of hydrogen via water electrolysis requires about 9 kg of water. However, in an industrial hydrogen plant based on Electrolysis-PEM, to obtain 1 kg of H₂, 17.5 liters of water are consumed [7] and this is the most efficient technology in the use of water. This means that this kind of plant must be installed in sites where water is abundant.



Data from [6]

Figure 1. Projected installed capacity in the Mexican electrical system by 2050 in scenario 3 of long-term scenarios published by CENACE.

3.2. Exercises of energy transition scenarios to clean energy in Mexico

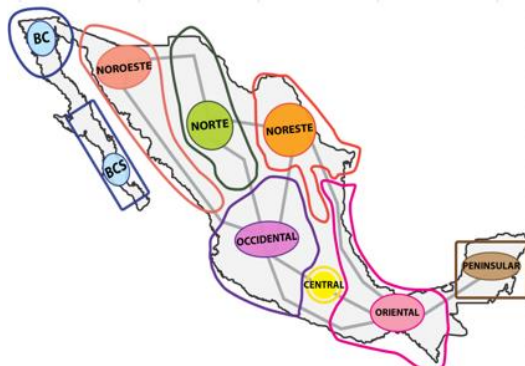
The present study compares two long-term energy transition scenarios in which a large amount of renewable energy is added. The first scenario does not consider new nuclear in the future, and the second does. The objective is to analyze how the inclusion of a small capacity of nuclear can improve the sustainability of the Mexican power system.

3.2.1. Methodology and common assumptions

The scenarios were created using SIMPLEX, a linear programming solver available in Excel. The objective function is based on the following assumptions to build the two scenarios:

- A modelling period from 2022 to 2050. The base year is 2021. Results are presented from 2030 to 2050.
- A simplified model of the national electrical system is used. This is represented by nine control regions, seven of which are in the national interconnected system (NIS) and the

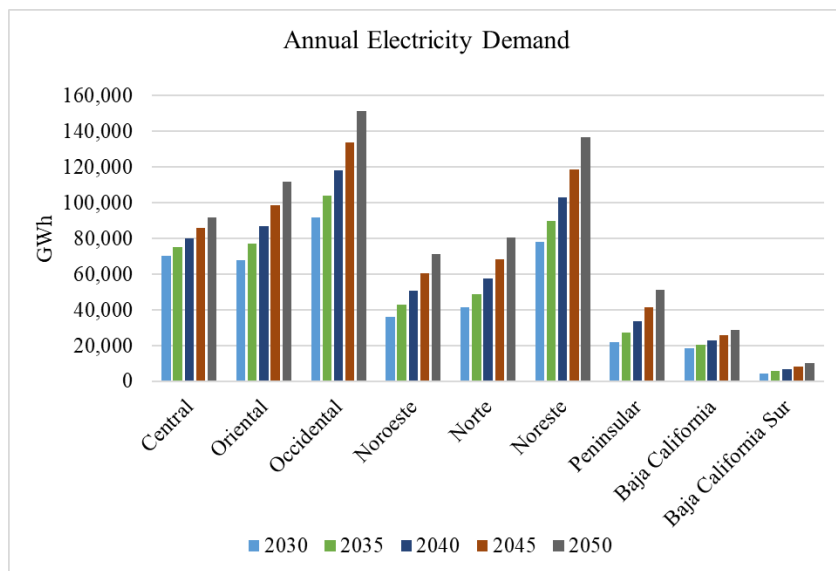
other two correspond to the isolated systems of Baja California (BC) and Baja California Sur + Mulegé (BCS). See Figure 2.



Source: Energy Planning Unit

Figure 2. Energy system representation in the model

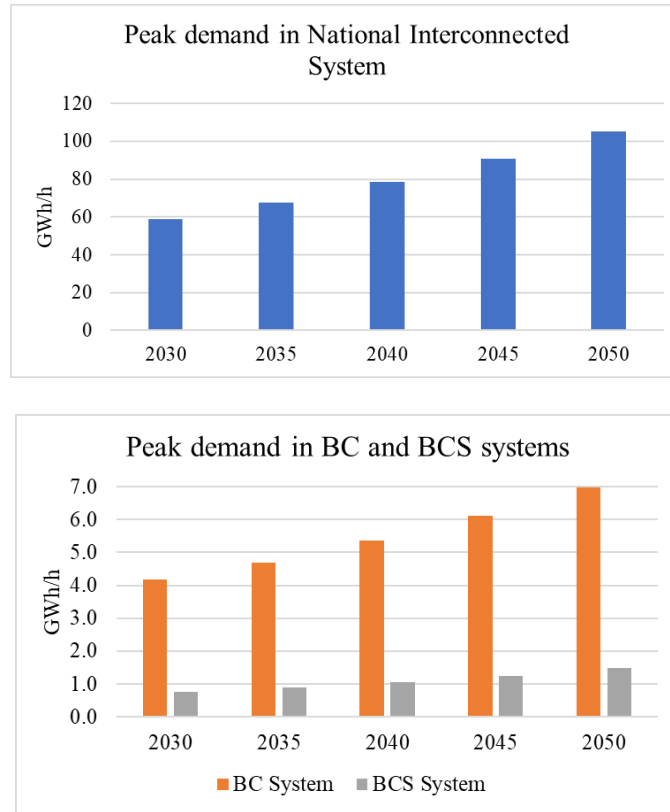
- c) Ten transmission links between regions are considered, as seen in Figure 2.
- d) The scenario considers the installed capacity in 2021, and the addition and withdrawal program established in PRODESEN 2021 is considered.
- e) The optimization model installs the capacity necessary to meet the proposed annual energy consumption in the SEN control regions. Energy demands in each region are the main constraints and are shown in Figure 3. The energy demand excludes the PV solar distributed generation. More scenarios could be generated by varying these restrictions.



Source: Calculated using historical data from PRODESEN and an exponential tendency.

Figure 3. Annual electricity demands by region

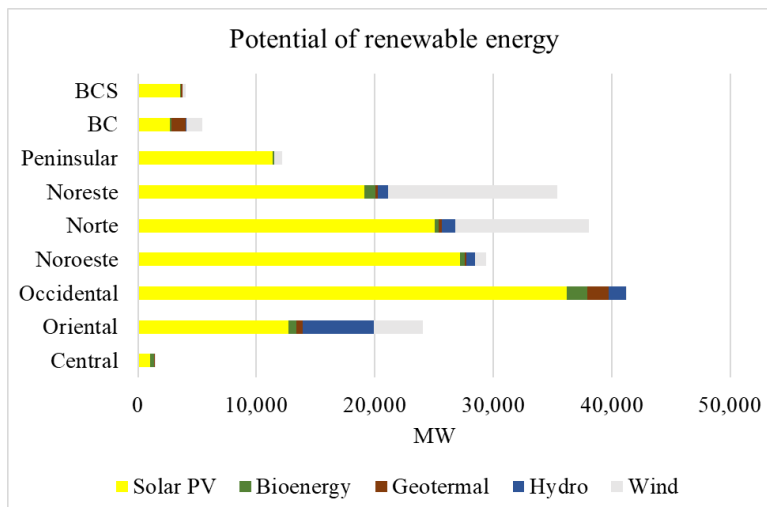
- f) The capacity to be installed must also meet the peak demands in each of the three systems: National Interconnected, Baja California and Baja California Sur with a reserve margin of 6% under the assumption that solar and wind energy are unavailable. Figure 4 shows the peak demands in each region.



Source: Calculated using historical data from PRODESEN and an exponential tendency.

Figure 4. Peak demand in each region

- g) The model considers energy lost in the transmission networks by exchange between regions. It also uses transmission capacity restrictions with data from PRODESEN documents. More scenarios could be generated by varying these capacities.
- h) Costs and parameters of technologies are generic, values from CFE reference documents. It considers the energy uses of the plants.
- i) It considers the installation of battery-based energy storage, which can serve as support to provide flexibility in the electrical system when the penetration of intermittent solar and wind energy increases. For every 100 MW of new wind or solar capacity, the model installs 10 MW of batteries and considers 10% losses in the battery charging process.
- j) Restrictions were imposed so the model does not install more nuclear capacity than is considered realistic considering the planning and construction time of new nuclear plants in Mexico. More scenarios could be generated by varying these restrictions.
- k) Realistic renewable energy potentials were considered: solar, wind, hydropower, geothermal and bioenergy. Figure 5 shows these renewable potentials in each region. More scenarios could be generated by varying these potentials.



Source: Information from Reference [8]

Figure 5. Renewable potentials considered

- l) The possibility of including marine energies was considered despite the high costs.
- m) A restriction was applied to meet the clean energy goals that Mexico has committed to. The aim was to reduce CO_{2eq} emissions.
- n) The combined cycle plants fueled with natural gas and hydrogen are not included, all the other technologies used in the CENACE scenario are incorporated.

3.2.2. Energy transition scenario without nuclear

This is an exercise to decarbonize the power sector without nuclear in the future. This means that only renewables must satisfy the restrictions described in section 3.2.1.

Mexico has abundant renewable natural resources, especially solar and wind energy. The estimation of the potential for the use of renewable resources depends on numerous factors. Based on a review of the atlases of renewable energy, available on the Ministry of Energy website, the renewable energy potentials that can be added to what is already installed in 2021 were assessed. The potential by type of renewable energy and for each control region were used to obtain an optimistic, but reasonable, deployment of renewable energies in the national electrical system for 2030-2050. Like many countries in the world, which are transitioning to clean energies, Mexico, should largely use solar and wind as clean energies, because they can be installed by public and private electric enterprises. This section presents a transition scenario where nuclear energy is not considered an energy option. Figure 6 presents the evolution of the generating capacity resulting from this scenario and Figure 7 shows results for the installed capacity by 2050 in the scenario without nuclear.

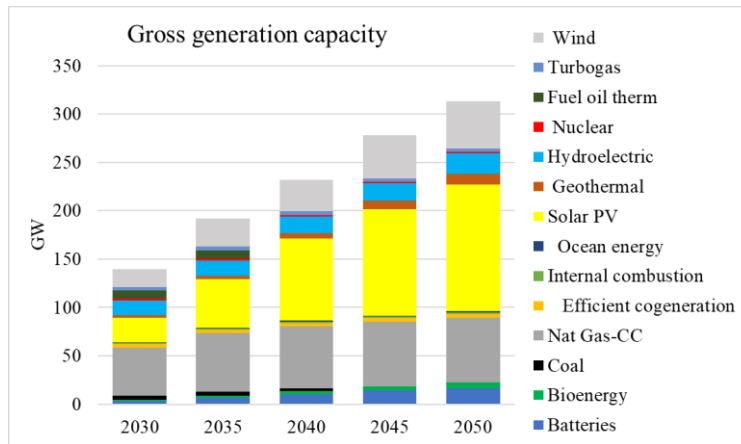


Figure 6. Capacity evolution in the transition scenario without nuclear

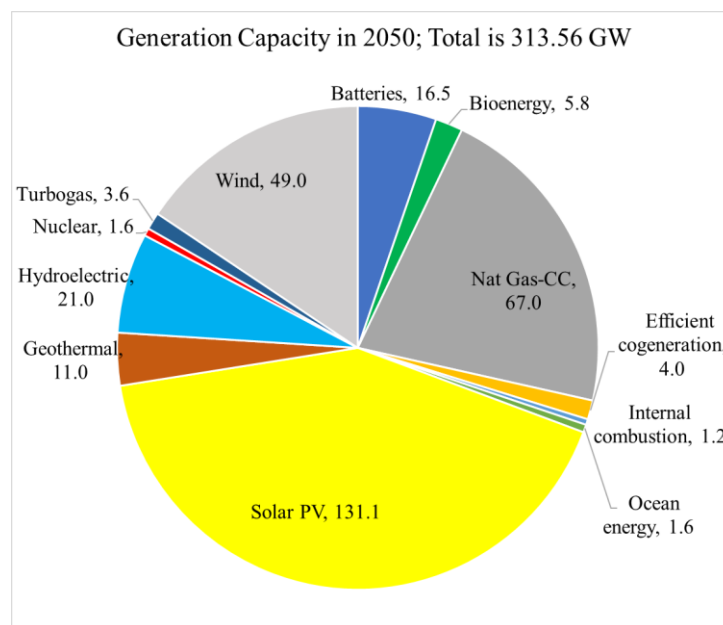


Figure 7. Installed capacity by 2050 in the transition scenario without nuclear

3.2.3. Energy transition scenario with renewables and nuclear

Nuclear capacity could be an excellent complement for wind and solar energy having intermittent or variable behavior. Nuclear capacity can be installed in Mexico with large or small reactor technologies as appropriate, considering the most suitable sites for nuclear energy to provide operational flexibility to the electrical system. Sites where conventional coal-electric and thermoelectric plants, which are the most polluting in the Mexican electricity generation park, could be replaced by modern and clean nuclear power plants.

For the transition to clean energy diversification in Mexico, SMR reactors represent the ideal. The use of SMRs is justified because the small capacity of SMRs can provide operational flexibility to the electricity system in terms of continuity of supply. The refueling outages of small nuclear units have a smaller impact than large plants. SMRs have advanced technology to regulate the frequency

and related services. Additionally, through cogeneration technologies, the heat generated can be redirected to industrial energy uses that are currently difficult to decarbonize. SMRs contain the energy to operate for at least 18 months without refueling and modern designs can operate for several consecutive years depending on fuel enrichment. SMRs are designed to operate preferably at 100% of their thermal capacity, distributing energy to electricity and thermal cogeneration uses, however, they can operate at lower power to follow the load demand. The exercise in planning an energy transition scenario with the implementation of nuclear energy focuses mainly on SMRs; however, the first reactors to be installed in the scenario are two large reactors because they have proven operation in other countries and can be planned for immediately in Mexico. Pending further discussion on the selection of the most suitable large nuclear reactor technology, the scenario with new nuclear capacity uses two AP1000 type reactors due to their advanced safety technology, their technological maturity, their capacity is less than others, and because the Laguna Verde site already has the basic infrastructure to house two reactors of that capacity in addition to the current reactors. The scenario considers that the LV1 unit will cease operations in 2050. The scenario studied starts installing nuclear power not before 2035 to give time for planning the nuclear roadmap. The resulting scenario is shown in Figure 8, and it reaches an installed capacity of 10,660 MW in 2050. A detailed graph for the year 2050 is presented in Figure 9.

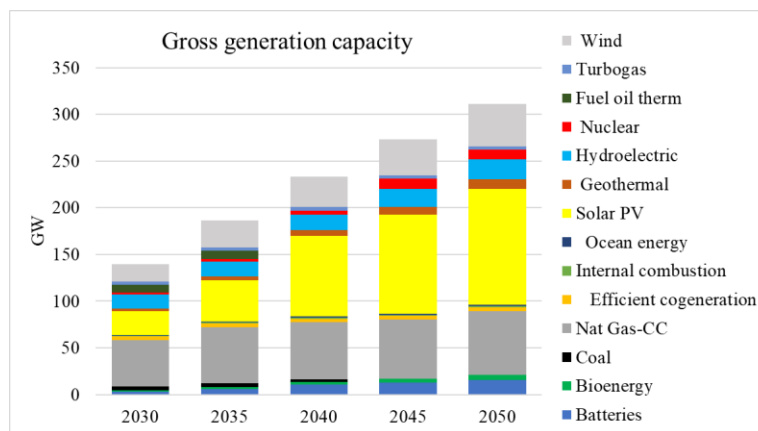


Figure 8. Generation capacity in the transition scenario with nuclear

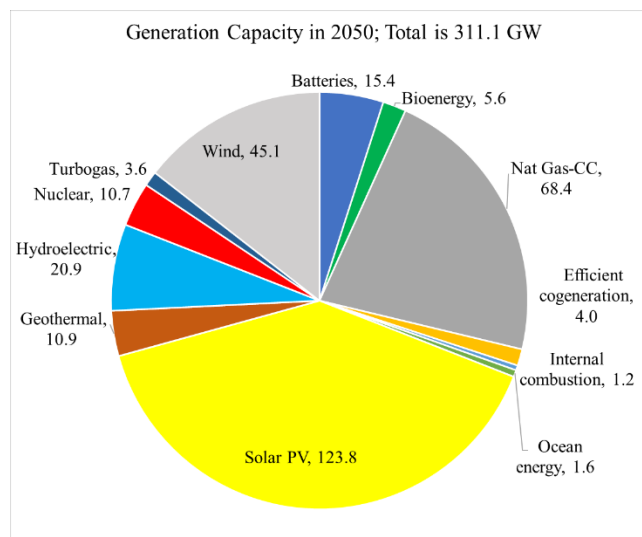


Figure 9. Generation capacity by 2050 in the transition scenario with nuclear

3.4. Comparison of Scenarios

Table II compares the two scenarios regarding the generation capacity, annual electricity production, clean energy participation, annual GHG emissions, and other key parameters.

Table II Comparison of scenarios

Parameters evaluated in the year 2050	Renewable Scenario with Nuclear	Renewable Scenario without nuclear
Inputs		
Electricity net demand BC (GWh)	28,631	28,631
Electricity net demand BCS (GWh)	10,302	10,302
Electricity net demand SIN (GWh)	694,576	694,576
Electricity net demand SEN (GWh)	733,508	733,508
Peak net demand BC (MW)	6,958	6,958
Peak net demand BCS (MW)	1,479	1,479
Peak net demand SIN (MW)	105,261	105,261
Outputs		
Total gross installed capacity (GW)	311.12	313.56
Electricity gross production SEN (GWh)	747.98	753,196
Electricity gross production BC (GWh)	29,533	29,575
Electricity gross production BCS (GWh)	10,302	10,487
Electricity gross production SIN (GWh)	707,944	713,134
Share of clean installed capacity (%)	76	77
Share of clean energy production (%)	84	78
Natural gas consumption (Thousands of millions m ³)	19.66	27.35
Annual GHG Emissions (Millions tCO _{2eq})	46.43	65.80
GHG Emission factor by (tCO _{2eq} /kWh net)	62.07	87.36
Emission of air pollutants SO ₂ +NO _x +PS (kg/GWh)	254.6	354.32
Share of intermittent capacity, solar+wind (%)	54.3	57.5
Capacity of batteries (%)	5.0	5.3
Annual losses in transmission (MWh)	5,161	7,621

4. CONCLUSIONS

By analyzing this exercise, it is observed that the use of nuclear energy in the Mexican power system can facilitate the insertion of renewable energies solar and wind and eliminate coal and oil in the mix. The scenario with nuclear progressively installs reactors in all the regions of the country, and in 2050 nuclear will contribute 3.4% of the total capacity and produce an average of 11.6% of the annual net electricity generation. This small portion of nuclear capacity has environmental advantages. To generate the same energy by 2050, in the transition scenario without nuclear, it is necessary to install 2,440 MW of additional capacity, compared to the scenario with nuclear. In the scenario with nuclear the share of clean energy is 84% versus 78% in the non-nuclear scenario. The annual GHG emissions are 29% lower, the consumption of natural gas is 28% lower, emissions of air pollutants are 28% lower, the capacity of batteries is 6% lower, and the transmission losses are 32% lower. Renewables with nuclear energy provide a better energy transition than the scenario with only renewable energy.

ACKNOWLEDGEMENTS

This study has been done on computers obtained with the budget of a PAPIIP-UNAM project no. IT102621, Modeling the energy transition to assess economic, environmental and social benefits in Mexico by 2030.

REFERENCES

1. Hannah Ritchie, “What are the safest and cleanest sources of energy?” Published online at *OurWorldInData.org*. Retrieved from: '<https://ourworldindata.org/safest-sources-of-energy>' [Online Resource] (2020).
2. United Nations, “Transforming our World: The 2030 Agenda for Sustainable Development”. [Online Resource] (2015).
3. “IAEA PRIS, Power Reactor Information System”. Last update on 2024-10-11. Retrieved from: <https://pris.iaea.org/pris/> (2024).
4. INPRO Membership | IAEA, <https://www.iaea.org/services/key-programmes/international-project-on-innovative-nuclear-reactors-and-fuel-cycles-inpro/membership>. (2024).
5. SENER, Programa de Desarrollo del Sistema Eléctrico Nacional (PRODESEN) Edición 2023-2037) (2023).
6. CENACE, Programa de Ampliación y Modernización de la Red Nacional de Transmisión y de los Elementos de las Redes Generales de Distribución que correspondan al mercado Mayorista PAMRNT 2021-2035. (2021).
7. IRENA and Bluerisk, Water for hydrogen production, *International Renewable Energy Agency*, Bluerisk, Abu Dhabi, United Arab Emirates. (2023).
8. Miguel Ángel Hernández Nava. Estado del arte y análisis de las estimaciones de potencial renovable en México y su posible integración en el Sistema Eléctrico Nacional. Tesis de Maestro en Ingeniería. Facultad de Ingeniería, UNAM. <http://132.248.9.195/ptd2022/noviembre/0833560/Index.html>. (2023).

Track 2

Reactor Physics, Fuel Cycle, and Non-Proliferation

BWR Fuel Lattices with Minor Actinides

Jose-Luis Montes-Tadeo, Eduardo Martínez Caballero, José Ramón Ramírez Sánchez

*Instituto Nacional de Investigaciones Nucleares
Carretera México-Toluca s/n, La Marquesa, Ocoyoacac,
Estado de México México CP 52750*

joseluis.montes@inin.gob.mx; eduardo.martinez@inin.gob.mx; ramon.ramirez@inin.gob.mx

Abstract

In this work, a method for carrying out the neutronic design of BWR fuel lattices is shown. Generated designs include a vector of minor actinides that were added to a pin in a typical 10x10 fuel assembly. This vector is composed of neptunium, americium and curium concentrations. The amounts of these concentrations were defined from the 3D simulation results of the nuclear reactor core operation. The choice of position in which the minor actinides were added is taken from previous results published by the same authors. So as to assess the proposed method, the main parameters of a fuel lattice used in the actual operation of a BWR reactor core were used as reference. The decision variables used of this design process were: average enrichment of U-235 [w/o], concentration of tri-oxide of gadolinium (w/o), neutronic multiplication factor in an infinite medium (k-infinity), and local power peaking factor of the fuel lattice. In addition to, a fixed average void fraction (%), and not presence of control rod is taken into account among other boundary conditions. Regarding to restrictions on decision variables, these include that k-infinity must be into the interval of ± 100 pcm with respect to reference value; the average enrichment of fuel lattice must be under the reference fuel enrichment but less than 1.0% with respect to the reference. A similar restriction is also assumed for the neutronic burnable poison concentration; local power peaking factor must not be greater than assumed reference. CASMO4 code was used for making the simulation of fuel lattices throughout the designing process. Obtained fuel lattices fulfilled each and every one of the restrictions imposed to them to be considered acceptable solutions. Finally, the differences between obtained results with respect to targets are into the intervals (0.00560, 0.84454), (-0.87566, 0.23360), (7.60838, 81.93513), and (0.14215, 1.77683) for average enrichment of U-235, (%), gadolinia (%), k-infinity (pcm), and Minimum Local Power Peaking Factor (%) of the fuel lattice, respectively.

1. INTRODUCTION

The neutronic design of fuel lattices has been addressed from different solution approaches [1, 2], among others. Furthermore, the transmutation of minor actinides has been studied in other works; i.e., [3, 4, 5, 6].

In the present work, an application of an evolutionary algorithm to the neutronic design when minor actinides are included into a BWR fuel lattice, is described.

The decision variables used in the design process were: a) average enrichment of U-235 (w/o), b) gadolinia concentration (w/o), c) k-infinity, d) local power peaking factor of the fuel lattice, and e) Np-237, Am-241, Am-243, Cm-244 concentrations (w/o).

2. METODOLOGY

The manner we proceed for making the designs of fuel lattice, taking into account the restrictions above mentioned, is described in the following.

The choice of pins inside of fuel lattice in which minor actinides are included was taken from reference [7]. In that work, it was found out that several locations showed an outstanding impact on the parameters on fuel lattice. The set of those locations is {v00, v05, v08, v26, v34, v45, v54}, Fig. 1.

In contrast to previous work [7], in present one, vector of minor actinides was not assumed as input data. In other words, the algorithm was looking for the concentrations to Np, Am, Cm isotopes. In such a way that, these added to the main decision variables a final solution to the design problem was obtained.

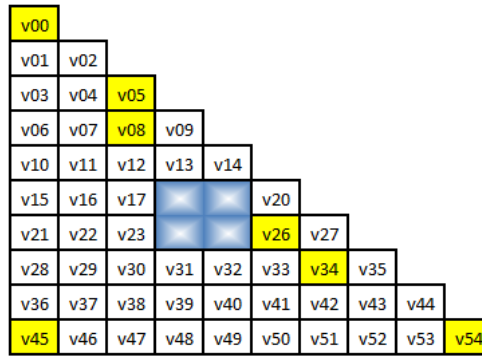


Figure 1. BWR fuel lattice with diagonal symmetry.

The evolutionary algorithm known as Differential Evolution (DE) [8] was used for carrying out the design process of fuel lattices. One of main reasons why this algorithm was selected is because it was created to work over continuous spaces. In the present paper, the concentrations of minor actinides are treated as continuous variables, as well as other decision variables.

The objective function (*OF*) used in the searching process is the following.

$$OF(x_n) = C + \sum_{n=1}^N w_n x_n \quad (1)$$

where w_n are selected according to the corresponding relative importance of x_n .

N stands for the number of main decision variables used in searching process. In this case, N was equal to 4.

C is an arbitrary constant value. In the present case, C was equal to 1.0.

In order to see details about how this algorithm works, we encourage readers to see reference [8].

3. RESULTS

Obtained results with the application of evolutionary algorithm are shown as follows.

Firstly, a representative series of obtained results is presented. This corresponds to fuel lattice that includes a vector of minor actinides in v00 fuel pin.

In Figure 2, the behavior of objective function (OF) throughout searching process is presented.

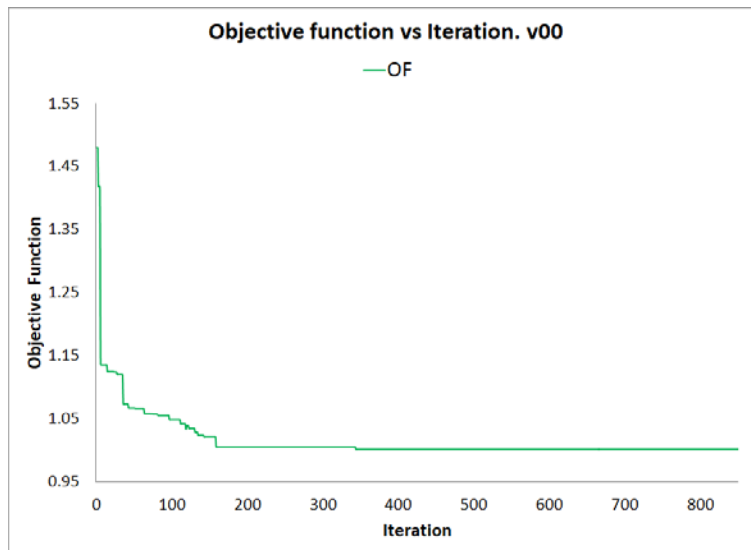


Figure 2. Objective function, v00

In Figure 3, the behavior of average enrichment of U-235 (w/o) of fuel lattice throughout of searching process is shown. R stands for the used reference value. This parameter must be inside the interval $(R \cdot 0.99, R)$ for being an acceptable solution.

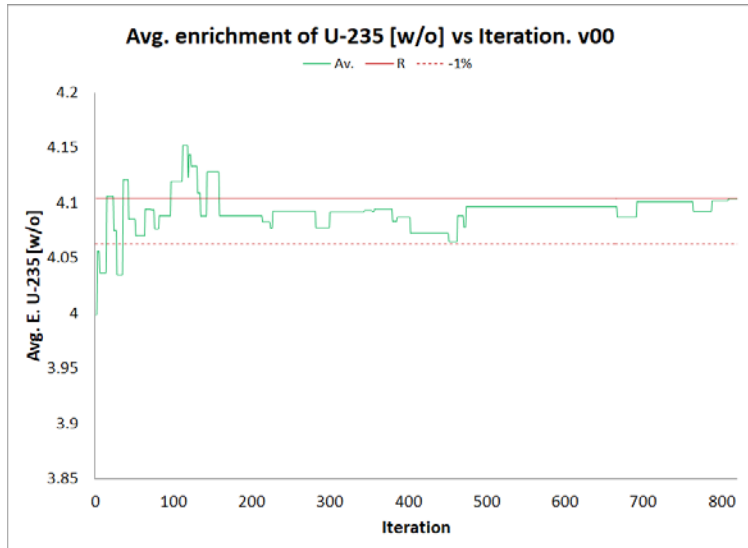


Figure 3. Average enrichment of U-235 (w/o) in the lattice, v00

In figure 4, the behavior of Gd_2O_3 concentration (w/o) of fuel lattice throughout of design process is shown. Acceptable solutions must be into the neighborhood defined by $\pm 1.0\%$ around R.

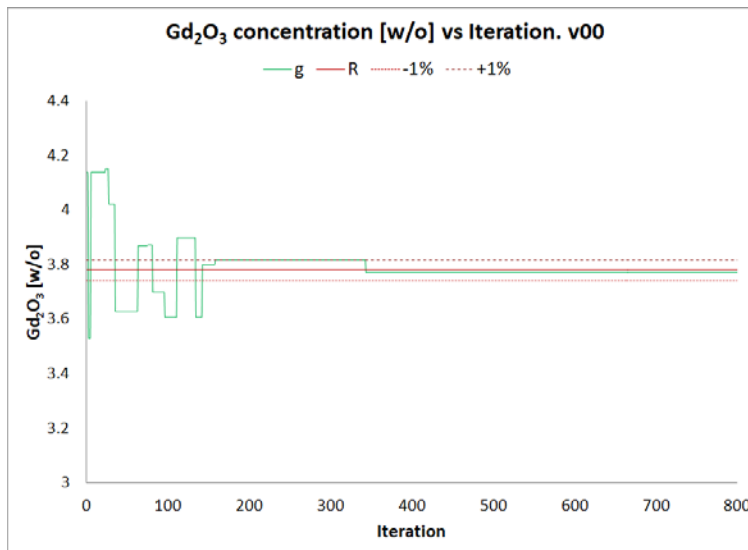


Figure 4. Concentration of Gd_2O_3 (w/o) in the lattice, v00

In figure 5, neutronic multiplication factor in an infinite medium of the fuel lattice is presented. This is the behavior of k -infinity throughout the searching process. For being considered as an acceptable solution, k -infinity must be into the interval $(R-100pcm, R+100pcm)$.

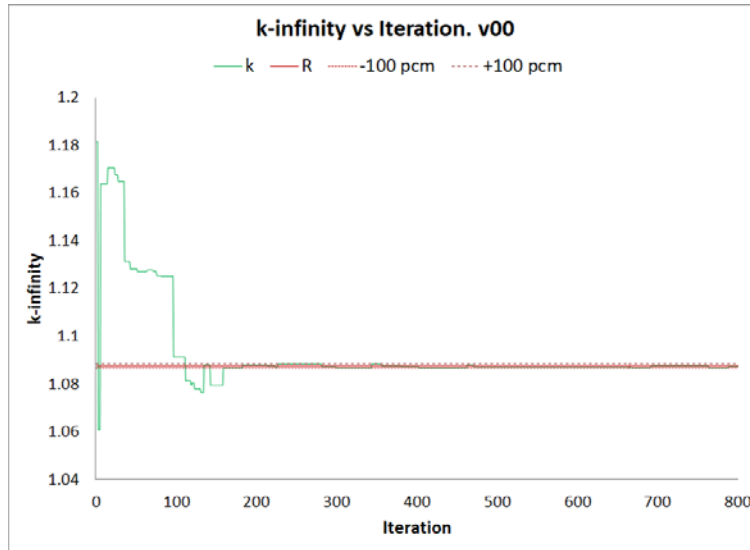


Figure 5. k-infinity of the lattice, v00

In figure 6, the behavior of the local power peaking factor of fuel lattice throughout the iterative process of design, is shown. In the case of LPPF, the established restriction consists of being less or equal to R reference value.

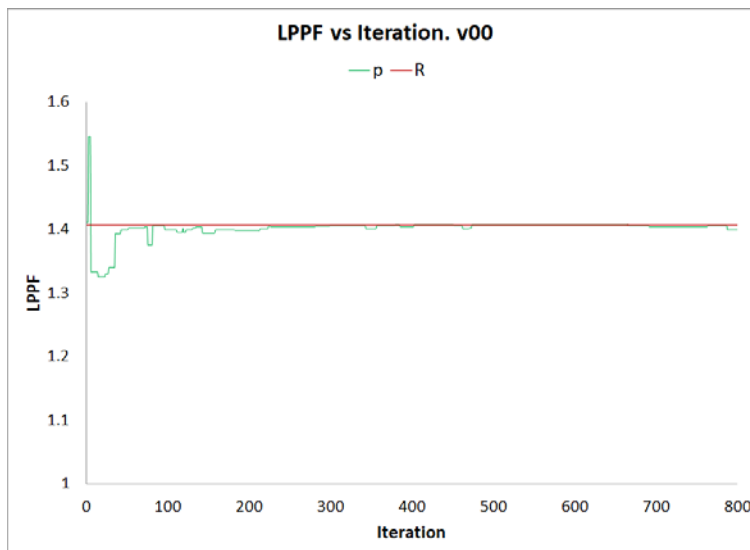


Figure 6. LPPF of the lattice, v00

In figure 7, the behavior of Np-237 concentration (w/o) added to pin v00 in the fuel lattice throughout the searching process is shown.

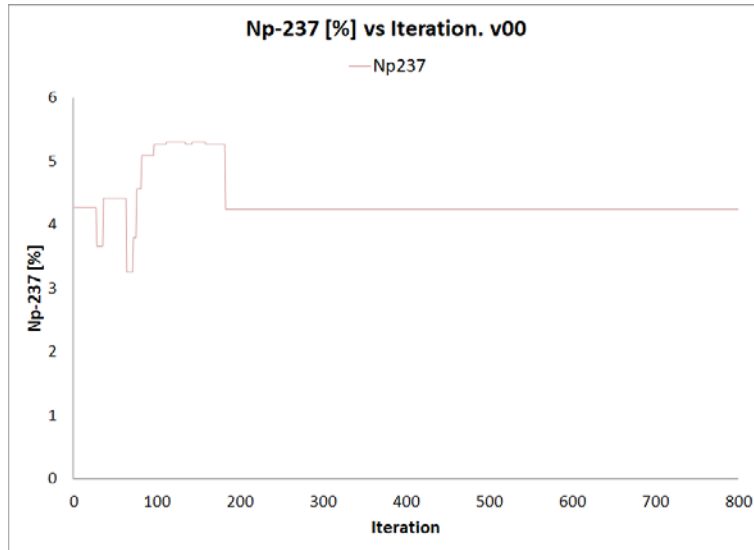


Figure 7. Np-237 (%) in the pin v00

In figure 8, the behavior of Am-241 concentration (w/o) added to pin v00 in the fuel lattice throughout the searching process is presented.

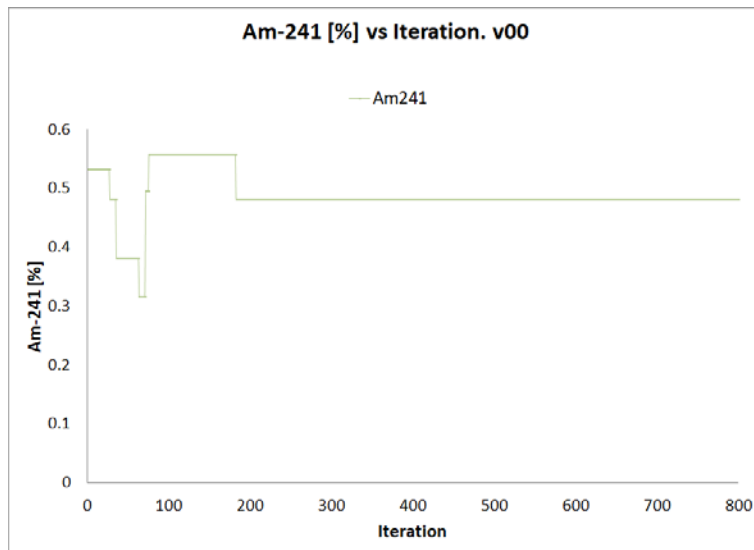


Figure 8. Am-241 (%) in the pin v00

In Figure 9, the behavior of Am-243 concentration (w/o) added to pin v00 in the fuel lattice throughout the searching process is presented.

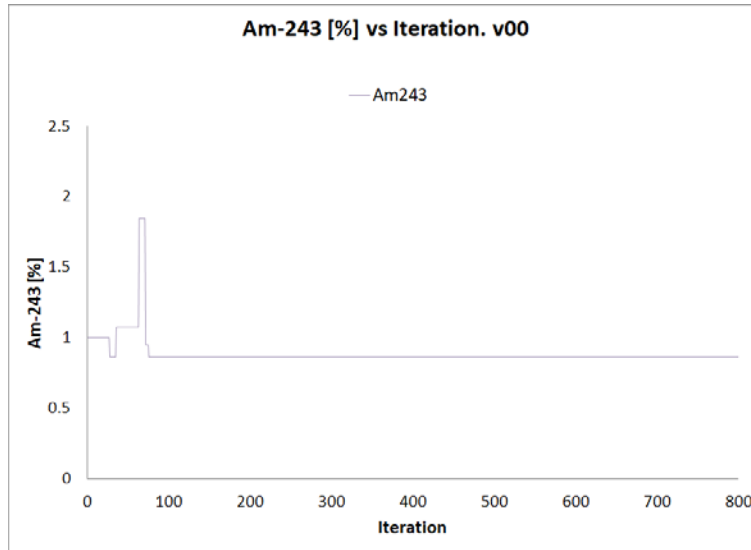


Figure 9. Am-243 (%) in the pin v00

In Figure 10, the behavior of Cm-244 concentration (w/o) added to pin v00 in the fuel lattice throughout the searching process is presented.

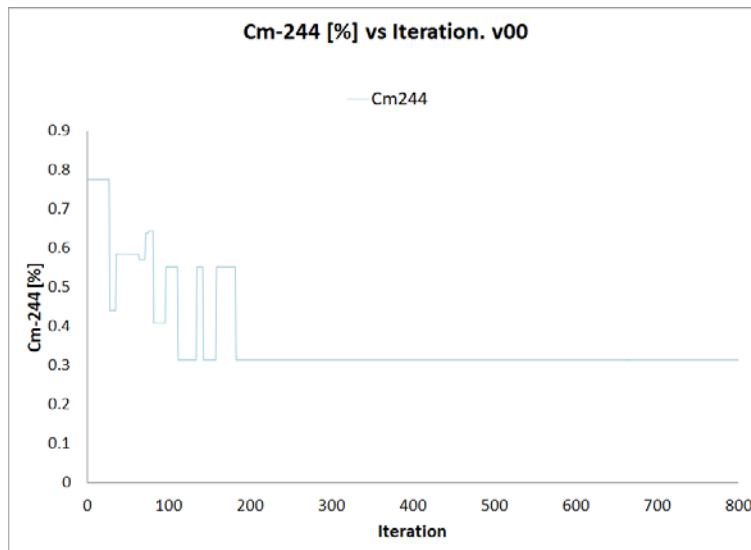


Figura 10. Cm-244 (%) de la varilla v00

A typical example of a designed fuel lattice is shown in Figure 11. In this figure, AcV stands for actinides vector, in red color. In UgG, U denotes uranium enrichment of pin [w/o], whereas G is the corresponding Gd_2O_3 content in the fuel pin, g indicates that pin has presence of gadolinia.

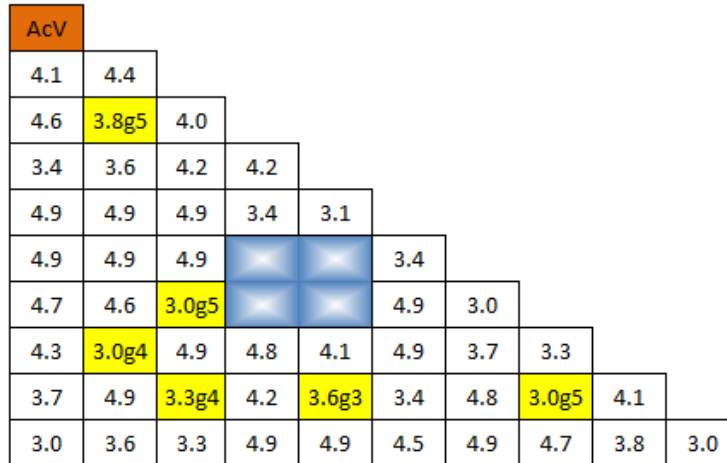


Figure 11. Fuel lattice with actinides vector in v00 position

In Table I, the differences of average enrichment of U-235 (w/o) between obtained results using the evolutionary algorithm with respect to reference are shown. EA, Ref stand for evolutionary algorithm and reference, respectively.

Table I. Differences in average enrichment of U-235 of the fuel lattice.

	Ref	EA	Δ
Lattice w/Act in	Avg. U-235 (w/o)	Avg. U-235 (w/o)	(Ref-EA)/Ref (%)
v00	4.104	4.10377	0.00560
v05	4.104	4.09663	0.17958
v08	4.104	4.10224	0.04288
v26	4.104	4.10334	0.01608
v34	4.104	4.06934	0.84454
v45	4.104	4.08622	0.43324
v54	4.104	4.10342	0.01413
Min		4.06934	0.00560
MAX		4.10377	0.84454

In Table II, the differences of Gd₂O₃ concentrations (%) between the obtained solutions by evolutionary algorithm against reference, are presented. EA and Ref stand for evolutionary algorithm and reference, respectively.

Table II. Differences in Gd₂O₃ concentration of the fuel lattice.

	Ref	EA	Δ
Lattice w/Act in	Avg. Gd ₂ O ₃ (%)	Avg. Gd ₂ O ₃ (%)	(Ref-EA)/Ref (%)
v00	3.78	3.77117	0.23360
v05	3.78	3.77117	0.23360
v08	3.78	3.77654	0.09153
v26	3.78	3.79430	-0.37831
v34	3.78	3.80854	-0.75503
v45	3.78	3.81310	-0.87566
v54	3.78	3.79885	-0.49868
min		3.77117	-0.87566
MAX		3.81310	0.23360

In Table III, the differences in pcm of k-infinity between the obtained solutions by the evolutionary algorithm with respect to the reference value, are shown. EA, Ref stand for evolutionary algorithm and reference, respectively.

Table III. Differences in k-infinity of the fuel lattice.

	Ref	EA	Δ
Celda c/Act en	k-infinity	k-infinity	(EA-Ref) (pcm)
v00	1.08757	1.08819	52.38775
v05	1.08757	1.08840	70.11846
v08	1.08757	1.08681	-64.29878
v26	1.08757	1.08766	7.60838
v34	1.08757	1.08844	73.49496
v45	1.08757	1.08854	81.93513
v54	1.08757	1.08812	46.47599
min		1.08681	7.60838
MAX		1.08854	81.93513

In Table IV, the differences of local power peaking factor between the obtained solutions by the evolutionary algorithm with respect to the reference value, are shown. EA, Ref stand for evolutionary algorithm and reference, respectively.

Table IV. Differences in LPPF of the fuel lattice

	Ref	EA	Δ
Lattice w/Act in	LPPF	LPPF	(Ref-EA)/Ref (%)
v00	1.407	1.402	0.35537
v05	1.407	1.402	0.35537
v08	1.407	1.382	1.77683
v26	1.407	1.401	0.42644
v34	1.407	1.405	0.14215
v45	1.407	1.391	1.13717
v54	1.407	1.401	0.42644
min		1.382	0.14215
MAX		1.405	1.77683

In Table V, the concentrations of minor actinides isotopes in different pins inside fuel lattices are shown. Here, M. Act stands for minor actinides.

Table V. Concentration of minor actinides in the pin.

Lattice w/M. Act in	Np237 (w/o)	Am241 (w/o)	Am243 (w/o)	Cm244 (w/o)
v00	4.24790	0.48093	0.86530	0.31429
v05	4.78935	0.48773	1.80678	0.64698
v08	2.77504	0.22305	2.16325	0.31429
v26	2.44181	0.24226	1.43785	0.78574
v34	5.30840	0.55782	1.73038	0.60348
v45	5.30840	0.32862	2.13376	0.31429
v54	2.12336	0.22305	0.86530	0.78574
min	2.12336	0.22305	0.86530	0.31429
MAX	5.30840	0.55782	2.16325	0.78574

4. CONCLUSIONS

The application of the evolutionary algorithm used in this work; it has permitted to obtain the expected results for the BWR fuel lattice design. Generated fuel lattices content a vector of Np-237, Am-241, Am-243 and Cm-244 concentrations (w/o) added to chosen locations inside the 10x10 fuel pins array. So as to assess the present application the main parameters of a fuel lattice used in the actual operation of a BWR reactor core were used as reference. The differences between obtained results with respect to targets are into the intervals (0.00560, 0.84454), (-0.87566, 0.23360), (7.60838, 81.93513) and (0.14215, 1.77683) for average enrichment of U-235, (%), gadolinia (%), k-infinity (pcm), and Minimum Local Power Peaking Factor (%) of the fuel lattice, respectively. According to the excellent obtained results, the application of present evolutionary algorithm is expected to be taken in to account in order to get a greater scope in this important topic.

Finally, the objective of the rods with minor actinides is their mass reduction through recycling, so the above does not replace the use of enriched uranium. In addition, this work is a preliminary study to improve the design of possible fuel assemblies with minor actinides incorporated in some rods.

ACKNOWLEDGEMENTS

Authors thank to Instituto Nacional de Investigaciones Nucleares (ININ) the support through projects SN-003 and CA410.

REFERENCES

1. J. L. Francois, C. Martín-del-Campo, R. Francois, L. B. Morales. “A practical optimization procedure for radial BWR fuel lattice design using tabu search with a multiobjective function”, *Annals of Nuclear Energy*, **30** (12) p. 1213-1229 (2003).
2. J.-L. Montes-Tadeo, R. Perusquía-del-Cueto, D. A. Pelta, J.-L. François, J.-J. Ortiz-Servin, C. Martín-del-Campo, A. Castillo, “A hybrid system for optimizing enrichment and gadolinia distributions in BWR fuel lattices”, *Progress in Nuclear Energy*, **119**, 103172 (2020).
3. Eduardo Martínez C., J. Ramón Ramírez S., Gustavo Alonso V. “Análisis de La Reducción de Radiotoxicidad basado en el Reciclado de Actínidos”, Tesis Doctoral, Escuela Superior de Física y Matemáticas – IPN, Diciembre de 2015.
4. F. Martín-Fuertes, “Technical notes with the specifications for calculations involving minor actinides recycling”, WP4 SP2.1, CIEMAT, July 2009.
5. Daniel Westlén, “Why Faster is Better - On Minor Actinide Transmutation in Hard Neutron Spectra”, Doctoral Thesis Stockholm, Sweden 2007.
6. J. Ramon R., G. Alonso, E. Martinez, R. Castillo , J. C. Palacios, Analysis of actinide recycling in a Boiling Water Reactor using CASMO-4/SIMULATE-3, *Progress in Nuclear Energy*, Vol. 89 (2016) 26 – 38.
7. E. Martínez C., J. L. Montes-Tadeo, “Estudio del Contenido de Actínidos Menores en Celdas de Combustible BWR”, *34 Congreso Anual de la Sociedad Nuclear Mexicana. Reactores Modulares Pequeños, una nueva perspectiva para la Energía Nuclear en México*, La Paz, Baja California Sur, México, del 27 al 30 de agosto (2023).
8. Storn, R., Price, K., “Differential evolution - a simple and efficient heuristic for global optimization over continuous spaces”, *Journal of Global Optimization*, **11** (4), p.341-359. (1997).

Analysis of Plutonium Production in a BWR Reactor

*Hernández Flores Juan Enrique**

*Facultad de Ciencias. Universidad Autónoma del Estado de México
Campus El Cerrillo, Piedras Blancas, Toluca de Lerdo, Méx*

**uaemjuan@outlook.com*

Ortiz Servín Juan José; Castillo Méndez José Alejandro

*Departamento Sistemas Nucleares, Instituto Nacional de Investigaciones Nucleares
Carr Toluca - México s/n, 52750 La Marquesa, Méx.*

juanjose.ortiz@inin.gob.mx; alejandro.castillo@inin.gob.mx

Abstract

This work shows a preliminary analysis of plutonium production in a Boiling Water Reactor (BWR). Using the fuel loading and control rod patterns optimization systems, developed at National Institute of Nuclear Research (ININ in Spanish), 3 reactor operation schemes were designed, for an 18-months equilibrium cycle. The first one generates the highest amount of energy; the second case, which is a family of 12 operation schemes, reaches the energy requirements; and the last case, which is a family of 5 operation schemes, does not reach the energy requirements. This operation cycle consists of two fresh fuel loading batches with the same uranium enrichment, but different amount of gadolinia. In addition, one of them is loaded in the center channels of the reactor core and the other one towards the periphery channels. The simulation of the reactor under the established conditions was done using SIMULATE-3 code. To analyze the *.sum output files, a computer program was developed in Fortran 90 to read the plutonium concentration of each fuel assembly throughout the operating cycle. The Pu239 concentration of the three mentioned cases was compared. It was observed that the Pu239 production in the cases where the energy requirements are not reached is lower in the fuel assemblies near the periphery of the reactor core. This is due to the density of control rods in that region of the reactor core, for the same cases is higher than in the cases where the energy requirements are met. The conclusion is that the high control rod density in the periphery of the reactor core influences the plutonium production and therefore the energy production. As a recommendation, it is suggested that a penalty factor can be added to the control rod pattern optimization systems to reduce the density of control rods near the reactor periphery.

1. INTRODUCTION

A Boiling Water Reactor (BWR) uses enriched uranium as the main fuel [1]. Typically, in a BWR, the enriched uranium is composed of 4% U235 and 96% U238. The fission of U235 produces the most energy in the reactor. On the other hand, fast neutrons are absorbed by U238 to

form U239, which, through beta decays and neutron absorption, generates the plutonium isotope family Pu239, Pu240, Pu241 and Pu242 [2]. Since Pu239 generates the other isotopes, it is expected to be the one with the highest production.

The breeding of plutonium is a sensitive issue due to the possibility of it being extracted from spent fuel for the purposes of nuclear weapons manufacturing [3]. In specialized literature it can be found studies aimed at reducing residual plutonium in spent fuel or methodologies to determine in which nuclear reactor the plutonium was produced [4]. Another strategy that has been implemented for the use of plutonium produced in nuclear reactors is to extract it and combine it with uranium for the manufacture of mixed fuel (MOX) [5]. Fredrikson et al. [6] made a study of how plutonium production is affected in three pressurized heavy water reactors as a function of fuel rod thickness, fuel density, initial uranium enrichment and power density, among others. On the other hand, breeding plutonium in nuclear reactors helps improve the utilization of uranium.

During normal operation of the BWR reactor, at the beginning of the cycle, the production of the plutonium isotopes is favored in the top part of the core due to the generation of voids. At the end of the operating cycle, when the lower part of the core has been overexposed to neutrons, energy production is shifted to the top of the core by the remaining U235 and Pu239 produced since the beginning of the cycle. Figure 1 shows the axial power relative behavior through of the operation cycle.

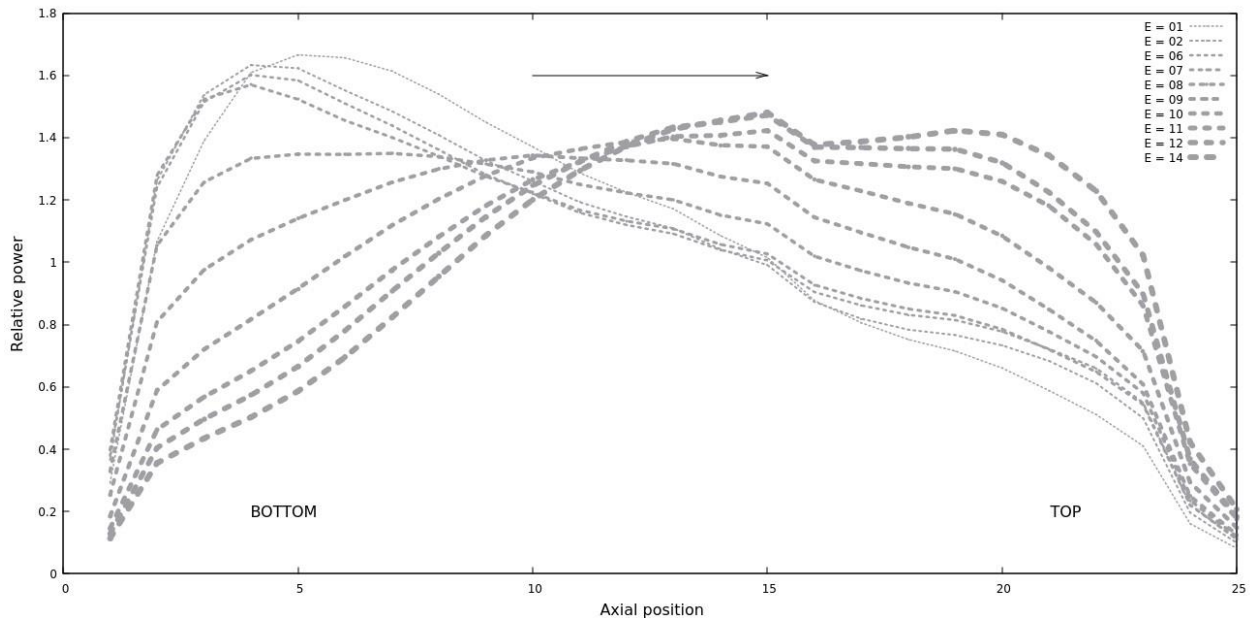


Figure 1. Axial power relative behavior through of the operation cycle

The control rods play a very important role in modeling of the axial power profile in the reactor core. The operating strategy called spectral shift favors a pronounced power peak in the bottom part of the core which helps to produce more plutonium in the upper part of the core. Consequently, the operating cycle produces more energy than without the spectral shift strategy.

The objective of this work is to show preliminary results of study the production of Pu239 by analyzing several control rod pattern schemes designed for an equilibrium operating cycle of a BWR reactor.

2. METHODOLOGY

An 18-month equilibrium cycle, consisting of a fresh fuel reloading fraction based on two batches, was used to conduct this study. R-type assembly with an average enrichment of 3.66% and 8 gadolinia rods at 5% from which 52 assemblies were loaded. Q-type assembly with average enrichment of 3.66% and 10 5% gadolinia rods from which 60 assemblies were loaded. Figure 2 shows the reactor positions where the Q- and R-type assemblies are placed for ¼ core symmetry.

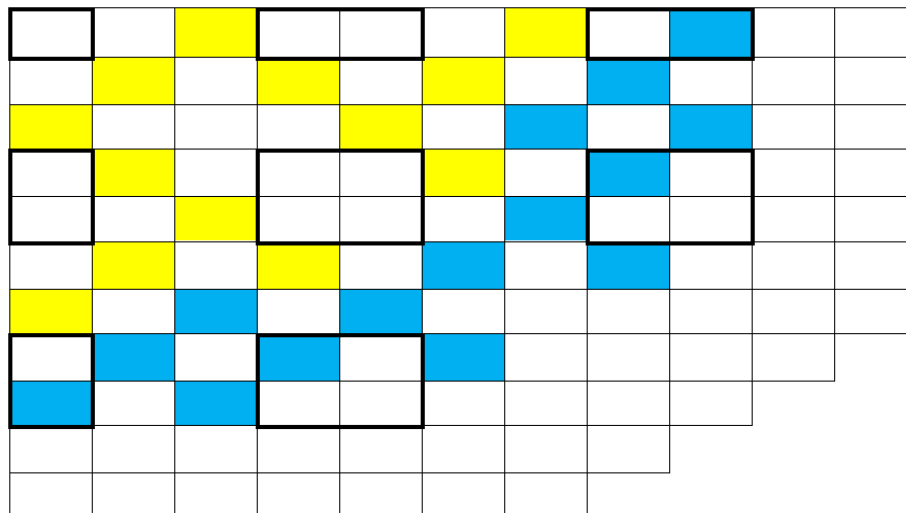


Figure 2. Location of fresh fuel assemblies type R (yellow) and Q (blue)

Control rod patterns and fuel loadings were designed for this operation cycle using Tabu Search [7] and Ant Colony Systems [8]. These operating scenarios were grouped under the following categories:

1. Optimal case denoted Max is the operation scheme with the highest energy production.
2. Twelve normal cases named BTG (Búsqueda Tabú General in Spanish), are operation schemes with acceptable energy production, but lower than the Optimal case.
3. Five non-optimal cases, named CHG (Colonia de Hormigas General in Spanish), refer to operation schemes with insufficient energy production according to the requirements.

The control rod patterns were designed for 12 burnup steps, for a cycle length of 11,846 MWD/KgU. Thermal limits throughout of the operating cycle in all scenarios are fulfilled.

All control rod pattern cases were simulated using SIMULATE-3 [9] code and the output files with the extension *.sum were obtained. For example, CHG01.SUM is the output file of the first

control rod pattern case of the non-optimal cases. The output files have information on the position of the control rods throughout the operating cycle and the production of the different plutonium isotopes.

To analyze the *.sum files, computer programs in Fortran 90 language were developed, compiled and executed in Ubuntu system. The *.sum files are formed by blocks of information containing a table with all the fuel assemblies of the reactor, their label identifiers and the specific weight of the produced isotopes such as neptunium and plutonium. The developed programs read the above information through the 12 burnup steps. The fuel assemblies are labeled with the following nomenclature NNT_{xxx}. Where NN is the cycle number in which that fuel assembly was first loaded, T is the type (R or Q) and xxx is a sequential number from 1 to 52 or 1 to 60, depending on the type. Since these are equilibrium cycles, the burnup history of the fuel assemblies over their lifetime can be reconstructed. The NN cycle represents the first burnup cycle of the assemblies, the NN-1 cycle represents the second burnup cycle of the assemblies, and so on. In this way, the developed programs build new information tables where the fuel type, the isotope concentrations and the fuel burnup from 0 to 50 MWD/KgU are included. There is a table for each of the cases of control rod patterns mentioned above. Figure 3 shows the behavior of plutonium isotopes over the lifetime of the fuel assemblies according to the Max case.

As can be seen, Pu239 shows the highest concentration of all. This is consistent with the production chain above mentioned. The 12 BTG cases have very similar behaviors among them and the 5 CHG cases have very similar behaviors among them. For this reason, the results shown below present average BTG and CHG behaviors.

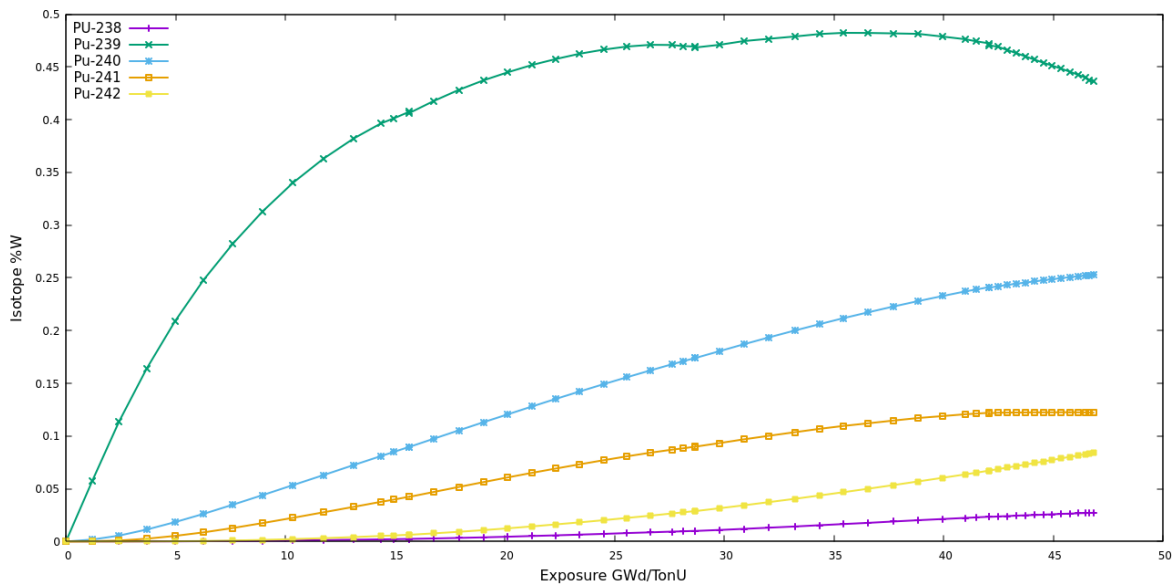


Figure 3. Plutonium isotope evolution in the core of the reactor core.

3. ANALYSIS OF PLUTONIUM PRODUCTION

To make the comparison of plutonium production of the CHG and BTG schemes against the Optimal Case (Max), the algebraic subtractions Max-BTGaverage and Max-CHGaverage were made for the R and Q assemblies of the Pu239 concentration. If the value of the subtraction is negative, it means that the BTG or CHG schemes produce more plutonium than the Optimum Case. The value of this subtraction, through the fuel burnup, is shown in Figure 4.

In Figure 4, it is observed that in the Q assemblies, loaded at the periphery of the core, less plutonium is generated in the CHG and BTG schemes than in the Optimal Case. This difference is more noticeable in the early burnup steps. On the contrary, in the R assemblies, the negative value of the subtraction points to higher plutonium production in the BTG and CHG assemblies compared to Max ones. It is inferred that the CHG schemes generate even less plutonium in the periphery assemblies than the BTG schemes.

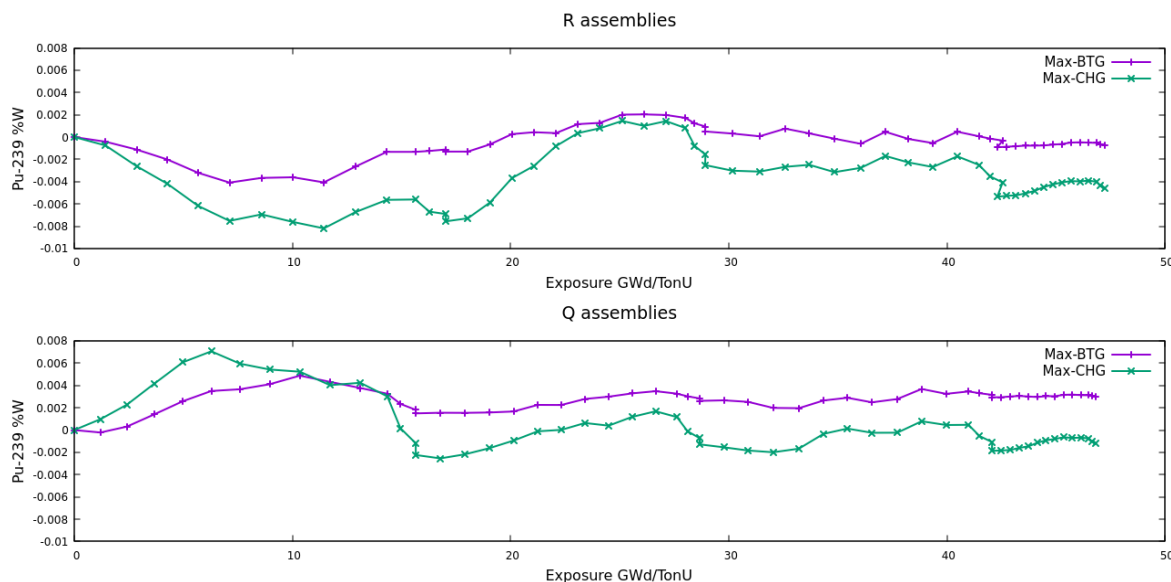


Figure 4. Comparison of Pu39 production: Max-BTG and Max-CHG.

Thus, it is the higher plutonium generation in the periphery fuel assemblies that achieves the reactor power requirements more easily.

To observe the influence of the control rods on plutonium production, new programs were designed to capture the control rod density from the *.sum files for each burnup step. Since the largest differences in plutonium production occur in the first operating cycle, only the behavior up to 12 MWD/KgU was considered. The reactor core was divided into two radial regions according to the distribution of the fresh fuel assemblies of the types Q and R. In Figure 2 the fuel assemblies surrounding the control rods of Sequence A2 are highlighted with thick line. In that Figure 2 the fresh fuel assemblies of the type R are in the center of the reactor and that there are 4 control rods (at 1/4 of the reactor core) controlling them. The Q-type fresh fuel assemblies

are located away from the reactor core and are controlled by another 4 control rods (at $\frac{1}{4}$ of the reactor core).

Figure 5 correlates the Pu239 production in the Q-type assemblies' region against the R-type assemblies' region for the Max, CHG-average and BTG-average cases. If the resulting lines have a slope at 45° it means that plutonium production occurs at the same rate in the two defined regions. If the curves are concave, it means that plutonium production in the R region occurs at a higher rate than in the Q region. Finally, if the curves are convex, plutonium production in the R region occurs at a lower rate than in the Q region.

Figure 5 shows that plutonium production occurs at a higher rate in the R region than in the Q region in all three schemes. But, in addition, plutonium production in the R region occurs at a higher rate in the CHG cases than in the other two. In other words, there is less plutonium production in the Q region of the CHG cases than in the other two. This could be the reason that the CHG cases do not meet the energy requirements. To understand why less plutonium is produced in the Q region of the CHG cases, the control bar patterns are analyzed below.

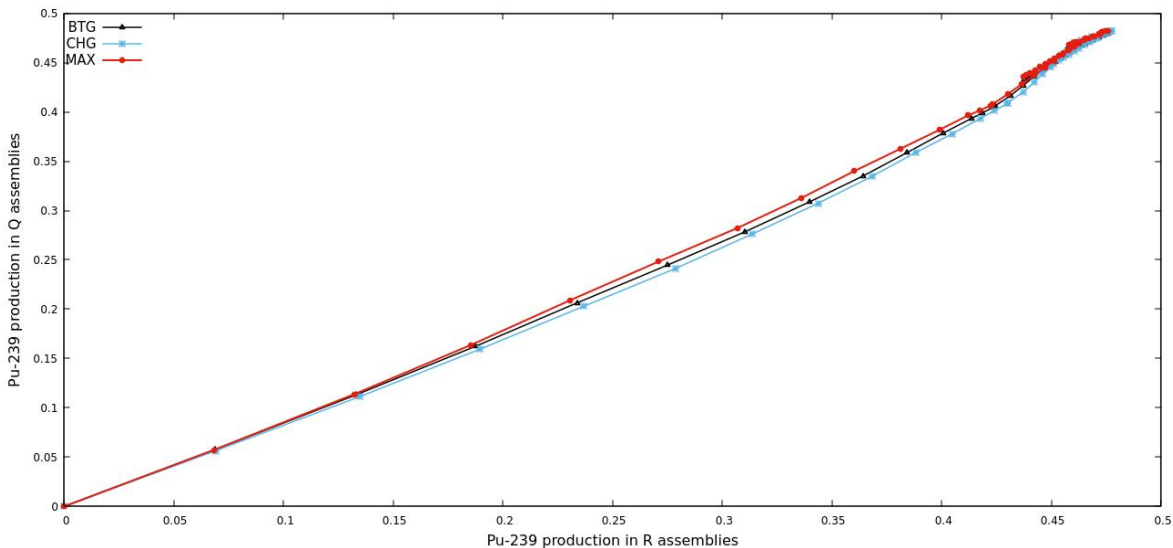


Figure 5. Comparison of Pu239 production in the Q and R fuel assemblies.

Control rods are introduced into the reactor from its bottom. They can be placed in 25 axial positions. A control rod totally inside the reactor is at position 00 and a rod totally outside the reactor is at position 48. The rods are placed in even numbers or notches, i.e. 00, 02, 04, ..., 46 and 48. It is assumed that the control rod patterns are designed applying a CCC type refuel, so only the control rods of Sequence A2 are used. The control rod density within the reactor core is defined as the number of control rod insertion notches used, divided by $24 \times \text{NBR}_i$ (number of control rods in radial region $i = R, Q$). NBR_Q equals 12 and NBR_R equals 9. This was done for each burnup step of the 3 operating schemes under study. A control rod density of 0 means all control rods are withdrawal. A control rod density of 1 means all control rods are fully inserted in the core.

Figure 6 shows the control rod density in the regions of the fuel assemblies Q and R. From the figure the control rod density in the R region is higher, in general terms, than in Q for all three cases. It should also be noted that the control rod density in the Q region of the CHG cases is higher than in the BTG and Max cases.

The control rods strongly model the behavior of the axial relative power profile of the fuel assemblies. This in turn, influences the production of voids in the upper part of the reactor core and consequently the plutonium production. As mentioned above, preliminary results of the study of plutonium production in a BWR reactor are presented in this work. In the following stages of the work, the shape of the axial power profile and the fraction of voids in the regions of Q and R assemblies will be analyzed.

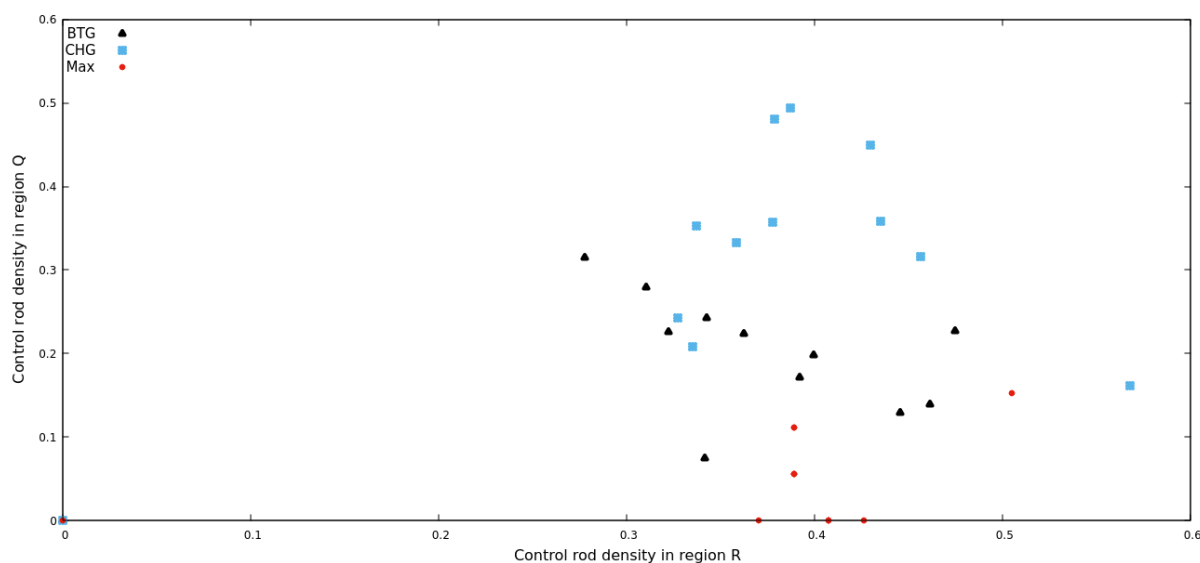


Figure 6. Comparison of Control Rod Density in Q and R assembly regions.

4. CONCLUSIONS

In this preliminary work, some interesting aspects of plutonium production in a Boiling Water Reactor were observed. Three cases of reactor operation were analyzed. In one of them, called Max, the highest amount of energy is obtained; the second case, called BTG, the energy requirements are reached; in the last case, the energy requirements are not reached. The three operation cases use two fresh fuel loading batches of two types called Q assemblies and R assemblies. Both have the same uranium enrichment but differ in the amount of gadolinia. In addition, the R-type assemblies are loaded at the reactor center and the Q assemblies are loaded at the periphery. The conclusions drawn are listed below:

1. In Q-type fuel assemblies more Pu239 is produced in the Max case than in the BTG and CHG cases.
2. In the R-type fuel assemblies, less Pu239 is produced in the Max case than in the BTG and CHG cases.

3. The control rod density is higher in the Q-assemblies region than in the R-assemblies region in the CHG case.
4. It is finally concluded that the high control bar density in the Q-assemblies region reduces the Pu239 production.

As feedback to the optimization systems developed at ININ, a term can be added in the objective function that penalizes control rod patterns with high rod density in the peripheral regions of the reactor.

Future work will include analysis of how plutonium is produced in the fuel assemblies that make up a control lattice, i.e., the control rod and the four fuel assemblies that surround it.

ACKNOWLEDGEMENTS

The authors wish to thank the National Institute for Nuclear Research for the support provided through the SN-003 project, for the development of this work. Similarly, student Juan Enrique Hernández Flores is particularly grateful to ININ for allowing him to develop his thesis work.

REFERENCES

1. Harvey W. Graves Jr. 1979, "Nuclear Fuel Management", John Wiley & Sons. ISBN 0-471-03136-4.
2. International Atomic Energy Agency, "Technical approaches for the management of separated civilian plutonium", IAEA Nuclear Energy Series No. NF-T-4.11.
3. Korobeynikov, V.V., Tikhomirov, B.B., Oussanov, V.I., Iougai, S.V., Pshakin, G.M., Chebeskov, A.N. (2004). Study of Proliferation Risk for Nuclear Fuel Cycles with Plutonium Breeding. In: Spitzer, C., Schmocker, U., Dang, V.N. (eds) Probabilistic Safety Assessment and Management. Springer, London.
4. J.M. Osborn, S.S. Chirayath, W.S. Charlton, "Neutronics Analysis of Fast Breeder Reactor Core to Support the Plutonium Fingerprinting for Forensics (PuFF) Project", INMM 54th Annual Meeting, 14-18 July 2013, Palm Desert, California, USA.
5. François J. L., Martín del Campo C., Hernández J. 2002. Design of an overmoderated fuel and a full MOX core for plutonium consumption in boiling water reactors. *Annals of Nuclear Energy*, Volume 29(16), Pp 1953-1965.
6. Fredrikson S., Hallander A. and Hedberg I. 2023. Assessment of how design and operational parameters affect plutonium production of PWHR. A study of the Ågesta, NRX and Candu reactors. PhD Thesis. Uppsala Universitet.
7. Fuel Loading and Control Rod Patterns in a BWR Using Tabu Search. Alejandro Castillo, Juan José Ortiz, José Luis Montes, Raúl Perusquía. *Annals of Nuclear Energy*. Vol. 34(2). Pp. 207-212. 2007.

8. A new system to fuel loading and control rod pattern optimization in Boiling Water Reactors. Juan José Ortiz, Alejandro Castillo, José Luis Montes, Raúl Perusquía. Nuclear Science and Engineering. Vol. 157, Pp. 236–244. 2007.
9. Dean, D. W., Rempe, K. R. Umbarger, J. 2005, "SIMULATE-3. Advanced Three-Dimensional Two-Group Reactor Analysis Code. User's Manual", Studsvik Scandpower INC. SSP-95/15 - Rev 3, Sweden 2005.

Burnup Analysis of Fuel Assemblies from the Last Operating Cycles of a BWR

Daniela Alejandra Arroyo García^{1*}

Universidad de Guadalajara

Blvd. Gral. Marcelino García Barragán 1421, Olímpica, 44430 Guadalajara, Jal.

daniela.arroyo6474@alumnos.udg.mx

Juan José Ortiz-Servin; Alejandro Castillo

Instituto Nacional de Investigaciones Nucleares

Carretera Toluca-México s/n 52750 La Marquesa, Mex.

juanjose.ortiz@inin.gob.mx; alejandro.castillo@inin.gob.mx

Daniel Tonalli Castillo Salinas

Instituto Politécnico Nacional, Escuela Superior de Física y Matemáticas

Avenida Instituto Politécnico Nacional s/n, Edificio 9, Unidad Profesional Adolfo López Mateos, colonia San Pedro Zacatenco, Gustavo A. Madero, 07738, Ciudad de México

dcastillos1400@alumno.ipn.mx

Abstract

In this paper we present the discharge burnup analysis of fuel assemblies of three end-of-life operation strategies of a Boiling Water Reactor (BWR). For this paper, a transition stage of 6 operating cycles at the end of the reactor's useful life was studied. The operating cycles considered were from 36 to 41. The strategies consider the reduction of fresh fuel assemblies loaded in these operating cycles, reducing the average uranium enrichment in these operating cycles and finally, equal length of such operating cycles. These strategies were designed using optimization systems based on heuristics techniques such as tabu search and neural networks. For each strategy, 5 families of operation cycles were designed. A computer program was developed in R-Studio to read and organize the information contained in the *.sum output files of SIMULATE-3 code. The program tracks fuel assemblies throughout the 6 operating cycles and identifies their discharge burnup. In addition, it builds histograms that show the number of fuel assemblies and their discharge burnup. With the information obtained from this computer program, it is possible to determine which is the best operation strategy at the end of the reactor's useful life from the point of view of fuel assembly utilization. Maximum, minimum and average discharge burnup values of all fuel assemblies of each family and strategy are also obtained. It was observed that the third strategy is the one that presents the best results, as it manages to have a greater number of fuel assemblies with discharge burnup of approximately 45 MWD/KgU and minimizes the number of fuel assemblies with 1 or 2 operating cycles (burnups of 10 and 20 MWD/KgU). This strategy requires 712 fresh fuel assemblies along the 6 operating cycles, which means that 72% of the fuel assemblies are used properly. In the first strategy, 70% have good use; while in the second one, less than half are well used.

1. INTRODUCTION

During a normal operation of a Boiling Water Reactor (BWR) the fuel assemblies are shuffled through several operation cycles generating energy from the fission of uranium (U235). The operation cycle is the period in which the most used fuel assemblies are replaced by new ones, the generating electricity process takes place, and the operative flexibilities are implemented. Depending on the position in which assemblies are loaded inside the reactor core, these are burned in different ways. Fuel assemblies in the center of the core burn up more than those on the periphery. The burnup of a fuel assembly is understood as the amount of energy produced by mass of uranium contained in it. At the end of the operating cycle, the reactor is shut down to start a new operating cycle and so a new recharge process. In each operating cycle, between 1/3 and 1/4 of the assemblies of the core are replaced.

The ideal situation would be to burn up the fuel assemblies as much as possible to ensure the best utilization of the uranium. However, as it was mentioned above, fuel assemblies are burned up differently, which implies that this is not always achieved. Researchers of ININ have been working to solve this problem. Recently, different strategies have been designed to obtain the latest operating cycles for a BWR reactor and so it was necessary to analyze the discharge burnup of these strategies, some of these results have been presented in the Mexican Nuclear Society Congresses [1, 2]. With all the above, it is essential to determine the use of uranium and to quantify the burnup of the fuel assemblies that are extracted from the reactor core at the end of its useful life. In this case, this is the goal of this research.

The study was conducted for the last 6 operating cycles of a typical Boiling Water Reactor.

2. METHODOLOGY

As it was mentioned, some strategies were designed to solve the problem of the last operating cycles of a BWR reactor, under this premise, the goal is to analyze the burnup of the fuel assemblies of these strategies. It is assumed that the last operating cycle of this reactor will be cycle 41, it is also assumed that the reactor operates under equilibrium cycles of 18 months until cycle 35. These strategies are described below:

1. Strategy 1. Decrease uranium enrichment of fuel assemblies from cycles 36 to 41. The length of the cycles is not 18 months.
2. Strategy 2. Decrease the fresh fuel loading fraction in cycles 36 to 41. The length of the cycles gradually decreases.
3. Strategy 3. Operate cycles 36 through 41 with the same cycle length.

These strategies were previously designed using the optimization systems developed in the Department of Nuclear Systems of the ININ [3, 4]. For each strategy, 5 families of possible solutions were designed. These solutions were simulated with SIMULATE-3 [5] code.

To perform this analysis, a computer program was developed to read the *.sum output files of SIMULATE-3 code. The program was created with R-Studio and it consists of three parts. In the first one, the output file of SIMULATE-3 is processed to identify the name of the fuel assemblies and its respective burnup value to create a data table for each operation cycle, each family and each

strategy. In the second part, the system reads the table of each cycle to create a new table with the name of all fuel assemblies (from cycle 36 to 41) and their final exposure values. Finally, for the third part, the system takes this database and determines the maximum, minimum and average burnup values of each family, along with the corresponding histogram. With this, the burnup of all fuel assemblies of each strategy can be visually compared.

3. RESULTS

Figures 1, 2 and 3 show the histogram of the families of cycles 36 to 41 of each strategy. The X-axis shows the discharge burnup of the fuel assemblies used in cycles 36 to 41, according to a discretization in ranges of 5 MWD/KgU. The Y-axis indicates the number of fuel assemblies within each burnup range.

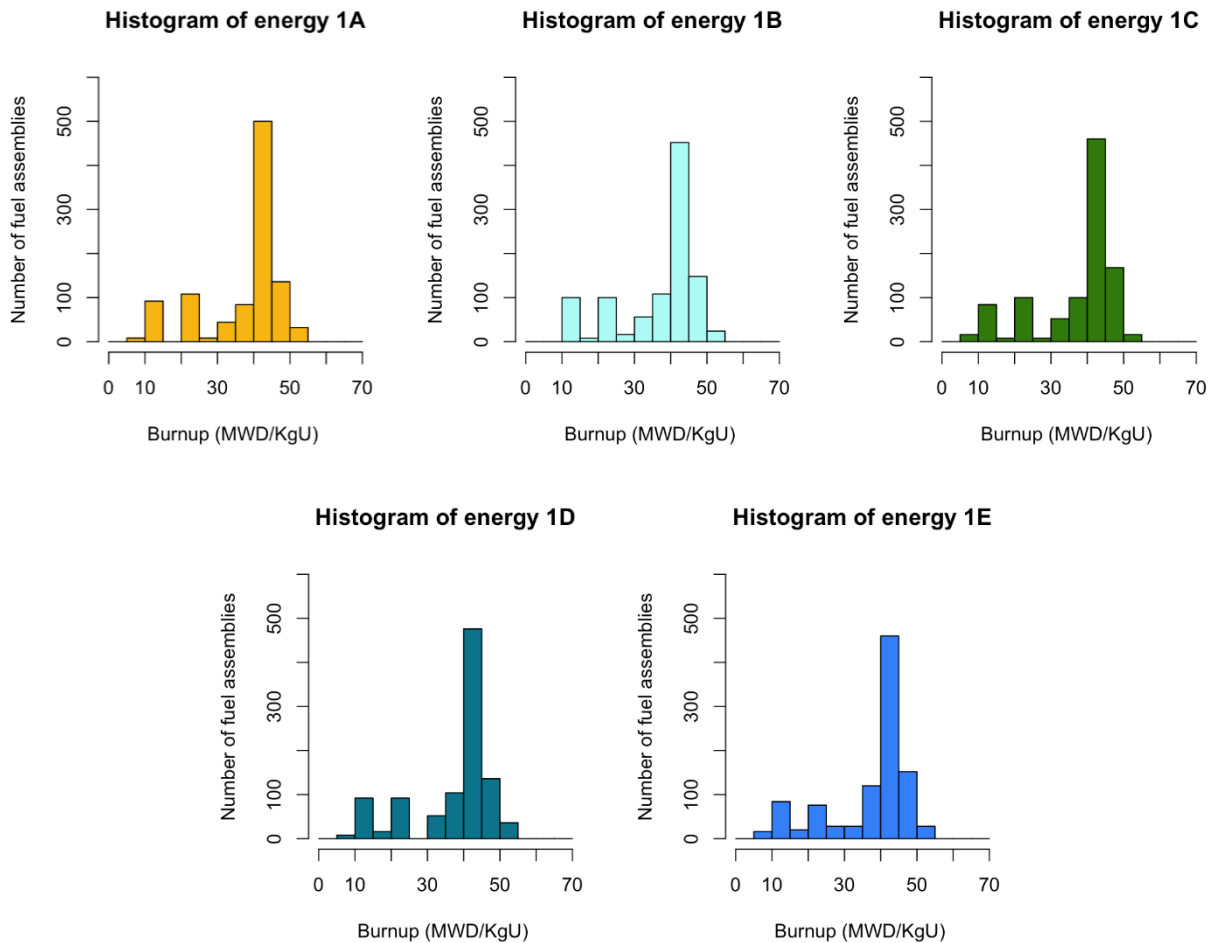


Figure 1. Histograms of Strategy 1 families.

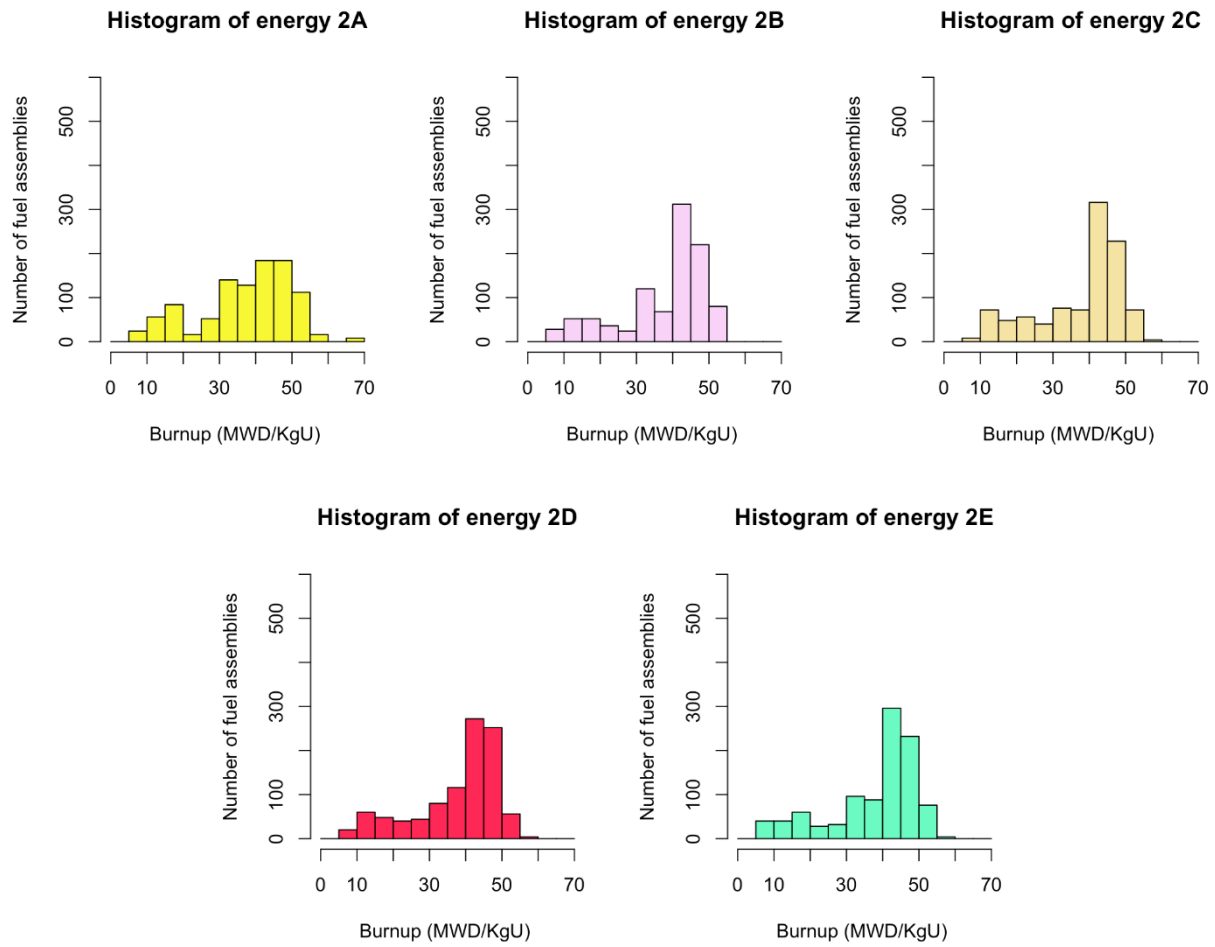


Figure 2. Histograms of Strategy 2 families.

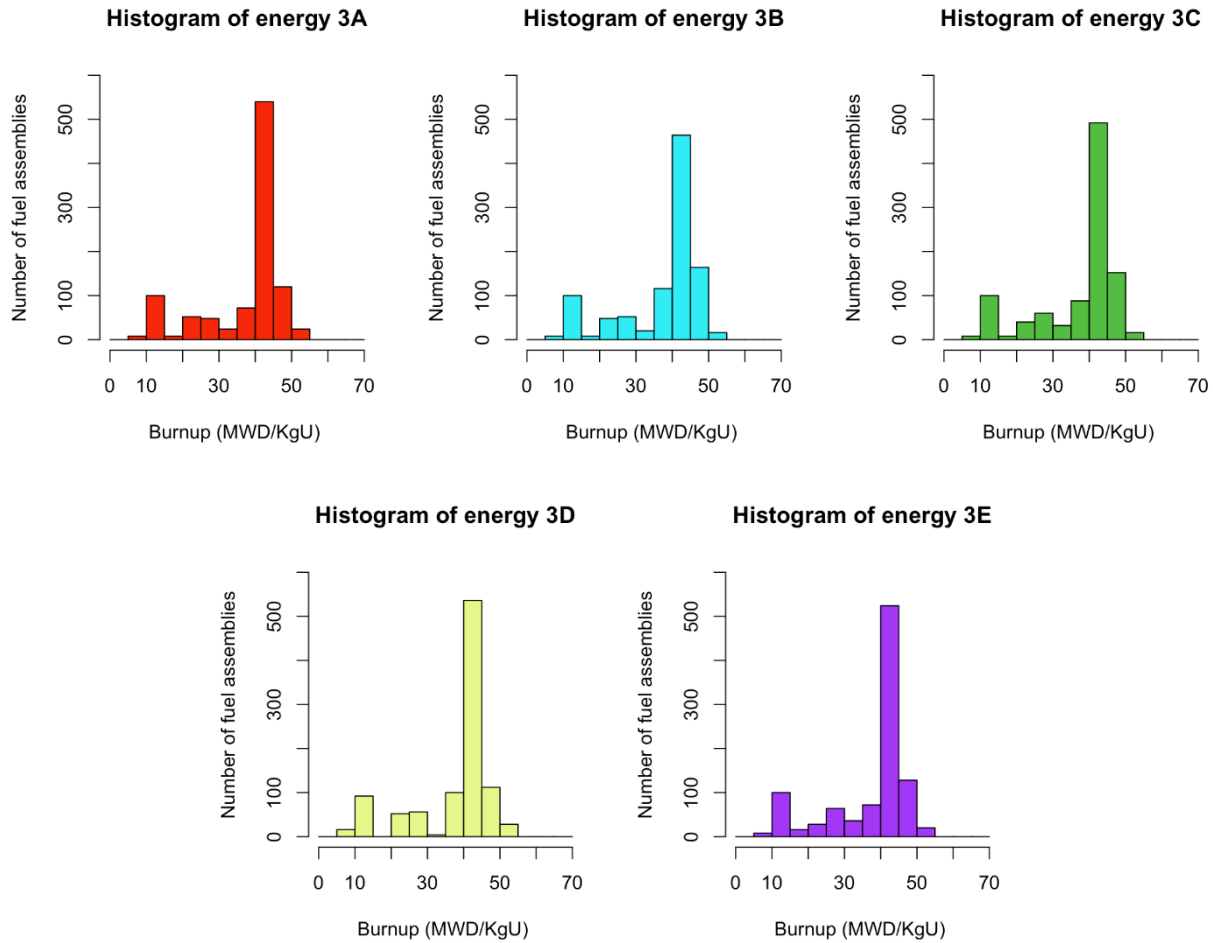


Figure 3. Histograms of Strategy 3 families.

Table I shows the maximum, minimum, and average discharge burnup of fuel assemblies for each family and strategy.

4. DISCUSSION

It is desirable to obtain histograms with a peak centered between 40 and 50 MWD/KgU of burnup (See Fig. 1, Family A). Under this situation, many fuel assemblies release their maximum available energy without exceeding the maximum burnup limit. In contrast, a histogram without peaks or more evenly distributed indicates that there are fuel assemblies that are not being used properly (see Fig. 2, Family A).

Table I. Mean, maximum and minimum exposure (MWD/KgU)

Family	<i>Average</i>	<i>Maximum</i>	<i>Minimum</i>
1A	37.145	53.057	9.521
1B	37.145	53.057	10.114
1C	37.145	53.057	7.810
1D	37.145	53.057	9.752
1E	37.145	53.057	6.794
2A	37.305	65.366	6.485
2B	37.756	54.945	8.245
2C	37.756	56.466	8.762
2D	37.756	56.699	8.710
2E	37.756	56.586	8.322
3A	37.696	53.057	9.544
3B	37.696	53.057	9.990
3C	37.696	53.057	8.171
3D	37.696	53.057	9.452
3E	37.696	53.057	8.009

From the histograms obtained, it is observed that the 5 families of Strategy 1 present peaks of 400 to 500 assemblies with burnup centered in the range of 40 to 45 MWD/KgU. There are two small peaks (approximately 100 fuel assemblies) centered at 10 and 20 MWD/KgU. These represent the fuel assemblies that are introduced in cycles 40 and 41. The E Family is the best one as its low peaks are appreciably of less than 100 fuel assemblies.

In Strategy 2, an almost uniform burnup distribution is observed in Family A, in the range between 30 and 50 MWD/KgU. In the rest of the families, there is a peak of approximately 300 assemblies in the range between 40 to 50 MWD/KgU. However, these peaks are not comparable to those in Strategy 1. The second highest concentration can be found at 50 MWD/KgU.

Strategy 3 resembles Strategy 1 in Families B and C where there are peaks of 400 to 500 assemblies at 45 MWD/KgU. However, in Families A, D and E, there are peaks with more than 500 assemblies in the 45 MWD/KgU, surpassing the peaks of Strategy 1. Most of the rest of the fuel assemblies are concentrated at 15, 35 and 50 MWD/KgU. Also, Strategy 3 achieves minimum burnup rates, higher than the other two strategies.

5. CONCLUSIONS

When comparing Strategy 2 with Strategies 1 and 3, it is clear that it does not achieve good use of fuel assemblies. In Family 2A it is even observed that there are fuel assemblies with an excessively high burnup. This means that this strategy, from the point of view of the discharge burnup analysis, must be rethought or discarded. Among Strategies 1 and 3, Strategy 3 turns out to be the best one, since it has higher peaks between 40 and 50 MWD/KgU.

Therefore, it is concluded that from the point of view of the discharge burnup analysis, Strategy 3 is the best option for the use of fuel assemblies at the end of the useful life of the nuclear power plant.

An important point as a future work is to conclude this analysis for all designed strategies and on the other hand, to support this research by doing an economic study.

ACKNOWLEDGEMENTS

The authors wish to thank ININ for the support provided through the SN-003 project, for the development of this work. Similarly, students Arroyo García and Castillo Salinas are particularly grateful to ININ for allowing them to develop their professional practices and their thesis work, respectively.

REFERENCES

1. José Alejandro Castillo Méndez, Juan José Ortiz Servín, José Luis Montes Tadeo, Raúl Perusquia del Cueto, José Luis Hernández Martínez, “Análisis de los últimos ciclos de la vida útil de un reactor nuclear BWR”, *XXXIII Congreso Anual de la Sociedad Nuclear Mexicana*, Veracruz, Veracruz, 13-16 de noviembre, p. 1-12 (2022).
2. José Alejandro Castillo Méndez, Juan José Ortiz Servín, José Luis Montes Tadeo, Raúl Perusquia del Cueto, “Últimos ciclos de operación para un BWR con patrones de barras de control”, *XXXIV Congreso Anual de la Sociedad Nuclear Mexicana*, La Paz, Baja California sur, 27-30 de agosto, p. 1-7 (2023).
3. Alejandro Castillo, Juan José Ortiz, José Luis Montes, Raúl Perusquia, “Fuel Loading and Control Rod Patterns in a BWR Using Tabu Search”, *Annals of Nuclear Energy*, **Vol. 34 (2)**, p. 207-212 (2007).
4. Juan José Ortiz, Alejandro Castillo, José Luis Montes, Raúl Perusquia, “A new system to fuel loading and control rod pattern optimization in Boiling Water Reactors”, *Nuclear Science and Engineering*, **Vol. 157**, p. 236–244 (2007).
5. W. D. Dean, *SIMULATE-3. Advanced Three-Dimensional Two-Group Reactor Analysis Code. User's Manual*, Studsvik Scandpower INC. SSP-95/15 - Rev 3, Sweden 2005.
6. Harvey W. Graves Jr., *Nuclear Fuel Management*, John Wiley & Sons, New York, USA (1979).

Development, Verification, and Validation of an Advanced Nodal Version of the AZKIND Code

Edmundo Leonardo Serrano Hernández, Edmundo del Valle Gallegos^{1}*
Instituto Politécnico Nacional, Escuela Superior de Física y Matemáticas
Av. IPN s/n, Col. Lindavista, México, Ciudad de México, 03020, México
eserranoh1500@alumno.ipn.mx; evalle@ipn.mx

Armando Miguel Gómez Torres
Instituto Nacional de Investigaciones Nucleares
Carretera Toluca – Estado de México s/n, 52750 La Marquesa, México
armando.gomez@inin.gob.mx

Abstract

The AZTLAN platform, to which AZKIND belongs, is a nationwide project led by the National Institute for Nuclear Research (ININ). This project aims to create a modeling platform for the analysis and design of nuclear reactors. The AZKIND code solves the time-dependent neutron diffusion equation for various energy groups in XYZ geometry. This is achieved through numerical methods, which are necessary due to the impossibility of obtaining an analytical result for most problems. Originally, AZKIND code used the Raviart-Thomas-Nedelec of zero index (RTN-0) nodal method to discretize the spatial variable. The advanced version of AZKIND, that is here described, together with some verification and validation exercises, includes an upgraded nodal method increasing the order to index 1 (RTN-1). The numerical results presented in this work demonstrated a higher accuracy in the solution.

1. INTRODUCTION

The computer code AZKIND (AZtlan KInetics in Neutron Diffusion) [1] calculates the solution of the time-dependent and stationary diffusion equation and is based on the multi-group diffusion theory. AZKIND uses the Galerkin finite element method and the Raviart-Thomas-Nedelec of zero index (RTN-0) nodal scheme to solve the equations with time dependence in cartesian coordinates. The RTN-0 nodal scheme is part of a series of finite element schemes developed in the last century by Hennart, J.P., et al [2]. These nodal methods use a simple representation of an otherwise complex system to classify small subdivisions of the problem referred to as "nodes". Each node is assumed to be homogeneous and assigned a value for each coefficient (average flux, material, etc.) that depends on its position. The objective of the nodal method is to deliver a specific value of the problem solution for each node. Nowadays, computational tools solve the neutron diffusion equation using nodal methods. These usually require complex and very fine

(*) Corresponding author: evalle@ipn.mx

meshing to deliver high-accuracy results. Implementing new nodal methods to the AZKIND code of the AZTLAN platform will increase its competitiveness against its counterparts, in addition to other features that make the project a worldwide reference.

2. THE DIFFUSION EQUATIONS AND THE FINITE ELEMENT METHODS TO APPROXIMATE THEIR SOLUTION

The central purpose of the AZKIND code is to determine how neutrons are distributed in the core of a fission reactor. This distribution can be modeled through the diffusion equation for various energy groups, either stationary or time – dependent.

Only in some cases it is possible to find an analytical solution to the diffusion equation, most of which are simplifications in which certain conditions of the problem are taken for granted. If the problem is not solvable analytically, a numerical method is used.

2.1. The Diffusion Equations

The time-dependent neutron diffusion equation is defined together with the system of equations for calculating the delayed neutron precursors in the system as follows [3]:

$$\begin{aligned} \frac{1}{v_g} \frac{\partial \phi_g}{\partial t} &= \nabla \cdot D_g(\vec{r}, t) \nabla \phi_g(\vec{r}, t) - \Sigma_{ag}(\vec{r}, t) \phi_g(\vec{r}, t) - \Sigma_{sg}(\vec{r}, t) \phi_g(\vec{r}, t) + \\ &\sum_{g'=1}^G \Sigma_{sg' \rightarrow g}(\vec{r}, t) \phi_{g'}(\vec{r}, t) + \chi_g (1 - \beta) \sum_{g'=1}^G v_{g'} \Sigma_{fg'} \phi_{g'}(\vec{r}, t) + \chi_g \sum_{i=1}^I \lambda_i C_i(\vec{r}, t) \\ \frac{\partial C_i}{\partial t} &= \beta_i \sum_{g'=1}^G v_{g'} \Sigma_{fg'}(\vec{r}, t) \phi_{g'}(\vec{r}, t) - \lambda_i C_i(\vec{r}, t) \end{aligned} \quad (1)$$

where the parameters involved have the usual meaning in nuclear reactor physics [3] and

$$\begin{aligned} g &= 1, \dots, G \\ i &= 1, \dots, I \\ \vec{r} &\in V \\ t &\in [0, T] \end{aligned}$$

Depending on the problem to be analyzed, the reactor core will always be delimited by imposed boundaries, marked to simplify the problem to some extent. The boundary conditions considered by AZKIND are: Dirichlet (null incoming neutron flux), Neumann (reflexion), and Robin (extrapolated boundary conditions) types.

2.2. Finite Element Method

The finite element method is a procedure based on creating subdivisions through the core. Each subdivision is assigned a set of parameters, each of which will have its own solution to the equation, known as discretization. The solution to the set of subdivisions follows the same rules as those that apply to standard discrete problems.

The main idea of the Galerkin method is that an approximation to the solution generated by a set of base functions different for each nodal method will be arranged on each element (the elements being each of the subdivisions of the space that constitute the domain to be analyzed).

The subspace defined by these basis functions will also delimit the precision of the approximation when compared to the solution generated by the nodal method.

2.3. Raviart-Thomas-Nédélec Nodal Methods

The original version of AZKIND program included the RTN of index 0, for the discretization. Although this method delivers acceptable results, as it will be shown in this work, a higher-order method (RTN-1) can, in theory, improve the accuracy of the results, and this hypothesis will be demonstrated throughout this document.

The method defines parameters to be interpolated on each of the grid cells, which are also known as cell moments. These moments are usually considered on vertices, sides, or cell averages, and the number of moments to interpolate will depend on the degree of the method.

The flow over these parameters is related to certain basis functions chosen depending on the method to be implemented. These functions are constructed by generating a system of equations with each cell's boundary conditions and appropriately applying the Legendre polynomials' properties.

In the paper "A general family of nodal schemes," Hennart, J.P. [2] introduced a family of nodal methods in 2 and 3 dimensions with general properties, including using cell sides as parameters and the averages of the moments over the whole cell.

The solution of each cell is defined as a linear combination of the cell moments defined for each nodal method. The cell moments must be defined within the polynomial space: Q_{ijk}

$$Q_{ijk} = \{ \xi^i \eta^j z^k \mid 0 \leq i \leq \ell; 0 \leq j \leq \ell; 0 \leq k \leq \ell \} \quad (2)$$

the indices i , j , and k will always be greater than or equal to zero and less than or equal to a certain parameter ℓ . This parameter gives the system degrees of freedom and is responsible for the method's accuracy.

2.3.1 Nodal method RTN-0

When the parameter ℓ is equal to 0, the indices $i, j,$ and k in (3) can only be 0, 0, and 0. This is reduced to 7 parameters to be interpolated: the moments 00 of the sides Left, Right, Near, Far, Bottom, and Top, as well as the moment 000 of the cell. These parameters are best represented in Figure 1.

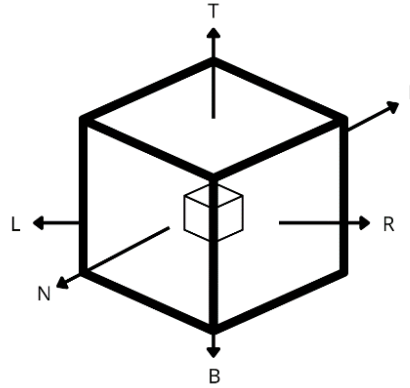


Figure 1. Graphical representation of the parameters to be interpolated for the RTN-0 nodal method.

The accuracy of this method is $O(h^2)$ [4].

2.3.2 Nodal method RTN-1

The nodal method becomes more complicated when the index is equal to 1. The total number of parameters to interpolate increases. In this case, are 32 parameters distributed throughout the cell: four for each side (the moments 00, 01, 10, 11) and eight for the cell (the moments 000, 001, 010, 011, 100, 101, 110, 111). These parameters are best represented in Figure 2.

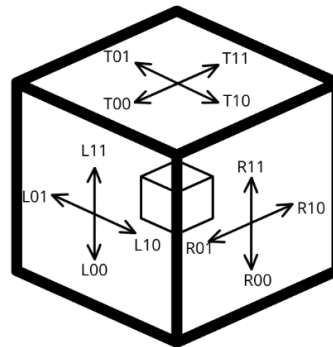


Figure 2. Graphical representation of some parameters to be interpolated for the RTN-1 nodal method.

The accuracy of this method is $O(h^3)$ [4].

3. BENCHMARK PROBLEMS

Different Benchmark problems with different conditions for the materials and geometry of the reactor, as well as the conditions of the nodal method involved, must be used to compare the results obtained for parameters such as neutron flux, power, and effective multiplication factor, and verify the new implementation. Two Benchmark problems were considered for the steady state and one more for the transient state. The three of them are described hereafter.

3.1 Steady State Benchmark Problems

3.1.1 Benchmark TWIGL

The Benchmark problem "TWIGL" [6] represents the core of a two-dimensional BWR reactor with the radial arrangement as in Figure 3.

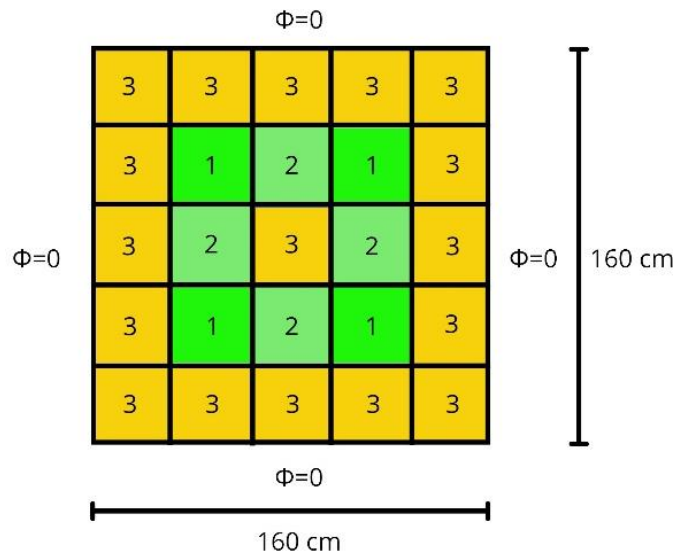


Figure 3. Radial representation of the TWIGL Benchmark

The numbers 1, 2, and 3 represent the three materials comprising the core: three fuels, two of them (1 and 2) with identical compositions, as seen in Table I. Two energy groups are considered: the fast group and the thermal group.

Table I. Characteristics of the materials that make up the core in the TWIGL benchmark

Mat	Group	$D_g (cm)$	$\Sigma_{ag} (cm^{-1})$	$\nu\Sigma_{ag} (cm^{-1})$	$\Sigma_{s1 \rightarrow g} (cm^{-1})$
1	1	1.4	0.01	0.007	-
	2	0.4	0.150	0.2	0.01
2	1	1.4	0.01	0.007	-
	2	0.4	0.150	0.2	0.01
3	1	1.3	0.008	0.003	-
	2	0.5	0.05	0.06	0.01

3.1.2 Benchmark IAEA

For the IAEA Benchmark [7] the following radial distribution of materials was considered (Figure 4):

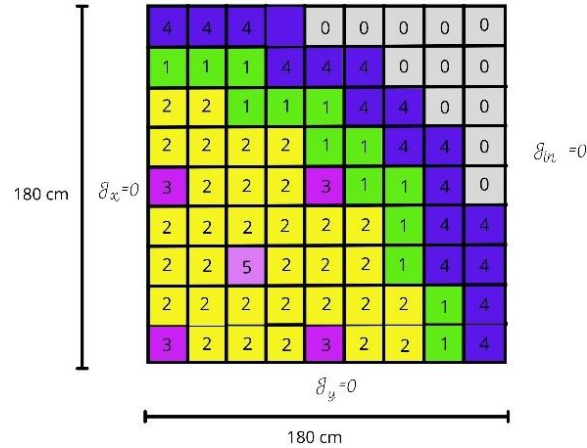


Figure 4. Radial representation of the IAEA Benchmark

Figure 5 represents the distribution of materials on the axial axis.

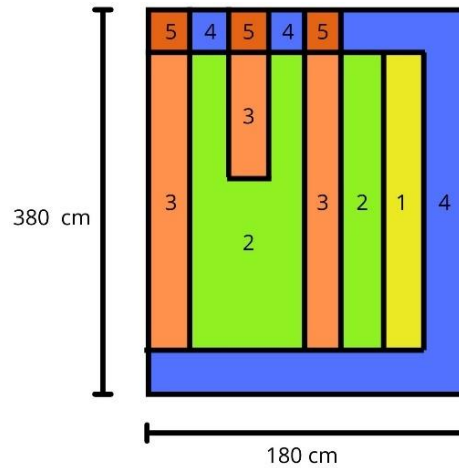


Figure 5. Axial representation of the IAEA Benchmark

The numbers represent the materials that make up the core: 1 and 2 represent the nuclear fuel, 3 represents a control rod with a larger Σ_a inserted into the fuel, 4 represents the moderator. In contrast, 5 represents the same control rod as 3 except that it is inserted to a certain extent. The nuclear parameters for each material in this exercise are presented in Table II.

Table II. Characteristics of the materials that make up the core in the IAEA benchmark

Mat.	Group	$D_g (cm)$	$\Sigma_{ag} (cm^{-1})$	$\nu\Sigma_{ag} (cm^{-1})$	$\Sigma_{s1 \rightarrow g} (cm^{-1})$
1	1	1.5	0.01	0.0	-
	2	0.4	0.08	0.135	0.02
2	1	1.5	0.01	0.0	-
	2	0.4	0.085	0.135	0.02
3	1	1.5	0.01	0.0	-
	2	0.4	0.13	0.135	0.02
4	1	2.0	0.0	0.0	-
	2	0.3	0.01	0.0	0.04

3.2 Transient Benchmark Problem

The results obtained by the transient benchmark are compared with those presented in the work of Kotchoubey, J. [8]. The method used in this reference is an analytical nodal method employed by two neutronics models: the NEU3 [9] and the NEU4 [10]; both models apply a transverse integration process to solve the time-dependent diffusion equation.

3.2.1 Benchmark TWIGL Transient

The transient Benchmark problem implemented was the same "TWIGL" benchmark described in section 3.1.1 above but now with time dependence.

The transient problem uses the result given by the stationary problem to approximate the initial flux. The initial power is also normalized to 1.

This problem has two versions based on two types of reactivity insertions: step perturbation at the cross-thermal absorption section of material one and ramp perturbation at the same cross-section [10]. Tests were performed on both versions; in the current work, only the results of the second version are presented. The following values are used for the delayed neutron fraction and decay constant, plus a time step of 0.005 seconds for 0.5 seconds.

$$\begin{aligned} \beta &= 0.0075 \\ \lambda &= 0.08s^{-1} \end{aligned} \tag{3}$$

During a ramp reactivity insertion, a step reactivity increase is considered before the ramp increase. In the case of the Benchmark above, the function determining the behavior of the absorption cross section of material 1 is defined as in Equation (4).

This equation is modeled in the general case in Figure 6.

$$\Sigma_{a,1}^2(t) = \begin{cases} \Sigma_{a,1}^2(0) \times (1 - 0.11667t) & \text{si } t \leq 0.2 \text{ seg} \\ \Sigma_{a,1}^2(0) \times 0.97666 & \text{si } t > 0.2 \text{ seg} \end{cases} \tag{4}$$

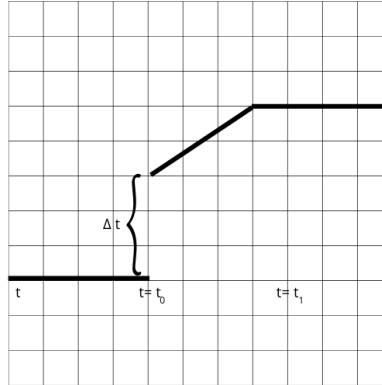


Figure 6. Change in the time of the absorption cross section during a ramp reactivity insertion in its general case

4. RESULTS

For all Benchmarks, the program's results were meticulously analyzed. The two nodal methods employed (RTN-0 and RTN-1) were compared. The program was executed with the finest mesh size available to obtain the most accurate results possible. The hypothesis stated at the beginning proved to be true. The RTN-1 nodal method is indeed more accurate. The error size obtained, which would define this accuracy, will depend on the complexity of the problem and the methods employed in the reference. All plots were generated in the Matlab graphical environment.

4.1 Steady State Benchmark Problems

4.1.1 Benchmark TWIGL

The program execution was carried out for different mesh sizes, in the case of the stationary "TWIGL" Benchmark: 8 and 4 cm. This is shown in Tables III and IV, where a comparison of the different values of the k_{eff} provided by the program is obtained, as well as a third value supplied by the KOMODO code [5], a program to which the Benchmark was implemented with the same conditions and the mesh size corresponding to each execution. To give context, this program uses polynomial and semi-analytic nodal methods.

Table III. Percentage errors obtained in the comparison of k_{eff} delivered by both nodal methods in the 8 cm mesh versus the 2 cm mesh for the TWIGL Benchmark.

		Mesh 8 cm		
			RTN-0	RTN-1
		k_{eff}	0.913477	0.913220
Mesh 2 cm	RTN-0	0.912988	0.0535%	0.0254%
	RTN-1	0.913054	0.0463%	0.0181%
	Komodo	0.913210	0.0292%	0.0010%

Table IV. Percentage errors obtained in the comparison of k_{eff} delivered by both nodal methods in the 4 cm mesh versus the 2 cm mesh for the TWIGL Benchmark.

		k_{eff}	Mesh 4 cm	
			RTN-0	RTN-1
Mesh 2 cm	RTN-0	0.912988	0.0304%	0.0254%
	RTN-1	0.913054	0.0232%	0.0181%
	Komodo	0.913210	0.0061%	0.0010%

Furthermore, with the AZKIND program, it is possible to obtain fairly good approximations for the axial and radial relative power and the average flux in both energy groups in the axial and radial planes. Although the accuracy for these parameters tends to vary a little more, it is possible to notice differences between the two methods. Plots were obtained for both nodal methods.

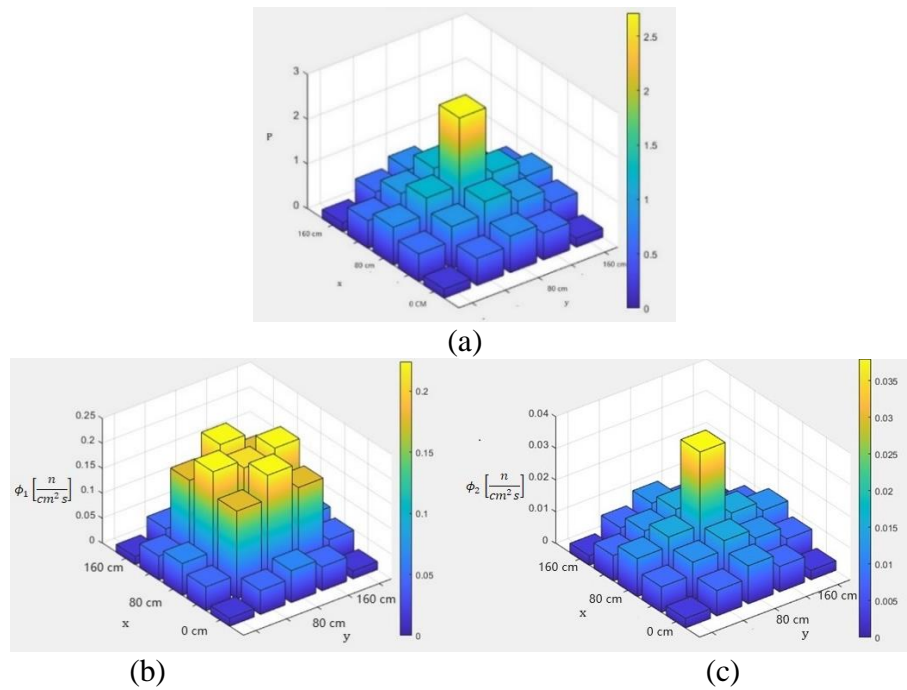


Figure 7. (a) relative power and (b) average flux of group 1 and (c) group 2 for the stationary TWIGL Benchmark problem using the RTN-1 nodal method.

4.1.2 Benchmark IAEA

Tables V and VI present the effective multiplication factor for this problem under the different methods. Again, the KOMODO program was executed under the same conditions to make appropriate comparisons.

Table V. Percentage errors obtained in comparing k_{eff} delivered by both nodal methods in the 10 cm mesh versus the 2.5 cm mesh for the TWIGL Benchmark.

		k_{eff}	Mesh 10 cm	
			RTN-0	RTN-1
Mesh 2.5 cm	RTN-0	1.028855	0.046%	0.027%
	RTN-1	1.027694	0.117%	0.042%
	Komodo	1.029070	0.067%	0.007%

Table VI. Percentage errors obtained in comparing k_{eff} delivered by both nodal methods in the 5 cm mesh versus the 2.5 cm mesh for the TWIGL Benchmark.

		k_{eff}	Mesh 5 cm	
			RTN-0	RTN-1
Mesh 2.5 cm	RTN-0	1.028855	0.005%	0.0277%
	RTN-1	1.027694	0.076%	0.042%
	Komodo	1.029070	0.026%	0.006%

These tables again show the accuracy of the RTN-1 nodal method since for the 5 cm mesh and the 10 cm mesh, the k_{eff} value is very similar to the k_{eff} value for the finer mesh and the RTN-0 nodal method. When the roles are reversed, the percentage errors are higher, meaning that the k_{eff} value in the RTN-0 nodal method is only close to the reference value when using a very fine mesh. The characteristics of the materials in the problem generate power peaks at the center of the reactor and valleys at the edges (due to reflector and boundary conditions). This is shown in Figure 8, which represents the relative radial power of the problem.

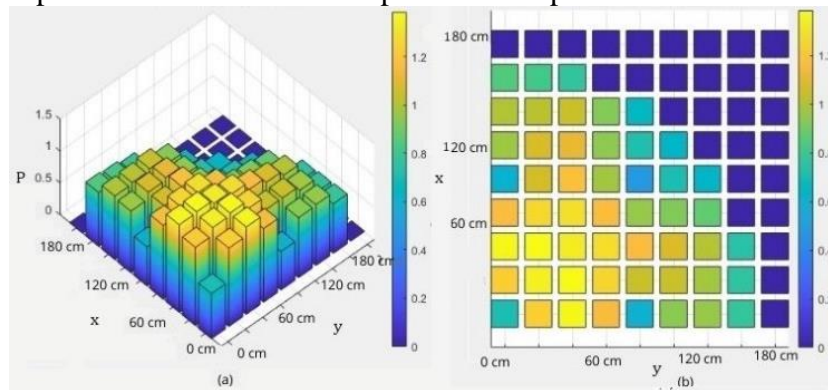


Figure 8. Relative radial power of the IAEA Benchmark problem under the RTN-1 nodal method viewed in (a) three dimensions and (b) two dimensions.

Since the problem is in three dimensions and there are changes along the reactor's z-axis, the relative power and average flux will not be constant over the axial plane. This relative power will be different for each assembly, and it is possible to analyze how it behaves for each assembly. The reactor's assembly 21 (the one with the control rod inserted at 100 cm) was chosen to exemplify this. The axial power is presented in Figure 9.

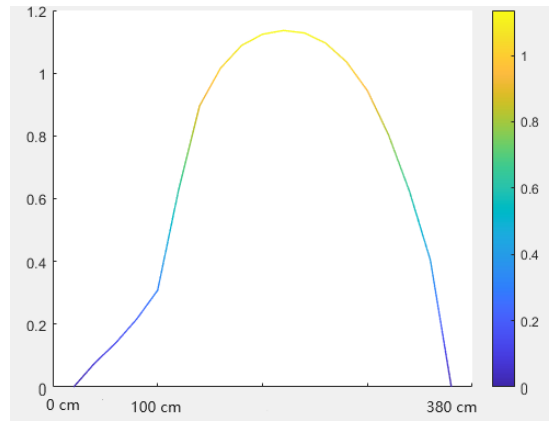


Figure 9. Relative axial power of the IAEA Benchmark problem under the RTN-1 nodal method

4.2 Transient Benchmark Problems

4.2.1 Benchmark TWIGL Transient

The AZKIND program takes the result of the static problem as the initial approximation of the transient problem. The ramp reactivity exhibits a smooth power change because the macroscopic absorption cross section in the problem changes linearly with the slope defined in Section 3.2.1 of the present work.

Figure 10 describes the relative power for the two nodal methods where it is possible to observe how smoothly the power grows until the final instant of the transient (presumably when the control rod is fully withdrawn). In this case, the difference between the two methods grows indefinitely but steadily. Table VII describes the difference in relative power more accurately at key moments of the transient.

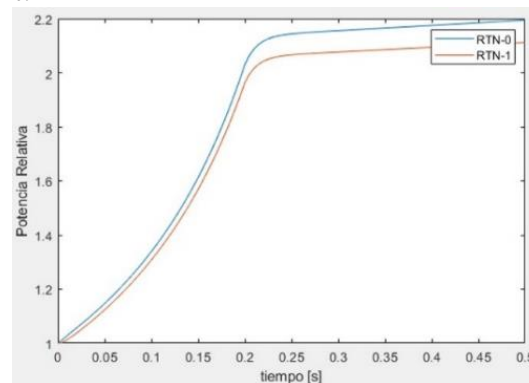


Figure 10. Relative power at different instants during the TWIGL transient problem by inserting ramp reactivity in the RTN-0 and RTN-1 nodal method

Table VII. Results of the power at the beginning and at the end of the transient in the TWIGL problem and its corresponding percentage errors

	Relative Power (0.1 s)		
	AZKIND	POLCA	e%
RTN-0	1.3390	1.308	2.315
RTN-1	1.3079	1.308	0.007

	Relative Power (0.5 s)		
	AZKIND	POLCA	e%
RTN-0	2.1946	2.111	3.809%
RTN-1	2.1118	2.111	0.037

4. CONCLUSIONS

The present work describes the improvement that was implemented in the AZKIND program by adding the RTN-1 nodal method, additionally to the RTN-0 method, originally included in code.

The theory claims that the RTN-1 nodal method is more accurate than the RTN-0 nodal method since the former uses 32 parameters to approximate the solution in comparison with the 7 parameters used in the RTN-0.

Using two stationary and one transient Benchmarks, it was verified that the RTN-1 nodal method delivered results very close to those delivered by different references used as references in this work, such as Komodo, which uses a semi-analytic nodal method, or POLCA, which uses very fine, and complex meshes.

It is well documented that when discretizing the space, a tiny mesh size is convenient for obtaining numerical solutions that are very close to the actual value using finite element methods. For the different benchmarks, the RTN-0 nodal method delivered accurate solutions only when very fine grids were used, which required very long computation times, while the RTN-1 nodal method delivered the same results with coarser meshes. Despite this, the fact that the number of parameters to interpolate is much larger in the RTN-1 nodal method translates into a larger number of equations to solve, which in turn results in a longer computational time and a need for more storage.

This is why it is foreseen the use of libraries such as the PETSc and SLEPc, which use sparse matrices, in order to accelerate the performance of the code. Although not implemented during this study's work, they should be seriously considered for future studies.

The AZKIND program is an excellent tool for modeling nuclear reactors. It is competitive with other nuclear codes developed in other countries that use other nodal methods or complex and fine meshes.

REFERENCES

1. Gómez Torres, A. M., Puente Espel, F., Del-Valle-Gallegos, E., Francois Lacouture, J. L., Martin del Campo, C., Espinosa Paredes, G. "Mexican platform for analysis and design of nuclear reactors", Proceedings of the International Congress on Advances in Nuclear Power Plants ICAPP (2015).
2. Hennart, J.P., *SIAM Journal on Scientific and Statistical Computing*, Vol. 7 (1986).
3. Duderstadt, J.J, Hamilton, L.J, *Nuclear Reactor Analysis*, John Wiley and Sons, New York (1976).
4. del Valle Gallegos, E., "Métodos Nodales en Difusión y Transporte de Partículas", Tesis Doctoral, ESFM-IPN, Mexico (1998).
5. Zimin, V. G., Ninokata, H. "Nodal neutron kinetics model based on nonlinear iteration procedure for LWR analysis," *Annals of Nuclear Energy*, Vol. 25 (1998).
6. Yuichiro, B., Tomohiro, E., Akio, Y., Yoshihiro, Y. "Explicit Time Integration Scheme Using Krylov Subspace Method for Reactor Kinetics Equation," *Journal of Nuclear Science and Technology*, Vol. 48, Nagoya, (2011)
7. Lawrence, R. D., "A Nodal Green's function Method for Multidimensional Neutron Diffusion Calculations," *Nuclear Science and Engineering*, Vol. 76, Urbana, Illinois (1979).
8. Kotchoubey, J., "POLCA-T Neutron Kinetics Model Benchmarking," Master of Science Thesis, KTH Royal Institute of Technology, Stockholm (2015).
9. Lindahl, S.-O., "POLCA7 - The NEU3 Neutronics Option.," " Technical report, Westinghouse Electric Sweden AB Report (2000).
10. Muller, E., "POLCA7 - The NEU4 Neutronics Option." Technical report, Westinghouse Electric Sweden AB Report (20
11. Camusso, C. P., Theler, G. G. "One- and two-dimensional diffusion kinetics benchmarks. Milonga capabilities to solve time-dependent neutron diffusion problems", SEAMPLEX (2017).

Preliminary Neutronic Design of a Multipurpose Nuclear Microreactor

Karina Cruz Vázquez and Emiliano Morones García

Universidad Nacional Autónoma de México, Facultad de Ingeniería, Departamento de Sistemas Energéticos.

*Av. Universidad 3000, C.U., 04510, Mexico City, Mexico.
kcvazquez.99@gmail.com; morones.e4@gmail.com*

Juan Luis François

Universidad Nacional Autónoma de México, Facultad de Ingeniería, Departamento de Sistemas Energéticos.

*Av. Universidad 3000, C.U., 04510, Mexico City, Mexico.
juan.luis.francois@gmail.com*

Abstract

The PAPIIT IN100824 project is an initiative for the design of a multi-purpose microreactor developed by UNAM, currently in the conceptual design stage. The microreactor has a thermal power of 15 MW_{th} , using heat pipes with sodium as coolant and TRISO particles as fuel. Two models were analyzed, the first is a fast microreactor originally proposed by the project research team and the second is a thermal microreactor proposed in this work. The Serpent Monte Carlo code with the JEFF-3.1 cross-section library was used to perform the calculations. For each model, the behavior of the effective neutron multiplication factor (k_{eff}), safety parameters such as temperature and void reactivity coefficient were analyzed. Fuel evolution was also analyzed over an operating period of 2,400 days for the fast and 3,500 days for the thermal design at full power. The results show that zirconium carbide (ZrC) proved to be the better reflector. Control rods insert enough reactivity for the safe shutdown of both microreactor concepts. The Doppler coefficient is negative for both models, and the void reactivity effect is negligible in the two microreactor designs. Finally, the thermal microreactor has a longer operating cycle length of approximately 9.5 years.

1. INTRODUCTION

In recent years, nuclear energy has become one of the energy alternatives to counteract the heavy dependence on fossil fuels and achieve the longed-for transition to clean, non-polluting energy. Energy from nuclear fission has a low environmental impact because greenhouse gas emissions from nuclear power plants are negligible compared to those from conventional thermal power plants. Currently, nuclear power accounts for about **10 %** of the world's electricity generation [1]. It is being considered as an important energy source for achieving the International Energy Agency's (IEA) Zero Net Emissions Scenario for 2050 (NZE Scenario) [1].

The NZE Scenario is a pathway for the global energy sector to achieve zero net CO_2 emissions and limit the rise in global temperatures to below pre-industrial levels by 2050 [2]. To achieve

this goal, the use of renewable energies such as solar, wind and water-based energy has been promoted. However, these are variable and intermittent energy sources that are climate-dependent and still face several challenges related to storage and availability. Nuclear power plants, on the other hand, are distributable sources of energy that can adjust their output according to electricity demand [3].

The IEA projects that nuclear electricity generation will have to double between 2020 and 2050 to meet net zero emissions ambitions [4]. The world needs to harness all low-carbon energy sources, so new nuclear reactor technologies, small modular reactors and microreactors are being researched and developed. Design advances are aimed not only at electricity production but also at non-electric applications such as district heating, hydrogen production, industrial process heat generation and desalination [3].

Microreactors are a smaller, simplified and flexible version of conventional reactors, designed to produce up to 10 MWe of electrical power. Because of their size, they can be designed in the factory and transported by truck and/or ship to their final destination. Like conventional reactors, they can use different types of coolant, such as light water, helium, molten salts or liquid metal. Some types of microreactors are turning to heat pipes (HP), a new and innovative alternative for the cooling system. Among the most common applications of these technologies are the supply of electricity to microgrids, remote off-grid areas and communities affected by natural disasters. They have also been conceived to support critical services such as hospitals, as well as for seawater desalination [5].

In this work, physic-neutronic studies are carried out on the core of a microreactor that is currently in the conceptual design phase. The project, called UNAM-DGAPA, PAPIIT IN100824: *Diseño conceptual de un microrreactor nuclear de usos múltiples* (2024-2026), was conceived and being developed by the Department of Energy Systems of the Faculty of Engineering of the *Universidad Nacional Autónoma de México* (UNAM).

2. MICROREACTOR

The microreactor proposed by the research team in the above mentioned project is based on the fast reactor and heat pipe technology currently under investigation. Due to the simplified and compact design envisaged, this nuclear system can be built in a controlled factory environment and transported to the final site. The design envisages the use of TRISO enriched uranium nitride particles as nuclear fuel, as well as heat pipes, with sodium as coolant, for heat extraction. The heat pipes reduce the use of internal components such as pumps and valves. Therefore, this decreases the likelihood of very common accidents in conventional reactors such as a Loss of Coolant Accident (LOCA). Table I summarizes the main characteristics of the microreactor.

Table I. Microreactor characteristics.

Thermal Power [<i>MWth</i>]	15
Coolant	HP
Fuel Type	TRISO
Reactivity control mechanism	Control Rods
Design Status	Conceptual Design

2.1. Reactor Core

The core is based on a solid hexagonal silicon carbide (SiC) matrix, a primary reflector of Beryllium oxide (BeO), and a secondary reflector of Zirconium silicide (Zr_3Si_2). The array contains 18 channels where the hexagonal control rods are inserted, 306 channels for the heat pipes containing sodium on the inside, 300 fuel assemblies and a central rod for an emergency shutdown. An overview of the reactor core cross-section is shown in Figure 1 and its dimensions are summarized in Table II.

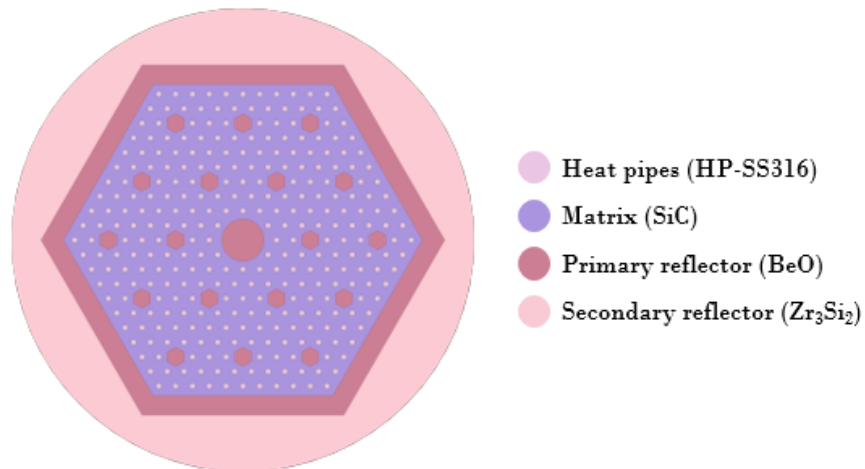


Figure 1. Model of the microreactor core in Serpent [6].

Table II. Main parameters of the microreactor core [6].

Parameter	Value
Core height [m]	185.5
Active core height [cm]	145.5
HP inner radius [cm]	1.25
HP outer radius [cm]	1.40
Primary reflector thickness [cm]	9.238
Secondary reflector thickness [cm]	110.0
Equivalent active core radius [m]	73.9

2.2. Fuel

Microencapsulated TRISO (tristructural isotropic) type particles are conceived for use as fuel. These particles were designed as a prototype safe nuclear fuel for high temperature gas-cooled reactors [7]. The overall diameter of a standard TRISO particle varies between 650 and 850 microns depending on the desired degree of burnup and the type of fuel used [8].

Each particle is composed of an enriched uranium nitride core (kernel). The kernel is encapsulated by three layers of ceramic and carbon-based materials to retain the release of fission products, which are the buffer layer, an inner pyrolytic graphite (IPyC) layer, a silicon carbide (SiC) layer and an outer pyrolytic graphite (OPyC) layer. Table III specifies the dimensions of the proposed fuel for the microreactor [9].

Table III. TRISO fuel dimensions [6].

Parameter	Value
Kernel Radius [mm]	0.400
Buffer Thicknes [mm]	0.090
IPyC Thickness [mm]	0.035
SiC Thickness [mm]	0.035
OPyC thickness [mm]	0.035
Enrichment [% ^{235}U]	19.75

Figure 2 shows an enlarged view of the reactor core. In the center of each fuel block is a heat pipe, surrounded by TRISO particles in a hexagonal configuration.

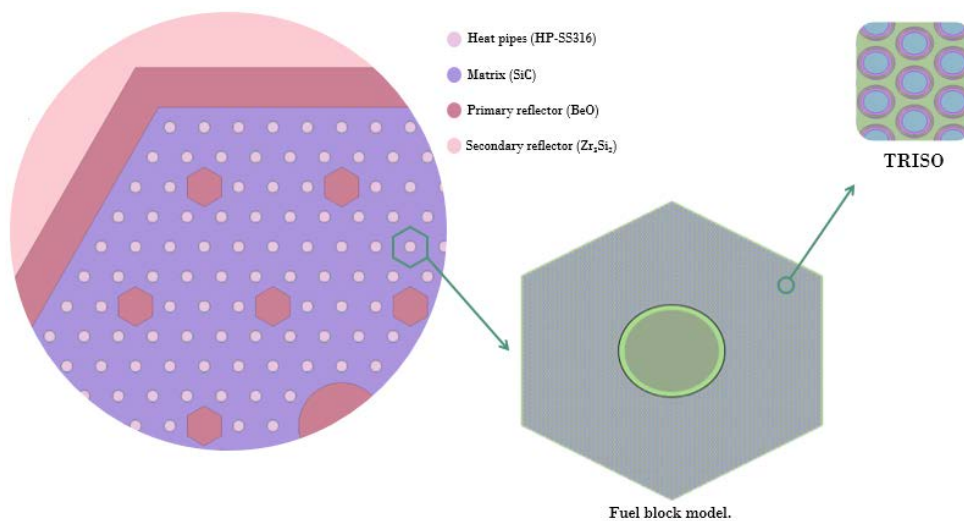


Figure 2. Fuel structure in the microreactor [6].

3. MATERIALS AND METHODS

Two microreactors with different spectra were studied: a fast one proposed by the project research team at the early stage of the project and a thermal one proposed in this work. The change from fast to thermal spectrum is achieved by replacing the silicon carbide matrix with a graphite (C) matrix. The following studies were carried out:

1. Determination of the axial and radial dimensions of the secondary reflector favoring the multiplicative properties of the medium.
2. Change of material of the secondary reflector of the fast microreactor.
3. Insertion of the boron carbide control rods.
4. Calculation of reactivity coefficients for fuel temperature and voids.
5. Calculation of the burnup to determine the operating cycle length.

The Serpent Monte Carlo code [10] with the JEFF-3.1 (Joint Evaluated Fission and Fusion [11]) cross-section library with 10,000 neutrons per cycle, 200 cycles and 30 inactive cycles was used for this work.

3.1. Determination of Reflector Dimensions

First, the diameter of the secondary reflector was varied between 105 cm and 165 cm and the behavior of the effective neutron multiplication factor was analyzed. Then, several simulations were performed by changing the axial thickness of the reflector between 5 cm and 60 cm. The objective of these simulations was to find the dimensions for which the behavior of k_{eff} has a minimum variation and starts to have a constant behavior, so that adding more reflector does not improve the k_{eff} and would imply a higher cost associated to the material that composes it.

3.2. Change of Secondary Reflector Material

Taking into account the potential of zirconium carbide as a reflector, it is proposed to change the material of the secondary reflector from silicide to zirconium carbide. The same procedure explained above was applied to determine the dimensions of the new reflector, compared with those obtained for the original reflector and choose the best option for the microreactor.

3.3. Control Rods

Boron carbide (B_4C) is an ideal material for control rods due to its high neutron absorption capacity, which is why it is taken into account for these simulations. The behavior of the effective neutron multiplication coefficient is analyzed and the behavior of the microreactor is observed when the control rods are inserted. Figure 3 shows model 1 of the microreactor core using B_4C in both the control rods and the central rod, while Figure 4 shows model 2 with the B_4C control rods and the BeO central rod. The simulations of these two models were done for both microreactors.

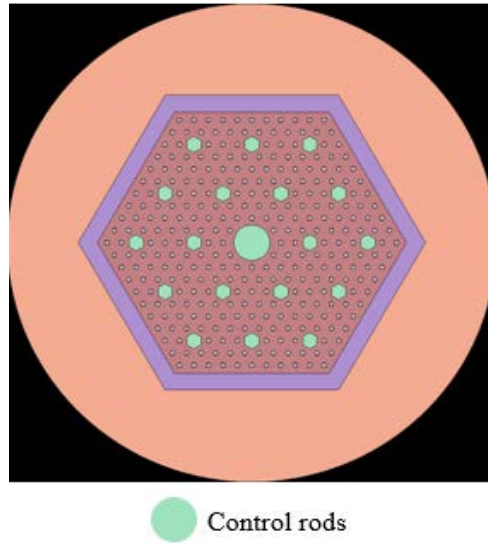


Figure 3. Model of the microreactor core in Serpent with control rods and central rod of B_4C .

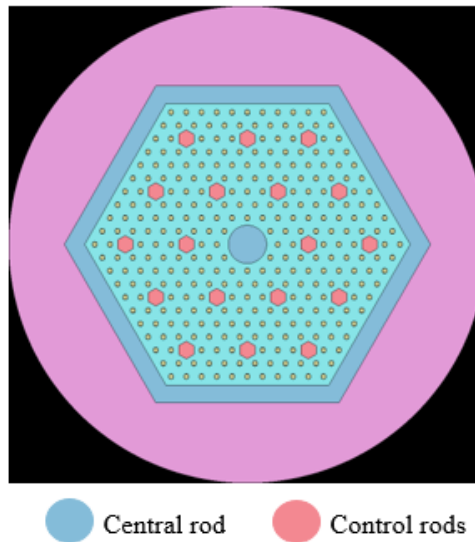


Figure 4. Model of the microreactor core in Serpent with B_4C control rods and the central BeO rod.

3.4. Calculation of the Temperature Reactivity Coefficient

The temperature reactivity coefficient, better known as the Doppler Coefficient, is one of the main safety parameters analyzed in the design of a nuclear reactor. This parameter describes the changes that occur in the reactor in terms of reactivity as a consequence of a variation in fuel temperature [12]. Table IV shows the temperatures that were considered with their respective cross sections in the Serpent JEFF-3.1 library for this simulation. The reactivity (ρ) and Doppler coefficient (α_f) were calculated using their respective definition formulae and approximating the differentials by linear variations as shown below:

$$\rho_i = \frac{k_{eff_i} - 1}{k_{eff_i}} \tag{1}$$

$$\alpha_f = \frac{\partial \rho}{\partial T} \approx \frac{\Delta \rho}{\Delta T} \approx \frac{\rho_i - \rho_{i-1}}{T_i - T_{i-1}} \tag{2}$$

Where subscript i refers to a specific temperature and subscript $i - 1$ refers to the previous temperature considered in the analysis.

Table IV. Temperatures considered in Serpent.

Temperature (K)	Library of cross-sections
600	.06c
1073.15	.09c
1500	.15c

3.5. Burnup Calculation

Finally, the fuel burnup calculation was performed to observe the behavior of k_{eff} and the fuel evolution for both the fast and thermal microreactor, during an operating time of 2400 and 3500 days at full power respectively. The studies were carried out with a small time interval and then with an interval of 100 days as time progresses. The objective of this simulation is to determine the operating cycle time of the microreactors.

4. RESULTS AND DISCUSSION

4.1. Determination of Reflector Dimensions

Figures 5 and 7 show, respectively, the behavior of the effective neutron multiplication factor as a function of the secondary reflector diameter for the fast and thermal microreactor. Figures 6 and 8 illustrate the variation of k_{eff} as a function of the axial thickness of the reflector for both microreactors. As expected, k_{eff} increases as the diameter and thickness increase, which is due to the fact that more neutrons are reflected to the active zone. This behavior continues until the dimensions of the reflector are comparable to its migration area. From this point on, the factor remains approximately constant.

The dimensions of the reflector in these microreactor simulations are shown in Table V. The results obtained show that ZrC is a better reflector material than BeO as the dimensions are smaller. These values were considered, since the results showed that from these dimensions

the relative error between one iteration and the previous one is less than 0.1 %, so that the k_{eff} does not have a considerable variation.

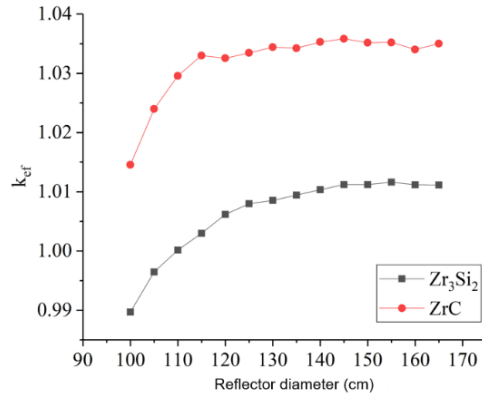


Figure 5. Effective multiplication factor as a function of reflector diameter in the fast microreactor.

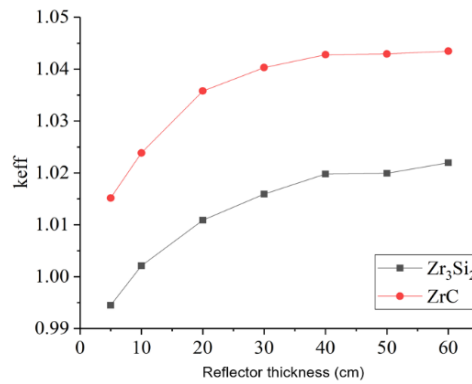


Figure 6. Effective multiplication factor as a function of the axial thickness of the reflector in the fast microreactor.

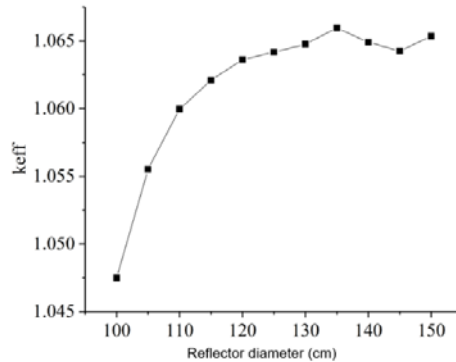


Figure 7. Effective multiplication factor as a function of reflector diameter in the thermal microreactor.

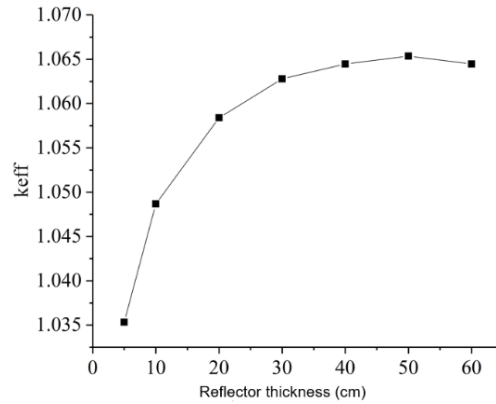


Figure 8. Effective multiplication factor as a function of the axial thickness of the reflector in the thermal microreactor.

Table V. Reflector dimensions.

		Diameter (cm)	Thickness (cm)
Fast	Zr_3Si_2	145	40
	ZrC	135	40
Thermal	Zr_3Si_2	125	30

4.2. Control Rods

Table VI shows the k_{eff} values of the two microreactors according to the material of the control rods and the central rod. As can be seen, k_{eff} has smaller values in the fast microreactor, what is expected since boron-10 captures more neutrons in the thermal region. According to these simulations, the control rods and the central rod fulfil the objective of inserting enough reactivity for the safe shutdown of the microreactor.

Table VI. k_{eff} values obtained in the Serpent simulations

	k_{eff}	
	1 st Model	2 nd Model
Fast	0.69690 ± 0.00056	0.71015 ± 0.00058
Thermal	0.73215 ± 0.00056	0.75015 ± 0.00056

4.3. Doppler Coefficient

Table VII shows the variations of k_{eff} as a function of fuel temperature variation for the two microreactor models. These results are plotted in Figures 9 and 10. It can be seen that as the fuel temperature increases, the reactivity decreases, which is associated with the Doppler effect. It can also be seen that all the values obtained for the Doppler coefficient are negative. However, for the thermal microreactor, even more negative values were obtained than for the fast microreactor, which contributes better to the self-controlled character of the reactor in transient states.

Table VII. Doppler coefficient.

	Temperature (K)	k_{eff}	Reactivity	Doppler Coefficient	ΔT (K)
Fast	600	1.05683 ± 0.00052	0.05377		
	1073.15	1.04265 ± 0.00049	0.04091	-2.720E-05	473.15
	1500	1.03440 ± 0.00047	0.03326	-1.792E-05	426.85
Thermal	600	1.07990 ± 0.00048	0.07399		
	1073.15	1.06291 ± 0.00052	0.05919	-3.128E-05	473.15
	1500	1.05309 ± 0.00052	0.05041	-2.055E-05	426.85

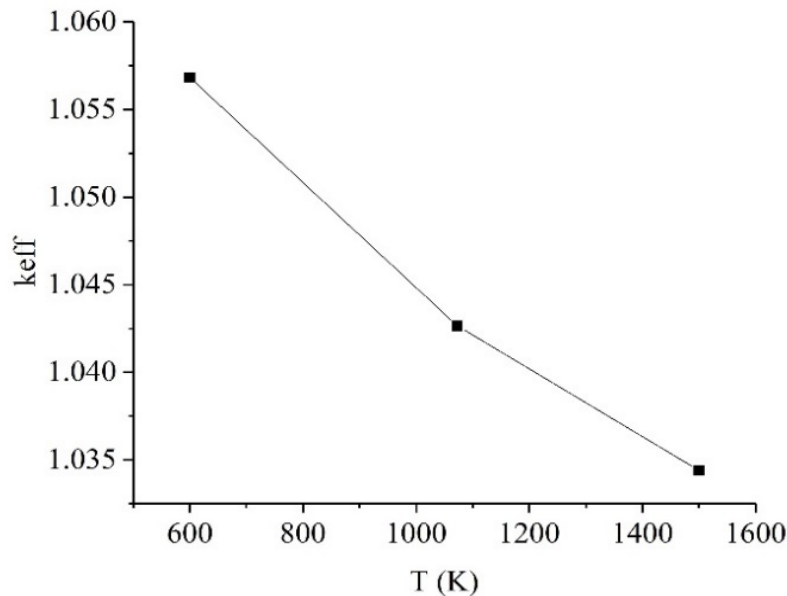


Figure 9. Variation of k_{eff} as a function of fuel temperature in the fast microreactor.

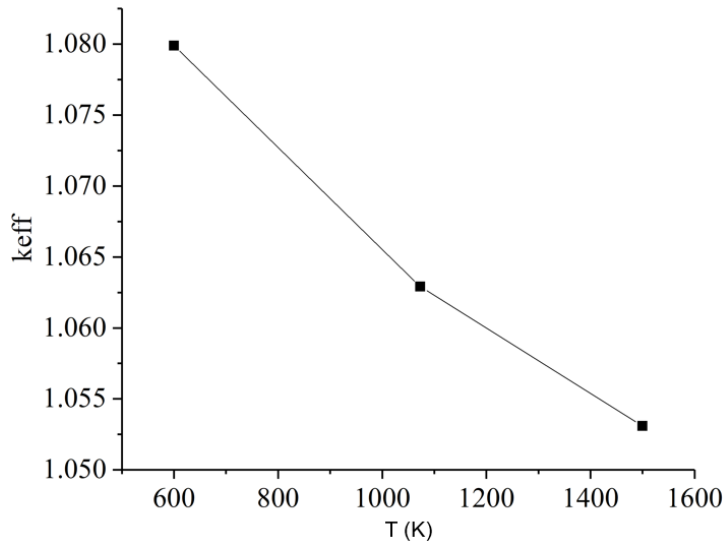


Figure 10. Variation of k_{eff} as a function of fuel temperature in the thermal microreactor.

4.4. Void Reactivity Effect

Sodium is a good coolant for fast reactors, but one of its main disadvantages is that it is very reactive in contact with water and air, and that the reactivity void coefficient tends to be positive in this type of reactors, which is a concern from the safety side. However, this is not a problem in this microreactor, since the presence of a monolithic core avoids the existence of coolant voids around the fuel, and the change of reactivity due to sodium density variation in the heat pipe is negligible, as can be seen in Tables VIII and IX, where the values of k_{eff} and the reactivity are shown. It can be seen that practically there is no change in the reactivity at different sodium densities, even more if the statistical error associated with the k_{eff} is considered.

Table VIII. Void reactivity effect for the fast microreactor.

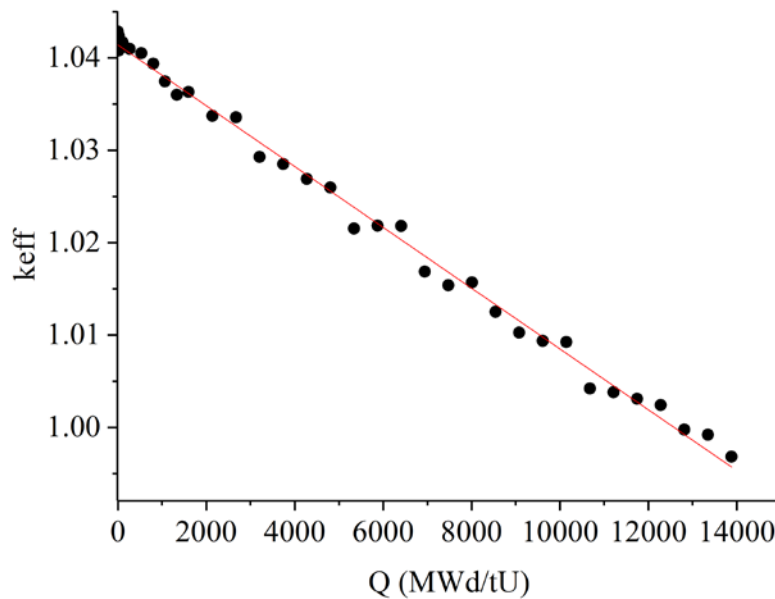
	Density (g/cm^3)	k_{eff}	Reactivity
Steam	0.00013020	1.04226 ± 0.00044	0.04055
	0.00006510	1.04192 ± 0.00051	0.04023
	0.00003255	1.04271 ± 0.00045	0.04096
Liquid	0.92700	1.04817 ± 0.00044	0.04596
	0.46350	1.04827 ± 0.00052	0.04605
	0.23175	1.04778 ± 0.00049	0.04560

Table IX. Void reactivity effect for the thermal microreactor.

	Density (g/cm^3)	k_{eff}	Reactivity
Steam	0.00013020	1.06320 ± 0.00050	0.05944
	0.00006510	1.06306 ± 0.00051	0.05932
	0.00003255	1.06408 ± 0.00046	0.06022
Liquid	0.92700	1.06851 ± 0.00050	0.06412
	0.46350	1.06958 ± 0.00051	0.06505
	0.23175	1.06849 ± 0.00051	0.06410

4.5. Burnup Calculation

Figures 11 and 12 show the variation of the neutron multiplication factor as a function of fuel burnup. As can be seen, k_{eff} decreases approximately linearly as the fuel burns up to a burnup of 13,824 MWd/tU. The parameter shows a relative decrease of 4.41 % in the fast microreactor and 6.83 % in the thermal microreactor. Interpolating the data obtained to a straight line gives a cycle length of 6.5 years for the fast reactor while for the thermal reactor it is 9.5 years.

**Figure 11. Variation of k_{eff} as a function of fuel burnup in the fast microreactor.**

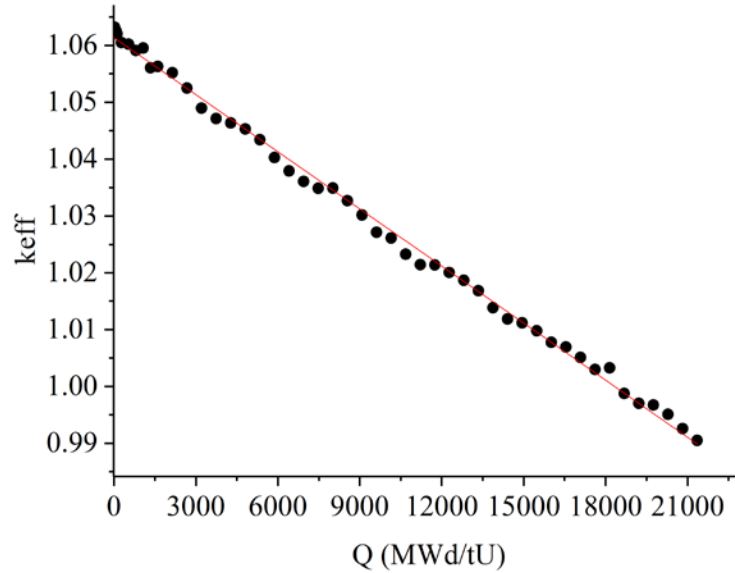


Figure 12. Variation of k_{eff} as a function of fuel burnup in the thermal microreactor.

5. CONCLUSIONS

From the study of the fast and thermal microreactor proposed in this work, the following conclusions can be drawn:

The k_{eff} for the thermal microreactor was shown to be 4.88% higher compared to the fast microreactor, using smaller reflector dimensions. The use of ZrC as a reflector material favors the increase of the neutron population in the core by reducing leakages. The thermal microreactor has a negative Doppler coefficient, which helps the safety. This microreactor was also found to have a longer operating cycle length of 9.5 years.

The microreactor design has the advantage of having a monolithic solid core and using heat pipes as coolant. This avoids creating voids in the core that eliminates the positive void reactivity coefficient issue present in fast reactors.

According to the results obtained in this work, the design of a thermal reactor can be chosen, however, to complete the design of said microreactor, additional studies should be considered in the future. Some of the recommended analyses are:

- Evaluation of the neutron performance of alternative nuclear fuels such as $(U - Pu)N, UC$ and thorium-based fuels.
- Thermohydraulic analysis
- Economic analysis

ACKNOWLEDGEMENTS

To the Consejo Nacional de Humanidades, Ciencia y Tecnología (CONAHCYT) for providing financial support to Karina Cruz Vázquez. To the Universidad Nacional Autónoma de México Mexico for its support through project PAPIIT IN100824: Diseño conceptual de un microrreactor nuclear de múltiples usos múltiples (2024-2026) and for facilitating the use of the MIZTLI supercomputer under the LANCAD-UNAM-DGTIC-253 project.

REFERENCES

1. “Web page of the International Energy Agency”, <https://www.iaea.org/energy-system/electricity/nuclear-power#tracking>
2. International Energy Agency, *Net zero roadmap a global pathway to keep the 1.5°C goal in reach*, 2023 update – Executive summary.
3. Organismo Internacional de Energía Atómica (IAEA), *Innovaciones nucleares para emisiones netas cero*, p. 4-5 (2023). www.iaea.org/es/bulletin
4. Morones E., François J. L., “Nuclear microreactors: Status review and potential applications; the Mexican case”. *Nuclear Engineering and Design*, Vol. 420, 113021, p. 1-8, 2024. <https://doi.org/10.1016/j.nucengdes.2024.113021>
5. IAEA, *Advances in Small Modular Reactor Technology Developments, A supplement to: IAEA Advanced Reactors Information System (ARIS), 2022 Edition*, International Atomic Energy Agency, Vienna, Austria (2022). <http://aris.iaea.org>
6. Morones E., *Diseño conceptual de un microrreactor nuclear multipropósito*, UNAM – Programa de Maestría y Doctorado en Ingeniería en Energía, Informe semestre 2024-2.
7. Félix Cancino Trejo, Eddie López Honorato, “Distribución del carácter de límite de grano en *SiC* y su efecto sobre la difusión de los productos de fisión en las partículas de combustible TRISO”, XXVIII Congreso Anual de la Sociedad Nuclear Mexicana - 2017 LAS/ANS Symposium, "New Technologies for a Nuclear Power Expansion Program", Ciudad de México, México, del 18 al 21 de junio de 2017.
8. García L., *Diseño conceptual de un sistema controlado por un acelerador para transmutación de residuos nucleares y aplicaciones energéticas*, Universidad Politécnica de Valencia, p. 19-21 (2012).
9. François J. L., *Module 1. Front-end of the nuclear fuel cycle*, p. 12-15. Coursera-UNAM <https://www.coursera.org/learn/nfm-frontend?specialization=nuclear-fuel>
10. Leppänen, J., *Development of a New Monte Carlo Reactor Physics Code*, In VTT Publications (Issue 640), p. 15-20 (2007).
11. Jiménez A., García N., Cabellos Ó., *Capacidades del sistema de códigos SCALE para el análisis de reactores rápidos avanzados*, Universidad Politécnica de Madrid, diciembre 2021.
12. Lima Y., *Estudio de la utilización del torio en reactores rápidos enfriados con gas*, Tesis de Maestría en Ingeniería, Universidad Nacional Autónoma de México, Ciudad de México (2018).

Neutronic Evaluation of Two Different Types of Fuel Material on the Performance of a Fast Nuclear Microreactor: First Approach to Mizton

Emiliano Morones-García and Juan-Luis François

*Universidad Nacional Autónoma de México, Facultad de Ingeniería, Departamento de Sistemas Energéticos, Paseo Cuauhnáhuac 8532, Col. Progreso, 62550 Jiutepec, Morelos, México
morones.e4@gmail.com; jlfl@fi-b.unam.mx*

Abstract

Nuclear microreactors are a type of Small Modular Reactor with power outputs from tens of kilowatts to 30 MWe. Conceived to be factory fabricated, transportable, and self-regulating; this nuclear technology could help decarbonize microgrids, remote off-grid areas, emergency power supply, space and naval applications, and non-electric applications. In contrast of the trend abroad to develop microreactor designs, there are currently no projects under development in Mexico or Latin America, even though some potential applications have been found. In case of Mexico, possible applications are power supply to isolated operations, integration with distributed electrical systems, or as an energy source to emerging megacities. Therefore, a high-temperature microreactor concept has been proposed as a possible solution to help address these potential niches. Mizton, as it is known, is a heat pipe cooled microreactor with power output of 15 MWt and its reference model contemplates the use of Fully Ceramic Micro-encapsulated (FCM) as fuel material with uranium nitride Tristructural Isotropic fuel particles. In this paper, a neutronic analysis of the reference model was performed, including the determination of the best zirconium carbide reflector dimensions. Next, an evaluation of the impact of the use of a solid uranium nitride annular fuel element on the performance of Mizton was carried out. The results obtained show that both models stay supercritical for ten years. However, the case with FCM fuel tends to subcriticality after that period of time. In addition, it was found that the substitution of silicon carbide in the matrix for the solid fuel hardened the neutron spectrum, increasing the conversion ratio and thereby the production of plutonium-239. Lastly, the radial and axial power peaking factors resulted lower with the alternative fuel and the power peaks shifted from the periphery to the center of the Mizton core in the radial distribution.

1. INTRODUCTION

Small Modular Reactors (SMRs) have taken the leading role in the development of nuclear technology. Incorporating modular manufacturing, factory production, portability, and scalable deployment in their designs, as well as the capacity to supply electricity to the grid and process heat to industrial applications [1], make them attractive for contributing to meeting climate goals.

A SMR is a nuclear reactor, physically smaller than the conventional ones, with a power output equal to or less than 300 MWe. Potential applications for SMRs include coal replacement for on-grid power, fossil cogeneration for industries, district heating, hydrogen and synthetic fuel production, and water desalination [1]. Particularly, there is a subset of SMRs called microreactors

that can help decarbonize microgrids for critical infrastructures, remote off-grid areas, emergency power supply, space and naval applications, and non-electric applications [2].

Microreactors have power outputs raging from tens of kilowatts to 30 MWe [3] and are characterized for been factory fabricated, transportable, and self-regulating. This technology, also known as nuclear batteries [4], offers benefits such as reduced facility footprint and emergency planning zone, as well as the exclusion area [5]. Although there are many microreactor designs under development around the world, most notably the Micro Modular Reactor, eVinci, and Aurora, all three in the United States, there are none in Mexico or any other Latin America country.

According to a market assessment carried out by the Idaho National Laboratory [2], power supply to isolated operations (mining industry, for example), integration with distributed electrical systems, or as an energy source to emerging megacities are possible applications in Mexico. For these reasons, the high-temperature microreactor concept, called Mizton, has been proposed as a possible solution to help address these potential niches.

Thus, the aim of this paper is to evaluate the preliminary neutronic design of the Mizton reference model, a fast microreactor with a Fully Ceramic Micro-encapsulated (FCM) fuel, and compare its performance with an alternative solid uranium nitride annular fuel. For this purpose, the neutron effective multiplication factor (k_{eff}), the neutron spectrum, the fissile mass evolution, and the core power distribution were analyzed. Additionally, the determination of the reflector dimensions was performed as part of the reference model analysis. The Serpent Monte Carlo Code [6] with ENDF/B-VII cross section library was used to perform the calculations. It should be noted that this paper only considers the neutronic analysis for the cases presented.

2. MIZTON MICROREACTOR

The Mizton reactor is a nuclear microreactor concept under development by the Group of Nuclear Engineering of the National Autonomous University of Mexico. Its design is based on heat pipe technology and is conceived to supply energy to a wide range of applications, either in the form of electricity or heat. As mentioned above, the fast neutron spectrum for Mizton is considered in this paper, as it would allow the use of alternative materials as nuclear fuel material (e.g. depleted uranium or thorium) and implement the Breed-and-Burn (B&B) fuel strategy.

In the Mizton reference model, a FCM fuel was selected as fuel material. The FCM consists of Tristructural Isotropic (TRISO) fuel particles embedded inside a matrix made of silicon carbide (SiC) instead of graphite, which is typically used in conventional high-temperature gas-cooled reactors [7]. In addition to the advantage of not using a moderator like graphite, the SiC matrix also offers enhanced irradiation stability, another barrier to fission product release, stability under steady state and transient conditions, long-term storage, proliferation resistance, and high thermal conductivity [7].

A uranium nitride (UN) kernel is adopted for the TRISO fuel because it provides a higher fissile atom density compared to uranium oxy-carbide or uranium dioxide kernels. Besides the fission product retention capability, this type of fuel is structurally more resistant to neutron irradiation, corrosion, and oxidation than traditional nuclear fuels, and is suitable for high-temperature

operation [8]. The specifications of the UN TRISO particles are presented in Table I. Note that fuel enrichment conforms to high-assay low-enriched uranium (HALEU) restrictions.

Table I. UN TRISO fuel specifications [9]

<i>Parameter</i>	<i>Value</i>
Kernel radius [mm]	0.400
Buffer thickness [mm]	0.090
IPyC thickness [mm]	0.035
SiC thickness [mm]	0.035
OPyC thickness [mm]	0.035
Kernel density [g/cm ³]	12.40
Buffer density [g/cm ³]	1.05
IPyC/OPyC density [g/cm ³]	1.90
SiC density [g/cm ³]	3.19
Enrichment [% ²³⁵ U]	19.75

Regarding the configuration of the heat pipes, sodium and SS316 stainless steel were selected as working fluid and shell material, respectively. Both materials are compatible to work together, and sodium allows operating temperatures between 500°C-1200°C [10]. Moreover, sodium has neutronic advantages that make it ideal for working inside the microreactor core, unlike lithium or potassium, which act as neutron poison [11].

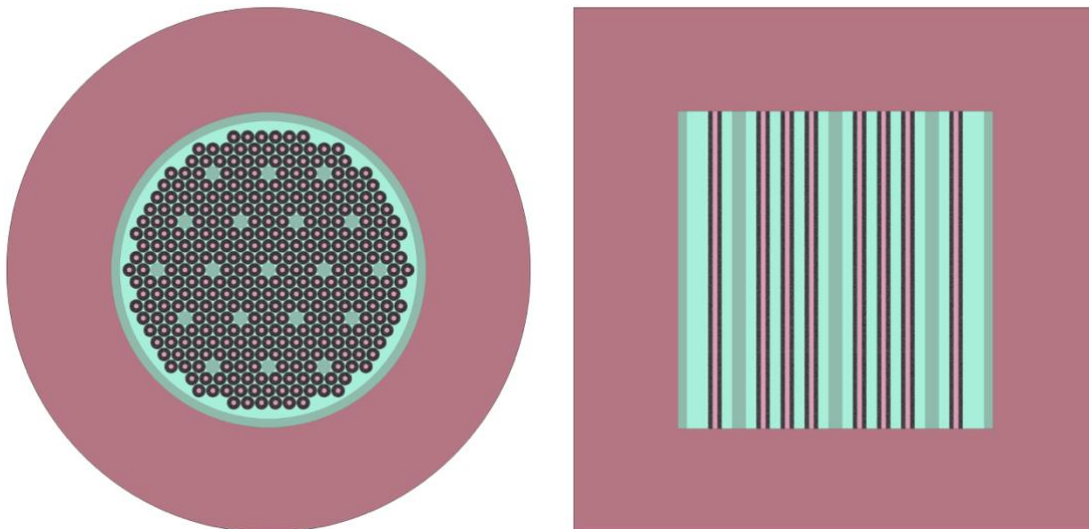


Figure 1. Cross-sectional and lateral view of the Mizton core (Serpent model)

The Mizton core is composed of 348 annular fuel elements arranged in a hexagonal lattice with a heat pipe in the central hole of each. Figure 1 shows the cross-section and lateral view of the Serpent model of the microreactor core. A 5-centimeter-thick beryllium oxide (BeO) ring axially surrounds

the active core. Also, there are 19 cylindrical BeO reflector/control rods distributed in the core. Table II shows the main parameters of the Mizton core. In this design of the reactor concept, the reflector/control rods operate only as a reflector.

Table II. Main parameters of the Mizton core

<i>Parameter</i>	<i>Value</i>
Thermal power [MWt]	15.0
Power density [mWt/particle]	12.19
Heat pipe inner radius [cm]	1.25
Heat pipe outer radius [cm]	1.40
Fuel inner radius [cm]	1.425
Fuel outer radius [cm]	3.80
Fuel pitch (hexagonal) [cm]	8.00
Packing fraction	0.55
Active core equivalent radius [cm]	85.5
Active core height [cm]	145.5
D/H ratio	1.18
BeO ring thickness [cm]	5.00

A more detailed view of Mizton can be seen in Figure 2. Like the fuel matrix, the monolith is also made of SiC. In addition, zirconium carbide (ZrC) was selected as the reflector material because it has demonstrated high reserve reactivity, relatively flat power and neutron flux distribution compared to silicon carbide or zirconium silicide [12]. Eliminating the use of a graphite reflector, besides avoiding neutron moderation, helps to reduce a significant amount of radioactive graphite that could become a waste management concern.

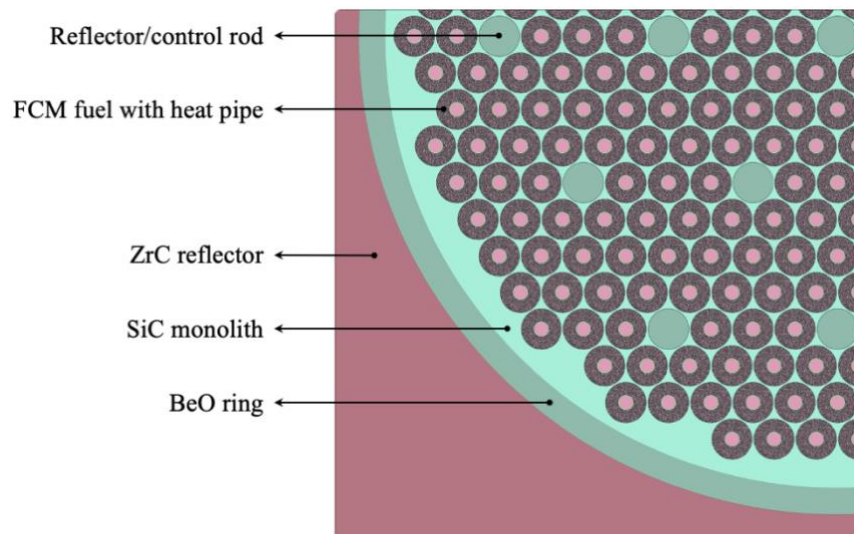


Figure 2. Cross-sectional view of a 1/4th of the core (Serpent model).

2.1. Reflector Study

Given that it is a fast reactor, where neutron leakages are greater compared to a thermal reactor, special care was taken to determine the size of the reflector. To find the minimum dimensions of the ZrC reflector at which the k_{eff} stops increasing, neutronics simulations were performed with the Serpent Monte Carlo Code using the ENDF/B-VII cross section library. The calculations were conducted with 10,000 neutrons per cycle, 300 active cycles, and 30 inactive cycles for a total of 3 million neutron histories. The variations of radius and thickness were from 110 to 165 cm and from 20 to 75 cm, respectively.

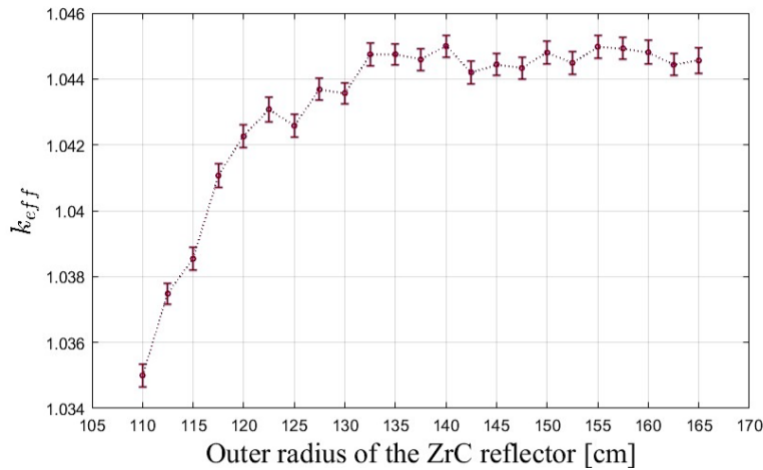


Figure 3. Evolution of the k_{eff} as a function of the ZrC reflector radius.

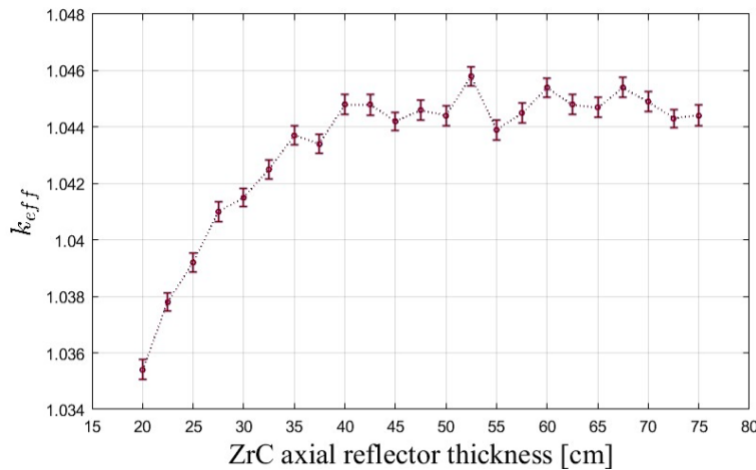


Figure 4. Evolution of the k_{eff} as a function of the ZrC reflector thickness.

Figure 3 and Figure 4 show the results obtained. As can be seen, the k_{eff} reached a maximum at 140 cm reflector radius and did not improve beyond this point. The same occurred when the reflector thickness reached 52.5 cm, where the value of k_{eff} was equal to 1.04578 ± 0.00033 .

3. BURNUP PERFORMANCE COMPARISON

Considering the previous results, the reference model achieves an operating cycle of approximately ten years (see Figure 5). However, the low fissile/fertile load that characterizes TRISO-based fuel, becomes an obstacle to implementing the B&B of fuel. Hence, it was considered necessary to evaluate the microreactor performance with another type of fuel material. In this manner, solid UN annular fuel elements were proposed as an alternative fuel. The enrichment for the alternative case was reduced to 10.6 [%²³⁵U], so that both scenarios started from the same reactivity point. All geometric parameters remained the same.

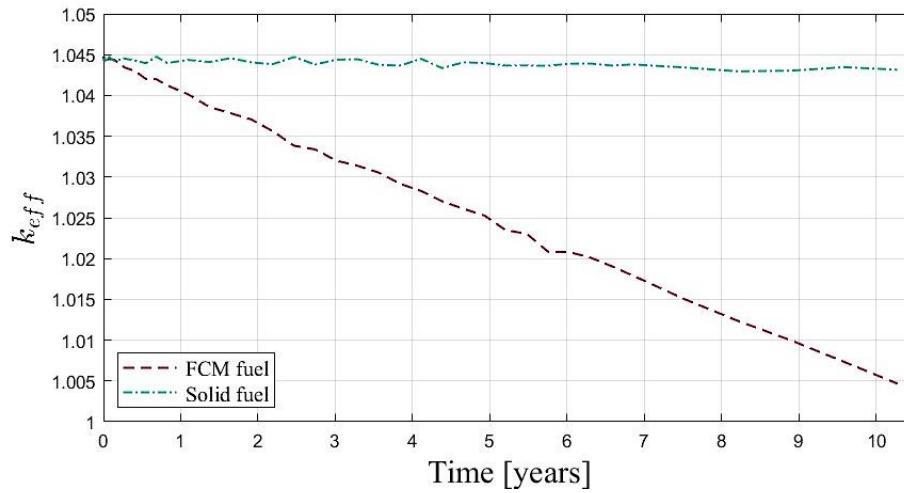


Figure 5. Evolution of the k_{eff} over time of the models with FCM and solid fuel.

First, the evolution of the k_{eff} over time was compared. It can be observed that both models remained supercritical throughout the cycle, as shown in Figure 5. Nevertheless, the k_{eff} in the reference model decreased and the microreactor tended to subcriticality after ten years. In contrast, the alternative case maintained almost constant reactivity, due to a higher initial fuel mass.

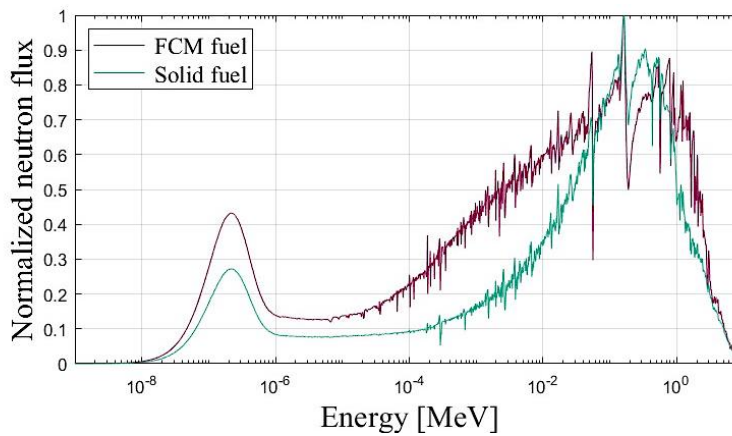


Figure 6. Neutron spectrum of the models with FCM and solid fuel.

With regard to the neutron spectrum, it was mostly fast for the two models, but harder in the case with solid fuel (see Figure 6). The substitution of the SiC matrix for the UN, decreased the amount of carbon in the fuel, resulting in less moderation in the core. In fact, as a result of the spectrum hardening, together with a higher initial fuel loading, the conversion ratio (0.80) was almost double that of the reference model (0.43).

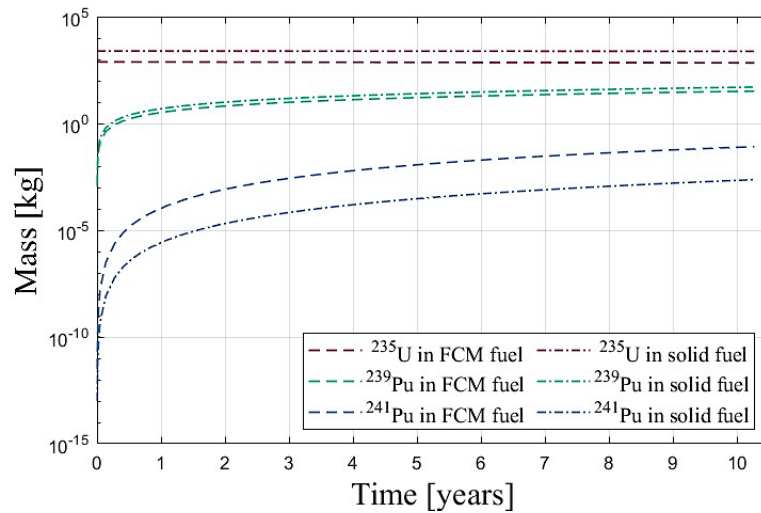


Figure 7. Fissile mass evolution of the models with FCM and solid fuel.

The difference between conversion ratios is also observed in the fissile mass production. Figure 7 shows the evolution of fissile isotopes of the two models. Although a B&B strategy is not implemented, plutonium-239 was bred in both cores, and due to the hardened spectrum, the alternative model ended up breeding more of this isotope. It is worth noting that the uranium-235 mass of the alternative model is three times higher than that of the reference model.

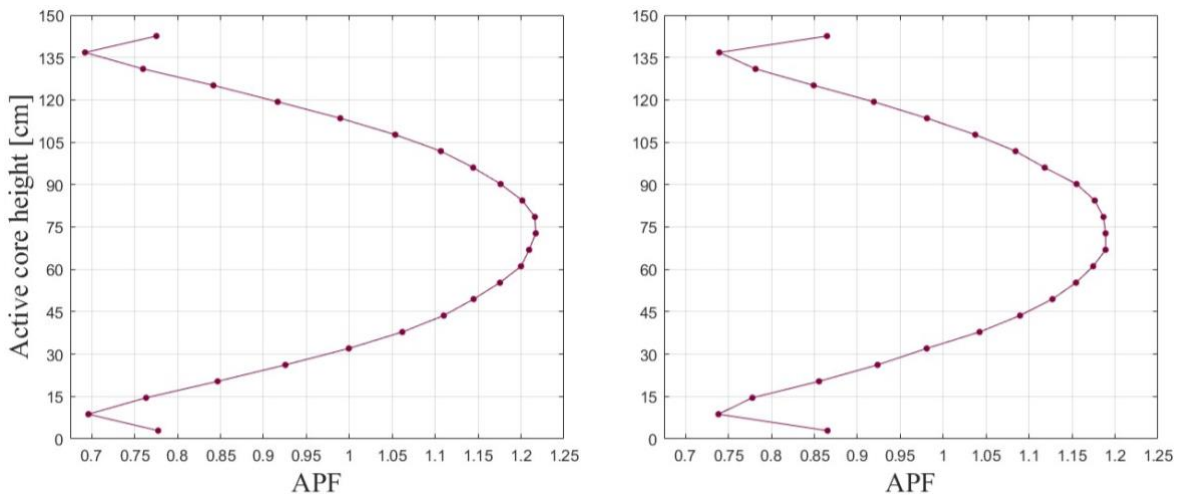


Figure 8. Axial power peaking factors (APF) distribution of the models with FCM (left) and solid (right) fuel.

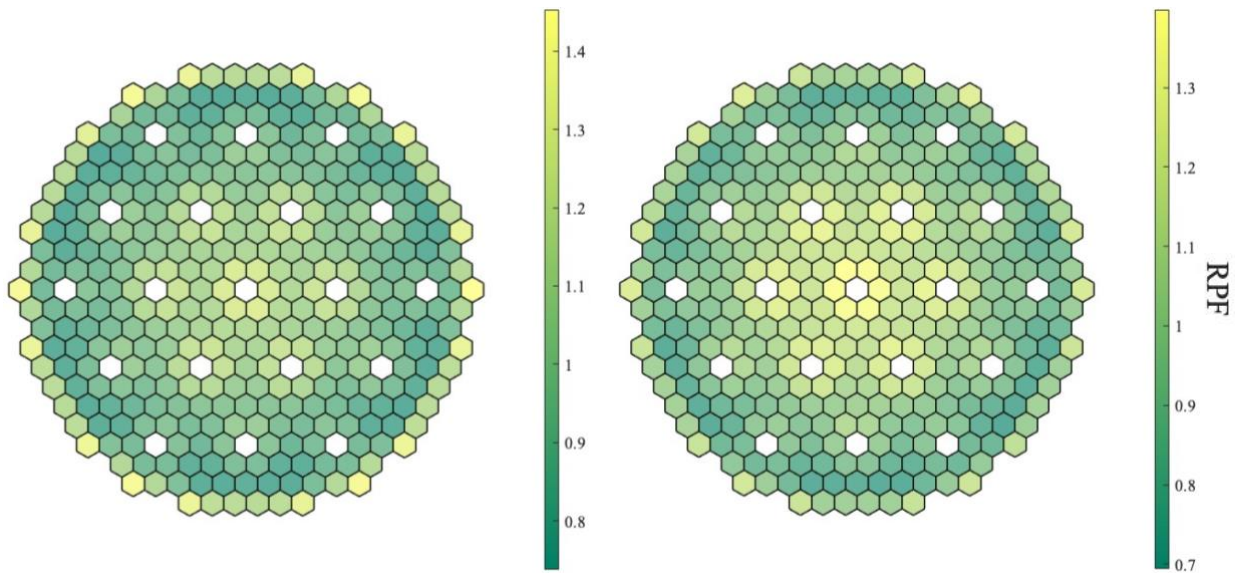


Figure 9. Radial power peaking factors (RPF) distribution of the models with FCM (left) and solid (right) fuel.

As for the core power distribution, Figure 8 and Figure 9 display the axial and radial power peaking factors distribution of the reference and alternative models. It is observed that the use of solid fuel resulted in lower peaking factors, both radially and axially. For the axial distribution, the profiles obtained show the expected figure, with the bulk of the power in the middle of the core. The APF behavior at the axial ends is a consequence of the reflector thickness. And for the radial distribution, the power peaks were shifted from the periphery to the center of the core by changing the fuel.

4. CONCLUSIONS

Neutronic evaluation of the Mizton microreactor performance showed similarities when using FCM and solid UN as fuel materials, with the evolution of the k_{eff} being the main difference. Although the k_{eff} of the reference model decreased with time, the microreactor was supercritical for more than ten years, which makes it more attractive compared to the alternative model due to the lower initial fissile load required (approximately one third less mass).

Nevertheless, the low conversion ratio of the reference model makes fuel breeding difficult. In this case, there are two possible solutions: to increase the packing fraction or to enlarge the core (radially and/or axially). The first one has a manufacturing limit, since it is hard to achieve high packing fractions; and the second would involve increasing the dimensions of the core, which could lead to exceeding the dimensional limit defined for a microreactor. Therefore, the implementation of a breed-and-burn fuel strategy is more viable with a solid UN as fuel material.

As future research, thermal-hydraulic and multi-physics analyses should be conducted, along with a cost assessment of the Mizton concept, in order to evaluate the heat pipes performance and the viability of the microreactor design.

ACKNOWLEDGEMENTS

To the National Council of Humanities, Science and Technology (CONAHCYT) for providing economic support to E. Morones-García for the accomplishment of this work that is part of his doctoral research. To the Universidad Nacional Autónoma de México for its support through project PAPIIT IN100824: Diseño conceptual de un microreactor nuclear de usos múltiples (2024-2026) and for facilitating the use of the MIZTLI supercomputer under the LANCAD-UNAM-DGTIC-253 project.

REFERENCES

1. “The NEA Small Modular Reactor Dashboard”, https://www.oecd-nea.org/upload/docs/application/pdf/2023-02/7650_smr_dashboard.pdf (2023).
2. Shropshire, D., Black, G., and Araujo, K., “Global Market Analysis of Microreactors”, United States, N. p., (2021).
3. “Advances in Small Modular Reactor Technology Developments”, https://aris.iaea.org/Publications/SMR_booklet_2022.pdf (2023).
4. Buongiorno, J., Carmichael, B., Dunkin, B., Parsons, J., & Smit, D., “Can Nuclear Batteries Be Economically Competitive in Large Markets?”, *Energies*, **14**(14), 4385 (2021).
5. Testoni, R., Bersano, A., & Segantin, S., “Review of nuclear microreactors: Status, potentialities and challenges”, *Progress in Nuclear Energy*, **138**, 103822 (2021).
6. Leppänen, J., Pusa, M., Viitanen, T., Valtavirta, V., & Kaltiaisenaho, T., “The Serpent Monte Carlo code: Status, development and applications in 2013”, *Annals of Nuclear Energy*, **82**, p. 142–150 (2015).
7. Terrani, K. A., Kiggans, J. O., Katoh, Y., Shimoda, K., Montgomery, F. C., Armstrong, B. L., Parish, C. M., Hinoki, T., Hunn, J. D., & Snead, L. L., “Fabrication and characterization of fully ceramic microencapsulated fuels”, *Journal of Nuclear Materials*, **426**(1–3), p. 268–276 (2012).
8. Grover, B., Maki, J., & Petti, D., “Completion of the first NGNP advanced gas reactor fuel irradiation experiment, AGR-1, in the advanced test reactor”, *Proceedings of HTR 2010*, Prague, Czech Republic, October 18-20, Paper 104 (2010).
9. Terrani, K. A., Jolly, B. C., & Harp, J. M., “Uranium nitride tristructural-isotropic fuel particle”, *Journal of Nuclear Materials*, **531**, 152034 (2020).
10. Wang, C., Li, J., Xu, B., & Wei, Z., “Design and Thermal Performance Research of Airfoil Alkali Metal High-Temperature Heat Pipe”, *Journal of Thermal Science and Engineering Applications*, **15**(4), (2023).
11. Guillen, D. P., “Review of Passive Heat Removal Strategies for Nuclear Microreactor Systems”, *Nuclear Technology*, **209**(sup1), S21–S40 (2023).
12. Pónya, P., Ding, C., Czifrus, Sz., & Shwageraus, E., “Evaluation of reflector design of ALLEGRO refractory core”, *Annals of Nuclear Energy*, **206**, 110602 (2024).

Helium Fraction Reactivity Effects in a Thermal Molten Salt Nuclear Reactor

Jesús Jorge Domínguez Alfaro, Gilberto Espinosa-Paredes, Alejandría Denisse Pérez-Valseca
Area of Engineering in Energy Resources, Metropolitan Autonomous University, CDMX 09340,
Mexico.

jorge.dominguez.alfaro@gmail.com; gepe@xanum.uam.mx; alepv@xanum.uam.mx

Roberto Lopez-Solis

National Institute for Nuclear Research (ININ), Toluca - México s/n, 52750 La Marquesa,
Mexico.

rcarlos.lope@gmail.com

Abstract

Molten salt nuclear reactors are high-efficiency reactors of Generation IV. This technology uses thorium or uranium fuel, providing a technological advantage because they can work as breeder or burner reactors, the fuel salt can be composed of uranium tetrafluoride (UF₄) or thorium tetrafluoride (ThF₄) dissolved in a mixture of salts, such as lithium fluoride with beryllium fluoride (LiF-BeF). This paper presents the effects of the reactivity due to helium volume fraction in a thermal molten salt nuclear reactor. The helium volume fraction reactivity is generated for the presence of helium bubbles, which is used to remove xenon present in liquid fuel. The models of neutron kinetics, heat transfer, and two-phase flow are solved and coupled in MATLAB and the reactivity coefficient associated with helium volume fraction was obtained using the stochastic Code Serpent version 2.1.30. The result shows that the reactivity per helium fraction has an impact on the thermal power, having a variation of 1.59% from the nominal value.

1. INTRODUCTION

The technologies of Generation IV (GENIV), seek to ensure that these reactors have an affordable cost, minimize the nuclear waste produced, and have high efficiency, the technologies that make up this generation are Molten Salt Reactor (MSR), Gas-cooled Fast Reactor (GFR), Lead-cooled Fast Reactor (LFR), Supercritical Water-cooled Reactor (SCWR), Sodium-cooled Fast Reactor (SFR) and Very High Temperature Reactor (VHTR). MSR technology is usually used with Thorium or Uranium fuel [1], which represents a technological advantage, due to the large reserves of thorium existing in nature. The reactor studied is a thermal spectrum reactor, it uses graphite as a moderator, the liquid fuel circulates in the core, and it has an inlet temperature to the core of 650°C and 750°C at the outlet of the core [2]. The dynamics of the MSR have unique characteristics compared to conventional reactors, this is because it is a circulating fuel reactor, i.e., there are migration of delayed neutron precursors in the circulating fuel [3].

In the molten salt reactor, the salt mixture is the coolant and fuel simultaneously. The molten salt circulates through the core, in this case, graphite, where the flow at the outlet of the core has a

higher temperature compared to the inlet. Then it circulates in an external circuit where the power generated by the fission is removed by heat exchangers. In general, it is found that the movement of delayed neutron precursors through the primary loop has a significant impact on transients at low reactor power or those with changes in the primary loop mass flow rate [4].

2. Description of the reactor

A thermal spectrum molten salt reactor is an advanced type of reactor that uses molten salts as both fuel and coolant, where the neutrons generated in fission interact with a moderator to reduce their energy to thermal levels, optimizing the efficiency of the nuclear reaction; the molten salts allow the reactor to operate at high temperatures and low pressures, which improves thermal efficiency and safety. Additionally, helium is introduced as an inert gas, forming bubbles within the fluid, playing a crucial role in controlling reactivity and managing the generated heat, facilitating the efficient extraction of heat and reducing gaseous fission products, which also contributes to safety by preventing the accumulation of radioactive gases in the system, see Figure 1.

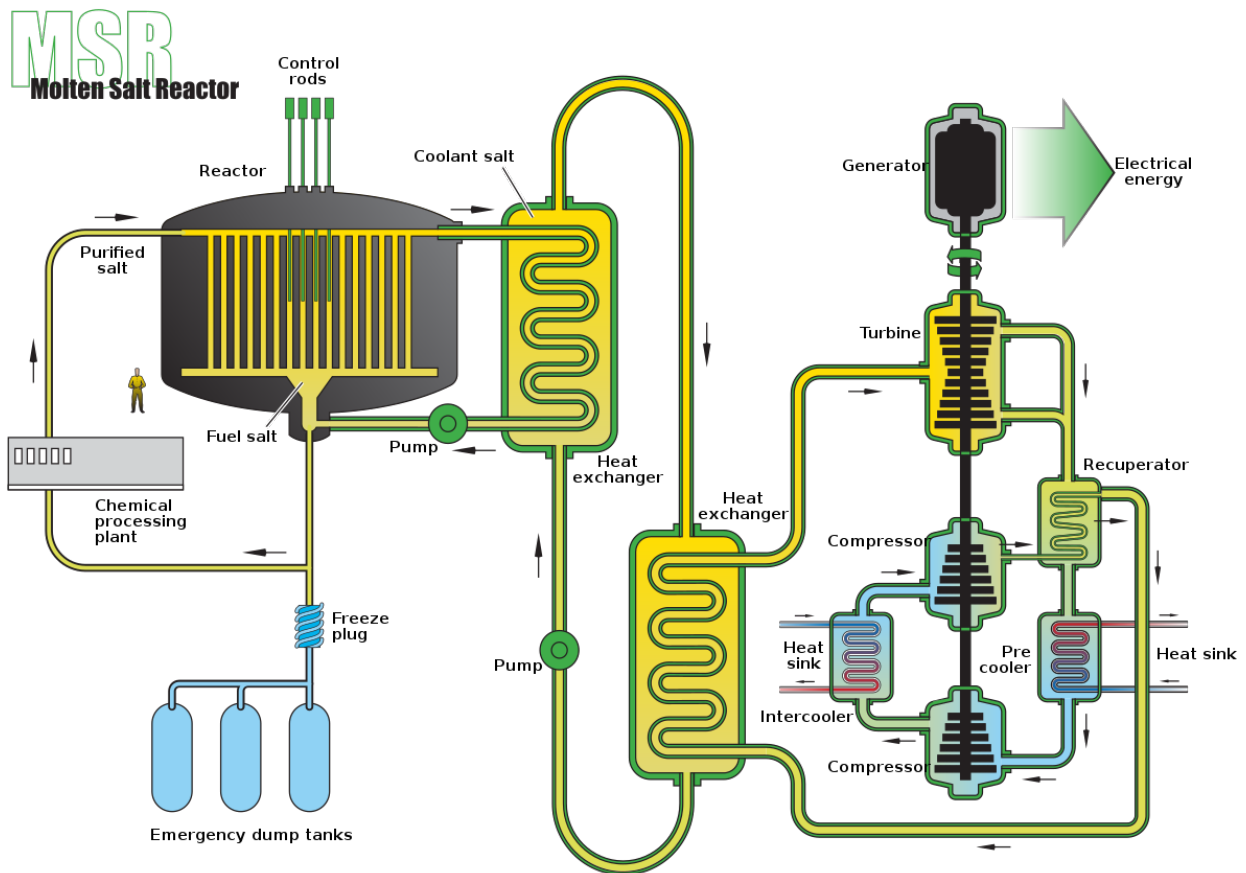


Figure 1. Molten Salt Reactor diagram [5].

3. Helium fraction reactivity coefficient

Helium is an inert gas so, in terms of safety, does not have a risk of a chemical reaction, also helps to homogenize the temperature inside the core, but the most important feature is its use for the extraction of xenon and other gaseous fission fragments. Xenon is a poison for the reactor because it has a very high neutron absorption cross section compared to other gaseous fission fragments, and it is obtained from the radioactive decay of iodine which is also a fission fragment. Throughout the paperwork, reference will be made to the helium fraction as ε_g , in addition, the reactivity coefficient of the helium fraction reactivity is ρ_{ε_g} .

3.1 Helium volume fraction approximation

The geometric model of the reactor consists of a simple cube of 10 cm per side which contains the fuel/coolant mixture salt. Neutronically, the walls have zero net neutron current condition (or infinite reflection) so it is equivalent to a reactor consisting of an infinite medium.

The salt (fuel/coolant) used was LiF-ThF₄-UF₄ with a mole fraction of 0.7750-0.1995-0.0255 respectively [6] with ²³³U as the only isotope in the U vector. Under nominal conditions (no helium bubbles present) the salt density is 4.266 g/cm³ and the atomic vector is shown in Table I.

Table I. Atomic fraction of LiF-ThF₄-UF₄

Isotope	Fraction
⁶ Li	1.405140E-02
⁷ Li	2.756682E-01
¹⁹ F	6.261682E-01
²³⁰ Th	1.491589E-05
²³² Th	7.456452E-02
²³³ U	9.532710E-03

In order to test the effect of the presence of helium in the reactor, helium bubbles of around 500 μm diameter are placed in random positions (but not superposed), the number of bubbles varies with the fraction of volume expected to be filled with helium.

To determine the reactivity helium fraction, the reactivity coefficient α_{ε_g} is required, which was obtained with Serpent version 2.1.30 [7] (nuclear reactor design code). A system of bubbles immersed in the liquid fuel was considered, and it was analyzed for a scenario of 1% mole fraction in a bare cube with a side of 10 cm, as shown in Figure 2 and the preliminary results of the reactivity coefficient are presented in Table II.

$$\alpha_{\varepsilon_g} = \frac{\partial \rho_V}{\partial \varepsilon_g}; \quad 0 \leq \varepsilon_g \leq 1 \quad (1)$$

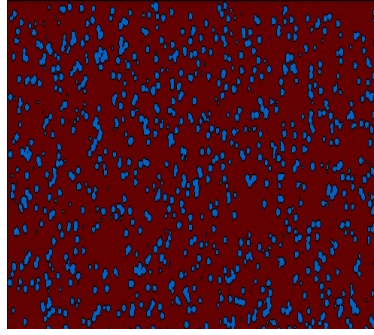


Figure 2. Bare cell with helium bubbles immersed in fuel salt.

Table II. Reactivity coefficient per helium gas fraction.

ε_g	0.00	0.001	0.002	0.003	0.004	0.005	0.006	0.007	0.008	0.009	0.01
α_{ε_g} (pcm)	0	-16	-27	-40	-51	-65	-75	-88	-102	-111	-124

The reactivity per helium fraction is

$$\rho_{\varepsilon_g} = \alpha_{\varepsilon_g} (\varepsilon_g(t) - \varepsilon_{g0}) \quad (2)$$

4. Mathematical models

In this Section, the mathematical models for thermal power, reactivity, heat transfer, and the two-phase flow are described, including the considerations and parameters used.

4.1. Thermal power

In a molten salt reactor, neutron density and concentration of neutron precursors are critical to maintaining and controlling the chain reaction. Considering the production and absorption of neutrons, the precursor concentration equation expresses the delayed neutrons that are transported by the movement of the liquid fuel, these equations allow modeling the dynamics of the reactor.

The thermal power in a nuclear reactor is given by [8]

$$\frac{dP}{dt} = \frac{\rho_{net}(t) - \beta}{\Lambda} P(t) + \lambda c \quad (3)$$

The delayed neutron precursor concentration is

$$\frac{dc(t)}{dt} = \frac{\beta}{\Lambda} n(t) - \lambda c(t) - \frac{c(t)}{\tau_C} + \frac{c(t - \tau_L)}{\tau_C} e^{(-\lambda \tau_L)} \quad (4)$$

Where $\rho_{net}(t)$ is the total reactivity, $\beta=240 \times 10^{-5}$ the effective delayed neutron fraction, $\Lambda=3.6 \times 10^{-4}$ s is the neutron lifetime, $P(t)$ is the power, $\lambda=5.0 \times 10^{-2}$ s⁻¹ the decay constant, $c(t)$ is the concentration of delayed neutron precursors, $n(t)$ the neutron density, $\tau_C=6$ s is the loop transient time, and $\tau_L=4$ s core transient time.

3.2. Reactivity

The reactivity in a nuclear reactor is a function of the temperature of the liquid fuel, the graphite moderation, and its temperature, and, in this work, the helium fraction. Reactivity equations incorporate terms that represent the dependence of parameters and allow the prediction of the reactor response during operational and transient changes.

The equation of reactivity is given by [8]

$$\rho(t) = \rho_{ext}(t) + \rho_{th}(t) \quad (5)$$

$$\rho_{th}(t) = \alpha_f (\langle T_l \rangle - T_{l0}) + \alpha_{gr} (T_{gr}(t) - T_{gr0}) + \alpha_{\varepsilon_g} (\varepsilon_g(t) - \varepsilon_{g0}) \quad (6)$$

The control signal is

$$\rho_{ext}(t) = \frac{\Lambda}{P(t)} \left[- \left(\lambda c + \frac{P}{\Lambda} (\rho_{th}(t) + \rho_0 - \beta) \right) + u_b \right] \quad (7)$$

$$u_b = k (P_{ref} - P(t)) \quad (8)$$

where $\rho_{ext}(t)$ is the external reactivity, α_f the fuel temperature reactivity coefficient, $\langle T_l \rangle$ the average fuel temperature, α_{gr} is the graphite temperature reactivity coefficient, the graphite temperature, α_{ε_g} is the reactivity helium fraction coefficient, $\varepsilon_g(t)$ the void fraction, ρ_0 the zero reactivity, k the proportional control gain, and $P_{ref} = 4000$ MWth is the reference power.

3.3. Heat transfer

In a molten salt reactor, heat transfer between liquid fuel and helium bubbles is a crucial phenomenon to the thermal performance of the reactor. The heat generated by nuclear fission in liquid fuel is transferred to helium bubbles through conduction and convection processes. This heat exchange affects the temperature of the fuel and, therefore, the neutron density and reactivity.

The graphite temperature and heat exchanger, are given by

$$\frac{dT_{gr}(t)}{dt} = \frac{K_{fgr}}{m_{gr}Cp_{gr}} (\langle T_l \rangle - T_{gr}(t)) + \frac{\gamma_g}{m_{gr}Cp_{gr}} P_0 n(t) \quad (9)$$

$$\frac{dT_{in}(t)}{dt} = \frac{\langle w_l \rangle}{m_h} (\langle T_l \rangle - T_{in}(t)) + \frac{k_{hs}}{m_h Cp_l} (T_s - T_{in}(t)) \quad (10)$$

where $K_{fgr} = 2.48 \times 10^7 \text{ WK}^{-1}$ heat transfer coefficient per area from fuel to graphite in the reactor, $m_{gr} = 1.22 \times 10^6 \text{ kg}$ graphite mass, $Cp_{gr} = 1.76 \text{ kJ kg}^{-1} \text{ K}^{-1}$ graphite specific heat, $\gamma_g = 0.97$ fraction of heat generated within the graphite, $\langle w_l \rangle$ fuel mass flow rate, $m_h = 5.38 \times 10^3 \text{ kg}$ fuel mass, $T_{in}(t)$ average fuel temperature in the heat exchanger, $k_{hs} = 2.32 \times 10^7 \text{ WK}^{-1}$ heat transfer coefficient per area in the heat exchanger, $Cp_l = 1.357 \text{ kJ kg}^{-1} \text{ K}^{-1}$ fuel specific heat, $T_s = 723.15 \text{ K}$ heat sink temperature.

Non-equilibrium two-phase flow heat transfers given by an upscaled model [9], describes how heat transfer occurs in a system where the gas and liquid phases are not in thermal or velocity equilibrium. This model is based on a scaling methodology, allowing the effects of interactions between the phases to be captured, such as the heat transfer between the gas bubbles and the surrounding liquid, as well as the velocity differences between both phases. This approach allows us to more accurately describe the macroscopic heat transfer phenomena in complex two-phase flow systems.

Liquid fuel:

$$\begin{aligned} (\rho Cp)_l \varepsilon_l \frac{\partial \langle T_l \rangle^l}{\partial t} - (\rho Cp)_l \langle T_l \rangle^l \frac{\partial \varepsilon_l}{\partial t} + (\rho Cp)_l \frac{\partial (\varepsilon_l v_{lz} \langle T_l \rangle^l)}{\partial z} + k_l \left(\frac{\partial \varepsilon_l}{\partial z} \frac{\partial \langle T_l \rangle^l}{\partial z} \right) = \\ \frac{\partial}{\partial z} \left(K_{llzz} \frac{\partial \langle T_l \rangle^l}{\partial z} \right) + \frac{\partial}{\partial z} \left(K_{lgzz} \frac{\partial \langle T_g \rangle^g}{\partial z} \right) + u_{llzz} \frac{\partial \langle T_l \rangle^l}{\partial z} + u_{lgzz} \frac{\partial \langle T_g \rangle^g}{\partial z} - a_v h (\langle T_l \rangle^l - \langle T_g \rangle^g) + \varepsilon_l \langle q_l'' \rangle^l \end{aligned} \quad (11)$$

Helium bubbles

$$\begin{aligned} (\rho Cp)_g \varepsilon_g \frac{\partial \langle T_g \rangle^g}{\partial t} - (\rho Cp)_g \langle T_g \rangle^g \frac{\partial \varepsilon_g}{\partial t} + (\rho Cp)_g \varepsilon_g \frac{\partial v_{gz} \langle T_g \rangle^g}{\partial z} + k_g \left(\frac{\partial \varepsilon_g}{\partial z} \frac{\partial \langle T_g \rangle^g}{\partial z} \right) = \\ \frac{\partial}{\partial z} \left(K_{ggzz} \frac{\partial \langle T_g \rangle^g}{\partial z} \right) + \frac{\partial}{\partial z} \left(K_{glzz} \frac{\partial \langle T_l \rangle^l}{\partial z} \right) + u_{ggzz} \left(\frac{\partial \langle T_g \rangle^g}{\partial z} \right) + u_{glzz} \left(\frac{\partial \langle T_l \rangle^l}{\partial z} \right) - \\ a_v h (\langle T_g \rangle^g - \langle T_l \rangle^l) \end{aligned} \quad (12)$$

where

$$\langle q^m \rangle^l = P(t)\varphi(z) / \varepsilon_l V \quad (13)$$

and Cp_g Helium specific heat, ε_l fuel fraction, v_{l_z} fuel velocity, ρ_l fuel density, ρ_g gas density, $\langle q_l \rangle^l = 1409.72 \text{ MWm}^{-3}$ volumetric power, $K_{\theta\theta_{zz}}$ effective thermal coefficient associated with the source, $u_{\theta\theta_{zz}}$ effective conductive-convective coefficient, $a_v h$ volumetric heat transfer coefficient, $\theta = l, g$, $\langle T_g \rangle^g$ gas temperature, $\langle T_l \rangle^l$ fuel temperature, $\varphi(z)$ flow profile, V volume.

3.4. Two-Phase Flow

The model describes the interaction between liquid fuel and helium bubbles inside the reactor. This model uses equations that consider surface velocities, phase velocities, and volumetric fractions.

The superficial velocities are obtained with the drift flux method is [10]

$$j_g = \varepsilon_g (C_0 j + v_{gj}) \quad (14)$$

where

$$C_0 = 1.2 - 0.2 \sqrt{\frac{\rho_g}{\rho_l}} \quad (15)$$

And

$$v_{gj} = \sqrt{2} \left(\frac{g\sigma(\rho_l - \rho_g)}{\rho_l^2} \right)^{0.25} \quad (16)$$

The superficial gas and liquid velocities are

$$j_l = v_l \varepsilon_l = v_l (1 - \varepsilon_g) \quad (17)$$

$$j_g = v_g \varepsilon_g \quad (18)$$

Then, the volumetric flux gas and liquid velocity are defined as

$$w_g = j_g A_{x-s} \rho_g \quad (19)$$

$$w_l = j_l A_{x-s} \rho_l \quad (20)$$

where $j_g = 0.02607$ m/s is the gas superficial velocity, j_l the fuel superficial velocity, $\varepsilon_g = 0.1$ the gas fraction, C_0 is the distribution parameter, j the total superficial velocity, v_{gj} is the slip velocity, g the gravitational acceleration, $\sigma = 0.2$ N/m the fuel surface tension, v_g is the gas velocity, w_g the gas flow, and A_{x-s} the surface area.

4. Numerical Experiments

4.1 Reactivity and Thermal Power

The main of this paper is to know if the consideration of the reactivity of helium fraction affects the behavior of the reactor.

In Figure 3, the change in reactivity when the term of reactivity helium fraction is presented. Is it possible to observe that the use of Eq. (2) in the reactivity function, generates a reduction of 0.07% of reactivity, using a helium gas fraction of $\varepsilon_g = 0.1$.

To compare the results, the value of total reactivity using and not using the helium fraction term is presented, in this way is possible to observe the influence of helium fraction in the dynamics of the reactor.

Power is directly related to reactivity and, consequently, it is affected by this reduction in reactivity, having a 1.59% reduction in thermal power, as shown in Figure 4. The change of power is due to the use of the thermal power model, which considers the proportional control term to reach a stabilized power.

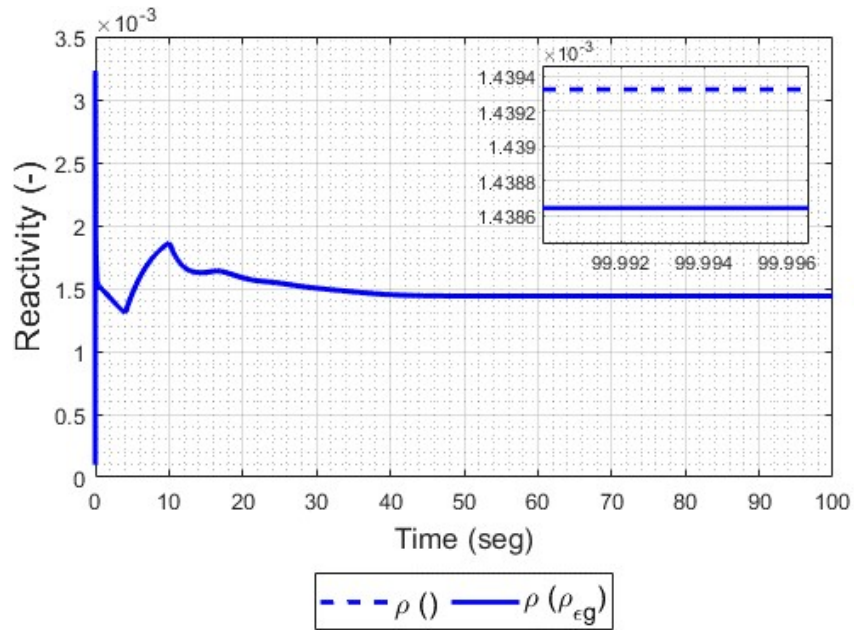


Figure 3. Reactivity per Helium fraction

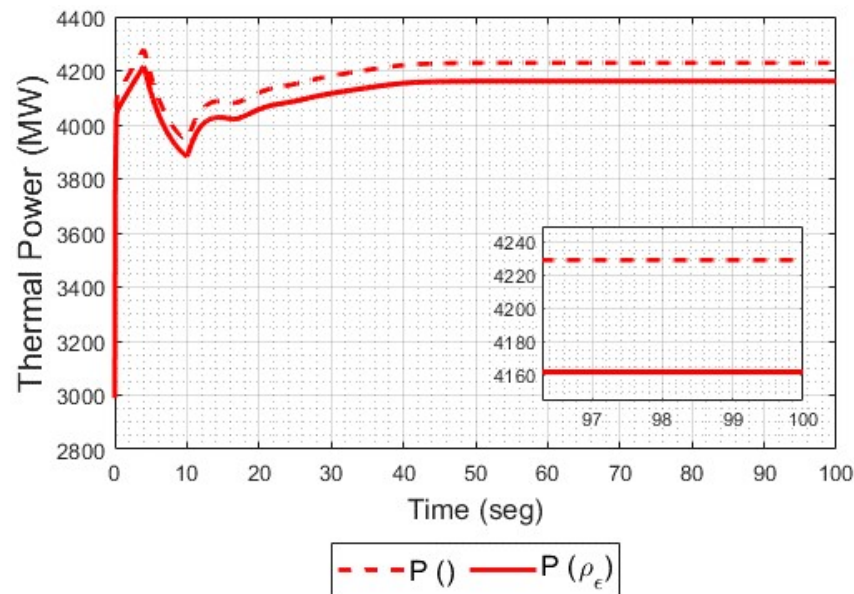


Figure 4. Thermal power

The results of the simulation are shown in Table III. It is represented by not using the reactivity per fraction of helium as $\rho()$, and by using the reactivity helium fraction by $\rho(\rho_{\epsilon g})$.

Table III. Thermal power and reactivity using reactivity per helium fraction

Parameter	$\rho(\)$	$\rho(\rho_{\varepsilon_g})$	Variation
Thermal power (MW)	4229.0015	4161.7479	-1.59%
Reactivity (-)	0.001434604	0.001445	-0.07%

5. CONCLUSIONS

Exploring the effect of reactivity helium fraction coefficient in a Molten Salt Reactor is relevant due to the number of helium bubbles inside and through the reactor, if the reactivity term affects the total reactivity, as a direct consequence the thermal power will be affected.

In this work, we observed that there is a power reduction effect due to considering the term of reactivity helium fraction term, reducing the thermal power by 1.59%, that is, the helium fraction will increase due to the effect of thermal expansion, which is a consequence of the increase in the temperature of the gas and to the effect of the increase in the temperature of the liquid fuel, and with this, the molten salt nuclear reactor could be controlled.

As a future work, a detailed model of the reactor core and helium bubble in Serpent is proposed, also analyzing the effects in the thermal model.

ACKNOWLEDGEMENTS

The authors acknowledge the financial support from the Basic Science and Frontier Project 2023-2024 Reference CBF-2023-2024-2023 founded by the National Council of Humanities, Sciences and Technologies CONAHCyT. Special thanks to CONAHCYT for the financial support given to Jesús Jorge Domínguez Alfaro during his PhD studies.

REFERENCES

1. Dolan T, *Molten Salt Reactors and Thorium Energy*. Woodhead Publishing (2017).
2. Muránsky O., Yang C., Zhu H., Karatchevtseva I., Sláma P., Nový Z. and Edwards L., "Molten salt corrosion of Ni-Mo-Cr candidate structural materials for Molten Salt Reactor (MSR) systems". *Corrosion Science* (2019).
3. Singh V., Wheeler A. M., Upadhyaya B. R., Chvála O. and Greenwood M. S., "Plant-level dynamic modeling of a commercial-scale molten salt reactor system". *Nuclear Engineering and Design*. (2020).
4. Wooten D. and Powers J. J., "A review of molten salt reactor kinetics models". *Nuclear Science and Engineering*. (2018).
5. "Generation IV International Forum Website", https://www.gen4.org/gif/jcms/c_9260/Public (2024)

6. Jaewoo Park, Amanda Leong, and Jinsuo Zhang. “Density Measurements of Molten Salts”. *Journal of Chemical & Engineering Data*, (1892-1898).
7. J. Leppänen, M. Pusa, T. Viitanen, V. Valtavirta, T. Kaltiaisenaho, “The Serpent Monte Carlo code: Status, development and applications in 2013”, *Annals of Nuclear Energy* (2015).
8. Zarei M., “Nonlinear dynamics and control in molten salt reactors”. *Nuclear Engineering and Design*, (2018).
9. Jiménez Balbuena, Z.I. “Transferencia de calor en un reactor nuclear de sales fundidas con efectos de inyección de burbujas de helio”. Tesis de Maestría. Universidad Autónoma Metropolitana-Iztapalapa (2021).
10. Zuber, N., & Findlay, J. A., “Average volumetric concentration in two-phase flow systems”. *Journal of Heat Transfer*, (1965).

AZIMUTAL, a Tool for the Visualization of Group Constants and Automation in the Generation of NEMTAB Files

Velazquez C. Saul Ricardo; del Valle G. Edmundo

*Escuela Superior de Física y Matemáticas – Instituto Politécnico Nacional
Av. Instituto Politécnico Nacional, S/N, Edif. 9, Unidad Adolfo López Mateos, Gustavo A.
Madero, CDMX, México.*

svelazquezc1400@alumno.ipn.mx; evalle@ipn.mx

Gomez T. Armando Miguel

*Departamento de Sistemas Nucleares – Instituto Nacional de Investigaciones Nucleares
Carretera Toluca – México, S/N, La Marquesa, México, 52750.*

armando.gomez@inin.gob.mx

Abstract

The development and features of AZIMUTAL (AZtlan Interface MUltiTool And Link), a graphical user interface for visualizing group constants generated by a code based on the Monte Carlo method, are described. The group constants are obtained for different universes, energy groups, burn-up steps, and branch combinations, to be later reordered in an automated way in NEMTAB files by AZIMUTAL to feed the input of some of the neutron codes developed by the AZTLAN platform (AZTRAN and AZKIND) or some other configuration required for the analysis of these group constants. The AZTLAN platform codes need these group constants to solve the corresponding equation (neutron diffusion equation or the neutron transport equation, both in multigroup). From the NEMTAB files, it is possible to visualize the group constants in graphs through the nuclear fuel-burnup steps, as a viewer has been generated within AZIMUTAL for this purpose. AZIMUTAL is responsible for searching and extracting information, reordering it, and writing new files of interest to the AZTLAN platform. It also communicates the user's options to the corresponding modules for generating plain text files or images in PNG format. In addition, as a support feature to the AZTLAN platform, it is possible to visualize the distribution maps of rods, materials, or thermal power in the reactor core found in the output file delivered by AZKIND to visualize more quickly the mentioned distributions axially or radially and allow the user to view data in other representations, delivering a folder with all the generated images. AZIMUTAL is built on the Flet framework, which is an adaptation of Flutter in Python and provides an attractive and modern user interface, as well as many of the most common Python libraries: Matplotlib, NumPy, SciPy, and Pillow, which are integrated into different points of the interface to perform mainly the graphics.

1. INTRODUCTION

The AZTLAN platform was born from the call to develop a computing platform for nuclear reactor analysis, a joint effort between the National Institute for Nuclear Research (ININ) who led the project, academic institutions such as the National Polytechnic Institute (IPN), the National Autonomous University of Mexico (UNAM), the Metropolitan Autonomous University (UAM) and institutions of the energy sector to provide Mexico with computational codes for the analysis of nuclear reactors at a competitive level [1].

The calculation considers a Multiphysics character in the reactor core, where neutrons interact with fissile and structural materials.

The AZTLAN platform has four working groups: a) Neutronics, b) Thermohydraulic, c) Coupling, d) Sensitivity and Uncertainty Analysis, and User Group. The neutronics working group oversees neutron code development, verification, and validation. This group is led by the Escuela Superior de Física y Matemáticas (ESFM), belonging to the IPN [2]. Some of its codes are mentioned below:

AZtlan neutron Transport for Reactor ANalysis (AZTRAN): Solves the neutron transport equations, in three dimensions, both in steady-state and in the transient (time-dependent) state in multi-energy groups [3][4].

AZtlan KInetics in Neutron Diffusion (AZKIND): Solves the neutron diffusion equations with G energy groups and I_p delayed neutron precursors [5][6].

In addition, AZKIND generates material and power distribution maps normalized to the average level value for each axial level of the nuclear reactor core. This code generates a plain text output file containing these maps.

The set of values

$$\left\{ \frac{1}{\nu}, \Sigma_t, D, \Sigma_R, \Sigma_S, \beta, \chi, \nu, \Sigma_f, \lambda \right\}$$

is necessary to know, to solve the equations that solve this pair of codes, so AZTRAN and AZKIND must be fed with these values through files in NEMTAB format; this format consists of a data table where each data is separated by a tabulator (or its equivalent in spaces) and each data table forms a group (in this case, a group of energy).

The AZTLAN platform obtains this set of values through the Serpent code [7]. Serpent is a Monte Carlo-based code developed by Finland's VTT Technical Research Centre. It is a multipurpose, three-dimensional, neutron, and photon transport code of continuous energy that exploits parallel computing. The AZTLAN platform codes use Serpent's automated burnup sequence to generate homogenized group constants collapsed into a few energy groups (hereafter only "group constants") through different burn-up steps.

The homogenized group constants have these characteristics:

- They are *group constants* because they depend on an energy group g and do not vary in that group.

- *homogenized* because all materials within the study geometry are considered to mix, resulting in spatial homogenization.
- *and collapsed to a few energy groups* for performing the calculations with H energy groups but presenting the results in G energy groups (by default, $H = 70$ and $G = 2$).

The Serpent code can deliver these group constants for different thermohydraulic variables to varying values of these variables if the user provides the necessary values for that activity in the input file. For example, if the thermohydraulic variables are fuel temperature (FT), coolant temperature (CT), void fraction (VF), and parts per million Boron ($ppmB$), then the group constants (GC) depend not only on the energy group (g), the geometry (u , from “universe”) and the nuclear burnup step (bs), but also on these variables, i.e.,

$$GC(bs, u, g) \rightarrow GC(bs, u, g, TF, TC, VF, ppmB) \quad (1)$$

Then, Serpent delivers a file extension: “.coe” containing group constants in the following arrangement

```
(Loop over executions)
* * * * *
* BRA_1 BRA_2 ...
* * * * *
BU * * * * *
      (Loop over universes)
      UNI N_para
            (Loop over group constants)
            PARA N_val VAL_1 VAL_2 ...
            ...
            (Ends loop)
            ...
            (Terminate loop)
            ...
            (Loop ends)
```

where

- * are values found in the Serpent output file but are not of interest for this work;
- BRA_n the name of the branch;
- BU the nuclear fuel burnup step;
- UNI is the name of the universe where the group constant was calculated;
- N_para is the total number of parameters to follow (vertically);
- PARA the name of the output variable;
- N_val the number of values that follow in the same row; and
- VAL_n the output values.

2. STRUCTURE OF AZIMUTAL

AZIMUTAL was born from programs written in Python [8] that were recreated, optimized, and combined to create new functionalities and improve existing ones. The current project integrates various modules and a user interface that allows the user to obtain a graphical and visualization environment for the data in the provided information files. Table 1 provides the environment and technologies used for this software.

Table I. Description of tools used in the development.

Type of technology	Name	Version
Programming language	Python	3.10.12
Native libraries	collections, os, re, sys	Not applicable
Third-party libraries	flet	0.22.0
	matplotlib	5.2.1
	numpy	3.8.2
	scipy	1.26.3
	pillow	10.2.0
Operative System	Ubuntu	22.04.3 LTS
Third-party packages	python3.10-venv	3.10.12
	python3-tk	3.10.8
	libgtk-3-dev	3.24.43

The project was divided into the following modules: Search and Extraction, Output Generator, Links, Graphical User Interface, and Miscellaneous.

2.1. Module: Search and Extraction

The search and extraction module processes user-supplied input and/or output files. In the case of Serpent files, two files are required: the input file with which Serpent was executed and the output file with `*.coe` extension or the input file and the output file with `*_res.m` extension.

The following parameters are obtained from the input file by string comparison search:

- Name of the case that Serpent solved,
- Nuclear fuel burnup steps and their unit of measurement,
- Number of (few) energy groups,
- Number of precursor groups for delayed neutrons,
- Names of universes,
- Names of branches, and
- Names and values of variables are defined in the branches.

For the case of searching branch names and extracting the values of the variables defined in the branches, the writing format of the branch cards must be considered, which is shown below:

```
branch  NAME_m  [ * * * ]
          [ * * * ]
          [ var  VNAME_1  VAL_1 ]
          ...
          [ var  VNAME_n  VAL_n ]
```

With m not necessarily equal to n.

To obtain this data, the input file should have a defined structure, which implies that the Serpent user follows a template and avoids the use of unnecessary line breaks between elements of the same card or sticks as closely as possible to the Serpent card writing guide. However, this standard is not currently available. One way to address this obstacle and analyze those cases that Serpent already ran was to process and format the input file so that it is easy to read by AZIMUTAL and follows a format like that shown in the Serpent usage guide. This process generates a temporary file, which contains the input data (without user comments) for the Serpent simulation.

Because it is necessary to have the group constants sorted for the correct writing of the NEMTABs (since the group constants depend on the branches, and the branches depend on the values of the variables defined in them), and many times in the input files in Serpent they are written at the user's discretion, it is convenient to sort the values of the variables in ascending order for each of the names of these variables so that the values are related to the name of the branch in the following way:

```
{ VAR_n: { BRA_n,m: VAL_m } }
```

where

- VAR_n is the name of the variable within the branch
- BRA_n,m is the name of the branch
- VAL_m is the variable value for BRA_n,m.

This way of structuring the data is made possible by a variation of the insertion sort algorithm, shown below

```
def insertion_sort(d:dict, p:list, v:str):
    for k in range(1, len(p)):
        while k > 0 and d[p[k]][v] < d[p[k-1]][v]:
            aux = p[k-1]
            p[k-1] = p[k]
            p[k] = aux
            k = k-1
```

Subsequently, a dictionary that stores all the group constants is generated with the data extracted and processed from the input file. The files are then written in NEMTAB format.

Then, a dictionary of dictionaries is created with the following form:

```
GC = { bc_n : { bs_n : { u_n : { c_n : [ ] } } } }
```

where

- bc are the branch combinations,
- bs are the nuclear fuel burnup steps,
- u is the name of the universe for the group constant, and
- c is the name of the group constant to extract and store.

So, calling $CG[bc][bs][u][c]$ accesses the list of constants that Serpent already sorts.

On the other hand, from the `coe` file, we get the values for each group constant. Because the `coe` file is written as a loop through bc , bs , and u , then the extraction is done through a *For loop*, which facilitates the storage of the data, since each of these blocks of information is equal to the previous one, resulting in reading patterns in the `coe` file.

The file `_res.m` file is written through the index generated for each combination obtained with the burn-up step, the branch combinations, and the universe for which the group constants are calculated. The way the data is sorted in this file is well defined, but the indexes are not, so it is convenient to build the branch combinations in order and then store the data through the burn-up stage and then the universe; the way the group constants are ordered is very similar to that of the `coe` file, with the difference that this file contains all the information concerning the execution of the problem with Serpent. This extraction feature from the `_res.m` is still under development and testing. However, the extraction from the `.coe` is the most valid as it was the first to be developed and the reason for the birth of AZIMUTAL.

Similarly, when it is necessary to obtain the data for visualization, this same GC dictionary is reconstructed, but from the NEMTAB files, and with the difference that another level is added to the dictionary: the energy group (or precursor group, or group to group, as the case may be).

When reading the AZKIND output files, keywords are searched to extract the data matrices representing the reactor core maps. In some cases, it is necessary to complete the matrix rows (in the power maps normalized to the average) because data are only found for those regions that produce power so that Matplotlib's generation of polygons is as controlled and standard as possible. At this point, the collections library is used to append zeros at the beginning and end of a list to complete the line.

In previous versions of the module in charge of reading AZKIND output files, the maps were stored in lists of sub-lists, which works adequately if there are no strange structural elements within the geometry of the core, which leads to the existence of regions where there is no power. Still, physically, there is in that region that needs to be displayed, which is why it was decided to use dictionaries of lists to respect these intermediate regions that do not produce power but exist. However, it makes the data structure more complex.

In addition, the module handling the output of files from AZNHEX version 3 is being developed. The main difference between the AZKIND output file and the AZNHEX output file is how the data is represented. While AZKIND represents them by levels, AZNHEX represents the whole core in a data matrix where the columns represent the axial level and the assembly number rows. This

difference requires generating an extra assembly index map to link this data matrix and obtain the diagrams by core plane in the same way as obtained from AZKIND.

2.2. Module: Output Generator

The output generation module oversees generating the NEMTAB files with the data stored in GC; for each universe, a new NEMTAB file is generated through a series of scripts, the format is generated, and the necessary data is written for each data table depending on the nuclear burn-up point, the combination of values for thermohydraulic variables and energy group. The structure of the NEMTAB files for two thermohydraulic variables is shown below

```
* VAR_1  VAR_2
   n      m
   V11    ...  V1n
   V21    ...  V2m
*
* -----
  (Loop over burnup steps)
* Burnup step  bs  units
bs
* -----
*
  (Loop over group constants)
* Group constant 1 (units) $short_name
*
  (Loop over groups)
* Group  g
GC[V11 V21][bs][c][g] ... GC[V1n V21][bs][c][g]
...
GC[V11 V2m][bs][c][g] ... GC[V1n V2m][bs][c][g]
*
  (Terminate loop)
*
  (Terminate loop)
END
  (Terminate loop)
* -----
```

where

- The * does not represent data; it is the character used to comment on lines in the file,
- *n* and *m* are the number of values for the thermohydraulic variables that were found,
- V1n and V2m are the values of these thermohydraulic variables, and each line corresponds to only one type of variable,
- *bs* is the nuclear fuel burnup step,
- *c* is the name of the group constant, and
- *g* is the energy group number.

On the other hand, images are generated for the distribution maps of rods, material, and power in the reactor core. This process is achieved with the dictionaries of data lists obtained through search and extraction; subsequently, using the Matplotlib and NumPy libraries, polygons are generated that represent each of the cells in the core in two dimensions. Then, the Pillow library is used to append important information to the final graph, as well as the images of the AZTLAN platform.

2.3. Module: Links

The inter-module link communicates the graphical user interface with the search, extraction, and output generation modules.

While the previous modules have methods to perform tasks, this module contains calls to several functions of the previous modules to separate the tasks more straightforwardly for the programmer. For example, this module receives parameters from the graphical user interface, calling modules to search and extract information. Once the information is obtained, output generation is called to get the required output files or images.

It is handy when coupling a graphical interface. In this case, it has been connected to Flet, which makes communication within AZIMUTAL easier.

2.4. Module: Graphical User Interface

The graphical user interface (GUI) was developed with Flet and Tkinter. Flet is a framework based on Flutter, and although it is mainly intended for developing mobile applications, it is also capable of developing desktop applications. On the other hand, Tkinter is intended for desktop applications of austere aesthetics but easy adaptation and enough documentation. Both are used because Flet offers user interaction features that are more intuitive and attractive, which gives the visual part a more modern look. At the same time, Tkinter has quite developed the file and folder finder, which is necessary for AZIMUTAL to know where to look for the files you require to analyze.

The graphical interface has multiple views that allow you to group AZIMUTAL's tools and a side menu that allows the user to move between them. The views are:

- **Home:** This section contains information about AZIMUTAL and the AZTLAN platform and sample images (see Figure 1).
- **Generate images (AZTLAN):** This section contains the tools for generating images of rods, material, or power distribution in the reactor core (see Figures 2 and 3).
- **Generate NEMTAB (Serpent):** This section contains the tools for generating NEMTAB files with the group constants obtained by Serpent. In this view, you can select the file from which the data are collected, the prefix, and the group constants to be recovered.
- **View from NEMTAB:** This view contains the graphics area and the different options to visualize the group constants obtained from the NEMTAB files. The controls and

options are generated dynamically with the data found in the files (see Figure 4). It is important to point out that it still needs to be supported to visualize NEMTAB files that do not come from the same execution from Serpent. In addition, the user can save the graph generated with AZIMUTAL.

The viewer can generate graphs of group constants for constants that depend only on the energy group, precursor, or group to group, as in the effective scattering sections. All plots are rectilinear (see Figure 5), except the scattering cross sections, which can be displayed in polar-type plots (see Figure 6).

For generating the graphs related to the practical group-to-group scattering sections, the SciPy library is used with the special.legendre(n) module generates a symbolic function of the Legendre polynomial of degree n. Thus, the module can evaluate the symbolic representation in the following way special.legendre(n)(x) where x is the point where the Legendre polynomial is evaluated.

To understand the construction of the effective group-to-group scattering section, it is necessary to understand the scattering matrices (S[0-7]) and scattering production matrices (SP[0-7]) delivered by Serpent.

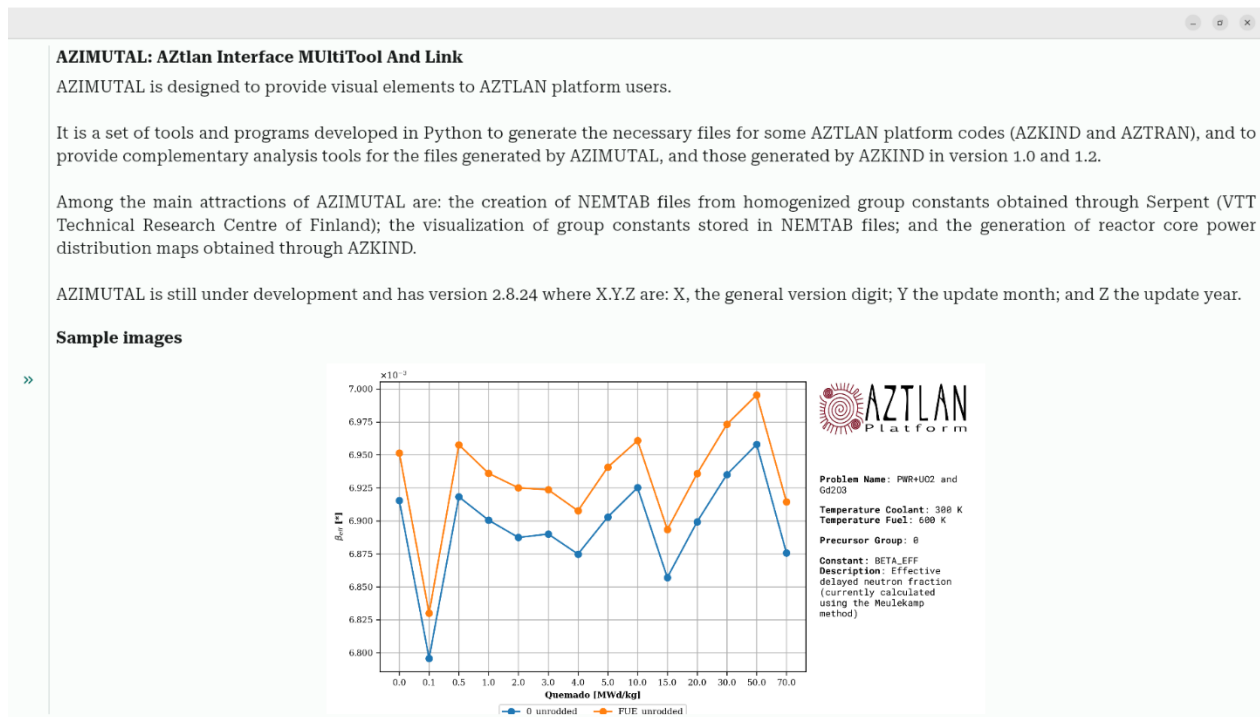


Figure 1. View of the AZIMUTAL home page, with information about the interface and the AZTLAN platform.

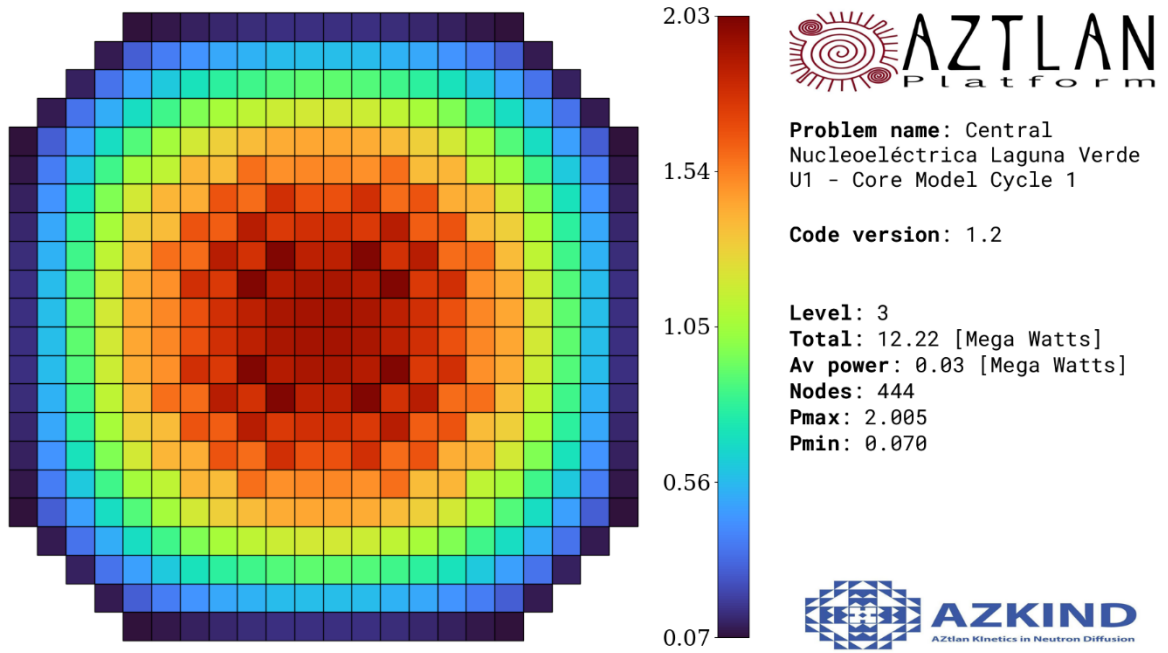


Figure 2. Normalized power distribution map for a BWR type reactor.

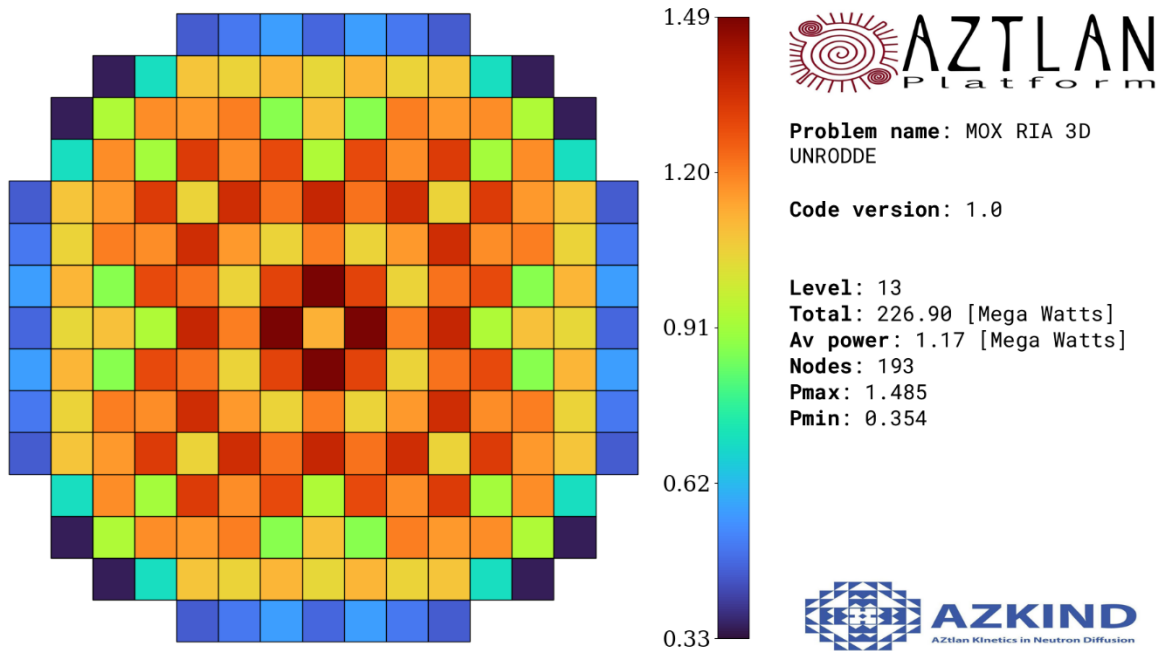


Figure 3. Normalized power distribution map for a BWR type reactor unrodded.

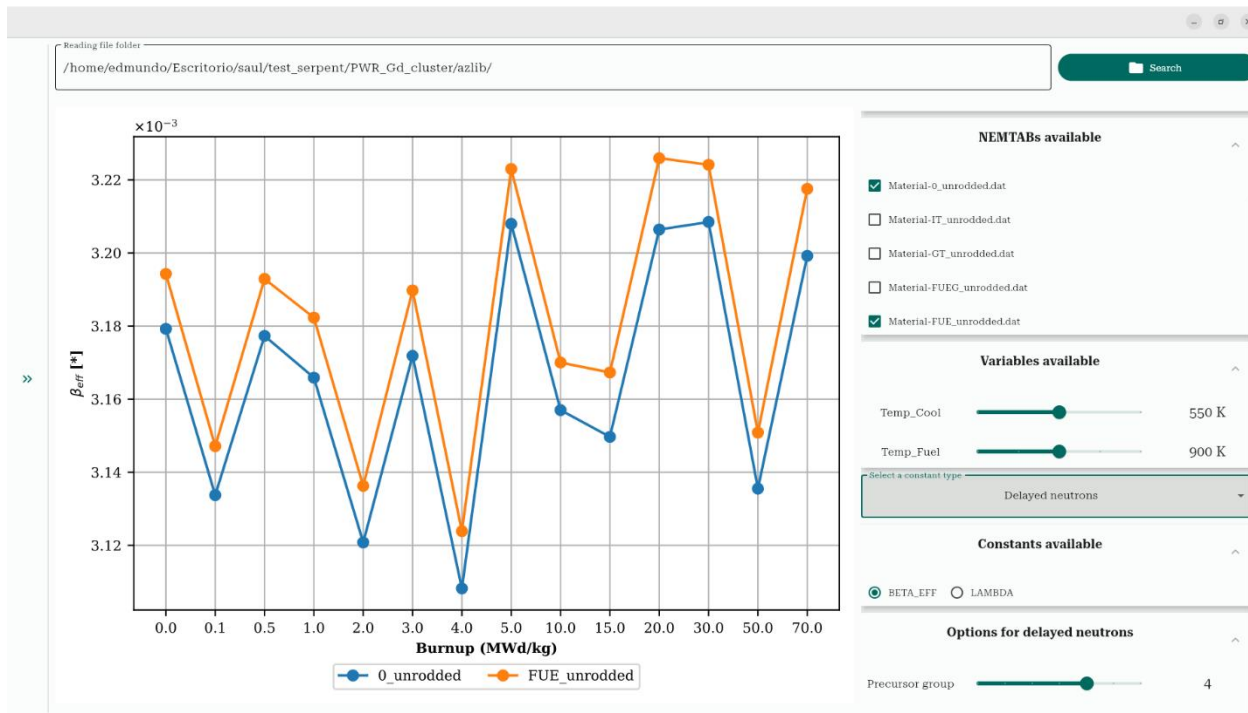
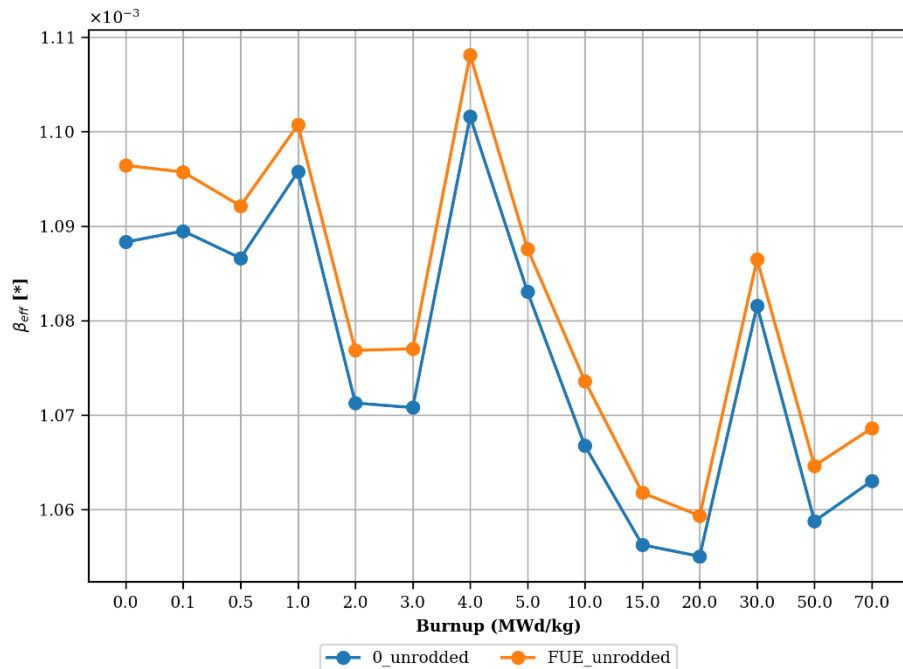
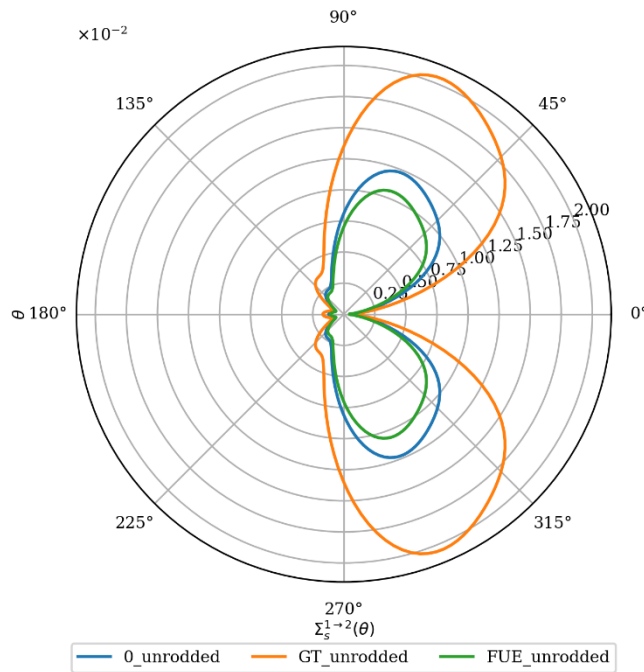


Figure 4. View of the plotting area of the obtained group constants stored in the NEMTAB files.



Problem Name: PWR+UO2 and Gd203
Temperature Coolant: 550 K
Temperature Fuel: 900 K
Precursor Group: 3
Constant: BETA_EFF
Description: Effective delayed neutron fraction (currently calculated using the Meulekamp method)

Figure 5. Chart of the effective beta group constant, obtained from one of the generated NEMTAB files, rectilinear plot.



Problem Name: PWR+UO2 and Gd203
Burnup Point: 15.0 MWd/kg
Temperature Coolant: 300 K
Temperature Fuel: 1200 K
Group to Group: 1 --> 2
Polynomial Degree: 7
Constant: B1_S
Description: From scattering matrices

Figure 6. Effective cross-sectional plot of group-to-group scatterplot, polar plot.

For g energy groups, the scattering matrices from group g to group g' take the following form:

$$\begin{pmatrix} \Sigma_{s,n}^{1 \rightarrow 1} & \dots & \Sigma_{s,n}^{g \rightarrow 1} \\ \vdots & \ddots & \vdots \\ \Sigma_{s,n}^{1 \rightarrow g} & \dots & \Sigma_{s,n}^{g \rightarrow g} \end{pmatrix}$$

where s is for scattering and $n = \{0, 1, \dots, 7\}$.

Then, the effective group-to-group scattering section can be constructed by (equation 2) in case it is required in a rectilinear graph type or by (equation 3) if required in a polar one.

$$\Sigma_s^{g \rightarrow g'}(\mu) = \sum_{n=0}^l \frac{2n+1}{2} \Sigma_{s,n}^{g \rightarrow g'} P_n(\mu) \quad (2)$$

$$\Sigma_s^{g \rightarrow g'}(\theta) = \sum_{n=0}^l \frac{2n+1}{2} \Sigma_{s,n}^{g \rightarrow g'} P_n(\cos \theta) \quad (3)$$

where P_n is the Legendre polynomial of degree n .

2.5. Module: Miscellaneous

This module handles objects, methods, and functions between the search and extraction module and the GUI module. It also has methods to handle errors presented during data search and extraction or data input through the GUI.

It relies on libraries such as *re* (regular expressions) to search for patterns in strings that do not comply with the expectations when reading the various types of files that need to be read.

3. CONCLUSIONS

It is useful to generate supporting codes and tools for collecting data from large files.

To create more robust reading methods, it is necessary to standardize the writing of input files for Serpent and those generated by AZKIND, although AZIMUTAL remedies this for the time being.

AZIMUTAL allows errors to be avoided due to the order of the data entered in the Serpent input file. Since this file allows some flexibility in its writing, in the past, the ordering of the data was done manually to generate the NEMTAB files; the automation methods in AZIMUTAL order the data and avoid the user having to intervene when generating the NEMTAB files by adding tags that facilitate the generation of graphs.

The generation of graphs from the NEMTAB files allows the user to visualize the evolution of the group constants through the burn steps to verify that the data obtained from the Serpent simulation are physically plausible. For the visualization of the effective scattering section, it is possible to visualize and identify whether the coefficients calculated by Serpent are suitable for constructing a univariate function from the Legendre polynomials.

In the case of image generation of the maps contained in the AZKIND output files, the application allows to quickly visualize the power distribution in the reactor core for the analyzed problem, as well as the distribution of materials; on the other hand, it is convenient to exploit the processing threads to the maximum to decrease the total image generation time; a possible implementation is with the thread library to generate two images simultaneously and, in theory, decrease the graphics generation time by half.

Although the graphical interface is versatile, several improvements are still needed to make the user experience more intuitive and to link the software developed on the AZTLAN platform.

ACKNOWLEDGEMENTS

Velazquez C. Saul Ricardo thanks the members of the AZTLAN platform for sharing the outputs of AZKIND and Serpent and clarifying theoretical and programming doubts about AZKIND and the primary use of AZIMUTAL within the platform. Also, a special thanks to CONAHCyT for its postgraduate financial support; this work would not have been achievable without their generous contributions.

REFERENCES

1. Gómez Torres, A.M., Puente Espel, F., del Valle Gallegos, E., Francois Lacouture, J.L., Espinosa Paredes, G., “Avances en el desarrollo de la plataforma mexicana para el análisis y diseño de reactores nucleares: AZTLAN platform”, *XXVIII Congreso Anual de la Sociedad Nuclear Mexicana. New Technologies for a Nuclear Power Expansion Program*, Ciudad de México, 18-21 Junio, (2017).
2. Gómez Torres, A.M., del Valle Gallegos, E., Espinosa Paredes, G, Francois Lacouture, J.L., “El Proyecto AZTLAN platform: un caso de éxito en la formación de recursos humanos en materia nuclear en México”, *XXXIII Congreso Anual de la Sociedad Nuclear Mexicana. Energía Nuclear: la fuente de energía más eficiente para mitigar el calentamiento global*, Veracruz, 13-16 noviembre, (2022).
3. Duran Gonzalez, J.A., del Valle Gallegos, E., Gómez Torres, A.M., “Implementación del método de descomposición en dominios en AZTRAN”, *XXX Congreso Anual de la Sociedad Nuclear Mexicana. Aplicaciones pacíficas de la energía nuclear en beneficio de México*, Monterrey, Nuevo León, 4-7 agosto, (2019).
4. Duran Gonzalez, J. A., “Development of an Upgraded Version of AZTRAN: A 3d Parallel Sn Transport Code for Light Water Reactor Analysis”, Doctoral thesis. Escuela Superior de Física y Matemáticas, Instituto Politécnico Nacional (2022).
5. Rodriguez Hernandez, A., "AZKIND: High Performance Computing Code Based on 3D Neutron Diffusion for Analysis and Simulation of Light Water Nuclear Reactors", Doctoral thesis. In preparation. ESFM-IPN. Mexico.
6. Rodríguez Hernández, A., Ramos Velázquez, D., Gómez Torres, A.M., Ceceñas Falcón, M., del Valle Gallegos, E., “Implementation of a thermal-hydraulic module in AZKIND for steady-state coupled calculations”, *XXX Congreso Anual de la Sociedad Nuclear Mexicana. Aplicaciones pacíficas de la energía nuclear en beneficio de México*, Monterrey, Nuevo León, 4-7 agosto, (2019).
7. Leppänen, J., et al. (2015) "The Serpent Monte Carlo code: Status, development and applications in 2013." *Ann. Nucl. Energy*, **82** (2015) 142-150.
8. Velázquez Cano, S.R., “Desarrollo de un programa de cómputo para la visualización, manipulación y análisis de secciones eficaces para la plataforma AZTLAN”. Bachelor's thesis. Escuela Superior de Física y Matemáticas, Instituto Politécnico Nacional. In preparation. Mexico.

Graphical Interface for Generating SERPENT Input for Light-Water Nuclear Reactors

Sergio Andrés Villamil Clavijo and Edmundo del Valle Gallegos

National Polytechnic Institute

Unidad Profesional Adolfo López Mateos, Zacatenco, Alcaldía Gustavo A.

svillamil2100@alumno.ipn.mx; evalle@ipn.mx

Armando Miguel Gómez Torres

National Institute for Nuclear Research (ININ)

Carr Toluca - México s/n, 52750 La Marquesa, Méx

armando.gomez@inin.gob.mx

Abstract

This article summarizes the development of a graphical interface designed to support the AZTLAN platform in obtaining cross sections, both at the fuel cell level and at the complete core level of light water reactors (pressurized water reactors—PWR and boiling water reactors—BWR). The graphical interface, developed in Python 3.11.4, uses the PyQt5 library. It allows the simplest manipulation of the SERPENT code and provides a visual environment that facilitates real-time design and modification of elements. The interface includes creating materials, fuel rods, fuel cell designs, and complete light water reactor cores. In addition, it allows modification of the boundary conditions to be implemented and the number of annular regions to be considered for the depletion or burning of each fuel material. Furthermore, it enables the extraction of homogenized group constants based on the number of energy groups, macroscopic cross sections, effective multiplication factor, and other SERPENT output information. The graphical interface exports all input data to a file with the extension `sp` corresponding to the SERPENT input file.

1. INTRODUCTION

The AZTLAN Platform [1] is an initiative created to unify efforts and provide tools for analyzing nuclear reactors. This effort enables Mexico to compete effectively in development of software for reactor analysis. The platform incorporates, modernizes, and improves the neutronics, thermohydraulic, and thermomechanical codes developed in Mexican higher education institutions and research institutions.

The AZTLAN platform neutron kinetics codes require libraries of cross-sections for various energy groups to generate consistent results that could be verified with experimental data or reference solutions. The accuracy and consistency of the results are quite sensitive to the cross

sections, which depend on many variables, such as energy, moderator temperature, and fuel temperature, among others (the discussion is expanded later). A methodology was developed to create libraries of cross-sections for a BWR reactor using the SERPENT [2] program, a three-dimensional Monte Carlo code with continuous energy. These libraries could be utilized by the AZKIND [3] and AZTRAN [4] codes, which are part of the platform neutronic codes and are based on multigroup theory, including delayed neutron precursors.

This work contributes to the AZTLAN platform and the methodology for obtaining cross-sections by developing a graphical interface that allows manipulation of SERPENT to produce input either at the fuel cell level or at the complete core level of a water reactor, including pressurized water reactors (PWR) and boiling water reactors (BWR).

1. Description of the graphical interface

The SERPENT input is structured using a card model, where each card has its syntax, arguments, and functions. These cards can be arranged in any order to form a block file. However, the graphical interface displays a light water core input and construction process in the sequence shown in Figure 1 (adapted from reference [4] for this document).

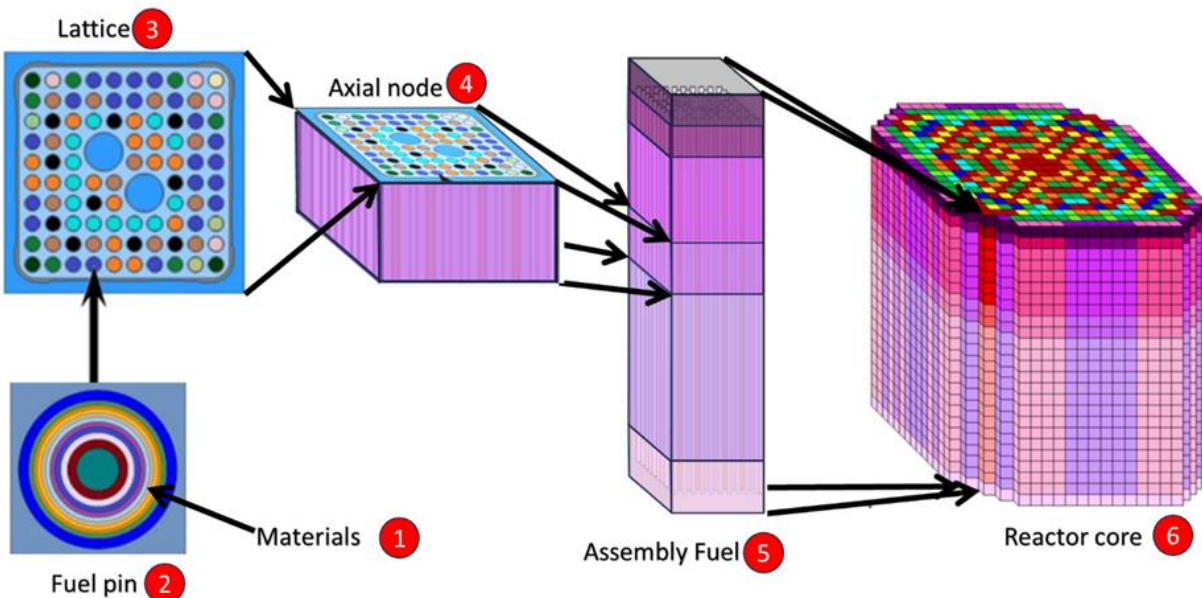


Figure 1. Input construction process for generating a core using the graphical interface.

The graphical user interface (GUI) was created with Python version 3.11.4 using the PyQt5 libraries and the Qt Designer tool. The main window (refer to Figure 2) consists of the standard menu bars and tabs corresponding to the steps outlined in Figure 1 and an additional tab for options.

It can be seen in Figure 2 that, at the top of the GUI, the user must enter the path to the cross-section libraries. Below the main window is a status bar displaying helpful tips for the user. This

is because the interface allows for various potential errors when exporting the designed reactor and running it with SERPENT. For example, component names should not coincide with SERPENT card names or contain special characters (mat, lat, pin, %).

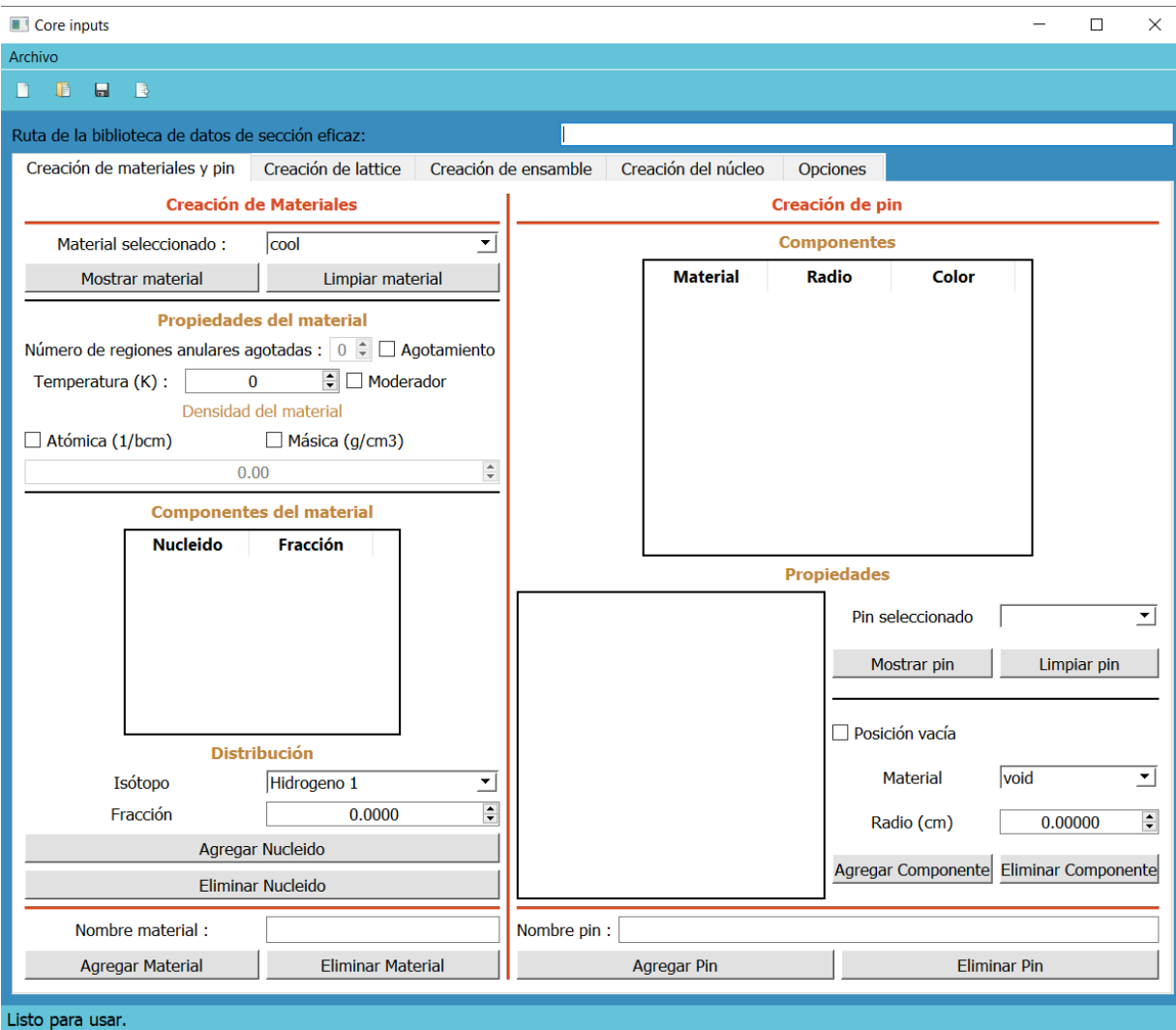


Figure 2. Designed graphical interface main window, material, and pin creation tab.

1.1. Description of Tab 1

The first tab contains two elements from Figure 1: material creation on the left and pin creation on the right. Each of these elements is described below.

1.1.1. Material creation

In the left section of the first tab (see Figure 2), materials can be created and their properties assigned. These properties include the number of annular regions to consider for depletion or burning, temperature, density (atomic or mass), the fraction of each isotope that composes it, and the name.

Among the isotopes available to create a material, some are usually used in the description of the core of a light water reactor [5]: Hydrogen 1, Bore 10, 11, Oxygen 16, Chromium 24, Iron 26, Nickel 28, Zirconium 40, Tin 50, Gadolinium 154, 155, 156, 157, 158, 159, 160, and Uranium 234, 235, 238.

The graphical interface includes predefined materials always available when the application is started. Which are:

- I. Uranium dioxide enriched to 3%.
- II. Water (cool) at a temperature of 600K, pressure of 7 MPa, and a void fraction of 40%.
- III. Water (moder) at a temperature of 600K, pressure of 7 MPa, and a void fraction of 0.0%.
- IV. The clad is composed mainly of Zirconium.
- V. The material of the boxes that contain the sets (box).

The properties of a saved material can be reviewed with the show button. Therefore, predefined materials can serve as examples or templates for new materials. Figure 3 illustrates one of the predefined materials, uranium dioxide enriched to 3% ^{235}U . Table 1 presents the composition and properties of all predefined materials.

Creación de Materiales

Material seleccionado :

Propiedades del material

Número de regiones anulares agotadas : Agotamiento

Temperatura (K) : Moderador

Densidad del material

Atómica (1/bcm) Máfica (g/cm3)

Componentes del material

	Nucleido	Fracción
1	Uranio 235	0.02644492
2	Uranio 238	0.85505247
3	Oxigeno 16	0.11850261

Distribución

Isótopo

Fracción

Nombre material :

Figure 3. Creation of materials, example 3% enriched uranium dioxide.

Material	Cool		Moder		Clad		Box		UOenrch3	
Temperature (K)	600		600		600		600		600	
Density (g/cm ³)	0.44376		0.7396		6.56		6.55		10.1	
Composition	Nuclide	Fraction	Nuclide	Fraction	Nuclide	Fraction	Nuclide	Fraction	Nuclide	Fraction
	Hydrogen 1	0.6667	Hydrogen 1	0.6667	Zirconium 40	0.98135	Zirconium 40	0.98135	Uranium 235	0.02644492
					Chromium 24	0.001	Chromium 24	0.001		
					Iron 26	0.0014	Iron 26	0.00135		
	Oxygen 16	0.3333	Oxygen 16	0.3333	Nickel 28	0.00065	Nickel 28	0.00055	Uranium 235	0.85505247
					Tin 50	0.0134	Tin 50	0.0145		
Oxygen 16					0.000104	Oxygen 16	0.00125	Oxygen 16		

Table 1. Composition and properties of all predefined materials.

1.1.1. Pin creation

On the right side of the first tab (see Figure 2) is the element to create a pin; two pins can be designed, as shown in Figure 4: the one with different annular regions (a) and the pin representing an empty position. (b).

The annular regions consist of materials defined previously in the material creation element. In Figure 4(a), the annular regions for the pin from different regions are related through the table at the top. Although it is not shown, the entire pin is immersed in a moderator by default. On the other hand, the empty position is a region where there is only a moderator.

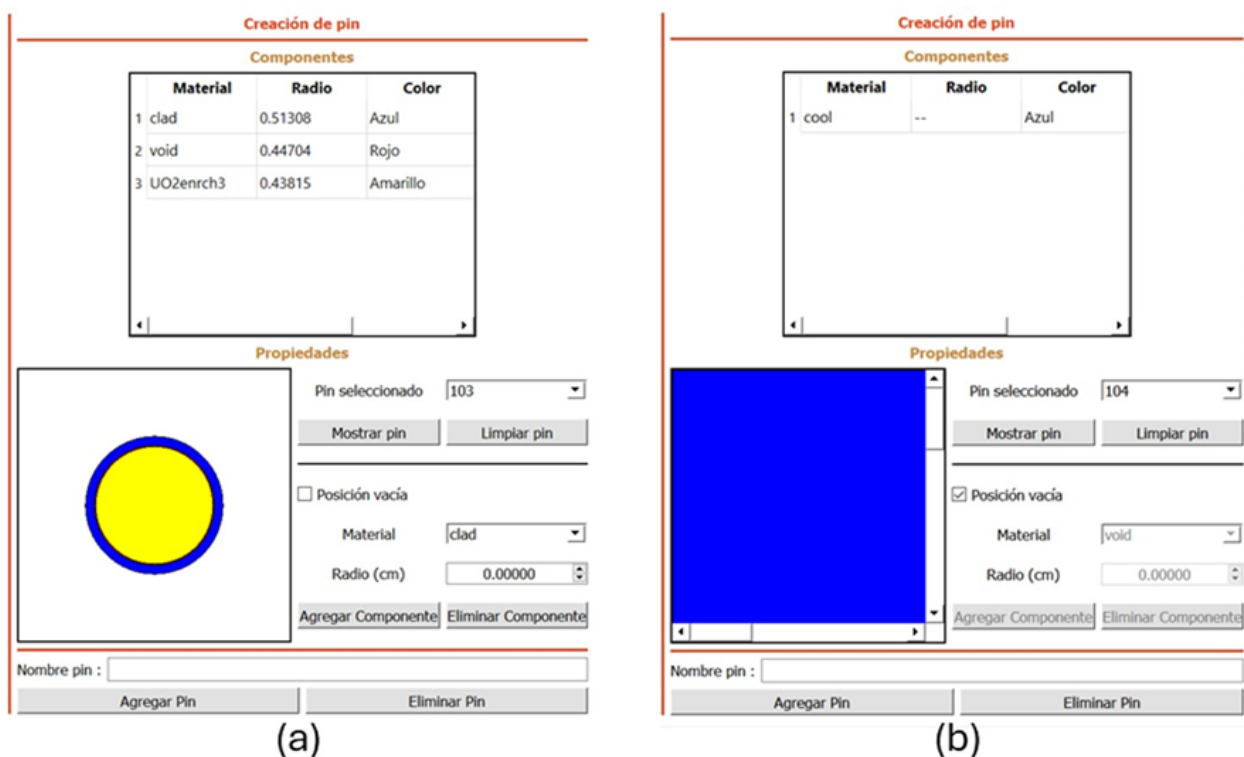


Figure 4. Creation of pins.

1.2. Description of Tab 2: Lattice Creation

Figure 5 shows the lattice creation tab divided into two modules. On the left side, there is a viewer that displays the lattice. Below the display is a box where the user can enter the number of pins to create a square arrangement. In this process, the pins will always have a representative radius. Likewise, the *pin pitch*, the separation due to the variation of this parameter, is a representation (scaled).

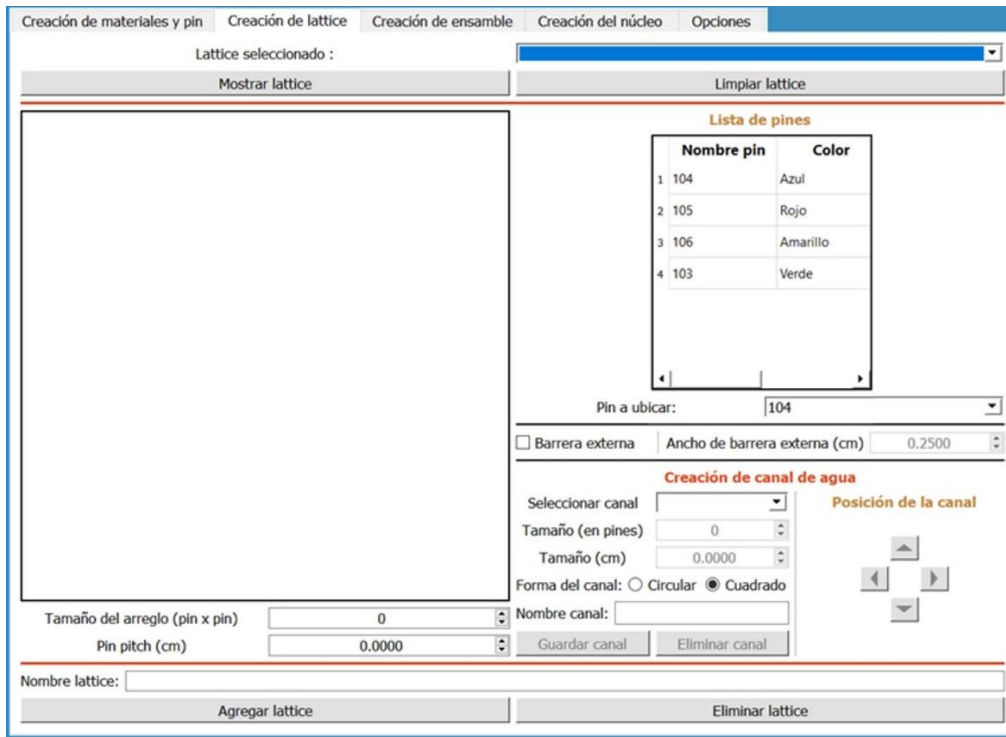
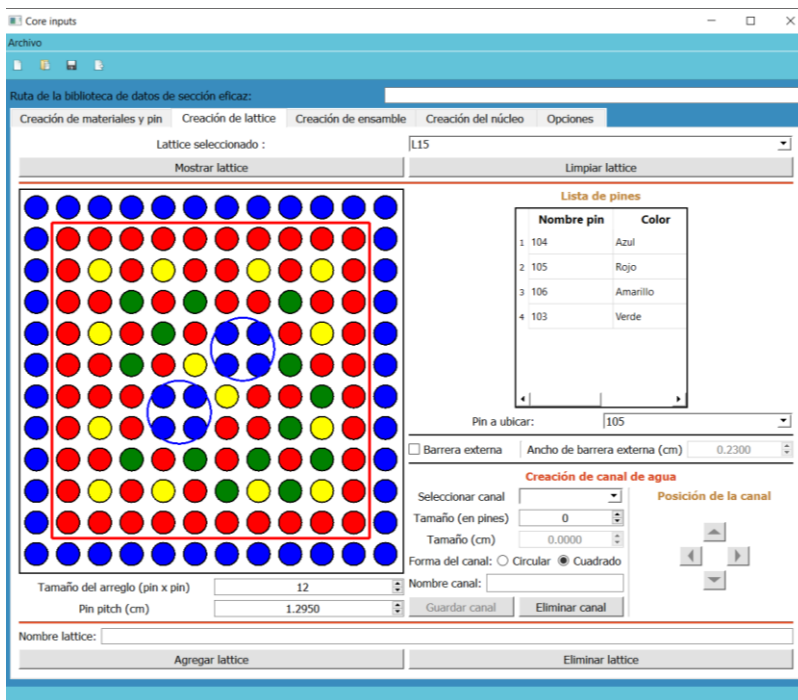


Figure 5. Lattice creation.

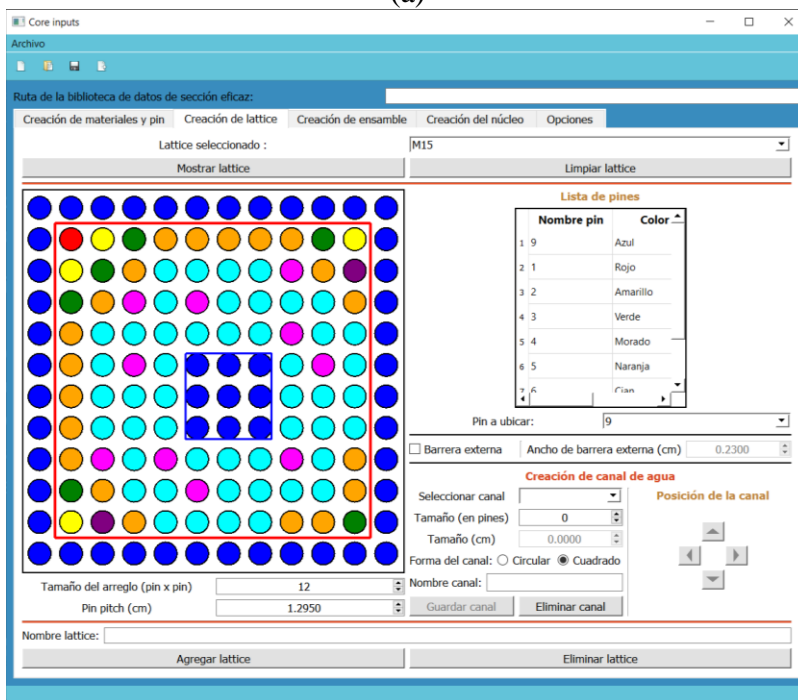
The module on the right side has a table with the heading "pin list." This table shows the relationship between the pins created in the previous tab and their corresponding colors. It helps distinguish the pins in the lattice arrangement. The pins in the table are just examples to help visualize how it works. Then, there is a section for adding an external barrier and water channels. This last section is typical of BWR reactors with more than one internal water channel.

The pins are located by adjusting the number of pins to be considered on each abscissa, then selecting the pin and *clicking* on the desired location. In Figures 6(a) and 6(b), the graphical interface displays the configuration of two *lattices* associated with two BWR reactors. Each *lattice* has a size of 11 x 11 pins and a *pin pitch* of 1.295 cm. The external barrier, represented by a square with a red line, has a width of 0.23 cm. It's important to note that the display does not modify the barrier width. The *lattice* called L15 (a) is composed of a distribution of four different pins and it has two circular water channels, while the *lattice* called M15 (b) is composed of a distribution of eight different pins and it has a larger square water channel.

The pins outside the external barrier are added to represent the conditions from an empty or absent position pin. It is important to note that the pin representing absence also indicates the locations where the coolant flows inside and outside the assembly. As a result, the pins positioned at the lattice border and inside the water channels are of this type.



(a)



(b)

Figure 6. Lattice example: BWR reactors.

The designed graphical interface does not separate the design into different tabs for each type of light water reactor (PWR and BWR). The options allow the information on each reactor to modify the variables necessary for the desired design. For instance, consider the *pin* size, *pitch*, and whether an external barrier should be added or not. Figure 7 displays a *lattice* of a PWR reactor featuring a 17 x 17-pin configuration. The *pin pitch* has been adjusted to 0.72 cm for visualization purposes, although the standard *pitch* is 1.625 cm.

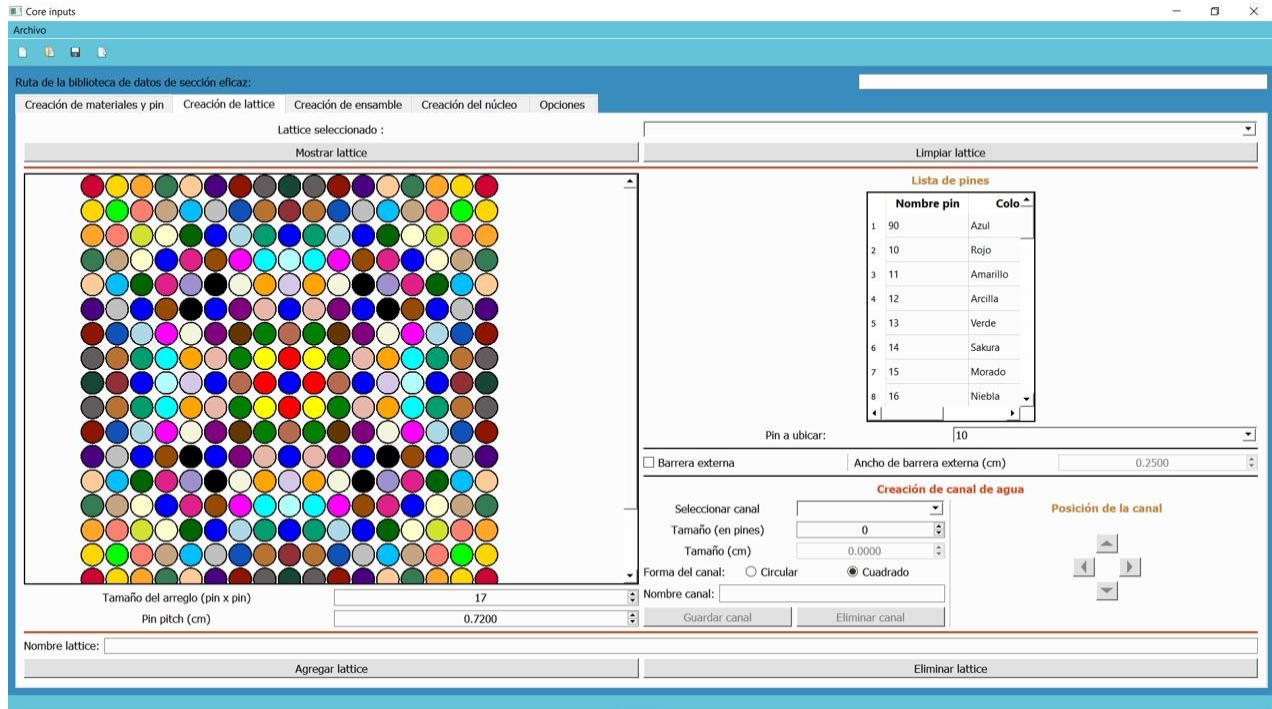


Figure 7. *Lattice* example: PWR reactors.

In this case, 40 different pins were used to create the arrangement. The control rods and instrumentation tube are removed, filling these spaces with coolant. This distribution was taken from an example on the Serpent Wiki [6] which is proposed that the burning of pins be studied in different positions.

1.1. Description of Tab 3: Assembly Creation

The assembly creation tab is shown in Figure 8. The tab is divided into two sections. On the left side is the viewer and the general characteristics of the assembly. On the right side is a table displaying the *lattices*, its vertical size in cm, the color representing it, and its position. The *lattice* is located by adjusting the number of nodes to be considered in the set, then the *lattice* is selected, and the desired node is *clicked*. In addition, Figure 8 illustrates assembly E56, consisting of 25 axial nodes, each with a height of 15.24 centimeters. Pre-designed lattices have been incorporated into this assembly. The overall size of the assembly is 411.48 cm, and variations in this parameter do not affect the representation displayed.

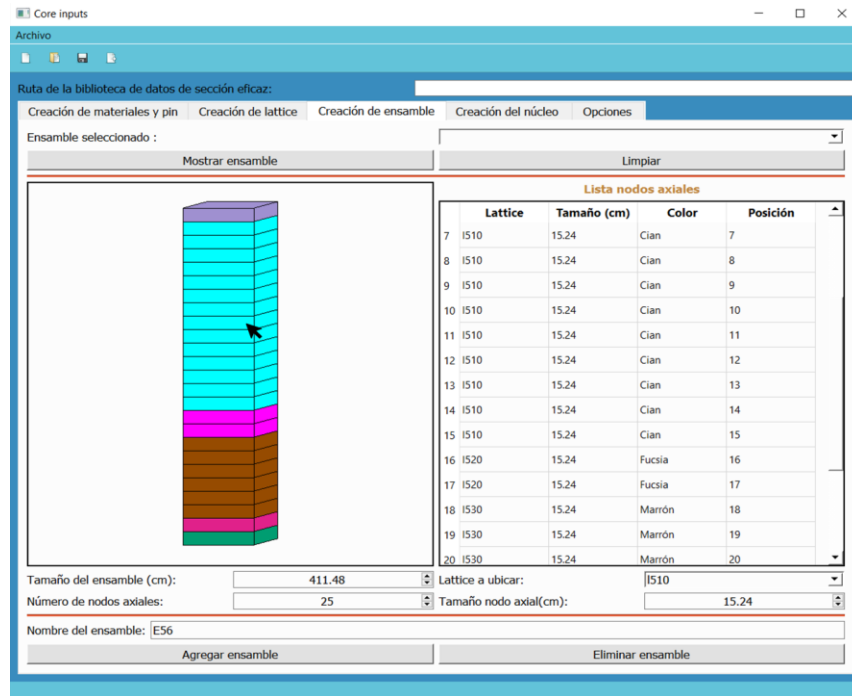


Figure 8. Assembly creation.

1.2. Description of Tab 4: Core Creation

Figure 9 shows the core creation tab, divided into two sections. At the top is the visualizer, which allows interaction through clicks to locate the assemblies. On the right side is a table that allows the user to relate the color to the assembly location. At the bottom are the general characteristics of the core, such as the size of the abscissa assemblies, the pitch for the assemblies, and the name of the designed core.

Figure 9 shows a BWR core named N1, with an abscissa of 25 assemblies and an assembly *pitch* of 15.24 cm. Nine different assemblies create a simple distribution. The first assembly designed in blue is an “assembly” made of a moderator, representing the fluid in which the core is immersed and allowing the void density to be modified axially according to the conditions of interest.

1.3. Additional options

Among the options available there are the boundary conditions offered by SERPENT: *black* (neutrons leaving the universe to die), reflective, and periodic; the neutron population and the number of cycles to be considered; group constants (specifying the number of energy groups) and effective sections.

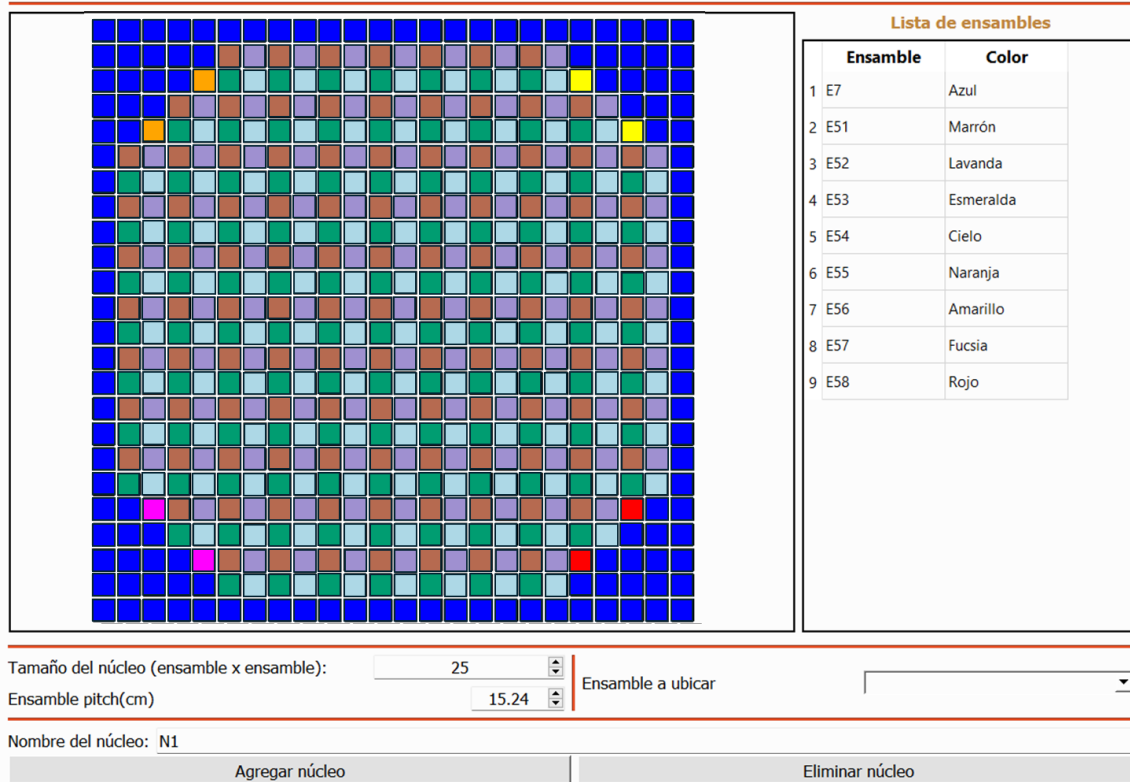


Figure 9. Core creation.

4. CONCLUSIONS

A graphical interface was developed that allows easier manipulation of SERPENT; it provides a visual environment that allows real-time visualization and modification of designed or modified elements, which allows the production of the input either at the fuel or the fuel cell level, the complete core of a light water reactor (pressurized water reactors (PWR) and boiling water reactors (BWR)). It also enables the user to select from the available options for the output provided by SERPENT. The graphical interface exports all entered data to a file with the extension *sp* corresponding to the SERPENT input file.

The graphical interface does not separate the design into tabs for each type of light water reactor (PWR and BWR). Instead, the options allow users to modify the variables necessary for their desired design for each reactor. These include the size of the pin, the number of pins per lattice, the void fraction of the moderator (reflected in the density), and the fuel type.

Future work will include the control rods definition and several additional options that SERPENT offers for calculation.

REFERENCES

1. A. M. Gómez Torres, F. Puente Espel, E. del Valle Gallegos, J.L. François, C. Martin del Campo, G. Espinosa Paredes, “Mexican platform for analysis and design of nuclear reactors.”
Proceedings of the International Congress on Advances in Nuclear Power Plants ICAPP, Niza, Francia (2015).
2. Jaakko Leppänen, Maria Pusa, Tuomas Viitanen, Ville Valtavirta, Toni Kaltiaisenaho, The Serpent Monte Carlo code: Status, development and applications in 2013, Annals of Nuclear Energy, Volume 82, 2015, Pages 142-150, ISSN 0306-4549, <https://doi.org/10.1016/j.anucene.2014.08.024>
3. Andrés Rodríguez Hernández, Armando Miguel Gómez Torres, Edmundo del Valle Gallegos, HPC implementation in the time-dependent neutron diffusion code AZKIND, Annals of Nuclear Energy, Volume 99, 2017, <https://doi.org/10.1016/j.anucene.2016.08.019>.
4. Julian Duran-Gonzalez, Edmundo del Valle-Gallegos, Melisa Reyes-Fuentes, Armando Gomez-Torres, Vicente Xolocostli-Munguia, Development, verification, and validation of the parallel transport code AZTRAN, Progress in Nuclear Energy, Volume 137, 2021, 103792, <https://doi.org/10.1016/j.pnucene.2021.103792>
5. Todd Allena, Jeremy Busby, Mitch Meyer. “Materials Challenges for Nuclear Systems”. Materials Today ,13 (2010).
6. “Serpent Wiki”, https://serpent.vtt.fi/mediawiki/index.php/Main_Page (2015).

First Steps on the Designing and Modeling of a Hight Temperature Gas-Cooled Microreactor

Roberto Lopez-Solis* and Celeste Montaña-Acevedo

*National Institute for Nuclear Research (Mexico)
Carr Toluca - México s/n, 52750 La Marquesa, Méx.
roberto.lopez@inin.gob.mx;
celes.jeanette@gmail.com*

Abstract

In this paper the process of selection of Microreactor (MR) technology, for further development, will be described along with a brief description of the first steps on modeling new reactor designs. The selection process consisted in identifying the desirable capabilities wanted in the final design and compare it with the features of the MR designs publicly available. These criteria included features such as transportability, relatively low power (less than 10 MWe) and the capability of lasting for years without the need of refueling, among others. The reactor type chosen was a Hight Temperature Gas-cooled Reactor (HTGR) due to the coincidence of this kind of reactor in the commercial designs publicly available that meet the previously established criteria. The chosen tool for neutronic modeling of the reactors was the stochastic code Serpent version 2.2.0. Prior to testing new designs of the core, an effort to validate the team capabilities for modeling an HTGRs was carried out, by using the FBMR-400 Pebble Bed as reference. The results obtained in this exercise were comparable with the ones available in references, giving confidence on the team's abilities to handle complex geometries and keep developing the next steps. This is only the first part of a bigger effort, and further stages of this work will be focused on finding geometry, materials, dimensions and other parameters with can lead to a critical Microreactor version of a HTGR.

1. INTRODUCTION

According to the International Atomic Energy Agency, small modular reactors (SMRs) are advanced reactors with a power output of less than 300 MWe [1]. Within this classification are micro-reactors (MRs), which are expected to generate no more than 20 MWe [2]. MRs can be used for electricity generation and even heat for secondary processes such as seawater desalination or hydrogen generation.

Their small size, initial costs and relatively low construction times make MRs an easier option to implement compared to large nuclear power plants.

Micro-reactors are not a new concept, the earliest examples of this technology date back to the 1950s, with reactors designed to operate on submarines in the US and the then Soviet Union [3]. In Mexico, important projects have been developed focused on the design of micro reactors, the most relevant being the MEX-15, proposed in the 1990s by researchers from the National Institute for Nuclear Research [4].

Due to their size and costs, MRs represent an attractive option to bring energy to regions with relatively low energy needs, to remote areas without existing electrical networks or during emergency situations due to natural disasters.

Currently (2024), Mexico is participating in the interregional project “IAEA INT2023: Supporting Member States Capacity Building on Small Modular Reactors and Micro-Reactors and their Technology and Applications as a Contribution of Nuclear Power to the Mitigation of Climate Change”, which aims to train countries interested in implementing a modular or micro reactor program in the future, which has made possible the training of Mexican specialists in these types of reactors.

Considering the mentioned background, it is possible to continue with the domestic development of realistic proposals for MRs, based on existing and proven technologies, with a long-term view of a possible expansion of the nuclear industry in Mexico.

In 2023 it was proposed and approved a project that aims, first of all, to contribute to the effort of in-house developments in nuclear reactor technology, particularly in MRs, and secondly, to study the coupling of nuclear systems to industrial processes for cogeneration. This is a two-year project which first year is aimed to find a MR configuration which can operate for a given life-time inside and that can be fitted in the limited space of a trailer container.

In this paper a brief description of the first stages of this development which consisted in the state-of-the-art study, the selection of criteria to meet, and the first efforts to make a neutronic model.

2. STUDY OF AVAILABLE DESIGNS

In this section a brief description of the state-of-the-art study will be given. Available information was collected on the microreactor concepts most advertised by their developers. The main sources were the portals and technical documents of the developers themselves, as well as the IAEA and NEA [5][6][7] and other compilation sources [8][9], as well as the webpages of the developers of each concept and the news portal World Nuclear News (WNN).

In order to keep the paper no longer than necessary, the Table I shows the main characteristics of each of the MR concepts studied.

One of the goals of the project is to design a MR that the whole reactor could be transported by train or trailer in order to be installed in a remote region or be temporally used in a place affected by a natural disaster in which the power generation/transmission has been affected, with that in mind, a reactor will be called “transportable” if its size is compact, if all its components are assembled at its manufacturing site and can be brought to the final location as a single unit, and if

it can be easily moved to the different location if needed, making it is a key feature in the selection of potential designs. Table I shows that, from the concepts studied, only three meet the transportability requirement.

Even though these three concepts are developed by different companies they present some coincidences on their features:

- Gas cooled
- TRISO Fuel
- Power of around 10 MWe or less

Table I. Microreactor concepts studied

Reactor	Developer	Transportable	Last News	Type	Power
eVinci	Westinghouse	No	2023 [10]	TRISO Fuel + Na Heat Pipes	200 kWe - 5 MWe
Aurora	Oklo Inc.	No	2024 [11]	SFR	2 MWe
Holos Quad	HolosGen	Yes	2019 [12]	HTGR	3 - 13 MWe
Xe-Mobile	X-Energy	Yes	2023 [13]	HTGR	2 - 7 MWe
SEALER	KTH	No	2023 [14]	LFR	55 MWe
U-Battery	Urenco + Others	No	2023 [15]	HTGR	4 MWe
PYLON	UltraSafe Nuclear	Yes	2024 [16]	HTGR	1.5 - 5 MWe
4S	Toshiba	No	2008 [17]	SFR	10 MWe
KLT-40	OKBM	No	2021 [18]	PWR	35 MWe
G4M	Gen4 Energy	No	2008 [19]	LFR	25 - 50 MWe
CLEAR-I	INEST	No	2019 [20]	LFR	10 MWt
MoveluX	Toshiba	No	Not in WNN [21]	SFR	3 - 4 MWe

Once the main features of the goal design were identified, the next logical step is to start modeling a first attempt of the reactor, an intermediate was testing its capabilities by working with a design available in the literature.

3. MODELLING OF REFERENCE EXERCISE

The Pebble Bed reactors concept was proposed and started development from the 1990s as a possible option of electricity generation for Eskom, the electric utility of South Africa. The Pebble Bed Modular Reactor PBMR-400 [22] is a 400 MWt/165MWe high-temperature gas-cooled reactor (HTGR) concept that incorporates a helium closed cycle primary coolant system to transport heat energy directly from the reactor to a recuperative Brayton cycle.

A brief description of the core will be given in this section, if the reader wants to know de design with more detail, full description of the geometry, materials and temperatures is included in the NEA/OECD PBMR-400 Neutronic/Thermal-Hydraulic Benchmark technical document [22].

The active core consist of a concentric cylinders 11.0 high, the first cylinder is 2.0 m diameter and is made of a solid monolith of graphite that acts as a central neutron reflector, in the next radial zone is a hollow ring 85 cm thick that contains about 452,000 fuel pebbles, in the outer-most region there is a radial neutron reflector 90 cm thick that consists in graphite just as in the central reflector. Outside the active zone described there are some other radial and axial regions containing axial reflector, gas plenums, and pressure vessels; for simplicity these are not described in detail.

The pebble is a 6.0 cm diameter graphite sphere that contains 15,000 TRISO particles which themselves consist of a 0.5 mm diameter fuel sphere follower by three carbon-compound layers, as shown in Figure 1.

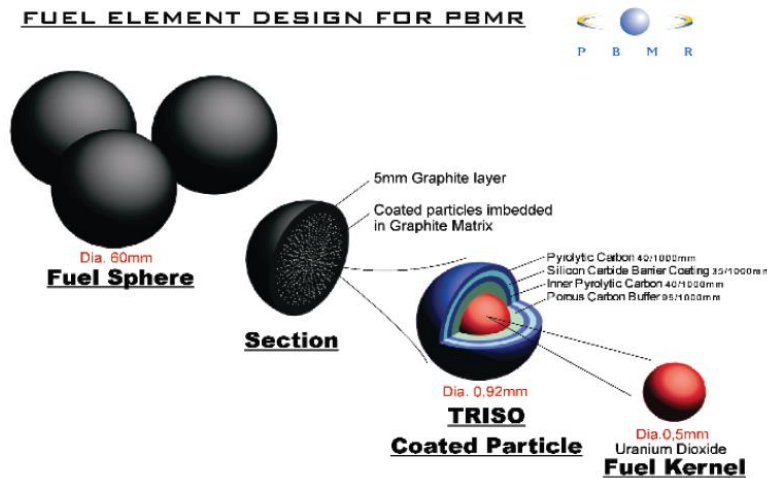


Figure 1. Fuel encapsulation for the PBMR-400 [10]

In order to test the group capabilities in modeling this kind of complex geometries, the results of one of the participants [23] of the benchmark are taken as reference with the objective to reproduce them.

The code used for this exercise was the stochastic code Serpent version 2.2.0, the Figures 2 and 3 show the geometric model of different regions of the core. As can be seen in Figure 3, the Serpent model takes into consideration all the regions considered in the reference, with that and the use of the same material definitions it can be considered that are equivalent models regarding the geometry and materials.

The parameters used in the Serpent simulations were 50,000 particles per cycle with 50/500 inactive/active cycles, which led to standard deviation of about 13 pcm. The run times vary depending on the number of cores used and what it was calculated, for example, using 16 cores times go from less than an hour in the cases where only reactivity was of calculated to up to a few hours in the cases where multiple detectors were used to calculate spectra, flux and power.

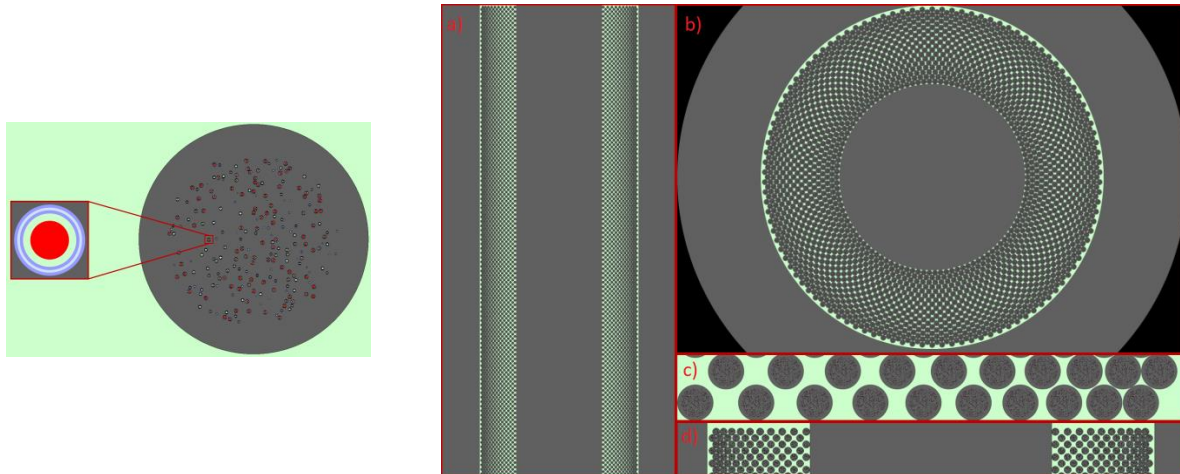


Figure 2. Model in Serpent of a TRISO inside a Pebble (left) and close-up to different regions on the core (right): longitudinal cut of the core (a), radial cross section of the core (b), two adjacent layers of pebbles (c), and upper section of the active core (d)

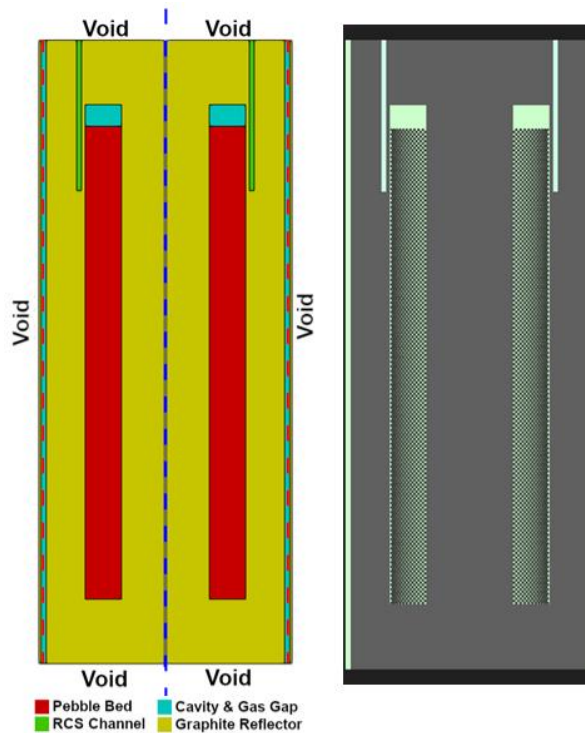


Figure 3. Comparison of geometric models of reference (left) and Serpent (right)

4. RESULTS AND DISCUSSION

In the mentioned reference, their results are compared against other participants in the benchmark, so it is a good reference to compare with. The compared parameters are:

- Fast Flux Axial Profile
- Thermal Flux Axial Profile

- Fast Flux Radial Profile
- Thermal Flux Radial Profile
- Power Axial Profile
- Power Radial Profile

In Figures 4, 5 and 6 the results obtained with Serpent are compared to the ones in the reference. As it can be seen on these figures, there is a good concordance among the calculated values in this exercise and the ones reported in the reference.

There is still chance of improvement in the power profile calculations where more discrepancies are observed against the references, this can be due to the fact that in Pebble Bed geometry Serpent doesn't calculate power profile directly as it does in regular geometries, for its calculation a detector had to be defined as $\kappa\Sigma_f$ as a way to calculate fission power, further studies can be done to define other indirect ways to calculate power, nevertheless, the results are on the same order and the plots shape are close to the consulted references.

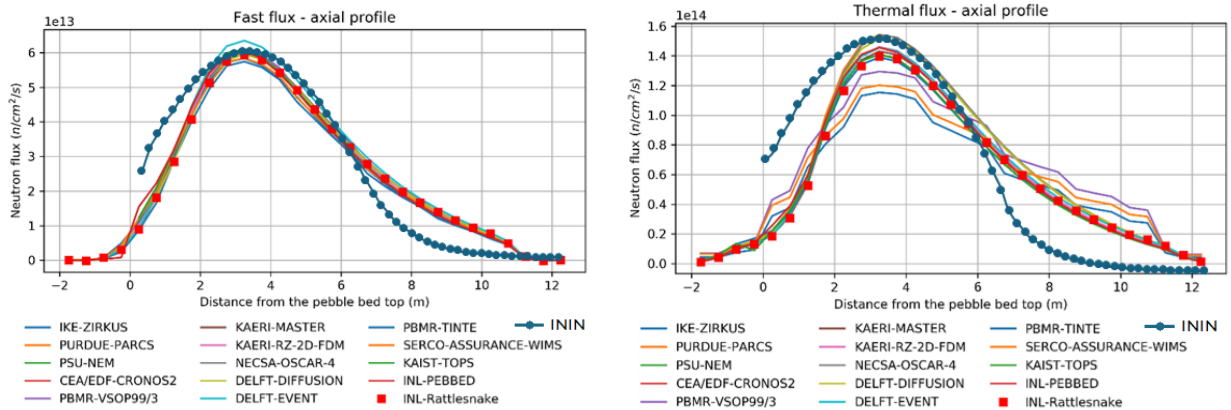


Figure 4. Comparison of obtained results with Serpent (ININ) against reference for the axial profile of fast (left) and thermal (right) flux

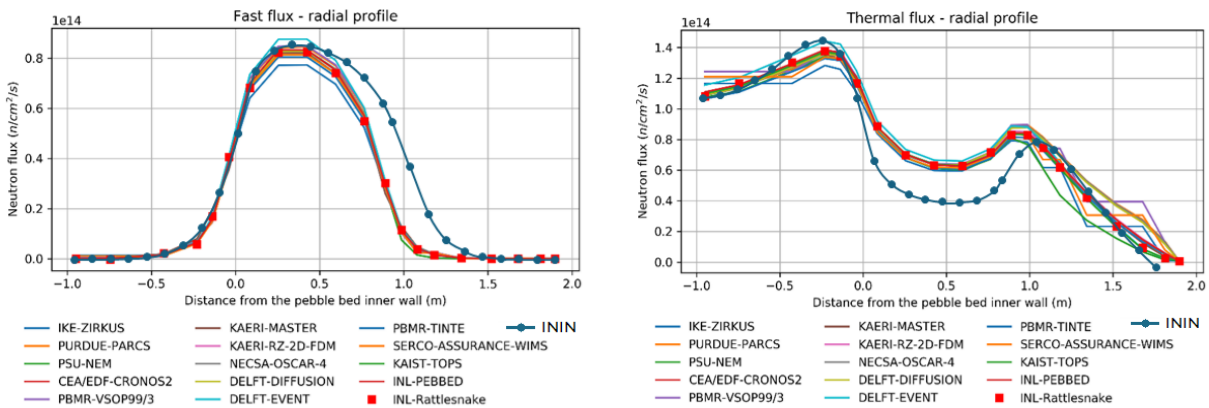


Figure 5. Comparison of obtained results with Serpent (ININ) against reference for the radial profile of fast (left) and thermal (right) flux

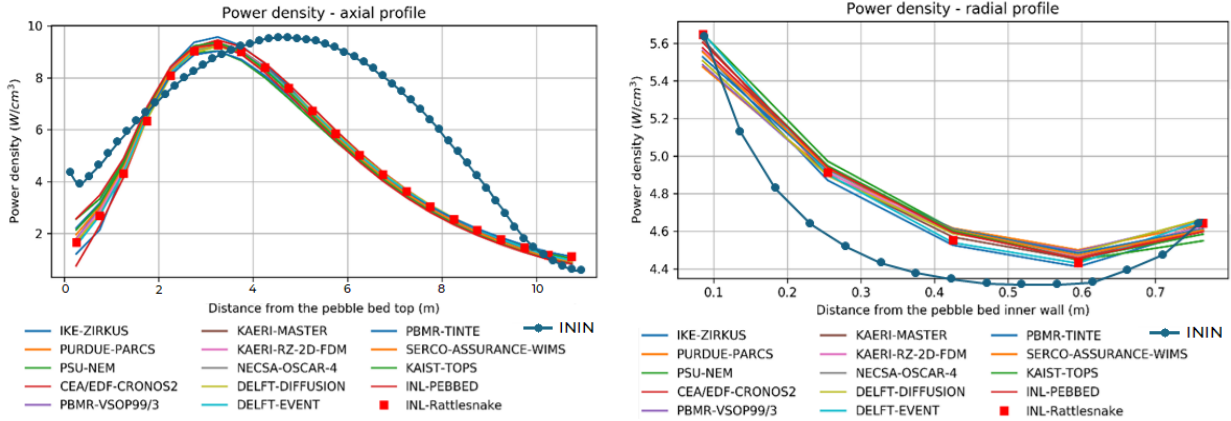


Figure 6. Comparison of obtained results with Serpent (ININ) against reference for the axial (left) and radial (right) power density profile

5. CONCLUSIONS

In this work the early stages of a project, which final goal is to design a MR, were shown, and these included: a) a bibliographical research of the current MR designs, b) the identification of key features wanted in the goal design, and c) the familiarity with the technology to develop (HTGR), its complexity and the challenges involved, by reproducing the results available from a Benchmark. With all this in mind the work done so far is fulfills the goal of the paper.

Further work will be aimed to use this experience in the modeling on new HTGR designs to find the right geometric and material combination that lead to a design that satisfies the features wanted for the new MR.

ACKNOWLEDGEMENTS

The authors thank the National Council of Humanities, Science and Technology (CONAHCYT) for the financial support given to Ms. Montaña-Acevedo during her masters.

REFERENCES

1. Liou, Joane. What are Small Modular Reactors (SMRs)? “International Atomic Energy Agency Website”, <https://www.iaea.org/newscenter/news/what-are-small-modular-reactors-smrs> (2021).
2. INL. Microreactors. “Idaho National Laboratory Webpage”, <https://inl.gov/trending-topics/microreactors/> (2024)
3. WNA. Nuclear-Powered Ships. “World Nuclear Association Information Library Webpage”, <https://world-nuclear.org/information-library/non-power-nuclear-applications/transport/nuclear-powered-ships> (2023)

4. Lucatero, M.A. *Diseño Conceptual Termohidráulico del Núcleo de un Reactor Nuclear de Investigación (MSc Dissertation in Spanish)*. National Polytechnic Institute, Mexico City, Mexico (1998).
5. IAEA. *Technology Roadmap for Small Modular Reactor Deployment (IAEA Nuclear Energy Series No. NR-T-1.18)*, International Atomic Energy Agency, Vienna, Austria (2021).
6. IAEA. *Advances in Small Modular Reactor Technology Deployments*, International Atomic Energy Agency, Vienna, Austria (2022).
7. NEA. *The NEA Small Modular Reactor Dashboard: Second Edition*, OECD Publishing, Paris, France, (2023).
8. Kadak, A. *A Comparison of Advanced Nuclear Technologies*. Columbia University Press, New York, New York, USA, (2017)
9. Testoni, R., Bersano, A., & Segantin, S. "Review of nuclear microreactors: Status, potentialities and challenges". *Progress in Nuclear Energy*, **138**, pp 103822, (2021).
10. WNN, First submissions for Canadian review of eVinci design. "World Nuclear News", <https://world-nuclear-news.org/Articles/First-submissions-for-Canadian-review-of-eVinci-de> (2023)
11. WNN, Oklo plans two plants in Southern Ohio. "World Nuclear News", <https://world-nuclear-news.org/articles/oklo-plans-two-plants-in-southern-ohio> (2023)
12. WNN, DOE announces funding for innovative nuclear technology. "World Nuclear News", <https://www.world-nuclear-news.org/Articles/DOE-announces-funding-for-innovative-nuclear-techn> (2018)
13. WNN, X-energy to develop second Project Pele microreactor design. "World Nuclear News", <https://www.world-nuclear-news.org/Articles/X-energy-to-develop-second-Project-Pele-microreact> (2023)
14. WNN, Studsvik considers SMR deployment at Nyköping site. "World Nuclear News", <https://world-nuclear-news.org/Articles/Studsvik-considers-SMR-deployment-at-Nykoping-site> (2023)
15. WNN, Urenco exits U-Battery micro-reactor project. "World Nuclear News", <https://www.world-nuclear-news.org/Articles/Urenco-exits-U-Battery-micro-reactor-project> (2023)
16. WNN, Fuel flexibility gives MMR range of power outputs. "World Nuclear News", <https://world-nuclear-news.org/Articles/Fuel-flexibility-gives-MMR-range-of-power-output> (2023)
17. WNN, Toshiba launches US nuclear company. "World Nuclear News", <https://world-nuclear-news.org/Articles/Toshiba-launches-US-nuclear-company> (2008)
18. WNN, Nuclear fuel report sees positive long-term future. "World Nuclear News", <https://world-nuclear-news.org/Articles/Nuclear-fuel-report-sees-positive-long-term-future> (2021)
19. WNN, First customer for Hyperion reactor. "World Nuclear News", <https://world-nuclear-news.org/Articles/First-customer-for-Hyperion-reactor> (2008)
20. WNN, Chinese lead-bismuth test reactor starts up. "World Nuclear News", <https://www.world-nuclear-news.org/articles/chinese-lead-bismuth-test-reactor-starts-up> (2019)
21. Toshiba, Pursuing Next-Generation and Advanced Reactors with Enhanced Safety. "Portal de Toshiba Global", <https://www.global.toshiba/ww/products-solutions/nuclearenergy/research/safety-reactor.html> (2024)
22. NEA. *PBMR Coupled Neutronics/Thermal-Hydraulics Transient Benchmark The PBMR-400 Core Design. Volume 1: The Benchmark Definition*. OECD Publishing, Paris, France, (2013).

23. Balestra, P., Schunert, S., Carlsen, R., Novak, A., DeHart, M., Martineau, R. "PBMR-400 Benchmark Solution of Exercise 1 and 2 Using the Moose Based Applications: MAMMOTH, PRONGHORN". *Proceedings of the International Conference on Physics of Reactors (PHYSOR 2020)*. Cambridge, U.K., March 29 - April 2, 2020.

Nuclear Technology Innovations and Export Controls

Eva Gyane
WiN Global
Franz-Siegel-Gasse 26
A-2380 Perchtoldsdorf
Austria
evagyane@gmail.com

Agostina Serrano Bentancour
WiN Argentina
Buenos Aires
Argentina
agos.serranob@gmail.com

Abstract

In the past decade, the rapid development of novel nuclear technologies has significantly influenced the global nuclear landscape. While these advancements hold great potential for peaceful applications, they also introduce complex challenges to the existing nuclear export control regime. The nuclear export control regime, grounded in the Treaty on the Non-Proliferation of Nuclear Weapons and reinforced by the Zangger Committee, the Nuclear Suppliers Group and United Nations Security Council Resolution 1540, has historically played a vital role in preventing the spread of nuclear weapons. These frameworks rely on control lists, which detail the technical specifications of items and technologies that require regulation. However, the advent of advanced manufacturing techniques, such as 3D printing, along with the integration of artificial intelligence, augmented reality, and robotics in nuclear applications, has complicated the task of defining suitable technical parameters for export controls. Additive manufacturing, for example, enables the precise production of components that could be used in uranium enrichment centrifuges or other sensitive nuclear equipment, challenging the traditional methods of export control. Similarly, AI and AR have the potential to enhance nuclear facility operations and training, but they also pose risks of being exploited for non-peaceful purposes. The increasing use of robotics in high-radiation environments, such as in nuclear decommissioning or potentially in clandestine facilities, further highlights the need to update existing control guidelines. The core challenge lies in ensuring that export controls effectively mitigate the risks of technology misuse without hindering their legitimate and peaceful applications. This paper provides a comprehensive review of the current nuclear export control framework, examining its evolution and the mechanisms it employs to prevent nuclear proliferation. It then delves into the specific challenges introduced by these novel technologies, analyzing their implications for the control regime. The paper concludes by advocating for a proactive and adaptive approach to maintaining a robust global nuclear export control system. This approach is essential for preventing the misuse of emerging technologies while simultaneously promoting peaceful nuclear cooperation, a balance that is critical for sustaining international security in an increasingly complex technological landscape.

1. INTRODUCTION

In recent years, there have been tremendous developments in nuclear technology innovation. Most of the novel technologies are dual-use, i.e. they may be used for both civilian and non-peaceful nuclear purposes. At the same time, nuclear export controls that strive to monitor the legitimate trade of certain strategic items and technology rely on the application of control lists, with detailed technical specifications of the controlled items. These control lists are updated on a regular basis, taking into account technological developments. Due to the dual-use nature of the novel technologies, it is mostly very difficult to define suitable technical parameters for controlling these technologies without hampering their peaceful applications. This paper will describe the major nuclear technology innovations and the challenges faced by the nuclear export control community to control such technologies.

2. NUCLEAR EXPORT CONTROL REGIME

Nuclear export controls aim to prevent states and unauthorized entities from acquiring materials, equipment, and technology that could be used to develop nuclear weapons, while ensuring that legitimate trade in these items is not hindering. The nuclear export control regime has its origins in the Treaty on the Non-proliferation of Nuclear Weapons (NPT) that was opened for signature in 1968 and entered into force in 1970. Article III.2 of the NPT has the following requirement: “Each State Party to the Treaty undertakes not to provide: (a) source or special fissionable material, or (b) equipment or material *especially designed or prepared* for the processing, use or production of special fissionable material, to any non-nuclear-weapon State for peaceful purposes, unless the source or special fissionable material shall be subject to the safeguards required by this Article” [1].

As the NPT did not specify what was meant by equipment or material especially designed or prepared (EDP), a committee, the Zangger Committee, was formed to define EDP. The Zangger Committee aimed to harmonize the interpretation of nuclear export control and produced a so-called “Trigger List”, a list of items that would “trigger” a requirement for safeguards and guidelines governing the export of those items to non-nuclear-weapon states not party to the NPT. These guidelines establish three conditions of supply: a non-explosive use assurance, an IAEA safeguards requirement, and a re-transfer provision that requires the receiving state to apply the same conditions when re-exporting these items. The International Atomic Energy Agency (IAEA) publishes the Zangger List on its website as INFCIRC/209¹

Following the “peaceful nuclear explosion” by India in 1974, using plutonium extracted from a reactor provided by Canada for peaceful research purposes, the Nuclear Suppliers Group (NSG) was created. Known originally as the “London Club”, it convened a series of meetings to facilitate a consistent interpretation of the obligations arising from the NPT and agreed on a set of Guidelines incorporating a Trigger List, taking into account the work already done by the Zangger Committee.

The NSG is a group of nuclear supplier countries (currently 48) which seeks to contribute to the non-proliferation of nuclear weapons through the implementation of two sets of Guidelines for

¹<https://www.zanggercommittee.org/download/18.6bee440115cab206b027e/1672310882695/infcirc209r3.pdf>

nuclear exports and nuclear-related exports, both published by the IAEA as INFCIRC/254 (subsequently amended)².

The aim of the NSG Guidelines is to ensure that nuclear trade for peaceful purposes does not contribute to the proliferation of nuclear weapons or other nuclear explosive devices, and that international trade and cooperation in the nuclear field is not hindered unjustly in the process [2]. By introducing order and predictability among supplier countries, the NSG Guidelines facilitate legitimate trade, enabling peaceful nuclear cooperation in a manner consistent with international nuclear non-proliferation norms.

The NSG Guidelines set forth conditions of supply to establish a baseline of responsible and safe supply behavior among suppliers in nuclear and nuclear-related transfers. These conditions include the requirement for IAEA safeguards, formal governmental assurances from recipients, provisions for re-transfer, physical protection measures, and a commitment to exercise particular caution in the transfer of sensitive facilities, technology and weapons-usable materials. The Guidelines also contain the “Non-Proliferation Principle” which seeks to cover the cases where adherence to the NPT or to a Nuclear Weapon Free Zone Treaty may not by itself be a guarantee.

The NSG Guidelines Part 1 governs the export of items that are especially designed or prepared for nuclear use. These include: (i) nuclear material; (ii) nuclear reactors and equipment therefore; (iii) non-nuclear material for reactors; (iv) plants and equipment for the reprocessing, enrichment and conversion of nuclear material and for fuel fabrication and heavy water production; and (v) technology (including software) associated with each of those items. The NSG Guidelines Part 2 governs the export of nuclear-related dual-use items and technologies, that is, items that have non-nuclear uses, for example in industry, but that can also make a major contribution to an unsafeguarded nuclear fuel cycle or nuclear explosive activity [3].

NSG participants review the Guidelines from time to time to ensure that they are up to date to meet evolving nuclear proliferation challenges and technology developments.

The Guidelines are implemented by each country in line with its national laws/practices, and decisions on export applications are made at the national level, following the respective export licensing requirements. The NSG encourages all states, including non-members, to adhere to the Guidelines.

The Zangger Committee Trigger List and the NSG Guidelines Part 1 have become almost identical over time. Together with NSG Guidelines Part 2 they have become the formal framework for nuclear and nuclear-related transfers, augmented by the United Nations Security Council Resolution 1540 (UNSCR1540), unanimously adopted on April 28, 2004.

The UNSCR1540 fills a gap in the nonproliferation regime by addressing the threat of terrorism and non-state actors and prescribes legally binding obligations for all UN member states to implement export controls. These obligations complement and enhance the nuclear export control regime, whose guidelines are implemented at the discretion of each participating government.

²<https://www.iaea.org/publications/documents/infircs/communications-received-certain-member-states-regarding-guidelines-export-nuclear-material-equipment-or-technology>

The nuclear export control regime, grounded in the NPT and reinforced by the Zangger Committee, the NSG, and UNSCR 1540, is crucial for preventing the proliferation of nuclear weapons while enabling legitimate trade, but the emergence of novel technologies demands continuous adaptation.

The international community must proactively address this challenge, updating and reinforcing export controls to prevent these new technologies from being exploited for nuclear weapons development. Maintaining this balance between fostering peaceful nuclear cooperation and preventing proliferation is critical, especially as the landscape of technology continues to evolve and present new risks.

3. NOVEL NUCLEAR TECHNOLOGIES

The past decade has seen a boost in the development of novel nuclear technologies, some of which have a potential to facilitate nuclear proliferation.

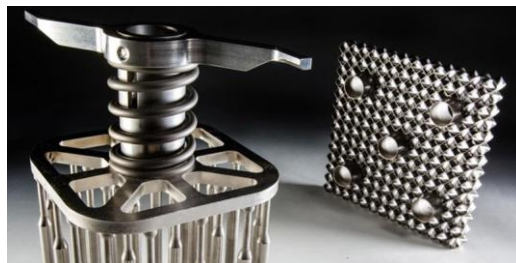
Advanced manufacturing techniques, such as 3D printing, now enable the production of nuclear fuel components with unprecedented precision. Digital twins provide virtual representations of nuclear energy systems throughout their entire lifecycle. By using real-time information and other data sources, the processes of design, licensing, construction, security, operation and maintenance, decommissioning, and waste disposal associated with nuclear energy utilization can be improved. Additionally, augmented and virtual reality technologies offer the capability to simulate the interior of nuclear facilities, for purposes such as training and advanced demonstrations.

3.1. Additive Manufacturing

The term additive manufacturing refers to the process of adding material to an object. This process is contrary to traditional manufacturing methods, which involve removing material from an existing piece of material. There are seven categories of additive manufacturing [4], with 3D printing being the most prominent one amongst them. 3D printing is a manufacturing method that involves building an object layer by layer with the use of a 3D printer and Computer-Aided Design (CAD) software.

In the nuclear field, 3D printing was successfully used by Framatome fuel experts from France, Germany and the USA to print stainless steel and nickel-based alloy fuel assembly components. The fuel assemblies were installed in the 1010 MWe pressurized water reactor at the Gösigen NPP in Switzerland in 2019 for a five-cycle programme as part of a qualification project [5].

Other companies have followed suite. For example, in 2020 Westinghouse Electric Co. announced that it had successfully installed a 3D-printed thimble plugging device in Exelon's Byron Unit 1 nuclear plant during its refueling outage [6]. In Figure 1 is displayed the Westinghouse's 3D-printed thimble plugging device.



**Figure 1. Westinghouse’s 3D-printed thimble plugging device
(credit: Westinghouse Electric Co.)**

Oakridge National Lab (ORNL) recently launched the Transformational Challenge Reactor (TCR) Program to bring to bear Additive Manufacturing (AM) and Artificial Intelligence (AI) to deliver enabling technologies for advanced reactors. Together with Advanced Methods for Manufacturing (AMM) and Nuclear Materials Discovery and the Qualification Initiative (NMDQi), the TCR aims to address the whole lifecycle of nuclear materials and related technologies [7]. Figure 2 shows thermal imaging of the direct deposition of stainless steel used to 3D print a component for a nuclear reactor.



**Figure 2. Use by ORNL of thermal imaging to monitor direct deposition of stainless steel to
3D print a reactor component
(credit: ORNL)**

From a non-proliferation perspective, the question arises whether AM, and in particular 3D printing, could be an enabling technology for the production of nuclear weapons, gas centrifuges or related components.

It has been assessed that additively manufacturing the plutonium or uranium core of a nuclear implosion device is more difficult than using conventional means. On the other hand, other parts of nuclear weapons, for example neutron reflectors made of beryllium-aluminum powders, or high explosives, could be produced using additive manufacturing technologies. 3D printers for

high explosives would need to be designed with the appropriate safety features in mind. Specifications for sealed electrical systems, spark-proof features and remote operation could be added as identifying parameters to the control lists [8].

3D printing could also be used to produce the high strength rotating components of simple gas centrifuges in large quantities as well as ancillary centrifuge equipment such as valves and sensors, thus bypassing the controls on the more complex uranium enrichment technologies.

The capabilities of AM machines do not make it easy to distinguish between those that are proliferation-relevant and those that are not. Defining controlled machines based only on the materials they use has limitations, especially if the materials have a variety of applications. For example, titanium may be produced by AM machines for civilian applications, such as dental implants.

In general, apart from their size, AM machines are hardly distinguishable by the type of object they are capable of producing, and there is significant overlap with many civilian uses that do not require licensing. Therefore, it is extremely challenging to define control parameters that could be added to control lists.

3.2. Artificial Intelligence (AI)

AI and machine learning are used in a number of nuclear applications. A nuclear Digital Twin is a virtual replica of a nuclear facility that allows operators to simulate operational scenarios and predict outcomes. It thereby serves as a risk-free “sandbox” to test and optimize strategies to enhance safety and efficiency of nuclear power plants and develop simulation tools.

AI can automate the process of detecting defects in nuclear fuel assemblies by analyzing data from sensors to predict failures before they occur and by inspecting fuel assemblies for defects. This enables proactive maintenance, reducing downtime and improving plant efficiency. At the same time it improves safety and reduces the time and cost compared with manual inspections.

From a nuclear emergency preparedness and response perspective, AI can be used to analyze relevant factors to predict potential radiation exposure levels during emergencies. This capability aids in the development of more accurate evacuation plans and enhances the overall effectiveness of emergency measures. By leveraging AI, authorities can make more informed decisions in real time, improving the safety of both personnel and the public.

Furthermore, AI can continuously monitor the reactor core, enabling early detection of transients and allowing operators to take prompt corrective action. It can analyze gamma spectroscopy data to detect anomalies that may otherwise go unnoticed.

On the military side, the integration of modern AI and machine learning programs into nuclear command, control, and communications (NC3) systems could have profound implications for global security. When implemented effectively, AI has the potential to reduce human error and bias in nuclear decision-making, thereby preventing critical mistakes during high-risk crisis scenarios [9]. By enhancing early warning systems, improving detection capabilities, and bolstering the resilience of second-strike options, AI could significantly strengthen nuclear

deterrence. However, it is essential to recognize that AI also has inherent limitations; if these are not addressed, they could raise the risk of nuclear use occurring suddenly and without warning. The improper use of AI in nuclear weapons operations could lead to catastrophic, world-ending consequences.

To take full advantage of these benefits, systems must take into account the strengths and limitations of humans and machines. Successful human-machine joint cognitive systems will harness the precision and speed of automation with the flexibility of human judgment and do so in a way that avoids automation bias and surrendering human judgment to machines [10]. AI is developing at a fast pace and it is difficult to imagine how AI could effectively be controlled by the current nuclear export control regime.

3.3. Augmented Reality (AR)

AR is a technology that allows overlaying of real-world objects and environments with 3D virtual objects using an AR device, and which allows the virtual to interact with the real-world objects to create intended meanings. AR enriches an image of the real world with computer-generated images and digital information. It seeks to change perception by adding video, infographics, images, sound, and other details [11].

In the nuclear sphere, AR has been used to create accurate visual representations of ionizing radiation to train radiological workers and radiological control technicians, thus enabling them to “see” radiation. Figure 3 presents the VIPER (Virtual Interaction with Physics Enhanced Reality) technology developed by ORNL [12]. AR has also been used in applications related to NPP maintenance work and to enable smart nuclear industrial infrastructure that a human can easily interact with to improve their performance in terms of safety, security, and productivity [13].

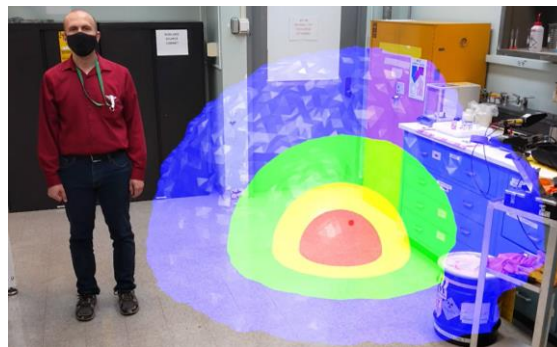


Figure 3. A still image from an ORNL video demonstrating the VIPER technology (credit: ORNL)

AR could be used in a number of nefarious ways, for example to simulate certain nuclear military operations or to train terrorists on the working and operation of nuclear installations, thus posing

a nuclear security threat. Regulating AR within the framework of the current nuclear export control regime presents a significant challenge.

To address these risks, it is vital to adopt strong security measures, including encryption and access controls, as well as monitoring usage. Restricting and overseeing AR content related to sensitive areas can effectively help prevent unauthorized access. Furthermore, collaborating with experts in cybersecurity, nuclear security, and AR technology is essential to establish comprehensive guidelines and best practices for the secure application of AR. Developing targeted training programs for personnel involved in AR will also strengthen security and minimize the risk of misuse.

3.4. Robotics

The key rationale of robotics application in the nuclear industry is to avoid human exposure to hazardous environments and tasks ranging from scrutiny and general maintenance to decontamination and post accidental activities. Robots are also used extensively in decommissioning activities. It is by radiation-resistant robots that the melted cores of the damaged Fukushima reactors are accessed.

To execute all these activities, robots need to incorporate artificial intelligence, improved sensors capability, enhanced data fusion and compliant humanlike leg and hand structures for efficient motions. The next generation of nuclear-related robotic systems is expected to work in full autonomous mode and could also deploy humanoid robots [14]. Figure 4 shows an image of melted fuel inside the core of a Fukushima reactor captured by a robot.



Figure 4. A robot-captured image of melted fuel inside the core of a Fukushima reactor (credit: IRID/Hitachi-GE Nuclear Energy, Ltd.)

Radiation-hardened robot technology is covered under Part 2 of the NSG Guidelines. From a non-proliferation perspective, it is essential to update the control parameters to keep pace with technological advancements. This will help prevent the misuse of such technology, for instance, in a clandestine reprocessing plant where it could be employed to extract weapons-grade plutonium.

4. CONCLUSIONS

The rapid evolution of nuclear technologies presents both opportunities and challenges for the nuclear export control regime, with significant implications for non-proliferation efforts. Emerging nuclear technologies, such as additive manufacturing (3D printing), AI, AR, and advanced robotics, have substantial potential to facilitate nuclear proliferation. These dual-use technologies can be applied in both peaceful endeavors and the development of nuclear weapons. Their ability to circumvent existing controls necessitates continuous scrutiny and updates to control lists to ensure they remain effective.

The challenges presented by some of the novel nuclear technologies covered in this paper are illustrative of many of the wider contemporary challenges to effective implementation of dual-use export controls triggered by technological developments. Defining clear technical parameters for controlling these novel technologies without impeding their peaceful applications is a persistent challenge. It is crucial to update the control parameters in the NSG and Zangger Committee lists to maintain the efficacy of these controls.

Technological advancement demands a coordinated and proactive international response. The challenge will lie in finding a balance between the precision of the technical parameters required to prevent an overlap with legitimate civilian applications and the desire to keep definitions broad enough to encompass emerging technologies effectively. This approach will help ensure that control lists remain relevant and effective as technology evolves. The international community must collectively work to strengthen and adapt the nuclear export control regime to meet the challenges posed by new technologies in a way that allows humanity to maximize the benefits of these technologies and their peaceful uses. Cooperation will be essential for successfully navigating these challenges.

ACKNOWLEDGEMENTS

This paper was written in a collaborative approach by the two authors. We extend our gratitude to WiN Global and WiN Mexico for the opportunity for presenting this paper at WiN Global 2024.

REFERENCES

1. United Nations. (1968). *Treaty on the Non-Proliferation of Nuclear Weapons (NPT)*. Available at <https://treaties.unoda.org/t/npt>
2. Nuclear Suppliers Group. (2022). *The Nuclear Suppliers Group: Its Guidelines, Origins, Structure, and Role - INFCIRC/539/Rev.8*. Available at <https://nuclearsuppliersgroup.org/images/Files%20and%20Documents/Documents/Publications/infcirc539r8.pdf>
3. Nuclear Suppliers Group. (2022). *The Nuclear Suppliers Group: Its Guidelines, Origins, Structure, and Role - INFCIRC/539/Rev.8*. Available at

<https://nuclearsuppliersgroup.org/images/Files%20and%20Documents/Documents/Publications/infncirc539r8.pdf>

4. Loughborough University Additive Manufacturing Research Group. (n.d.). *The seven categories of additive manufacturing*. Available at <https://www.lboro.ac.uk/research/amrg/about/the7categoriesofadditivemanufacturing/>
5. World Nuclear News. (2020, November 5). *URANIUM & FUEL: 3D-printed fuel parts complete initial irradiation cycle*. Available at <https://www.world-nuclear-news.org/Articles/3D-printed-fuel-parts-complete-initial-irradiation>
6. The Fabricator. (2020, May 18). *Westinghouse installs 3D-printed fuel component inside nuclear reactor*. Available at <https://www.thefabricator.com/additivereport/product/additive/westinghouse-installs-3d-printed-fuel-component-inside-nuclear-reactor>
7. Oak Ridge National Laboratory. (n.d.). *Transformational Challenge Reactor (TCR)*. Available at <https://tcr.ornl.gov/>
8. Brockmann, K., & Kelley, R. (2018, April). *The challenge of emerging technologies to non-proliferation efforts: Controlling additive manufacturing and intangible transfers of technology*. Stockholm International Peace Research Institute. Available at https://www.sipri.org/sites/default/files/2018-04/sipri1804_3d_printing_brockmann.pdf
9. Rautenbach, P. (2022, September). *Integrating artificial intelligence into nuclear control*. Arms Control Association. Available at <https://www.armscontrol.org/act/2022-09/features/integrating-artificial-intelligence-nuclear-control>
10. Depp, M., & Scharre, P. (2024, January 16). *Artificial intelligence and nuclear stability*. War on the Rocks. Available at <https://warontherocks.com/2024/01/artificial-intelligence-and-nuclear-stability/>
11. Sruthy. (2024, March 9). *What is augmented reality – Technology, examples & history*. Software Testing Help. Available at <https://www.softwaretestinghelp.com/what-is-augmented-reality/>
12. American Nuclear Society. (2023, May 8). *ORNL-developed AR tool will help workers “see” radiation*. Nuclear Newswire. Available at <https://www.ans.org/news/article-4976/ornldeveloped-ar-tool-will-help-workers-see-radiation/>
13. Mascareñas, D., et al. (2019, June 25). *Augmented reality for enabling smart nuclear infrastructure*. *Frontiers in Built Environment*, 5, 82. <https://doi.org/10.3389/fbuil.2019.00082>
14. Priyanka, K., & Barani Krishnan, G. V. (2018). *Robotics for nuclear power plants*. *International Journal of Engineering Research & Technology (IJERT)*, *Confcall - 2018 Conference Proceedings*. Available at <https://www.ijert.org/robotics-for-nuclear-power-plants>

Two Alternative Proofs to an Inequality Related to a Periodic Power Variation in a Nuclear Reactor

Carlos Antonio Cruz López and Gilberto Espinosa Paredes

*Universidad Autónoma Metropolitana.
cacl.nucl@gmail.com ; gepe@xanum.uam.mx*

Juan Luis François Lacouture

*Universidad Nacional Autónoma de México.
juan.luis.francois@gmail.com*

Abstract

In the context of nuclear reactor dynamics, the Inverse Method determines the type of reactivity that produces a desired behavior in the neutron density (or power level). This method is a fundamental part of programming the control-rod motion of a nuclear reactor. It allows interpreting the power responses in transient analysis from an analytical point of view. In mathematical terms, the Inverse Method also provides important information about the solution of the Neutron Point Kinetics Equations for non-constant reactivities, as the conclusion of the impossibility of using the Laplace transform to solve them, as well as the exponential order of the solutions. One of the earliest applications of this method was related to the study of periodic power variations and reactor oscillator experiments, in which nuclear parameters were measured in unsteady configurations of nuclear fuel, also known as unsteady piles. These experiments mainly aimed to infer the behavior of nuclear devices in extreme conditions. In this context, an important theoretical finding was discovered related to the reactivity that produces a periodic power: it has a negative bias, i.e., the average integral over the extension of the period is negative. To prove this last result, it is necessary to analyze an inequality that is far from being trivial because it requires using Riemann-sums and results related to unordered pairs. In the present work, two alternative methods to prove this inequality are analyzed, which use techniques different from those reported in the literature. The first method consists of applying the integral version of the Jensen inequality, simplifying the proof. The second method addresses a case where assumptions are made over the period. Even when these results are theoretical in nature, they are very relevant because they provide alternative methods to analyze inequalities in the context of nuclear reactor dynamics. Additionally, the analysis of these types of results is a matter of interest to generalize them to the fractional calculus approach, which is a recent line of research.

1. INTRODUCTION.

The time evolution of the neutron population in a nuclear reactor can be modeled using a mass balance approach, where gains and losses are considered. For this task, it is possible to use the one-point assumption, which considers that the spatial flux and the parameters involved do not change with time [1, p. 234]. Assuming this, it is possible to simplify the original system by using the separation of variables, leading to the following set of differential equations:

$$\frac{dn(t)}{dt} = \frac{\rho(t) - \beta}{\Lambda} n(t) + \sum_{i=1}^m \lambda_i C_i(t), \tag{1}$$

$$\frac{dC_i(t)}{dt} = \frac{\beta_i n(t)}{\Lambda} - \lambda_i C_i(t), \quad 1 \leq i \leq m, \tag{2}$$

where $n(t)$ and Λ are the numeric neutron density and the mean neutron generation time [1, p. 238]. $C_i(t)$, λ_i and β_i are the concentration, the decay constant and the fraction of the i -group of precursors of delayed neutrons, respectively. $\rho(t)$ is the reactivity, which can be defined as a measure of the deviation from the critical state [2, p. 7], given by:

$$\rho(t) = \frac{k(t) - 1}{k(t)}, \tag{3}$$

with $k(t)$ the multiplication factor, and:

$$\beta = \sum_{k=1}^m \beta_i. \tag{4}$$

The system given in Eqs. (1-2) is known as the Neutron Point Kinetics Equations (NPKE). As it can be observed, reactivity behavior governs the linearity of the system. Indeed, as Lewins has pointed out [3, p. 59], the system is linear when the reactivity $\rho(t)$ is assumed to be a function that only depends on time, t . Nevertheless, this last assumption is usually valid only in the first stages of the operation of a nuclear reactor, where the feedback effects can be neglected [1, p. 233]. For later stages, on the other hand, ρ can also depend on other variables that are coupled to the power and hence to the neutron density, resulting in the nonlinearity of the system due to the product $\rho \cdot n(t)$ appearing in Eq. (1) [3, p. 60]. As a consequence of this fact, analytical solutions of the NPKE for non-constant reactivities are scarce and commonly expressed in non-closed forms, requiring advanced and approximate methods as the ones developed in [4-6].

Fortunately, from the point of view of the reactor control, it is more adequate to invert the problem in the sense of determining the reactivity $\rho(t)$ that will be associated to a given numeric neutron density $n(t)$ (or to a power $P(t)$). This is the main idea behind the Inverse Method (IM), in which the system given in Eqs. (1-2) is rewritten as follows [1, p. 248]:

$$\rho(t) = \beta + \Lambda \frac{d}{dt} [\ln(n(t))] - \beta \int_0^\infty D(\tau) \frac{n(t - \tau)}{n(t)} d\tau, \tag{5}$$

being $D(\tau)$ the Delayed Neutron Kernel defined as:

$$D(\tau) \equiv \sum_{i=1}^m \frac{\lambda_i \beta_i}{\beta} \exp(-\lambda_i \tau). \tag{6}$$

In this context, the adjective “inverse” means that the behavior of $n(t)$ is known, being usually the desired behavior of the reactor and having the objective determining what value of $\rho(t)$ is associated to it, inverting in this way the original problem of finding $n(t)$ for a specific behavior

of the reactivity. There are several physical and mathematical applications of this method, related to the control of a nuclear reactor, the analysis of the feedback process, and the validation of the analytical models. Among the examples of the first case is the prediction of the negative sign of the average reactivity, ρ_{av} , associated with a periodic power variation. This last relationship can be written in terms of the following inequality:

$$\rho_{av} = \frac{1}{T} \int_0^T \rho(t) dt < 0, \quad (7)$$

where T is the period of the power (or the neutron density), i.e., $n(t) = n(t + qT)$, for $q \in \mathbf{Z}$. This conclusion, simple in appearance, is actually a powerful result that serves to validate the behavior of approximate solutions [7, pp. 155, 165, 230]. In order to prove it, it is necessary to show the following inequality:

$$\int_0^T \frac{n(t - \tau)}{n(t)} dt \geq T, \quad (8)$$

where τ is an arbitrary real number. As it can be observed, (8) is a general statement that is valid for any periodic positive function, regardless of whether it is the numeric neutron density, the power, or any other physical quantity. In the context of nuclear engineering, the only proof of this inequality was proposed by Ergen [8, p. 705], who applied the Rearrangement Inequality (RI) [9], expressing the integral of Eq. (8) in terms of Riemann's sums. In the present work, two alternative proofs to this inequality are developed, considering different approaches that use convexity, as well as a relationship between the arithmetic and the geometric mean.

The discussion of these alternative proofs is important for four reasons: firstly, there are some issues related to the formalism of the Ergen proof, such as the fact that the RI is applied initially to finite sums, not to infinite ones. On the contrary, the proposed proofs do not face these issues and are more rigorous. Secondly, one of the alternative proofs is extremely brief compared to the Ergen discussion, where it is necessary to justify several steps. Thirdly, from a pedagogical and research points of view, it is adequate to establish classical results of the theory of NPKE in terms of more advanced and sophisticated mathematical tools, with the purpose of exploring new approaches. Finally, in the context of the relatively recent research line of Fractional Calculus, it is important to determine what results of the classical theory remain valid with this new type of operators, and therefore these inequalities require a new detailed analysis. The structure of the present works is as follows: Section 2 contains an analysis of the Ergen's original proof, formalizing several steps and exemplifying the techniques used in it. Section 3 contains the first alternative proof using the integral version of the Jensen inequality as well as some results of periodic functions. A weaker proof based on some assumptions of the period is given in Section 4, and Section 5 contains the conclusions.

2. INVERSE METHOD, INEQUALITY AND ERGEN'S SOLUTION

2.1 The Importance of the Inverse Method

As it was mentioned in the Introduction, the IM provides relationships between the reactivity and the power behavior, using the integral transformation given in Eq. (5). This method overcomes

some limitations related to the nonlinearity of NPKE, providing important physical and mathematical information of the nuclear reactor. As a first example, IM allows interpreting measures of the power in transient analysis, expressed in terms of feedback mechanisms. According to Akcasu *et al.* [7, p. 91], this last can be carried out by inserting an initial reactivity, after which the associated power variation is measured using experimental means. Then, the IM uses this power profile and estimates the corresponding reactivity, which will include the inserted one as well as the feedback effects. Using this procedure, which combines experimental and theoretical estimations, it is possible to validate analytical methods related to reactivity insertions and describing feedback effects.

IM also can be used to estimate the exponential order of the neutron density for the case of a ram reactivity, $\rho(t) = at + b$, with $a \neq 0$, where it can be shown that $n(t)$ behaves as $\exp(a\beta t^2/2\Lambda)$ [7, p. 107]. This last fact leads to the conclusion that the Laplace transform cannot be applied to solve the NPKE for this type of reactivity [7, p. 107], being necessary to use other methods, as the one proposed by Smets [10] of the developed my Amano [6]. This finding is relevant because a direct proof of this impossibility using convergence criteria is very complicated or it may not even be possible [11].

Another important application of the IM is the study of power oscillations, which are related to the dynamic stability of a nuclear reactor. The power can exhibit these oscillations due to the delay of some feedback effects, as occurs in the case of the negative temperature coefficient, which does not immediately compensate the excess of reactivity due to a change in the power level [8, p. 702]. Additionally, the analysis of these oscillations is part of the early studies of the instabilities of nuclear piles, as the ones carried out by Wigner [12, p. 529], representing the first attempts to estimate nuclear parameters in extreme conditions. In this context of power oscillations, the description of the reactivity is fundamental, particularly the conclusion that, on average, this is negative. This last fact is expressed in terms of the inequality given in (8), whose development is discussed in the following section.

2.2 Building the Inequality

After integrating Eq. (5) and dividing it by T , it follows that:

$$\begin{aligned} \rho_{av} &= \frac{1}{T} \int_0^T \rho(t) dt = \beta + \frac{\Lambda}{T} \int_0^T \frac{d}{dt} [\ln(n(t))] dt - \frac{\beta}{T} \int_0^T \int_0^\infty D(\tau) \frac{n(t-\tau)}{n(t)} d\tau dt \\ &= \beta \left(1 + \frac{\Lambda}{\beta T} \int_0^T \frac{d}{dt} [\ln(n(t))] dt - \frac{1}{T} \int_0^\infty D(\tau) \int_0^T \frac{n(t-\tau)}{n(t)} dt d\tau \right). \end{aligned} \quad (9)$$

The integral involving the logarithm is cancelled after observing that the property of periodicity, $n(t) = n(t + T)$, implies that $\ln(n(T)) = \ln(n(T + T))$:

$$\int_0^T \frac{d}{dt} [\ln(n(t))] dt = \ln(n(T + T)) - \ln(n(T)) = 0. \quad (10)$$

Since $\beta > 0$, it is possible to conclude that the negative sign of the average ρ_{av} of Eq. (9) is reduced to the following inequality:

$$1 - \frac{1}{T} \int_0^\infty D(\tau) \int_0^T \frac{n(t-\tau)}{n(t)} dt d\tau < 0, \quad (11)$$

which in turn is reduced to:

$$\int_0^\infty D(\tau) \int_0^T \frac{n(t-\tau)}{n(t)} dt d\tau > T. \quad (12)$$

It is possible to simplify this last relationship with the purpose of writing it in terms of a single integral instead of a double one. For this task, it is necessary to consider the following normalized relationship:

$$\int_0^\infty D(\tau) d\tau = 1, \quad (13)$$

that fulfills the Delayed Neutron Kernel [7, p. 92]. Since the most nested integral involving the quotient $n(t-\tau)/n(t)$ will produce a continue function $H(\tau)$, it is possible to write:

$$\int_0^\infty D(\tau) \int_0^T \frac{n(t-\tau)}{n(t)} dt d\tau = \int_0^\infty D(\tau) H(\tau) d\tau. \quad (14)$$

If $H(\tau) \geq T$:

$$\int_0^\infty D(\tau) H(\tau) d\tau \geq \int_0^\infty D(\tau) T d\tau = T \underbrace{\int_0^\infty D(\tau) d\tau}_{\text{Using Eq. 13}} \geq T. \quad (15)$$

Therefore, from the last analysis it follows that proving the inequality given in (12) is equivalent to prove that $H(\tau) \geq T$, i.e.:

$$\int_0^T \frac{n(t-\tau)}{n(t)} dt \geq T, \quad (16)$$

which is the same expression mentioned in the Introduction. Before concluding this section, it is worth mentioning that the only cases where the equality is obtained is when $\tau = qT$. Nevertheless, since this parameter is running in the positive real numbers in the double integral in Eq. (9), it follows that the strict inequality is obtained if these last cases (that are finite) are omitted.

2.3 Transforming the Integral to a Sum

It is possible to interpret the left side of (16) under the concept of Riemann integral. From this theory, it is known that [13, p. 296]:

$$\int_0^T f(t) dt = \lim_{N \rightarrow \infty} \frac{T}{N} \sum_{k=1}^N f\left(\frac{kT}{N}\right), \quad N \in \mathbf{N}. \quad (17)$$

Applying (17) to the left side of (16), and considering a product of functions, it follows that:

$$\int_0^T \frac{n(t-\tau)}{n(t)} dt = T \lim_{N \rightarrow \infty} \frac{1}{N} \sum_{k=1}^N n\left(\frac{kT-\tau}{N}\right) \cdot \left(\frac{1}{n\left(\frac{kT}{N}\right)}\right). \quad (18)$$

Using the following notation:

$$a_k = n\left(\frac{kT-\tau}{N}\right), \quad b_k = \frac{1}{n\left(\frac{kT}{N}\right)}, \quad (19)$$

the Eq. (18) can be rewritten as:

$$T \lim_{N \rightarrow \infty} \frac{1}{N} \sum_{k=1}^N a_k b_k. \quad (20)$$

In this point it is necessary to reproduce an important theorem that is the core of Ergen's proof.

2.4 Rearrangement Inequality

Theorem 1. *Let $a_i, b_i, 1 \leq i \leq N$, two sets of real numbers. Then the sum:*

$$\sum_{i=1}^N a_i b_i, \quad (21)$$

is greatest when a_i, b_i are monotonic in the same sense and least when they are monotonic in opposite sense; that is to say:

$$\sum_{i=1}^N a_{\sigma_1(i)} b_{\sigma_2(N+1-i)} \leq \sum_{i=1}^N a_i b_i \leq \sum_{i=1}^N a_{\sigma_1(i)} b_{\sigma_2(i)}, \quad (22)$$

where $\sigma_1(i), \sigma_2(i)$ are permutation functions of the set $\{1, 2, \dots, N\}$ with:

$$a_{\sigma_1(1)} \leq a_{\sigma_1(2)} \leq \dots \leq a_{\sigma_1(n)}; \quad \text{and} \quad b_{\sigma_2(1)} \leq b_{\sigma_2(2)} \leq \dots \leq b_{\sigma_2(n)}.$$

The inequality given in Eq. (22) is known as the Rearrangement Inequality (RI), and its proof was provided by Hardy *et al.* [9, p. 261] using elementary techniques of algebra. A brief example of its application will be analyzed to clarify the present discussion. First, the following set of numbers will be considered:

$$\begin{aligned} a_1 &= 2, & a_2 &= 7, & a_3 &= 1, & a_4 &= 4; \\ b_1 &= 10, & b_2 &= 2, & b_3 &= 9, & b_4 &= 1. \end{aligned} \quad (23)$$

As it can be observed, the original indexation (the lower right index) represents an arbitrary order of the numbers. These sets can be reordered in ascending monotonic fashion, defining the following permutation functions:

$$\begin{aligned} \sigma_1(1) = 3, \quad \sigma_1(2) = 1, \quad \sigma_1(3) = 4, \quad \sigma_1(4) = 2; \\ \sigma_2(1) = 4, \quad \sigma_2(2) = 2, \quad \sigma_2(3) = 3, \quad \sigma_2(4) = 1. \end{aligned} \tag{24}$$

Using them, the following relationship is obtained (the original indexation is shown in the underbrace symbols):

$$\begin{aligned} \underbrace{a_{\sigma_1(1)}}_{a_3} \leq \underbrace{a_{\sigma_1(2)}}_{a_1} \leq \underbrace{a_{\sigma_1(3)}}_{a_4} \leq \underbrace{a_{\sigma_1(4)}}_{a_2}, \\ \underbrace{b_{\sigma_2(1)}}_{b_4} \leq \underbrace{b_{\sigma_2(2)}}_{b_2} \leq \underbrace{b_{\sigma_2(3)}}_{b_3} \leq \underbrace{b_{\sigma_2(4)}}_{b_1}. \end{aligned} \tag{25}$$

Computing the sums that appear at the extremes of (22):

$$\begin{aligned} \sum_{i=1}^4 a_{\sigma_1(i)} b_{\sigma_2(4+1-i)} &= a_{\sigma_1(1)} b_{\sigma_2(4)} + a_{\sigma_1(2)} b_{\sigma_2(3)} + a_{\sigma_1(3)} b_{\sigma_2(2)} + a_{\sigma_1(4)} b_{\sigma_2(1)} \\ &= a_3 b_1 + a_1 b_3 + a_4 b_2 + a_2 b_4 = 1 \cdot 10 + 2 \cdot 9 + 4 \cdot 2 + 7 \cdot 1 = 43, \end{aligned} \tag{26}$$

and similarly:

$$\begin{aligned} \sum_{i=1}^4 a_{\sigma_1(i)} b_{\sigma_2(i)} &= a_{\sigma_1(1)} b_{\sigma_2(1)} + a_{\sigma_1(2)} b_{\sigma_2(2)} + a_{\sigma_1(3)} b_{\sigma_2(3)} + a_{\sigma_1(4)} b_{\sigma_2(4)} \\ &= a_3 \cdot b_4 + a_1 \cdot b_2 + a_4 \cdot b_3 + a_2 \cdot b_1 = 1 \cdot 1 + 2 \cdot 2 + 4 \cdot 9 + 7 \cdot 10 = 111. \end{aligned} \tag{27}$$

Therefore, the [Theorem 1](#) states the following inequality:

$$43 \leq \sum_{i=1}^N a_i b_i \leq 111, \tag{28}$$

where the middle sum represents an arbitrary ordering of the elements. In other words, the sum of the product of any permutation of the elements a_i, b_i lies in such range.

2.5 Ergen's Proof

The proof developed by Ergen consists of applying [Theorem 1](#) to the sum of [Eq. \(20\)](#). Nevertheless, even when the justification can be deduced straightforwardly, it is not evident nor obvious, and the explanations reported in the literature are not given in detail (see, for example [\[7, p. 92\]](#) and [\[8, p. 705\]](#)). In the present work the following formal justification is provided: firstly, it is necessary to observe that under the range of the periodicity, the functions $n(t)$ and $n(t - u)$ produce the same values, i.e., they have the same image of real numbers denoted by Ω :

$$n(t): [0, T] \rightarrow \Omega, \quad n(t - u): [0, T] \rightarrow \Omega. \tag{29}$$

This can be exemplified in [Figure 1](#), where an arbitrary periodic profile for the numeric neutron density is assumed. In that scheme, a negative variable u , with $-u < T$ is considered, which is equivalent to introducing a displacement in the domain of the function, represented with the vertical dot lines in light blue color. Therefore, the integral of the function $n(t - u)$ over the interval $[0, T]$ takes into account the same points of the integral of $n(t)$, but in a different order. In the first case, the summation inside of the integral begins in the point $t = -u$, and ends in $t = T - u$. Nevertheless, due to the periodicity, the same area under the curve is computed in both cases, but in the last one it runs over a modified domain. Since the present problem was transformed to the sum given in [Eq. \(20\)](#), it is necessary to extend the relationship [\(29\)](#) to discrete sets, instead of continuous ones. For such task a partition, $t_i, 1 \leq i \leq N$ of the interval $[0, T]$ of length T/N will be introduced, which allows defining the following set:

$$\Omega_1 = \{a_i \mid a_i = n(t_i), 1 \leq i \leq N\}. \tag{30}$$

This represents a discrete set of images of the function $n(t)$, under the partition mentioned before, and related to the Riemann sum given in [Eq. \(20\)](#). Since we do not have information about the monotonicity of the function, it is necessary to define a permutation, $\sigma_1(i), 1 \leq i \leq N$, that allows ordering such values in an ascending way:

$$a_{\sigma_1(1)} \leq a_{\sigma_1(2)} \leq \dots \leq a_{\sigma_1(N)}. \tag{31}$$

Similarly, another discrete set is defined as follows:

$$\Omega_2 = \left\{ b_i \mid b_i = \frac{1}{n(t_i)}, 1 \leq i \leq N \right\}. \tag{32}$$

It is worth mentioning that all the elements of the set Ω_2 are well defined because $n(t) > 0$, for all $t \in [0, T]$. Since the numbers b_i are the inverse of the elements in the set Ω_1 , it follows that, under the same permutation $\sigma_1(i)$, the following descending order is obtained:

$$b_{\sigma_1(1)} \geq b_{\sigma_1(2)} \geq \dots \geq b_{\sigma_1(N)}. \tag{33}$$

In other words, when the elements a_i are ordered in an ascending way, then their inverses are ordered in a descending way. Therefore, it is possible to conclude that:

$$\sum_{i=1}^N a_{\sigma_1(i)} b_{\sigma_1(i)} = \sum_{i=1}^N a_{\sigma_1(i)} \left(\frac{1}{a_{\sigma_1(i)}} \right) = \sum_{i=1}^N 1 = N, \tag{34}$$

which in virtue of [\(31\)](#), [\(33\)](#) and [Theorem 1](#), represents the lower bound of the sum given in [\(22\)](#). Therefore, it follows that the integral written using [Eq. \(20\)](#) fulfills the following relationship:

$$T \lim_{N \rightarrow \infty} \frac{1}{N} \sum_{k=1}^N a_k b_k \geq T \lim_{N \rightarrow \infty} \frac{1}{N} \underbrace{\sum_{i=1}^N a_{\sigma_1(i)} b_{\sigma_1(i)}}_{\text{Lower bound of Theorem 1}} \geq T \lim_{N \rightarrow \infty} \underbrace{\frac{1}{N} N}_{\text{By Eq. (34)}} \geq T, \tag{35}$$

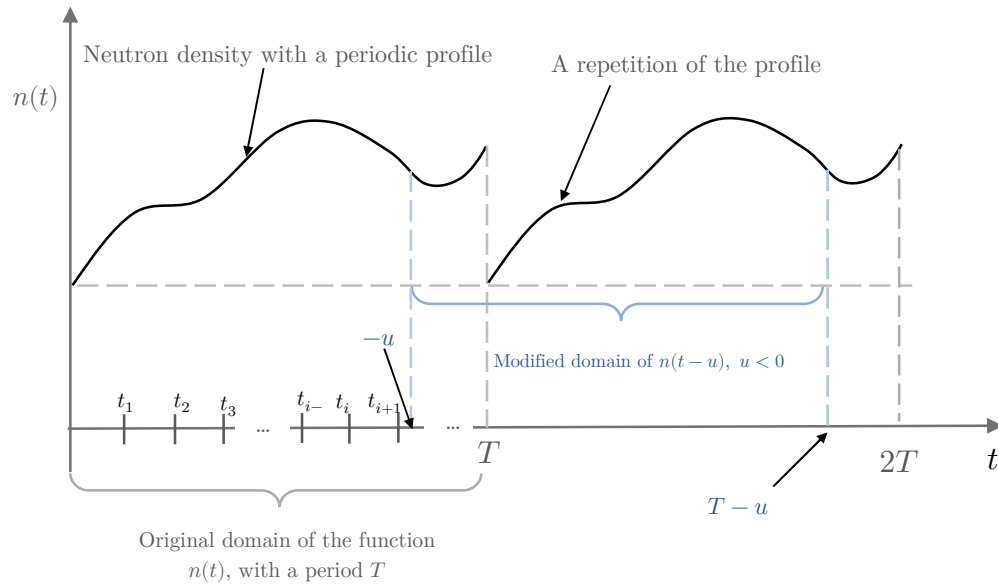


Figure 1. A scheme of an example of a periodic numeric neutron density with an arbitrary profile

which, as it was discussed in Section 2.3, is equivalent to the desired inequality given in (16).

3. FIRST ALTERNATIVE PROOF

3.1 Symmetry Under the Integral

As consequence of (29) and following the idea behind the Figure 1, it is possible to state the following result for a continuous function of period T :

$$\int_0^T f(t)dt = \int_b^{T+b} f(t)dt, \text{ for } b \in \mathbf{R}. \quad (36)$$

This last relationship can be rigorously proved by defining a function $F(x)$ as:

$$F(x) = \int_x^{x+T} f(t)dt, \text{ for } x \in \mathbf{R}, \quad (37)$$

and applying the Fundamental Theorem of Calculus [13, p. 310]:

$$\frac{d}{dx} F(x) = \underbrace{f(x+T) - f(x)}_{\text{Using the fact that } f(x+T)=f(x)} = 0. \quad (38)$$

Therefore, the function $F(x)$ is constant, which implies that it is the same for any x value, particularly for $x = 0$ and $x = b$, i.e., $F(0) = F(b)$:

$$\underbrace{\int_0^T f(t)dt}_{F(0)} = \underbrace{\int_b^{T+b} f(t)dt}_{F(b)}. \quad (39)$$

Using a change of variable given by $t = \tau + b$ in the second integral, it follows that:

$$\int_b^{T+b} f(t)dt = \int_0^T f(\tau + b)d\tau. \quad (40)$$

Therefore, it follows:

$$\int_0^T f(t + b)dt - \int_0^T f(t)dt = 0, \text{ for all } b \in \mathbf{R}. \quad (41)$$

3.2 Motivation of the Alternative Proof

The first alternative proof arises from trying to apply the elementary property of the periodic function, $f(t + T) - f(t) = 0$, to the integral in the left side of (16). Certainly, the term in the integral is a quotient, not a subtraction, which suggests us that a transformation is required with the purpose to apply the mentioned property. In other words, it would be desired to express:

$$\frac{n(t - \tau)}{n(t)} \rightarrow n(t - \tau) - n(t), \quad (42)$$

which implies that a logarithm is necessary. Such function can be introduced as follows:

$$\int_0^T \frac{n(t - \tau)}{n(t)} dt = \int_0^T e^{\ln(n(t-\tau)-n(t))} dt, \text{ for } \tau \neq T. \quad (43)$$

The value $\tau = T$ is excluded, because in such case the argument of logarithm is zero, which is not defined. Nevertheless, it is clear that for $\tau = T$ (also for $\tau = 0$), the argument inside the integral is 1, and the inequality can be easily proved, because it is reduced to the trivial case where the numerator and the denominator are equal. Therefore, we can exclude these values in the present analysis. Eq. (43) represents the motivation and the main idea behind the alternative proof and due to the presence of the exponential function, it allows using the integral version of Jensen Inequality.

3.3 The Integral Version of the Jensen Inequality

Jensen inequality is a powerful result that relates convex and concave functions. Its integral version can be state as follows [14, p. 1]:

Theorem 2 (Jensen Inequality). *For an integrable function g , over $[c, d]$, and a convex function h , over the same interval, it follows that:*

$$h\left(\frac{1}{d-c} \int_c^d g(t)dt\right) \leq \frac{1}{d-c} \int_c^d h(g(t))dt. \quad (44)$$

Since the exponential function is a convex function, it is possible to apply Jensen inequality to Eq. (43) as follows:

$$\int_0^T e^{\ln(n(t-\tau)-n(t))} dt \geq T \exp\left(\frac{1}{T} \int_0^T \ln((n-\tau) - n(t)) dt\right) \quad (45)$$

3.4 First Alternative Proof

Since $n(t)$ is periodic, it follows that $n(t) = n(t + T)$, therefore $\ln(n(t)) = \ln(n(t + T))$, which implies that $\ln(n(t))$ is also periodic. Therefore, it is possible to apply the result given in (41) and therefore:

$$\int_0^T \ln((n(t-\tau)) - n(t)) dt = 0. \quad (46)$$

Therefore, inequality (45) is equivalent to:

$$\int_0^T \frac{n(t-\tau)}{n(t)} dt \geq T \exp(0) = T, \quad (47)$$

which proves the desired result, ending the proof.

3.5 The Work of Christian Blatter

As it can be observed, the proof given in the last subsection can be written in a few lines, compared with the proof developed by Ergen, which was formally justified in Section 2.5. The properties of the periodic function serve as a guide to build the inequality; therefore, this last proof is more intuitive and direct. Even more, this first alternative proof does not require using Riemann-sums or permutations and only requires concepts of convexity, which, in our opinion, makes it more elegant.

Unfortunately, after a careful analysis and search, we found that the mathematician Christian Blatter got ahead of us and published a similar result nearly twelve years before. Therefore, we cannot credit ourselves for being the first ones to discover this alternative proof. Certainly, Blatter shared his result on a question-and-answer (Q&A) website [14] and not in a peer-reviewed journal, and his proof requires justification of all the steps provided in the present work. Additionally, this author developed his proof in a general context, and not in the nuclear engineering field. Nevertheless, his procedure is similar to the one discussed in the present article, and therefore he deserves the credit for being the first one to have this idea, even when we independently rediscovered his result.

As a consolation prize, the discovery of the Blatter's solution allows us to learn of a different approach proposed by Rijul Saini, which will be discussed in the following section.

4. SECOND ALTERNATIVE PROOF

4.1 A Weaker Proof

It is possible to propose a weaker proof of the inequality, assuming some relationships between the period T and the variable τ . Even when this weaker result cannot be used to show the negative bias of the average reactivity (because in the general case, no assumption is made), the discussion of the procedure behind it is very useful to provide some insight of an alternative approach that can be applied in the fractional case. Therefore, we concluded it is important to add the following discussion about the proof developed by Rijul Saini [14], which we found in the same entry of the (Q&A) website where the Blatter's found was found.

4.2 Rewritten the Inequality

Under an elementary change of variable, $z = t - \tau$, it is possible to show that:

$$\int_0^T \frac{n(t-\tau)}{n(t)} dt = \int_{-\tau}^{T-\tau} \frac{n(z)}{n(z+\tau)} dz \stackrel{\text{by virtue of Eq.(40)}}{=} \int_0^T \frac{n(t)}{n(t+\tau)} dt \quad (48)$$

where in the last integral the relationship $z \rightarrow t$ has been used only for notation. For a $K \in \mathbf{N}$:

$$\begin{aligned} \int_0^{KT} \frac{n(t)}{n(t+\tau)} dt &= \int_0^T \frac{n(t)}{n(t+\tau)} dt + \int_T^{2T} \frac{n(t)}{n(t+\tau)} dt + \dots + \int_{(K-1)T}^{KT} \frac{n(t)}{n(t+\tau)} dt \\ &\stackrel{\text{Using Eq.(40)}}{=} K \int_0^T \frac{n(t)}{n(t+\tau)} dt. \end{aligned} \quad (49)$$

4.3. The Assumption Over the Period

For the particular case where τ and T are rational and are related as:

$$\tau = \frac{K}{q} T, \quad q \in \mathbf{N}, \quad (50)$$

it follows that:

$$KT = q\tau \rightarrow \int_0^{KT} \frac{n(t)}{n(t+\tau)} dt = \int_0^{q\tau} \frac{n(t)}{n(t+\tau)} dt. \quad (51)$$

Therefore, using (50), the following equality is obtained:

$$K \int_0^T \frac{n(t)}{n(t+\tau)} dt = \int_0^\tau \frac{n(t)}{n(t+\tau)} dt + \int_\tau^{2\tau} \frac{n(t)}{n(t+\tau)} dt + \dots + \int_{(q-1)\tau}^{q\tau} \frac{n(t)}{n(t+\tau)} dt. \quad (52)$$

The core of Saini's proof consists of grouping all the terms under the same domain, which can be carried out considering the following change of variable:

$$\int_{r\tau}^{(r+1)\tau} \frac{n(t)}{n(t+\tau)} dt \stackrel{t=z+r\tau}{=} \int_0^\tau \frac{n(z+r\tau)}{n(z+(r+1)\tau)} dz, \quad r \in \mathbf{Z}_{\geq 0}. \quad (53)$$

Therefore, the sum given in Eq. (53) can be written as follows:

$$\int_0^\tau \sum_{r=0}^{q-1} \frac{n(z+r\tau)}{n(z+(r+1)\tau)} dz. \quad (54)$$

This last relationship exhibits an interesting behavior, which can be observed using the following notation $\omega_r(z) = n(z+r\tau)$:

$$\begin{aligned} \sum_{r=0}^{q-1} \frac{n(z+r\tau)}{n(z+(r+1)\tau)} &= \frac{n(z)}{n(z+\tau)} + \frac{n(z+\tau)}{n(z+2\tau)} + \dots + \frac{n(z+(q-1)\tau)}{n(z+q\tau)} \\ &= \frac{\omega_0(z)}{\omega_1(z)} + \frac{\omega_1(z)}{\omega_2(z)} + \dots + \frac{\omega_{q-1}(z)}{\omega_q(z)}, \end{aligned} \quad (55)$$

and using that:

$$\omega_0(z) = \underbrace{n(z) = n(z+KT)}_{\text{By periodicity of } n(t)} = \underbrace{n(z+q\tau)}_{\text{Using Eq. (50)}} = \omega_q(z), \quad (56)$$

the following sum is obtained:

$$\sum_{r=0}^{q-1} \frac{n(z+r\tau)}{n(z+(r+1)\tau)} = \frac{\omega_q(z)}{\omega_1(z)} + \frac{\omega_1(z)}{\omega_2(z)} + \dots + \frac{\omega_{q-1}(z)}{\omega_q(z)}. \quad (57)$$

In the last expression, indexes in the numerator are “shifted” in one place with respect to the indexes in the denominator. This arrangement resembles the displacement discussed in the Ergen’s proof, and it is useful for building the desired inequality.

4.4 The Procedure of Saini

For a set of non-negative real numbers, c_1, c_2, \dots, c_q it follows that:

$$\sum_{r=1}^q c_r \geq q \sqrt[q]{c_1 c_2 \dots c_q}. \quad (58)$$

which is known as the Inequality of Arithmetic and Geometric Means [9, p. 16]. If this result is applied to Eq. (56), it follows that:

$$\frac{\omega_q(z)}{\omega_1(z)} + \frac{\omega_1(z)}{\omega_2(z)} + \dots + \frac{\omega_{q-1}(z)}{\omega_q(z)} \geq q \sqrt[q]{\frac{\omega_q(z)\omega_1(z)\dots\omega_{q-1}(z)}{\omega_1(z)\omega_2(z)\dots\omega_q(z)}}. \quad (59)$$

The term inside the root is equal to 1, because it involves the same product that appears in the denominator but in different order, then it follows that:

$$\frac{\omega_q(z)}{\omega_1(z)} + \frac{\omega_1(z)}{\omega_2(z)} + \dots + \frac{\omega_{q-1}(z)}{\omega_q(z)} \geq q. \quad (60)$$

Therefore, combining the previous steps, it follows that:

$$K \int_0^T \frac{n(t)}{n(t+\tau)} dt = \int_0^\tau \sum_{r=0}^{q-1} \frac{n(z+r\tau)}{n(z+(r+1)\tau)} dz \geq \int_0^\tau q dz = \underbrace{q\tau}_{\text{By Eq. (50)}} = KT. \quad (61)$$

Considering the extremes of the last relationship, the desired inequality is proved. Even when Saini offers another proof for a different case, where the quotient T/τ is assumed irrational, such procedure also requires some assumptions between T and τ , and therefore we do not consider it as a general method in the context of the present work.

5. CONCLUSIONS

The present work studied an inequality related to the negative bias of the reactivity. Such inequality is built using the Inverse Method and plays an important role in validating approximate analytical solutions of Neutron Point Kinetics Equations. It can be proved using three different methodologies, the earliest one proposed by Ergen, who used Riemann sums and the Rearrangement Inequality. The present work developed a rigorous formalization of such proof, filling the theoretical gaps in the literature and exemplifying the mathematical methods behind it. This last represents an important contribution from a pedagogical and research points of view and allows identifying of the main steps, which essentially are related to a displacement in the domain of a periodic function. Additionally, two alternative proofs were discussed: the first using the integral version of the Jensen inequality and the second using the inequality between the arithmetic and geometric means. In the first case, a very short proof is obtained because the convexity of the exponential function allows the inequality to be expressed as a difference instead of a quotient. This procedure was originally proposed by Christian Blatter, even when some steps in his proof were not explicitly justified. On the other hand, making some assumptions about the period and its relationship with a displacement variable, allows building a weaker proof, which only requires elementary arithmetic results. Therefore, it is possible to conclude that the inequality can be proved with alternative methods, one of them most sophisticated and direct, providing more mathematical tools to explore such relationship in the context of other approaches to the dynamics of nuclear reactors, such as as the fractional approach, among others.

6. ACKNOWLEDGEMENTS

The authors appreciate the financial support received from the Consejo Nacional de Humanidades, Ciencia y Tecnologías, CONAHCYT, under the program “Estancias Posdoctorales por México, 2022”, with the project entitled: “Desarrollo de modelos fenomenológicos energéticos de orden fraccional, para la optimización y simulación en reactores nucleares de potencia”, as well as to the

project “Reactores nucleares pequeños y microreactores para la transición energética de México”, by which the present work was possible. Author Carlos Antonio Cruz López also acknowledges the help and guidance of Professor Mónica Báez regarding some key points of the first alternative proof.

7. REFERENCES

1. Duderstadt, J. J., Hamilton, L. J. *Nuclear Reactor Analysis*. John Wiley and Sons. United States of America. 1976.
2. Oka, Y., Suzuki, K. *Nuclear Reactor Kinetics and Plant Control*. Springer. Japan. 2008.
3. Lewins, J. *Nuclear Reactor Kinetics and Control*. Pergamon Press. United States of America. 1978.
4. Zhang, F., Chen, W. Z., Gui, X. W. Analytic Method Study of Point-Reactor Kinetic Equation when Cold Start-up. *Annals of Nuclear Energy*. **Vol. 35**, pp. 746-749 (2008).
5. Palma, D. A. P., Martínez, A. S., Gonçalves, A. S. Analytical Solution of Point Kinetics Equations for Linear Reactivity Variation During the Start-up of a Nuclear Reactor. *Annals of Nuclear Energy*. **Vol. 36**, pp. 1469-1471 (2009).
6. Amano, F. Approximate Solution of One-Point Reactor Kinetic Equations for Arbitrary Reactivities. *Journal of Nuclear Science and Technology*. **Vol. 6**, pp. 646-656 (1969).
7. Akcasu, Z., Lellouche, G. S., Shotkin, L. M. *Mathematical Methods in Nuclear Reactor Dynamics*. Academic Press. New York, London. 1971.
8. Ergen, W. K. Kinetics of Circulating Fuel Nuclear Reactor. *Journal of Applied Physics*. **Vol. 25**, pp. 702-711 (1954).
9. Hardy, G. H., Littlewood, J. E., Pólya, G. *Inequalities*. Cambridge At the University Press. Great Britain (1934).
10. Smets, H. B. Exact Solution of the Reactor Kinetics Equations for Linear, Exponential, or Reciprocal Reactivity Dependence on Time. *Bulletins de l'Académie Royale de Belgique*. Vol. 45, pp. 256-271 (1959).
11. Cruz-López, C.A., Espinosa-Paredes, G., Vidales-Basurto, C. Analytic Solution of Neutron Point Kinetics Equations for Linear Ramp Reactivities, $\rho(t) = at + b$. A Theoretical and Computational Approach. To be Submitted to *Computer Physics Communications*.
12. Wigner, E. P. *The Collected Works of Eugene Paul Wigner*. Part A. Volume V. Springer Verlag, Berlin Heidelberg, 1992.
13. Stewart, J. *Calculus*. Seventh Edition. Brooks/Cole. CENGAGE Learning. United States of America, 2008.
14. Nazari Pasari, S., Barani, A., Abbasi, N. Generalized Integral Jensen Inequality. *Journal of Inequalities and Applications*. Vol. 2024, pp. 1-11.
15. “Q&A site related to the inequality”. <https://math.stackexchange.com/questions/190881/integral-inequality-on-a-periodic-function/190952#190952> (2012).

Solution of the neutronics benchmark of the NuScale-like core using the AZTRAN code

J. Vicente Xolocostli Munguía and Armando M. Gómez Torres

Instituto Nacional de Investigaciones Nucleares

Carretera México – Toluca SN, La Marquesa, Ocoyoacac, CP 52750, México

vicente.xolocostli@inin.gob.mx; armando.gomez@inin.gob.mx

***Julián A. Durán González, Gianfranco Huaccho Zavala, Alejandro Campos Muñoz
and Víctor H. Sánchez Espinoza***

Karlsruhe Institute of Technology (KIT), Institute of Neutron Physics and Reactor Technology

Hermann-von-Helmholtz-Platz 1, 76344 Eggenstein-Leopoldshafen, Germany

julian.gonzalez@kit.edu; gianfranco.zavala@kit.edu; alejandro.munoz@kit.edu;

victor.sanchez@kit.edu

Edmundo del Valle Gallegos

Instituto Politécnico Nacional, Escuela Superior de Física y Matemáticas

Gustavo A. Madero, 07738, Ciudad de México, México

evalle@ipn.mx

Abstract

This paper describes the use of the AZTRAN code-optimized version for neutronics modeling of the 3D full-core neutronics benchmark, which is based on the NuScale small modular reactor (SMR) concept. The benchmark specifications were developed in the Euratom McSAFER project's framework and were recently published. The AZTRAN code was created for the AZTLAN Platform project, an initiative to establish a Mexican Platform to analyze and design nuclear reactors. AZTRAN solves the multi-group discrete-ordinate form of the neutron transport equation in 3D Cartesian geometry by applying the nodal RTN-0 method and the domain decomposition method for parallelization. In the past, this code has been verified and validated using the C5G7 MOX benchmark in a stationary state and for several time-dependent cases, obtaining solutions close to the reference and highly satisfactory acceleration results, demonstrating the correct implementation of the parallel algorithm. The NuScale-like core model benchmark is considered a good candidate for evaluating the performance of the software in a real industrial environment and to test if the AZTRAN code is ready to model detailed cores and obtain accurate results with reasonable running times. A comparison of the effective multiplication factor k_{eff} and core power distribution (axial and radial) among AZTRAN, PARCS, and the Monte Carlo code SERPENT is presented here. Results obtained with the AZTRAN code for the NuScale-like core are in excellent agreement compared with PARCS and SERPENT codes (reference solution). The verification and validation procedures for the AZTRAN code will focus on a time-dependent scenario in the near term.

1. INTRODUCTION

The AZTLAN Platform project [1] aimed to develop a modeling Mexican platform for nuclear reactor design and analysis. A module of the AZTLAN Platform called AZTRAN code [2, 3] uses the nodal method Raviart-Thomas-Nédélec of index zero (RTN-0) on Cartesian geometry along with the discrete coordinates (S_N) approach to solve the 3D neutron transport equation. Cross sections created externally by SERPENT code can be used with AZTRAN. It solves the eigenvalue problem and establishes the desired conditions for the neutron distribution for a given medium. This version of the AZTRAN code incorporates the use of the NEMTAB format for cross sections, in addition to being a version that can be executed in parallel, thanks to the domain decomposition implementation that takes advantage of the computing power available. Another advantage of this version is the possibility of generating output files of the neutron flux and power distribution in the format VTK (Visual Toolkit). The Visualization Toolkit (VTK) is a powerful free software system for 3D computer graphics, image processing, and scientific visualization, which is compatible with ParaView, an open-source multiple-platform application for visualization.

The NuScale-like reactor benchmark is used to continue the efforts to verify and validate the AZTRAN code. The benchmark describes a NuScale-like core model developed in the framework of the Euratom McSAFER project [4]. Code-to-code comparison can ascertain neutronic tools and computational techniques intended for SMR applications. The McSAFER project was a three-year H2020 Euratom initiative to utilize high-fidelity multi-physics reactor analysis tools created in the previous European projects NURESAFE [5], HPMC [6], and McSAFE project [7], seeking to improve safety analysis approaches for SMRs.

This paper performs the benchmark analysis using the Monte Carlo code SERPENT for cross-section generation and as a reference solution. It also presents comparisons with the deterministic codes AZTRAN and PARCS.

2. BENCHMARK SPECIFICATIONS

This benchmark is devoted to static neutronics calculations of the NuScale-like core in its Beginning of Life (BOL) state [4]. Depletion analysis and Xe/Sm poisoning modeling are not considered. The benchmark specifications contain all necessary information required for the neutronic modeling, including:

- Fuel loading pattern and location of control rod assemblies (CRAs) within the core
- Radial and axial layouts of all core components and their relevant dimensions
- Imposed operating temperatures required to select appropriate temperature-dependent cross-section data or to activate suitable temperature treatment
- Description of materials comprising the core and their detailed isotopic compositions

The provided NuScale core specifications are primarily derived from a public version of the Final Safety Analysis Report (FSAR) submitted to the US Nuclear Regulatory Commission (NRC) as a part of the Design Certification Application [8] and were detailed described in [4]. To facilitate the understanding of the model in this work, a brief description of the model's main

characteristics is presented, clarifying that all the figures and tables detailing the core configuration have been taken from reference [4].

2.1. Radial core layout

The radial layout of the initial NuScale-like core is shown in Figure 1. The core is loaded with 37 all-fresh no-Xe UO₂ fuel assemblies at six different U-235 enrichment levels, which were adjusted to approximate batch-wise U-235 content at the beginning of the equilibrium fuel cycle. Four fuel assemblies contain 16 fuel pins with Gd₂O₃ burnable poison (Fig. 1, left). In total, there are 7 different fuel assembly types.

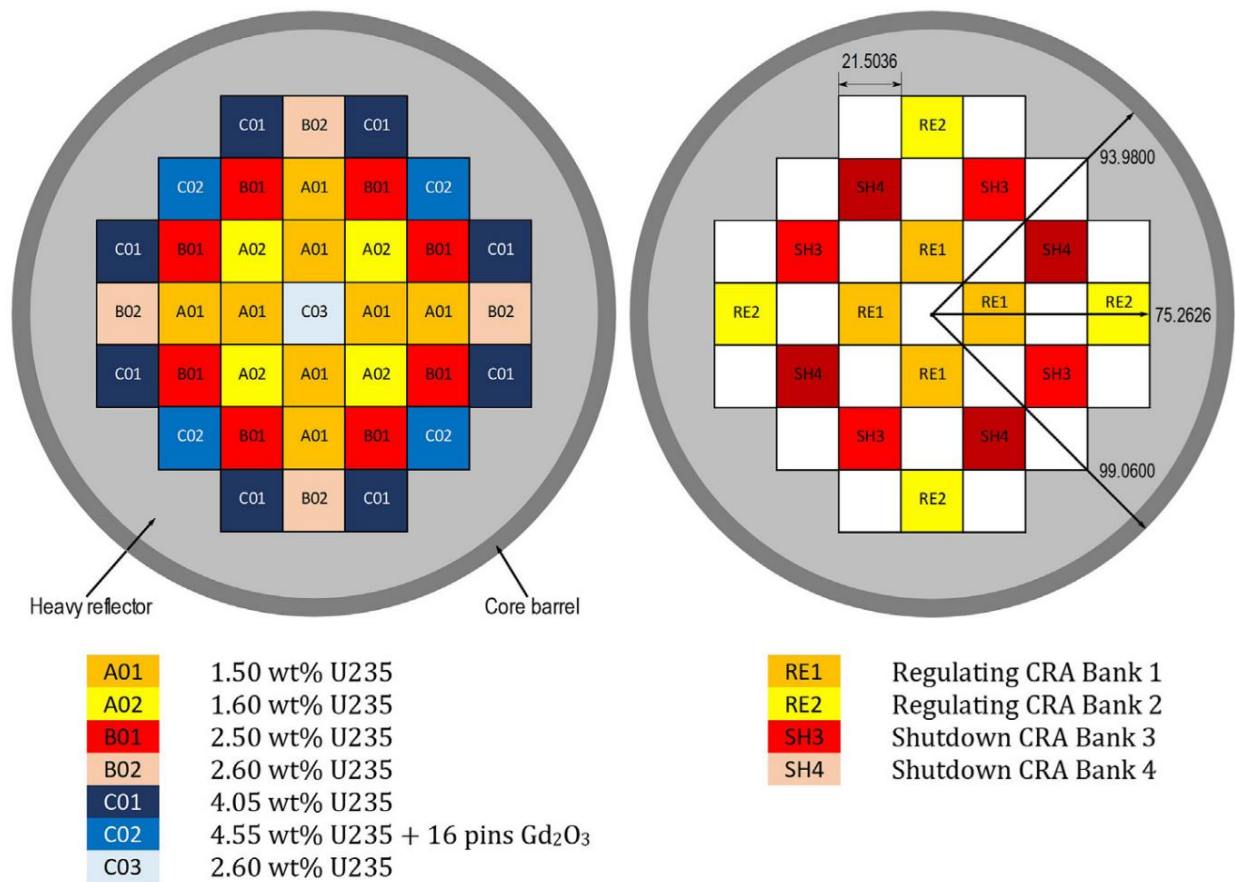


Figure 1. Core loading pattern and control rod assembly locations (dimensions in cm) [7]

The core is regulated and controlled by 16 control rod assemblies (CRA) divided into two regulating (RE) and two shutdown (SH) banks, as shown in Figure 1, right. The core is surrounded by a heavy steel reflector and bounded by a cylindrical core barrel. The inner and outer radii of the core barrel are shown in Figure 1, right.

The actual dimensions and locations of the coolant channels are unavailable in the FSAR. Therefore, the radial heavy reflector for the case modeled in [4] is simplified as a homogeneous

mixture of steel and water. Since the deterministic codes used in this paper cannot model a cylindrical barrel and define a core model that could be compared directly with SERPENT, the radial configuration modeled in this work was modified, as shown in Figure 2.

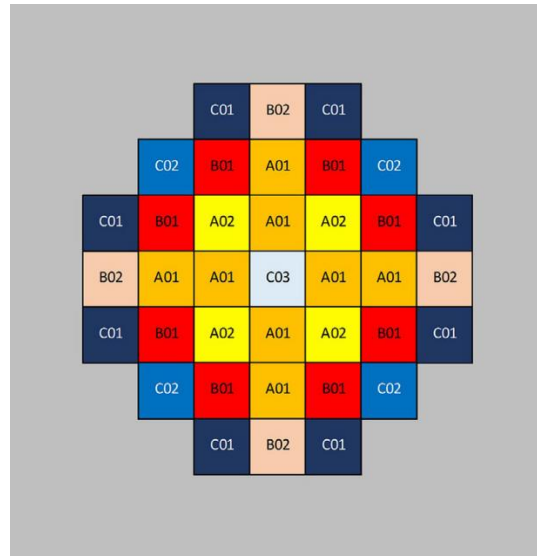


Figure 2. Radial configuration of the NuScale-like core used in this work

2.2. Radial layouts of fuel assemblies

All fuel assemblies utilized in NuScale have a typical 17x17 lattice. The fuel rod pitch inside the assembly is 1.2598 cm, and the fuel assembly pitch inside the core is 21.5036 cm. The resulting inter-assembly gap is explicitly modeled.

Fuel assemblies listed in the left panel of Figure 1, except the C02 type, do not contain any burnable poison (BP). These fuel assemblies comprise 264 fuel rods and 24 guide tubes (GT) to insert control rods. In addition, the assemblies contain a central instrumentation tube, which is modeled as an empty guide tube in this benchmark. The locations of fuel rods and GTs are shown in Figure 3, left.

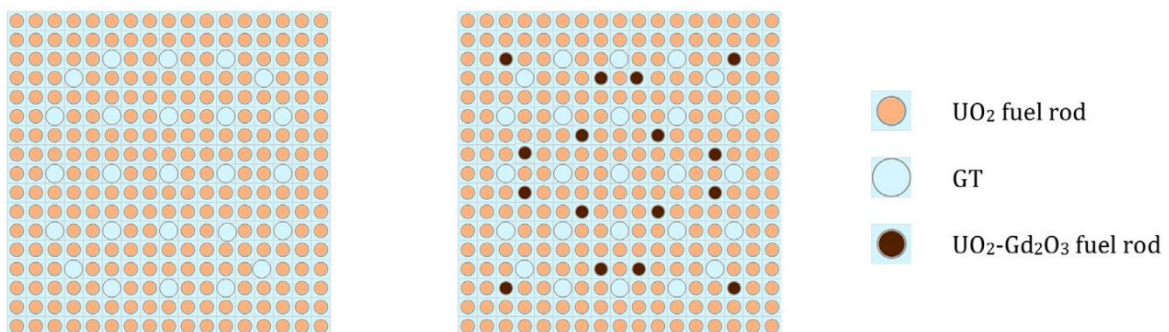


Figure 3. Radial layouts of fuel assemblies: un-poisoned (left) and poisoned (right) [7].

Some fuel assemblies are loaded with integral burnable poison (BP) as a homogeneous mixture of UO₂ and gadolinia (Gd₂O₃) to cope with initial excess reactivity. However, the actual BP configuration is not publicly available (e.g., the amount of gadolinia, the number of BP pins per

fuel assembly, the BP location within the fuel assembly, etc.). The benchmark specification [7] assumed that the fuel assemblies with the highest U-235 enrichment (the C02 type) contain 16 gadolinia BP rods. The placement of BP in fuel assemblies of the C02 type is shown in Figure 3, right.

2.3. Axial and radial structures of fuel rods, guide tubes, and control rods

The axial structure and dimensions of fuel rods and Guide Tubes (GTs) are presented in Figures 4 and 5. In the original Benchmark specification, Control Rods (CR) are also provided; however, in this exercise, only the All Rods Out (ARO) configuration is studied. For this reason, specifications for control rods were not considered. For a complete description, the reader is invited to consult the reference [4]. The following assumptions and simplifications were considered in this analysis in agreement with [4]:

- The fuel rod is constructed as a combination of three different heterogeneous pin-cells: the fuel, the plenum, and the end cap. These pin cells are defined in Figure 5, including radial dimensions and materials. A detailed isotopic composition of every material is provided in [4].
- In Figure 4, the “coolant” region above the end cap of the fuel rod contains homogeneous coolant.
- The bottom and top nozzle parts of fuel assemblies are modeled as homogeneous mixtures of steel and coolant as specified in [4].
- The bottom and top nozzles constitute axial boundaries of the core.
- The whole fuel stack height of 200 cm is composed of a single material for a specific fuel rod type.

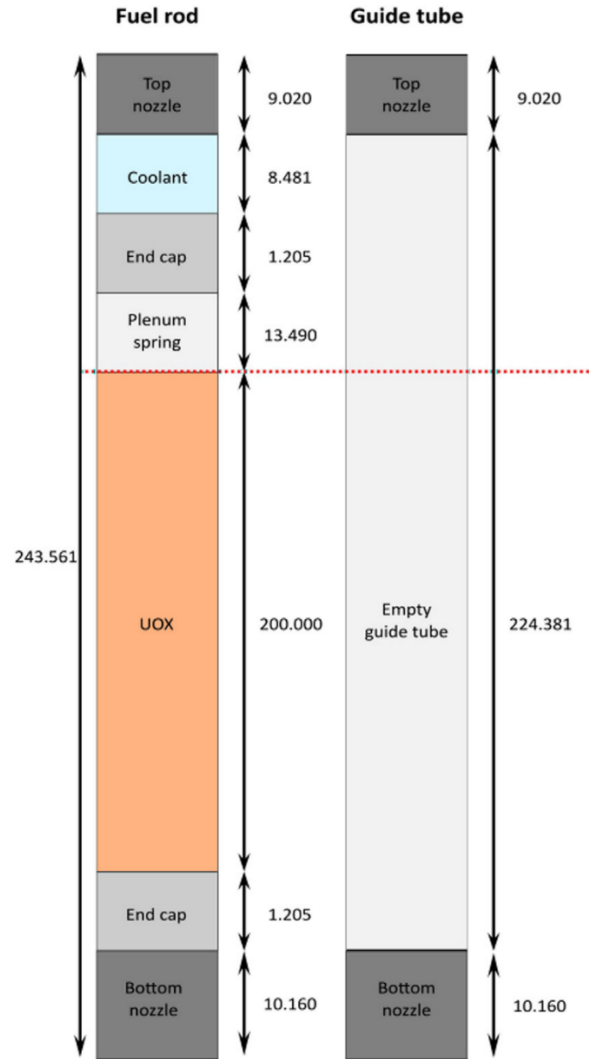


Figure 4. Axial structure and alignment of the different components of the NuScale core (all dimensions in cm)

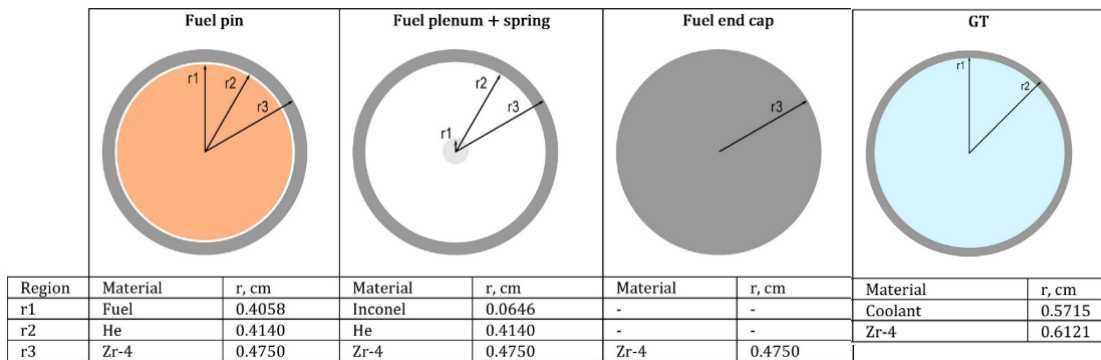


Figure 5. Radial pin-cells forming up the fuel rods and guide tube

2.5. Materials

A summary of the materials used for the different parts of the NuScale model is given in Table I.

Table I. Materials used for different parts of the NuScale core model

Part	Material
Fuel pellets	UO ₂ or UO ₂ þGd ₂ O ₃
Fuel rod cladding	Zr-4 (replaces M5®)
Fuel rod plenum springs	Inconel
Fuel rod lower-end cap	Zr-4
Fuel rod upper-end cap	Zr-4
Coolant	H ₂ O with 1000 ppm boron
Guide tube	Zr-4

All material compositions are provided in [4] as number densities (ND) to facilitate the modeling and avoid misinterpretations. The volume fractions for regions modeled as homogeneous mixtures and the compositions for different materials are also provided in [4].

2.6. Operating conditions

Operating conditions for the model and generation of cross-sections are given following:

- A power of 160 MW
- A uniform fuel temperature of 900 K
- A uniform coolant temperature of 600 K
- The content of soluble boron is 1000 ppm (Composition was showed in Table I)
- The position of CR is 100% withdrawal

3. RESULTS

3.1. The SERPENT Model

To perform the benchmark simulation in AZTRAN, it was necessary to build a model in the Monte Carlo code SERPENT [9]. This model was the base for the comparison of AZTRAN and PARCS codes, and with this model, the cross sections for the deterministic codes AZTRAN and PARCS were generated. The SERPENT input of the benchmark corresponds to the ARO configuration (All Rods Out). The materials and operation conditions are listed in the previous tables. Figures 6a and 6b show the generated SERPENT model for radial and axial, respectively.

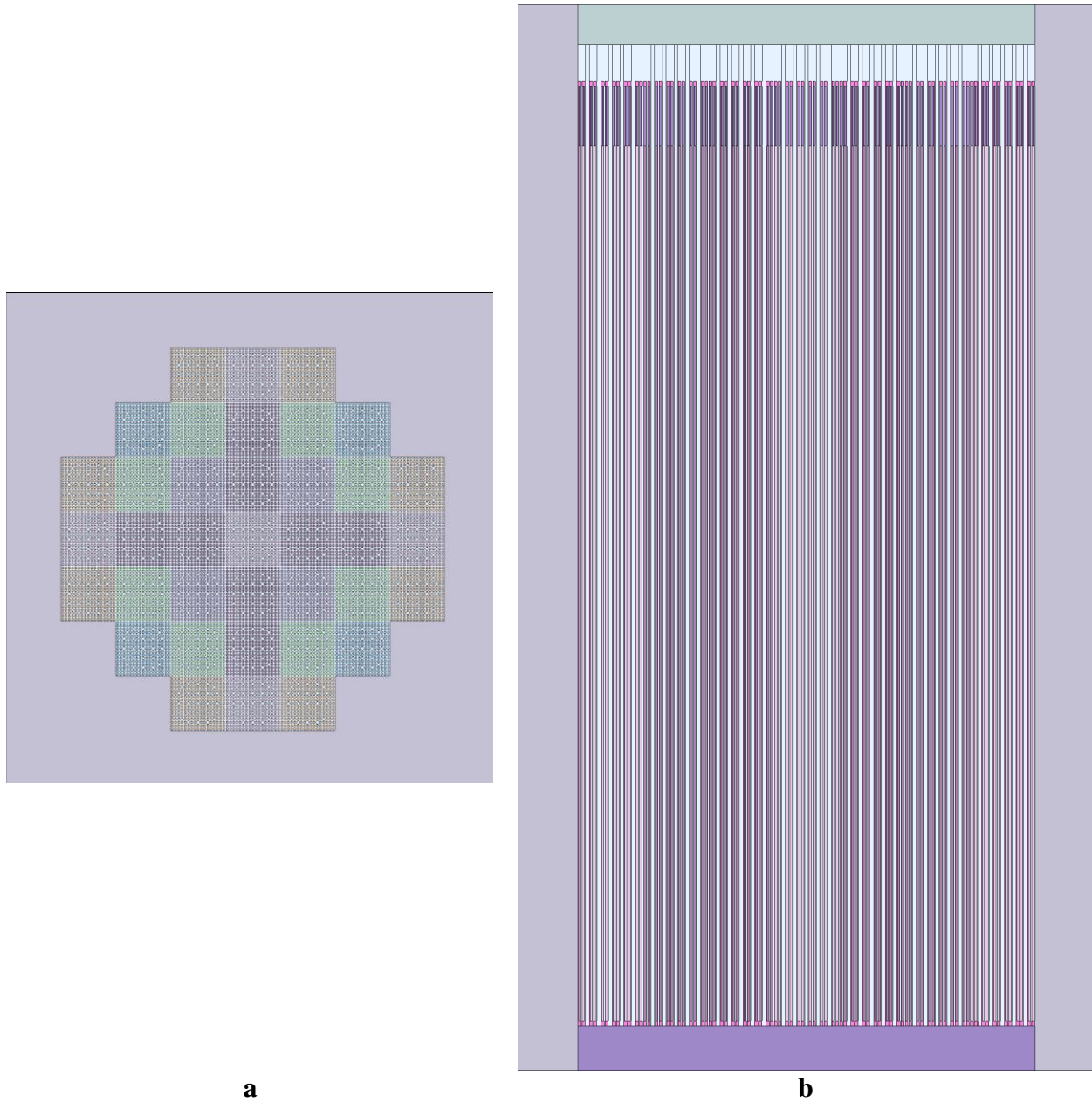


Figure 6. Radial (a) and Axial (b) geometry configurations from SERPENT benchmark NuScale model.

The results of effective multiplication factor k_{eff} and power profiles will be shown in conjunction with the comparisons with the other codes in the following section.

3.2. Results of the comparison between AZTRAN and PARCS codes

For the comparison, the NuScale benchmark analysis was made in two ways, considering the whole core, first at assembly level and, second at pin level.

3.2.1. k_{eff} and power results with assembly-based model

Table II compares the effective multiplication factor k_{eff} and the corresponding error between AZTRAN and PARCS codes concerning SERPENT. Furthermore, to accurately describe error (deviation from reference data-solution) in radial power distribution, two metrics used for comparison of results were used: Power-Weighted Error (PWE) and Error-Weighted Error (EWE). Both were defined as a weighted average of the error by Eq. (1) and Eq. (2), respectively, and the assembly power relative error (%), e_i , was defined by Eq. (3) to describe accumulated error accurately (where, $calc$ and ref are the calculated and reference values, respectively.) [10]. Figure 7 shows the relative errors regarding SERPENT for radial power distribution in both codes.

$$PWE = \frac{\sum_i |e_i| ref_i}{\sum_i ref_i} \quad (1)$$

$$EWE = \frac{\sum_i |e_i| |e_i|}{\sum_i |e_i|} \quad (2)$$

$$e_i = \frac{calc_i - ref_i}{ref_i} \times 100 \quad (3)$$

Table II. Comparisons of k_{eff} value and accumulated power errors obtained with assembly-based model

SERPENT	AZTRAN S16	PARCS SP3
1.03046	1.03186	1.03219
Error (pcm)	140	173
PWE (%)	1.6396	1.8761
EWE (%)	2.0713	2.2712



Figure 7. The assembly-based model compares Relative errors with the SERPENT code of radial power distribution for AZTRAN (left) and PARCS (right).

3.2.2. k_{eff} and power results with a pin-based model

Table III compares the effective multiplication factor k_{eff} and the corresponding accumulated error between AZTRAN and PARCS codes concerning SERPENT. Figure 8 shows both codes' relative radial errors regarding SERPENT for radial power distribution.

Table III. Comparisons of k_{eff} value and accumulated power errors obtained with pin-based model.

SERPENT	AZTRAN S16-P	PARCS SP3 P
1.03046	1.03176	1.03236
Error (pcm)	130	190
PWE (%)	1.2936	1.7620
EWE (%)	1.6046	2.1683

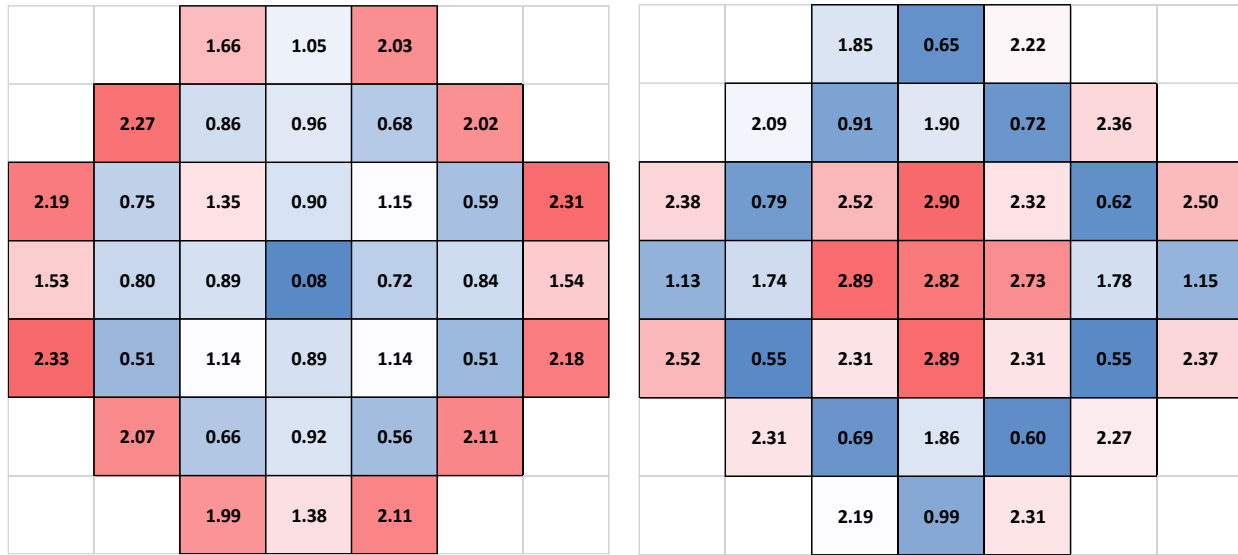


Figure 8. Relative errors comparison with SERPENT code of radial power distribution for AZTRAN (left) and PARCS (right), with detail pin-by-pin

Table IV summarizes all results for k_{eff} value and accumulated error in power distribution.

Table IV. Comparison of effective multiplication factor and power distribution with detail by assembly (A) and pin-by-pin (P)

	SERPENT	AZTRAN S16-A	AZTRAN S16-P	PARCS SP3 A	PARCS SP3 P
k_{eff}	1.03046	1.03186	1.03176	1.03219	1.03236
Error (pcm)		140	130	173	190
PWE (%)		1.6396	1.2936	1.8761	1.7620
EWE (%)		2.0713	1.6046	2.2712	2.1683

Comparing the k_{eff} with SERPENT code, a better approximation of the values was obtained with AZTRAN than those calculated with PARCS, both at the assembly- and pin-based level where the lowest difference in pcms can be observed. However, it is essential to clarify that the PARCS results correspond to an SP3 approximation; meanwhile, the AZTRAN solution used was the S16.

When relative errors for radial power distribution are compared with SERPENT, the results again better approximate AZTRAN at the assembly and pin-by-pin levels, as shown by the values of PWE and EWE.

Figure 9 shows a 3D full-core power distribution of the NuScale SMR concept at assembly and pin-by-pin levels. The detailed power behavior in the core can be observed; this is part of the AZTRAN code's capabilities to generate 3D VTK files for post-processing with ParaView (power distribution, neutronic fluxes, etc.).

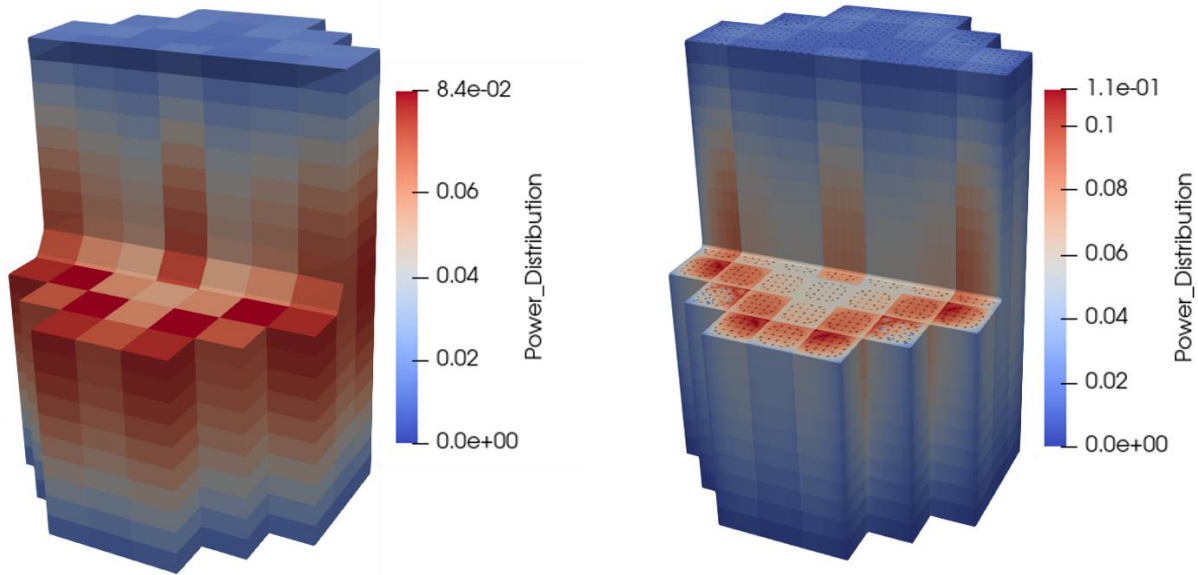


Figure 9. Core power distribution with AZTRAN at assembly level (left) and pin-by-pin (right)

4. CONCLUSIONS

This work presents a neutronics comparative analysis of an ARO 3D NuScale-like core. The comparison is considered as a reference solution, the one obtained using the Monte Carlo code SERPENT.

The parallel optimized version of the AZTRAN (AZtlan neutron Transport for Reactor ANalysis) code has been developed, improving the code's calculation capabilities.

The whole core was verified in two ways: first, at the assembly level, and second, at the pin-by-pin level. The results show very accurate results for AZTRAN regarding reference code SERPENT and deterministic code PARCS for both models, but it is possible to obtain the best results with the pin-based model; obviously, this calculation required much more computing time to run. It is essential to clarify that the PARCS results correspond to an SP3 approximation; meanwhile, the AZTRAN solution used was the S16, which, in theory, has better precision. Thus, the comparison against SP3 could be considered fair, and the authors do not want to conclude anything in a direct comparison, but just as an additional result coming from a very well-known and well-validated code as PARCS, to confirm that the development of AZTRAN is moving in the correct direction.

Hence, this benchmark's analysis serves as a new verification and validation exercise of AZTRAN, considering a more sophisticated computational case dedicated to steady-state and

transient SMR-like cores. Besides, this AZTRAN version can generate VTK files for post-processing with PARAVIEW and obtain 3D visualizations of power distribution or neutron fluxes.

Finally, the confidence obtained with this comparative approach encourages further development and improvements of the AZTRAN code, such as control rod movements for transient analysis by coupling it with thermal-hydraulics codes in the short and medium term.

REFERENCES

1. A. M. Gómez Torres, F. Puente Espel, E. del Valle Gallegos, J.L. François, C. Martin del Campo, G. Espinosa Paredes, “AZTLAN: Mexican Platform for Analysis and Design of Nuclear Reactors,” Proceedings of the International Congress on Advances in Nuclear Power Plants ICAPP, Nice, France (2015).
2. Julian Duran-Gonzalez, Edmundo del Valle-Gallegos, Melisa Reyes-Fuentes, Armando Gomez-Torres, and Vicente Xolocostli-Munguia, “Development, verification, and validation of the parallel transport code AZTRAN,” *Prog. Nucl. Energy*, 137 (2021), <https://doi.org/10.1016/j.pnucene.2021.103792>.
3. Vicente Xolocostli Munguía, Roberto Carlos López Solís, “AZTRAN 2.0 AZTLAN TRANSPORT NEUTRONIC CODE: User Manual” (2022).
4. Emil Fridman, Yurii Bilodid, Ville Valtavirta, Definition of the neutronics benchmark of the NuScale-like core, *Nucl. Eng. Technol.*, 55 (2023), 3639-3647, <https://doi.org/10.1016/j.net.2023.06.029>.
5. B. Chanaron, Overview of the NURES SAFE European project, *Nucl. Eng. Des.*, 321 (2017) 1e7, <https://doi.org/10.1016/j.nucengdes.2017.09.001>.
6. C. Demazière, V.H. Sanchez-Espinoza, B. Chanaron, Advanced numerical simulation and modeling for reactor safety - contributions from the CORTEX, HPMC, McSAFE and NURES SAFE projects, *EPJ Nucl. Sci. Technol.* 6 (2020), <https://doi.org/10.1051/epjn/2019006>.
7. V.H. Sanchez-Espinoza, L. Mercatali, J. Leppänen, E. Hoogenboom, R. Vocka, J. Dufek, The McSAFE project - high-performance Monte Carlo based methods for safety demonstration: from proof of concept to industry applications, in PHYSOR 2020, 2020, <https://doi.org/10.1051/epjconf/202124706004>.
8. US NRC, NRC to Issue Rule Certifying NuScale Small Modular Reactor, US NRC, Office of Public Affairs, Washington, DC, 2022
9. Leppänen, J., Pusa, M., Viitanen, T., Valtavirta, V., Kaltiaisenaho, T., 2015. The Serpent Monte Carlo code: status, development, and applications in 2013. *Ann. Nucl. Energy* 82, 142–150.
10. T. Kozlowski, T. J. Downar, PWR MOX/UO₂ Core Transient Benchmark (Final Report), OECD Nuclear Energy Agency, Rep. NEA/NSC/DOC (2006)20, 2007.

Mexican Results on the Refined Phase of the NEA Lead-cooled Fast Reactor Benchmark

Roberto Lopez-Solis y Armando Gomez-Torres

National Institute for Nuclear Research

Carr Toluca - México s/n, 52750 La Marquesa, Méx

roberto.lopez@inin.gob.mx; armando.gomez@inin.gob.mx

Edmundo del Valle-Gallegos

National Polytechnic Institute – Physics and Mathematics Higher School

Av. Instituto Politécnico Nacional s/n, Gustavo A. Madero, 07738 CDMX

edmundo.delvalle@gmail.com

Abstract

This paper presents the Mexican team's work in the refined phase of the NEA/OECD Lead-cooled Fast Reactor Benchmark. The Benchmark consists of three independent exercises: a 2D pin-level exercise, a 2D subassembly/supercell-level exercise, and a 3D full-core-level burnup exercise. The core described in the Benchmark is based on the ALFRED Lead Fast Reactor design. It contains Fuel Subassemblies, Control and Safety Rods, Reflectors, and Shielding Subassemblies. In this refined phase, specifications not previously clearly defined were clarified to avoid confusion among participants, such as temperatures in different regions, material densities, and geometries under given temperatures, and an alternative method to simplify the burnup of the whole core. The Benchmark in the reported stage is still in the blind phase. Hence, no data was previously available to compare so this is the first comparison with other participants. Participation in the Benchmark implies a very complex exercise in developing methodologies of core modeling, the presented results are generally consistent with those of the other participants. The participation in this exercise can be considered a success even if there is still some refinement to be done.

1. INTRODUCTION

The Generation IV International Forum (GIF) is an international organization with its stated goal being "*the development of concepts for one or more Generation IV systems that can be licensed, constructed, and operated in a manner that will provide a competitively priced and reliable supply of energy ... while satisfactorily addressing nuclear safety, waste, proliferation, and public perception concerns*", and coordinates the development of GEN IV technologies [1].

One of the six technologies the GIF chose for further development is the Lead-cooled Fast Reactor (LFR). This reactor features a fast neutron spectrum, high-temperature operation, and cooling by either molten lead or lead-bismuth eutectic (LBE). Both support low-pressure operations, have excellent thermodynamic properties, and are relatively inert regarding interactions with air or water [2].

The Advanced Lead Fast Reactor European Demonstrator (ALFRED) design is a 300 MWth pool system developed to demonstrate the viability of European LFR (ELFR) technology. It is based on proven and available technology [3].

The OECD/NEA Expert Group on Physics of Reactor Systems (EGPRS) is coordinating different benchmarks for various reactors, including an LFR based on the ALFRED concept [4].

The LFR Benchmark has the following purposes:

- a) To familiarize participants with the physics of an LFR core.
- b) Practice with the neutronics of an LFR core.
- c) Assess confidence in the capability of simulating an LFR core.

This work presents the results of the Mexican team that participated in the Benchmark [4] and compares its results with those of other participants.

2. BENCHMARK DESCRIPTION

The EGPRS Lead-cooled Fast Reactor (LFR) Benchmark [4] technical specifications document has been distributed to all participants. It contains all the temperature, geometric, and material data needed to model the core based on the ALFRED Reactor.

This work does not intend to describe the ALFRED core in depth (the reader is encouraged to visit reference [3] if interested); nevertheless, a brief description will be given.

ALFRED is a 300MWth LFR design cooled by pure lead, which operates at 400°C (inlet) and 520°C (outlet). The core consists of 253 subassemblies (SAs), see Figure 1, which include:

- 134 Fuel SAs (56 inner / 78 outer) or FAs.
- 16 Neutron Absorber SAs (12 Control Rods CRs / 4 Safety Devices SDs).
- 1 Test Assembly (TA) in the center of the core.
- 102 Peripheral SAs (48 Reflector Assemblies RA / 54 Shield Assemblies SA).

Every SA inside the core is 171.0 cm long and has a pitch of 16.7 cm between adjacent SAs. The Control Rods and Safety Devices are placed at different axial positions depending on the stage of the core life cycle. Figure 2 shows the positions of the Control Rods at the beginning, middle, and end of the cycle, along with the positions of the Safety Devices when inserted and not inserted.

The Benchmark consists of 3 different exercises, each with sub-exercises. The following section describes them.

The calculated parameters include the infinite and effective neutron multiplication factor (k_{∞} , k_{eff}), different microscopic cross section including fission, capture and inelastic scattering (σ_f , σ_c , σ_i), different macroscopic cross section including and fission (Σ_{tr} , Σ_f), thermal fission factor (η), thermal utilization factor (f), the average number of neutrons released by fission (ν), among others.

2.1. First Stage: 2D Pin-Level

In this stage, a single fuel pin is modeled. The pin is encased by a hexagonal wall, which reflects the geometry. The cell is considered infinitely long (equivalent to a 2D model).

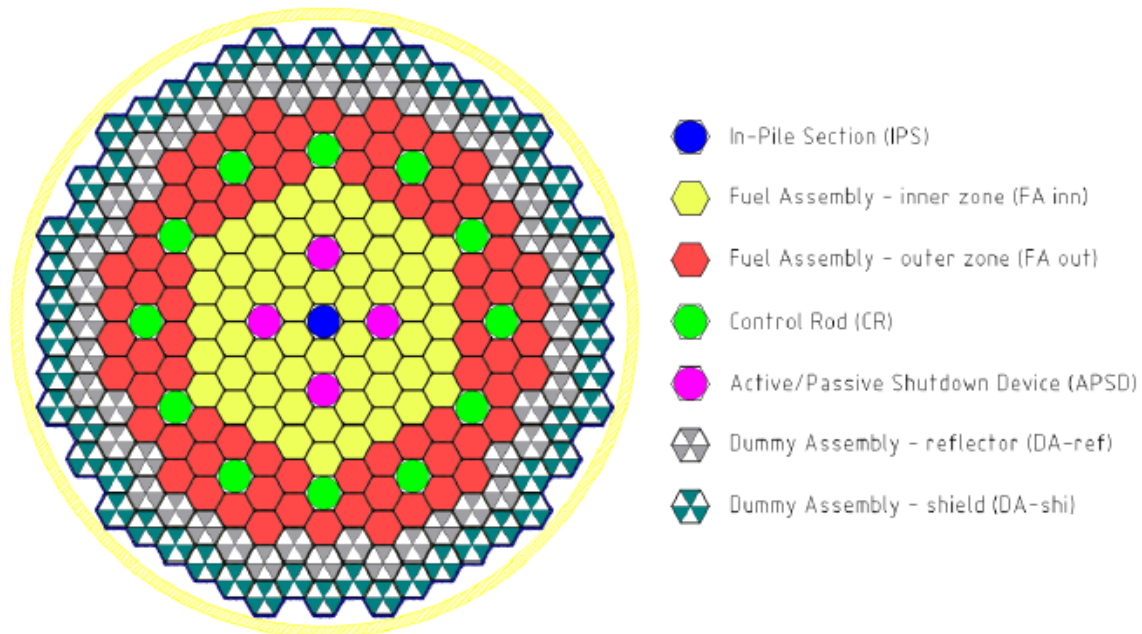


Figure 1. ALFRED Core Radial Layout [4]

A set of parameters is expected to be calculated:

- k_{∞} .
- key 1-group cross-sections.
 - ν , fission and capture for ^{239}Pu , ^{241}Pu , ^{235}U and ^{238}U (+ inelastic scattering).
 - Capture for ^{56}Fe and ^{208}Pb (+ inelastic scattering).
 - Neutron spectrum at a given 172 groups discretization.
- Criticality Factors: η , f , Σ_{tr} .
- Sensitivity/Uncertainty Analysis.

2.2. Second Stage: 2D Subassembly/Supercell-Level

At this stage, the models consist of a whole Fuel Subassembly or a super-cell of a Non-Fuel SA surrounded by FAs. This stage consists of three different exercises:

- a) Heterogeneous model of the cell of a fuel assembly.
- b) Heterogeneous model of a super-cell of a control rod subassembly surrounded by fuel assemblies.
- c) Heterogeneous model of a super-cell of a shield subassembly surrounded by fuel assemblies.

The parameters to be calculated are very similar to the previous stage except for the neutron spectrum and the inclusion of few-group macroscopic cross-sections:

- k_{∞} .
- key 1-group cross-sections for main isotopes and criticality factors (as in First Stage).
- Macroscopic few-group cross-sections.
- Sensitivity/Uncertainty Analysis.

2.3. Third Stage: 3D Full-Core Level

At this stage, a study on the reactivity control and shutdown systems is performed at a whole-core scale. The core is simulated without burnup at different configurations of the CRs and SDs to calculate the reactivity swings due to the rod insertion.

In reality, the core FAs are divided into five batches and every year; the most burnt batch is removed from the core and replaced by a fresh one, so every batch spends five years inside the reactor. To simplify the calculations, the Benchmark provides a methodology for an equivalent single-batch burnup; this methodology was used for these calculations.

The expected results are the following:

- k_{eff} at the Beginning of Life (BOL).
- Δk of Control Rods (CRs) and Shutdown Devices (SDs) at BoL.
- Δk of the core between Beginning and End of Life (BOC-EOC).
- Power distribution by assembly (at BOL and EOC).
- Mass balances of given isotopes.

2.4. Participants

Due to the great opportunity that participating in this Benchmark represents, various institutions participated. As it can be seen in Table I, there is no single code or methodology used which adds an extra.

Table I. Participants and methodologies used in the Benchmark

Country	Institute	Code	Library	Exercise
Belgium	SCK-CEN	Serpent 2.2.1	ENDF/B-VIII.0, JEFF-3.1.1, JEFF-3.3, JENDL-5, JEFF-4T3	1 st Stage
Italy	Newcleo	OpenMC	ENDF/B-VIII.0	1 st Stage
Mexico	ININ	Serpent 2.1.30	ENDF/B-VII.0	All Stages
Spain	CIEMAT	EVOLCODE (MC)	JEFF-3.1	1 st Stage
Spain	UTC	SCALE 6.2.4 (KenoVI and NEWT) and OpenMC	ENDF/B-VII.0	1 st Stage
USA	NCSU	Serpent 2.2.1 and LUPINE	ENDF/B-VII.1, ENDF/B-VIII.0, JEFF-3.1.1	All Stages

3. BENCHMARK RESULTS

In this section, the results obtained by ININ will be compared with the ones available. Only the

most representative parameters will be presented, so the paper will not be extended more than necessary.

3.1. First Stage: 2D Pin-Level

Figure 2 shows the normalized spectrum when the cell is filled with inner and outer fuel. There is good concordance among the participants, so most lines overlap.

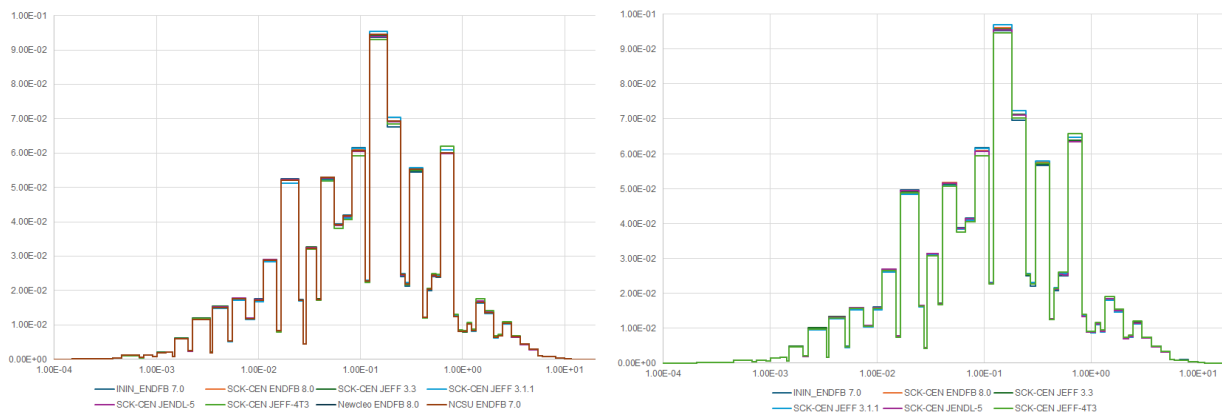


Figure 2. Normalized neutron spectrum for 2d cell using inner (left) and outer (right) fuel

Table II shows the k_{∞} values for the cells when using inner and outer fuel. In both cases, ININ's results are slightly lower (around 300 pcm) than those of the other participants. Further refinement must be done in later stages.

Table II. Results of k_{∞} value in Stage 1

	Inner Fuel		Outer Fuel	
	k_{∞}	Diff	k_{∞}	Diff
ININ ENDFB 7.0	1.32812	-1.75%	1.51436	-1.48%
SCK-CEN ENDFB 8.0	1.35581	0.30%	1.54243	0.35%
SCK-CEN JEFF 3.3	1.36173	0.74%	1.54767	0.69%
SCK-CEN JEFF 3.1.1	1.35336	0.12%	1.54077	0.24%
SCK-CEN JENDL-5	1.34666	-0.38%	1.53277	-0.28%
SCK-CEN JEFF-4T3	1.35950	0.57%	1.54461	0.49%
Newcleo ENDFB 8.0	1.35581	0.30%	Not Reported	
CIEMAT JEFF 3.1	1.35683	0.37%	Not Reported	
UPC-1 ENDFB 7.0	1.35029	-0.11%	Not Reported	
UPC-2 ENDFB 7.0	1.34528	-0.48%	Not Reported	
NCSU ENDFB 7.0	1.35625	0.33%	Not Reported	
Average	1.35179		1.53710	

Tables III and IV show the results of some of the microscopic cross sections (σ) calculated for the inner and outer fuel, respectively. As can be seen, good concordance among all participants was obtained.

Table III. Results of some microscopic cross sections for Stage 1 (inner fuel)

	$^{235}\text{U } \sigma_f$		$^{239}\text{Pu } \sigma_f$		$^{241}\text{Pu } \sigma_f$	
	Value [b]	Diff	Value [b]	Diff	Value [b]	
ININ ENDFB 7.0	1.8304	0.19%	1.7256	-0.06%	2.4168	0.46%
SCK-CEN ENDFB 8.0	1.8306	0.20%	1.7252	-0.08%	2.3964	-0.39%
SCK-CEN JEFF 3.3	1.8352	0.45%	1.7383	0.68%	2.3965	-0.38%
SCK-CEN JEFF 3.1.1	1.8196	-0.40%	1.7125	-0.82%	2.4163	0.44%
SCK-CEN JENDL-5	1.8247	-0.12%	1.7230	-0.21%	2.3469	-2.44%
SCK-CEN JEFF-4T3	1.8132	-0.75%	1.7402	0.78%	2.3811	-1.02%
Newcleo ENDFB 8.0	1.8307	0.20%	1.7252	-0.08%	2.3965	-0.38%
CIEMAT JEFF 3.1	1.8139	-0.71%	1.7163	-0.60%	2.4161	0.43%
UPC-1 ENDFB 7.0	1.8235	-0.19%	1.7329	0.36%	2.4618	2.33%
UPC-2 ENDFB 7.0	1.8355	0.47%	1.7282	0.09%	2.4277	0.91%
UPC-3 ENDFB 7.0	1.8358	0.48%	1.7273	0.04%	2.4162	0.43%
NCSU ENDFB 7.0	1.8304	0.19%	1.7252	-0.09%	2.3962	-0.40%
Average	1.82695		1.72666		2.40571	

Table IV. Results of some microscopic cross sections for Stage 1 (outer fuel)

	$^{235}\text{U } \sigma_f$		$^{239}\text{Pu } \sigma_f$		$^{241}\text{Pu } \sigma_f$	
	Value [b]	Diff	Value [b]	Diff	Value [b]	
ININ ENDFB 7.0	1.7601	0.28%	1.6997	-0.18%	2.3286	0.94%
SCK-CEN ENDFB 8.0	1.7600	0.28%	1.7008	-0.12%	2.3100	0.13%
SCK-CEN JEFF 3.3	1.7628	0.44%	1.7130	0.60%	2.3110	0.18%
SCK-CEN JEFF 3.1.1	1.7495	-0.32%	1.6886	-0.84%	2.3292	0.96%
SCK-CEN JENDL-5	1.7557	0.03%	1.6987	-0.24%	2.2654	-1.80%
SCK-CEN JEFF-4T3	1.7429	-0.70%	1.7161	0.78%	2.2974	-0.41%
Average	1.75517		1.70281		2.30694	

Tables V and VI show the results of η and Σ_{tr} for the cases with inner and outer fuel, respectively; as it can be seen, a good concordance among participants is found.

Table V. Results of η and Σ_{tr} for Stage 1 (inner fuel)

	η		Σ_{tr}	
	Value	Diff	Value [cm^{-1}]	Diff
ININ ENDFB 7.0	1.3769	-0.23%	0.2756	2.07%
SCK-CEN ENDFB 8.0	1.3958	1.14%	0.2730	1.11%
SCK-CEN JEFF 3.3	1.4008	1.50%	0.2767	2.45%
SCK-CEN JEFF 3.1.1	1.3926	0.91%	0.2820	4.43%
SCK-CEN JENDL-5	1.3877	0.55%	0.2818	4.35%
SCK-CEN JEFF-4T3	1.4023	1.61%	0.2722	0.81%
Newcleo ENDFB 8.0	1.4050	1.81%	0.3120	15.52%
CIEMAT JEFF 3.1	1.4094	2.12%	Not Reported	
UPC-1 ENDFB 7.0	1.4250	3.26%	0.2730	1.11%
UPC-2 ENDFB 7.0	1.1464	-16.93%	0.2074	-23.20%
UPC-3 ENDFB 7.0	1.4135	2.42%	0.2421	-10.36%
NCSU ENDFB 7.0	1.4055	1.85%	0.2746	1.70%
Average	1.38007		0.27004	

Table VI. Results of η and Σ_{tr} for Stage 1 (outer fuel)

	η		Σ_{tr}	
	Value	Diff	Value	Diff
ININ_ENDFB 7.0	1.5626	-10.97%	0.2704	-0.45%
SCK-CEN ENDFB 8.0	1.5836	-9.78%	0.2679	-1.39%
SCK-CEN JEFF 3.3	1.5880	-9.52%	0.2712	-0.15%
SCK-CEN JEFF 3.1.1	1.5818	-9.88%	0.2766	1.84%
SCK-CEN JENDL-5	1.5752	-10.26%	0.2767	1.85%
SCK-CEN JEFF-4T3	1.5885	-9.49%	0.2670	-1.69%
Average	1.57995		0.27163	

3.2. Second Stage: 2D Subassembly/Supercell-Level

Only two participants, ININ and North Carolina State University (with three different libraries), published results in this stage. The results will be shown and compared by separating them into sub-exercises. To use shorter names, ININ with ENDFB 7.0 will be called only ININ, and North Carolina State University with ENDFB 7.1, ENDFB 8.0, and JEFF 3.1 will be called NCSU-1, NCSU-2, and NCSU-3, respectively.

Tables VII and VIII show the results of the Fuel Assembly cell sub-exercise, and Table IX shows the value of k_{∞} and the only microscopic cross-section requested ($^{10}\text{B } \sigma_c$) in the sub-exercises of absorber and shielding super-cells (region of interest surrounded by two rings of fuel).

Table VII. Results of the different parameters in Stage 2 (FA cell)

Parameter	ININ	NCSU-1	NCSU-2	NCSU-3
k_{∞}	1.26226	1.29206	1.29448	1.29751
$^{208}\text{Pb } \sigma_i$ (coolant) [b]	2.30240E-02	2.40392E-02	2.34549E-02	2.43532E-02
$^{208}\text{Pb } \sigma_c$ (coolant) [b]	6.68360E-04	6.70505E-04	6.72806E-04	6.81725E-04
$^{56}\text{Fe } \sigma_c$ (cladding) [b]	7.41589E-03	7.22894E-03	8.06362E-03	6.88245E-03
$^{238}\text{U } \sigma_i$ (fuel) [b]	9.38862E-01	9.43963E-01	9.46224E-01	8.53220E-01
$^{235}\text{U } \sigma_f$ (fuel) [b]	1.90462E+00	1.89635E+00	1.89882E+00	1.88268E+00
$^{238}\text{U } \sigma_f$ (fuel) [b]	3.36502E-02	3.41283E-02	3.41477E-02	3.36205E-02
$^{239}\text{Pu } \sigma_f$ (fuel) [b]	1.76514E+00	1.76016E+00	1.75893E+00	1.74619E+00
$^{241}\text{Pu } \sigma_f$ (fuel) [b]	2.51009E+00	2.49332E+00	2.48029E+00	2.49955E+00
$^{235}\text{U } \nu$ (fuel) [b]	2.50555E+00	2.45857E+00	2.45310E+00	2.45485E+00
$^{238}\text{U } \nu$ (fuel) [b]	2.72480E+00	2.74024E+00	2.72191E+00	2.76074E+00
$^{239}\text{Pu } \nu$ (fuel) [b]	3.00698E+00	2.93870E+00	2.93590E+00	2.93713E+00
$^{241}\text{Pu } \nu$ (fuel) [b]	3.01690E+00	2.96378E+00	2.96360E+00	2.96995E+00
$^{235}\text{U } \sigma_c$ (fuel) [b]	5.50580E-01	5.46638E-01	5.41788E-01	5.38926E-01
$^{238}\text{U } \sigma_c$ (fuel) [b]	2.89811E-01	2.84993E-01	2.80933E-01	2.83785E-01
$^{239}\text{Pu } \sigma_c$ (fuel) [b]	4.96569E-01	4.90803E-01	4.88827E-01	4.89074E-01
$^{241}\text{Pu } \sigma_c$ (fuel) [b]	4.43118E-01	4.37974E-01	4.33974E-01	4.72307E-01
η	1.33863E+00	1.36521E+00	1.36989E+00	1.37127E+00
Σ_{tr} [cm^{-1}]	2.78933E-01	2.81746E-01	2.80035E-01	2.83001E-01

Table VIII. Results of Σ_{fiss} and Σ_{capt} in Stage 2 (FA cell)

Parameter [cm^{-1}]	ININ	NCSU-1	NCSU-2	NCSU-3
Σ_f (Group 1)	1.86144E-04	6.43764E-03	6.45908E-03	6.52353E-03
Σ_f (Group 2)	4.96009E-04	2.83434E-03	2.86191E-03	2.82683E-03
Σ_f (Group 3)	6.27454E-04	1.62345E-03	1.62914E-03	1.63306E-03
Σ_f (Group 4)	6.39973E-04	2.01312E-03	2.03003E-03	2.00970E-03
Σ_f (Group 5)	1.31781E-04	6.18360E-03	5.91612E-03	6.07015E-03
Σ_f (Group 6)	2.75635E-09	5.36035E-02	5.29444E-02	5.52993E-02
Σ_f (Group 7)	1.59896E-11	4.44347E+00	4.89202E+00	2.40652E+00
Σ_c (Group 1)	3.00082E-05	1.02875E-03	1.15330E-03	1.02231E-03
Σ_c (Group 2)	1.62292E-04	9.02617E-04	8.91988E-04	9.51273E-04
Σ_c (Group 3)	5.77864E-04	1.44609E-03	1.42591E-03	1.46174E-03
Σ_c (Group 4)	1.64040E-03	4.96382E-03	4.97613E-03	4.94655E-03
Σ_c (Group 5)	3.39966E-04	1.56215E-02	1.57403E-02	1.57719E-02
Σ_c (Group 6)	5.53407E-09	1.11604E-01	1.10235E-01	1.21414E-01
Σ_c (Group 7)	1.01835E-11	3.18661E+00	3.56929E+00	1.67744E+00

Table VII shows good concordance of results between the two participants regarding the microscopic cross-sections and other parameters, but Table VIII is explicit that there are significant differences in the macroscopic cross sections calculations; this can be due to the methodology used in its calculations, unfortunately having only two participants makes challenging to assess the precision. The same happens in the super-cell sub-exercises; a good concordance is found in the calculated microscopic parameters (see Table IX) but not in the macroscopic (not shown here), where the same trend as Table VIII was observed.

Table IX. Results in Stage 2 (Absorber and Shield super-cell)

Parameter	ININ	NCSU-1	NCSU-2	NCSU-3
k_∞ (Control SA)	1.15553	1.15456	1.15542	1.15976
^{10}B σ_c (Control SA) [b]	2.48795E-04	2.47191E-04	2.06347E-04	2.44655E-04
k_∞ (Shield SA)	1.24205	1.26071	1.26261	1.26555

3.3. Third Stage: 3D Full-Core Level

In this exercise, the entire core is modeled and burned for 5 effective years. Some parameters related to the burnup are requested, such as the mass balance (at the beginning of life BoL and end of life EoL) or the reactivity swing along the core life; other parameters requested are related to the effect of insertion of control rods and the effects of voids. These parameters are listed here:

- **dk_swing [in pcm]**: criticality swing between Beginning and End of a cycle.
- **doppler [in pcm]**: Doppler constant for which the fuel temperature is increased by 600 K.
- **pb_void_activeheight [in pcm]**: lead void reactivity for which the lead density is set to zero on the sole active region.
- **pb_void_wholeheight [in pcm]**: lead void reactivity for which the lead density is set to zero on the whole S/A height.
- **pb_void_wholecore [in pcm]**: lead void reactivity for which the lead density is set to zero on the whole core.
- **control_rods_worth [in pcm]**: all control rods are inserted in the active region.

- **safety_devices_worth [in pcm]:** all safety devices are inserted in the active region.

Table X shows the results for the parameters listed previously, and Tables XI, XII, and XIII show the mass balances of the main fuel components for the inner core, outer core, and full core. In this exercise, only one NCSU result is reported, and it is done with the code LUPINE using the ENDFB VII.0 library, so it will only be called NCSU.

Table X. Results of reactivity parameters in Stage 3

Parameter	ININ	NCSU
k	1.03134E	1.04185
control_rods_worth	-5.17578E+03	8.97180E+03
safety_devices_worth	-2.83418E+03	4.53990E+03
dk_swing	-5.19257E+03	-2.11815E+03
doppler	-5.74091E+02	-5.47036E+02
pb_void_activeheight	5.07827E+02	4.75903E+02
pb_void_wholeheight	-3.65757E+03	-6.00326E+03
pb_void_wholecore	-7.78514E+03	-9.73958E+03

Table XI. Mass balances at BoL and EoL in the inner core

Mass [kg]	ININ		NCSU	
	BoL	EoL	BoL	EoL
Uranium	7.63603E+02	6.66962E+02	2.54745E+03	2.30813E+03
Plutonium	1.87253E+02	1.71793E+02	6.48860E+02	6.04820E+02
Americium	2.49884E+00	4.29701E+00	8.55000E+00	1.56100E+01
²³⁸ U	7.62071E+02	6.66048E+02	2.54234E+03	2.30453E+03
²³⁹ Pu	1.06499E+02	9.55090E+01	3.69040E+02	3.38410E+02
²⁴¹ Pu	1.14296E+01	8.40878E+00	3.96100E+01	2.92300E+01

Table XII. Mass balances at BoL and EoL in the outer core

Mass [kg]	ININ		NCSU	
	BoL	EoL	BoL	EoL
Uranium	8.79677E+02	7.72578E+02	3.30197E+03	3.10008E+03
Plutonium	2.96990E+02	2.50454E+02	1.15792E+03	1.04516E+03
Americium	3.96325E+00	6.91820E+00	1.52500E+01	2.86400E+01
²³⁸ U	8.77912E+02	7.71307E+02	3.29534E+03	3.09427E+03
²³⁹ Pu	1.68911E+02	1.32309E+02	6.58550E+02	5.67900E+02
²⁴¹ Pu	1.81277E+01	1.33952E+01	7.06800E+01	5.36100E+01

The results parameters from Tables X to XIII are somewhat comparable, at least in order of magnitude.

In the reactivity parameters (Table X), a couple of NCSU values were in opposite signs, which is expected since the insertion of control or safety rods should have a negative effect on the reactivity. Having positive values is not right. It could be an interpretation error, and the value could have been calculated first with the rods inserted and then extracted. Still, no explanation of this was included in the NCSU results.

Table XIII. Mass balances at BoL and EoL in the whole core

Mass [kg]	ININ		NCSU	
	BoL	EoL	BoL	EoL
Uranium	1.64328E+03	1.43954E+03	5.84942E+03	5.40820E+03
Plutonium	4.84243E+02	4.22247E+02	1.80678E+03	1.64999E+03
Americium	6.46209E+00	1.12152E+01	2.38000E+01	4.42500E+01
²³⁸ U	1.63998E+03	1.43736E+03	5.83768E+03	5.39879E+03
²³⁹ Pu	2.75409E+02	2.27818E+02	1.02759E+03	9.06310E+02
²⁴¹ Pu	2.95573E+01	2.18040E+01	1.10290E+02	8.28400E+01

From Tables XI to XIII, the first thing to show is that both models do not start with the same amount of fuel at the BoL, which is a significant discrepancy since both participants based their models on the same benchmark definitions. However, it was also found that both showed the same tendencies; this happens when the results of one participant show an increase or decrease in mass, and the other shows it, too, in the same proportion. This fact leaves a positive feeling on the team.

4. CONCLUSIONS

Participation in the Benchmark was a positive experience for the ININ team since it involved modeling highly complex geometries, and the expected results included parameters that the team had never calculated in previous activities.

The results show a good general agreement with the data available from other participants, but there is still room for further improvement.

Regrettably, most participants published only part of the results asked in the Benchmark, either for not participating in the stage or not including all the results in a given stage. As a result, ININ's team completed all the tasks but could not compare all the results. When discrepancies are found but only two participants reported results, the uncertainty is left on which is correct.

REFERENCES

1. "Wikipedia – Gen. IV Reactor," https://en.wikipedia.org/wiki/Generation_IV_reactor (2024)
2. "GEN IV International Forum Website - Lead-Cooled Fast Reactor (LFR)" https://www.gen-4.org/gif/jcms/c_9358/lfr (2024)
3. IAEA. *Status of Innovative Fast Reactor Designs and Concepts: A Supplement to the IAEA Advanced Reactors Information System (ARIS)*. IAEA Publishing, Vienna, Austria (2013).
4. Grasso, G. *EGPRS Lead-cooled Fast Reactor (LFR) Benchmark (Technical Report NEA/NSC/WPRS/DRAFT)*. OECD Publishing, Paris, France (2022)

Results of Mexico's Participation in the Extension Phase of Neutronics Benchmark of the CEFR Reactor Start-Up Test

Roberto Lopez-Solis*, Armando Gomez-Torres, Juan Galicia-Aragon
National Institute for Nuclear Research

Carr Toluca - México s/n, 52750 La Marquesa, Méx

roberto.lopez@inin.gob.mx; armando.gomez@inin.gob.mx; jgaliciaa87@gmail.com

Edmundo del Valle-Gallegos

National Polytechnic Institute – Higher School of Physics and Mathematics

Av. Instituto Politécnico Nacional s/n, Gustavo A. Madero, 07738 CDMX

edmundo.delvalle@gmail.com

Abstract

Since 2018, the China Institute of Atomic Energy (CIAE) has proposed a benchmark based on the start-up tests of the China Experimental Fast Reactor (CEFR) due to the large amount of experimental data obtained during those tests. The benchmark represents an excellent opportunity for code validation and testing of nuclear reactor modeling methodologies and capabilities. This paper shows the results of the Mexican team's participation in the CEFR Start-Up Test Neutronic Benchmark extension exercise. The extension exercise was proposed in 2022 and consists of five work packages or exercises in which the team participated. The results of the blind phase were available for the participants after the midterm Research Coordination Meeting. The primary tool used by the team, was the stochastic code Serpent version 2.2.0. The results were consistent with the ones obtained and reported by other teams, which gives confidence in the team's capabilities to handle this kind of project.

1. INTRODUCTION

The China Experimental Fast Reactor (CEFR), located at the China Institute of Atomic Energy (CIAE), is the first fast reactor in China, and it reached its first criticality in 2010. It is a 65MWth pool-type sodium-cooled fast-spectrum reactor. The first loading of the reactor core was uranium dioxide fuel, with the enrichment of ^{235}U at 64.4%.

In 2018, the CIAE proposed via an IAEA Coordinate Research Project, a benchmark based on the start-up tests of the CEFR due to the large amount of experimental data obtained [1]. This benchmark represents an important opportunity for V&V of nuclear codes, which benefit the worldwide fast reactor community. The physical start-up of CEFR consisted of a series of experiments carried out in four aspects: 1) criticality experiments, 2) measurement of control rod worth, 3) measurement of reactivity coefficients, and 4) foil activation measurements.

Several institutions worldwide participated in reactor core modeling activities to calculate the desired neutronic parameters established in the benchmark using stochastic and deterministic nuclear codes. Mexico was not the exception and participated in all of those exercises. Its results have been used to validate codes and develop methodologies for reactor analysis [2][3][4]. The code of choice was the stochastic code Serpent version 2.2.0 [5] with the microscopic cross-section's library ENDFB VIII.0.

By the end of 2022, due to the great success of the Benchmark, an extension of this benchmark was proposed, aiming more complex calculations with the CEFR model further to validate the participants' codes, models and nuclear data [6]. These extension exercises were seven: burn-up, deep penetration, neutron dynamics, neutron spectrum, group constant, kinetics parameters, and reactivity spatial distribution. The Mexican team participated in five of these seven exercises.

In this paper, Mexico's participation in the Benchmark extension is compared with the available results from other participants. Most of participants used stochastic neutronic codes, with this consideration, the comparison against Mexico's results is fair. It is important to note that the available data are blind results and will likely be further refined. Still, this comparison is a good exercise for testing the modeling methodologies.

2. CEFR CORE

This section will provide a brief description of the CEFR core. For a more detailed description of geometry or materials, the reader is encouraged to visit references [1] and [6].

The core of nominal loading consists of 79 fuel subassemblies (SA), 8 control SAs, one neutron source SA, 394 stainless steel (SS) SAs, and 230 boron shielding SAs, as shown in Figure 1.

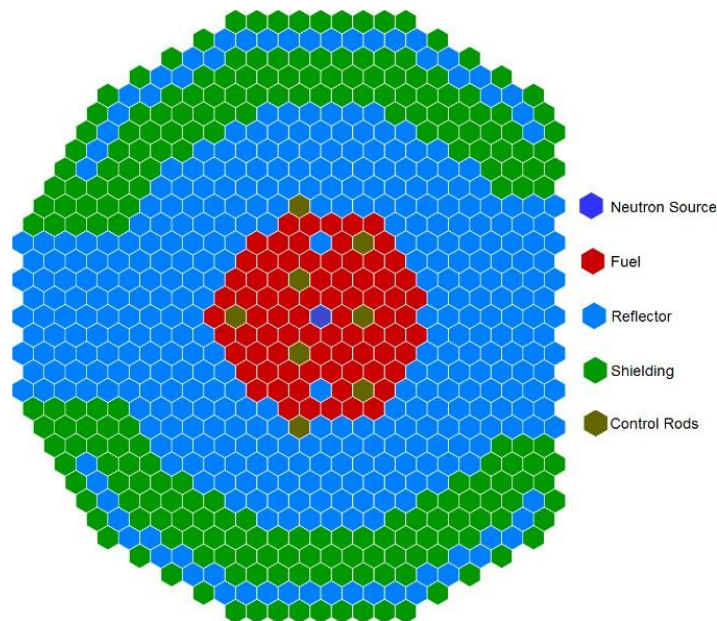


Figure 1. CEFR core layout when fully loaded

The external shape and dimension of all SAs are almost the same, while the inner structure varies on the specific SA type. The SAs are seated on a supporting structure, with the nozzle inserted to accept the sodium flow, while the top of the SAs are free for axial expansion; radially, the gap between SAs is kept by spacer pads on the SA head. The sodium flows upwards through the channels inside the SA and the gap between the SAs. Due to the different positions in the core and different cooling needs, the reactor core is divided into different flow-rate zones; subsequently, the nozzle of SAs is specially designed to obtain a specific flow rate, which does not influence the neutronics calculation.

3. BENCHMARK EXTENSION EXERCISES

As mentioned previously, the Benchmark extension consists of seven exercises, in which Mexico participated in five; unfortunately, results for one of those (group constants exercise) were unavailable, so this will not be presented since there are no other results to compare. This section will briefly describe the exercises, and the results will be compared against those of other participants. If the reader is interested in a more detailed description of the exercises, is encouraged to read reference [6].

3.1. Burn-Up Exercise

Participants are expected to carry out burn-up calculations for one refueling cycle, i.e., 80 days at nominal full power (80 EFPDs), with fixed control rods at given positions. Fuel, structural material, and coolant temperatures are also provided depending on the core region. Figures 2, 3, and 4 show the results obtained by the team (in red) compared to those of the other participants in the benchmark.

The expected results include:

- Burn-up reactivity loss of each time step (0, 1, 2, 6,10, 20, 30, 40, 50, 60, 70 and 80 days)
- Burn-up axial distribution in 5 cm thick layers, 0 cm being the core’s midplane
- Mass of key nuclides
-

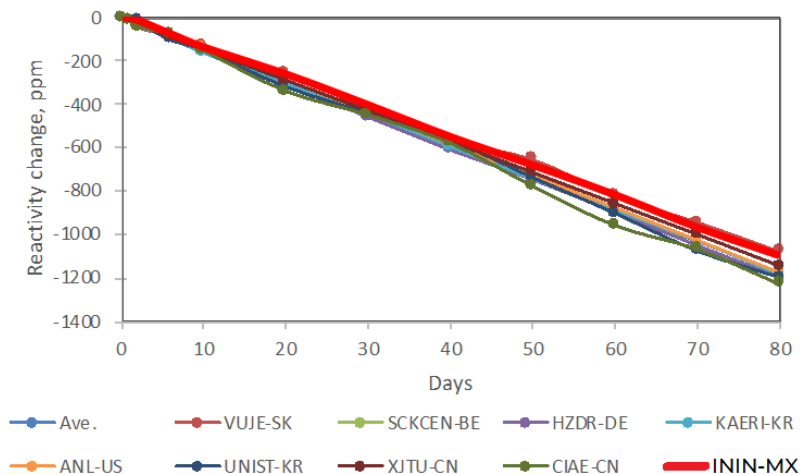


Figure 2. Reactivity loss (in pcm) with burn-up

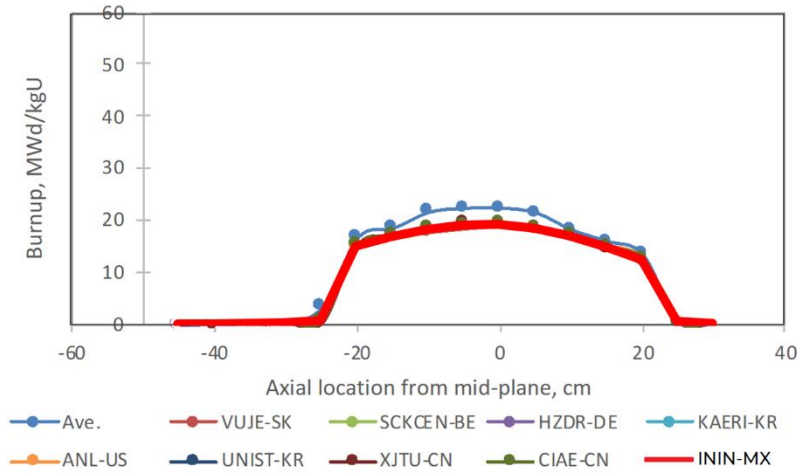


Figure 3. Burn-up axial distribution

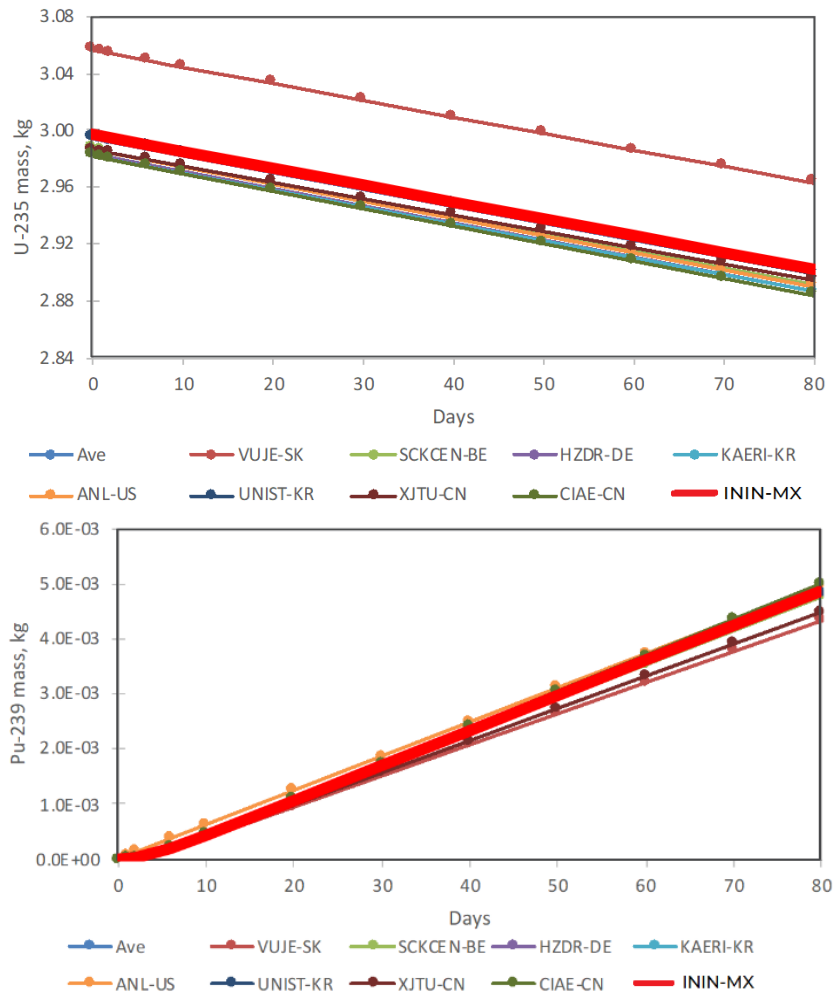


Figure 4. Mass evolution with burn-up time of ^{235}U (top) and ^{239}Pu (bottom)

As seen in Figures 2, 3, and 4, the results are well concordant with those of the other participants.

In Figure 4, the results are shown only for 235U and 239Pu, but the same concordance was found for the rest of the nuclides tracked.

3.2. Neutron Spectrum Exercise

In this work package, the neutron spectrum is calculated at the mid-plane of two given subassemblies (2-2 and 7-5). The energy is divided with a 33-group structure, also given in the specifications.

The results of this exercise were compared against the available data, as shown in Figure 5 in red. The results are comparable to those of the other participants, so most lines overlap.

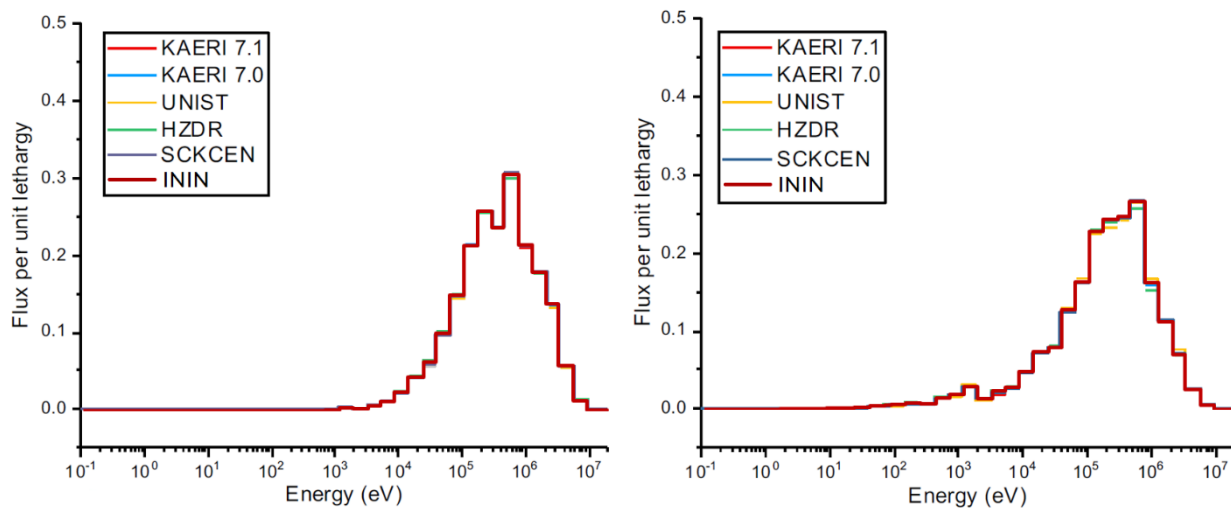


Figure 5. Comparison of spectra in subassembly 2-2 (left) and 7-5 (right)

3.3. Kinetics Parameters Exercise

In this work package, participants are expected to calculate the core's kinetics parameters at the operation-loading cold state, i.e., the status at which most experiments were conducted.

The expected outputs include the decay constant of each delayed neutrons groups λ_i and the fraction of each group β_i . As is commonly done, the delayed neutrons are divided into six groups based on the life of precursors.

Figures 6 and 7 show the participants' results for this exercise; the libraries sort the plots using ENDFB 7.0, 7.1, and 8.0. As it can be seen in the mentioned figures, there is a significant influence on the library selected since good concordance among the results that used the same libraries is observed. Nevertheless, it is also observed that results with ENDFB 7.0 and 8.0 are very close to each other; this information is especially essential in the group fraction section of the exercise since the CIAE (the only other participant using version 8.0) didn't report results.



Figure 6. Decay constants λ_i [sec⁻¹] for different delayed neutron precursor groups

3.4. Reactivity Spatial Distribution Exercise

The spatial distribution presents the neutronics characteristics of the core and serves as an input to the safety analysis; the axial distribution of the fuel density reactivity coefficient at a given FA position (2-2) was calculated and reported. The fuel density reactivity is calculated by reducing the fuel density by 1% while keeping the rest of the materials untouched.

Figure 8 shows the Mexican results (red line) compared to the other exercise participants. There was good agreement among all the participants.



Figure 7. Fraction of delayed neutron precursor groups β_i

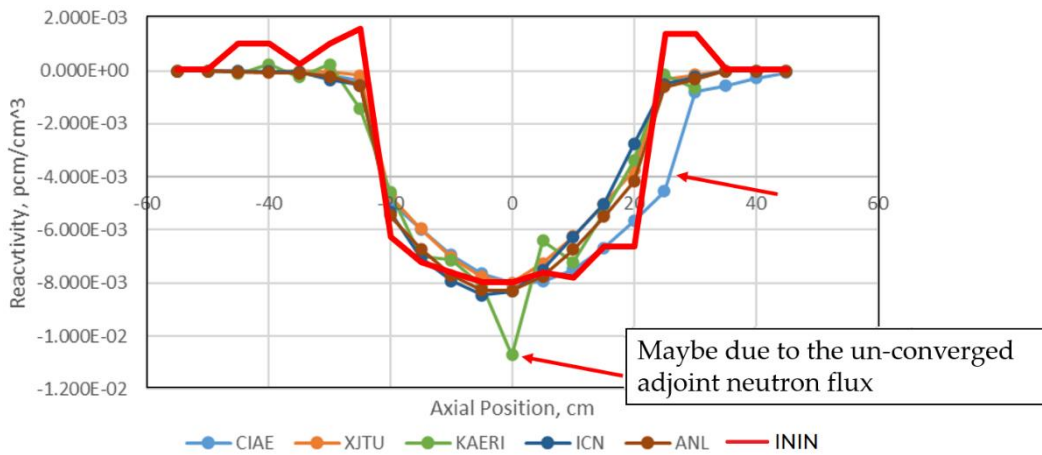


Figure 8. Axial distribution of fuel density reactivity

It is important to note that this exercise involves minor variations in big-sized models such as whole assembly and even full core level, so the tracking of reactivity is hard to do (just a few pcm in peak changes), and even a difference of 1 pcm leads to a significant change in the plot; however, even with these complications, the presented results are a good match.

4. CONCLUSIONS

The work shown here continues the previous work done by the Mexican team in the CEFR Benchmark and serves as a conclusion for its participation since it is the last set of exercises in the benchmark.

The results presented are in good concordance with those from other participants, confirming the team's good practices in modeling and analyzing nuclear reactors, particularly Sodium Fast Reactors.

These were blind results comparisons, so further work will include the refinement of the models in cases where improvement is still needed and the writing of the Mexican team report for the final version of the Benchmark document (TECDOC from IAEA).

REFERENCES

1. Xingkai Huo, *Neutronics Benchmark of CEFR Start-Up Tests*, China Institute of Atomic Energy, Beijing, China (2019).
2. Muñoz-Peña, G, Galicia-Aragon, J, Lopez-Solis, R, Gomez-Torres, A, del Valle-Gallegos, E. "Verification and Validation of the SPL Module of the Deterministic Code AZNHEX through the Neutronics Benchmark of the CEFR Start-Up Tests." *Journal of Nuclear Engineering*. **4**(1), pp 59-76. (2022).
3. Galicia-Aragon, J., Lopez-Solis, R., Gomez-Torres, A., Palacios-Hernandez, J., Del-Valle-Gallegos, E. "Verification and validation of the CEFR Serpent model for the generation of reference solutions and Cross Sections database for the deterministic code AZNHEX." *Proceedings of the International Conference on Fast Reactors and Related Fuel Cycles FR22*. Vienna, Austria. April 19-22, (2022).
4. Lopez-Solis, R., Muñoz-Peña, G., Del-Valle-Gallegos, E., Gomez-Torres, A., Galicia-Aragon, J., Palacios-Hernandez, J., "Verification of the SPL module of the neutron diffusion code AZNHEX through Neutronics Benchmark of CEFR Start-Up Tests." *Proceedings of the International Conference on Fast Reactors and Related Fuel Cycles FR22*. Vienna, Austria. April 19-22, (2022).
5. Leppänen, J., et al. (2015) "The Serpent Monte Carlo code: Status, development and applications in 2013", *Annals of Nuclear Energy*, **82**, pp 142-150. (2015)
6. Xingkai Huo, Xu Li, *Technical Specifications for the Extension Phase of Neutronics Benchmark of CEFR Start-Up Tests (Technical Document KY-IAEA-CEFRICRP-002)*, China Institute of Atomic Energy, Beijing, China. (2022).

Track 3

Nuclear Reactor Thermal- hydraulics and Safety

Hot channel analysis of the NuScale core with ATFs using Computational Fluid Dynamics

Yosvany Pérez González and Juan Luis François Lacouture

Universidad Nacional Autónoma de México, Facultad de Ingeniería, Departamento de Sistemas Energéticos.

Av. Universidad 3000, C.U., 04510, Mexico City, Mexico.

ypglez96@gmail.com ; juan.luis.francois@gmail.com

Fabián Luis Mena de la Noval

Universidad Nacional de Pernambuco

Av. Prof. Luis Freire No. 1000, C. Universitaria, CEP 50740-540, Brasil.

fabian.mena@ufpe.br

Abstract

The VOYGTR™ or commonly denoted as NuScale is a compact, integral, pressurized water small modular reactor (SMR) that is part of the third generation of nuclear reactors. It is the only SMR application that has been submitted for evaluation and approval by the U.S. Nuclear Regulatory Commission. Its economic, technological and safety advantages make it a viable and promising option for power generation. Since the Fukushima accident, the study of accident-tolerant fuels has aroused considerable interest associated with the decrease in the probability of core damage in the event of a severe accident. In this paper, a computational model based on CFD codes is presented to perform a hot channel analysis of the NuScale core using the conventional fuel and three ATFs under stationary operating conditions. The model allows obtaining and analyzing the thermal-hydraulic properties of the main core components. As results, it was observed the coolant temperature and density axial profiles vary by less than 2 % when the alternative fuels are used and proposed coatings do not influence the maximum temperature reached in the fuel rods. Also, maximum fuel temperature decreases significantly when the metallic fuel is used, due to the better thermal conductivity of this ATF compared to the conventional UO₂.

1. INTRODUCTION

The unsustainable nature of the current global energy scenario has greatly contributed to the search for alternatives to displace primary fossil fuel sources and address the environmental problems the planet faces. The energy transition to affordable and non-polluting energies is precisely one of the proposed objectives by the United Nations (UN) in its Agenda for Sustainable Development [1]. For these reasons, renewable energies have aroused considerable interest in recent years and their deployment has been on the rise. In 2022, these sources provided 30 % of global electricity generation [2]. Although a considerable growth in this contribution is planned and estimated, there are still limitations in availability, generation capacity and storage.

Nuclear power is considered another viable and promising option to achieve sustainable development goals. The possibility of expanded generation, negligible greenhouse gas emissions, low cost and strict safety levels in electricity generation are the main potentialities of nuclear fission energy. Many countries have opted to use this source to diversify their energy matrix. In France, for example, 62.6 % of electricity demand is met by nuclear energy [3].

However, major challenges remain to ensure the sustainability of the nuclear energy industry. The main challenges to be faced include to avoid the proliferation of nuclear weapons, to reduce construction and operating costs, to improve efficiency in power generation and safety systems, as well as to solve the problems associated with the storage of long-lived radioactive waste. Generations III and III+ of advanced nuclear systems promote the improvement of safety through the incorporation of completely passive safety systems and the maximum utilization of nuclear fuel. Among the reactors of these generations, Small Modular Reactors (SMRs) stand out for their feasibility and potential advantages. SMRs are, as their name suggests, small reactors (approximately half the size of conventional Light Water Reactors), capable of generating up to 300 MWe. The ability to adapt to regions with weak grids and the modular and integral character are the main advantages of these nuclear systems. Modularization allows module-by-module construction in the controlled environment of a factory and subsequent transportation to the site, which significantly reduces construction costs. Because each module can operate independently, the costs associated with operation and maintenance are reduced, as one or more modules can be shut down for failures or maintenance actions without the need to shut down the entire plant [4]. Currently, there are several SMR designs in the planning and design stages, as well as some in operation and construction. The only SMR that has been submitted for licensing by the U.S. Nuclear Regulatory Commission (NRC) is the VOYGR™, developed by NuScale Power, LLC and commonly referred to as NuScale [5].

Although the safety of nuclear power reactors has always been a priority, the lessons learned from the three most serious accidents in the nuclear industry highlight the need for improvement and the search for excellence in safety systems. The Fukushima Daichii accident in 2011 contributed to the deployment of research on fuels capable of tolerating the consequences of a severe accident for a longer period than the conventional UO₂ fuel. These were called Accident Tolerant Fuels (ATFs). One of the most studied ATF concepts is the use of coatings on conventional fuel. Commonly, metallic coatings are discussed, such as chromium and iron alloys, chromium and aluminum, or a combination of layers of both. Ceramic coatings such as chromium titanium nitrides and chromium titanium zirconium carbides have also been proposed [6]. Several investigations have been developed to evaluate ATFs and different fuel coating materials in the NuScale. A neutron analysis of the reactor core using ATFs with different coating materials is presented in [7]. Conventional UO₂ fuel and uranium silicide, as well as claddings of chromium and an iron-chromium-aluminum alloy were studied. A neutronic and thermal-hydraulic coupled calculation methodology is implemented in [8] to evaluate ATFs performance in the NuScale. Uranium oxide and silicide with and without coatings of Zr, FeCrAl and SiC were studied. A decrease in the infinite neutron multiplication factor was observed when the ATFs were used. Also, the use of ATFs reduces the radial power peak factors and the maximum temperature registered in the fuel rods.

In this paper a hot-channel analysis is performed on the NuScale core to evaluate the performance of three ATFs. The research presented in [7] is used as a reference. A model based on

Computational Fluid Dynamics (CFD) codes is presented for the study and analysis of the thermal-hydraulic properties of the main reactor core components under stationary operating conditions.

2. MATERIALS AND METHODS

This section summarizes the main operating parameters of NuScale and the core configuration. The hot-channel calculation methodology implemented to evaluate the thermal-hydraulic performance of three ATFs under stationary operating conditions is also described.

2.1. NuScale Modular Power Reactor

The initial design of a NuScale plant envisions the installation of 1 to 12 independent modules, each one with a power capacity of 160 MWt (45 MWe). Each module includes an integral pressurized water reactor (iPWR) operating in a natural circulation regime with 100 % passive and independent safety systems. The reactor is located inside a 20 m high pressure vessel that is submerged underwater in a stainless-steel pool. Figure 1 shows the main components of a NuScale nuclear power plant module. The main design characteristics of the reactor are presented in Table I [9][10].

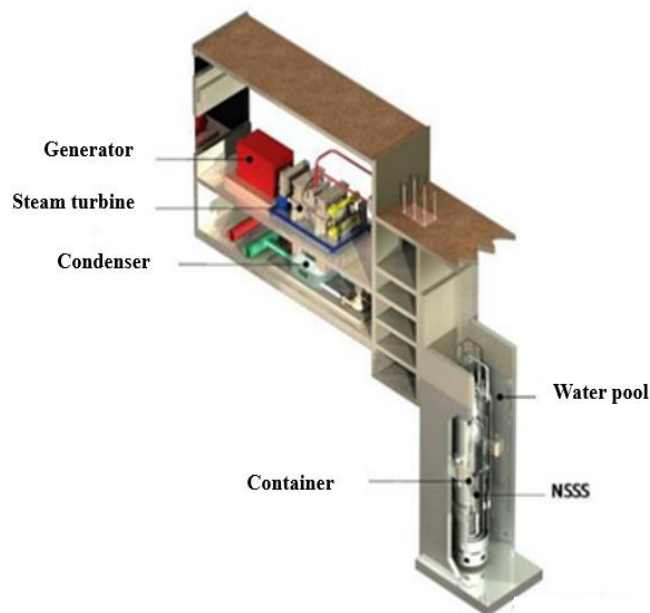


Figure 1. Main components of a NuScale power plant module [10].

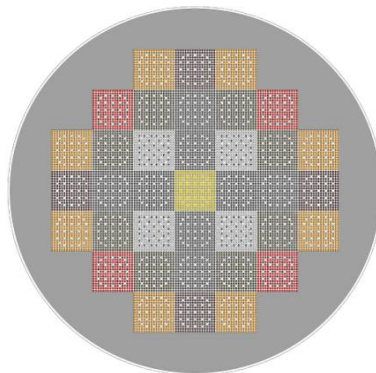
Table I. Main characteristics of the NuScale reactor [9].

Parameter	Value/Description	Unit
Thermal power	160	MWth
Electrical output	45	MWe
Coolant and moderator	Light water	
Fuel	UO ₂ (<4.95 wt% U ²³⁵)	
Operating pressure	12.76	MPa
Coolant inlet temperature	531.48	K
Average coolant temperature rise	310.93	K
Coolant mass flow rate	587.16	kg/s
Reactivity control mechanisms	Control rods/H ₃ BO ₃	
Burnable poison	Gadolinium	
Active core height	2	m
Pressure vessel height	20	m
Vessel outside diameter	2.83	m

In addition to the small core size, the NuScale reactor differs from conventional PWRs in its integral character. All secondary cycle components required for steam generation are included inside the pressure vessel. The Nuclear Steam Supply System (NSSS) consists of the core, a helical steam generator and a pressurizer, all of them incorporated inside the pressure vessel.

2.1.1. NuScale core configuration

The NuScale core design is based on conventional PWRs designs. It consists of an array of 37 fuel assemblies arranged in an octagonal shape, surrounded by a stainless-steel reflector that greatly improves the thermal utilization of the fuel by significantly reducing neutron leakage in the radial direction. A cross-sectional view of the reactor core is shown in Figure 2.

**Figure 2. Reactor core cross section [7].**

Each fuel assembly consists of a 17x17 square array, 24 guide tubes and a central instrumentation tube. The 264 fuel rods are supported by 5 separator grids. Gadolinium is used as a burnable

poison to control the excess of reactivity at the start of the cycle. Gadolinium oxide is homogeneously mixed with UO_2 and rods with this composition are distributed in certain regions of the assembly. The fuel rods are separated from the claddings (fabricated with alloy 304SS) by pressurized helium [7]. Figure 3 shows the cross section of the typical NuScale fuel assembly. Table II describes its main geometrical characteristics.

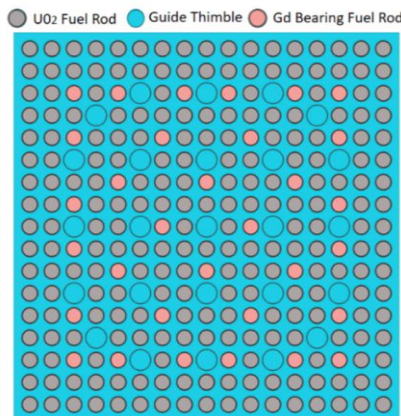


Figure 3. Cross section of the typical NuScale fuel assembly [7].

Table II. Main geometrical characteristics of the NuScale fuel assembly [9].

Design parameter	Value [cm]
Fuel pellet diameter	0.81153
Cladding outside diameter	0.94996
Cladding inside diameter	0.82804
Fuel rod pitch	1.25984
Fuel assembly pitch	21.50364
Control rods outside diameter	0.96774
Control rods inside diameter	0.87376

2.2. Hot Channel Methodology

One aspect to consider in any design study or analysis of a nuclear reactor is the close relationship between the thermal-hydraulic properties of the core components and the physical-neutron parameters. In a LWR, when the coolant water rises through the core, there are significant changes in its density, which produces variations in its neutron moderating power. This causes the power release profiles and multiplicative properties of the medium to vary. As the energy released because of fission varies, changes in the density of the water will occur again and so on. For this reason, it is necessary to use computational tools such as coupled neutron-thermal-hydraulic analyses to evaluate reactor performance and safety parameters. This neutron-thermal-hydraulic phenomenon is stronger in BWRs, where cooling water boiling occurs and

consequently more abrupt density and temperature changes are observed than in PWRs, where there is no phase change of the pressurized water.

In this regard, hot channel studies are fundamental. In this type of analysis, the hottest reactor channel is studied, that is, the one in which the highest heat energy is released or the one with the highest peak power factor. If this channel satisfies the limits established in the thermal safety parameters, such as power release and maximum fuel temperature, the rest of the channels or assemblies must also satisfy these requirements. The analysis is greatly simplified in this way.

In this paper, a hot channel analysis is developed to evaluate the thermal-hydraulic performance of ATFs in the NuScale core under stationary operating conditions. The following fuels are proposed for study and performance analysis:

1. Conventional UO_2 fuel
2. Conventional UO_2 fuel with chromium coating ($\text{UO}_2\text{-Cr}$).
3. Conventional UO_2 fuel with an iron, chromium and aluminum alloy coating ($\text{UO}_2\text{-FeCrAl}$).
4. Metallic alloy U-10Zr fuel

The implemented methodology is described below:

1. Obtaining the axial power profile in the reactor core for each analyzed fuel. These distributions were obtained from a previous neutronic study presented in [10].
2. Determination of the radial power peak factors in the core, to select the hot channel (the one with the highest peak power factor). These factors were also presented in [10].
3. Obtaining the axial power distribution for the hot channel. This profile is obtained as the product of the radial peak power factor and the average axial power distribution in the core described in the first step of the methodology.
4. Determination of the radial peak power factors for each fuel rod in the hot channel. These factors were approximated by performing a single fuel assembly neutronic calculation in an infinite medium. Probabilistic SERPENT code was used to perform the calculation.
5. Obtaining average volumetric power profiles for each channel fuel rod. The average axial volumetric power profile for each fuel rod is obtained as the product of the channel axial power distribution and the radial peak factor corresponding to each rod.
6. Introduction of the average volumetric power profiles for each fuel rod of the channel as boundary condition for the thermal-hydraulic calculation in the model. A fourth-degree polynomial fit was applied to the profiles to obtain continuous equations for the released power in each fuel element.
7. Analysis of results.

2.3. Thermal-hydraulic Model Based On CFD Codes

The development of computer science has made Computational Fluid Dynamics (CFD) a powerful numerical calculation tool for nuclear reactors. The thermal-hydraulic properties of fuel assemblies can be predicted with high accuracy through its use. For this purpose, CFD codes solve the equations of conservation of energy, mass and momentum in discretized control volumes. The CFD codes system inserted in the ANSYS-CFX 18.1 software is used in this work.

The analysis with this software is performed in three fundamental stages: pre-processing, solver and post-processing. Figure 4 shows the relationship between the elements compounding the CFD analysis in ANSYS-CFX 18.1.

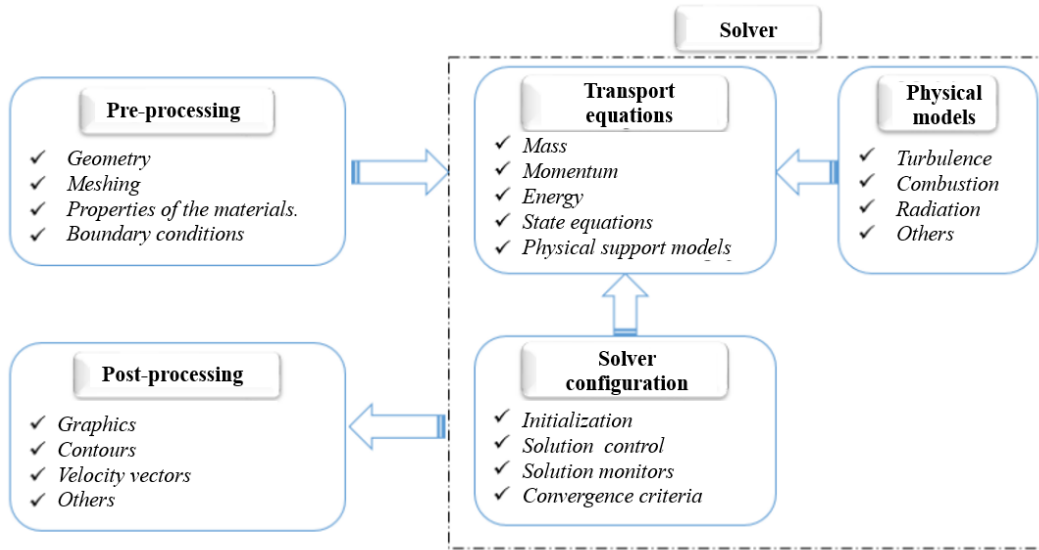


Figure 4. Relationship between the elements on a CFD analysis [11].

2.3.1. Geometry

In this work, one-eighth of the typical NuScale fuel assembly is analyzed. By taking advantage of the symmetry, the computational cost of the calculations and the processing time are reduced. The geometry was constructed using the Space Claim Design Modeler 18.1 tool, considering the geometrical characteristics presented in Table II (Figure 5).

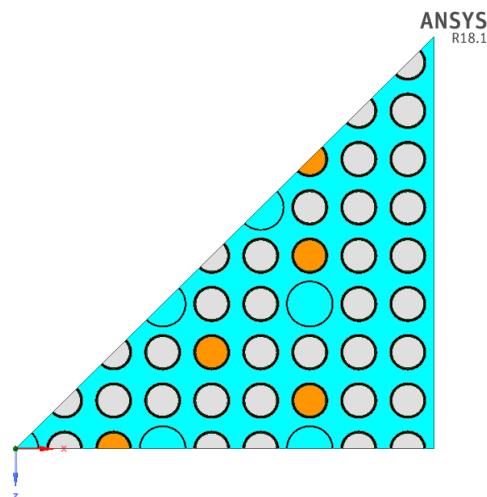


Figure 5. Cross section of an eighth of the NuScale fuel assembly.

2.3.2. Meshing

A three-dimensional mesh was constructed of prismatic and hexahedral elements for the spatial discretization of the eighth of the assembly. Sweep meshing methods were used to discretize the fuel, claddings and helium, and the Multizone method to discretize the coolant region. Inflations were added at the cladding-refrigerant separation interfaces to capture the phenomena associated with the formation of convective boundary layers. Figure 6 shows an overview of the generated meshing.

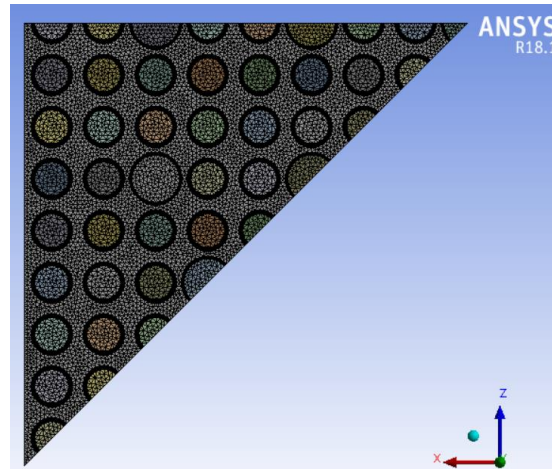


Figure 6. Overview of the generated meshing.

A mesh sensitivity analysis was performed to obtain the radial and axial dimensions of the finite volumes that ensure that the relative error in each considered variable in one iteration and the previous one is less than 1 %. The coolant is the element of the assembly that experiences the greatest variations in temperature and density. For this reason, for the sensitivity study, these variables were analyzed at distributed points in the assembly with meshes of different axial and radial dimensions. Considering the results, the selected mesh has 628,280 elements of 0.001 m length in the radial direction and 0.1 m in the axial direction. To analyze the mesh quality, quality indicators are used. The Orthogonal Quality indicator reports an average value of 0.94627 (1 is the best value [12]), while Skweness reports an average of $8.17 \cdot 10^{-2}$ (0 is the best value [12]). These values reveal the generated meshing has a good quality.

2.3.3. Boundary conditions and physical models

Two main boundary conditions were established for the coolant: inlet mass flow rate and outlet static pressure. These parameters coincide with those shown in Table I. Volumetric heat sources are introduced in the fuel rods as boundary conditions. The results of neutron calculations presented in [7] and [10] are used to obtain the equations for the axial and radial distributions of average volumetric heat. The axial and radial peak power factors in the reactor core were also considered.

The main heat transfer models used are Total Energy for the coolant, to include the kinetic energy effects of the fluid, and Thermal Energy, for the rest of the elements. The RSM-SSG model is used to simulate turbulence.

2.3.4. Thermophysical properties

The thermophysical properties of water are selected from the International Association for the Properties of Water and Steam (IAPWS) [13]. The IAPWS-IF97 library is used in ANSYS-CFX 18.1. Helium properties are assumed constant and equal to those reported in the ANSYS-CFX 18.1 libraries. The main properties of the 304 SS alloy used in the fabrication of combustible assemblies vary with temperature according to the equations presented in [14]. The variation of the main thermophysical properties of UO_2 with temperature is extensively discussed in [15] and [16]. Since the density of the metallic fuel U-10Zr does not vary considerably with temperature, a constant value of density is assumed. The used equations to evaluate its thermophysical properties were selected from [17].

3. RESULTS AND DISCUSSION

Figures 7 and 8 show the axial profiles of the average coolant temperature and density for each studied case. As expected, the average water temperature increases as it rises through the core due to heat transfer with the fuel. No significant variation of average coolant temperature or density is registered when the fuels UO_2 , UO_2 -Cr and UO_2 -FeCrAl are used. The coolant temperature increases from 531 K at the inlet to 571 K at the outlet of the assembly, while density decreases from 796 kg/m^3 to approximately 726 kg/m^3 . A slight difference in the axial profile of coolant temperature and density is observed when the metallic fuel U-10Zr is used. Outlet average values of 576 K and 714 kg/m^3 are registered for this case. This is because the highest radial peak power factor was obtained for this fuel, so more power is released in this case and more heat is released to the coolant. However, the noticed deviations are less than 2 %.

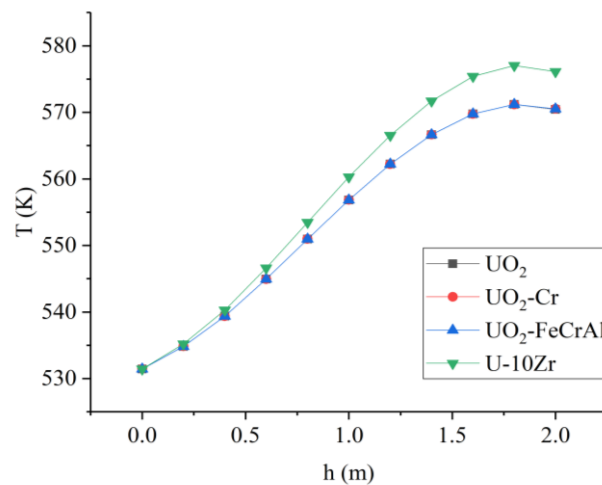


Figure 7. Axial profile of coolant temperature.

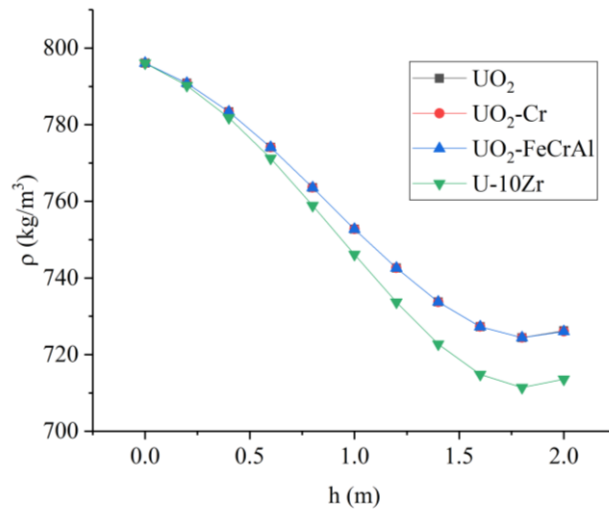


Figure 8. Axial profile of coolant density.

Radial distribution of the coolant temperature at the outlet of the fuel assembly is shown in Figure 9 for the analyzed cases. A similar behavior is observed when the conventional fuel UO_2 is used with or without the proposed coatings. The maximum temperatures are registered in the central space between the fuel rods with the highest radial peak power factors. The minimum temperature value is reached in the corner of the fuel assembly, because of the existence of a large volume of coolant and the relatively low radial peak power factor of the rods in this region. Low temperature values are also registered in the surrounding area of the guide tubes and the central instrumentation tube, due to the absence of heat generation in this region. Temperature variations between 17 K and 22 K can be observed in the radial direction for all the studied cases, obtaining values of up to 584 K when the metallic fuel is used.

Axial profiles of the maximum temperatures of the analyzed fuels are presented in Figure 10. These distributions are linked to the axial power profiles in the reactor core. The maximum values of fuel temperature (816 K for UO_2 and $\text{UO}_2\text{-Cr}$, 817 K for $\text{UO}_2\text{-FeCrAl}$ and 716 K for U-10Zr) are approximately registered at a height of 1.1 m. A significant decrease of about 100 K is obtained when the metallic fuel is used, due to the better thermal conductivity of this fuel compared to the conventional. Also, the use of the proposed coatings does not significantly influence the maximum temperature registered in the fuel.

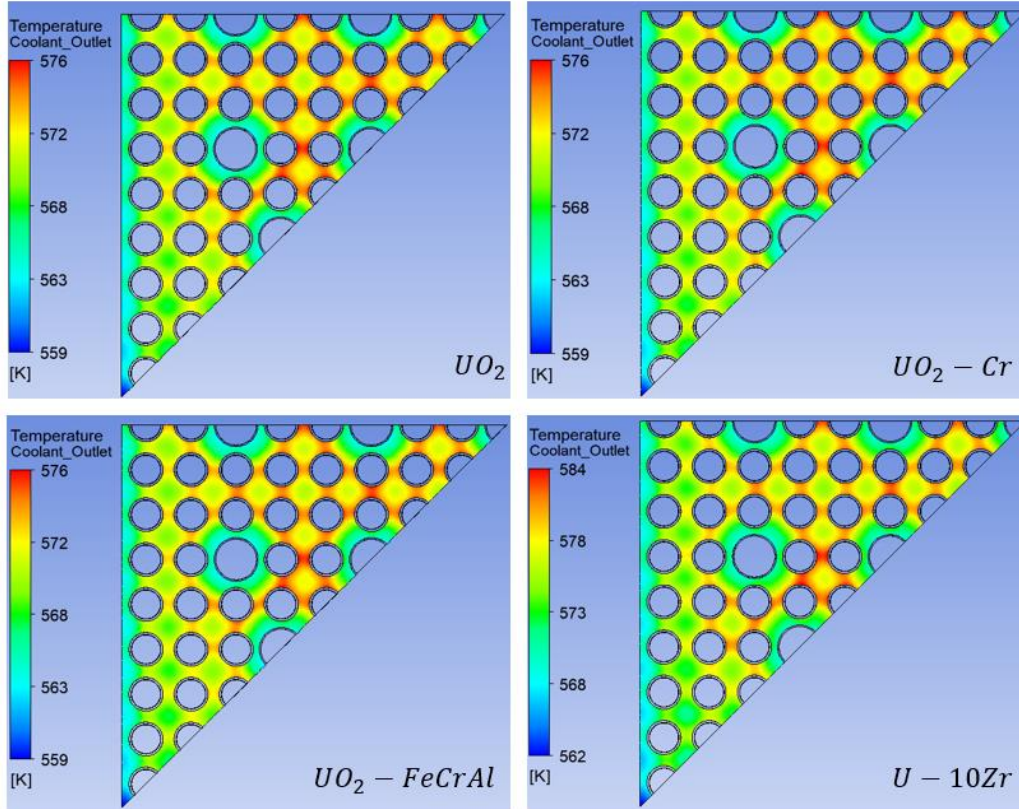


Figure 9. Radial distribution of the coolant outlet temperature.

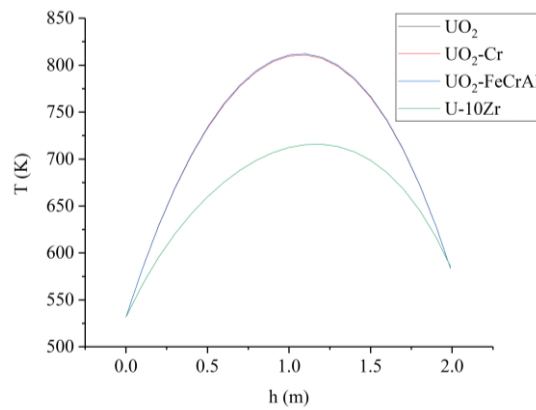


Figure 10. Axial profile of the maximum fuel temperature.

The radial temperature distribution of UO_2 , $\text{UO}_2\text{-Cr}$, $\text{UO}_2\text{-FeCrAl}$ and U-10Zr fuel rods at a height of 1.1 m is shown in Figure 11. As expected, maximum values are observed at the center of the rods with a higher radial peak power factor. Due to heat transfer, temperature decreases in radial direction until minimum values are reached at the helium-fuel interface. The maximum values observed are well below the fuel melting temperatures, which allows reactor operation with wide safety margins, even more so in the case of metallic fuel.

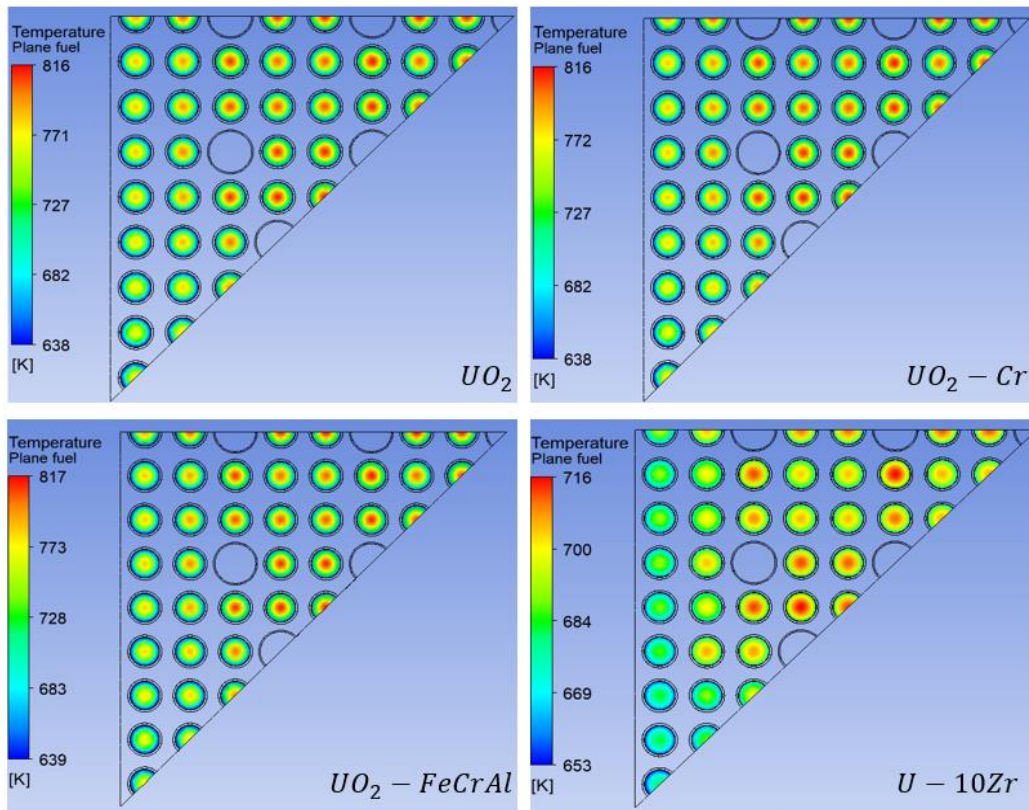


Figure 11. Radial distribution of the temperature registered on fuel rods of UO_2 , $\text{UO}_2\text{-Cr}$, $\text{UO}_2\text{-FeCrAl}$ and U-10Zr .

4. CONCLUSIONS

The presented computational model based on CFD codes allowed performing a hot channel analysis on the NuScale core using different ATF's in steady-state operating conditions. The main thermal-hydraulic properties of the critical fuel assembly were obtained and analyzed, demonstrating once again the effectiveness of CFD codes in predicting the thermal-hydraulic behavior of a nuclear reactor core.

The use of the proposed ATF's do not considerably vary the axial distributions of temperature and average coolant density, where the maximum relative deviation is less than 2 %. This allows the reactor to operate within the same operating parameters as when using conventional UO_2 fuel.

When analyzing the maximum temperature reached in the fuel rods, a decrease of up to 100 K was observed when using ATFs based on metallic fuel, which allows the safe operation of the reactor. The use of the considered coatings does not influence the maximum temperature reached in the fuel rods. These coatings are fundamental in the case of severe accidents by increasing the margin of time allowed to mitigate an emergency and avoid core meltdown.

ACKNOWLEDGEMENTS

To the *Consejo Nacional de Humanidades, Ciencia y Tecnología (CONAHCYT)* for providing financial support to Yosvany Pérez González for the completion of this work, which is part of his master's degree research.

To the *Universidad Nacional Autónoma de México*, for its support through the research project *Nuclear reactors and nuclear fuel cycles*.

REFERENCES

1. “Sustainable development goals”, United Nations (UN), <https://www.un.org/sustainabledevelopment/> (2023).
2. IRENA, *World Energy Transitions Outlook 2023: 1.5°C Pathway*, International Renewable Energy Agency, Abu Dhabi (2023).
3. “Power Reactor Information System (PRIS, IAEA). Country Statistics (France)”, IAEA, <https://pris.iaea.org/PRIS/CountryStatistics/CountryDetails.aspx?current=FR> (2024).
4. IAEA, *Advances in Small Modular Reactor Technology Developments, A supplement to: IAEA Advanced Reactors Information System (ARIS), 2022 Edition*, International Atomic Energy Agency, Vienna, Austria (2022).
5. “Application Documents for the NuScale US600 Design”, <https://www.nrc.gov/reactors/new-reactors/smr/licensing-activities/nuscale/documents.html#dcApp> (2020).
6. NEA and OECD, *State-of-the-Art Report on Light Water Reactor Accident-Tolerant Fuels*, Nuclear Energy Agency and Organization for Economic Co-Operation and Development, NEA No. 7317, Boulogne-Billancourt, France (2018).
7. S. Pino-Medina and J.L. François, “Neutronic analysis of the NuScale core using accident tolerant fuels with different coating materials”, *Nuclear Engineering and Design*, **Volume 377**, 111169 (2021).
8. Honghao Yu et. al., “Analysis of neutron physics and thermal hydraulics for fuel assembly of small modular reactor loaded with ATFs”, *Annals of Nuclear Energy*, **Volume 152**, 107957 (2021).
9. “NuScale Standard Plant Design Certification Application, Chapter Four: Reactor, NuScale Power LLC, 2020”, <https://www.nrc.gov/reactors/new-reactors/smr/licensing-activities/nuscale/documents.html#dcApp> (2020).
10. S. Pino Medina, *Evaluación del uso de combustible avanzado en el reactor nuclear modular e integral NuScale*, Tesis de Maestría en Ingeniería, Universidad Nacional Autónoma de México, Ciudad de México, México (2020).

11. Y. Pérez González, *Evaluación del desempeño de mezclas homogéneas de óxidos de Torio y Uranio como combustibles alternativos en un reactor nuclear refrigerado por agua supercrítica*, Universidad de La Habana, La Habana, Cuba (2020).
12. ANSYS Inc., 2010. ANSYS CFX Solver Theory Guide. Canonsburg, PA.
13. IAPWS, *Revised Release on the IAPWS Industrial Formulation 1997 for the Properties of Water and Steam*, International Association for the Properties of Water and Steam, Switzerland (2007).
14. D.P. Bentz and K.R. Prasad, *Thermal Performance of Fire Resistive Materials I. Characterization with Respect to Thermal Performance Models*, National Institute of Standards and Technology, Gaithersburg, U.S. (2007).
15. IAEA, *Thermophysical properties database of materials for light water reactors and heavy water reactors, Final report of a coordinated research project 1999-2005*, International Atomic Energy Agency, Vienna, Austria (2006).
16. IAEA, *Thermophysical Properties of Materials for Nuclear Engineering: A Tutorial and Collection of Data*, International Atomic Energy Agency, Vienna, Austria (2008).
17. D.E. Janney and S.L. Hayes, “Experimentally known properties of U-10Zr alloys: a critical review”, *Nuclear Technology*, **Volume 203(2)**, p. 109-128 (2018).

Development of a Reactor Building model of a BWR5 for the calculation of fission product masses with the MAAP5 code

Ortega, Blanca¹

*Universidad Nacional Autónoma de México
Facultad de Ingeniería, Ciudad Universitaria
Ciudad de México
bj.ortegachagoyan@gmail.com*

Ortiz, Javier²; Vias, Jorge²; Martínez, Eduardo²; Amador, Rodolfo²

*Instituto Nacional de Investigaciones Nucleares
Ocoyoacac, Estado de México*

*Javier.Ortiz@inin.gob.mx; Jorge.Vias@inin.gob.mx; Eduardo.Martinez@inin.gob.mx;
Rodolfo.Amador@inin.gob.mx*

Abstract

The secondary containment, also known as the Reactor Building, acts as the ultimate physical barrier to prevent the release of fission products during an accident. Therefore, it is crucial to model this structure to evaluate its effectiveness in retaining such products. In this research, a model of the Reactor Building has been developed for the MAAP5 code, and it has been coupled to a Mark II type primary containment model previously designed for a BWR5, to the end of quantifying the impact of such containment structure on fission product retention. A description of the new secondary containment model is presented in this paper. The results at nominal steady state showed that the coupled model is adequate to provide the initial values in the simulation of an accident. The scenario chosen for this comparative analysis of fission product retention is an unmitigated SBO. The simulation covers three hours of steady state and 24 hours from the onset of the event. Some relevant results of key events during the progression of this severe accident are presented. Regarding fission product release analysis, the results show a reduction of the total mass of vapors and aerosols released in 24 hours by 42.9% when the Reactor Building model is coupled. In addition, for the noble gases Xe and Kr, the release is reduced from 78.1% to 33.7%; for the compounds CsI and RbI, the releases are 22.1% and 7.7%, respectively; and finally, for CsOH and RbOH, the values are 33.6% and 17.6%, respectively. Thus, this research study shows the importance of having a Reactor Building for fission product retention, even in the catastrophic scenario simulated here, and therefore it should not be excluded in such kind of analyses.

1. INTRODUCTION

The secondary containment in a Boiling Water Reactor (BWR) plant is commonly known as the Reactor Building, which acts as the ultimate physical barrier to prevent the release of fission products during an accident. In general, this structure is not considered in the safety analyses in order to keep a high level of conservatism for the fission product releases results. However, it is clear that sedimentation of fission products in form of particles or aerosols is a phenomenon that must be taken into account for a correct prediction of the masses to eventually be released to environment. While the sedimentation process is expected to occur on the floors and walls of the drywell, and also on the major equipment within this area, it is clear that those kinds of fission products will reach the secondary containment when the drywell or wetwell are breached by degradation of seals, because of high temperature, on the penetrations to the primary containment, or leakage induction because of high pressure. When in the Reactor Building, the incoming particulate or aerosol fission products will remain airborne or can sediment depending on the conditions within this structure.

There is not much scientific literature on the topic of analyzing the impact of the secondary containment on fission product retention, and even most of the work was performed during the 80s and 90s, last century. However, there is renewed interest on studying the efficiency of the different actions that can be carried out during a severe accident, to mitigate or delay the release of fission products, as for example spraying in the Reactor Building or keeping a negative pressure, versus, outside atmospheric pressure, via the Standby Gas Treatment System. Therefore, it has been considered a milestone to study and model this structure to evaluate its effectiveness in retaining such products for a BWR5 with Mark I primary containment. In this research, a model of the Reactor Building has been developed for the Modular Accident Analysis Program MAAP code, and it has been coupled to the Mark II type primary containment primary model developed for the same code.

The software used in this research was MAAP version 5. This computer code simulates the response of diverse types of nuclear power plants during severe accidents and addresses the full spectrum of important phenomena that could occur during an accident, simultaneously modeling those related to thermal-hydraulics and fission products. Its models include the primary system, the core, and the containment structures. When used, MAAP requires a set of initiating events and operator actions, to then predict both the thermal-hydraulics and transport of fission products over all the volumes in the nodalization model of the entire plant as the accident progresses. For these reasons, MAAP5 is often referred to as a comprehensive severe accident analysis code.

Fission products are atoms resulting from the separation of a heavy nucleus into two new ones. These can be non-radioactive or radioactive at different levels depending on the energy they need to release to reach a state of stability, i.e. to become stable atoms. This atomic nucleus splitting phenomenon is called fission process. During normal operation these fission products are retained by various safety barriers, which may be affected during a major accident depending on the situation, so they may end up being released into the environment.

In this work, the efficiency of a new nodalization model of a Reactor Building to retain particulate and aerosol fission products is quantified, by the simulation of an unmitigated Station

Blackout event with the code MAAP5. This severe accident scenario is also known as Short Term SBO (STSBO) because it is assumed that no cooling emergency system is available to face the progression of the accident. Results of the steady state period, timing of key events during the progression of the scenario, and finally results of retention of fission products when the Reactor Building model is used versus when only using the original Mark II primary containment model are presented, along with some conclusions of this work.

2. METHODOLOGY

The present research is the continuation of the work carried out by a team at the Nuclear Systems Department of the Nuclear Research National Institute (ININ of Mexico). This team developed a nodalization model of the Mark II primary containment and its internals. This Mark II has two main zones, the drywell and the wetwell. In MAAP, the different areas or volumes in nodalization model are called nodes, that is, a node is a geometric division representing a given space, which may or may not have physical barriers. The analyst proposes the criteria to create the full nodalization model. In the drywell there is the reactor vessel, as well as 9 nodes that represent important areas of this zone, and in wet well there is a division of 3 nodes for the suppression pool and 3 nodes for suppression chamber. Additionally, 6 nodes are used to represent the geometry of the downcomers. This nodalization model also has 36 heat structures. The flow paths between the volumes of the model consist of 26 junction-type and 2 failure-type paths. Figure 1 shows a scheme of the whole plant nodalization model, but without showing the different volumes of the Mark II original model.

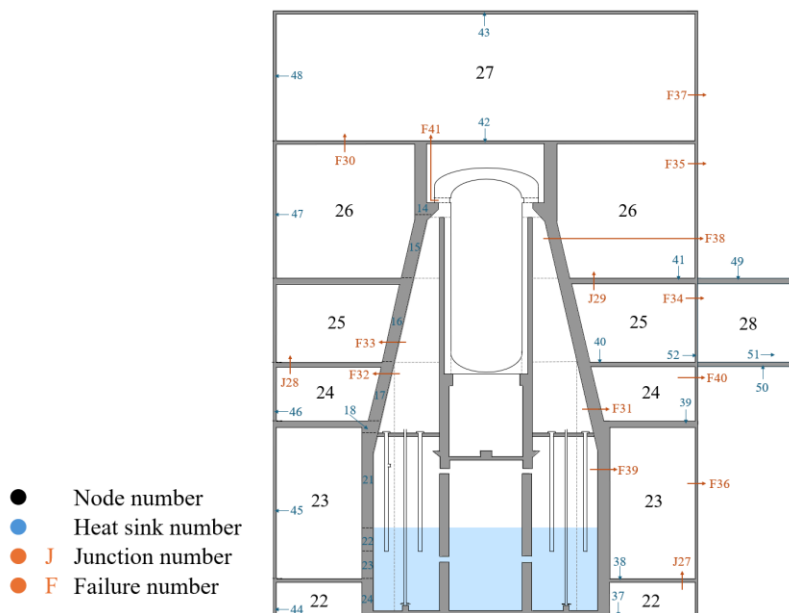


Figure 1. Graphical representation of the generated model of the reactor building with number of nodes, junctions, and heat sinks.

The process of creating the reactor building model consisted of generating first a single node model, to couple it to the original Mark II model. Then, it is necessary to determine if the

previously validated steady state is still being satisfied, and in case correcting errors if they arose. If this simulation reached the stability criteria, it was considered successful. Then a second model of the reactor building was created, but this time it was conformed of two nodes. The same coupling and correction, if needed, process was repeated. This is repeated until a model with the desired number of nodes is obtained. In this case, it was considered that the Reactor Building can be divided into 6 nodes to show those zones with more relevance for fission product transport. In addition, one more node was added to represent a control room, but such room model is not realistic, and it is used just as an example of nodalization options outside the containments. Thus, the final model has a total of 28 nodes, and node number 29 corresponds to the environment. Figure 1 shows the scheme of the Reactor Building model developed for this study, and Table I shows a summary of the diverse components of the model.

Table I. Summary of number of nodes, heat sinks and junctions of the Building Reactor model.

Primary Containment, Mark II	
Total number of nodes	21
Total number of junctions	26
Secondary Containment, building reactor	
Total number of nodes	6
Total number of nodes of control room	1
Total number of horizontal head sinks	9
Total number of vertical head sinks	7
Total number of junctions	3
Total number of the failures in the nodes	1
Total number of the failures in the Mark II nodes and Building reactor nodes	5
Total number of the failures in Building reactor nodes and environment	4
Total number of the failures in Mark II nodes and environment	1
Total number of the failures in Mark II nodes and Building reactor nodes	1

3. RESULTS OF THE SIMULATIONS

3.1. Steady state

Clearly, no impact should be expected on the results of the key variables of the heat balance of the primary system, or Nuclear Steam Supply System (NSSS) for a BWR, for the plant nominal steady state, simply because there is not a connection of the heat structures composing the Reactor Pressure Vessel (RPV) with the new Reactor Building heat structures. However, the Mark II walls heat structures are now also heats structures for the Reactor Building, so these heat structures can induce changes from the nominal values previously obtained for the Mark II volume on pressure and temperature. As an example of results, the differential range in which the pressures for the nodes of the Reactor Building all fall within 0.6% difference from the nominal value. Figure 2 shows the profiles of pressure within the Reactor Building nodes. Table II shows the description of the nomenclature used in Figure 2. Regarding the temperature results in the

same nodes, all of them (22 to 27) show the same value for the temperature, while node 28 does show a change, although it might not seem very noticeable, which corresponds to a difference of 2.2% from the nominal value.

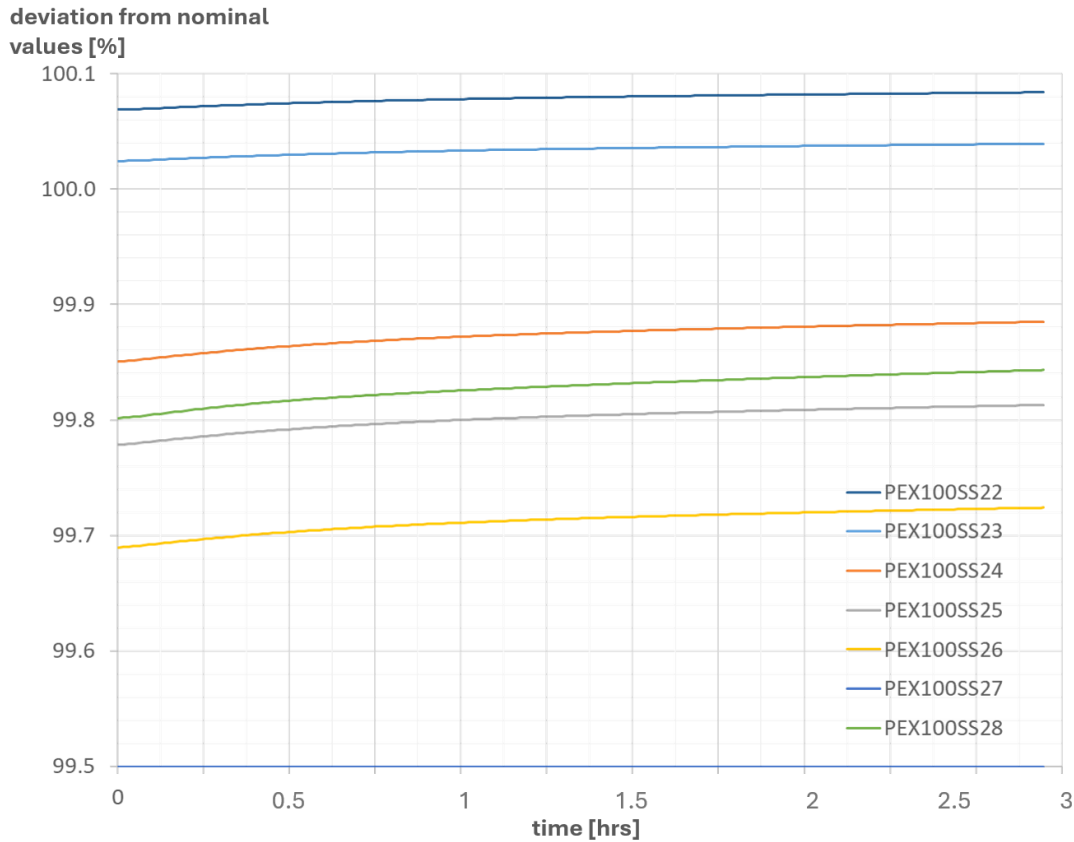


Figure 2. Pressure profile in the 6 nodes of the Reactor Building and in the Control Room.

Table II. Description of the variables plotted in Figure 2.

Parameter	Variable in Figure 1
Average pressure at node 22	Pa PEX100SS22
⋮	⋮
Average pressure at node 28	Pa PEX100SS28

3.2. Accident scenario

The steady state begins at time 0 second of the simulation and it ends at time 10,800 second (3 hrs), and also the time at which the initiating events are triggered, which include battery power interruption, loss of AC power, loss of diesel generators, and therefore loss of all Emergency Core Cooling Systems (ECCS), plus loss of the RCIC because no DC power available.

The following progression of images (Figure 3) shows the graphical representation of the main events that occurred during the accident, 1) steady state operation, 2) pressure increase in the vessel, 3) decrease of water level in the vessel, core uncovering, 4) core damage, increase of melt

percentage, 5) increase of melt percentage, increase of fission product release to coolant system, 6) core mass relocation to the lower plenum, 7) vessel failure, fission product distribution in primary containment, 8) Mark II primary containment failure, 9) connection openings determined by structural failures, fission product distribution in secondary containment, 10) distribution of fission products from the reactor building to the environment and to the control room. Table III shows a comparative of the timing of relevant events when using or not the Reactor Building model.

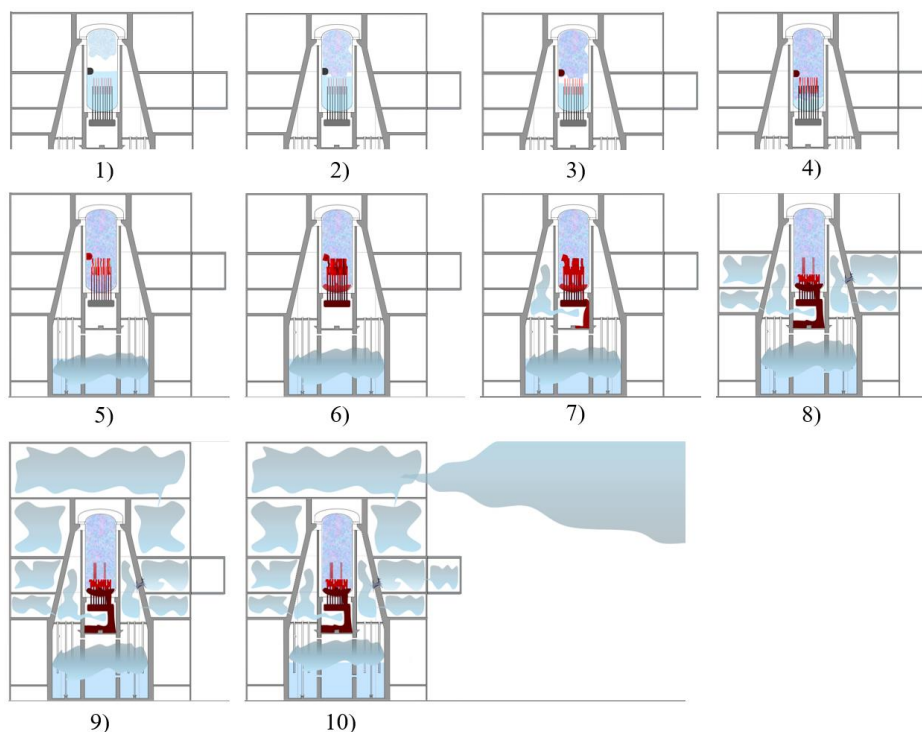


Figure 3. Progression of representative events during the unmitigated SBO accident in the generated Mark II plus reactor building model for a BWR5.

Table III. Summary of figures of merit between the two models.

	Taking t=0 with steady state				No steady state			
	M2+RB		M2		M2+RB		M2	
	sec	hrs	sec	hrs	sec	hrs	sec	hrs
Discovery of the core	12896.3	3.58	12897.7	3.58	2096.3	0.58	2097.7	0.58
Relocation of material to the lower plenum	14864.3	4.13	14886.1	4.14	4064.3	1.13	4086.1	1.14
Vessel failure	26406.5	7.33	24480	6.80	15606.5	4.33	13680	3.80
M2 containment failure	58143.37	16.15	57007.7	15.84	47343.37	13.15	46207.7	12.84
RB failure	59805.2	16.61	-	-	49005.2	13.61	-	-
Mass of H ₂ generated in the core (kg)	M2+RB				410.6			
	M2				385.8			

The two models were simulated with the same steady state time and the same at which the initiating events were triggered, so they showed similar responses, however, there are differences in the timing of the events. One way to better compare the performance of the two models is to verify the behavior of key variables in the primary system. Figure 4 shows the resulting profiles for the main variables are pressure and temperature (TGPS M2+RB and TGPS M2), corresponding to the gas temperature in the primary system, for the model with the Mark II plus the Reactor Building and the Mark II-only model, respectively. Similarly, the pressure variable in the primary system (PPS M2+RB and PPS M2) is also shown in Figure 4. Table IV shows the description of the nomenclature used in Figure 4.

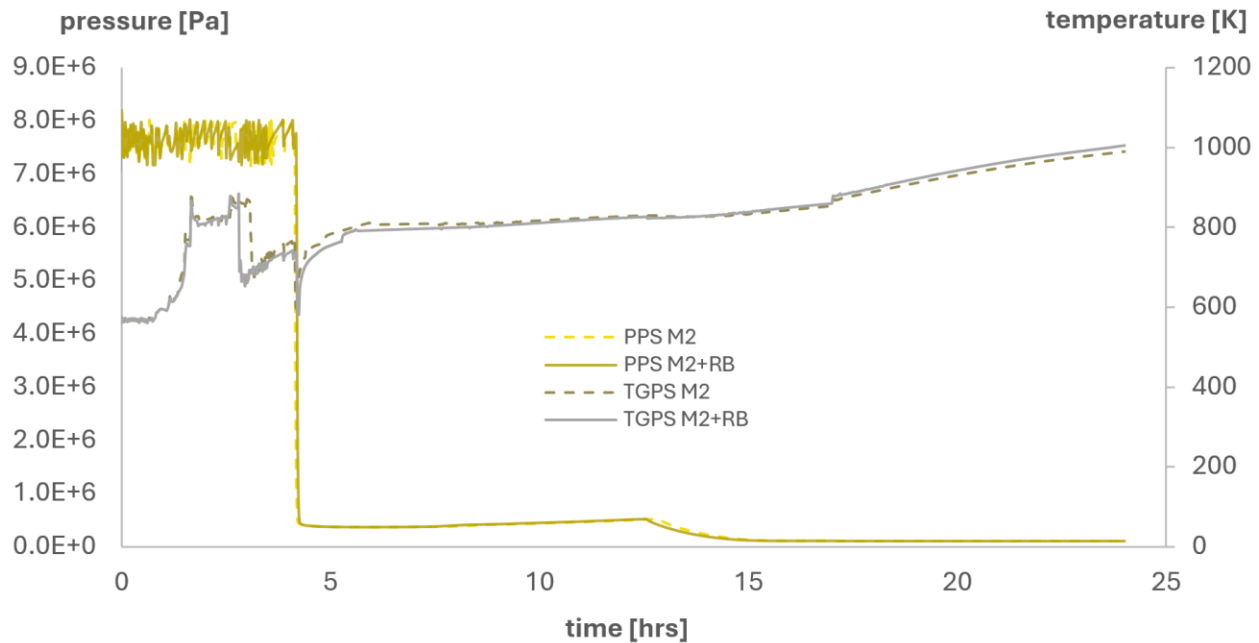


Figure 4. Comparison between models with and without reactor building during a severe accident in MAAP5.05.

Table IV. Description of the variables plotted in Figure 4.

Parameter	Variable in Figure 4	
Primary System Gas Temperatures (PS) with primary containment only	K	TGPS M2
PS gas temperatures with primary and secondary containment	K	TGPS M2+RB
PS average pressure only with primary containment	Pa	PPS M2
Average PS pressure with primary and secondary containment	Pa	PPS M2+RB

Since the behavior and values are very similar for pressure and temperature in the primary system for both models, one can be confident that no significant errors were committed during the model construction process and the coupling methodology.

To facilitate the analysis of the fission product mass tracking and to do the comparison between the two models (M2 and M2+RB), the primary containment was divided into its main parts as

explained before. MAAP5 groups the fission products into 18 different sets, although some of them are not applicable to BWRs, as the group for silver (Ag), or the group for the uranium oxide, because it is not a fission product. Thus, only 16 of the 18 groups are actually tracked all over the nodalization model. Figure 5 shows a comparative of the profiles of distribution of the total mass of fission products in diverse zones of both containments. For example, the total mass of fission products, including the noble gases, in the drywell is obtained by summing up the contribution in each of the 9 nodes that compose that containment zone. Table V shows the description of the variables plotted on Figure 5.

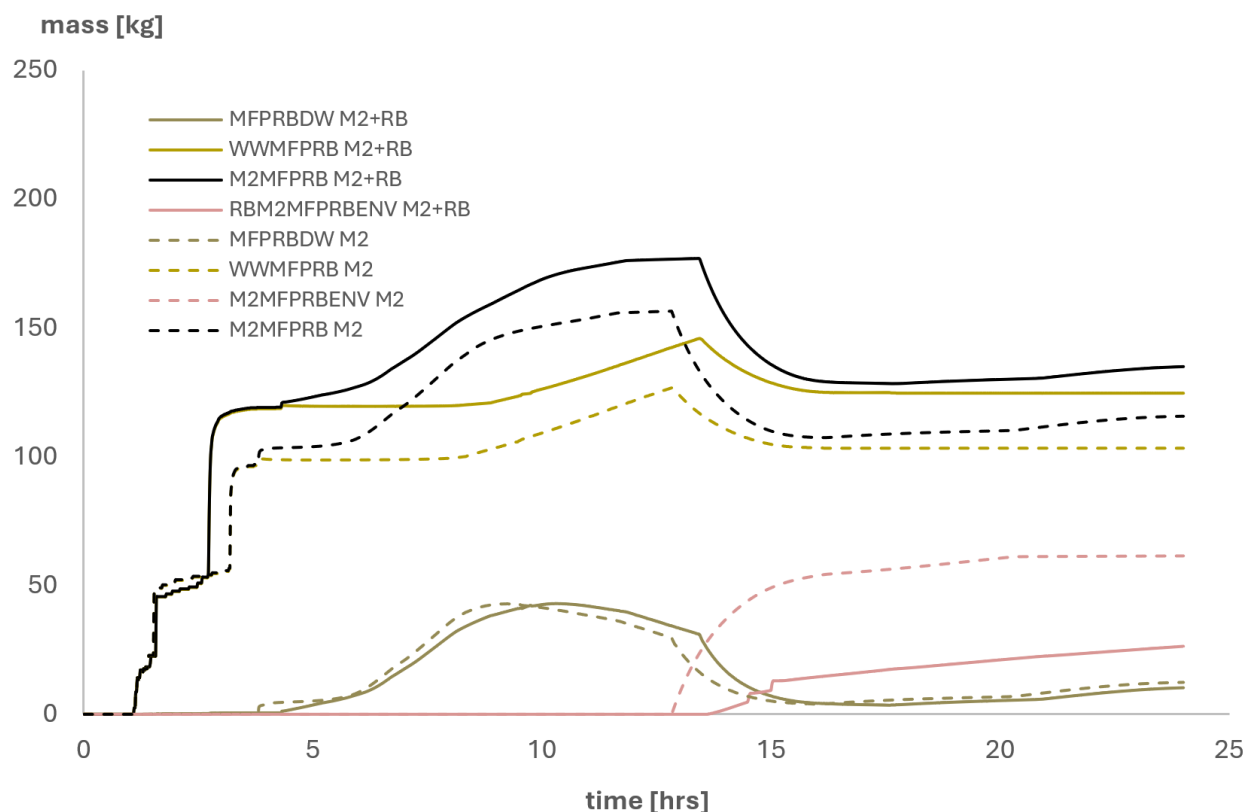


Figure 5. Comparison of fission products for model M2 and M2+RB within primary containment and ambient.

Table V. Description of the variables plotted in Figure 5.

Parameter		Variable in Figure 5
Mass of fission products in the dry well with the M2 model and with the M2+RB respectively.	kg	MFPRBDW M2/ M2+RB
Mass of fission products in the wet well with the M2 and M2+RB models, respectively.	kg	WWMFPRB M2/M2+RB
Total mass of fission products in primary containment with the M2 and M2+RB models, respectively.	kg	M2MFPRB M2/ M2+RB
Mass of fission products in the environment with the M2 and M2+RB model respectively	kg	RBM2MFPRBENV M2/ M2+RB

For the two models, the appearance of fission products in the primary containment around the first hour is consistent with to the uncovering of the core. Some of these fission products remain in the primary system and other are dragged by the steam and discharged through the SRVs in the wet well. Fission product generation continues until vessel failure, which further allows outflow from the RPV to the drywell and a subsequent distribution in the primary containment. Of the most relevant analyses that can be carried out with the help of Figure 6 is to study the correct distribution of fission products, as a consequence of diverse systems actuation, for example the opening and closing signals of the relief valves during the first stage of the accident explain the presence of products in the wet well. Moreover, during this time there are still no fission products in the environment, simply because there are no connections opened (failures or leaks) at this time period. Table VI shows the description of the variables plotted on Figure 6. Note that significant difference in the mass values between Figures 5 and 6. This is because some of the variables that the code MAAP uses to provide with such data include the mass on no-radioactive aerosols formed from the degradation of structural material in the core or from the MCCI phenomena in the pedestal once the RPV has failed.

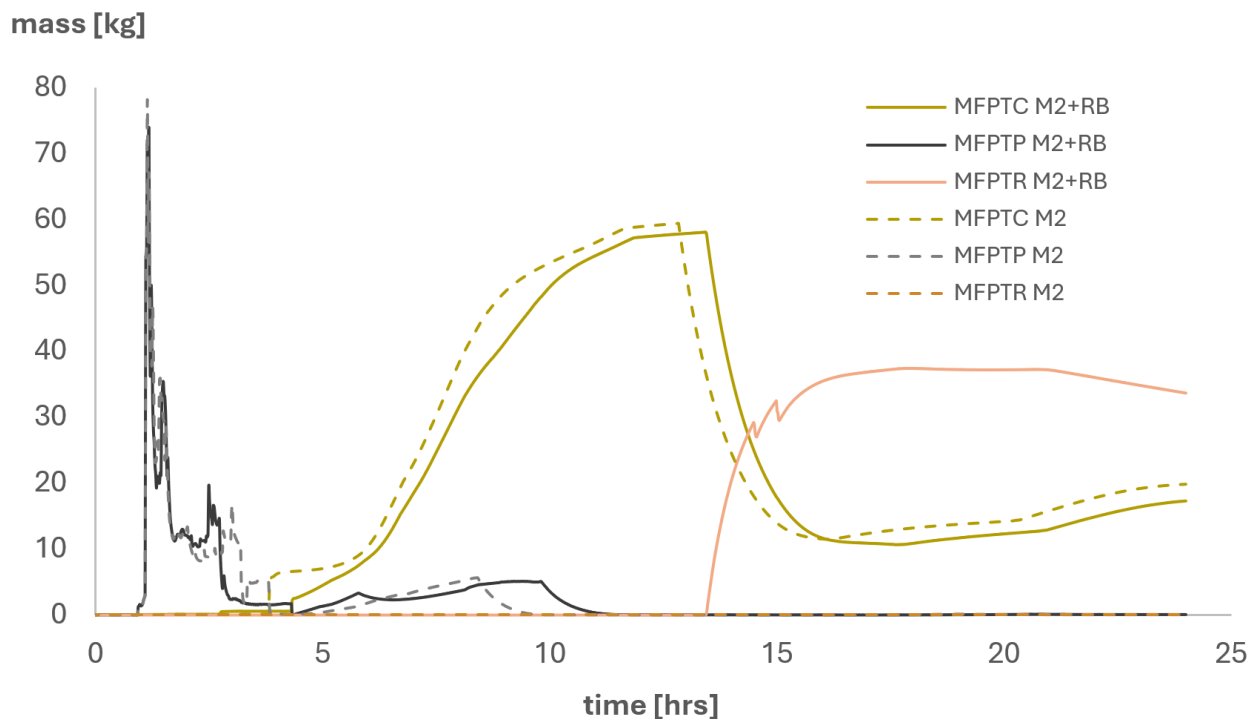


Figure 6. Comparative masses of volatile fission products in Primary System, Mark II and Reactor Building.

Table VI. Description of the variables plotted in Figure 6

Parameter	Variable in Figure 6
Mass of volatile fission products in the Mark II with the M2 and M2+RB models, respectively.	kg MFPTC M2/ M2+RB
Mass of volatile fission products in the primary system	kg MFPTP M2/ M2+RB

with the M2 and M2+RB model respectively		
Mass of volatile fission products in the reactor building with model M2 and M2+RB respectively.	kg	MFPTR M2/ M2+RB

The failure, assumed here to occur because over pressure, of the primary containment (5*) happens at 12.83 hrs (46,207 s) for the M2 model and 13.15 hrs (58,140 s) for the M2+RB model. Therefore, there is now release of fission products in the environment due to the existence of a direct connection (of the type FAILURE) to the environment for both models. One also can note the corresponding decrease of fission products in the drywell. In addition, for the M2+RB model, an increase in fission product masses is observed in the reactor building and later also in the control room. The time shift in the mass values in the control room is due to the transport models used by MAAP to estimate the time it takes for particles and gases to move through the different levels and through the different connections of the model.

As a summary, in this work, of the efficiency of a Reactor Building to avoid the release of fission products, the results showed a reduction of the total mass of vapors and aerosols released in 24 hours by 42.9% when the Reactor Building model is coupled. In addition, for the noble gases Xe and Kr, the release is reduced from 78.1% to 33.7%; for the compounds CsI and RbI, the releases are 22.1% and 7.7%, respectively; and finally, for CsOH and RbOH, the values are 33.6% and 17.6%, respectively.

4. CONCLUSIONS

A secondary containment model, i.e., of the Reactor Building, of a BWR plant with a Mark II type primary containment has been developed for the MAAP5 code. Although some volume conditions in specific nodes indicate the need to review with more detail the heat transfer structures between the drywell and the wet well, as well as between the two containments, the coupled primary-secondary containments model is suitable to provide a nominal steady state for accident simulation. Then, the simulation of an unmitigated SBO was carried out, and the results show that the proper coupling of a Reactor Building model is significantly positive in fission product retention gain, as the results show that a 42.9 % reduction of the total mass of vapors and aerosols that would be released within 24 hours has been obtained.

From the results of this research study, it has been shown the importance of having a Reactor Building for fission product retention, even in the catastrophic scenario simulated here, and therefore it should not be excluded in such kind of analyses.

ACKNOWLEDGEMENTS

The first author of this paper would like to express her sincere thanks to the institution CONAHCYT for its support through a fellowship to obtain the Degree of master's in science in Energy Engineering, at Facultad de Ingeniería of the Universidad Nacional Autónoma de México. The funding and additional resources provided were essential for the development of this research and the completion of this paper. I am also deeply grateful to the Department of Nuclear Systems at the National Institute for Nuclear Research for their continuous support,

advice and training. Finally, I would like to express my deepest gratitude to the National Autonomous University of Mexico for welcoming me and providing me with an integral education.

REFERENCES

1. IAEA. “Severe accident management programmes for nuclear power plants: Safety Guide”, *International Atomic Energy Agency*, Viena, Australia, July, No. SSG-54 (2019).
2. IAEA. “Status and Evaluation of Severe Accident Simulation Codes for Water Cooled Reactors”, *International Atomic Energy Agency*, Viena, Australia, June, TECDOC-1872 (2019).
3. IAEA. “Technical meeting on the status and evaluation of severe accident simulation codes for water cooled reactors”, *International Atomic Energy Agency*, Viena, Australia, October, TECDOC-1872 (2017).
4. IAEA. “The Chernobyl accident: updating of INSAG-1/INSAG-7. A report by the International Nuclear Safety Advisory Group”, *International Atomic Energy Agency*, Viena, Australia, No. 75-INSAG-7 (1992).
5. Mitchell Rogovin, director, George T. Frampton, Jr. deputy director. “Three Mile Island, a report to the commissioners and to the public”, *Nuclear regulatory commission special inquiry group*. Vol. 1 (1979).
6. Mora, Heriberto Sánchez. “Uncertainty and sensitivity analysis of the core degradation of a BWR during an unmitigated SBO”, *Instituto Politecnico Nacional*, México (2023).
7. N Kelly, D L, Jones, K R, Dallman, R J, & Wagner, K C. “An assessment of BWR (boiling water reactor) Mark-II containment challenges, failure modes, and potential improvements in performance”, *Nuclear Regulatory Commission*, United States. UREG/CR-5528; EGG-2593; ON: TI9001562 (1990).
8. Nishimura, Satoshi, Hiwatari, Ryoji, Furuya, Masahiro, & Yoshihisa Nishi. “Severe accident analysis of a representative BWR plant with MAAP and MELCOR. Station blackout in a BWR-5 with advanced Mark-II containment”, *Atomic Energy Society of Japan*, Tokyo, Japan, N. p. (2014).
9. OIEA. “El accidente de Fukushima Daiichi. Informe del Director General”. *Organismo Internacional de Energía Atómica*. GC(59)/14 (2015).
10. “Organismo Internacional de Energía Atómica”, [Glosario de Seguridad del OIEA: Edición de 2018 | OIEA \(iaea.org\)](#) (2018).

Multiphysics and multiscale analysis of HTR-10 reactor

Erick Josué Yescas-Pozos, Gilberto Espinosa-Paredes

Alejandría Denisse Pérez-Valseca

Área de Ingeniería en Recursos Energéticos

Universidad Autónoma Metropolitana, Unidad Iztapalapa

cbi2223804744@xanum.uam.mx, gepe@xanum.uam.mx, alepv@xanum.uam.mx

Abstract

Due to the growing concern about greenhouse gases, the need arises to study alternative energy sources that can meet the needs of today's world. Nuclear energy, during its operation, does not emit greenhouse gas emissions, besides having a high-power density, which is a viable option to achieve a world of zero emissions. Nuclear reactors are systems with many physical phenomena involved that together determine the safety and power delivered by the reactor. The physical phenomena of interest, taking as a reference the HTR-10 nuclear reactor located at Tsinghua University, China, are neutron diffusion, heat transfer in the fuel and coolant. This work presents the numerical simulation of the HTR-10 reactor, taking a simplified and homogeneous geometry, and considering a porous medium in the core. The neutronic model was developed from the Diffusion equation, considering every part of the reactor, i.e., core, axial, and radial reflector, and for thermal hydraulics, a porous media model was applied.

1. INTRODUCTION

High-temperature gas-cooled reactors (HTGR) are part of the next generation of nuclear reactors. HTGRs were developed in Germany and the United States during the 1950s. This type of reactor usually uses helium as a coolant and graphite as the moderator, one difference of this technology taking as a reference the reactors used today for power generation is the form of fuel used [1]. Each fuel element, which is usually spherical or tube-shaped, contains small spheres smaller than 1 mm in diameter called TRISO particles wrapped in pulverized graphite, the TRISO particles are responsible for initiating the fission reactions. Due to the shape of the fuel and the fissile material being coated inside the TRISO particle, fission products produced during normal reactor operation or in an accident are encapsulated inside the TRISO particle [2].

The first HTGR reactor to use TRISO fuel particles and become standardized today is the 21.5 MWth UK Dragon reactor [3]. Thanks to the fact that the Dragon reactor demonstrated the viability of this type of technology, the AVR demonstration reactor of the Federal Republic of

Germany differs in that now its fuel elements are spherical with a diameter of 6 cm housing the TRISO particles, this reactor began its operation in 1967 and has a thermal power of 46 MWth. In the United States, the Peach Bottom Unit started its operation in 1967 and provided a thermal power of 115 MWth and the fuel configuration used was in the form of tubes and prisms [4].

Subsequently, the last two test reactors were built following the development of the three previously mentioned reactors and the extensive accumulation of experimental and developmental data. Japan's High Temperature Test Reactor (HTTR), which started operation in 1998 and is currently in operation, has a thermal power of 30 MWth and uses prism-shaped fuel elements. The 10 MWth high temperature reactor, HTR-10, is the last test reactor of this type of HTGR technology, it started its operation in 2000 and is currently in operation, the fuel element used is a pebble bed [3]. Figure 1 presents the fuel design used by the HTR-10 and HTTR reactors. A summary of the main characteristics of the HTGR test reactors is presented in Table 1.

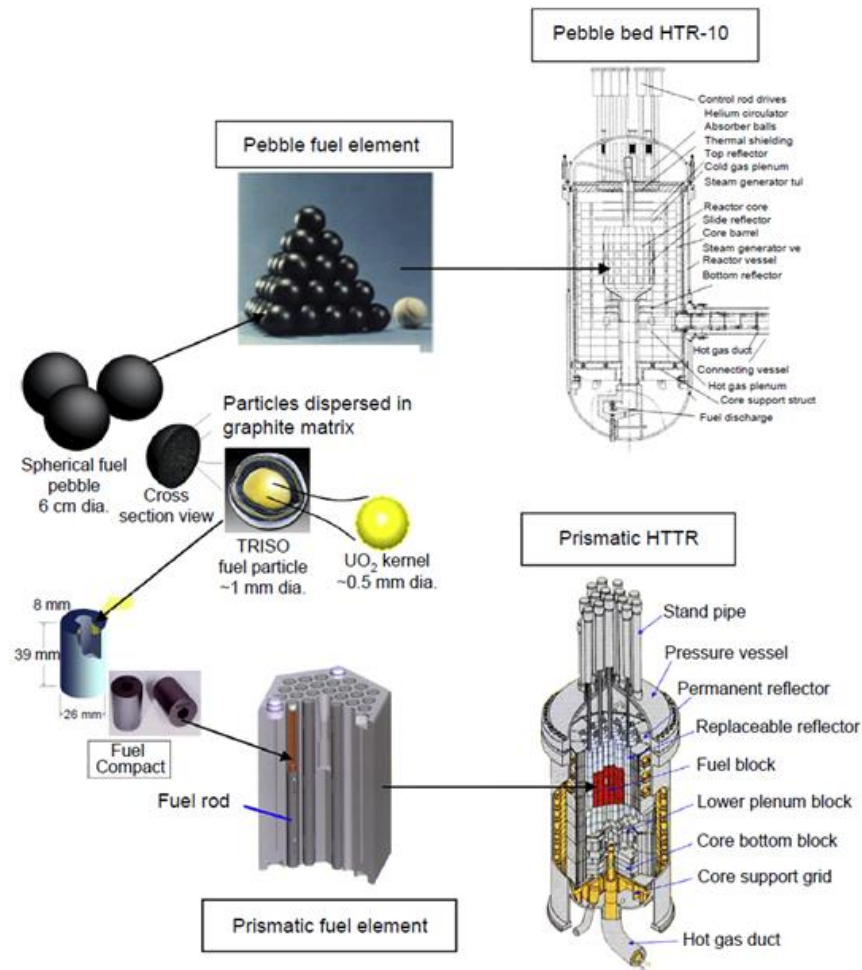


Figure 1. Design of a pebble-bed and prismatic reactor [3]

Table I. Main parameters of HTGR test reactors [3, 4].

Parameter / Reactor	Dragon	Peach Bottom	AVR	HTTR	HTR-10
Criticality /Closing	1964/1976	1967/1974	1967/1988	1998/ operating	2000/ operating
Thermal power (MWth)	20	115	46	30	10
Net electrical power (MWe)	---	40	15	---	2.5
Helium pressure (Bar)	20	24	11	40	30
Inlet helium temperature (°C)	350	340	260	---	250
Outlet helium temperature (°C)	750	715	950	900	700
Core diameter (m)	1.1	2.8	3	---	1.8
Core height (m)	1.6	2.3	3	---	1.97
Power density (MW/m ³)	14	8.3	2.2	2.5	2
Fuel element	Tube	Tube	Esphere	Prismatic	Esphere
Fuel cycle	Various	235U/Th	235U/Th	U235/UO ₂	U235/UO ₂

2. DESCRIPTION OF THE HTR-10 REACTOR

The HTR-10 nuclear reactor fuel is spherical in shape and is referred to as a pebble bed in which the interior of each pebble contains approximately 8,300 TRISO particles. Each TRISO particle consists of the spherical Kernel, the Buffer layer which is responsible for providing a volume due to its porosity to contain the gaseous fission residues; the inter-pyrolytic pyrolytic carbon (IPyC) layer functions as a barrier for the fission products; the silicon carbide (SiC) layer, like the IPyC layer, functions as a second barrier for the fission products, but its main function is to guarantee that there will be no problems with any expected condition in the reactor core; the outer pyrolytic carbon (OPyC) layer protects the SiC layer from any damage in the coating process. (Figure 2) [5].

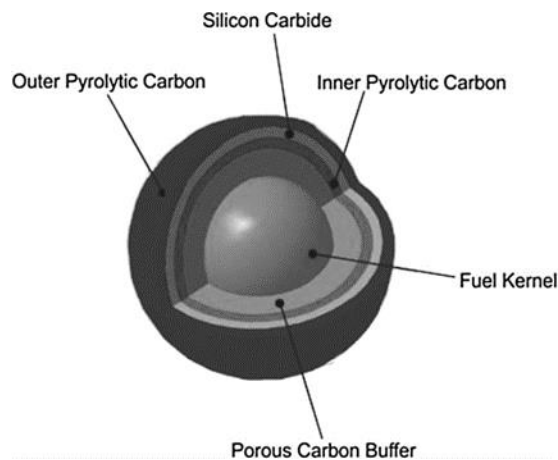
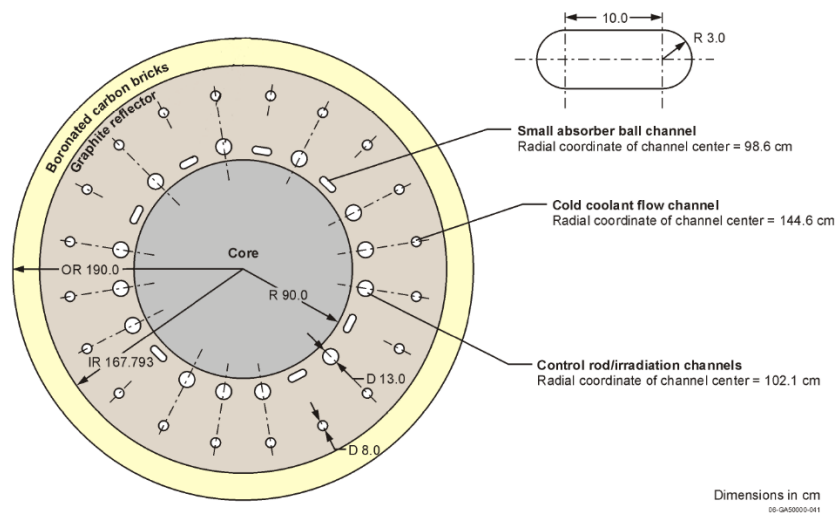


Figure 2. TRISO particle [6]

Table II. Radius of TRISO particle and pebble materials [7]

Material	Radius (μm)
UO ₂	251
Buffer	3425
IPyC	3824
Sic	4177
Opyc	4577
Graphite matrix	25000
Graphite clad	30000

The radius of the reactor is 90 cm and the active core height is 197 cm. The lateral reflector is 77.793 cm thick, 90 cm thick upper reflector, and a graphite lower reflector, "to return the escaping neutrons to the reactor core. The reactor has two shutdown systems, the first one consists of 10 control rod channels with a diameter of 13 cm which are placed symmetrically in the lateral reflector approximately at a radius from the center of the channel to the center of the core of 101.1 cm, the material is B₄C [8]. The second system consists of 7 ducts similarly located in the axisymmetric region of the 160×60 mm control rods through which graphite absorber balls are deposited, in this same region 3 other channels can be used for irradiation tests or control rods [9]. In the reflector are located 20 channels through which circulates the coolant (helium) with a diameter of 8 cm and with a distance from center to center of 144.6 cm [10], this can be seen in Figure 3.

**Figure 3. Upper view of the HTR-10 nuclear reactor [11]**

The core outlet temperature of helium is 700°C and the inlet core temperature is 250°C. In Figure 4, the helium flow is shown, at the beginning it travels through the entire containment vessel of the reflected core. Then, the helium circulates from bottom to top through the coolant channels. The reactor core has a 50 cm diameter drainage system through which the burned pebbles are removed and recirculated back into the core until they are completely burned, each pebble can be

recirculated 10 to 15 times; an advantage of this reactor is that it can be refueled while in operation. In total, the reactor contains 27,000 fuel elements inside the core [12].

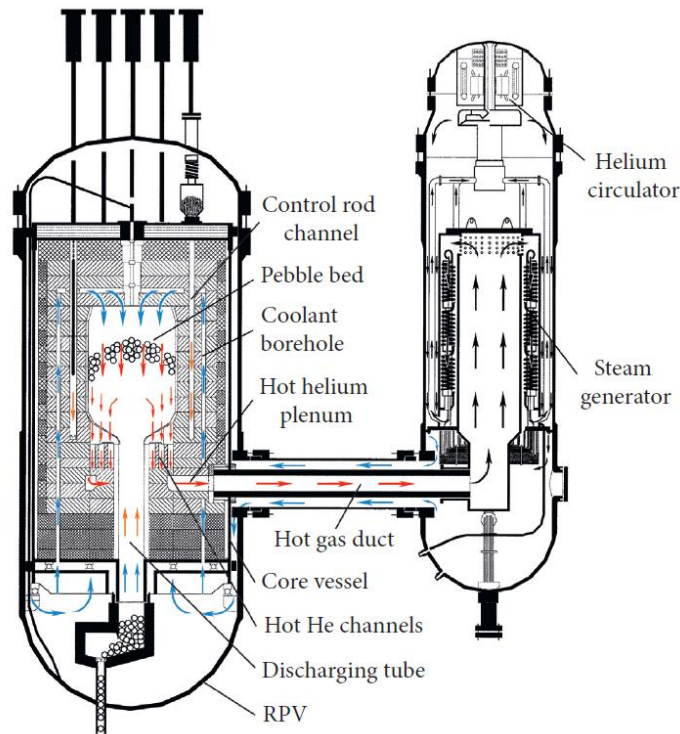


Figure 4. HTR-10 reactor with the primary steam generator system [13]

In Table III, the reactor design values required to carry out the numerical experimentation are presented.

Table III. HTR-10 reactor reference values [9, 12, 14]

Thermal power	MW	10
Active core volume	m ³	5
Thermal power density	MW/m ³	2
Helium pressure	MPa	3
Helium inlet temperature	°C	250
Helium outlet temperature	°C	700
Mass flow helium	kg/s	4.32
Fuel	---	UO ₂

U-235 enrichment of fuel elements	%	17
Spherical fuel diameter	mm	60
Number of spherical fuel elements	---	27,000
TRISO number in a fuel element		8,300
Maximum fuel temperature	°C	918.7
Maximum fuel surface temperature	°C	876.7
Reactor core diameter	cm	180
Active core height	cm	197

3. MATHEMATICAL MODELING

In this section the equations of neutron diffusion in the bare reactor and the reflector, heat transfer in the fuel, heat transfer in the fluid, and momentum balance in the fluid are presented. It should be recalled that the numerical simulation was done in a 3D model in cylindrical coordinates.

Starting from the general neutron diffusion equation for a single neutron group and, considering the definitions of the effective and infinite multiplication factor, diffusion length, the half-life of neutrons in a finite reactor, the instantaneous neutron generation time, reactivity, and in the source term the instantaneous and delayed neutrons are considered is how Eq. 1 is obtained.

The theory of a single neutron group is used because it reduces the computational time during the simulations, in addition to the fact that the reactor under study is thermal and therefore the neutrons that dominate are the thermal ones.

3.1 Equation of neutron kinetics in the bare reactor

The fission reactions are carried out in the bare reactor, the core has a radius of 90 cm and is 197 cm high. The governing equation is Eq. 1. the first term of the equation from left to right represents the accumulation, the second term is the neutron escape term, the third term represents the neutron absorption, the fourth term represents the instantaneous neutron production and the fifth term is the delayed neutron production.

$$\frac{1}{v} \frac{\partial \phi_C(\mathbf{r}, t)}{\partial t} = D_C(\mathbf{r}) \nabla^2 \phi_C(\mathbf{r}, t) - \Sigma_{ac}(\mathbf{r}) \phi_C(\mathbf{r}, t) + \frac{1}{v} \left(\frac{\rho(\mathbf{r}, t) - \beta}{\Lambda} + \frac{1}{l_n} \right) \phi_C(\mathbf{r}, t) + \sum_{i=1}^6 \lambda_i C_i(\mathbf{r}, t) \quad (1)$$

$$\frac{dC_i(\mathbf{r},t)}{dt} = \frac{\beta_i}{\Lambda} \frac{\phi_c(\mathbf{r},t)}{\nu} - \lambda_i C_i(\mathbf{r},t) \quad (2)$$

the boundary conditions are:

B.C.1 $\phi_c(\mathbf{r},t) = 0$ in $\mathbf{r} = \tilde{\mathbf{r}}_c$

B.C.2 $C_i(\mathbf{r},t) = 0$ in $\mathbf{r} = \mathbf{r}_c$

B.C.2 $-D_c(\mathbf{r})\nabla\phi_c(\mathbf{r},t) = \nabla C_i = 0$ in $\mathbf{r} = 0$

Where \mathbf{r}_c refers to the group of coordinates found at the bare reactor boundary, on the other hand, $\tilde{\mathbf{r}}_c$ is the group of coordinates extrapolated at the bare reactor boundary.

3.2. Equation of neutron kinetics in the bare reactor

For the governing diffusion equation in the reflector, as the core is fully reflected and symmetrical, it is necessary to divide the reflector into 3 parts (Figure 5): side, top and bottom reflector, and top and bottom corner reflector. The thickness of the upper reflector is 90 cm, the lower reflector is 121.236 cm thick, and the side reflector is 77.793 cm. For the reflector equation, the neutron diffusion equation is used for a single energy group but without taking into account the source term, because the reflector is not a multiplicative system.

$$\frac{1}{\nu} \frac{\partial \phi_R(\mathbf{r},t)}{\partial t} - D_R(\mathbf{r},t)\nabla^2 \phi_R(\mathbf{r},t) + \Sigma_{aR} \phi_R(\mathbf{r},t) = 0 \quad (3)$$

The boundary conditions for equation 3 are as follows:

B.C.1 $\phi_c(\mathbf{r},t) = \phi_R(\mathbf{r},t)$ in $\mathbf{r} = \mathbf{r}_c$

B.C.2 $-\mathbf{n} \cdot (-D_c \nabla \phi_c(\mathbf{r},t)) = -\mathbf{n} \cdot (-D_R \nabla \phi_R(\mathbf{r},t))$ in $\mathbf{r} = \mathbf{r}_c$

B.C.3 $\phi_R(\mathbf{r},t) = 0$ in $\mathbf{r} = \mathbf{r}_r$

where \mathbf{r}_r is the group of coordinates of the outer surface of the reflector.

3.3. Heat transfer in the fuel

The heat transfer model in the fuel is located directly in the pebbles, where all fission reactions occur. As it can be seen, the core is considered a porous medium through which the coolant flow passes. The first term from left to right represents the accumulation, the second term is the conduction term which describes the diffusion of the material due to a temperature gradient, the third term is the interstitial convective heat transfer and describes the heat transfer that received or released when the temperatures are different between the fluid and the porous medium and finally, the fourth term represents a source or sink.

$$(\theta\rho Cp)_s \frac{\partial T_s(\mathbf{r},t)}{\partial t} = \nabla \cdot (\theta_s k_s \nabla T_s(\mathbf{r},t)) + q_{sf} (T_f(\mathbf{r},t) - T_s(\mathbf{r},t)) + \theta_s Q_s(\mathbf{r},t) \quad (4)$$

The boundary conditions for equation 4 are the following:

$$\text{B.C.1 } -\mathbf{n}_s \cdot (-k_s \nabla T_s(\mathbf{r},t)) = 0 \text{ in } \mathbf{r} = \mathbf{r}_t$$

where $\theta = 1 - \varepsilon_p$ is the solid volume fraction of the porous media, \mathbf{r}_t is the group of coordinates of the area by which fluid flows through the upper and lower reflector and the core walls.

3.4. Heat transfer in the coolant

The fluid heat transfer model consists of three regions, the upper reflector which is where the coolant enters, immediately the fluid enters the core and then the coolant exits through the lower reflector. Both the upper and lower reflectors were considered to place two domains together, the central part that has the same radius as the core and the outside, this was done as a first approximation to be able to study the phenomena of the core only. For this case in the fluid equation, the source term is eliminated, and the convection term is added, which is the second term from left to right; the convection term describes the heat transfer due to the fluid motion.

$$\varepsilon_p (\rho Cp)_f \left(\frac{\partial T_f(\mathbf{r},t)}{\partial t} + \mathbf{u}_f \cdot \nabla T_f(\mathbf{r},t) \right) = \nabla \cdot (\varepsilon_p k_f \nabla T_f(\mathbf{r},t)) + q_{sf} (T_s(\mathbf{r},t) - T_f(\mathbf{r},t)) \quad (5)$$

The boundary conditions for equation 5 are as follows:

$$\text{B.C.1 } -\mathbf{n}_f \cdot (-k_f \nabla T_f(\mathbf{r},t)) = 0 \text{ in } \mathbf{r} = \mathbf{r}_t$$

$$\text{B.C.2 } T_f(\mathbf{r},t) = T_{inlet} \text{ in } \mathbf{r} = \mathbf{r}_{inlet}$$

$$\text{B.C.3 } -\mathbf{n}_f \cdot (-k_f \nabla T_f(\mathbf{r},t)) = 0 \text{ in } \mathbf{r} = \mathbf{r}_{outlet}$$

Where \mathbf{r}_{inlet} is the group of coordinates where the helium enters through the upper reflector and \mathbf{r}_{outlet} is the group of coordinates of the channel where the helium flux exits through the lower reflector.

As can be seen, the heat boundary conditions in the coolant and the core share the same boundary, $\mathbf{r} = \mathbf{r}_t$, this is because in the core region, there is the solid phase and the fluid phase.

3.5. Momentum balance in a free medium

The momentum balance equation in a free medium has two domains: the central part of the lower and upper reflector, the fluid enters through the upper part of the upper reflector, then in the

lower part of the core it enters the lower reflector and exits through the lower reflector. The first term of the equation from left to right is the accumulation term, which tells us how the fluid behaves over time; the second term is the convective term which describes the change in the amount of motion in the fluid itself; the third term is the pressure gradient which describes the pressure differences in the fluid; the fourth term which is the divergence of the stress tensor describes how due to the motion of the fluid and the viscous forces of the fluid, there is a dissipation of energy; and finally there is the gravity term.

$$\rho \frac{\partial \mathbf{u}(\mathbf{r}, t)}{\partial t} + \rho (\mathbf{u}(\mathbf{r}, t) \cdot \nabla) \mathbf{u}(\mathbf{r}, t) = -\nabla \cdot (p\mathbf{I} + \boldsymbol{\tau}) + \rho \mathbf{g} \quad (6)$$

3.6. Momentum balance in porous medium

The momentum balance equation in a porous medium has only the core as its domain since this is where the pebbles are located. As can be seen, compared to the equation in a free medium, three more terms are added after the stress tensor $\mu\kappa^{-1}$. This is the Darcy term describing the flow resistance in the porous medium; the next term is the Forchheimer term $\beta\rho|\mathbf{u}(\mathbf{r}, t)|$ which introduces a nonlinear effect due to flow inertia at higher velocities; and Q_m Represents an additional force that could be due to different effects such as momentum sources.

$$\frac{\rho}{\varepsilon_p} \left(\frac{\partial \mathbf{u}(\mathbf{r}, t)}{\partial t} + (\mathbf{u}(\mathbf{r}, t) \cdot \nabla) \frac{\mathbf{u}(\mathbf{r}, t)}{\varepsilon_p} \right) = -\nabla \cdot (p\mathbf{I} + \boldsymbol{\tau}) - \left(\mu\kappa^{-1} + \beta\rho|\mathbf{u}(\mathbf{r}, t)| + \frac{Q_m}{\varepsilon_p^2} \right) \mathbf{u}(\mathbf{r}, t) + \rho \mathbf{g} \quad (7)$$

In this case the boundary conditions are shared since the porous medium is in the medium through which the helium flow circulates, i.e., they share the same domain.

Its boundary conditions are

$$\text{B.C.1 } \mathbf{u}(\mathbf{r}, t) = \mathbf{u}_{inlet} \text{ in } \mathbf{r} = \mathbf{r}_{inlet}$$

$$\text{B.C.2 } p(\mathbf{r}, t) = p_{outlet} \text{ in } \mathbf{r} = \mathbf{r}_{outlet}$$

$$\text{B.C.3 } \mathbf{u}(\mathbf{r}, t) = 0 \text{ in } \mathbf{r} = \mathbf{r}_t$$

In this case \mathbf{r}_t is the group of coordinates where the fluid has contact with the solid surface of its domains which are the top reflector, bottom reflector, and core, therefore, the velocity of the fluid in the direction tangential to the surface shall be equal to the velocity of the same surface.

4. RESULTS

To perform the physical phenomena mentioned above, a simplified geometry of the HTR-10 reflected reactor was constructed in which the reactor core, the total reflector, the control rod channels, and the absorber balls are considered. The geometries that make up the reflected reactor are presented in Figure 5.

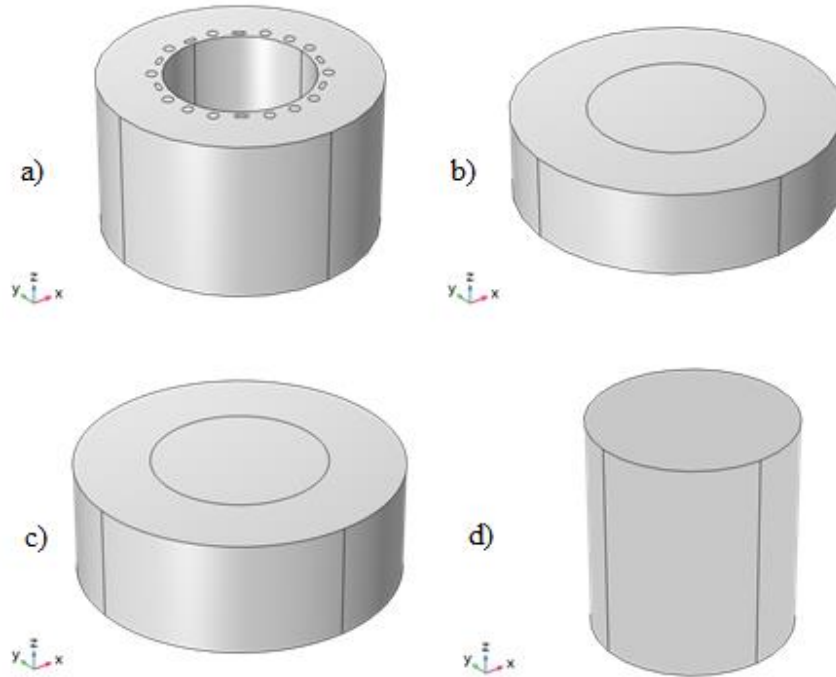


Figure 5. a) Side reflector with control rod channels and absorber balls b) Top reflector c) Bottom reflector d) Core reactor

4.1. Neutron diffusion

The behavior of the neutrons in the bare reactor and the reflector are shown separately (Figures 9 and 10), and the behavior of the neutrons in both regions is presented in Figure 11.

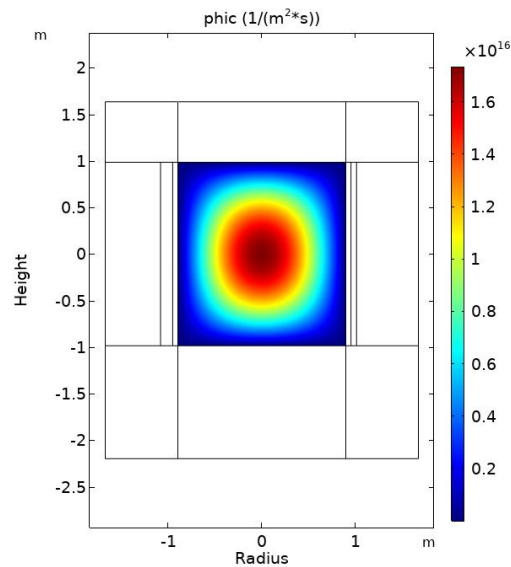


Figure 9. Neutron diffusion in the core

As it can be seen, the highest neutron concentration is found in the center of the bare reactor, which complies with the neutron diffusion theory for a single group.

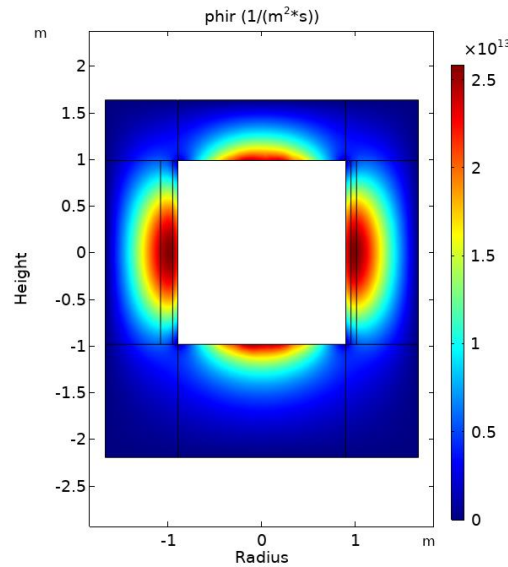


Figure 10. Neutron diffusion in the reflector

It can be seen in Figure 10 that the reflector, more specifically at the outer limits of the reflector the neutron flux is zero. The rectangle in the center belongs to the reactor core and its behavior is shown in Figure 9.

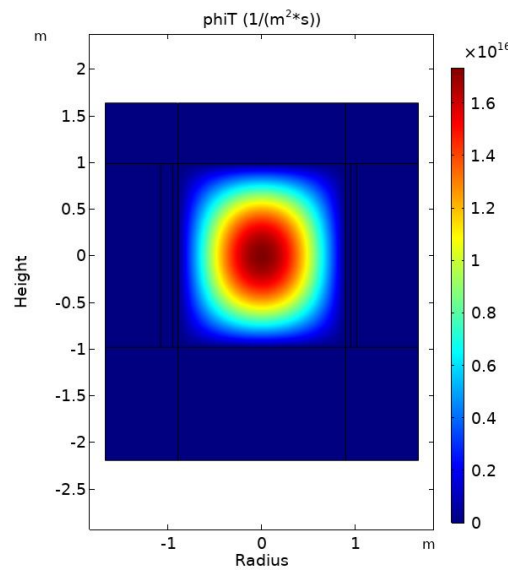


Figure 11. Core-reflector neutron diffusion

Figure 11 shows the behavior of the neutron flux when the core and the reflector are joined. It can be seen that when they are joined, information is lost from the reflector due to the fact that the order of magnitude is lower than the core itself.

4.2. Heat transfer

The following are several experiments that take place in the working fluid and fuel, results are shown in a stationary form in which the coolant inlet temperature (THe) and the coolant mass flow (F) are varied.

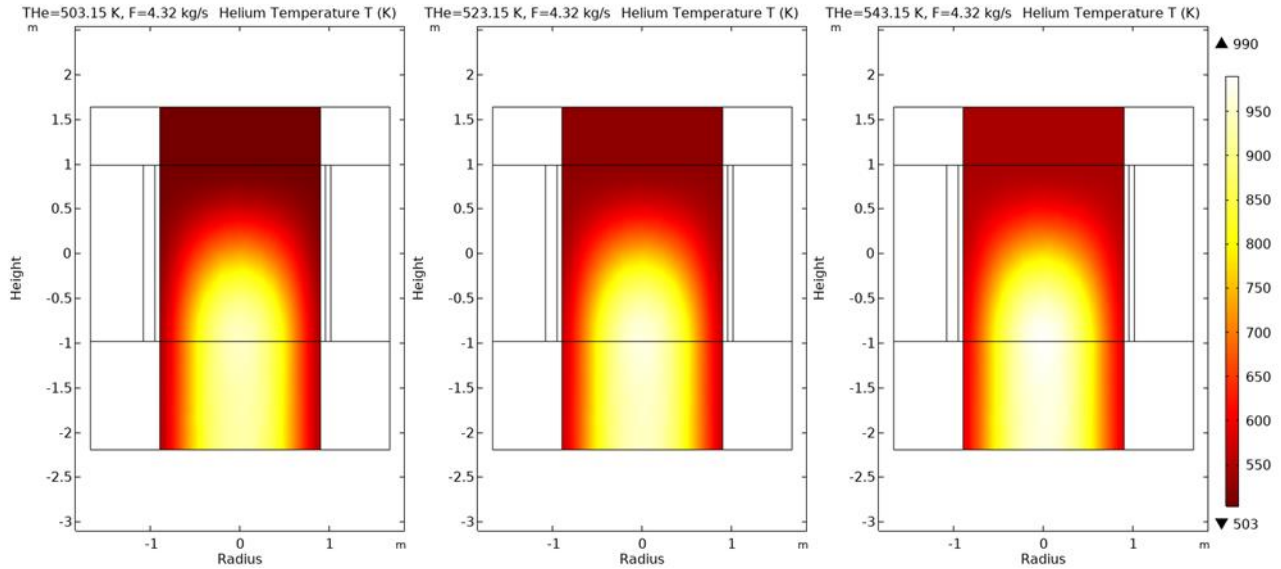


Figure 12. Coolant temperature varying helium inlet temperature (2D)

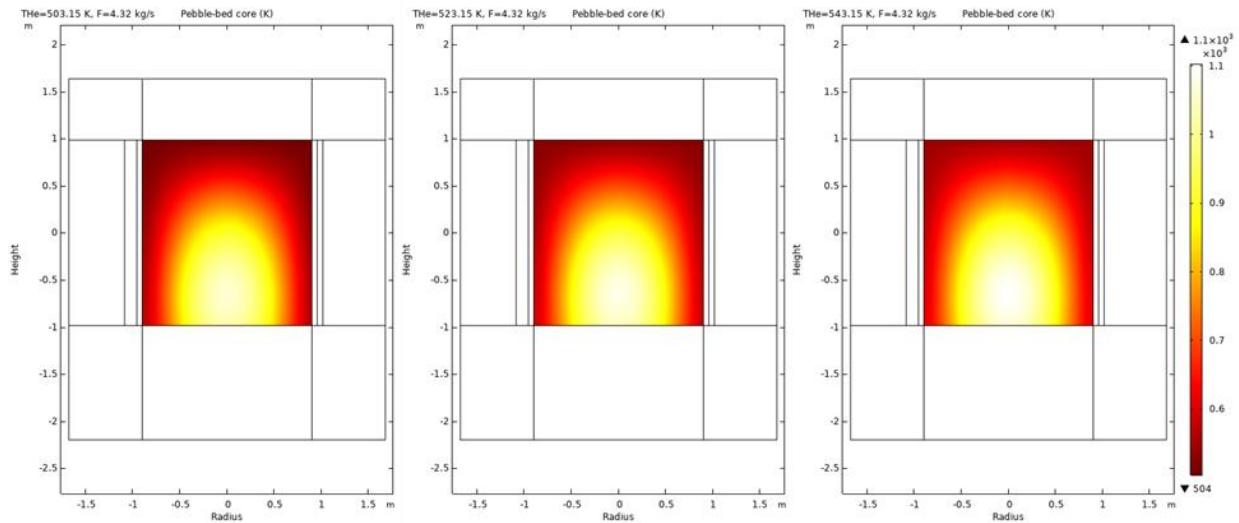


Figure 13. Pebble-bed core temperature helium inlet temperature (2D)

As is presented in Figures 12 and 13, when inlet mass flow rate is increased, the temperature reached by the helium flow and the Pebble-bed core increases and vice versa, in addition, it is fulfilled that the highest temperature is at the bottom of the core.

Next, 1D axial plots are shown next, and the helium and Pebble-bed core temperature and the velocity field will be studied, this study was carried out along the Pebble-bed core and in the center of it, i.e., with a radius equal to zero.

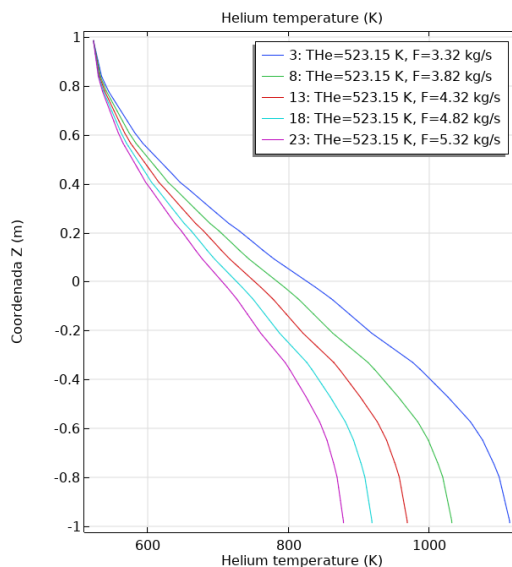


Figure 14. helium temperature varying mass Flow

In Figure 14, it is possible to observe that the helium inlet flow rate decreases, the longer the helium is in contact with the Pebble-bed core, the more heat it supplies, so the helium temperature increases, and the opposite happens when the mass flow rate is increased.

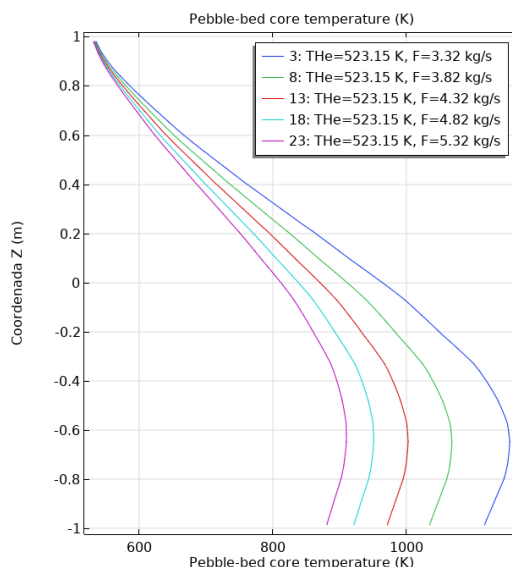


Figure 15. Pebble-bed core temperature varying mass flow

For the case of the Pebble-bed core temperature, the same thing happens, as the mass flow decreases the core temperature also increases, on the other hand, when the mass flow increases, the core temperature decreases because there is a faster exchange of energy between the helium flow and the core.

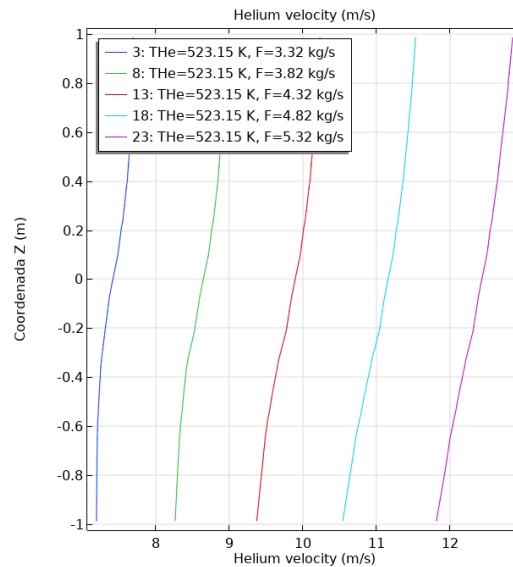


Figure 15. Helium velocity varying mass flow

In this case, the temperature that is supplied from the Pebble-bed core to the helium is directly influenced by the velocity that the helium reaches, i.e., the higher the temperature, the higher the dynamic viscosity of the helium, the higher the resistance to flow, and vice versa.

According to the work developed by Rodriguez et al. (2021), the maximum coolant temperature is 1,139 K and the highest surface temperature of the fuel is 1,222 K, in this work, the coolant temperature is 970 K and the fuel surface temperature is 1,002.6 K, comparing both results, there is an error of 15% for the coolant temperature and 17% for the fuel temperature, however, it should be clarified that the results of this article were simulated in an Intel Core i9 14900k processor with 3.2 GHz, while the reference article uses a cluster of 24 Intel 3.6 GHz CPUs, which is a great computational advantage since having a greater number of CPUs allows a much finer meshing and the simulation times are shortened. Also, we should consider that in this work, the model is for the core, while in the work of Rodriguez et al. (2021), the model includes the complete vessel and all the phenomena inside it, which could affect the approximation of results. In future work, the secondary system of the gas reactor will be included.

4. CONCLUSIONS

The results obtained are acceptable compared with the literature on this type of reactor. The temperature either for the helium coolant flow or for the pebble-bed core is always found to be higher in the lower part of the core, due to the gas flow and heat source.

The neutron processes show correct results according to the neutron diffusion theory for a single group. It is possible to consider that this approximation gives a good approximation.

In further studies, it is planned to couple neutronic processes, including control rod reactivity, with thermohydraulic processes. This will be done to study the behavior of the reactor itself and demonstrate that it is reliable. The inclusion of the control rods, which are a safety system,

reactivity by Doppler effect due to fuel temperature, reactivity by thermal expansion, among others, are an important factor in the coupling of the neutronic processes and the reactor thermalhydraulics. This coupling will ensure that in any accident simulation the coupled model will reach a new steady state without jeopardizing the integrity of the reactor.

ACKNOWLEDGEMENTS

The authors acknowledge the financial support from the Basic Science and Frontier Project 2023-2024 Reference CBF-2023-2024-2023 founded by the National Council of Humanities, Sciences and Technologies CONAHCyT. Erick Josue Yescas Pozos acknowledges the CONAHCyT for the support received during his Master's studies.

REFERENCES

1. Mears, L. D., & Goodjohn, A. J., "Situación del desarrollo y diseño de los reactores de alta temperatura refrigerados por gas". *International Atomic Energy Agency*, https://www.iaea.org/sites/default/files/31304793639_es.pdf (1989).
2. Sowby, D., Thorne, M., Bridges, B. A., double diamond anniversary—Kyshtym, A., Wakeford, R., & McNally, R. J., The Windscale reactor accident—50 years on. *Journal of Radiological Protection*, **27**, 211-215 (2007).
3. Yan, X. L., "Very high-temperature reactor", In *Handbook of Generation IV Nuclear Reactors*, Woodhead Publishing (2016).
4. Cacuci, D. G. (Ed.), *Handbook of Nuclear Engineering*, Springer Science & Business Media (2010).
5. George, A. P., "Introduction to the Pebble Bed Modular Reactor (PBMR)". *Exelon Generation. South Africa*, DOCUMENT No.: 009949-185 (2001).
6. Espinosa-Paredes, G., Castillo-Jiménez, V., Herranz-Puebla, L. E., & Vázquez-Rodríguez, R., "Analysis of the interfacial heat transfer process in a pebble fuel". *Progress in Nuclear Energy*, **65**, 15-31 (2013).
7. Cho, N. Z., Yu, H., & Kim, J. W., "Two-temperature homogenized model for steady-state and transient thermal analyses of a pebble with distributed fuel particles", *Annals of nuclear energy*, **36**(4), 448-457 (2009).
8. Yuanqiang, W., Xingzhong, D., Huizhong, Z., & Zhiyong, H., "Design and tests for the HTR-10 control rod system", *Nuclear Engineering and design*, **218**, 147-154 (2002).
9. Gao, Z., Shi, L., "Thermal hydraulic calculation of the HTR-10 for the initial and equilibrium core", *Nuclear Engineering and Design*, **218**, 51-64 (2002).
10. Terry, William K., et al., "Evaluation of the HTR-10 Reactor as a Benchmark for Physics Code QA. No. INL/CON-05-00852", *Idaho National Lab. (INL)*, Idaho Falls, ID (United States) (2005).
11. Agus, W., & Azizul, K., "Calculation reactivity of HTR-10 control rods using scale", *International Atomic Energy Agency* (2019).
12. IAEA, Xu, Y. "The HTR-10 project and its further development", *International Atomic Energy Agency*, No. INIS-XA--524 (2002).
13. Sun, S., Zhang, Y., & Zheng, Y., "Research on Influence of Different Simulation Methods of Bypass Flow in Thermal Hydraulic Analysis on Temperature Distribution in HTR-10", *Science and Technology of Nuclear Installations*, 4754589 (2020).

14. Jeong, H. D., Chang, S. H., “Estimation of the fission products, actinides and tritium of HTR-10”, *Nuclear Engineering and Technology*, **41**, 729-738 (2009).
15. Rodríguez, A. G., Mazaira, L. Y. R., Hernández, C. R. G., Dominguez, D. S., & de Oliveira Lira, C. A. B. An integral 3D full-scale steady-state thermohydraulic calculation of the high temperature pebble bed gas-cooled reactor HTR-10. *Nuclear Engineering and Design*, **373**, 111011. (2021)

Development of a BWR5 Reactor Building model for on-site and off-site dose calculations with MAAP5-DOSE

Ortega, Blanca

*Universidad Nacional Autónoma de México
Facultad de Ingeniería, Ciudad Universitaria
Ciudad de México*

bj.ortegachagoyan@gmail.com

Ortiz, Javier; Vias, Jorge;

*Instituto Nacional de Investigaciones Nucleares
Ocoyoacac, Estado de México*

Javier.Ortiz@inin.gob.mx; Jorge.Vias@inin.gob.mx

Abstract

The assessment of off-site dose and in the control room (in-site) dose is a requirement in the safety analyses of a nuclear power plant, for the design basis analysis. This type of analysis gives credit to retention of fission products in the secondary containment, also known as the Reactor Building in BWR plants, and it also allows for the use of the Alternative Source Term methodology in the dose calculation. Thus, in this work, a nodalization model of the Reactor Building has been developed for the MAAP5 code, and it has been coupled to a Mark II type primary containment implemented for BWR/5 design. The final model of the Reactor Building has 6 nodes for the building levels and a representative node for the control room. The integral model, composed by the Mark II and the Reactor Building, has a total of 28 nodes, 29 junctions, 14 failures, and 52 heat sinks. This expanded model was tested first for the steady state case, and then during the simulation of an unmitigated SBO, in order to verify the proper coupling of the primary and secondary containments. The results showed no impact on the key variables of the steady state heat balance and on the core degradation process, indicating that the coupling was successful. Then, this integral mode, in conjunction with the Alternative Source Term methodology, was tested for dose calculation during the progression of the unmitigated SBO, with the code MAAP-DOSE. The event simulation covers three hours of steady state and 24 hours of accident scenario from the onset of the event. The final dose results show a reduction of 43.1 % of off-site dose when the integral nodalization model is used, in comparison to the use of only the Mark II primary containment model. Therefore, this work sows the importance of having a secondary containment in dose calculations.

1. INTRODUCTION

Nuclear power plants have a series of engineered barriers to avoid the progression of accidents and for mitigation actions, when they occur, based on the Principle of Defense in Depth. A severe accident in a nuclear reactor could involve damage to biota if there is a release of radioactive material into the environment. The effect that ionizing radiation from those materials will depend on the nature of the fission products being released.

Activity, exposure and dose are fundamental concepts in the assessment of risks associated with ionizing radiation in nuclear environments or in emergency situations, such as accidents at nuclear power plants. Activity refers to the amount of radiation emitted by a source in a given period of time, measured in becquerels (Bq) [1]. This measurement allows us to quantify the number of radioactive particles released from a decaying substance. Exposure, on the other hand, refers to the amount of radiation absorbed by a material or organism. It is measured in units such as roentgen PRA or coulomb per kilogram (C/kg). Exposure is crucial for assessing the potential adverse effects of radiation on human health and the environment [1], [2]. Dose, finally, is the amount of energy deposited by radiation in a material or tissue. It is expressed in grays (Gy) or sieverts (Sv). It is important to distinguish between the absorbed dose, which indicates the amount of radiation actually received by an object, and the absorbed dose rate, which refers to the speed with which this radiation is absorbed by the tissue, thus determining the severity of biological effects [3].

There are several software systems, commonly known as codes, that allow the modeling of a nuclear power plant, with its emergency and mitigation systems. These tools can be used to simulate accident scenarios and analyze the progression of events, and also analyze the distribution of hydrogen or fission products in the primary containment, in the event of a vessel failure. In addition, some codes allow the calculation of doses inside the containments as well as in the environment. One code that can perform such tasks is the Modular Accident Analysis Program (MAAP), which addresses the full spectrum of important phenomena that could occur during an accident, simultaneously modeling those related to thermal-hydraulics and fission products. It is in MAAP where the modeling of the plant is done. However, there is an optional module that allows dose analysis, referred as to DOSE, which contains the physics model that calculate dose rate and total dose at specified containment nodes, as well for off-site locations. DOSE can be run simultaneously with MAAP5 to calculate dose and rates during the progression of the accident or as a stand-alone module, but in this case requires much more data. Thus, a MAAP-DOSE model must be developed in order to perform dose analysis ([4], [5]) and the user must specify a source term for transport and analysis.

The assessment of off-site dose and in the control room (in-site) dose is a requirement in the safety analyses of a nuclear power plant, for the design basis analysis. This type of analysis gives credit to retention of fission products in the secondary containment, also known as the Reactor Building in BWR plants, and it also allows for the use of the Alternative Source Term methodology in the dose calculation. Thus, in this work, a nodalization model of the Reactor Building has been developed for the MAAP5 code, and it has been coupled to a Mark II type primary containment implemented for BWR/5 design. This integral nodalization model, in conjunction with the Alternative Source Term methodology, was tested for dose calculation

during the progression of the unmitigated SBO, with the code MAAP-DOSE. The dose results are presented in this paper.

2. METHODOLOGY

The present research is the continuation of the work carried out by a team at the Nuclear Systems Department of the Nuclear Research National Institute (ININ of Mexico). The current Mark II model for the code MAAP5 has a total of 36 heat structures, a total of 21 nodes, 26 junctions, and 2 failures. Additionally, MAAP5 requires a minimum number generate the inputdeck, both for the geometric structures and also for the environmental and operating conditions of the reactor. To mention just a few of the many input variables, to generate a single node model, MAAP5 requires about 50 variables, so the total number of variables in MAAP to generate a full plant model is generally over 5000 [6], [7], [8]. As an example, Table I shows some of the main variables required to describe a node.

Table I. Examples of the main variables to create a node in MAAP5.

Variables	Description
VOLRB(i)	the total volume of gases and liquids in the iv'th compartment
AGKEY(i)	the largest characteristic total cross-sectional area in the iv'th compartment through which the gas flows.
XDGKEY(i)	the iv'th compartment hydraulic diameter associated with parameter AGKEY(i)
ASEDRB(i)	the iv'th compartment aerosol aerosol sedimentation area
TGRB0(i)	the initial gas temperature in the iv'th compartment
PRB0(i)	the initial pressure in the iv'th compartment
XHBRRB(i)	the characteristic height of the iv'th compartment for combustible gas burns
XRBLK(j,i)	i'th height lookup entry for iv'th compartment, and
VRBLK(j,i)	i'th volume lookup entry for iv'th compartment

The coupling process between the two models of primary and secondary containments is not a simple or quick task. In this work, it was first considered to represent the Reactor Building by a single node, being the geometry of this node a rectangle. Thus, with a single node representing the Reactor Building, the connections between the primary and secondary containment models were updated, including the review of those that corresponded to a connection to the environment. After the coupling process is completed (between the primary containment and the Reactor Building nodes), a simulation of only the steady state was performed to verify that no input errors are committed. Once this run is completed without generating any output errors and the results obtained for the main variables of the steady state heat balance are satisfactory, the coupling process is considered successful.

The next step is to create a new model for the Reactor Building with more nodes. In this case, a nodalization model with two nodes was created, for which the adjustment of the junctions between the primary containment, the secondary containment, and the environment is carried out

again. Additionally, the adjustment of the heat sinks is performed, because it must be correctly set the contact surfaces between the two containments.

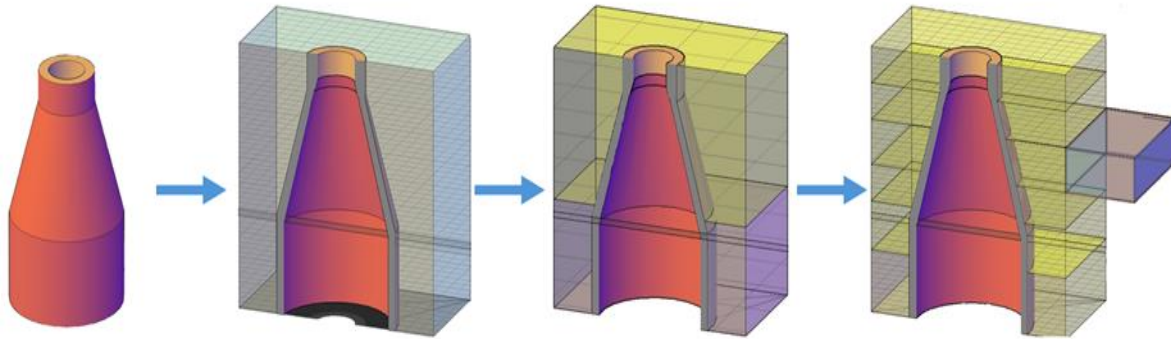


Figure 1. Node augmentation process of the reactor building model.

Once the new Reactor Building model is coupled to the Mark II primary containment, the steady state is simulated again, and errors, if any, are corrected and simulated again. This sequence is repeated as more nodes are incorporated to the model until the coupling of the final integral model is deemed to have been done correctly. For each of these models and simulations, checks were performed on all variables that, although unchanged, could be indirectly affected by the changes and the overall coupling. At no time changes were made to the dimensions of the primary containment nodes, only adjustments were made to the junctions, their numbering and the contact that the heat sinks have between the nodes. The process to achieve the final Mark II model coupled to the new Reactor Building model is shown in Figure 1.

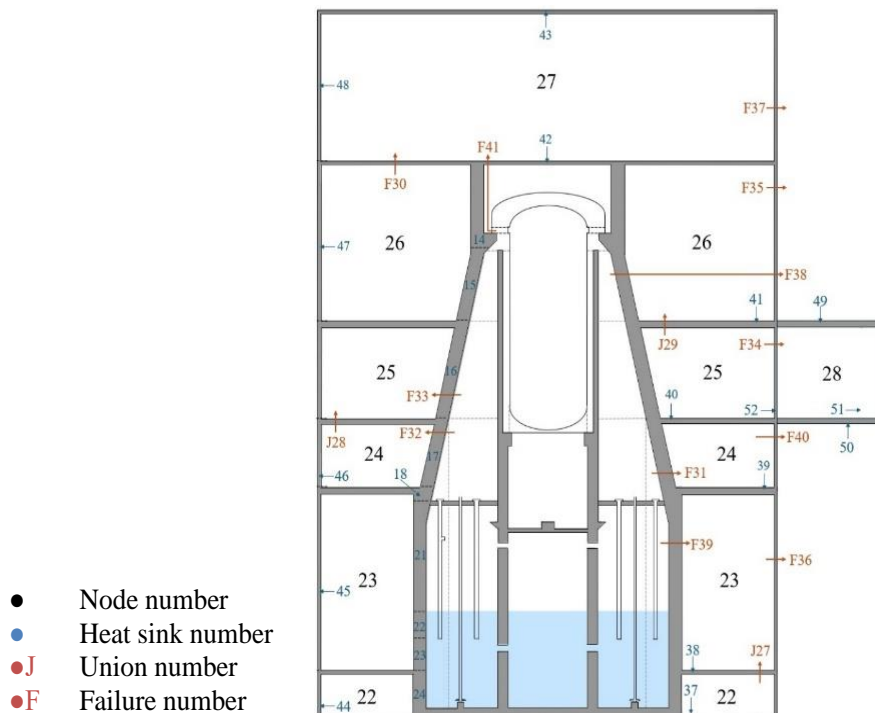


Figure 2. Graphical representation of the generated model of the reactor building with number of nodes, junctions, and heat sinks.

The final model developed in this research is based largely on material provided in [9]. As shown in Figure 1, only 6 levels were considered for the model developed, which are considered as adequate representatives for dose calculations for the entire volume of the building. In addition, the new coupled Mark II and Reactor Building (M2+RB) model has 3 new junctions and 12 failures between the Mark II, the reactor building and the environment. Figure 2 shows the full nodalization model developed for this work.

3. INITIATING EVENT

For this case study, an SBO will be taken as the initiating event, which will be understood for this work as the loss of internal and external AC energy. Additionally, there is not any type of mitigation actions during the progression of this accident. Given that the objective of this research is to estimate the dose in-site and off-site, the simulation of a scenario without any type of mitigation will yield more conservative results, because the accident reaches the periods of the failure of the vessel and the two containments.

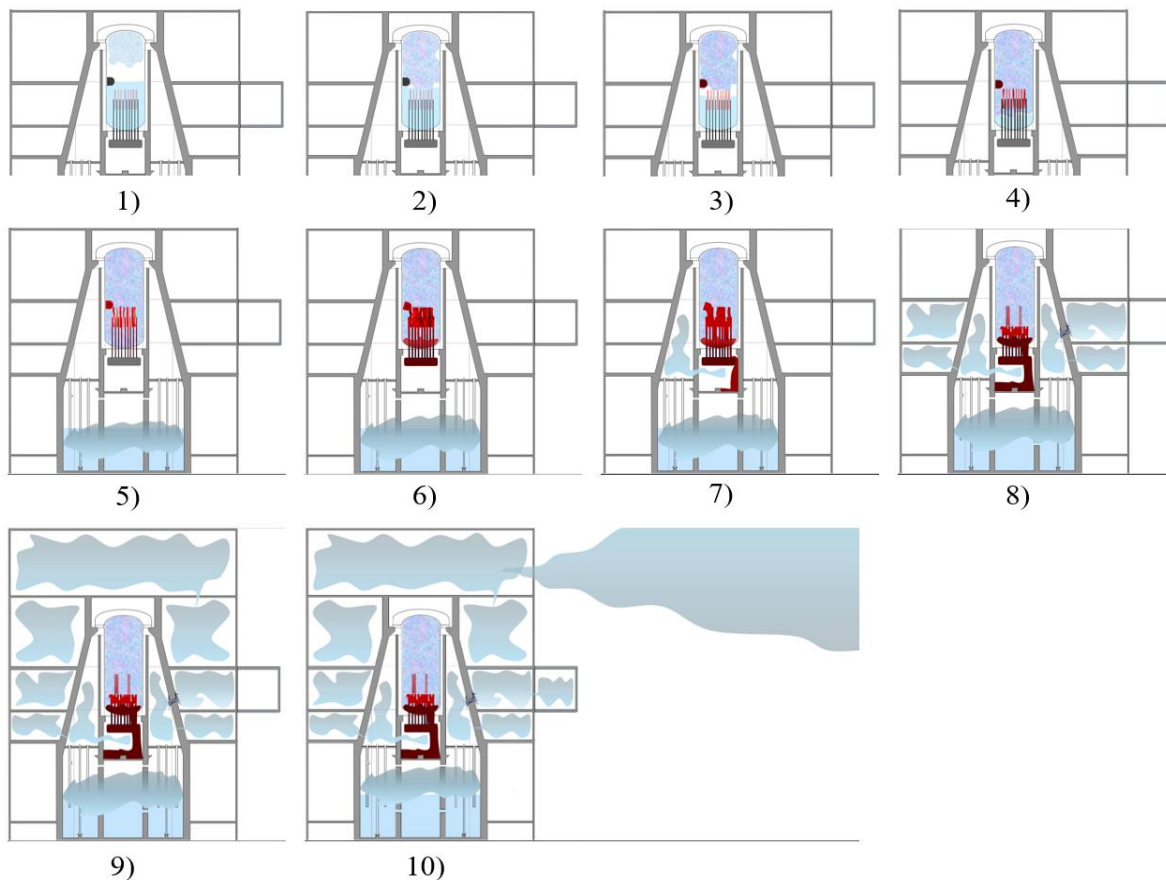


Figure 3. Progression of representative events during the unmitigated SBO accident in the generated Mark II plus reactor building model for a BWR5.

Table III. Summary of figures of merit between the two models.

Event / timing	Nodalization model			
	M2+RB		M2	
	sec	hrs	sec	hrs
Discovery of the core	2096.3	0.58	2097.7	0.58
Relocation of material to the lower plenum	4064.3	1.13	4086.1	1.14
Vessel failure	15606.5	4.33	13680	3.80
M2 containment failure	47343.37	13.15	46207.7	12.84
RB failure	49005.2	13.61	-	-

Figure 3 shows the graphical sequence of the main events that occurred during the accident: 1) steady state operation, 2) pressure increase in the vessel, 3) decrease of water level in the vessel, core uncovering, 4) core damage, increase of melt percentage, 5) increase of melt percentage, increase of fission product release to coolant system, 6) core mass relocation to the lower plenum, 7) vessel failure, fission product distribution in primary containment, 8) Mark II primary containment failure, 9) connection openings determined by structural failures, fission product distribution in secondary containment, 10) distribution of fission products from the reactor building to the environment and to the control room. Table III shows a comparative of the timing of relevant events when using or not the Reactor Building model.

4. DOSE RESULTS

Figure 4 shows the comparison of the resulting cumulative dose profiles at two off-site distances, from the BWR plant in consideration, when using only the Mark II primary containment model and when using the new integral mark II plus Reactor building model, and Table IV presents the description of the nomenclature used on Figure 4.

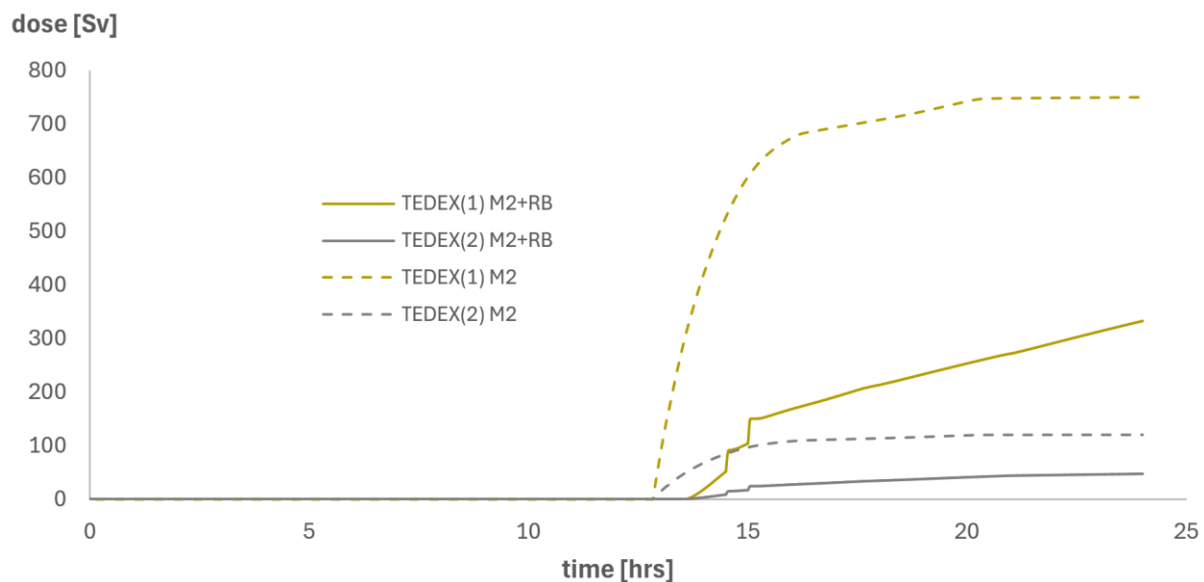


Figure 4. Comparison of cumulative dose results for the two nodalization models.

Table IV. Description of variables plotted in Figure 4.

Parameter		Variable in Figure 4
Dose at distance 1 with the M2 and M2+RB model	Sv	TEDEX (1) M2/ M2+RB
Dose at distance 2 with M2 and M2+RB model	Sv	TEDEX (2) M2/ M2+RB

Figure 5 shows the comparison of the resulting dose rate profiles at the same two off-site distances shown in Figure 4, when using only the Mark II primary containment model and when using the new integral mark II plus Reactor building model, and Table V presents the description of the nomenclature used on Figure 5.

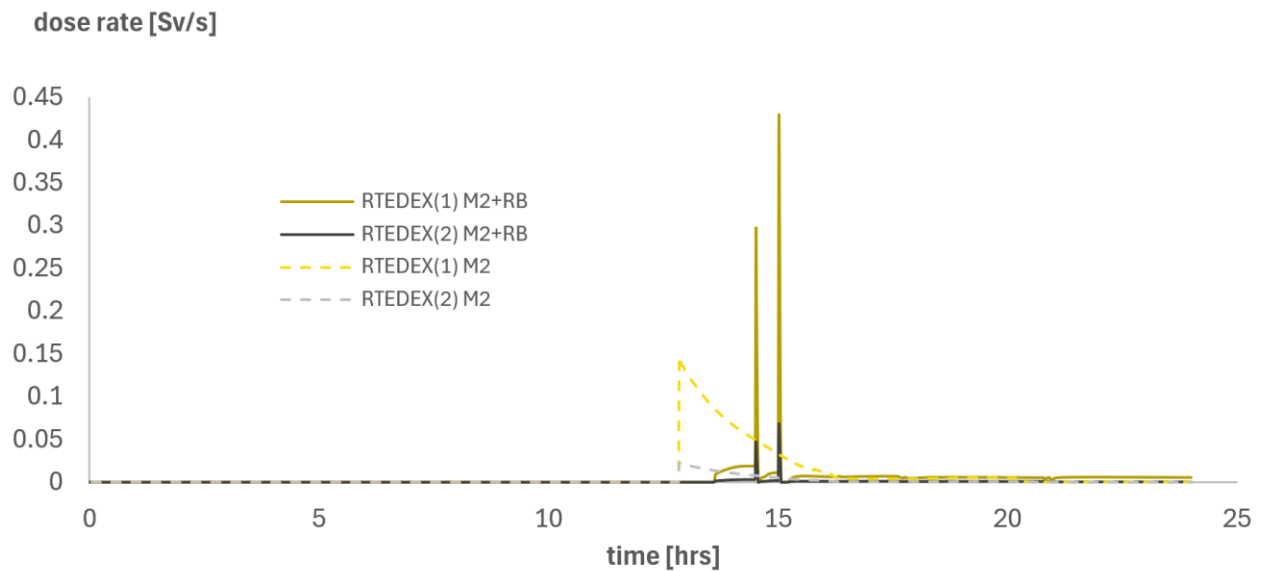


Figure 5. Comparative Dose rate results for the two nodalization models.

Table V. Description of the variables graphed in Figure 5.

Parameter		Variable in Figure 5
Dose rate at distance 1 with M2 and M2+RB model	Sv/s	RTEDEX(1) M2/ M2+RB
Dose rate at distance 2 with M2 and M2+RB model	Sv/s	RTEDEX(2) M2/ M2+RB

Figure 5 shows that the profiles are markedly different between the two nodalization models, clearly reflecting the assumptions used in the simulation. For example, in the M2 model, a single release phase is observed, as only the conditions necessary for continuous leakage occur, which decreases in magnitude over a period of 15,000 seconds. Although the dose rates at the two distances are significantly lower than in the M2+RB model, because of the single release point, the dose accumulation at the end of the 24-hour simulation is 2.25 times higher at distance 1 and 2.55 times higher at distance 2, as illustrated in Figure 4.

Regarding the M2+RB model, there are two clear release moments, which correspond first to a leak and then to the failure of the Reactor Building. Such a failure is due to a hydrogen deflagration. The cumulative Dose in this case increases (almost) linearly but does not reach the magnitude of the M2 model results because there is a significant retention of fission products in the Reactor Building at the end of the 24 hours of the simulation.

The release of products to the environment is ultimately determined by the release route or mode of containment failure: either by failure due to overpressure, release through leaking or unfiltered vent routes, or by corium penetration through the concrete foundation. This depends on the size and number of leaks or gaps that may form. The most significant results include cumulative doses and dose rates, which are a direct result of the activities and thus fission product masses at each node. The assumptions for the simulated scenario are quite extreme to provide a clear view of the impacts of mitigation measures in future studies. In addition, the use of the AST option to calculate doses showed a considerable impact on the results too, as only aerosols are retained in water volumes, while most of the noble gases, which account for a large part of the total activity, are released.

5. CONCLUSIONS

The simulation of an unmitigated SBO in a BWR plant with Mark II type Primary Containment has shown that the proper coupling of a Reactor Building model is significantly positive in fission product retention gain, and as a major consequence on markedly reduction on accumulated dose and dose rates at two different off-site locations. The integral mode, in conjunction with the Alternative Source Term methodology, was used to simulate an unmitigated SBO for a lapse of 24 hours, with the code MAAP-DOSE. The final dose results show a reduction of 43.1 % of off-site dose when the integral nodalization model is used, in comparison to the use of only the Mark II primary containment model. Therefore, this work sows the importance of having a secondary containment in dose calculations.

ACKNOWLEDGEMENTS

The first author of this paper would like to express her sincere thanks to the institution CONAHCYT for its support through a fellowship to obtain the Degree of master's in science in Energy Engineering, at Facultad de Ingeniería of the Universidad Nacional Autónoma de México. The funding and additional resources provided were essential for the development of this research and the completion of this paper. I am also deeply grateful to the Department of Nuclear Systems at the National Institute for Nuclear Research for their continuous support, advice and training. Finally, I would like to express my deepest gratitude to the National Autonomous University of Mexico for welcoming me and providing me with an integral education.

REFERENCES

1. H. Cember, *Introduction to health physics*, McGraw-Hill, New York, EE.UU (1996).
2. EPRI, “MAAP5 User's Manual: Calculation of In-Plant and Ex-Plant Dose and Dose Rates”, *Electric Power Research Institute*, **Volume 1**, Revision 0.6 (2021).
3. EPRI, “MAAP5 User's Manual: Phenomenology Models”, *Electric Power Research Institute*, **Volume 2** (2008).
4. EPRI, “Modular Accident Analysis Program 5 (MAAP5) Applications Guidance Desktop Reference for Using MAAP5 Software-Phase 3 Report”, *Electric Power Research Institute* (2017).
5. IAEA. “Status and Evaluation of Severe Accident Simulation Codes for Water Cooled Reactors”, *International Atomic Energy Agency*, Viena, Australia, June, TECDOC-1872 (2019).
6. F. P. M. B. Reeves, “1-MAAP5 Generalized Containment Model Volumes, Junctions, and Heat Sinks”, *Electric Power Research Institute* (2022).
7. F. P. M. B. Reeves, “2 -MAAP5 Standalone Containment Model Standalone Model and External Source Flows”, *Electric Power Research Institute* (2022).
8. T. S. C. C. D. Fujiwara, “Module 15 - Reactor Building Model: Volumes, Junctions, and heat sinks”, *Electric Power Research Institute* (2017).
9. L. 1. & 2, “Final Safety Analysis Report”, *Nuclear Regulatory Commission* (2000).

Unprotected Transients Simulations of a Liquid Metal-cooled Fast Reactor

Alejandría D. Pérez Valseca, Rodolfo Vázquez-Rodríguez
Metropolitan Autonomous University – Iztapalapa
San Rafael Atlixco 186, Iztapalapa, 09340 Mexico City, Mexico.
alepv@xanum.uam.mx; rwr@xanum.uam.mx

Abstract

The safety in nuclear reactors is one of the goals of the GenIV reactors. The safety analysis includes the simulation of different transient events derived from insertion or reactivity, loss of coolant, or loss of heat skin. The lead-cooled fast reactor is one of the six designs of Generation IV reactors, currently, the research and investigation of this technology are growing, and now is in the phase of simulations in a steady state and transients, to decrease the risk of accidents when the reactors be built. This work analyzes steady state and transient events in a Lead-cooled fast reactor. The tool used is one homemade code, this code solves a system of energy, mass, and momentum balance equations by applying numerical methods. The transients simulated are the Unprotected Transient Over Power, with insertion of reactivity in the core, and Unprotected Loss of Flow. The lead-cooled fast reactor was selected because it is one of the designs of Generation IV nuclear reactors under development.

1. INTRODUCTION

Nuclear technology applied to the energy industry originated in the 1950s, when the prototypes of nuclear reactors, also known as experimental reactors, belonging to Generation I, were developed [1]. In the 1970s, Generation II reactors were created, characterized as the first commercial reactors for electricity generation. The systems developed were BWR (Boiling Water Reactor), and PWR (Pressurized Water Reactor), both of which are LWR (Light Water Reactor). In this generation, the CANDU reactor (CANada Deuterium Uranium) was created.

The designs of Generation II were improved in Generation III. The reactors developed in this generation are known as advanced reactors. Following Generation III, we have Generation III+, which aims to create reactors with evolutionary designs that yield economic improvements, making them more competitive, and where technological advancements allow for faster construction.

Advanced thermal reactors and fast neutron spectrum reactors are part of Generation IV. The Generation IV (GIV) of nuclear reactors emerged by creating highly economical designs with increased safety, minimal radioactive waste, and the purpose of not promoting proliferation [1]. The International Forum on Generation IV (GIF) originated in the year 2000 when the Office of

Nuclear Energy, Science, and Technology of the U.S. Department of Energy convened a group of expert representatives from different countries. As a result, GIF has led international efforts for over a decade to develop next-generation nuclear systems. The four main driving objectives for developing this new technology were sustainability, economy, safety and reliability, proliferation resistance, and physical protection [2].

Six technologies were selected for development from the proposed technologies: Gas-Cooled Fast Reactor (GFR), Lead-Cooled Fast Reactor (LFR), Molten Salt Reactor (MSR), Supercritical-Water-Cooled Reactor (SCWR), Sodium-Cooled Fast Reactor (SFR), and Very High-Temperature Reactor (VHTR). Many of these designs are currently under development, indicating that they will be the reactors of the coming decades [2].

2. REACTOR DESCRIPTION

Among the six systems proposed by the GIF (Generation IV International Forum) in Generation IV for research and development, the Lead-cooled Fast Reactor, Sodium-cooled Fast Reactor, and Gas-cooled Fast Reactor have been selected by the European Union for focused research. These systems are considered the most promising candidates for a closed fuel cycle, ensuring highly efficient utilization of uranium resources, and minimizing the generation of long-lived waste [3].

The Lead-Cooled Fast Reactor (LFR) covers the concepts of the Generation IV reactors (Generation IV International Forum, 2002), which was selected by the European Union together with the Sodium-cooled and the Gas-cooled Fast Reactors. The LFR features a fast neutron spectrum, high temperature operation, and cooling by molten lead or lead-bismuth eutectic (LBE), low-pressure, and chemically inert liquids with very good thermodynamics [4].

The Advanced Lead Fast Reactor European Demonstrator (ALFRED), is a small-size pool type LFR of 300MWth, considered in this study to stand-alone core sensitivity and uncertainty analysis from Monte Carlo simulations. The main technological constraints, goals, and choices for the ALFRED core design are given by Grasso *et al.* [3]. The primary characteristics of the reactor are presented in Table I [3].

Table I. Main parameters of the ALFRED reactor [3].

Parameter	Units	Value
Thermal Power	MW	300
Fuel type	-	MOX
Maximum fuel temperature	°C	2000
Maximum Pressure	MPa	5 MPa
Clad material	-	15-15 Ti
Maximum clad temperature	°C	550
Inlet temperature of the coolant	°C	400
Outlet temperature of the coolant	°C	480
Maximum coolant velocity	m/s	3

In Table II, the properties of the coolant (lead) are presented, in this work, the properties are considered constant.

Table II. Properties of coolant [3].

Property	Units	Value
Density	Kg m ⁻³	10520
Specific Heat	J kg ⁻¹ K ⁻¹	147.3
Thermal Conductivity	W m ⁻¹ K ⁻¹	17.1
Viscosity	Pa s	0.1998

3. MATHEMATICAL MODEL

3.1. Neutronics

The neutron density is calculated using the neutron point kinetics equations with six precursors of delayed neutrons. The model is given by:

$$\frac{dn(t)}{dt} = \left(\frac{\rho_t - \beta}{\Lambda} \right) n(t) + \sum_{i=1}^6 \lambda_i C_i(t) \quad (1)$$

$$\frac{dC_i(t)}{dt} = \frac{\beta_i}{\Lambda} n(t) - \lambda_i C_i(t) \quad \text{for } i = 1, 2, \dots, 6 \quad (2)$$

Where $n(t)$ is the normalized neutron density, t is the time, ρ_t is the total reactivity, β is the total fraction of the delayed neutron, Λ is the mean neutron generation time, λ_i is the decay constant of delayed neutron precursor, C_i is the concentration of the i -th delayed neutron precursor.

The total reactivity considers the external reactivity, Doppler effects, and expansion effects in fuel, clad, and coolant:

$$\rho_t = \rho_0 + \underbrace{1.1K_D \ln \left(\frac{\langle T_f \rangle_{out}}{\langle T_f \rangle_{in}} \right)}_{\text{Doppler}} + \underbrace{\alpha_f \Delta \langle T_f \rangle}_{\text{Fuel expansion}} + \underbrace{\alpha_{cl} \Delta \langle T_{cl} \rangle}_{\text{Clad expansion}} + \underbrace{\alpha_c \Delta \langle T_c \rangle}_{\text{Coolant expansion}} \quad (3)$$

Where ρ_0 is the reactivity in a stationary state, K_D is Doppler constant, α is the thermal expansion coefficient and the subscripts f, cl, c correspond to fuel, clad, and coolant respectively. And $\Delta \langle T_f \rangle = \langle T_f \rangle - \langle T_f \rangle_0$, $\Delta \langle T_{cl} \rangle = \langle T_{cl} \rangle - \langle T_{cl} \rangle_0$, $\Delta \langle T_c \rangle = \langle T_c \rangle - \langle T_c \rangle_0$, the subscript 0 refers to the steady state. The nuclear parameters used in these simulations are presented in Table III.

The thermal power in the subchannel is given by:

$$P(t, z) = P_0 n(t) \psi(z) \quad (4)$$

Where P_0 is nominal thermal power per fuel rod and $\psi(z)$ is the axial power distribution.

Table III. Reactivity coefficients [5].

Coefficient	Units	Value
K_D	pcm	-555 pcm
α_f	pcm/K	-0.232 pcm/K
α_{cl}	pcm/K	0.045 pcm/K
α_c	pcm/K	-0.271 pcm/K

3.2. Fuel heat transfer model

The temperature distribution in the annular fuel pin, considering each section of the rod is given by:

$$(\rho Cp)_\gamma \frac{\partial T_\gamma}{\partial t} = \frac{k_\gamma}{r} \frac{\partial}{\partial r} \left(r \frac{\partial T_\gamma}{\partial r} \right) + q'''(t, z) \quad \text{for } \gamma = f, cl, c \quad (5)$$

$$q'''(t, z) = 0 \quad \text{in } \gamma = cl, c \quad (6)$$

The initial condition is given by $T(r, 0) = f(r)$, and the boundary conditions are:

$$\frac{dT_f}{dr} = 0 \quad \text{at} \quad r = r_0 \quad (7)$$

$$-k_g \frac{dT_g}{dr} = h_g (T_f - T_g) \quad \text{at} \quad r = r_f \quad (8)$$

$$-k_{cl} \frac{dT_{cl}}{dr} = h_g (T_g - T_{cl}) \quad \text{at} \quad r = r_g \quad (9)$$

$$-k_{cl} \frac{dT_{cl}}{dr} = h_c (T_{cl} - T_c) \quad \text{at} \quad r = r_{cl} \quad (10)$$

Where ρ is the density, Cp is the specific heat capacity, k is the thermal conductivity, h_c is the coolant heat transfer coefficient, h_g is the gap conductance, subscript g refers to gap section, and q''' is the heat source given by:

$$q'''(t, z) = \frac{P(t, z)}{V_f} \quad (11)$$

Where $P(t, z)$ is the subchannel power and V_f is the fuel volume. The physical properties of the fuel as a function of temperature are given by Carbajo et al. [6].

3.3. Thermofluid model

The thermofluid in the core is modeled using mass, energy, and momentum balances Eq. 12-14, the physical properties of the coolant are given in Table II.

$$\alpha_c \rho_c \frac{\partial T_c}{\partial t} - \frac{\partial G}{\partial z} = 0 \quad (12)$$

$$\frac{\partial T_c}{\partial t} = \frac{P_m h_c (T_{cl} - T_c)}{A_f \rho_c C p_c} - \frac{G}{\rho_c} \frac{\partial T_c}{\partial z} \quad (13)$$

$$\frac{\partial G}{\partial t} = -\frac{\xi_{fr}}{2} \left(\frac{G^2}{\rho_c L} \right) - \frac{\partial}{\partial z} \left(\frac{G^2}{\rho_c} \right) - \rho_c g \quad (14)$$

In these equations G is the mass flux, P_m is the wet perimeter, A_f is the flow area (cross-sectional area), L is subchannel length and g is the gravitational acceleration. In the momentum balance given by Ec. (14), the friction coefficient is calculated with the following equation:

$$\xi_{fr} = \frac{0.210}{\text{Re}^{0.25}} \frac{L}{D_h} \left[1 + \left(\frac{l_p}{D_{rod}} - 1 \right)^{0.32} \right] \quad (15)$$

Where D_{rod} is the rod diameter, the rod pitch l_p . The hydraulic diameter for each array is given by:

$$D_h = \frac{4}{\pi D_{rod}} \left(\frac{\sqrt{3}}{2} l_p^2 - \frac{\pi D_{rod}^2}{4} \right) \quad (16)$$

4. RESULTS AND DISCUSSION

In the study of nuclear reactors, the analysis of the responses in steady state and with some transients is important from the point of view of safety, since it allows determining the limits and characteristics of the materials, as well as identifying possible control systems (i.e., flow and temperature of the reactor and control rods).

During the study of transient states, it is necessary to know a) if after the variation produced the reactor reaches another stationary state, which means that the system is stable, and b) if it is stable, how it behaves the reactor throughout the transition between the initial and final steady states.

4.1 Steady-state

In the stationary state it can be observed which are the nominal operating characteristics of the reactor, that is, without any disturbance.

In Figure 1, the radial profile at different heights of a fuel rod is presented, the first section (FUEL) corresponds to the fuel, the next is the gap and the third is the clad (CLAD). At the beginning of the bar there is the lowest temperature in all sections, in the intermediate part there is the highest axial temperature, and radially it is the highest in the fuel and gap area, however in the clad section, it is less than the temperature at the top of the bar. This behavior is because the axial power distribution of the reactor is not uniform.

In Figure 1, the axial profile of temperatures in the fuel rod and the coolant is presented, the fuel profile follows the axial power distribution. The temperature of the coolant increases due to the absorbed heat flow, the coolant inlet temperature is 673.15K and the outlet is 753.15K.

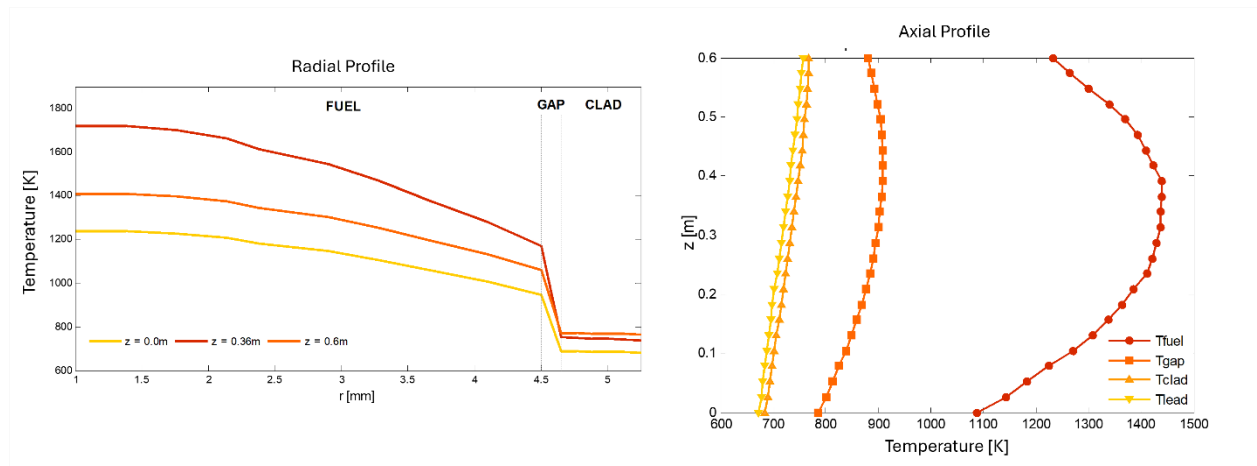


Figure 1. Steady-state temperatures profile of ALFRED reactor.

4.2 Transient state

A transient is defined as an event in a nuclear power plant, which proceeds from a normal state to an abnormal state. This event is produced when there is a disturbance that generates a change in the operating parameters.

In this work, numerical experimentation was carried out with two transients to the reactor: (1) Unprotected Transient Over Power, with insertion of reactivity in the core and, (2) Unprotected Loss of Flow, simulating a change in the inlet velocity of coolant.

The first transients can be generated by insertion or extraction of the control rod, it was considered that the reactivity changes from +20 pcm, -20 pcm, +10 pcm, and -10 pcm, these changes are considered as an Unprotected Transient Over Power. In Figure 2, the effect of reactivity change on power is presented, for positive reactivity changes power increases, and, for negative changes power decreases.

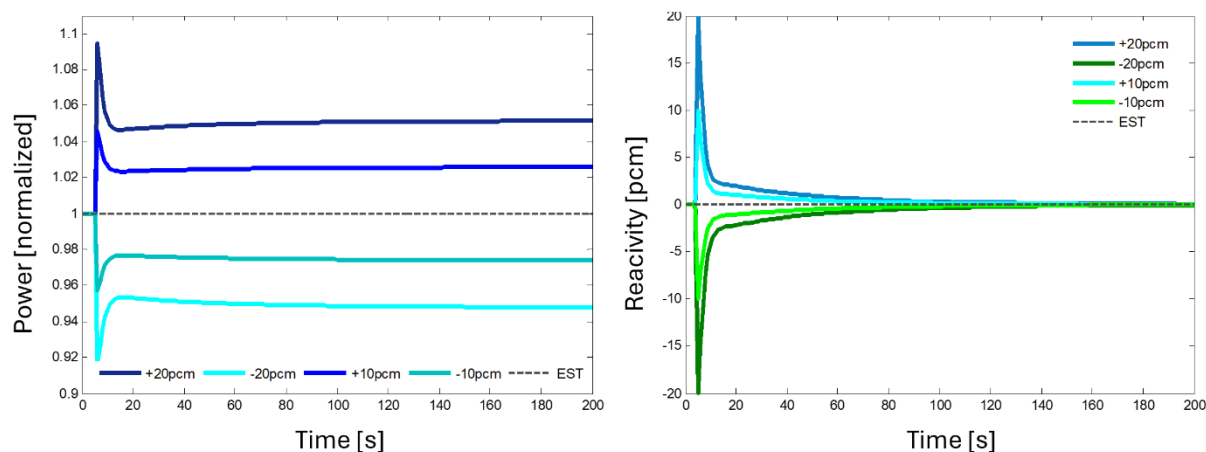


Figure 2. Power and reactivity behavior during an Unprotected Transient Over Power.

The second transient simulation was the change of inlet coolant velocity, which means a change in the mass flow. The nominal speed is 2 m/s, the proposed variations are 1 m/s, 1.5 m/s, 2.5 m/s and 3 m/s. In Figure 3, the results of the transient are presented.

In this case, the effect of variation in velocity is more representative when the value is lower than the nominal, this is due to the change in reactivity. If the velocity decreases, the power decreases; followed by a coolant temperature increase, as well as the fuel, gap, and cladding, a decrease in reactivity will appear.

In Figure 3, is possible to observe the effect of this transient on the reactivity. Like the power behavior, the effect is greater when velocity decreases. During the first 20 seconds, there is a large change in reactivity, and then the reactivity decreases to reach a steady state again.

In the opposite case, when the velocity increases, the reactivity increases and in the same way the power, although the effect is less.

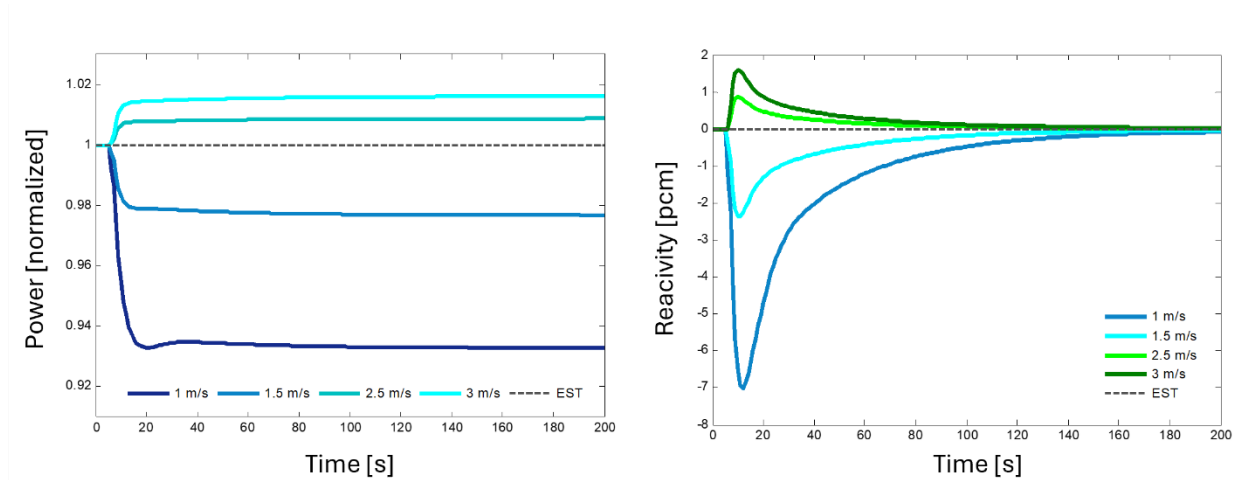


Figure 3. Power and reactivity behavior during an Unprotected Loss of Flow.

5. CONCLUSIONS

Numerical experiments were carried out in a steady state, obtaining results of temperatures within the margins established in the ALFRED design. These temperatures are important for the safe operation of the reactor. The maximum fuel temperature was 1720.06 K, which remains below the design limit, which is 2273.15 K. The maximum temperature of the cladding obtained is 749.43 K, that is, 73.72 K less than the design limit. The outer coolant temperature was 753 K, which is equal to the limit established in the ALFRED design.

From the beginning of the transient state, the system returns to a steady state after 150 seconds approximately (in typical reactors it is an order of magnitude less). For the Unprotected Loss of Flow Accident, the highest temperatures were obtained with 1 m/s, for the fuel it is 1290.48 K, 800.72 K for the cladding, and 783.85 K for the coolant lead outlet.

The power, when the speed is 1 m/s, is 0.93 and the reactivity is -7 pcm, where the greatest contribution is negative due to refrigerant expansion. In the reactivity transient, Unprotected transient Over Power, with an increase of 20 pcm, the power increased by 10%. The fuel temperature is 1293 K, the clad is 736.91 K and the coolant is 720.46 K.

The simulations carried out show the importance of having tools to simulate the behavior of the reactor under transient events to know if the reactor maintains the power and reactivity under the limits, impacting the temperature of the fuel rod, coolant, and structural materials.

ACKNOWLEDGEMENTS

Pérez-Valseca, acknowledges the financial support from the Basic Science and Frontier Project 2023-2024 Reference CBF-2023-2024-2023 founded by the National Council of Humanities, Sciences and Technologies, CONAHCyT.

REFERENCES

1. Generation IV International Forum. *A Technology Roadmap for Generation IV*. Nuclear Energy Systems, Issued by the U.S. DOE Nuclear Energy Research. Advisory Committee and the Generation IV International Forum, GIF-002-00. 2002.
2. “*Generation IV International Forum Website*”, https://www.gen4.org/gif/jcms/c_9260/Public. (2024)
3. Grasso G, Petrovich C, Mattioli D, Artioli C, Sciora P and Gugiu D, “The core design of ALFRED, a demonstrator for the European lead-cooled reactors”. *Nuclear Engineering Design* **287**: 287–301 (2014)
4. Alemberti, A., Smirnov, V., Smith, C.F., Takahashi, M., “Overview of lead-cooled fast reactor activities”. *Prog. Nucl. Energy* **77**, 300–307. (2014)
5. Aufiero M, Cammi A, Fiorina C, Luzzi L, Sartori A, “A multi-physics time-dependent model for the Lead Fast Reactor single-channel analysis”, *Nuclear Engineering and Design* **256**:14–27 (2013).
6. Carbajo JJ, Yoder GL, Popov GS and Ivanov VK, “A review of the thermophysical properties of MOX and UO₂ fuels”, *Journal of Nuclear Materials*. **299**:181–198 (2001).

Track 4

Operation, Maintenance, Materials, and New Designs

Probabilistic Risk Assessment of the HVAC Extraction Hoods of a Radioisotope Plant

Omar Pérez Parrazal and Pamela F. Nelson

School of Engineering, National Autonomous University of Mexico

C.U., Coyoacán, 04510, Mexico City, CDMX

parrazalomar@gmail.com; pnelson_007@yahoo.com

Abstract

This paper presents the advance in a pilot case study on the design of the Heating Ventilation and Air Conditioning System (HVAC) system of a radioisotope production plant. The objective of the project is to develop a methodology to incorporate risk analysis into all stages of plant design. This methodology is to be incorporated into a nonmandatory appendix for the “Plant System Design Standard” (PSDS), under development by the American Society of Mechanical Engineers (ASME). The analysis presented here provides an example of how to perform risk evaluation for initial design. The accident sequences developed include impacts on health, safety, and environment (HSE) as well as on production. This pilot case study presents an example of a Probabilistic Risk Assessment model of the extraction hoods section of the exhaust system of the HVAC. A schematic diagram was used to develop its fault tree to obtain its probability of failure. The component with the highest contribution to risk was identified. A modification in the design was made to calculate the failure probability reduction. An event tree was developed for the “Spill and spray accident” and used to identify the consequences of different combinations of failures. Once all the systems in the event tree are modeled, it will be possible to determine other changes to the design that will reduce HSE and production impacts. Further uses of the methodology will include being able to use the results to identify the dose in REM for the different sequence frequencies and compare to the frequency-consequence curve used for nuclear reactor design.

1. INTRODUCTION

Risk, as defined in this paper, is the chance or probability that a person will be harmed or experience an adverse health effect if exposed to a hazard. Risk can be characterized by identifying what can go wrong, how often something will go wrong, and what are the negative impacts when something goes wrong. In general, risk is in all activities and everywhere around us, and there are diverse methodologies to carry out risk analysis, either qualitatively (Checklist, PHA, What-if, FMEA or HAZOP, etc.) or quantitatively (FMECA, HAZOP with frequency and consequence classification, counting by parts, Fault trees, Event Trees, LOPA, PRA, etc.) depending on the depth of the analysis.

Of these risk analysis methods, the PRA methodology is used the least in the industrial sectors. Risk evaluation on an operating plant or for plant/system design has been adopted by the nuclear industry. It is beginning to be used by other industries with applications like in electrical transmission systems [1] and railway lines [2]. A new standard is being developed by American Society of Mechanical Engineers (ASME) that focuses on design for any technology-neutral facility (electrical power generation, oil refining, oil and natural gas production, petrochemical, chemical, pharmaceutical, etc.), with potential for significant hazards to the health and safety of the public, the worker, and the protection of the environment. In this context, plant risk is characterized by identifying the scenarios that can have an adverse impact on the operation and the health, safety, environment (HSE) from both internal and external sources.

The assessment of the frequency and consequence of those scenarios that can lead to interruption in production as well as to HSE impacts is performed. This analysis considers the probability that plant equipment and associated design features can prevent or mitigate the impacts of these events. [3] If it is found that the design does not prevent or mitigate the impacts sufficiently, changes are made to the design in order to reduce the risks.

As a way to cover this necessity for a technology-neutral design standard, ASME has embarked on the development of this Plant System Design Standard (PSDS). The objective of this paper is to describe the pilot study being conducted to support the research project “ASME STLLC Project 200: Target Reliability for Mechanical Fluid Systems”. This study applies the PSDS to improve the design of a radioisotope production plant, and the results of some improvements on the HVAC system are presented here.

2. RISK EVALUATION FOR INITIAL DESIGN USING PSDS

As mentioned above, the ASME PSDS (in process of development) will provide a new approach for designing production plants with potential for significant hazards to the health and safety of the public, the worker or the environment. [3]

This Standard has three main focuses:

- Incorporate and integrate systems engineering design processes, practices, and tools with traditional architect engineering design processes, practices and tools.
- Conduct plant process hazard evaluation and risk analysis in the early phases of design that:
 - Provide early identification of hazards and strategies to avoid and mitigate them.
 - Advance as the design matures.
 - Provide structure to the development of a quantitative risk assessment.
- Incorporate and integrate risk informed probabilistic design processes, practices and tools with traditional deterministic design processes using reliability and availability targets.

This paper concentrates on the second bullet, that is, conducting risk analysis of the design. In this case, the plant already exists, and the objective is to show how to use the Standard to improve the design.

2.1. Risk Evaluation for Initial Design Activities

Of all activities included within the standard, this activity evaluates risks based on available design information and generates process, production, external hazards, and risk information to inform design. This information includes the lists of hazards or initiating events, sequences and likelihoods, consequences, and recommended functions for barriers to be included in the design to avoid or mitigate identified hazards. It also includes the validation of risk evaluation results against stakeholder identified HSE objectives and production goals. [4]

Risk evaluations at the beginning of initial design are limited by available design information and the conformed contract technical requirements (CCTRs). As design evolves, additional design information is developed enabling the evaluation of risks in more detail. This is an iterative exchange of information between risk evaluation and design. The initial risk evaluation outputs represent available information at the completion of initial design. At this early stage of design, it is expected that the low level of design detail and hazard information will constrain development of risk sequences, consequences, and evaluations.

To develop this risk evaluation for initial design it is necessary to carry out the following activities:

1. *Define the design information and the conformed contract technical requirements (CCTRs):* At the beginning of the initial design, it is necessary to collect all the information provided by the customer and the norms and regulations that pertain to the project. The documents expected to be obtained are: technical requirements, customer requirements, regulatory requirements, license design requirements, siting requirements and site conditions, industry codes and standards, design criteria, production and performance goals, HSE objectives and measures, process descriptions, identified hazardous materials and associated requirements and regulatory, early risk evaluations, etc.
2. *Identify hazards and initiating events:* In this section, lists of hazards and initiating events need to be compiled to perform risk evaluations that inform initial design for applicable plant operating states. The hazards and initiating events that affect HSE, production or both typically included are:
 - Internal related hazards and initiating events, such as failure of equipment and human errors.
 - External related hazards and initiating events, such as earthquakes and floods.
3. *Identify sequences:* Generate initial lists of potential event sequences that can result in HSE or production consequences. A sequence typically includes: initiating events, subsequent failure events, plant responses, preventive and mitigative actions, and resulting consequences. The health, environmental, and safety consequences typically include both on-site and off-site. The initial sequence lists also include any assumptions, open items, and missing information related to identifying the sequence.
4. *Characterize unavailabilities:* Determine unavailabilities of plant primary functions considering uncertainties, dependencies, and impacts. The unavailability of a system or component includes its failure, as well as the time it is not available for service due to inspection, maintenance and testing.
5. *Evaluate likelihoods:* Estimate probabilities that will be used to establish the HSE and production risks to inform initial design.

6. *Evaluate consequences*: Generate a list of potential consequences to be used as inputs to the characterization of risk activities and inform initial design.
7. *Characterize risk*: In this section, the output is a description of the risk associated with the plant. This requires a characterization of the risk level represented by each sequence, the unavailabilities, the likelihood, and the resulting consequences.
8. *Determine acceptable risk*: In this section, a comparison is made between the characterized risk levels based on the current design and the originating HSE and production goals established for the facilities in order to determine if the risk is acceptable. If the originating goals are satisfied, then the design continues to its next logical phase, if the goals are not met, then the reasons for not meeting the goals are identified and provided as an input for the next step for further evaluation.
9. *Define targets and barriers*: If the risk goals are not met, barriers are needed to reduce the risk. These can be physical (such as a wall), adding another cooling train, or something organizational, such as adding emergency procedures and training on them. In order to reduce the risk, it may also be necessary to adjust the unavailabilities of the systems and components. This can be accomplished by replacing components with lower probability of failure, or implementing or designing components that require less maintenance, inspection and testing.
10. *Document availability targets*: This final section is performed by repeating the step 4, with the updated information resulting from the changes proposed in the targets and barriers section, the risk and unavailability targets for HSE and production, and the new risk characterization. Risk targets can be expressed in terms of unavailability targets. Availability targets can be determined from unavailability targets as they are complementary mathematical functions.

3. CASE STUDY

The Heating Ventilation and Air Conditioning System (HVAC) from a Radioisotope Production Facility (RPF) was chosen for a pilot case study for the project. For the focus of this paper, only the extraction hoods section of the HVAC are addressed. The information collected in this section corresponds to the activities of the first three steps in Section 2.

3.1. Radioisotope Production Facility

Radioisotope production facilities (RPF) are typically production plants where radioisotopes are extracted from spent fuel reprocessing (LEU or HEU) or produced through cyclotrons by the bombardment of stable isotopes with protons to convert them into radioisotopes. Some radioisotopes produced have proven to be useful for diverse industries such as medical, industrial, food and agriculture, environmental, and even some daily life products applications.

The vast majority of demand for fission radioisotopes is for ^{99}Mo (for obtaining $^{99\text{m}}\text{Tc}$ due to its medical applications). Supply capacity is always substantially below demand due to decay of ^{99}Mo in transit.

The type of plant used for this case study is a LEU reprocessing plant for obtaining ^{99}Mo and a lot of the information is available in the World Nuclear Association web page. [5]

3.2. HVAC System

The HVAC system, also referred to as the ventilation system, is designed to ensure that temperature, relative humidity, and air exchange rates are within the design-basis limits for personnel and equipment. It should be designed to ensure that all normal sources of airborne radioactive material are controlled so that occupational doses do not exceed the requirements of Title 10, Code of Federal Regulations, Part 20, “Standards for Protection Against Radiation” (10CFR20).

3.2.1. Design basis

The HVAC is designed to:

- Maintain the number of air changes per hour to achieve acceptable activity concentrations.
- Confine the environment of areas or systems with hermetic valves in case of emergencies, avoiding the dispersion of contaminated air.
- Ensure a direction of air flow inside the building from the areas with the lowest risk to the areas with the highest risk of contamination, by staggering pressures.
- Guarantee environmental protection, filtering and controlling (through deferred monitoring of gases and aerosols), the air that is expelled outside. All air released into the atmosphere is previously subjected to absolute HEPA filters that guarantee an efficiency of 99.97%, and if necessary, it is also passed through activated carbon filters.
- The combined application of the principles of source reduction and the introduction of multiple barriers of protection for members of the public through the use of multiples stages of air purification.
- Confine significant quantities of radioactive material through redundancy, maintaining a high degree of continuity in the production processes.

3.2.2. System description

The ventilation of the production facility as a closed-circuit introduces a dynamic protection barrier for the public; in the working zones a mixture of open-circuit and closed-circuit combination is used to achieve an adequate economy and safety. The ventilation system consists of two subsystems:

- The injection system maintains the activity concentrations of the work environment to acceptable values, applying dilution principles.
- The extraction system, that is done through four subsystems segregated according to actual or potential air contamination: Cells and Glove Boxes, Radiochemical Hoods, Hot Hallway, and the upper and lower production and controlled zones. The purification of the extracted air is carried out with absolute filters and activated carbon absorbers. The use of purification steps is a combined application of the principles of source reduction and multiple barriers of protection for members of the public.

From the Control Room it is possible to manually enable an additional activated carbon stage for the extraction of cells and glove boxes and another for the extraction of the hot corridor.

3.2.3. Extraction hoods

The extraction hoods section of the HVAC consists of 3 sections:

1. Hermetic closure: This section serves as a barrier in case of emergencies avoiding the dispersion of contaminated air. It is composed of an automatic hermetic shut-off valve in series with a manual regulation damper.
2. Air filtering: This section consists of two HEPA absolute filters in parallel in simultaneous operation. Each HEPA filter has its pair of manual closure dampers to favor dynamic confinement, as well as to serve as a barrier for maintenance of the HEPA filter.
3. Air extraction: This section consists of two centrifugal fans in parallel, one in use and one in standby. The fan expels the filtered air to the outside. Each centrifugal fan has its own manual closure damper and automatic damper. The manual damper function is a barrier for when maintenance is needed and the automatic damper function as a regulator of the extraction air.

A schematic view of the extraction hoods of the HVAC system is shown below in Figure 1.

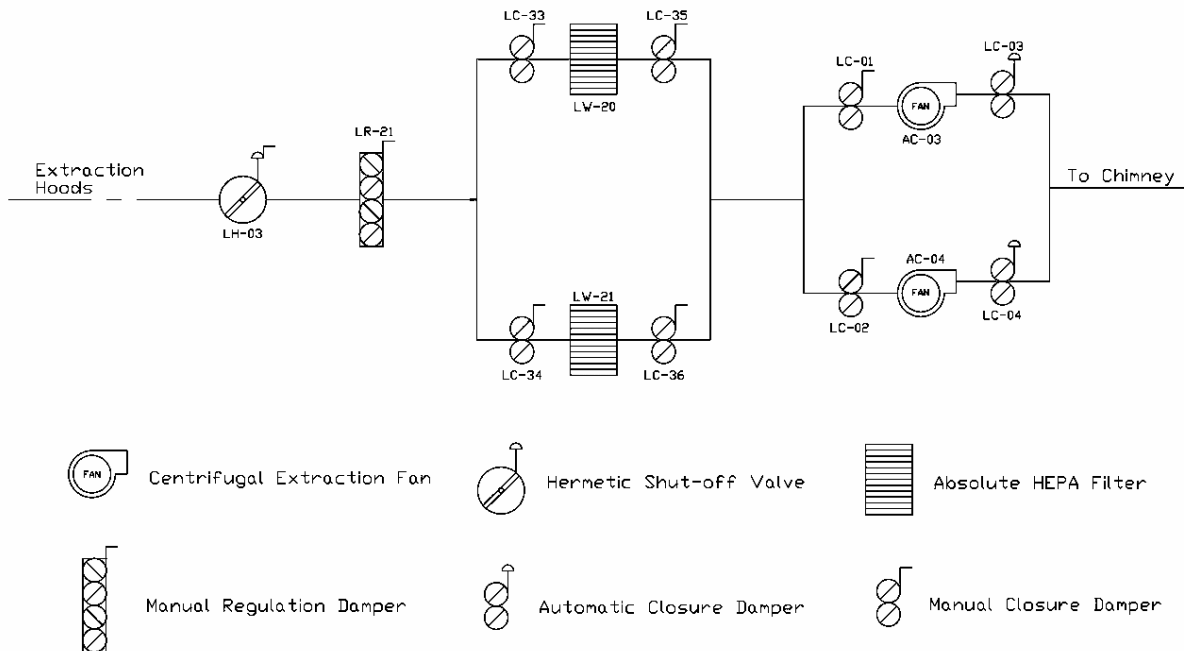


Figure 1. HVAC Extraction Hoods System

3.3. Spill and Spray Accident Analysis

Liquid solution spill and spray events causing radiological exposure present a hazard to workers from direct exposure and inhalation to the public in the unmitigated scenario. The Process Hazard Analysis (PHA) reviewed for this study [6] also identifies fissile solution leaks with worker safety concerns.

3.3.1. Initial Conditions

Initial conditions of the process are described by a tank filled with process solution. Multiple vessels are projected to be at initial conditions throughout the process, and the PHA reduced the variety of conditions to the following three configurations that span the range of potential initial conditions:

- A process tank containing low-dose uranium solutions, with no or trace quantities of fission product radionuclides located in a contact maintenance-type of enclosure typical of the target fabrication systems.
- A process tank containing high-dose uranium solutions located in a hot cell-type of enclosure typical of the irradiated target dissolution system.
- A process tank containing ^{99}Mo product solution located in a hot cell-type of enclosure typical of the molybdenum purification system (this condition does not lead to a criticality safety concern).

In each case, a vessel is assumed to be filled with process solution appropriate to the process location with the process offgas ventilation system operation. A level of monitoring system is available to monitor tank transfer and stagnant storage volumes on all tanks processing LEU or fission product solutions.

3.3.2. Identification of initiating event conditions

The accident initiating event is generally described as a process equipment failure, but also could be operator error or an event initiated by a fire/explosion. Multiple mechanisms were identified during the PHA that result in the equivalent of a failure that spills or sprays the tank contents, resulting in rapid and complete draining of a single tank to the enclosure in the vicinity of the tank location.

3.3.3. Description of accident sequence

The accident sequence is described as follows:

1. The accident starts depending on the failure
 - a) Tank leakage: Process vessel failure or personnel error cause the tank contents to be emptied to the vessel enclosure floor in the vicinity of the leaking tank.
 - b) Spray leakage: The process line, containing pressurized liquid, ruptures or develops a leak during a transfer, spraying solution into the source or receiver tank enclosure and transferring leaked material to an enclosure floor in the vicinity of the leak.
2. Tank liquid level monitoring and liquid level detection in the enclosure floor sump region alarms, informing operators that a tank leak has occurred.
3. Processing activities in the affected system are suspended based on the location of the sump alarm.
4. Operators identify the location of the leaking vessel and take actions to stop additions to the leaking tank.

5. A final stable condition is achieved when solution accumulated in the sump has been transferred to a vessel available for the particular sump material and removed from the enclosure floor.

3.3.4. Barrier function

The process vessel enclosure floor, walls, and ceiling will provide a barrier that prevents transfer of radioactive material to an uncontrolled area during a liquid spill or spray accident. For accidents involving high-dose uranium solutions and ⁹⁹Mo product solutions, the process vessel enclosure floor, walls, and ceiling will provide shielding for the worker. The enclosure structure barriers are to function throughout the accident until (and after) a stable condition has been achieved.

The process enclosure secondary confinement (or ventilation system) will provide a barrier to prevent transfer of a radioactive material to an uncontrolled area during a liquid spill or spray accident from radioactive material in the airborne particulate and aerosols generated by the event. The secondary confinement system is to function throughout the accident until a stable condition has been achieved.

The process enclosure sump system represents a component credited for preventing the occurrence of a solution-type accidental nuclear criticality due to spill or spray of fissile material. The sump system is to function throughout the accident until a stable condition has been achieved.

4. Probabilistic Risk Assessment Application

In order to quantify the models, a generic database “Component Reliability Data for Use in Probabilistic Safety Assessment” [7] was used to prepare an analysis using the PRA methodology through the application program Saphire 8.

4.1. Event tree

Event trees are specific diagrams to help represent the spectrum of possible outcomes of sequences of events from an initiating event to an end state [8]. These event trees are modeled as in the following example (Figure 2):

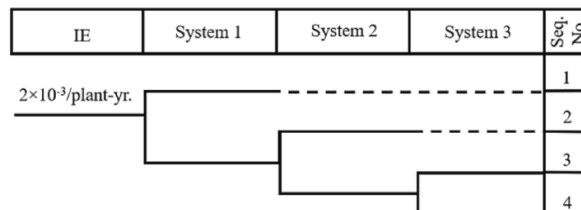


Figure 2. Event tree

The event tree designed for the “Spill and Spray Accident” shown in Figure 3, presents six end states that present different results depending on how the accident develops.

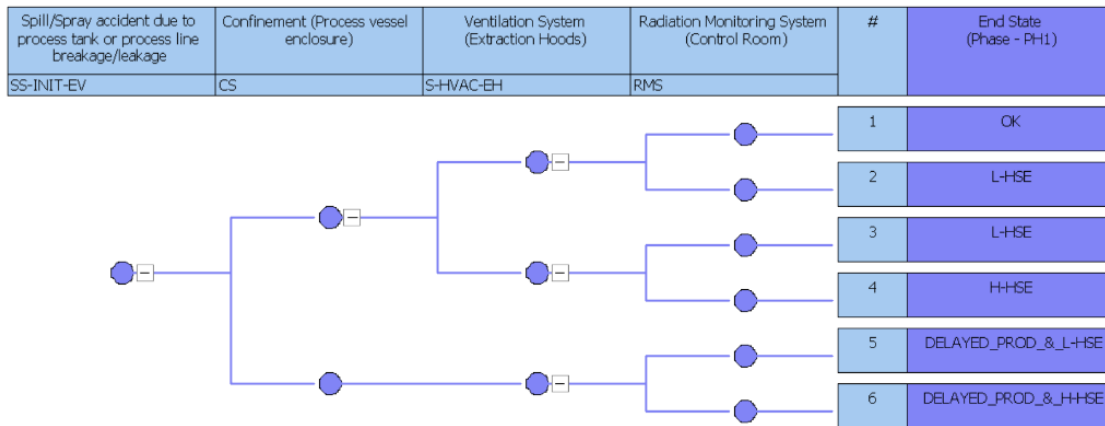


Figure 3. Spill and spray accident event tree

4.1.1. Sequence 1 (end state OK)

For this first end state, it is considered that after the initiating event, every mitigation system will operate as is intended and no HSE target will be affected.

4.1.2. Sequence 2 (L-HSE)

For this second end state, the Radiation Monitoring System fails in a way that the worker does not receive notification, or the notification is delayed, so the worker receives a low dose for being in or near the place of the initiating event. Only a low dose is received because the other mitigation systems are working as intended.

4.1.3. Sequence 3 (L-HSE)

For this third end state, the system that fails is the HVAC causing a little release from the confinement where the accident occurred, but the workers are aware of the event and actions being taken for mitigating this accident. Because of this, this accident can cause a low dose exposure for the workers repairing the section that failed in the HVAC system or a small radioactive release to the environment.

4.1.4. Sequence 4 (H-HSE)

For this fourth end state, the confinement is the only system and barrier that functions. This sequence causes the workers receive a higher dose than before for being near or in contact with the place of the accident due to the failure of the alarms and notifications of the Radiation Monitoring System. Also, a small amount of radioactive release to the environment can be produced.

4.1.5. Sequence 5 (Delayed_Prod_ & L-HSE)

For this fifth end state, if the process vessel enclosure or the sump (confinement) where the accident occurs fails, the ventilation system cannot maintain the pressure inside thus failing the confinement of a radioactive release of the room, which can affect the workers. Since the Radioactive Monitoring System remains functional, the workers can receive timely notification and actions can be performed. However, because there are several actions necessary to correct the failures, the workers are distracted from the production activities which causes production delays. For the same reason, low dose to workers is also considered.

4.1.6. Sequence 6 (Delayed_Prod_ & H-HSE)

For this sixth end state, all systems may fail causing radiation release that may affect the workers and a small release to the environment until some worker identifies the accident and actions are taken for mitigating the accident.

4.2. Fault tree

In order to be able to evaluate the frequency of the sequences in the event tree, a fault tree is developed for each system in the event tree headers. Fault trees are specific diagrams to model failures of components in a system or mitigating functions [8]. Fault trees are modeled using the symbols in the following example (Figure 4).

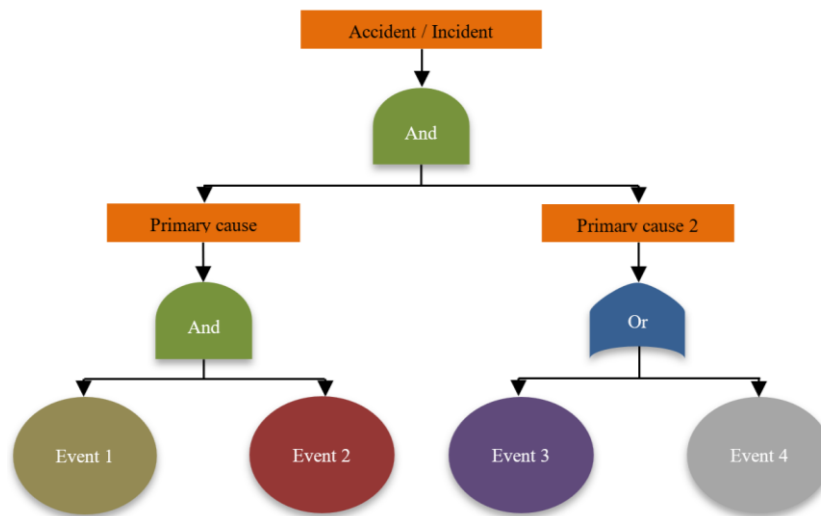


Figure 4. Fault tree logic

Logic commands are used in the fault trees. In the example, “And” refers to the failure of Event 1 and Event 2 lead to the failure of Primary cause, and “Or” means that the failure of the Event 3 or Event 4 leads to failure of Primary cause 2. The “And” means the probabilities of Event 1 and Event 2 are multiplied to get the probability of failure of Primary cause, and in the case of the “Or” the probabilities are summed.

The HVAC extraction hoods fault tree was developed based on the schematic diagram presented in Figure 1 and shown in Figure 5. (For practical purposes, the fault tree only shows the section where the component with the highest risk appears due to the length of the complete diagram).

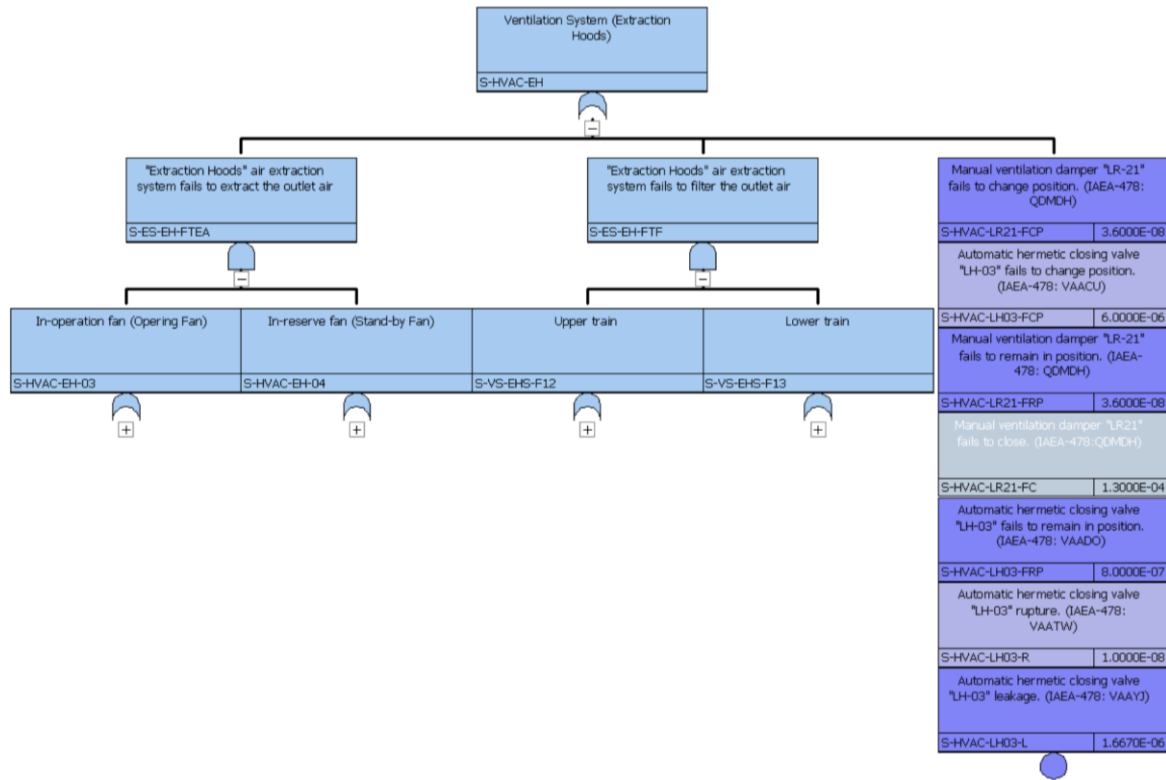
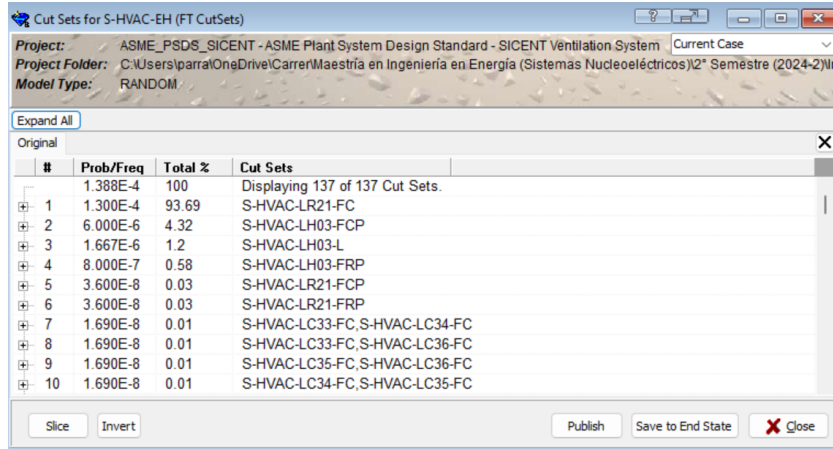


Figure 5. HVAC extraction hoods fault tree

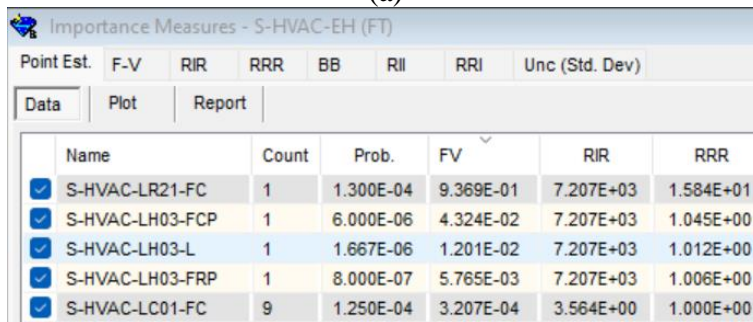
4.3. Results

The fault tree was evaluated to calculate the probability of failure of the extraction hoods section of the HVAC, the cut sets and the importance measures. The cut sets contain every combination of components that fail the system. The risk importance measures are indexes to rank structures, systems, and components (SSCs), with the Fussell-Vesely (F-V) and the Risk Increase Ratio (RIR) and Risk Reduction Ratio (RRR). F-V measures the contribution of the component to the failure probability and RIR measures the risk increase if that component always fails and RRR measures the risk reduction when the component never fails.

Figure 6 shows the failure probability of the HVAC Extraction Hoods section is 1.39E-04 with 137 cut sets, and the component that contributes most to system failure is the failure to close the manual damper, "S-HVAC-LR21" with high importance measure for F-V of 0.937 and a RIR of 7.21E+03. (Threshold values are 0.005 for F-V and 2 for RIR). This failure contributes 93.69% to the probability of failure of the Extraction Hoods section.



(a)



(b)

Figure 6. (a) First fault tree results (b) First importance measures

One possibility to reduce the design failure probability, is to change the component to another model (from a manual regulation damper to an automatic one) with a lower failure probability (1.2E-06). The new results (Figure 7) show that the failure probability of the system decreases from 1.39E-04 to 9.96E-06. This contribution of this failure reduces to only 12.05% probability of failure of the Extraction Hoods section. This represents a large reduction in system failure probability, demonstrating the use of PRA in design.

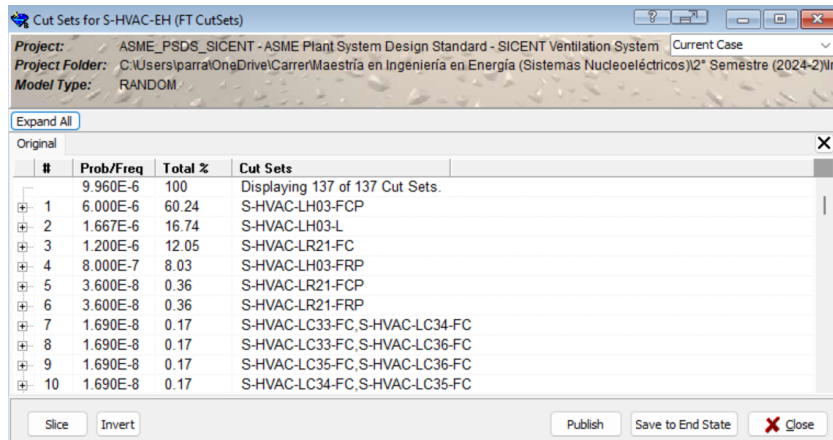


Figure 7. Second fault tree results

5. CONCLUSIONS

The application of this new PSD standard is helping define the documentation basis for understanding the purpose of the system itself, to identify hazards, initiating events and sequences, and for characterizing unavailabilities and evaluating the likelihoods and consequences, at least for this section of the HVAC system.

Also, while applying this standard, the application of the PRA methodology for characterizing the system using fault trees and event trees for the accident, as well as the HSE targets, are showing how it can be applied for any neutral-technology production plan.

The results demonstrate how the components that most affect the system can be identified and modified. In this case, when the damper “LR-21” fails to close, the extraction hoods section of the HVAC fails. It was shown how to improve the system design by reducing its probability of failure.

This pilot case requires further work, including the use of PRA methodology to define unavailability targets for the systems to meet the HSE and production goals. For future work it is expected to obtain the results of the event tree for the “Spill and Spray accident” for the complete HVAC system and prepare a graph that can help visualize the relation of the failure frequency of the sequences to the radiation dose emitted. This will be completed using regulations and norms that are relevant to this type of production plant.

ACKNOWLEDGEMENTS

Thanks to the ASME STLLC Project 200: Target Reliability for Mechanical Fluid Systems and to the National Council of Humanities, Science and Technology (CONAHCYT) for providing economic support to Omar Pérez for the accomplishment of this work that is part of his master’s research.

REFERENCES

1. Oliva, J. D. J. R. (2019). The application of Probabilistic Safety Assessment to Electric Transmission Systems. <https://www.redalyc.org/journal/3291/329164315008/movil/>
2. Grande Andrade, Zacarias, Enrique Castillo Ron, Maria Nogal, y Alan O’Connor. «Probabilistic Safety Analysis of High Speed and Conventional Lines Using Bayesian Networks». En *XII Congreso de ingeniería del transporte. 7, 8 y 9 de Junio, Valencia (España)*, 362-71. Editorial Universitat Politècnica de València, 2016. <https://doi.org/10.4995/CIT2016.2015.3428>.
3. Ralph S. Hill, deLamare M., (2023), The ASME Plant Systems Design Standards, Bechtel, Virtual Technology Expo 2023.
4. 2-2.2 Risk Evaluation for Initial Design (H.3), 20240217 H.3 for Ballot.

5. “World Nuclear Association: Radioisotopes in Medicine” <https://world-nuclear.org/information-library/non-power-nuclear-applications/radioisotopes-research/radioisotopes-in-medicine>
6. Northwest Medical Isotopes, LLC “Part Two, Construction Permit Application, Chapter 13, Part 2 of 2”, ML15210A122. <https://www.nrc.gov/docs/ML1521/ML15210A122.pdf>
7. Agency, International Atomic Energy. «Component Reliability Data for Use in Probabilistic Safety Assessment». Text. *Component Reliability Data for Use in Probabilistic Safety Assessment*. International Atomic Energy Agency, 1988. <https://www.iaea.org/publications/733/component-reliability-data-for-use-in-probabilistic-safety-assessment>.
8. “U.S.NRC: Probabilistic Risk Assessment (PRA)”, <https://www.nrc.gov/about-nrc/regulatory/risk-informed/pr.html>
9. Castillo Hernández O. “Desarrollo de una metodología de diseño informada en riesgo de reactores nucleares”, [Tesis de doctorado]. UNAM <https://ru.dgb.unam.mx/handle/20.500.14330/TES01000850345>
10. Bartholdt, Michael, Bernd Bertsche, y Rudiger Schmidt. “Determining availability targets — A value managerial approach”. *2016 Annual Reliability and Maintainability Symposium (RAMS), Reliability and Maintainability Symposium (RAMS), 2016 Annual*, 1 de enero de 2016, 1-6. <https://doi.org/10.1109/RAMS.2016.7448085>.
11. Castillo-Hernández, Orestes, Manuel Perdomo-Ojeda, C. R. Grantom P.E., y Pamela F. Nelson. “Risk-informed design of advanced nuclear reactor: A target unavailability approach”. *Nuclear Engineering and Design* 416 (1 de enero de 2024): 112787. <https://doi.org/10.1016/j.nucengdes.2023.112787>.

Safety Analysis Methodology Development for Multipurpose Nuclear Microreactors.

Liz A. Ambruster Sánchez and Pamela F. Nelson
Universidad Nacional Autónoma de México Facultad de Ingeniería,
C.U., Coyoacán, 04510, CDMX, México
lizadeanezambrustersanchez@gmail.com; pnelson_007@yahoo.com

Abstract

Nuclear microreactors, also known as nuclear batteries, are highly innovative projects within the nuclear industry. They can generate from 1 to 20 MWth. They have very advanced technologies and offer many advantages: small size with the possibility of transport, low environmental footprint, long periods of operation without the need for refueling, diverse industrial and energy production applications, passive safety and factory assembly. The biggest barrier they face in order to operate is their licensing process since the current rules and regulations are obsolete compared to the variety of designs and technologies implemented by the new microreactor models. Other regulations are being developed such as 10CFR part 53 and the Licensing Modernization Project by the industry. Standards such as ASME's Plant System Design Standard is under development and forms the basis for this pilot case study presented in this paper. While these only instruct on what must be complied with, they do not explain how it should be done. In this paper, a safety analysis methodology for nuclear microreactors is developed from their initial design stage, providing an iterative process that can help reduce uncertainty for licensing and assure safe and productive designs. The prototype analyzed is the Mizton microreactor that is being developed at UNAM. This microreactor is in the initial design phase and is expected to be a high-energy neutron reactor cooled by heat pipes filled with liquid sodium. During this study, microreactor systems that have not yet been defined by the designer were assumed, such as the reactivity control mechanisms (ESS, Control Drums) and the primary and secondary containment, to be able to evaluate the core's safety. For this, a support matrix of function availability was developed, and five initiating events were modeled in the SAPHIRE software to reveal their sequences. The final states of these sequences are evaluated based on the dose according to the recommendation of the License Modernization Project (LMP).

1. INTRODUCTION

Nuclear batteries, or microreactors, are currently one of the most innovative projects in the nuclear industry and the ones that are most challenging for engineers and physicists to make them a reality. The small footprint they leave on the environment compared to large nuclear power plants; their high energy density; their ability to constantly generate from 1 to 20 MWe for long periods of time without the need for refueling; the promise of easy transportation and their diverse applications in the energy industry, mining, urban development and even maritime propulsion; are just some of their advantages.

Microreactor designs vary from the neutron spectrum to the type of coolant. The expectations are that some will be operational in 2026, such as eVinci (Westinghouse), Ubattery (Urenco) and Micro Modular Reactor (MMR, UltraSafe Corporation). [1]

One of the main limitations that prevents these new designs from being put into operation is their licensing. The norms and regulations in the nuclear industry seek to guarantee, above all, the safety of these facilities, but these rules are governed by standards based mainly on analysis of nuclear plants that have been operating since the 1960s and which are mostly light water reactors (LWR) [2].

A harmonization of nuclear standardization was considered necessary to allow the development of new norms and standards focused on the technology that characterizes each new reactor design [2]. These norms have been developed by several international organizations dedicated to the nuclear industry such as the International Atomic Energy Agency (IAEA), the Nuclear Regulatory Commission (NRC) of the United States, the American Nuclear Society (ANS) and the American Society of Mechanical Engineers (ASME) who is recently developing the Plant System Design standard (PSDS) intended to provide detailed guidelines on the design of systems in advanced industrial plants.

To date, no regulatory effort has materialized to speed up the licensing of these new microreactors, since the great diversity of designs and technologies prevents a standardization of licensing methodologies and processes.

The PSDS focuses on ensuring that the design of an industrial plant meets the requirements necessary to operate safely, efficiently and reliably. There is no reason to separate microreactors from the definition of an advanced industrial plant just because they belong to the nuclear industry.

Mexico is currently developing a microreactor design called MIZTON, since the benefits offered by this technology could have a large share in the national market, especially for operation in isolated areas and for distributed energy generation [3].

The Mizton, a microreactor being developed at UNAM, is in its initial design stage, so it requires a safety analysis for its future licensing, which, if carried out from this moment, would guarantee a faster and more efficient start-up.

For this reason, this work aims to develop a safety analysis methodology for multipurpose nuclear microreactors from their initial design stage, taking as a prototype the Mizton microreactor and following the requirements established in the PSDS. The risk analysis portion of the methodology is supported by the SAPHIRE software.

2. NORMS AND STANDARDS INVOLVED IN THE LICENSING OF NUCLEAR MICROREACTORS.

Mexico has one nuclear power station with two reactors, the Laguna Verde Nuclear Power Plant in Veracruz with BWR-5 technology from General Electric, a North American company. Mexico follows the regulations of the United States Nuclear Regulatory Commission (USNRC), that is, the Code of Federal Regulations (CFR).

10 CFR Part 50 provides an important regulatory framework of the NRC for all types of nuclear energy production and utilization facilities. Its approach, although somewhat outdated for new

technologies, ranges from design, construction and operation to decommissioning, but always ensuring the safety of the public, the environment and the workers at the facility [4].

According to this regulation, microreactors must submit a licensing application demonstrating that they comply with all Health, Safety and Environment (HSE) safety requirements and this must include a safety assessment just before their start-up or construction.

10 CFR Part 52 streamlines this process by reducing start-up times, as it allows for the granting of construction and operation licenses, it also facilitates standardization, making it easier to obtain a design certification that can be easily marketed while ensuring safety, and it is also flexible in terms of technology, since unlike Part 50, it allows for the innovation and applicability of new techniques as long as they demonstrate compliance with safety and reliability requirements; aspects that make it very attractive for the licensing of microreactors, but it is still mostly directed at light water-cooled reactors [4]. A probabilistic risk assessment (PRA) is now required for a license request.

Since many of the new reactors seeking licensing are advanced non-light water reactors, the Probabilistic Risk Assessment Standard for Advanced Non-Light Water Reactor Nuclear Power Plants was written (ASME/ANS) RA-S-1.4-2021)

Part 53 of the 10 CFR, like the previous ones, focuses on safety, but with a more modern approach. It makes the licensing process for new technologies and advanced reactor designs more flexible and is currently under revision [4]. This regulation is aimed to provide a more risk-informed approach for reactors that are not light water-cooled.

One thing that all these regulations and standards have in common is that they are designed for specific technologies. Since risk analysis can be performed for any industry, risk analysis standards could be applied to any technology in any industry. Thus, the idea of writing a standard which uses risk analysis to support design independent of the industry. Some standards recommend performing a PRA of the facility, but what methodology exists to perform this study when there is not enough information about the facility being designed? Is it advisable to perform an analysis as complex and expensive as a PRA for a facility with inherent safety and for which there is no operational experience or failure rate databases?

For the licensing of microreactors, regulations, requirements and standards need to be updated. However, since their designs and models are not standardized, and their applications are varied, as are their technologies, the how to comply to the requirements in the PSDS is the topic of this work.

2.1. Plant System Design Standard (PSDS)

The PSDS focuses on integrating risk and performance considerations into the design process, promoting safe and efficient designs. It requires performing a probabilistic risk analysis (PRA) to identify and mitigate possible accidents by adapting to the technological characteristics of the facility.

For example, maintenance on a turbine generator involves having to assemble and disassemble a scaffold to perform maintenance on a valve at a height of three meters, which can cause a worker injury, the need for more than one worker to perform the action as well as involving a significant

amount of time. If the need for such maintenance had been foreseen from the initial design stage, then a ladder would have been added, allowing quick and safe access for maintenance.

This is precisely what the PSDS promotes. It focuses on ensuring that the design of plant systems meets the necessary requirements to operate safely, efficiently and reliably by optimizing them. The standard characterizes plant risk by identifying scenarios that may result in an adverse impact, assessing the likelihood and consequences of those scenarios, and attesting to the likelihood that plant equipment and associated design features can prevent or mitigate the impacts of these events.

It states that a risk characterization should begin with a comprehensive list of hazards and initiating events that includes an assessment of applicability to the plant based on its design and physical location. These include external events, such as hurricanes and seismic events, as well as internal, such as pipe breaks. Design and operational requirements for the plant's full operational capability should be defined, as well as requirements for responding to events that could lead to adverse outcomes.

This activity assesses risks based on available design information and generates information about the process, production, external hazards, and risks to inform the design. Figure 1 shows the activities pursued by this standard schematically. It is possible to appreciate the feedback nature of each process. Section H.3 of the PSDS refers to the risk analysis at a plant function level to support initial design of the plant. Once the results are obtained and provided to the designer, changes made to the design, the risk analysis is updated using the H.4 requirements at a system level, and again the interaction with the designer provides an updated design, which now can be taken to the component level in order to achieve a final design (section H5 of PSDS).

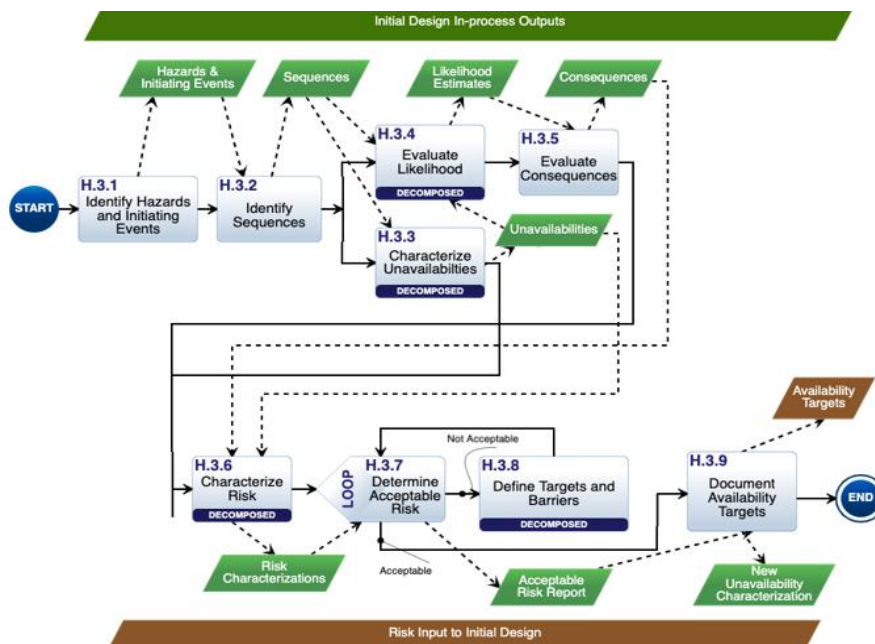


Figure 1: Risk assessments for initial design in PSDS

3. MICROREACTOR CHARACTERISTICS: ADVANTAGES AND DISADVANTAGES

Microreactors are a very promising energy production option for developing industries. Their power ranges from 1 to 20 MWe, reaching a maximum of 50 MWe [5]. They can produce electricity and generate large amounts of heat to be used in the production of olefins and chemical compounds that can be used as starting materials for the manufacture of plastics, detergents and adhesives; all without greenhouse gas emissions. They can also be used in the production of high-temperature hydrogen for heating and cogeneration [6].

The main advantages of these energy sources include the reduction of financial capital costs due to the possibility of total or partial assembly in the factory. They will be installations with a low environmental footprint because, compared to large nuclear plants, they do not require as many components or external safety systems and their high-power density is an aspect that favors this. The possibility of being transportable to a site in an emergency is an aspect that makes them attractive to countries prone to natural disasters. The new intrinsic technology in microreactors is expected to allow them to operate for periods between 3 and 20 years without the need for refueling or maintenance, and they will be self-regulating and with passive safety [5].

Microreactor designs vary in their neutron spectrum, in the coolant, and even in the choice of materials or heat exchangers [5]. The first microreactors are expected to be operational in 2026, with the most advanced designs being Ubattery (Urenco), Micro Modular Reactor (MMR, UltraSafe Corporation) and eVinci (Westinghouse) [1]

The greatest current challenges to see microreactors operating are both their economic viability and competitiveness in the market with renewable technologies, as well as having political support for their development and implementation of prototypes that demonstrate their technological and safety strengths. There is also a need to improve the licensing process, which delays testing and prototype construction times. The rules and regulations in the nuclear industry seek, above all, to guarantee the safety of these facilities, but these rules are governed by standards based mainly on analyses of nuclear plants that have been operating since the 1960s and which are mostly light water reactors (LWR) [2].

3.1 Mizton: Microreactor in Design Stage by UNAM

Mizton is currently a high-temperature, heat-pipe-cooled (HP) fast microreactor. It will be capable of generating 15 MW of thermal power and its core is expected to remain critical for at least 8 years of operation without the need for refueling.

The core is composed of a hexagonal silicon carbon (SiC) matrix containing embedded triso fuel with an enrichment of 19.75% and cooled by heat pipes filled with sodium. It has two reflectors, the primary one made of beryllium oxide (BeO) and the secondary one made of zirconium carbide (ZrC) as shown in Figure 2. Table I shows the dimensions of Mizton that are currently being considered. [7]

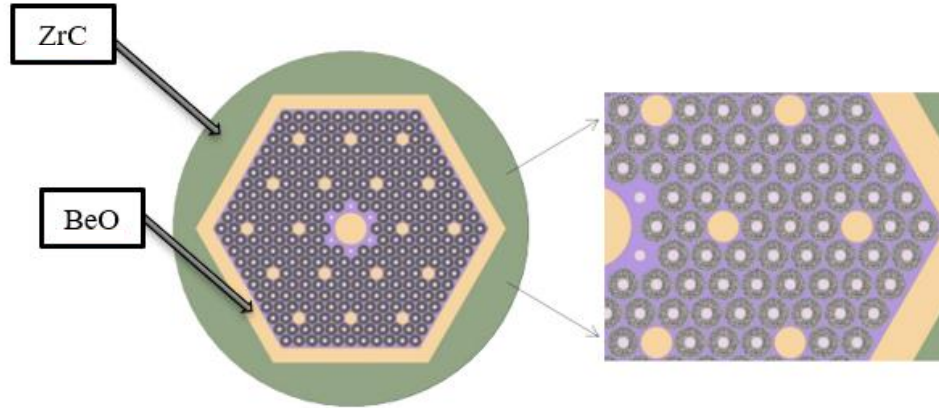


Figure 2: Mizton core with ZrC secondary reflector and BeO primary reflector

Table I: Mizton parameters with their dimensions.

Parameter	Value
HP internal radius [cm]	1.25
External radius of HP [cm]	1.40
Radius (eq.) of active core [cm]	80.0
Height of active core [cm]	145.5
Thickness of primary reflector [cm]	47.5
Radius of secondary reflector [cm]	135.0
Height of core [cm]	185.5
Power [MWt]	15

It is worth noting that the current Mizton design exceeds the width limit for standardized containers for transporting microreactors according to ISO 668 (International Organization for Standardization [ISO], 2020) as shown in Table II. This issue is fed back to the designer for further analysis.

Table II: ISO Standard Containers

Length	Width	Height	Mass
12.192 [m]	2.438 [m]	2.591 [m]	36,000 kg
40 [ft]	8 [ft]	8.5 [ft]	79,000 [lb]

4. RESULTS: APPLICATION OF THE PSD STANDARD TO THE MIZTON MICROREACTOR

The methodology for Mizton's safety assessment is still under development but is governed by the guidelines of the PSD standard, which can be seen in Figure 1. The application process of this methodology is an iterative process.

The safety assessment process for any microreactor or facility in general, according to the PSD standard, requires certain information from the Conformed Contract Technical Requirements (CCTRs) and processed by part D.3 of the Standard. This information defines the operation of the plant and its modes, the maintenance concept, operating diagrams of the facility are obtained, as well as descriptions of the equipment involved and the mass and energy flows involved, the materials considered with their respective regulations in case of being dangerous, intermediate and final products, characterization of waste with the applicable regulations, responses to emergency conditions, HSE objectives are defined, as well as the regulatory documents applicable for the operation of the facility and the variables that restrict it.

In this work, a block diagram of the equipment and functions required for Mizton to be viable is shown in Figure 3. This is adapted from Westinghouse's eVinci microreactor design. [8] As can be seen, the control drums and emergency shutdown control rods (ESS) are considered in the initial design for the reactivity control function.

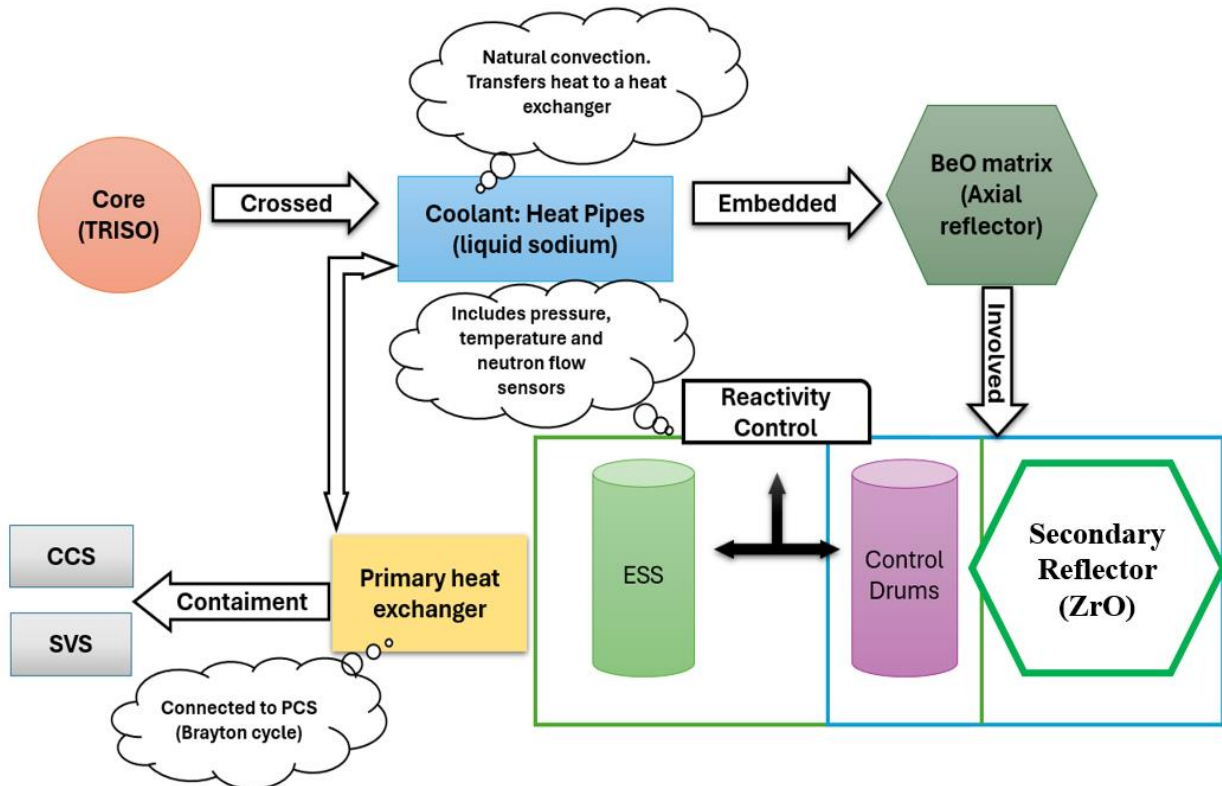


Figure 3: Mizton block diagram

The boron concentration of the control drums is not homogeneously distributed in their geometry. They have a mechanism that allows them to rotate around the core of the microreactor and on their own axis. This rotation occurs automatically in correspondence with the calibration of the internal sensors in the core, but also manually by the operators from an external control panel. The ESS or emergency shutdown control rods have this same characteristic. [9]

In the current Mizton thermohydraulic models, the heat transfer from the heat exchanger to the secondary circuit is being considered to occur through a Brayton cycle to improve the efficiency of the system and also to avoid accidents due to the sodium-water reaction.

Two containment barriers were also added for this initial study: the CCS as the main containment barrier for fission products and allows heat exchange with the environment. The safe vault system (SVS) protects the microreactor from external agents such as floods, strong winds, fires and terrorist attacks.

In this paper, only the full power operating state was considered and for this, three designs functions were considered:

- 1- Reactivity Control
- 2- Heat Removal
- 3- Radioactive Material Containment.

4.1 Identification of Hazards and Initiating Events.

There are many methods available to identify the hazards and initiating events that are capable of triggering accident sequences (FMEA, what-if, other studies, etc.). Based on studies carried out on the eVinci microreactor [8], it was possible to postulate several similar initiating events for Mizton, such as the following:

- Emergency reactor trip (human error or sensor failure)
- Failure of the primary heat exchanger or the secondary circuit system.
- Rupture of the primary heat exchanger tube.
- Multiple ruptures of heat pipe seals (more than three)
- Primary containment rupture

Once the initiating events have been postulated, it is possible to develop accident sequences. For this purpose, five event trees were modeled using the SAPHIRE software. Figure 4 shows the event tree obtained considering an emergency trip of the microreactor. The three functions mentioned above are necessary for success in the event tree. The different combinations of failures define the sequences. For example, sequence 4 involves the emergency shutdown initiating event, the success of the reactivity control but failure of the heat removal with the secondary system the containment functions. In this case, the end state is the frequency of dose levels, which will be calculated later.

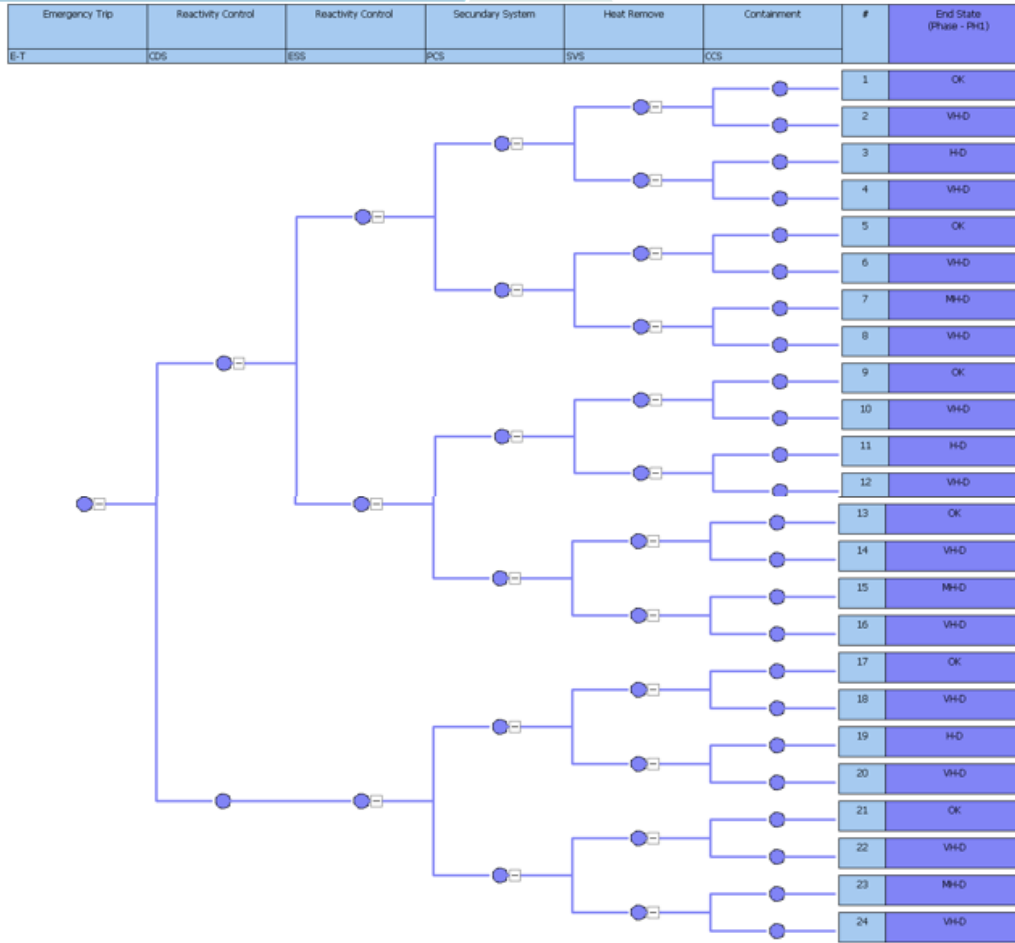


Figure 4: Event tree for an emergency trip of Mizton

The final states of the sequences are postulated as a function of dose according to the recommendations of the Licensing Modernization Project (LMP). The goal is to compare the dose and frequencies calculated for the Mizton microreactor with the dose versus frequency curve, as shown in Figure 5 [10].

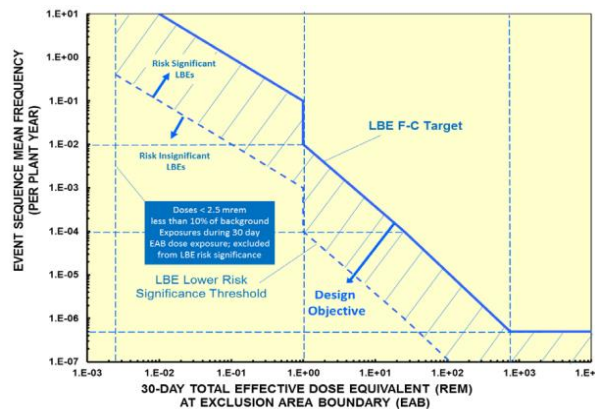


Figure 5: Frequency-dose curve [10]

4.1.1 Risk characterization for Mizton

In order to calculate the risk, it is necessary to define the contribution of each function to the total unavailability. In this project, unavailability is defined as the sum of all the times that systems or components are unavailable to perform their function due to failure, maintenance, inspection, testing, human error, etc. For this purpose, a support matrix was developed to define unavailability contributors as well as if the failures impact production and/or health, safety, environment (HSE). For each function, the maintenance activities should be defined, the downtime estimated and the total downtime, or unavailability, is calculated for each function. These values will be used as the failure unavailabilities for each header in the event tree. In this way, the frequencies of the sequences are determined.

The results of the support matrix are shown in Table III, which only represents a small part of the availability matrix, since it does not yet include the unavailability contributors such as planned and unplanned maintenance, testing and inspection.

Table III: Support matrix for Mizton

Modes of operation	Design Functions	Systems involved	Production	HSE Impact			Design dependencies	
							Support for other functions	Compatible with other functions
Full Power Operation				Health	Safety	Environment		
	1	CDS	x	N/A	x	N/A	2, 3	2
	1	ESS	x	N/A	x	N/A	2,3	2
	2	Secondary	x	x	x	x	1, 3	1
	2	SVS	N/A	x	x	x		
	3	CCS	N/A	x	x	x	N/A	N/A
	3	SVS	N/A	x	x	x	N/A	N/A
Total	3		2	2	3	2		

The Secondary system refers to the system to which the microreactor is coupled, given the application that is decided to be granted to it, and which will therefore have a greater number of subsystems and components, which can be a greater source of unavailability of the primary system.

Depending on the maturity of the design and the studies carried out, this matrix becomes more complex and other modes of operation are analyzed, giving rise to other contributors to unavailability.

5. CONCLUSIONS

Safety assessments of nuclear plants should be carried out at all stages, including the design. The PSD standard demonstrates this by providing a possibility of optimizing the designs of new

advanced plants and of progressing in the risk analysis at the same time to achieve the licensing of the designs in a shorter period.

The process is long and iterative as presented in the paper, but it gives us an insight into the next steps, which is to evaluate probabilities and characterize unavailability at the system level and finally at the component level.

The analysis presented here is to support the development of the methodology and be able to apply it to the design of a microreactor. The Mizton model does not yet have the reactivity control mechanisms or the mass flows of coolant to be managed defined yet, but the model shown in this paper establishes the relationships between the systems and examines their dependencies. It is also evident that microreactors, although tiny compared to large nuclear power plants, will most likely require some maintenance, which will be implemented in future work.

The sequences are preliminary, but the methodology becomes clearer as the requirements are applied to the actual design task. A great deal of work lies ahead, including obtaining the source term, quantifying the sequences and defining the availability targets in order to comply with the production and safety goals of the Mizton microreactor.

ACKNOWLEDGEMENTS

To the Risk-Informed Plant Design team for instructing and supporting me in my ongoing studies on Safety Analysis and Nuclear Safety in general.

To the National Council of Humanities, Science and Technology (CONAHCYT) for providing economic support to Liz Adaneaz for the accomplishment of this work that is part of her Master's research. To the Universidad Nacional Autónoma de México for its support through project PAPIIT IN100824: Diseño conceptual de un microreactor nuclear de múltiples usos múltiples (2024-2026).

REFERENCES

1. Peinado Pérez, Ángel. "Reactores Modulares Horizontes 2030", *Nuclear España*, **Vol. Divulgación**, [Art.-Reactores-Modulares.pdf \(revistanuclear.es\)](#) (julio-2022).
2. Jayarajan, Nayara and Piotukh, Volha. "La reglamentación de los diseños de reactores innovadores", IAEA Website [6432425es.pdf \(iaea.org\)](#), **Vol. Boletín IAEA** (septiembre-2023).
3. Morones-García, Emiliano y François, Juan Luis. "Nuclear microreactors: Status review and potential applications; the Mexican case", *Nuclear Engineering and Design*, **Vol 420**, (2024).
4. United States Nuclear Commission (NRC). "Regulations 10CFR", *NRC Website* [Regulations \(NRC, 10 CFR\) | NRC.gov](#)

5. G. Black, D. Shopshire, K. Araújo y A. van Heek. “Prospects for Nuclear Microreactors: A Review of the Technology, Economics, and Regulatory Considerations”, *Nuclear Technology*, **Volume 209**, p. S1-S20, (2023).
6. Midgley, Emma. “Descarbonizar las industrias con la ayuda de microrreactores y reactores nucleares pequeños”, IAEA Website [6431213es.pdf \(iaea.org\)](#), **Vol. Boletín IAEA** (septiembre-2023).
7. Morones-García, Emiliano y François, Juan Luis. “Neutronic Evaluation of Two Different Types of Fuel Material on the Performance of a Fast Nuclear Microreactor: First Approach to Mizton” *35th SNM Annual Congress*, Ciudad de México, October 28, (2024)
8. Miaoli, Andrea; Detar, Heather y Haessler, Richard. “Westinghouse eVinci™ Micro-Reactor Licensing Modernization Project Demonstration” *Southern Company*. (August-2019)
9. D. A. Ricaurte, L.C. Igua, J.C. Vargas y H. D. Olaya “Modeling of the core and analysis of the operation of a nuclear microreactor”, *Ciencia en Desarrollo*, **Vol 14**, (2023).
10. Nuclear Energy Institute. *Modernization of Technical Requirements for Licensing of Advanced Non-Light Water Reactors. Risk-Informed Performance-Based Technology Inclusive Guidance for Non-Light Water Reactor Licensing Basis Development*, Washington, D.C, United States (2017)

Risk-Informed Design: A New Approach in the Nuclear Industry

Orestes Castillo Hernández

*Comisión Nacional de Seguridad Nuclear y Salvaguardias
Dr. Barragán 779, Narvarte Oriente, Benito Juárez, 03020 Mexico City, Mexico.
orestes.castillo@cnsns.gob.mx*

Pamela F. Nelson

*Universidad Nacional Autónoma de México
Av. Universidad 3000, Coyoacán, 04510, Mexico City, Mexico
pnelson_007@yahoo.com*

Abstract

This article explores a comprehensive risk-informed design methodology specifically developed for critical sectors such as nuclear power plants. The methodology emphasizes the integration of risk analysis with financial evaluation to enhance safety, economic efficiency, and compliance with regulatory standards. It follows a structured, iterative process that spans five key stages: pre-conceptual, conceptual, preliminary, final, and plant-in-operation design. Each stage involves multiple iterations, applying standardized risk analysis techniques, including Failure Modes and Effects Analysis (FMEA), Hazard and Operability Study (HAZOP), and Probabilistic Risk Assessment (PRA), to continuously refine and improve the design. A primary objective of this methodology is to ensure adherence to regulatory criteria, which is crucial for obtaining necessary design licenses and ensuring the plant's legal operation. By addressing potential hazards and their consequences early in the design process, the approach not only enhances safety but also optimizes economic performance by balancing construction costs with operational expenses. This dual focus on safety and cost efficiency enhances technological competitiveness and overall profitability. This process involves identifying hazards, initiating events, and potential sequences of events, and assessing the unavailability of essential functions to meet safety and production goals. An important contribution of the article is the development of an integrated risk index for situations where computational modeling of consequences is impractical. This index utilizes expert judgment to translate qualitative risk assessments into quantitative targets. The article also addresses cost and availability optimization through a bi-objective approach, balancing these factors at both component and system levels. This approach is particularly useful for managing complex systems and large-scale plants, employing techniques such as the Unified Non-dominated Sorting Genetic Algorithm III evolutionary model to handle non-linearity and system interdependencies effectively. The methodology is detailed in a comprehensive flowchart that guides the design process from establishing production and safety targets to the iterative optimization of risks and costs. This structured approach ensures that the final design aligns with regulatory requirements and achieves optimal safety and economic performance, thereby facilitating a well-balanced and efficient design process.

1. INTRODUCTION

Current research in the design of critical sectors, such as nuclear power plants, focuses on the iterative integration of risk analysis with financial analysis. This approach offers numerous benefits, including a safety-oriented design and economic optimization that adheres to the prevailing regulatory criteria. Additionally, an optimized design that considers both initial construction and operational costs significantly enhances technological competitiveness and profitability.

Risk-informed design is an iterative process divided into five main stages: pre-conceptual, conceptual, preliminary, final, and plant-in-operation design. Each stage involves multiple iterations to achieve continuous improvement and accurate analysis. Throughout the process, standardized risk analysis methodologies, such as Failure Modes and Effects Analysis (FMEA), Hazard and Operability Study (HAZOP), and Probabilistic Risk Assessment (PRA), are applied and introduced from the early design stages based on the available information [1], [2], [3].

Furthermore, risk-informed design establishes the foundation for obtaining a design license, as a core component of this methodology is compliance with regulatory criteria. In addition, risk analysis is a key requirement set by regulatory institutions for license approval. Thus, risk-informed design not only enhances safety and economic efficiency but also facilitates compliance with regulations necessary for the legal and safe operation of the plant.

This work presents risk-informed design in a general and global context, tailored to the complexity of the industry in question. It outlines various strategies based on the nature of regulatory criteria, technological complexity, and available information. In other words, it encompasses design strategies applicable to both technologically advanced plants, such as advanced nuclear reactors, and relatively simple facilities, such as an isotope center.

Another crucial aspect of risk-informed design is assessing the nature and magnitude of potential event consequences. The frequency of an event in the design is directly related to its potential consequences; specifically, an event with severe consequences should occur less frequently than one with relatively minor consequences within the same facility's design. This approach allows for the adjustment of design and prevention measures based on the potential impact of events, ensuring more effective and balanced cost management.

2. INITIAL DESIGN

Risk-informed design offers a comprehensive risk assessment during the early design phase. This assessment identifies hazards, initiating events, and sequences of events, and evaluates the availability of essential functions needed to meet safety and production targets established by regulatory criteria and contract technical requirements.

The goal of the risk assessment process in the early design stages is to identify and evaluate facility-specific risks based on the available design information. This assessment provides insights into risks associated with processes, production, and external hazards, which are used to inform the design and validate the results against safety targets and production goals.

During the early design phases, risk assessments are limited by the available information, regulatory criteria, and contract technical requirements. As the design evolves, additional information becomes available, allowing for more detailed risk assessments. Given the preliminary nature of this phase, qualitative risk assessment methods such as HAZOP, FMEA, What-if analyses, and checklists are employed to adequately inform the evaluations. Initial phases are also developed to incorporate PRA.

The early design phases are structured into several key activities:

Identification of Hazards and Initiating Events: This activity focuses on generating lists of hazards and initiating events, both internal and external, based on the available information. These lists also include assumptions, pending items, and missing information related to the identified hazards.

Identification of Sequences of Events: This involves developing lists of possible sequences of events that could lead to safety or production consequences. It considers initiating events, subsequent failures, plant responses, and both preventive and mitigating actions.

Characterization of Unavailability: This activity assesses the unavailability of the plant's primary functions, accounting for uncertainties, dependencies, and impacts. It is divided into four sub-activities:

- Identification of primary functions and areas of uncertainty in the design.
- Identification of sources of unavailability and their impacts, including hardware failures, maintenance issues, human errors, and other factors.
- Evaluation of dependencies between functions, determining how the absence of one function might affect other primary functions.
- Final characterization of unavailability, calculating the total projected unavailability and its contribution to the design targets for safety and production.

The outcomes of the initial design activities include lists of hazards, sequences of events, and estimates of unavailability, along with documentation of assumptions, missing information, and unresolved questions. This process provides a comprehensive risk assessment in the early design phase, evaluating the availability of essential functions to meet safety and production targets and comply with industry regulatory criteria

3. RISK TARGET BASED ON EVENT SEQUENCES AND CONSEQUENCES

On numerous occasions, regulatory criteria associated with technology in the design phase establish quantitative limits for sequences of events, based on the associated consequences.

Therefore, if the consequences of a specific sequence are known, it becomes feasible to determine its risk target, according to regulatory criteria and previously calculated consequences.

However, for many sequences related to severe accidents, experimental evaluation of the consequences, even on a small scale, becomes impractical due to the magnitude of such events. However, it is feasible to model the consequences of each sequence in the design through the use of computational models supported by scientific data. These models simulate the physical and chemical processes that describe the inventories and transport mechanisms of hazardous substances over time. Examples of software that can model the consequences of an event are MELCOR and MAAP in the nuclear industry [4].

It is essential to emphasize that the consequences are calculated for each sequence, since the magnitude of the effects of an accident depends on the specific sequence that triggers the damage state. In other words, different sequences can lead to different consequences.

3.1. Example of the Relationship Between Regulatory Criteria, Consequences and Risk Targets in the Nuclear Industry

Based on the review of existing regulatory criteria and consequence calculations, targets are established for the acceptable frequency of each sequence based on its consequences in the nuclear industry. These targets can be represented graphically in a frequency-consequence curve for all sequences in the design. This plot uses the frequency metric of sequences of events in relation to their associated off-site radiological consequences [5]. Figure 1 shows the most commonly used curve in the literature. [5], [6], [7], [8], [9]. Table 1 shows the frequency or frequency range determined by the regulatory criteria, the regulatory criteria and their corresponding reference.

Table I: U.S. regulatory criteria for drawing the F-C curve.

Regulatory criteria	Frequencies (/plant-year)	Consequences (REM)	Reference
10 CFR 20	>10 ⁻¹	<1	[10]
(EPA-PAG)	10 ⁻¹ to 10 ⁻²	1	[11]
10 CFR 50.34	10 ⁻² to 10 ⁻⁴	1 to 25	[12]
QHO	10 ⁻⁴ to 5x10 ⁻⁷	25 to 750	[13]

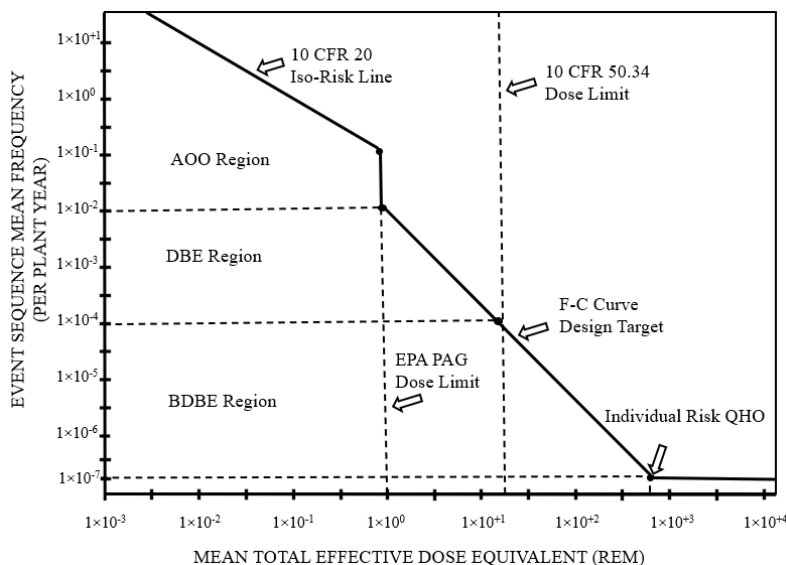


Figure 1: Frequency-Consequence curve [14].

However, in many conventional industry designs such as an isotope center, both the limits of regulatory criteria and the consequences are defined qualitatively, and their translation to a quantitative frequency is facilitated through the intervention of expert judgments. The subsequent section develops an integrated risk index with the purpose of converting the qualitative characteristics of the sequences into a quantitative frequency, using expert judgement in the industry under design.

3.2. Integrated Risk Index

For numerous technologies, developing computational models to assess accident consequences proves impractical due to their limited impact or the absence of necessary tools for model creation. Nevertheless, in a risk-informed design, understanding or, at the very least, evaluating the consequences of each sequence or group of sequences is crucial. The objective is to establish a target value or range for the risk associated with these sequences, thereby facilitating an optimal transfer to the component level.

The proposed methodology aims to analyze the consequences of sequences lacking computational modeling and not constrained by a strict frequency limit defined by regulatory criteria. The goal is to propose a quantitative risk target, allowing for a more flexible and adaptive assessment in situations where regulatory limitations may not directly apply. To conduct this analysis, the following steps are proposed:

- List and precisely define the relevant qualitative criteria characterizing the impact level of the analyzed sequence. These criteria may encompass factors such as potential impact, recovery time, types of consequences (economic, environmental, health implications for occupationally exposed operators or the public), among others.
- Assign numerical scores to each qualitative level of every criterion. For instance, if terms

like "low," "medium," and "high" are used, numerical values such as 1, 2, and 3 can be respectively assigned.

- Establish the relative importance of each criterion by assigning weights. Some criteria may be more critical than others, necessitating a greater weight in the overall evaluation of the risk index.
- Normalize the scores for each criterion (by dividing each score by the maximum possible value, which could be the range or standard deviation). This is crucial to ensure equitable contribution of all criteria to the index.
- Multiply the normalized scores of each criterion by their respective weights and sum these products. The result is a quantitative measure representing the weighted combination of all criteria.
- Additionally, a matrix is required that correlates the severity of event consequences with their frequency of occurrence. The matrix may include, for example, three levels of severity (low, medium, and high). The proposed target frequency for each level is based on existing regulatory criteria, the policies of the company owning the technology, and expert judgment.

When calculating the index, it is compared with the possible maximum and minimum values obtained. Based on this comparison, the corresponding level of importance and the associated risk target are assigned.

3.3. Distribute a Global Target for the Plant at the Sequence Level

The risk associated with a facility is a useful measure, especially for comparing plants with the same purpose but different designs. If a predefined risk value is established in the design provisions or regulatory requirements, this value becomes a design target for the facility. Therefore, it is essential to consider this target when calculating and distributing risk at both the sequence and unavailability levels, for systems and components. Ideally, the resulting risk from the design should be close to or lower than this predefined value, provided that achieving this does not incur a disproportionate cost.

Mathematically, the total risk of the plant is obtained by the Boolean sum of the risks associated with each sequence. To avoid arbitrary division, a preliminary assessment of the sequences can be conducted. For instance, methodologies described in Section 3.2 for conventional facilities or in Section 3.1 for advanced nuclear reactors can be employed. A proportionality factor is then established between the preliminary risk result for the plant and the predefined target. This proportionality factor is applied to each sequence risk value, thus adjusting the risk of the sequences to meet the pre-established total risk of the plant.

If the risk distribution at the sequence level results in an increased risk, it is necessary to demonstrate that the applicable regulatory criteria for these sequences are not violated.

Ultimately, decisions must be made regarding which sequences can have their risk adjusted and which cannot. The updated values obtained will then serve as new targets for the sequences, ensuring that the system designs adhere to these criteria.

4. UNAVAILABILITY AND COST OPTIMIZATION

The remaining problem is to allocate unavailability to components and systems in an optimal manner, while ensuring that risk targets for the sequences are met. An initial approach explored in the literature starts with an analysis of the importance of components at the plant level. Based on the Pareto principle [15], this approach optimizes only the costs and reliability of the most critical components at the plant level, while the sequences conform to their risk targets [16]. Mathematically it is expressed by expression 1.

$$\begin{aligned}
 & \text{Min} \quad |MCS_m (BE) - T_m| \quad m = 1, \dots, M \\
 & \text{Min} \quad Cost(C) \\
 & \quad BE_1, \dots, BE_i \quad i = 1, \dots, I \\
 & \quad C_1, \dots, C_i \quad i = 1, \dots, I \\
 & \quad C, BE \in \Omega
 \end{aligned} \tag{1}$$

Where M is the sequences number, T_m is the target of the sequence m , BE is the probability of the basic events, i is the number of options available in the design for each component, C is the cost of the component i , $Cost$ is the cost of the plant, and Ω is the objective space.

However, since the total number of combinations, as defined in Equation 2, depends on the number of components to be optimized and the options available for each, the objective space in optimization can become extremely large for complex plants such as nuclear reactors. Therefore, decomposing the problem into more manageable subproblems emerges as a viable option.

The expression defining the number of combinations in the objective space is:

$$\Omega = \prod_{n=1}^N m_n \tag{2}$$

Where N is the total number of components that make up the plant or system to be designed, and m is the number of options for component n

In cases where decomposing the optimization problem into subproblems is feasible, it is logical to perform such decomposition at the system level. Dividing the objective space in this manner reduces the complexity of the problem in each subspace. This facilitates the use of more specific and efficient optimization methods for each subspace—methods that might not be applicable to the entire problem due to its size or complexity and improves convergence towards an optimal solution [17], [18], [19]. Furthermore, working at the system level can simplify the interpretation

of results and control over the optimization process, allowing for the evaluation and adjustment of solutions at the system level before integrating them into a plant level.

Therefore, the following section defines the problem at the system level, and the main problems for a full integration in the plant.

5. SYSTEM-LEVEL COST AND UNAVAILABILITY OPTIMIZATION PROBLEM

Dividing the optimization problem at the system level involves translating the constraints that ensure compliance with regulatory criteria into risk targets at the system level. This process is accomplished by developing unavailability targets for the systems, which ensure that both regulatory criteria and risk targets related to accident sequences are met.

Optimization at the system level should result in an optimal design where the system's unavailability converges with the established objective. Among the various formulations explored, bi-objective optimization—considering both costs and the distance to the unavailability targets has proven to be the most effective in addressing the problem. This approach guarantees convergence to the objective and, additionally, provides solutions on both sides of the unavailability target. Mathematically it is expressed by expression 3.

$$\begin{aligned}
 & \text{Min} && |MCS_m (BE) - T_{sys} | && m = 1, \dots, M \\
 & \text{Min} && Cost(C) && \\
 & && BE_1, \dots, BE_i && i = 1, \dots, I \\
 & && C_1, \dots, C_i && i = 1, \dots, I \\
 & && C, BE \in \Omega &&
 \end{aligned} \tag{3}$$

Where T_{sys} is the unavailability target for the system

Figure 2 shows an example of the calculation distribution using this approach, and the Unified Non-dominated Sorting Genetic Algorithm III (UNSGA-III) evolutionary optimization model was used to resolution model[20], [21], [22].

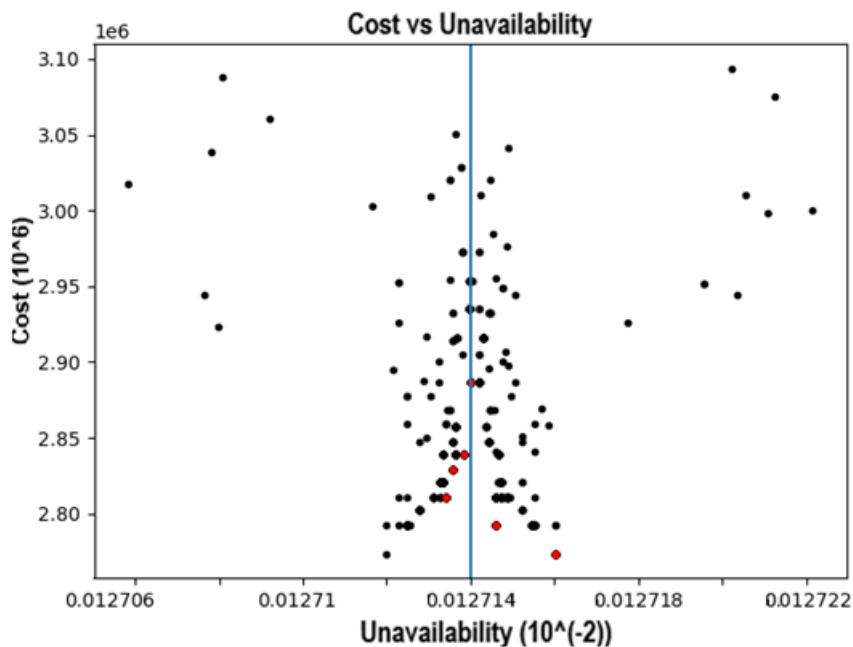


Figure 2: Calculation example for a system with this approach

6. PROBLEM OF PROPOSING UNAVAILABILITY TARGETS FOR SYSTEMS

Distributing sequence risk targets into unavailability targets for systems to meet regulatory criteria given the consequences of each sequence is a mathematically complex problem. The unavailability of the systems is not independent of each other because there are interdependencies among systems, such as shared components or functional dependencies as with supporting systems. The interdependencies among systems are so robust in a PRA that considering or dismissing dependencies yields sequential results which may differ by several orders of magnitude and may not reflect the actual facility's capabilities.

Nonlinearity and the interdependencies among systems make it impractical to model the problem as a system of equations where the variables are the systems' unavailability. One potential solution is to take the variables to the component level or, preferably, to the basic event (BE) level. Thus, the interdependencies among systems are included in the model, and the BEs can be considered independent variables. Then, it is only necessary to calculate the systems' minimal cut sets with the value obtained from the sequences to achieve the unavailability target. Even though the issue is at the BE level, it remains a non-linear problem. Therefore, a multi-objective optimization method is utilized to solve it. Moreover, in a multi-objective model, multiple solutions are obtained.

In the early phases of design, the lack of detail on BE of the components in Fault Tree (FT) models poses a significant challenge. However, in the conceptual design stage, it is feasible to develop at least one BE that represents the unavailability of each system. This includes not only main systems, but also supporting systems. In a logical approach, systems dependent on the supporting systems should incorporate the dependency by an external transfer to the FT of the

supporting system, or by directly incorporating the unavailability of the supporting system within the FT of the dependent system, depending on the modeling strategy used.

The goal in this phase is to model all functional dependencies between the systems. Once this is achieved, the next crucial step involves identifying as many sequences of events as possible that could lead to an accident. Furthermore, it is imperative to establish risk targets for each of these sequences, either through regulatory criteria or through expert judgment.

At this point, an unavailability target can be calculated for each system. The underlying strategy is to minimize the discrepancy between the outcome of each sequence and its stated risk target. This approach not only provides a basis for assessing and managing risk, but also helps optimize the availability and reliability of systems during the design process. Mathematically the optimization problem is expressed in expression 4.

$$\begin{aligned} \text{Min} \quad & |MCS_m (BE) - T_m| \quad m = 1, \dots, M \\ & BE_i^{\text{min_value}} \leq BE_i \leq BE_i^{\text{max_value}} \quad i = 1, \dots, I \\ & BE \in \Omega \end{aligned} \quad (4)$$

Where m is the sequences number, i is the BE number, T_m is the target of the sequence, $BE_i^{\text{min_value}}$ is the minimum probability of the BE_i , $BE_i^{\text{max_value}}$ is the maximum probability of the BE_i and Ω is the objective space.

7. GENERAL METHODOLOGY

Figure 3 presents a general flowchart of the proposed methodology for risk-informed design. The process begins with identifying and establishing production and safety targets for the facility, in accordance with existing regulatory criteria, as shown in Box 1 of the diagram.

In the initial stages, a comprehensive functional analysis should be developed. Additionally, where possible, unavailability values should be assigned to primary and secondary functions and functional failure sequences using expert judgment, as indicated in Box 2 of the diagram.

As the design progresses, potential initiating events or hazards, their frequencies, and potential accident sequences need to be identified. The potential consequences should then be quantified. Based on regulatory criteria, likelihood targets for the sequences must also be proposed, optimizing against these criteria. A design that deviates significantly from regulatory criteria could be very costly, while one that does not meet the established criteria would be unsafe and unprovable. Therefore, to achieve an optimal design and comply with regulatory criteria, risk objectives must be set for the sequences, as indicated in Box 3 of the flowchart.

To iteratively reduce risk uncertainty and optimize costs, unavailability and cost optimization are performed, as reflected in Box 6. However, if technological complexity prevents this optimization, the objective space is divided into smaller subspaces. In this case, unavailability

objectives need to be proposed for individual systems, as shown in Boxes 4 and 5 of the flowchart.

If design distortions are detected and the final design of the systems does not meet the established objectives, unavailability objectives must be reestablished for the non-optimized systems, as indicated in Box 7 of the flowchart.

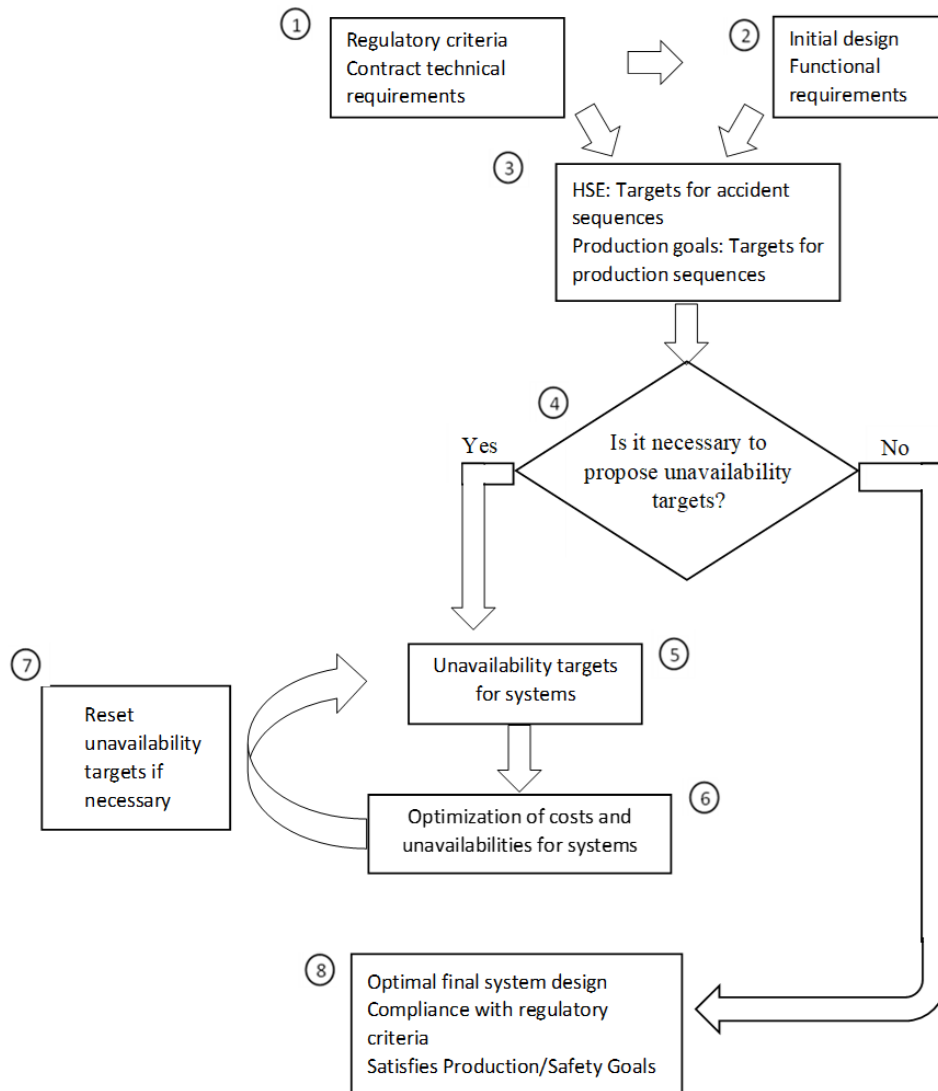


Figure 3: Flowchart of methodology

8. CONCLUSIONS

Recent design research highlights a growing trend towards integrating risk analysis from the early stages of the design process, alongside financial analysis. This approach not only enhances safety and economic efficiency but also facilitates compliance with regulatory requirements.

This paper presents a developing risk-informed design methodology that combines deterministic methods with multi-objective optimization models to achieve efficient and precise designs. The methodology is adaptable to varying levels of technological complexity, whether for advanced facilities or simpler systems.

A critical component of risk assessment in risk-informed design is understanding the consequences associated with sequences of events. Regulatory criteria often impose quantitative limits on the likelihood of these sequences based on their consequences, enabling the determination of appropriate risk targets for each.

For technologies where computational consequence modeling is impractical, the paper proposes an integrated risk index. This index uses qualitative criteria and expert judgments to establish quantitative risk objectives for sequences, thereby facilitating risk assessment and management in scenarios where regulatory constraints may not directly apply.

Cost and availability optimization is central to the design process. It is recommended to begin with an analysis of the importance of components and apply principles such as Pareto to optimize the costs and reliability of key components. Additionally, decomposing the problem into more manageable subproblems is explored as a strategy to address complexity in large plants, proposing unavailability objectives for the involved systems.

The interdependence between systems and their non-linearity makes the establishment of unavailability objectives a complex mathematical challenge. Modeling at the basic event level and employing multi-objective optimization methods are suggested to tackle these challenges. The optimization approach has proven effective in balancing costs and unavailability objectives, utilizing evolutionary models such as UNSGA-III.

The paper concludes with a general methodology that includes identifying production and safety objectives, performing functional analysis, identifying initiating events, quantifying consequences, and iteratively optimizing risks and costs. This methodology also considers subdividing the objective space into more manageable subspaces when technological complexity necessitates it.

ACKNOWLEDGEMENTS

Thanks to the ASME STLLC for supporting the Research Project 200: Target Reliability for Mechanical Fluid Systems.

REFERENCES

- [1] J. You, S. Lou, R. Mao, and T. Xu, “An improved FMEA quality risk assessment framework for enterprise data assets,” *Journal of Digital Economy*, 2022.
- [2] Z. Du, S. Yu, and Z. Chen, “Enhanced minimum-cost conflict risk mitigation-based FMEA for risk assessment in a probabilistic linguistic context,” *Comput Ind Eng*, 2022.

- [3] J. Liu, D. Wang, Q. Lin, and M. Deng, "Risk assessment based on FMEA combining DEA and cloud model: A case application in robot-assisted rehabilitation," *Expert Syst Appl*, 2023
- [4] K. Wagner, C. Faucett, R. Schmidt, and D. Luxat, "MELCOR Accident Progression and Source Term Demonstration Calculations for a Heat Pipe Reactor."
- [5] W. L. Moe and A. Afzali, "Modernization of technical requirements for licensing of advanced non-light water reactors: selection and evaluation of licensing basis events," 2019
- [6] W. L. Moe and A. Afzali, "Modernization of technical requirements for licensing of advanced non-light water reactors: safety classification and performance criteria for structures, systems, and components," 2020.
- [7] W. L. Moe and A. Afzali, "Modernization of technical requirements for licensing of advanced non-light water reactors: risk-informed and performance-based evaluation of defense-in-depth adequacy," 2020.
- [8] W. L. Moe and A. Afzali, "Modernization of technical requirements for licensing of advanced non-light water reactors: probabilistic risk assessment approach," 2020.
- [9] M. Holbrook, "Next Generation Nuclear Plant Licensing Basis Event Selection White Paper," 2010.
- [10] CFR, "Part 20—standards for protection against radiation."
- [11] U.S. EPA, "Protective action guides (PAGs)." [Online]. Available: <https://www.epa.gov/radiation/protective-action-guides-pags>
- [12] CFR, "Part 50—domestic licensing of production and utilization facilities."
- [13] W. L. Moe, "Risk-Informed Performance-Based Technology. Inclusive Guidance for Advanced Reactor Licensing Basis Development (NEI 18-04) development," 2019.
- [14] O. Castillo-Hernández, M. Perdomo-Ojeda, C. R. Grantom, and P. F. Nelson, "Risk-informed design of advanced nuclear reactor: A target unavailability approach," *Nuclear Engineering and Design*, 2023.
- [15] Y. Amiel and F. Cowell, "Monotonicity, dominance and the Pareto principle," *Econ Lett*, 1994.
- [16] D. Mandelli, T. Anselmi, C. Smith, S. Lawrence, and C. Otani, "Reliability and Integrity Management Program Implementation Approach Final Report," 2022, Accessed: Jun. 06, 2023. [Online]. Available: <http://www.art.inl.gov>.
- [17] M. Meselhi, R. Sarker, D. Essam, and S. Elsayed, "A decomposition approach for large-scale non-separable optimization problems," *Appl Soft Comput*, 2022.
- [18] Y. Sun, X. Li, A. Ernst, and M. N. Omidvar, "Decomposition for Large-scale Optimization Problems with Overlapping Components," 2019.
- [19] A. Sinha, D. Pujara, and H. K. Singh, "Decomposition of Difficulties in Complex Optimization Problems Using a Bilevel Approach," 2024, [Online]. Available: <https://arxiv.org/abs/2407.03454v1>
- [20] J. Blank, K. Deb, and P. C. Roy, "Investigating the normalization procedure of NSGA-III," *International Conference on Evolutionary Multi-Criterion Optimization*, 2019.
- [21] K. Deb and H. Jain, "An evolutionary many-objective optimization algorithm using reference-point-based nondominated sorting approach, Part I: Solving problems with box constraints," *IEEE Transactions on Evolutionary Computation*, 2014.
- [22] H. Jain and K. Deb, "An evolutionary many-objective optimization algorithm using reference-point based nondominated sorting approach, Part II: Handling constraints and extending to an adaptive approach," *IEEE Transactions on Evolutionary Computation*, 2014.

Integration of the Equipment Reliability Process and Ageing Management for the Safe and Reliable Long Term Operation of NPP's.

Aida Liliana Medina Almazán
Comisión Federal de Electricidad/ LVNPP
Carretera Cardel- Nautla Km. 42.5
C.P. 91476
Alto Lucero, Veracruz, MEXICO
aida.medina@cfe.mx

Abstract

In this paper it is described how the Equipment Reliability Process, through its Life Cycle Management (LCM) Module, is integrated together with the Ageing Management Process in order to guarantee the Safe and Reliable Long Term Operation of LVNPP. An example of how Life Cycle Management interacts with ageing management is provided. Also, an obsolescence case needing a deep design analysis to be long term solved is provided.

1. INTRODUCTION

Life Cycle Management (LCM) is one of the Modules of the Equipment Reliability Process [1] but it is also one of the Criteria of the WANO PO&C 2019-1 [2] related with Long- Term Equipment Reliability. LCM is the integration of the ageing management and financial planning, in order to optimize the operation, maintenance and service life of Structures, Systems and Components (SSC).

LCM assures that the **vulnerabilities** related with **ageing** and **obsolescence** are: 1. Identified; 2. Risk ranked; 3. Analyzed and 4. Eliminated or mitigated. Thus, LCM comprises detailed technical and financial analyses, together with the strategic planning process.

LCM credits the actions that are taken by other process, for example, Preventive Maintenance (PM) Programs, Corrective Action Program and Work Management (WM) Process; however, LCM does not duplicate (but it complements) the function of other process, such as those related with NUREG 1800 [3], NUREG 1801 [4], License Renewal Application (LRA) / Aging Management Review (AMR).

There are many actions that are taken, and interactions between them, in order to guarantee the Safe and Reliable Long Term Operation of LVNPP, as it will be described in the next sections.

2. LIFE CYCLE MANAGEMENT (LCM)

The objective of the LCM process is to assure that the major assets will not fail due to the

impossibility of carry out the projects that represent the highest cost, such as major inspections, refurbishments and replacements. It is necessary to implement actions prior to failure for the replacement and/ or refurbishment, or to implement design changes of SSC required for safe and reliable operation. LCM process implies to establish a monetary threshold to provide additional detailed technical, cost and impact analysis. This allows developing and implementing long range plans to address current equipment reliability problems and likely future equipment and obsolescence issues.

LCM process requires that age- related mechanisms are well understood for major components and families of subcomponents, at the time that engineering personnel are cognizant of generic industry issues and of advances in technology.

2.1. LCM integration with Aging Management.

LCM does not necessary implies a Long Term Operation (LTO, operation beyond the design life time) or a Period of Extended Operation (PEO, operation beyond the first licensed operating period, as the case of LVNPP). In the case of LRA, it addresses aging management of passive components and structures important to safety, whilst the scope of LCM includes these, plus active and passive components not important to safety, but whilst ageing or obsolescence could have a negative impact in monetary terms, such as cost of repairs, cost of replacements, loss of power generation.

2.1.1. Example of a Mechanical Component managed by Aging Management but requiring a LCM evaluation.

One example of a component managed by both, ageing management and LCM are the Reactor Recirculating (RRC) System discharge valves, which typically are gate valves and whose body is managed by Aging Management Programs (AMP's) such as One Time Inspection, Water Chemistry, Flow Accelerated Corrosion, Stress Corrosion Cracking, and Time Limited Aging Analysis (TLAA).

RRC system consists of two recirculation loops external to the reactor vessel. These loops provide the piping path for the driving flow of water to the reactor vessel jet pumps. Each loop contains one high capacity motor- driven recirculation pump, a flow control valve, and two motor- operated gate valves (one at the suction of the loop and the other one at the discharge of the loop). The recirculation loops are part of the reactor coolant pressure boundary and are located inside the drywell structure.

Depending on the design, some Recirculation Loops have a configuration that produces fatigue cracking in the gate of the discharge valves. Such ageing mechanism (fatigue cracking) have caused problems since the early stages of operation, being possible that such valves have reached its economic end of life, having in mind that the economic end of life is reached when the present worth cost of anticipated repairs equals or exceeds the cost of replacement [5].

For the economic assessment of this example, it has to be considered the cumulative cost related

to the installation of special devices every time that it is needed to isolate the recirculation pumps for maintenance during outages, the radiation exposure and rad waste management costs, which is added to the cost of repairs and replacement of broken gates; such cumulative cost must be compared with the cost of replacement of those valves.

The technical analysis has to consider the installation of a different design of valve, that not experiment such ageing mechanism; for example, the recirculation flow control valves are ball valves that do not present such problem, thus a ball valve design could be considered for the replacement of the recirculation discharge valves. When the replacement is performed, the new valves will also be in the scope of AMP's (body of the valve) and of PM, which will be programmed through the WM process.

2.2. Obsolescence Program.

Obsolescence is a challenge in all the industries. The obsolescence program has as objective to solve reactive and proactive obsolescence cases, being applicable for all the SSC of LVNPP, no matter its safety class (safety and non-safety related components) or its criticality classification (single point vulnerability, critical, non-critical and run to failure components).

Reactive Obsolescence is detected when an urgent need is present, for example, during the spare parts purchasing process.

Proactive Obsolescence means the identification of obsolete components before that its replacement is urgent. This kind of obsolescence is the one that is part of the LCM.

The obsolescence list includes instrumentation, mechanical, electric and civil components, thus in order to have a solution for the cases it is necessary a multidisciplinary team for the evaluation and/ or proposal of replacements. Such multidisciplinary team is formed by the different disciplines of Engineering staff, design engineering, programs and components engineering, and systems support engineering.

Once an obsolescence case is identified, whether proactive or reactive, it is risk ranked, analyzed and a replacement is proposed. An obsolescence case is considered resolved when the replacement is received on site.

2.2.1 Example of an Obsolescence Case that requires a deep design analysis in order to be Long Term solved.

One example of an obsolete mechanical component is the unloading valve of the Electrohydraulic Control (EHC) System. Recently, the spare parts area asked to the Obsolescence Program Coordination to confirm the obsolescence of these valves. By contacting the manufacturer, it was confirmed that the model of the EHC unloading valves has been obsolete for many years, with no manufacturer replacement.

These valves are not safety related components (they are not needed to shut down

the nuclear reactor and maintaining it in a safe-shutdown condition), but they are critical components, whose failure could produce a significant power transient ($\geq 20\%$ and $\leq 50\%$ Nominal Thermal Power). EHC system is out of the scope of LRA.

EHC System has the function of regulating the position of the turbine control valves. EHC system is composed by various subsystems. One of them is the Electrohydraulic Fluid Subsystem which supplies Fyrquel EHC at high pressure to control the turbine control and bypass valves; to open and close the interceptor control valves and the turbine main stop valves; to operate the air pilot valves, including two pilot trip valves of the turbine main stop valves.

The Electrohydraulic Fluid Subsystem has a hydraulic control block, to which two electrical pumps supply hydraulic fluid at 65 l/min and 175 kg/cm². Each pump has an **unloading valve** that is designed to control the pressure at the fluid header, relieving the discharge pressure of the pump to a deposit when a pressure of 127 kg/cm² is reached. If the pressure decreases until 106 kg/cm², the discharge valve closes in order to re-pressurize the circuit, maintaining the pressure of EHC system in the range of 106 kg/cm² to 127 kg/cm².

The critical characteristics of the obsolete discharge valve are: nominal size NG10 according to ISO 4401-05; maximum flow rate 80 l/min; two pressure adjustments 106 ± 3 kg/cm² (to close) and 127 ± 3 kg/cm² (to open); flange construction; operation temperature 55°C; adjusted by screw; differential pressure 25.5 kg/cm² (25 bar). The manufacturer of the valve has in the market a valve of similar geometry but with different nominal size (NG6) and different maximum flow rate (30 l/min), thus this valve cannot be used and the manufactures cannot carry out a special run to manufacture the obsolete valve, but they recommended: 1) to adopt as replacement a special cartridge solution from other manufacturer and, 2) the reconditioning of the valves that have been retired from service.

Finally, the strategy taken by the Obsolescence Program to face the described case is:

- a) Short term solution: Reconditioning by the manufacturer the unloading valves available on site (Maintenance strategy).
- b) Long term solution: It is necessary to find the best design solution in order to provide the function of the discharge valves of the control block of EHC system, which is to maintain the pressure of the EHC System in the range of 106 ± 3 kg/cm² to 127 ± 3 kg/cm².

3. CONCLUSIONS

LCM and AMP's are dynamic processes, whose scope is actualized as the condition of the components is modified (replaced, refurbished, design changed, etc).

The interaction between different processes of the plant is carried out in a systematic way, which contributes to the Long Term Equipment Reliability, and consequently to the safe and reliable long term operation of LVNPP.

REFERENCES

1. INPO AP-913 Rev. 6, “Equipment Reliability Process Description” (2018).
2. WANO PO&C/ 2019-1, “WANO Performance Objectives and Criteria” (2019).
3. NUREG 1800 Rev. 2, “Standard Review for Review of License Renewal Applications for Nuclear Power Plants” (2010).
4. NUREG 1801 Rev. 2, “Generic Aging Lessons Learned (GALL) Report” (2010).
5. EPRI 1021066, “Plant Support Engineering: Feedwater Pump Turbine Mechanical Hydraulic Controls End-of-Life Report” (2010).

Track 5

Environment and Non-Electric Applications

Performance and Degradation pathways of Erythrosine by Ionizing Radiation in Aqueous Solutions

Amira Zaouak and Ahlem Noomen*

Laboratory on Energy and Matter for Nuclear Sciences Development, Tunisia. National Center for Nuclear Sciences and Technologies

Sidi Thabet Technopark 2020 Ariana Tunisia

amirazaouak@gmail.com, noomenahlem2000@yahoo.fr

Haikel Jelassi

Laboratory on Energy and Matter for Nuclear Sciences Development, Tunisia. National Center for Nuclear Sciences and Technologies

Sidi Thabet Technopark 2020 Ariana Tunisia

haikel.jelassi@gmail.com

Abstract

The study explored the degradation and color removal of erythrosine dye using gamma radiation. It also assessed the impact of different radiation doses on UV-visible spectroscopy, pH, chemical oxygen demand (COD), total inorganic carbon (TOC), kinetic behavior, and colorimetric measurements. Results showed that the absorption peak at $\lambda=528$ nm and the color difference (ΔE^*) increased with higher radiation doses. The kinetic analysis revealed that the degradation of erythrosine followed a pseudo-first-order reaction. At a dose of 15 kGy, the efficiency of removing the dye, COD, and TOC was 97% and 81%, respectively

1. INTRODUCTION

Xanthene dyes are noted for their brilliant shades and strong fluorescence. Erythrosine is used for colouring pharmaceuticals and food products [1]. Many studies have shown that this class of dyes have great toxicity and can lead to neurological, developmental tumours due to their carcinogenic properties. These dyes are difficult to remove by traditional treatment procedures. Several classic methods for treatment of industrial wastewater contaminated by dyes have been reported in the literature. In fact, these methods such as biological processes, chemical coagulation, photochemical process, adsorption on activated carbon, coagulation, and flocculation are ineffective for destruction of organic compounds and have several limitations for wastewater treatment [2-10]. However, these techniques, such as advanced oxidation processes (AOPs) and radiation technologies (including gamma and electron irradiation), have emerged as promising alternatives for treating water contaminated with organic compounds. These methods have particular distinct advantages. It is the production of radical species like hydroxyl radicals that have particular distinct advantages like strong ability to oxidize organic compounds leading to their degradation.

These species are considered the most powerful oxidizing agents in aqueous solutions. They do not produce sludge and produce toxic intermediates at low level [11-15]. In this work, we were interested in the degradation of Erythrosine in aqueous solutions using gamma radiation. This compound can be considered as a model molecule of those widely used for coloring food products. This type of organic pollutant is hardly biodegradable by conventional techniques given their complex chemical structures.

2. MATERIALS AND METHODS

Erythrosine, also known as Red No. 3, is an organoiodine compound, specifically a derivative of fluorone. It is cherrypink synthetic dye and primarily used for food coloring. It is the disodium salt of 2,4,5,7-tetraiodofluorescein. Its chemical structure is shown in Figure.1. The molecular formula of the dye is $C_{20}H_6I_4Na_2O_5$ and molecular weight is $879.856 \text{ g mol}^{-1}$. Stock solution of 1 g/L Erythrosine (Sigma Aldrich) was prepared by dissolving the dye in ultrapurified water. The ultrapurified water was obtained by passing distilled water through a Barnstead Easypure II Thermo Scientific Water Purification System.

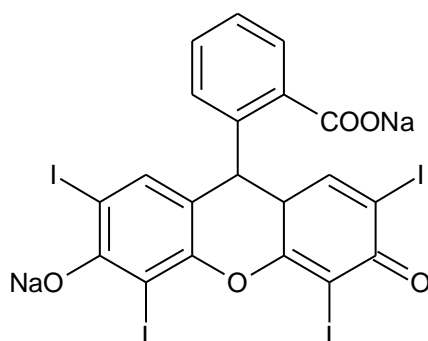


Figure 1. Structural chemical formula of Erythrosine dye

2.1. Irradiation methodology of samples

Samples of Erythrosine (150 mg/L) were irradiated by the Cobalt 60 gamma source installed, since 1999, in the National Centre for Nuclear Sciences and Technologies (CNSTN) at Sidi-Thabet, Tunisia [16]. The irradiation procedure was done at room temperature in the inner zone of the gamma irradiator chamber. In order to determine the dose rate at the chosen irradiation position, dosimetry process was performed using Red Perspex dosimeters. The method of dose rate measurement is well described [17]. The measured rate dose was found 47.62 Gy/min. To get reliable and reproducible results all samples were irradiated at the same fixed position in the radiation field.

2.2. Analytical methods

In this study, several spectroscopic methods were used. Quantitative analysis for the irradiation and un-irradiated solutions of Erythrosine were done by UV-visible spectroscopy using the UV-

visible UNICO 2080 spectrophotometer. Chemical Oxygen Demand (COD) measurements were carried using an equipment type Hanna (HI 83212). Total Organic Carbon (TOC) measurements were carried using TOC –VCSH Shimatzu type analyzer.

3. RESULTS AND DISCUSSION

3.1. Changes of absorption spectra of Erythrosine

The absorption spectra of the un-irradiated and irradiated aqueous Erythrosine solutions at 150 ppm concentration at different doses (from 1 to 10 kGy) are represented in Figure.2. The UV–visible spectrum of un-irradiated solution showed three absorption peaks situated in the UV region ($\lambda = 315, 265$ and 225 nm) and a single peak positioned in the visible region at $\lambda = 528$ nm

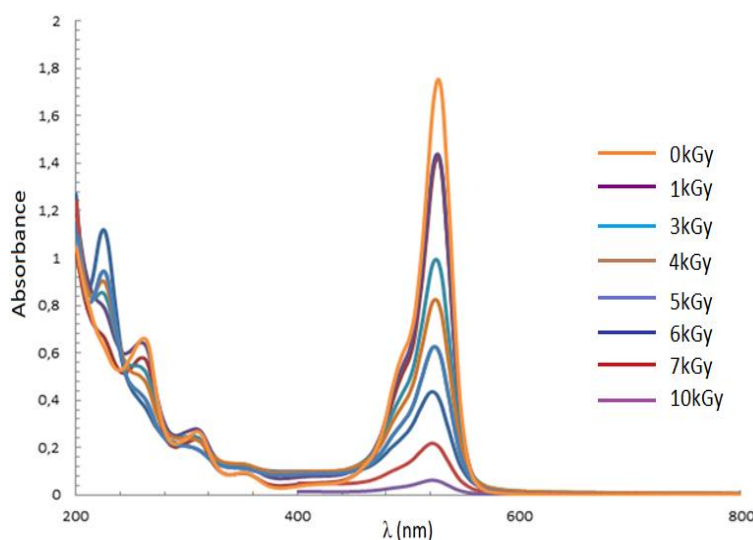
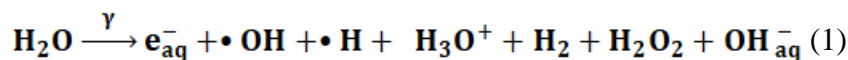


Figure 2. Absorption spectra of un-irradiated and irradiated erythrosine (150 mg/L) aqueous solutions at different doses (from 1 to 10 kGy)

We noted that after treatment, absorbance decreases with increasing irradiation dose for all bands. Nevertheless, the absorption bands in the UV region diminished less rapidly compared to visible band and disappeared almost completely at 10 kGy. This result show that the peak at 528 nm is the characteristic peak of the dye colour and his disappearance at can be explained by the rupture of characteristic chromophoric group. While the persistence of the UV bands proved also that the cleavage of the dye molecule led to the increase of the aromatic groups and therefore requires a longer irradiation time to degrade them. Indeed, these results are in agreement with the literature [11-15]. In fact, it is important to note that the radiolytic degradation process in aqueous solutions results by interaction between γ ray and water molecules. They generate many species such as hydroxyl radical, hydrated electron, hydrogen radical, dihydrogen and water oxygen according to the equation below:



Many studies showed the importance of these radical species especially hydroxyl radicals because they can react rapidly with non-selective manner with organic compounds and leading to the destruction of their chemical structure [18-20].

3.2. Kinetic study

Erythrosine According the Beer-Lambert law, the concentration (C) of the solution is linearly proportional to the absorbance (A) of the light by the dye:

$$A = \varepsilon \times l \times C \quad (2)$$

Where A is absorbance, l is the path length of the sample (1 cm), C is the concentration of the dye in the solution and ε is the molar absorptivity obtained by calibration curve. In order to assess the impact of contaminant load on the removal of target contaminant by gamma-ray irradiation, kinetic study was applied. According to the spectra of figure 2, we focused on the major peak of the chromophore at 528 nm in the visible region.

The graph representing $\ln(C_0) - \ln(C) = k_{app} \times t$ is given in Figure 3. It shows a linear behavior, signature of a pseudo first order degradation of Erythrosine solution. The resulting apparent rate constant value is approximately $k_{app} = (0.0144 \pm 0.007) \text{ min}^{-1}$.

An Adj R-square was found to be $R^2 = 0.9942$.

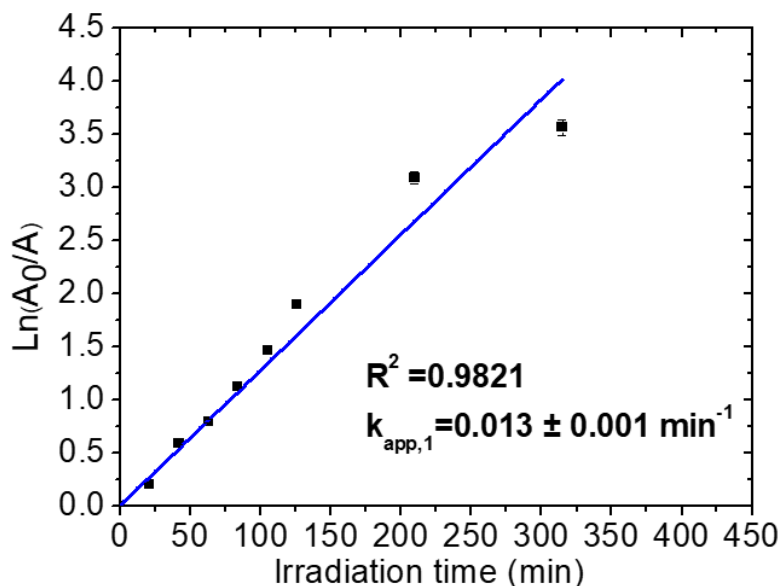


Figure 3. Logarithmic (C_0/C) as function of time exposition in min. Linear fit in gray line was done in order to extract a apparent constant $k_{app} = (0.013 \pm 0.001) \text{ min}^{-1}$ with $R^2 = 0.98212$.

3.3. Study on the variation of COD and TOC during radiolysis

Monitoring the progress of mineralization was performed by COD measurements and TOC analysis. The COD evolution during electrolysis is given in Figure 4 at different doses. It was found that the degradation is the fastest and the percentage of elimination of organic matter is the most important when the dose is the highest. So, a high rate of COD elimination close to 95% was obtained when the dose is 10 kGy. This results shows that the mineralization of aromatic

intermediates resulting from the cleavage of the starting molecule was achieved. These results are comparable to those obtained in previous studies and may be explained in a similar manner [18-21].

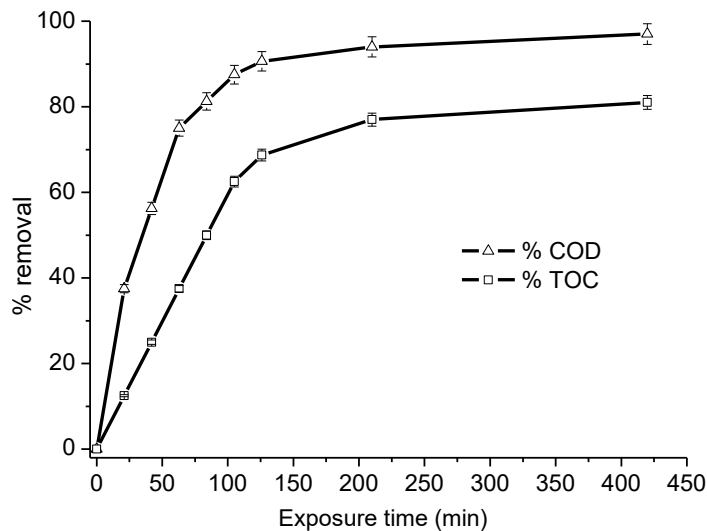


Figure 4. % COD and %TOC removals of aqueous solution erythrosine at different doses.

In addition, the mineralization process by gamma radiation was confirmed by control of % TOC removal. The behavior of the TOC as a function of the dose showed in Figure 4 highlights a rapid elimination of TOC at the beginning of treatment (for lower doses). This first observation allows us to assign that a rapid degradation of the cyclic intermediates took place. A slowdown was obtained later due to more time consuming degradation of aliphatic intermediates [22-23].

4. CONCLUSION

This work reports the degradation by gamma radiation of Erythrosine which can be considered as a model molecule of xanthene dyes. Such organic pollutants are not readily biodegradable. The results showed that gamma radiation treatment was quite efficient for degradation of the aqueous solutions of Erythrosine. The % Chemical Oxygen Demand (COD) and Total Organic Carbon (TOC) were influenced by the applied doses. After applying 10 kGy dose, 95% COD removal, 80% TOC reduction were observed. Thus, it can be concluded that gamma radiation treatment efficiently decolorize and degrade the dye effluents. An estimation of the kinetics of degradation was given. Finally, the above studies encourage the gamma radiation treatment as a promising method for mineralization of dye effluents coming from industries.

ACKNOWLEDGEMENTS

This work has been realised with the financial support of the Ministère de l'Enseignement Supérieur et de la Recherche Scientifique (Tunisia).

REFERENCES

1. R. Jain, M. Bhargava, N. Sharma, "Electrochemical degradation of erythrosine in pharmaceuticals and food product industries effluent", *Journal of Scientific and Industrial Research*, **64**, p.191 (2005).
2. Y. Wong, Y.S. Szeto, W.H. Cheung, G.McKay, "Adsorption of acid dyes on chitosan-equilibrium isotherm analyses", *Process Biochemistry*, **39**, p.695 (2004).
3. M.T, Yagub, T.K. Sen, H. Ang, "Equilibrium, Kinetics, and Thermodynamics of Methylene Blue Adsorption by Pine Tree Leaves", *Water Air Soil Pollution*, **223**, p.5267 (2012).
4. S. Alahiane, S., Qourzal, M. El Ouardi, M. Belmouden, A. Assabbane, Y. Ait-Ichou, "Adsorption and photocatalytic degradation of indigo carmine dye in aqueous solutions using TiO₂/UV/O₂" *Journal of Materials and Environmental Sciences*, **4**, p.239 (2013).
5. N.M, Mahmood, B. Hayati, M, Arami, C. Lan, "Adsorption of textile dyes on Pine Cone from collared: kinetics, equilibrium and thermodynamic studies", *Desalination*, **268**, p.117 (2011).
6. P.K. Malik, S.K. Sanyal "Kinetics of decolorization of azo dyes in wastewater by UV/H₂O₂ process", *Separation and Purification Technology*, **36**, p.167 (2004).
7. A. Zaouak, F. Matoussi, M .Dachraoui, " Electrochemical degradation of a chlorophenoxy propionic acid derivative used as an herbicide at boron-doped diamond", *Desalination and Water Treatment*, **52**, p.1662 (2014).
8. A. Zaouak, F. Matoussi, M .Dachraoui, "Electrochemical oxidation of herbicide bifenox acid in aqueous medium using diamond thin film electrode", *Journal of Environmental Science and Health, Part B* ,**48**, p.878 (2013).
9. A. Zaouak, F. Matoussi, M. Dachraoui, "Investigation of the anodic oxidation of aryloxy propionic acid derivatives in acetonitrile", *Journal of Materials and Environmental Sciences* **1**, p.138 (2015).
10. P. Canizares, R. Paz, C. Saez, M.A. Radrigo "Costs of the electrochemical oxidation of wastewaters: a comparison with ozonation and Fenton oxidation processes", *Journal of Environmental Management*, **90**, p.410 (2009).
11. N. Getoff, W. Lutz, "Radiation induced decomposition of hydrocarbons in water resources", *Radiation Physics and Chemistry*, **25**, p.21(1985).
12. M. Hosono, H, Arai, M. Aizawa, L. Yamamoto, K. S, "Decoloration and degradation of azo dye in aqueous solution supersaturated with oxygen by irradiation of high energy electron beam", *International Journal Applied Radiation and Isotopes*, **44**, p.199 (1993).
13. J. Hoigne, H. Bader, "The role of hydroxyl radical reactions in ozonation processes in aqueous solutions" *Water Research*, **10**, p.377 (1976).
14. J. Paul, D.B. Naik, S. Sabharwal "High energy induced decoloration and mineralization of Reactive Red 120 dye in aqueous solution: a steady state and pulse radiolysis study", *Radiation Physics and Chemistry*, **79**, p.770 (2010).

15. J. Paul, K.P. Rawat, K.S.S. Sarma, S. Sabharwal, “Decoloration and degradation of Reactive Red-120 dye by electron beam irradiation in aqueous solution”, *Applied Radiation and Isotopes*, **69**, p.987 (2011).
16. O. Kadri, F. Gharbi, K. Farah “Monte Carlo improvement of dose uniformity in gamma irradiation processing using the GEANT4 code”, *Nuclear Instruments and Methods in Physics Research*, **239**, p.391 (2005).
17. K. Farah, T. Jerbi, F. Kuntz, A. Kovacs, “Dose measurements for characterization of a semi-industrial cobalt-60 gamma-irradiation facility” *Radiation Measurement*, **41**, p.201 (2006).
18. F. Azara, H.B.Yanga, L.Venaultb, S. Faurea, “ Degradation of erioglaucine dye under γ -irradiation”. *Procedia Chemistry*.**7**, p.647 (2012).
19. Y.-P Chen, S.-Y., H.-Q. Liu, Yu, H Yin, Li, Q.-R. “Radiation-induced degradation of methyl orange in aqueous solutions”, *Chemosphere*. **72**, 532 (2008).
20. J. Grodkowski, J.Mirkowski, M. Páusa, N. Getoff, P Popov, “ Pulse radiolysis of aqueous diphenyloxide”. *Radiation Physics and Chemistry*, **69**, p.379 (2004).
21. H. Suzuki, S. Yamagiwa, S. Araki, H. Yamamoto, “Effects of Advanced Oxidation Processes on the Decomposition Properties of Organic Compounds with Different Molecular Structures in Water”, *Journal of Water Resource and Protection*, **8**, p.823 (2016).
22. Zaouak A, Matoussi F, Dachraoui M., Electrochemical degradation of a chlorophenoxy propionic acid derivative used as an herbicide at boron-doped diamond, *Desalination and Water Treatment*, **52**, p1662 (2014)
23. Zaouak A, Noomen A, Jelassi H., Degradation mechanism of losartan in aqueous solutions under the effect of gamma radiation. *Radiation Physics and Chemistry*.**184**,p. 109435 (2021)

Neutron Activation Analysis and Atomic Absorption Spectrometry of Watermelon Rind as Potential Bioadsorbent for Toxic Metals Decontamination of Water

Samreen Shehzadi^{1*}, Sadia Kanwal², Tanveer Ahmad¹ and Yasir Faiz¹

^{1*}Pakistan Institute of Nuclear Science and Technology, P.O. Nilore, Islamabad, Pakistan, sshehzadi11@hotmail.com

²Pakistan Institute of Engineering and Applied Sciences, Nilore, Islamabad, Pakistan, kanwalsadia855@gmail.com

Abstract

Water pollution due to toxic heavy metals is a serious issue in the developing countries as a consequence of uncontrolled disposal of agricultural, industrial and domestic discharge directly into water bodies and soil. Among various toxic metals, lead and cadmium are considered as extremely toxic and carcinogenic for human beings. Bio-adsorption is considered as relatively simple, cost effective, eco-friendly and excellent tool for toxic metals removal from contaminated water. Therefore, a study was conducted in 2023 with the objectives to develop low cost bio-adsorbent from agro-waste material and explore its potential for toxic metals (Pb and Cd) removal from contaminated water. Watermelon rind (WMR) was prepared as bio adsorbent and was analyzed for its various parameters including major and trace elements using neutron activation analysis (NAA) and Atomic Absorption Spectrometry (AAS) technique. Batch experiments were conducted to study the effect of adsorbent dose, solution pH, contact time, agitation speed and temperature on lead and cadmium removal from aqueous solutions. Physico-chemical analysis of WMR revealed that it had high nutrient composition with N (3.2 %), total organic C (24 %), total P (0.33 %) and C: N (7.5) with no Pb and Cd toxicity. NAA showed that WMR had K (3.0%), Ca (1.2%), Na (0.16%) and Fe (0.03%) with no toxic metals contents (Hg, As, Co). The study revealed that maximum removal of Pb (81.54%) and Cd (86%) were obtained at dose rate of 1 gL⁻¹ and 8 gL⁻¹ respectively at pH (5.2 for Pb and 6 for Cd) at 25°C, 100 rpm agitation speed, for 25 minutes contact time. The Langmuir adsorption isotherm showed that WMR had maximum adsorption capacity of 82.46 mg/g for Pb and 55.45 mg/g for Cd. Fourier transform infrared (FTIR) spectroscopy of WMR showed the presence of functional groups like hydroxyl and carboxyl as contributors for lead and cadmium adsorption. The findings indicate that WMR is cost effective and eco-friendly agricultural waste with great potential as bio-adsorbent for Pb removal compared to Cd from contaminated water.

Keywords: Bioadsorbent, Watermelon rind, Lead, Cadmium, Neutron Activation Analysis, AAS, Wastewater

1. INTRODUCTION

Heavy metal pollution is the major concern particularly due to their toxic, carcinogenic, non-biodegradable nature and their tendency to bio accumulate which causes lethal effects on human beings. Heavy metals are considered as primary contaminants due to their toxicity and mobility in natural water systems [1]. The prevalence of various industries including mining, waste recycling, solid waste disposal activities, battery operations and other urban activities have contributed to the heavy metal contamination in rivers, lakes and other water sources. According to an estimation of the United Nation, almost 80% of all the industrial and municipal wastewater in the developing countries is dumped into the environment without any prior treatment. [2].

Among various heavy metals, lead and cadmium are considered as extremely toxic and carcinogenic for human beings. Lead is generated from anthropogenic sources such as thermal energy stations, coal combustion and battery manufacturing industries. Lead causes serious health issues like hypertension, stomach pain, renal dysfunction, fatigue, insomnia, arthritis and hallucination [3]. Long term exposure to lead is associated with mental retardation, allergies, psychosis, autism, brain and kidney damage and in certain cases even cause death [4]. Cadmium is a toxic, non-biodegradable heavy metal that persists in the environment for a long time. Its

pollution in natural water bodies mainly arises due to the discharge of wastes and effluents from industries such as electroplating, metallurgical processes, plastic and battery manufacturing industrial practices [5]. Cadmium causes serious health hazards to humans as it can stimulate the respiratory tract, triggers loss of smell, vision and hearing. Moreover, when cadmium binds with cystine rich proteins such as metallothionein, its level increases 3,000 fold which in turn causes liver problems like hepatotoxicity and nephrotoxicity in kidneys [6].

Therefore, efficient removal of these toxic metals from contaminated water is one of the foremost challenges. In recent years, bioadsorption is found to be the most promising technique for heavy metals removal as it is cost effective, convenient and easy to operate. Low cost bioadsorbents derived from agricultural wastes such as sugar cane bagasse, rice husk, fruit wastes and saw dust etc. are being used for heavy metals removal. Among these, fruit wastes (e.g. peels, seeds, rinds and shells) have the highest potential as active bioadsorbents for wastewater treatments.

Watermelon (*Citrulluslanatus*) belonging to the family cucurbitaceae is one of the top summer fruits grown in warmer regions and is widely used everywhere in the world, including Pakistan. Watermelon rind (WMR) represents 30% of the fruit which is discarded after fruit consumption as waste [7]. Watermelon rind consists of cellulose, proteins, pectin and carotenoids. These polymers are rich in functional groups including carboxyl, hydroxyl and amine which play an important role for binding heavy metals. These functional groups bind metals through ion exchange by transferring hydrogen ions or through complex formation by sharing an electron pair [8]. Based on these properties; watermelon rind is used as efficient and low-cost bioadsorbent.

Therefore, the present study was undertaken with the aims to investigate 1. The Physico-chemical characteristics of WMR using neutron activation analysis (NAA) and Atomic Absorption Spectroscopy (AAS); 2. The effects of different parameters (i.e. adsorbent dose, pH, contact time temperature and agitation speed) on adsorption performance of WMR for lead and cadmium removal from aqueous solution. 3. The maximum adsorption capacity of WMR using adsorption isotherms.

2. MATERIALS AND METHODS

The study was carried out at the Central Analytical Facility Division (CAFD), Pakistan Institute of Nuclear Science and Technology (PINSTECH), in Islamabad, Pakistan in 2023. WMR was selected as bioadsorbent, its preparation, physico-chemical analysis and batch experiments were performed for exploring its potential for removal of toxic metals from contaminated water are mentioned below:

2.1 Preparation of Bioadsorbent (WMR)

Watermelon samples were collected from local markets in Islamabad for bioadsorbent preparation with simple pre-treatment. The preparation scheme of adsorbent is given in figure 1. The watermelon peel samples were brought to the laboratory at CAFD, PINSTECH. After cutting, WMR were separated from the fruit pulp, thoroughly washed with tap water and cut into smaller pieces before rinsing with distilled water three times. Subsequently, WMR pieces were left to air-dry at room temperature, then dried in a laboratory oven at 60°C until a constant weight was achieved. Once dried, the cut pieces were ground, finely powdered, sieved through a mesh

no. 30 (600 μm), and carefully stored in an airtight container with appropriate labelling for subsequent analysis.

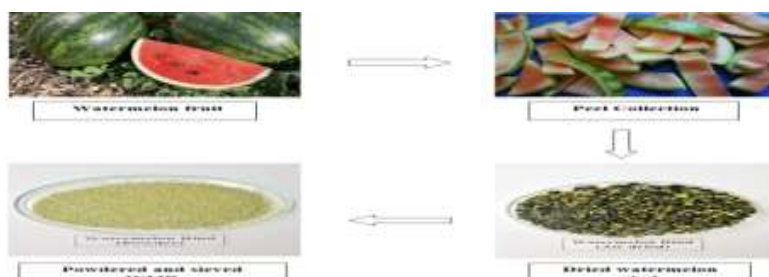


Figure 1. Schematic diagram of preparation of adsorbent (WMR)

2.2 Characterization of WMR

After preparation, WMR (adsorbent) was analyzed for its various physico-chemical characteristics including moisture content, pH, EC, total organic carbon, total nitrogen and phosphorus. In addition, major and trace elements were analyzed using neutron activation analysis (NAA) and Atomic Absorption Spectrometry (AAS). The WMR samples were analyzed using the NAA technique; approximately 100 mg aliquots of the samples (in triplicate) were sealed in clean polyethylene capsules and packed together with two standards: NIST 1752 (Citrus Leaves) and NIST 1753 (Tomato Leaves) in polyethylene irradiation rabbits. The sealed rabbits were irradiated using three different protocols in the miniature neutron source reactor (MNSR) at the Pakistan Research Reactor-2 (PARR-2) irradiation facility, with a thermal neutron flux of 1×10^{12} n/cm²/s. Optimal conditions for obtaining interference-free photopeaks of the target elements were achieved by adjusting the irradiation and cooling times (Table I). After irradiation, the samples and standards were allowed to decay for a predetermined period (as shown in Table-I), transferred to clean, pre-weighed counting containers, and subsequently measured using gamma spectroscopy. The Gamma spectrometry system used consists of a high purity germanium detector (80% rel. efficiency and FWHM of 1.9 keV at the 1.33 MeV peaks of ⁶⁰Co) along with relevant electronics. Recorded spectra were evaluated with ANGES program (IAEA version 1.0.0.2).

Table I. Irradiation, decay and counting time schemes for determination of elements using NAA

Irradiation time	Decay time	Counting time	Elements measured
2 min	5 min	100 sec	Al, K, Mg, Mn, Na, V
1 hour	2 days	900 sec	As, K, La, Na, Sb
5 hours	2-3 weeks	7200 sec	Ce, Co, Cr, Cs, Fe, Lu, Rb, Sb, Sn, Sr, Zn

2.2.1 Quality assurance (QA)

To ensure data quality, reference materials (RMs) NIST 1752 (Citrus Leaves) and NIST 1753 (Tomato Leaves) were analyzed alongside the samples. A t-test confirmed excellent agreement between our data and the certified values for all elements ($p < 0.05$), with relative standard deviations below 20%. Limits of detection (LODs) were calculated as three times the standard deviation of the measured counts. Whereas Mg, Zn, Cu, Pb, Cd analyses were performed using

AAS Hitachi Z- 8000. Fourier transform infrared spectroscopy (iS50 FTIR (Thermo Scientific)) of WMR was also performed in order to determine its various active functional groups involved in lead and cadmium adsorption. The analytical procedures and instruments used for physicochemical analyses of WMR are described in Table II.

Table II. The analytical procedures and instruments used for characterization of WMR

Physico-chemical Parameters	Instruments/model
Moisture	Oven dried method
pH	HANNA HI 2211, pH meter
EC _e	Cond 7110, WTW
Total Organic Carbon	Spectrophotometer (Spectonic+20)
Nitrogen	Kjeldahl method
Mg, Zn, Cu, Mn, Pb, Ni	AAS (Hitachi Z-8000)
Cd	ICP-OES (Thermo iCAP-6500)
Functional Groups	iS50 FTIR (Thermo Scientific)

2.3 Batch Experiments for Lead and Cadmium Adsorption

Experiments were conducted in batch mode to investigate the adsorption of Pb and Cd by WMR. From the stock solutions of Pb and Cd (1000 mg L⁻¹), 50 mg L⁻¹ Pb and 50 mg L⁻¹ Cd solutions were prepared. The effect of five parameters including adsorbent dose, solution pH, contact time, agitation speed and temperature were systematically studied. Each parameter was altered progressively while keeping the others constant to understand its specific effect.

2.3.1 Study of Adsorption parameters

To investigate the impact of adsorbent dose on Pb adsorption, a range of WMR doses (0.15gL⁻¹-5gL⁻¹) were applied, whereas for Cd adsorption, dose was studied in the range of 0.15gL⁻¹-12gL⁻¹. The effect of solution pH on Pb adsorption was explored within a pH range of 2-10. Conversely, for Cd, the pH influence was studied within a pH range of 4-9. The desired pH levels were achieved by using 0.1M HCl or 0.1N NaOH to 50µg mL⁻¹ Pb and Cd solutions. To assess the impact of contact time, experiments were conducted with varying shaking times (0-50 minutes). The effect of shaking speed on the adsorption was monitored at varying speeds (0-250 rpm). The influence of temperature on adsorption process was investigated over a range of temperatures (15°C - 40°C). After the adsorption process, the solutions were filtered and Pb and Cd concentrations were determined using AAS and ICP-OES respectively.

The adsorption capacity (q_e) and removal efficiency of the bio-adsorbent (WMR) were determined at equilibrium using the equations 1 and 2:

$$q_e = \frac{C_i - C_e}{W} \times V \quad (1)$$

$$\% \text{ Removal Efficiency} = \frac{C_i - C_e}{C_i} \times 100 \quad (2)$$

Where q_e = Adsorption capacity (mg g⁻¹); C_i = Initial metal concentration (mgL⁻¹); C_e = Metal concentration at equilibrium (mg/L); W = Weight of the adsorbent (grams); V = Volume of the solution (Litre)

2.4 Study of adsorption isotherms

Six solutions with concentrations of 30, 40, 50, 60, 70 and 80 mg L⁻¹ were prepared by proper dilutions of stock solutions of Pb and Cd. The adsorption experiments were carried out using 1 g L⁻¹ of WMR for Pb and 8 g L⁻¹ for Cd. The mixtures were agitated at 100 rpm at 25°C for 25 minutes. At the end, suspensions were filtered and the supernatants were analyzed for Pb and Cd. The obtained experimental data were employed to apply two isotherm models, Langmuir and Freundlich, in order to comprehend the adsorption characteristics at equilibrium.

2.4.1 Langmuir Isotherm

After experimentation, Langmuir adsorption isotherm was devised by using Langmuir expression. Equation 3 and its linear form given in equation 4 stand for the Langmuir Isotherm:

$$q_e = \frac{q_{max} K_L C_e}{1 + K_L C_e} \quad (3)$$

$$q_e = \frac{1}{K_L q_{max}} \times \frac{1}{C_e} + \frac{1}{q_{max}} \quad (4)$$

Where q_{max} = maximum adsorption capacity (mg/g); K_L = Langmuir isotherm constant (L/mg)

The separation factor (R_L), illustrates the adsorption possibility either favourable ($0 < R_L < 1$) or unfavourable ($R_L > 1$). R_L was determined using equation 5:

$$R_L = \frac{1}{1 + C_i \times K_L} \quad (5)$$

2.4.2 Freundlich Isotherm

Freundlich isotherm is represented by using the equations 6 and 7:

$$q_e = K_f C_e^{1/n} \quad (6)$$

$$\log q_e = \log K_f + \frac{1}{n} \log C_e \quad (7)$$

Where K_f = Freundlich constant, a measure of adsorption capacity; q_e = Amount of metal adsorbed (mg/g); C_e = Concentration of adsorbate at equilibrium (mg/L); $1/n$ = adsorption intensity that corresponds to the adsorption process either favourable ($0.1 < 1/n < 0.5$) or unfavourable ($1/n > 2$).

2.5 Fourier Transform Infrared Spectroscopy (FTIR)

The FTIR study of WMR was taken into account before and after adsorption process.

3. RESULTS AND DISCUSSION

3.1 Physico-chemical characteristics of WMR

The results regarding physico-chemical characteristics of WMR are mentioned in Table III & IV. The results (Table III) showed that WMR had a pH of 5.37, EC of 5.09 mS cm⁻¹, moisture content of 4.24 % and phosphorus contents of 0.33%. The results also revealed that WMR is a good source of total organic carbon (24 %) and nitrogen (3.22 %) with a narrow C: N ratio of 7.5.

The neutron activation analyses (Table IV) depicted that WMR is enriched with K (3.0 %), Ca (1.10 %), and Fe (0.03%). Moreover it had Br of 17.23 mg kg⁻¹ and Al of 216 mg kg⁻¹ whereas no toxic metals (Cr, As, Hg, Co) were detected. The AAS analysis indicated that WMR had Mg (34.15 mg kg⁻¹), Zn (17.68 mg kg⁻¹), Cu (7.46 mg kg⁻¹) and Mn contents of 11.15 mg kg⁻¹. In addition, toxic heavy metals (Pb, Cd, As, Hg, Ni) were not detected in WMR which was the safe indication for its use as an adsorbent.

Table III. Physico-chemical characteristics of WMR

Parameters	Unit	Value
pH		5.37
EC	mS cm ⁻¹	5.09
Moisture	%	4.24
Phosphorus	%	0.33
Total Organic Carbon	%	24.0
Nitrogen	%	3.22
C:N	--	7.50

Table IV. Elemental composition of WMR using NAA & AAS

Element	K	Ca	Na	Fe					
NAA (%)	3.0	1.10	0.16	0.03					
Element	Br	Al	Sn	Rb	Se	Cr	Hg	As	Co
NAA (mg kg ⁻¹)	17.23	216	0.15	25.91	*ND	ND	ND	ND	ND
Element	Mg	Zn	Cu	Mn	Pb	Cd	Ni		
AAS (mg kg ⁻¹)	34.15	17.68	7.46	11.15	ND	ND	ND		

*ND= Not detected

3.1.1 FTIR Spectra of WMR

The FTIR spectra of WMR before adsorption (Figure 2) showed that the peak at 3322 cm⁻¹ revealed the presence of O-H group of alcohol which confirmed the subsistence of hydroxyl group containing compounds such as lignin and pectin. The band present at 2913cm⁻¹ and 2847 cm⁻¹ indicated the C-H stretching of alkanes. The band present at 1733cm⁻¹ implied the evidence of C=O stretching vibrations due to the presence of either carboxylic acids or their esters. The medium band at 1583 provided a clear indication of C=C stretching in ring structure (cyclic

alkenes). The medium peak at 1321 cm^{-1} pointed out the presence of O-H bending of phenol whereas the prominent peak at 1039 cm^{-1} indicated the C-O stretching (primary alcohol). The confirmation of hydroxyl group (O-H stretch), carbonyl group (C=O) and C-O stretch demonstrated the presence of cellulose, hemicelluloses and lignin compounds in WMR. The data revealed that it had many active sites (functional groups) such as hydroxyl and carboxyl linkages which were highly helpful in binding Pb & Cd ions with them for their removal from water [9].

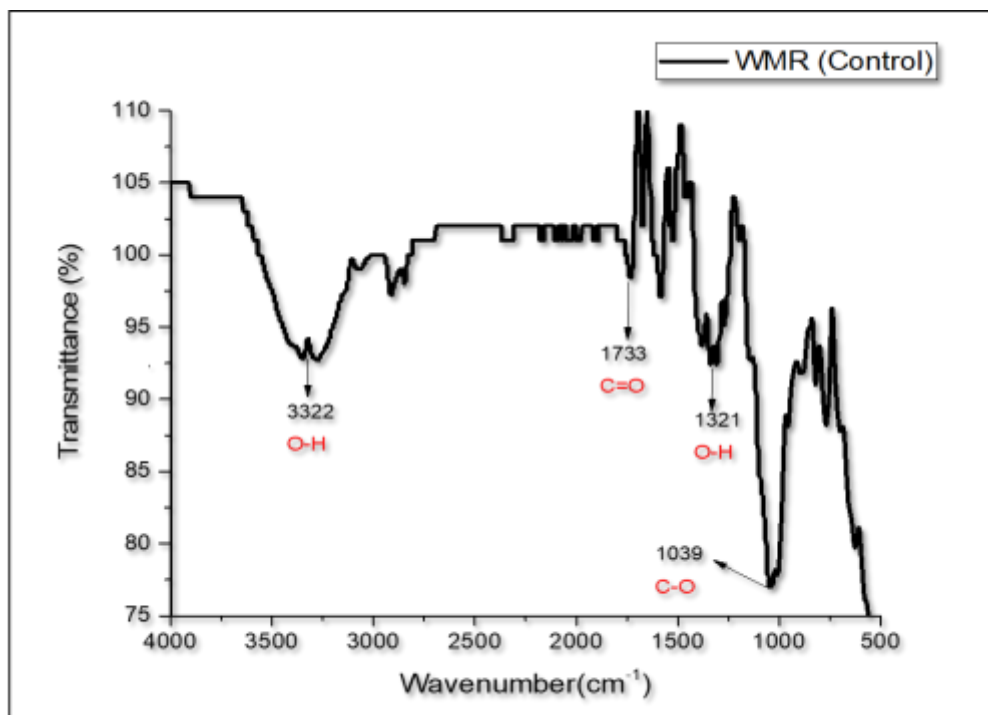


Figure 2. FTIR Spectra of WMR before adsorption

3.2 Effect of various parameters on lead adsorption

Lead adsorption by WMR as affected by various factors including adsorbent dose, solution pH, contact time, agitation speed and temperature is depicted in figure 3a - 3e.

3.2.1 Effect of adsorbent dose

The impact of adsorbent dose on Pb adsorption was monitored by varying concentrations of WMR ranged from 0.15 gL^{-1} to 5 gL^{-1} (figure 3a). The results revealed that initially as the WMR dose increased from 0.15 gL^{-1} to 0.25 gL^{-1} , the Pb removal increased from 47.6% to 76.3% respectively. The maximum Pb removal (81.54%) was obtained at a dose of 1 gL^{-1} . The further increase in dose (2 gL^{-1}) had reduced the Pb removal to 66.55% sharply. After further increasing the WMR dose up to 5 gL^{-1} , the Pb removal remained almost the same (nearly 55%). The increase in Pb uptake by increasing WMR dose was linked to the accessibility of more binding sites for Pb adsorption. The reduction in Pb removal at higher WMR doses could be apprehended as a result of aggregation of WMR particles which led to the decrease in surface area of WMR [10]. The optimum WMR dose of 1 gL^{-1} was selected for further experiments.

3.2.2 Effect of solution pH

The pH of the solution is a critical factor that significantly affects metal adsorption. The effect of pH was monitored at different pH ranging from 2 to 10 (figure 3b). The Pb removal increased from 29.6% to 55.6% as the pH increased from 2 to 3. Further increase in pH (4 & 5) led to the increase in Pb removal (80.3% & 81.5% respectively). The maximum Pb removal was attained at pH 5 (81.54%). After further increasing the pH from 6 to 8, the Pb removal gradually dropped from 81.5% to 40.8% respectively. By increasing pH up to 10, no remarkable change was observed in Pb removal. These results could be comprehended by contemplating the phenomenon of competing H^+ ions with Pb ions. Under conditions of extremely low acidity, H^+ ions contend with Pb ions for the adsorption sites that are accessible. As the pH is increased, deprotonation of some binding groups occurred, which lessened the competition between Pb ions and H^+ ions, thus more binding sites were provided for Pb ions adsorption. After further increasing the pH >4 , the decline in Pb removal was due to the precipitation of Pb ions [10].

3.2.3 Effect of contact time

The effect of shaking time on Pb adsorption was studied from 0 to 50 minutes (figure 3c). At zero contact time, 62% Pb was removed by WMR. A sharp increase in Pb removal (77%) was observed up to 5 minutes of contact time. However, a gradual increase in Pb removal was observed from 5 to 25 minutes. The graph depicted that the maximum Pb removal (81%) was attained at 25 minutes. However, its removal decreased to 79.1% at 30 minutes. The further increase in the contact time (up to 50 minutes), had no significant impact on Pb removal as it remained constant (nearly 79%). The increase in Pb adsorption by increasing contact time could be due to the existence of more binding sites for Pb uptake. The gradual reduction in Pb removal after increasing the contact time above 25 minutes could be credited as gradual adsorption of Pb ions onto the WMR surface which caused its slow uptake even at higher contact time ranges [11].

3.2.4 Effect of agitation speed

The impact of agitation speed revealed that an increase in Pb removal (74.5% to 81.5%) was observed with an initial rise in shaking speed from 0 to 100rpm (figure 3d). The graph showed that the maximum Pb removal (81.54%) was obtained at 100 rpm. The further increase in agitation speed (150 rpm) led to reduction in Pb removal (76.29%). It was observed that further increase in stirring speed up to 250 rpm had not significantly affected Pb removal as it remained almost constant (77%). These results could be described by keeping in consideration the fact that lower speeds caused the inappropriate dispersion of WMR particles into the Pb containing solution, thus leading towards the poor availability of active binding sites for Pb removal. On the contrary, high shaking speed vigorously circulated the WMR particles into the Pb containing solution which resulted into the insufficient time for binding Pb ions with adsorbent [12].

3.2.5 Effect of temperature

The figure 3e depicted that initially, by increasing the temperature from 15°C to 25°C, the Pb removal showed an increment from 76.5% to 81.5% respectively that showed maximum Pb removal. It was observed that further increase in temperature (upto 30°C) declined the Pb removal

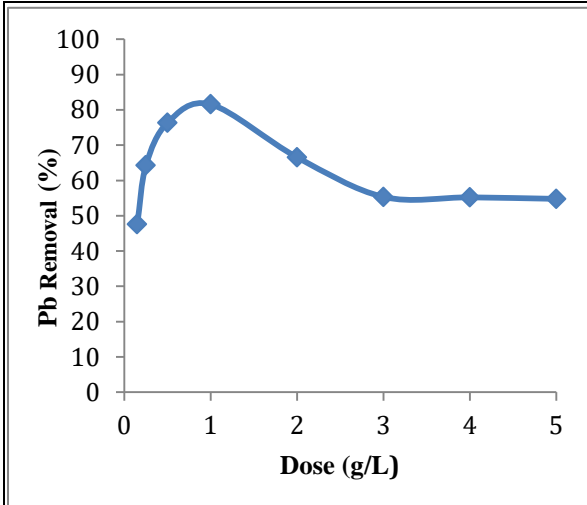


Figure 3a. Effect of Adsorbent dose on Pb removal (pH 5.2, Pb conc. $50\mu\text{g mL}^{-1}$, contact time 25 minutes, agitation speed 100 rpm, temperature 25°C).

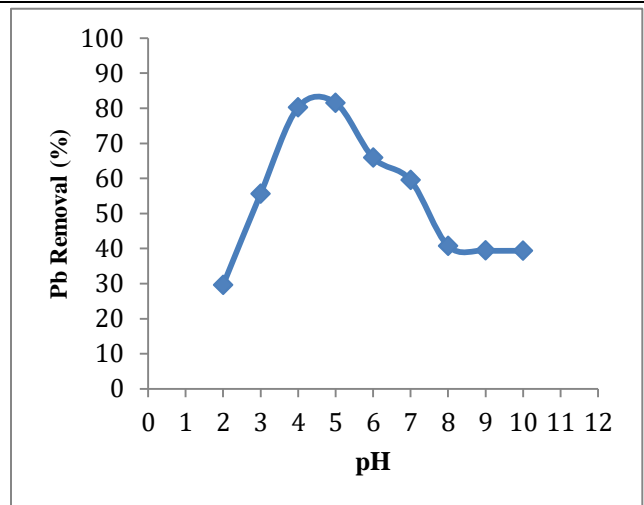


Figure 3b. Effect of pH on Pb removal (adsorbent conc. 1gL^{-1} , Pb conc. $50\mu\text{g mL}^{-1}$, contact time 25 minutes, agitation speed 100 rpm, temperature 25°C).

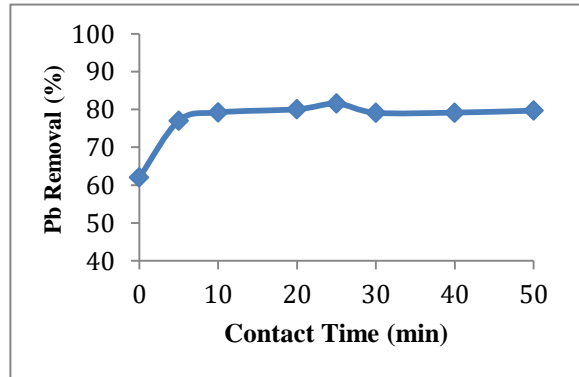


Figure 3c. Effect of contact time on Pb removal (adsorbent conc 1gL^{-1} , Pb conc. $50\mu\text{g mL}^{-1}$, pH 5, agitation speed 100rpm, temperature 25°C).

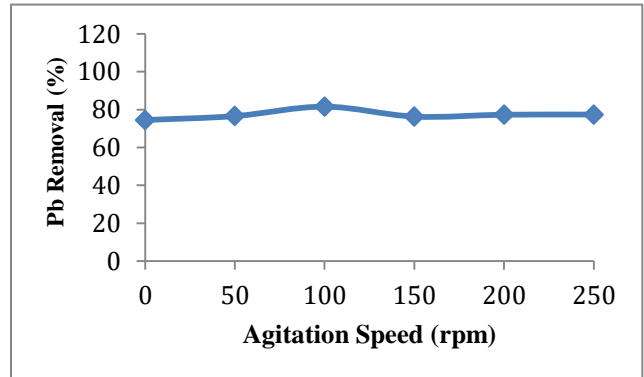


Figure 3d. Effect of agitation speed on Pb removal (adsorbent conc. 1gL^{-1} , Pb conc. $50\mu\text{g mL}^{-1}$, pH 5.2, contact time 25 minutes, temperature 25°C).

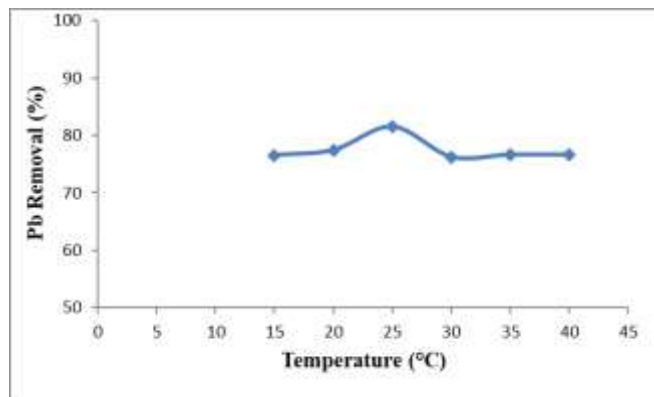


Figure 3e. Effect of temperature on Pb removal (Adsorbent dose 1gL^{-1} , Pb conc. $50\mu\text{g mL}^{-1}$ pH 5.2, contact time 25 minutes, agitation speed 100 rpm)

(76.2%), which remained constant (76%) by further increasing the temperature upto 40°C. These results explained that the initial rise in Pb adsorption with the increase of temperature led to the development of Pb ions from the contaminated water onto the unoccupied sites of WMR [13]. On the other hand, reduction in Pb removal at higher temperature was due to the weakened adsorption interactions between Pb ions and WMR surface which supported physio-sorption [14].

3.3 Effect of various parameters on cadmium adsorption

Cadmium adsorption by WMR as affected by various factors including adsorbent dose, pH, contact time, agitation speed and temperature is depicted in Figures 4a-4e

3.3.1 Effect of adsorbent dose

The impact of adsorbent dose on Cd removal was investigated across varying concentrations of adsorbent, ranging from 0.15 g L⁻¹ to 11 g L⁻¹ (Figure 4a). The findings indicated that initially, increasing the WMR dose from 0.15 g L⁻¹ to 0.25 g L⁻¹ resulted in Cd removal increment of 29% to 36%. Subsequent increments in WMR dose up to 1g L⁻¹ led to a Cd removal of 57%. Notably, a substantial increase in Cd removal (71%) was observed as the dose was elevated from 1 to 2 g L⁻¹. Moreover, a gradual rise in Cd removal was observed upon further increasing the dose up to 6 g L⁻¹. The peak removal of Cd, reaching 86.3%, was attained with 8 g L⁻¹ dose of WMR. However, a further increase in the dose (9 g L⁻¹) reduced Cd removal to 84.4%. The results demonstrated that subsequent increase in dose (10 - 11 g L⁻¹) had minimal impact on Cd removal, maintaining a consistent removal rate (84%). The escalation in Cd removal as the dose increased was linked to the heightened availability of active sites for Cd adsorption. Conversely, the decline in Cd uptake at higher doses could be attributed to the competition between previously adsorbed Cd ions and incoming Cd ions. Furthermore, aggregation of adsorbent particles led to the reduction in surface area of WMR. This can also be speculated from the results that increase in adsorbent dose at constant Cd concentration limited the degree of freedom of Cd ions and the constant volume of Cd solution caused the impregnation of binding sites which ultimately decreased the adsorption capacity and Cd removal.

3.3.2 Effect of solution pH

The effect of pH on Cd removal by WMR was studied at pH ranges of 4-9 (figure 4b). The results divulged by figure 4b indicated that firstly, increase in Cd removal from 82.6 % to 83.1 % was noted as the pH was increased from 4 to 5. At pH 6, maximal Cd removal (86.3 %) was obtained. Further rise in pH to 7, Cd removal gradually decreased to 84.5 % which remained almost the same by increasing the pH up to 9. These results could be comprehended by keeping in focus the competitive phenomenon of H⁺ ions with the Cd²⁺ ions. In conditions of lower pH, elevated concentrations of H⁺ ions lead to a competitive interaction with Cd²⁺ ions for the active sites that are available. The increase in pH caused the deprotonation of some functional groups (-COOH, -NH₂) which made the surface of WMR negatively charged due to the decrease in hydronium ions, thus making the WMR surface more available for cadmium ions instead of hydronium ions. After further increasing the pH above 6, a decline in Cd removal was perceived due to the

precipitation of Cd^{2+} ions as the Cd^{2+} ions reacted with hydroxides ions and precipitate the Cd^{2+} ions as cadmium hydroxides. The optimum pH of solution selected for further experiments was 6.

3.3.3 Effect of contact time

The influence of contact time on Cd adsorption was examined within a time range of 0 to 50 minutes (figure 4c). The results indicated that at zero contact time, there was 60.7% Cd removal. The results further showed that with the rise of stirring time up to 5 minutes, a sharp rise in Cd uptake was observed (83.6%). A gradual increase in Cd removal (from 83.9% to 86.3%) was noticed as the stirring time was increased from 5 to 25 minutes. The highest Cd removal (86.3%) was attained at 25 minutes. The increase in contact time up to 30 minutes led to reduction in Cd adsorption (84.8%). Further increment in agitation time till 50 minutes had no significantly impact on Cd removal. The increase in Cd uptake with the increase of contact time was the consequence of more availability of active sites and adequate time for binding the Cd^{2+} ions with active functional sites present on the WMR surface. The gradual reduction in Cd removal after increasing the contact time above 25 minutes could be regarded as the saturation of adsorbent surface with maximum Cd^{2+} ions adsorption which ultimately declined the Cd removal.

3.3.4 Effect of agitation speed

The impact of agitation speed on Cd removal was assessed by varying the speeds in the range of 0 to 250 rpm (figure 4d). Initially, escalating the agitation speed from 0 rpm to 50 rpm resulted in a notable rise in Cd removal (71.8% - 81.7%). Subsequently, further elevating the agitation speed up to 100 rpm led to the highest increase in Cd removal (86.3%). However, increasing the agitation speed beyond 150 rpm caused a reduction in Cd removal (83.2%), which remained relatively stable with subsequent increases in agitation speed up to 250 rpm. These results could be interpreted by keeping in consideration the aspect adsorbate (Cd) solution to bind the Cd ions with them, thus leading towards the poor availability of active binding sites for Cd adsorption. While on the contrary, high shaking speeds vigorously circulated the adsorbent particles into the Cd solution which caused the insufficient time for binding Cd ions with the adsorbent [15].

3.3.5 Effect of temperature

Variations in temperature (15°C to 40°C) were observed on Cd adsorption by WMR (figure 4e). At first, with the increase of temperature from 15°C to 25°C, the Cd removal showed an increment from 81.9% to 86.3% respectively showing maximum removal. The further increase in temperature (30°C) decreased the removal (85.4%) which remained constant up 40°C. The initial increase in Cd removal with temperature was attributed to the adsorption of Cd ions from the solution onto the unoccupied binding sites of WMR, facilitated by the lower temperature. On the other hand, reduction in Cd removal at higher temperature was the consequence of weakened adsorption interactions between the Cd ions and WMR surface.

3.4 Adsorption Isotherms

Adsorption isotherms depict the distribution of adsorption molecules between the solid and liquid phases at equilibrium during the adsorption process [16]. These isotherms are important to

indicate the interaction of adsorbates with adsorbents; therefore, correlation of equilibrium data by using adsorption equations is essential for practical adsorptive processes [17]. An adsorption isotherm offers essential insights into adsorption capacity, binding strength and surface properties of the adsorbent, aiding in comprehending how the adsorbate binds with the adsorbent. The Langmuir isotherm explains monolayer adsorption of adsorbates on the adsorbent surface, while the Freundlich isotherm describes adsorption taking place on a heterogeneous surface of the adsorbent [18].

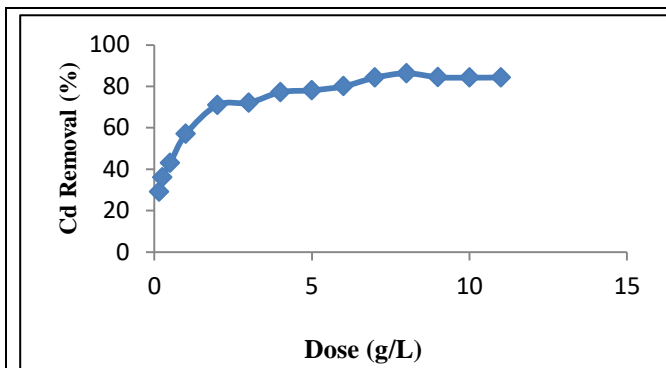


Figure 4a. Effect of adsorbent dose on Cd removal (pH 6, Cd conc. 50 mgL⁻¹, contact time 25 minutes, agitation speed 100rpm, temperature 25°C).

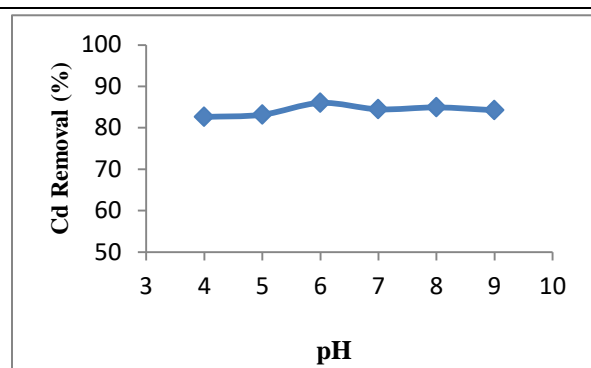


Figure 4b. Effect of pH on Cd removal (adsorbent dose 8gL⁻¹, Cd conc. 50 mgL⁻¹, stirring time 25 minutes, agitation speed 100 rpm, temperature 25°C).

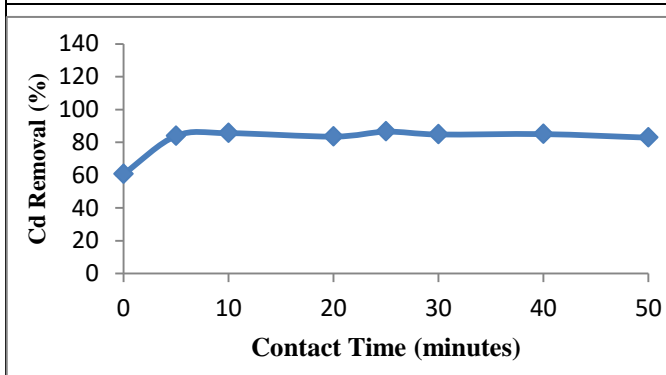


Figure 4c. Effect of contact time on Cd removal (adsorbent dose 8 gL⁻¹, pH 6, Cd conc. 50mgL⁻¹, agitation speed 100 rpm, temperature 25°C).

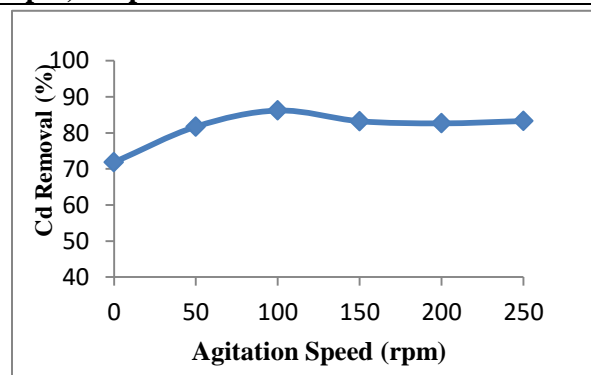


Figure 4d. Effect of agitation speed on Cd removal (adsorbent dose 8gL⁻¹, pH 6, Cd conc. 50 mgL⁻¹, contact time 25 minutes, temperature 25°C).

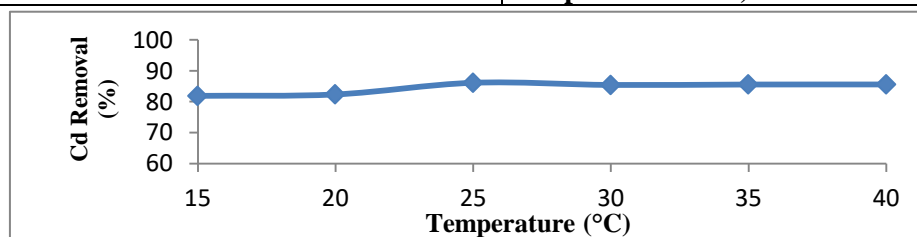


Figure 4e. Effect of temperature on Cd removal (adsorbent conc. 8gL⁻¹, pH 6, Cd conc. 50mgL⁻¹, contact time 25 minutes, temperature 25°C)

3.4.1 Adsorption Isotherms for Lead

3.4.1.1 Langmuir Isotherm

The Langmuir adsorption isotherm indicates correlation coefficient value ($R^2 = 0.998$) which suggested that Langmuir isotherm was valid to explain adsorption of Pb on WMR surface. The Langmuir model is presented in figure 5. The maximum capacity of WMR for Pb adsorption was found 82.46 mg/g (Table V). The value of separation factor (R_L) was less than 1 (0.486) which indicated that adsorption of Pb onto WMR surface was favorable. The Langmuir constant (K_L) is attributed towards bond energy for binding of Pb with WMR by complex formation reactions.

3.4.1.2 Freundlich Isotherm

The Freundlich isotherm for Pb (figure 6), presenting the parameters K_f (ultimate adsorption capacity) and n , which were computed from the graph of $\log C_e$ vs $\log q_e$. The Freundlich isotherm parameters are mentioned in Table VI. Freundlich constant (K_f) calculated from Freundlich isotherm was 1.51 with ($R^2=0.997$). The parameter 'n' indicates the level of adsorption intensity for Pb on WMR. The 'n' value of 1 signifies linear adsorption, while a value less than 1 indicates chemical adsorption. Conversely, if 'n' >1, it implies physical adsorption [19]. The value of n (0.676) indicated that Pb adsorption on WMR involves chemical processes.

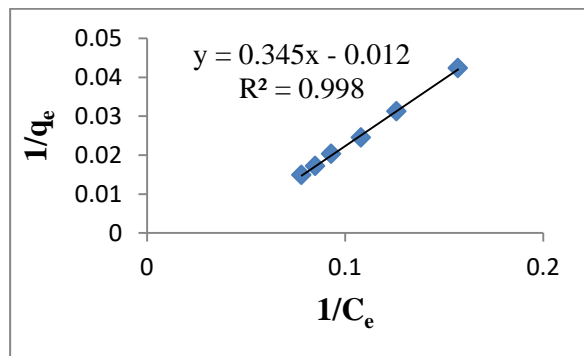


Figure 5. Langmuir isotherm for Pb

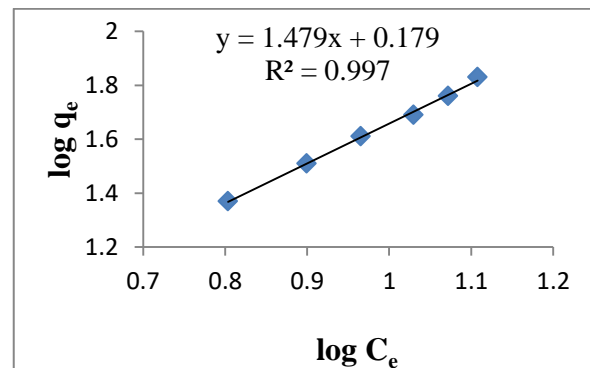


Figure 6. Freundlich Isotherm for Pb

Table V. Langmuir Isotherm parameters for Pb

Metal	Slope	Intercept	R^2	q_{max} (mg/g)	K_L	R_L
Pb	0.345	0.012	0.998	82.461	0.035	0.486

Where K_L = Langmuir constant, R_L = Separation factor, q_{max} = Maximum adsorption capacity, R^2 value describes the well fitted model for adsorption

Table VI. Freundlich Isotherm Parameters

Metal	Slope	Intercept	R^2	1/n	n	K_f
Pb	1.479	0.179	0.997	1.477	0.676	1.51

3.4.2 Adsorption Isotherms for Cadmium

3.4.2.1 Langmuir Isotherm

Langmuir isotherm for Cd adsorption (figure 7) with corresponding parameters is given in Table VII. The Langmuir isotherm model yielded an R^2 value of 0.976, affirming the accordance of Cd adsorption with the Langmuir isotherm model. Additionally, the maximum adsorption capacity (q_{max}) of WMR for Cd was found 55.45 mg/g. The separation factor i.e. R_L value below 1 (0.696), indicated the good loading of Cd adsorption onto the WMR surface.

3.4.2.2 Freundlich Isotherm

The Freundlich isotherm for Cd (figure 8) with corresponding parameters are presented in Table VIII. K_f (Freundlich constant) calculated from Freundlich isotherm was 1.056. The value ($R^2 = 0.978$) indicated that Freundlich isotherm model fits well for Cd adsorption. The value of n indicates the nature of the adsorption process. The value of $n > 1$ (1.156) indicated that Cd adsorption onto WMR surface was a physical phenomenon.

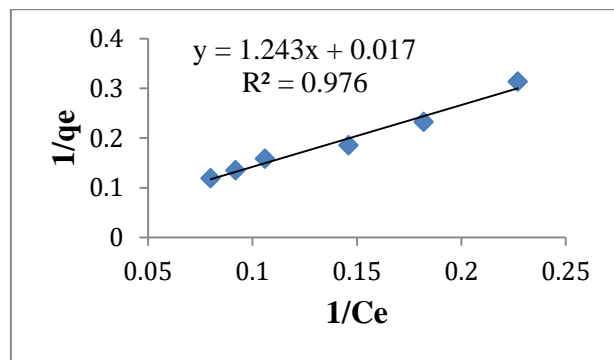


Figure 7. Langmuir Isotherm for Cd

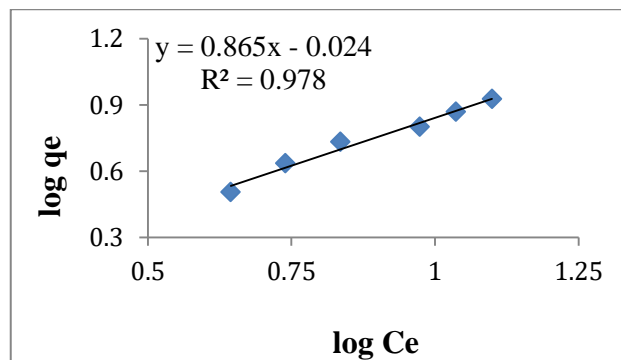


Figure 8. Freundlich Isotherm for Cd

Table VII. Langmuir isotherm parameters for cadmium

Slope	Intercept	K_L (L/mg)	C_o	q_{max}	R_L	R^2
1.243	0.017	0.015	30	55.45	0.696	0.976

Table VIII. Freundlich isotherm parameters for cadmium

Slope	Intercept	R^2	1/n	n	K_f
0.865	0.024	0.978	0.865	1.156	1.056

3.5 Fourier Transform Infrared (FTIR) Analysis

The FTIR spectra of WMR material after Pb and Cd adsorption are shown in figure 9 & 10. These spectra were obtained from scanning in the range of $500-5000\text{ cm}^{-1}$

3.5.1 FTIR Spectra of Lead loaded WMR

The adsorption mechanism of Pb on WMR is attributed to the active sites and bonds present within the rind. FTIR spectra of lead containing WMR, shifts in peaks related to the functional groups involved in lead adsorption were observed (figure 9). Specifically, the spectra indicated shifts in peaks associated with C=C, C=O (Esters), O-H (Phenol), and C-O (Primary alcohol) from 1583, 1733, 1321, and 1039 cm^{-1} to 1618, 1686, 1301, and 1046 cm^{-1} , respectively. These shifts could be attributed as changes by keeping in view the fact that counter ions associated with carboxyl and hydroxyl groups are major contributors in lead adsorption [20].

3.5.2 FTIR Spectra of Cadmium loaded WMR

The FTIR analysis of Cd adsorbed WMR showed distinct functional groups like hydroxyl, carboxyl, and carbonyl groups present in cellulose, hemicellulose and pectin that contribute to cadmium adsorption (figure 10). Additionally, the FTIR spectra of cadmium-loaded WMR demonstrated shifts in peaks corresponding to O-H (Alcohol), C=O, O-H (Phenol), and C-O (Primary alcohol) from 3322, 1733, 1321 and 1039 cm^{-1} to 3304, 1636, 1412 and 1028 cm^{-1} respectively. This was observed from the spectra of pure and cadmium containing watermelon rind that the strong band of C=O (at 1733 cm^{-1}) present in the pure WMR shifted to 1636 cm^{-1} which could be attributed as the pi-metal ion interaction of C=O group with Cd ions [10].

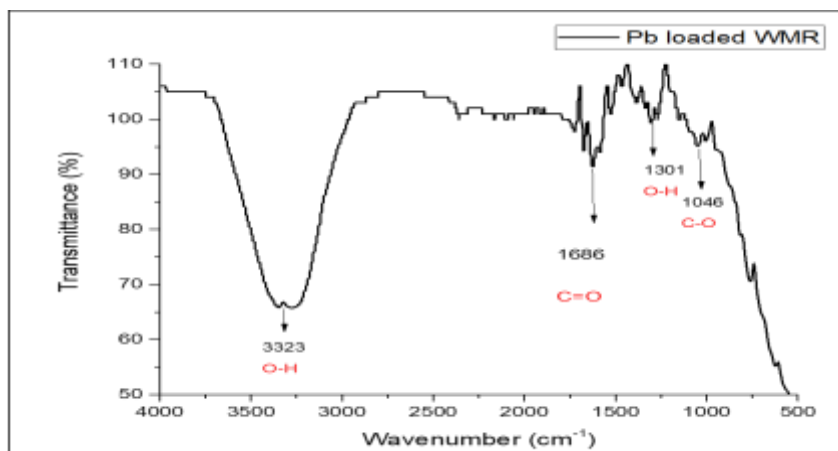


Figure 9. FTIR spectrum of Pb loaded WMR

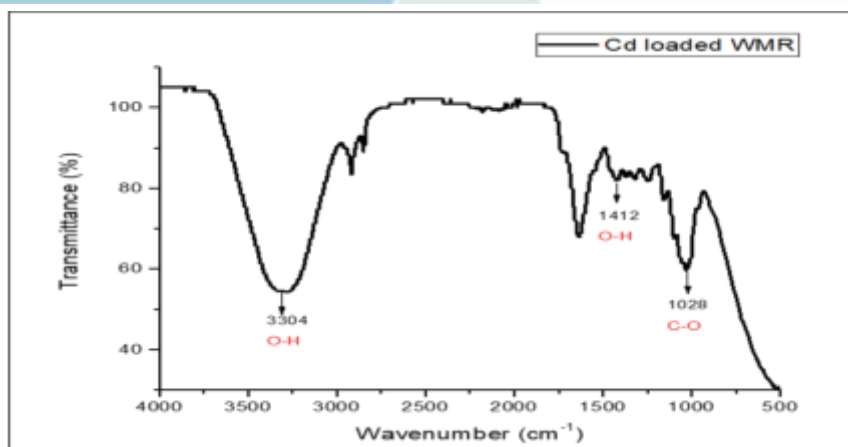


Figure 10. FTIR spectrum of Cd loaded WMR

4. CONCLUSIONS

The watermelon rind (WMR) investigated in the study exhibited good potential for removal of Pb and Cd from aqueous solution. FTIR spectra of WMR indicate the presence of functional groups like hydroxyl and carboxyl as contributors for metal adsorption. The Langmuir adsorption isotherm showed that WMR had maximum adsorption capacity of 82.46 mg/g for Pb and 55.45 mg/g for Cd showing 48.71% more potential to adsorb Pb as compared to Cd. The study concludes that instead of chemicals, cost-effective and eco-friendly agro-waste material like WMR can be used efficiently to remove toxic metals (Pb, Cd) from wastewater to overcome water pollution.

ACKNOWLEDGEMENTS

The research support and facility provided by Central Analytical Facility Division and Chemistry Division, PINSTECH is highly acknowledged.

REFERENCES

- [1] L. Joseph, B.-M. Jun, J. R. Flora, C. M. Park, and Y. Yoon, "Removal of heavy metals from water sources in the developing world using low-cost materials: A review," *Chemosphere*, **Vol. 229**, p. 142-159 (2019).
- [2] Wastewater The Untapped Resource. The United Nations World Water Development Report. 2017, UNESCO.
- [3] J. AguilarRosero, M. E. Urbina-López, B. E. Rodríguez-González, S. X. León-Villegas, I. E. Luna-Cruz, and D. L. Cárdenas-Chávez, "Development and characterization of bioadsorbents derived from different agricultural wastes for water reclamation: a review," *Applied Sciences*, **Vol. 12**, no.5, p. 2740(2022).

- [4] B. Debnath, W. S. Singh, and K. Manna, "Sources and toxicological effects of lead on human health," *Indian Journal of Medical Specialities*, **Vol. 10**, no. 2, p. 66 (2019).
- [5] C. Bhattacharjee, S. Dutta, and V. K. Saxena, "A review on biosorptive removal of dyes and heavy metals from wastewater using watermelon rind as biosorbent," *Environmental Advances*, **Vol. 2**, p. 100007(2020).
- [6] P. Amoatey, and R. Bani, *Wastewater management*. INTECH Open Access Publisher (2011).
- [7] L. K. Munishi, P. A. Ndakidemi, W. Blake, S. Comber, and T. H. Hutchinson, "Toxic metals in East African agro-ecosystems: Key risks for sustainable food production," *Journal of Environmental Management*, **Vol. 294**, p. 112973 (2021).
- [8] V. Masindi, P. Mkhonza, and M. Tekere, "Sources of Heavy Metals Pollution," *Remediation of Heavy Metals*, p. 419-454 (2021).
- [9] G. A. El-Din, A. Amer, G. Malsh, and M. Hussein, "Study on the use of banana peels for oil spill removal," *Alexandria engineering journal*, **Vol. 57**, no. 3, p. 2061-2068 (2018).
- [10] Q. Wang, Y. Wang, L. Yuan, T. Zou, W. Zhang, X. Zhang, L. Zhang, X. Huang, "Utilization of low-cost watermelon rind for efficient removal of Cd (II) from aqueous solutions: Adsorption performance and mechanism elucidation," *Chemical Engineering Journal Advances*, **Vol. 12**, p. 100393 (2022).
- [11] M. A. Abd-Elaziz, M. Taha, M. Gahly, and H. Hefnawy, "Removal of Fe⁺³ and Pb⁺² ions from aqueous solutions by adsorption using banana peels" *Zagazig Journal of Agricultural Research*, **Vol. 49**, no. 6, p. 853-864 (2022).
- [12] A. U. Augustine, B. Ishaq, T. M. Akpomie, and R. Odoh, "Removal of Lead (II) and Iron (II) ions from Aqueous Solutions Using Watermelon (*Citrillus Lanatus*) Peels as Adsorbent." *Open Access Journal of Chemistry*. **Vol. 3**, .no.1, p.1-7 (2019).
- [13] T. F. Akinhanmi, E. A. Ofudje, A. I. Adeogun, P. Aina, and I. M. Joseph, "Orange peel as low-cost adsorbent in the elimination of Cd (II) ion: kinetics, isotherm, thermodynamic and optimization evaluations," *Bioresources and Bioprocessing*, **Vol. 7**, no. 1, p. 1-16(2020).
- [14] Q. Wu, Y. Xian, Z. He, Q. Zhang, J. Wu, G. Yang, X. Zhang, H. Qi, J. Ma, Y. Xiao and L. Long "Adsorption characteristics of Pb (II) using biochar derived from spent mushroom substrate" *Scientific Reports*, **Vol. 9**, no. 1, p. 15999 (2019).
- [15] E. A. Ofudje, I. A. Adeogun, M. A. Idowu, S. O. Kareem, and N. A. Ndukwe, "Simultaneous removals of cadmium (II) ions and reactive yellow 4 dye from aqueous solution by bone meal-derived apatite: kinetics, equilibrium and thermodynamic evaluations," *Journal of Analytical Science and Technology*, **Vol. 11**, p. 1-16 (2020).
- [16] G. Vilardi, L. Di Palma, and N. Verdone, "Heavy metals adsorption by banana peels micro-powder: Equilibrium modeling by non-linear models," *Chinese Journal of Chemical Engineering*, **Vol. 26**, no. 3, p. 455-464 (2018).
- [17] P. V. Sierra-Trejo, E. Guibal, and J. F. Louvier-Hernández, "Arsenic sorption on chitosan-based sorbents: comparison of the effect of molybdate and tungstate loading on As (V) sorption properties" *Journal of Polymers and the Environment*, **Vol. 28**, p. 934-947 (2020).
- [18] M. A. Mahmoud, and M. M. El-Halwany, "Adsorption of cadmium onto orange peels: isotherms, kinetics, and thermodynamics," *Journal of Chromatography Separation Technique*, **Vol. 5**, no. 5. P 1-6 (2014).
- [19] N. B. Dewage, R. E. Fowler, C. U. Pittman, D. Mohan, and T. Mlsna, "Lead (Pb²⁺) sorptive removal using chitosan-modified biochar: batch and fixed-bed studies," *RSC advances*, **Vol. 8**, no. 45, p. 25368-25377 (2018).
- [20] Huosheng, Li, J. Xiong, T. Xiao, J. Long, Q. Wang, K. Li, X. Liu, G. Zhang and H. Zhang "Biochar derived from watermelon rinds as regenerable adsorbent for efficient removal of thallium (I) from wastewater," *Process Safety and Environmental Protection*, **Vol. 127**, p. 257-266(2019).

Potential use of the TRIGA Mark III Reactor for neutrographies

*Hernández-Galeana Jaime**

*National Institute for Nuclear Research (ININ-México)
Carr. México-Toluca s/n, 52750 La Marquesa, Méx.
jaime.hernandez@inin.gob.mx;*

Montaño-Acevedo Celeste and Olguín-Rodríguez Itzel

*celes.jeanette@gmail.com;
itzel_ad2@hotmail.com*

Abstract

This article describes the neutrography tests carried out in the TRIGA Mark III Reactor of the National Institute for Nuclear Research. In the west tangential beamport 1, a digital camera was installed to obtain neutrographies, this beamport has the necessary parameters to perform the technique. Several tests were carried out with different collimation systems, resolution tests were performed and irradiation parameters were optimized, such as reactor operating power and exposure time, thus obtaining neutrographies where the difference in materials and thicknesses can be clearly seen.

1. INTRODUCTION

Neutrography is a non-destructive testing technique similar to radiography, both of which photograph the interior of solid structures, in the case of neutrography, by means of a beam of neutrons, and radiography by X-rays. Neutrons are strongly absorbed by light elements such as hydrogen, cadmium and boron, and interact differently with matter. This technique offers additional information to that obtained with X-ray radiographs.

2. EXPERIMENTAL AND THEORETICAL METHODOLOGY

The system to obtain neutrographies (Figure 1) is mainly based on a neutron source, a collimator and a detector [1].

A proper installation of neutrographies must meet certain specifications to obtain the best images [2], for example:

- Have a collimated thermal neutron flux of the order of 10^8 n/cm² s.
- Low intensity of gamma radiation (the ratio of thermal neutrons to gammas is of the order of at least 10^5 n/cm² mR).
- A low fast neutron intensity or cadmium ratio greater than 2.4.

- The ratio of $L/D > 100$, where L is the distance from the aperture of the first collimator to the screen and D is the diameter of the collimator.

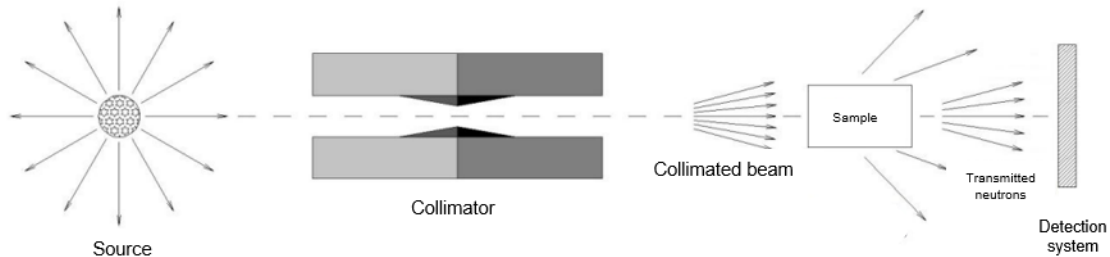


Figure 1. System to obtain neutrographies [1].

2.1 Reactor Facility for Neutrographies

The National Institute for Nuclear Research has a TRIGA Mark III type nuclear research reactor. This reactor has several experimental facilities, internal (inside the core) and external (outside the core), among the external facilities are the tangential and radial tubes. [3]

At the north end of the pool, next to the thermal column, there are two tubes that penetrate from west side of the pool concrete to the east side, passing through the interior of the pool tangentially to the reactor core, these are called tangential beam tubes.

The tangential tubes have a total length of 828.91 cm, their external part is made of steel with a thickness of 0.635 cm, they have a diameter of 25 cm and their internal part (inside the pool) is made of aluminum with a thickness of 0.703 cm and a diameter of 20 cm.

In the reactor, the tangential port west 1 (Figure 2, blue color) was enabled in the past to obtain film neutrographies. The radial tubes have higher neutron and gamma radiation fields than the tangential tubes, while the latter have lower intensity radiation fields and higher neutron/gamma ratio; with respect to the neutron spectrum, the radial tubes have a higher fast neutron component than the tangential tubes.

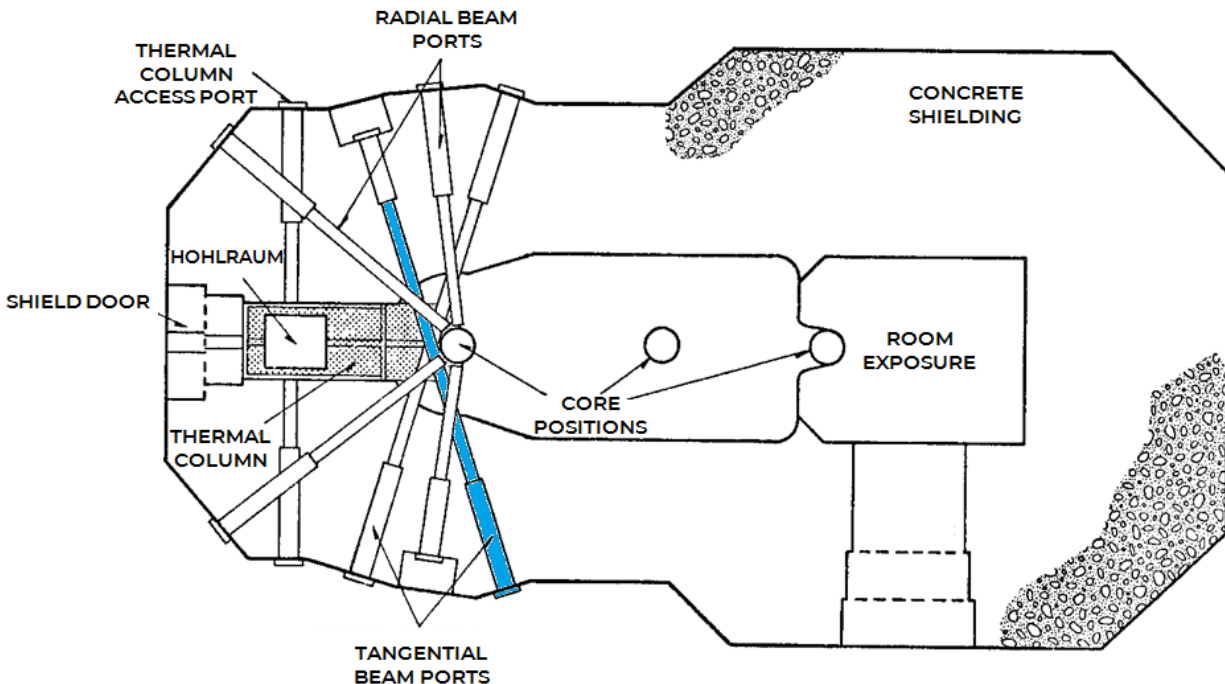


Figure 2. TRIGA Mark III Reactor facility [3].

The orders of magnitude of the fluxes in the radial ports are; thermal flux 10^8 n/cm² s and epithermal flux 10^5 n/cm² s. In the tangential ports those are; thermal flux 10^7 n/cm² s and epithermal flux 10^5 n/cm² s [4].

The shielding allows personnel operating the digital camera to work in the vicinity of the reactor since the exposure rate is in the order of 0.1 mR/h. To open the beam ports it must be taken into account that the reactor must be turned off and away from the thermal column position, it must be between the central position and the exposure room.

2.2 Digital System to Obtain Neutrographies

As mentioned earlier, to obtain neutrographies, a neutron source, a neutron collimation system, a neutron detection system, shielding and radiation safety are needed. The TRIGA Mark III Reactor produces a constant and controlled neutron flux.

The neutron imaging detection system use a detector comprised of 2 parts: a scintillation screen (LiF:ZnS) and a CCD camera. The images were obtained with a Sony VS60 digital camera (Figure 3) connected to the computer by means of Artemis Capture software [5].

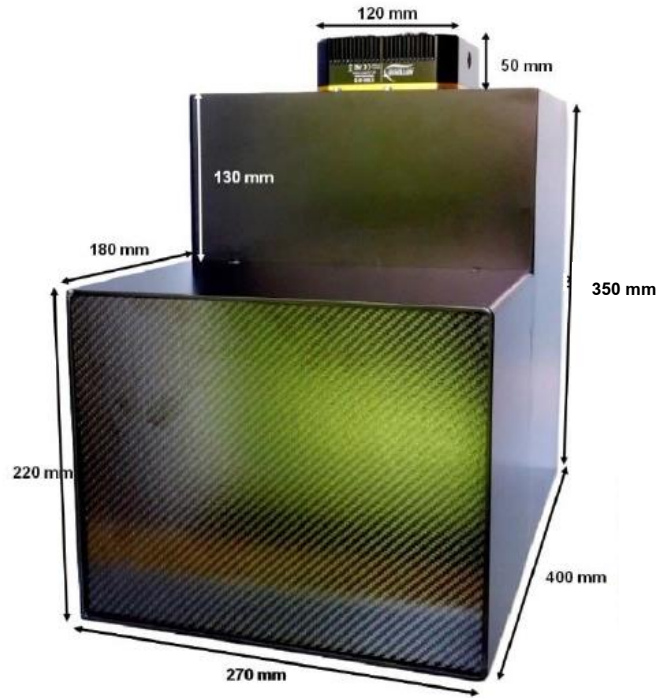


Figure 3. Digital camera to obtain neutrographies.

The first collimation system (Figure 4) had already been used to obtain film neutrographies in the 90's [6], so we decided to make the first tests of digital neutrographies with this system. In this case, $L = 204$ cm and $D = 3$ cm, therefore, $L/D = 68$. The collimators used are also shown in this image, the first one is 15.7 cm long, with an external diameter of 20 cm and an internal diameter of 3 cm. It is composed of the following materials: 10 cm of borate paraffin, a boron plate of 0.2 cm thickness, a space without material of 0.5 cm and 5 cm of lead. The second is a diverging collimator with a length of 49.66 cm, 25 cm outside diameter, 7 cm smaller inner diameter and 18.7 cm larger inner diameter. It is composed of the following materials: 2.6 cm of lead, 47 cm of paraffin and a 0.06 cm thick cadmium plate.

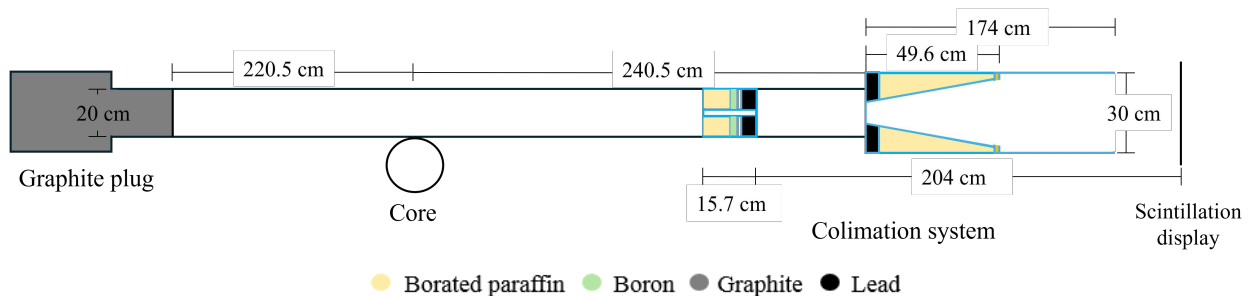


Figure 4. First collimation system.

As camera shielding, 10 cm of borated paraffin and 10 cm of lead were used around the digital camera and the electronics were also well shielded so that they would not be damaged by gamma radiation. Additionally, a beam catcher was placed at the back of the camera to stop the neutron beam and the gamma radiation component.

The digital camera (scintillation screen) was placed 16.5 cm from the beam port, and a computer-controlled sample holder was placed between the beam port and the camera, allowing the personell to be up to 20 m away from the system.

To improve the imaging results, it was decided to put the collimators together (Figure 5) obtaining an $L/D = 63.5$ and continuing to use the same shielding.

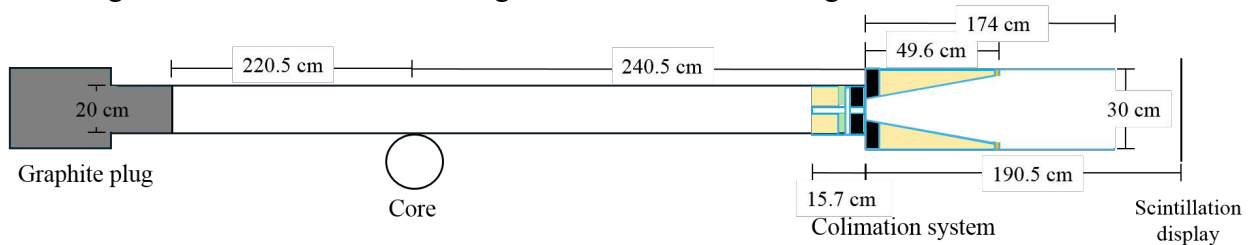


Figure 5. Second collimation system.

Since the best results are obtained with a ratio of $L/D > 100$ [2], it was decided to increase the distance from the collimator to the scintillator screen (L) by moving the camera farther away from the beam port. Figure 6 shows the diagram of this new system with which we obtained a ratio of $L/D = 109.6$. In this case a different shielding was used, 40 cm x 40 cm x 60 cm borated concrete blocks were used to increase the beam line between the beam port and the camera. The shielding used in the two previous collimation systems was placed 120 cm away from the beam port.

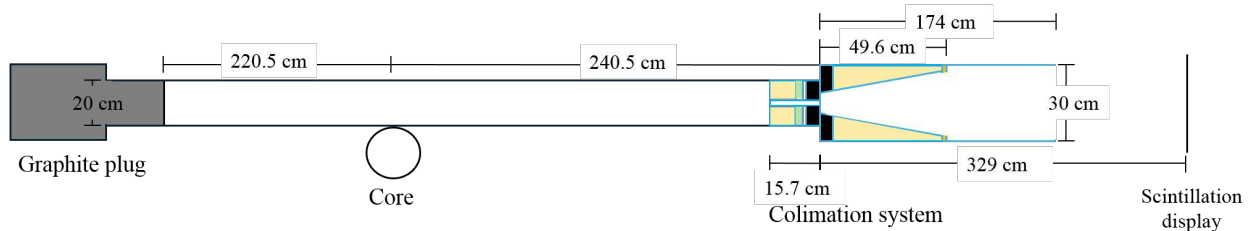


Figure 6. Third collimation system.

2.3 Power and Exposure Time Tests

The first neutrographies were obtained from a timer (Figure 7), using the first collimation and shielding system (Figure 4). Different powers (P) and exposure times (t_e) were chosen (Table 1) to compare the results and make an analysis to find the best combination of these parameters, and thus obtain a good image quality in the neutrographies.



Figure 7. Neutrographed sample (Timer).

Table I. Irradiation parameters - Timer, test 1.

Power (kW)	10	50	100	200	200
t_e (s)	1	5	10	5	1

A second series of tests was performed by setting the exposure time of the camera at 5 s and varying the power according to Table 2, the arrangement of the collimation system was changed to observe if the flux increased and the image improved by putting the collimators together as described in Figure 5.

Table II. Irradiation parameters – Timer, test 2.

Power (kW)	200	300	400	500	600	700	800	900	1000
t_e (s)	5	5	5	5	5	5	5	5	5

The third series of tests was performed with the second collimation and shielding system 2 (Figure 5), the exposure time was increased to 30 s and neutrographies were taken at powers of 200 kW, 500 kW and 1 MW (Table 3).

Table 3. Irradiation parameters – Timer, test 3.

Power (kW)	200	500	1000
t_e (s)	30	30	30

2.4 Resolution tests

A device with image resolution indicators was designed and built (Figure 8), the material used was a mixture of polyethylene, boron and paraffin. The device has 9 mm, 6 mm and 3.2 mm

diameter holes as well as the corresponding distance between them; the size of the smallest visible hole defines the sensitivity or resolution of the images. Tests were carried out with the irradiation parameters mentioned in Table 4.

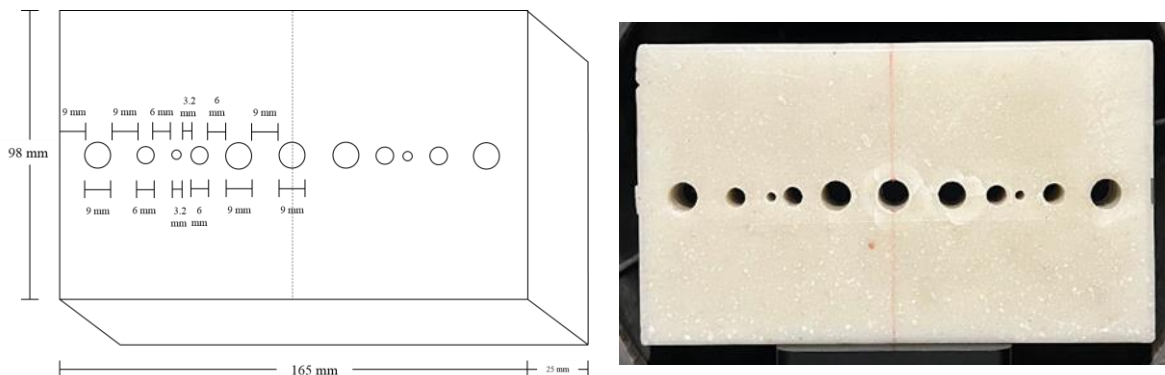


Figure 8. Device with resolution indicators.**

Table 4. Irradiation parameters - Resolution test

Power (kW)	t_e (s)
250	30
	60
	90
	120
500	30
	60
	90
	120

2.5 Materials test.

An electronic device (Figure 9) with diverse components and materials was used to evaluate the potential application of the neutrographies. The electronic device contains isolating material, screws, electrical connections, carcass, terminal connections and a semiconductor device. These components are made of different materials such as aluminium, silicon, copper, plastic, ceramic and other possible alloys.

The objective was to identify the different components previously described as well as to observe the differences in neutron attenuation in various materials. For this task, the following materials were placed on the back of the sample: a copper wire, a cadmium plate and a tin solder wire.

**Designed by Aguilar-Hernández F., and manufactured by Ortega-Velázquez B.

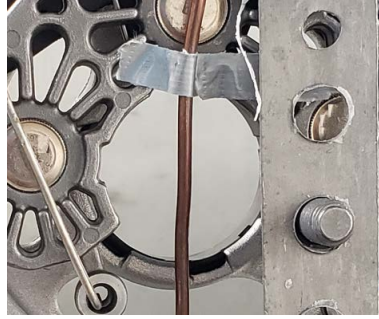


Figure 9. Electronic device with other materials.

The neutrography of the electronic device with the other materials was obtained with a power of 500 kW and an exposure time of 120 s. A neutrography of the neutron beam without sample (Open Beam) was obtained with the same irradiation parameters and a dark image with the same exposure time but without beam was also obtained to remove electronic noise.

The third collimation and shielding system were selected (Figure 6) to perform this neutrography.

2.6 Data Processing

The ImageJ [8] program for processing a scientific images we use to data processing. The detection system is not homogeneous over the area illuminated by the neutron beam. Hence, in addition to the neutrography containing the electronic device a second image without the sample has to be taken. This open beam image contains the same inhomogeneities as the neutrography, just without the sample. Additionally, the camera of the detector system has a certain thermal noise and offset. These two components are an additive component. Hence, an image containing this offset called dark image has to be acquired. The dark image (electronic noise) is subtracted from the neutrography of the electronic device. The Neutrography obtained is then divided by the Open Beam to remove the gamma spots (white spots), thus the image obtained allows us to specifically visualize the components of the electronic device.

3. RESULTS

3.1 Power and Exposure Time Test Results

From the neutrographies obtained with the parameters in table 1, it was observed that the sharpness improves with higher power and exposure time. From these neutrographies (table 2) it was observed that the higher the power, the higher the contrast and the lower the roughness of the images [7]. Between each pair of consecutive images there is no evident change.

Comparing the neutrographies obtained with the same powers and different exposure times (1, 2 and 3 tables) we observed greater sharpness and less roughness in the images as the exposure time increased. Figure 10 shows the change in image quality depending on power and exposure time

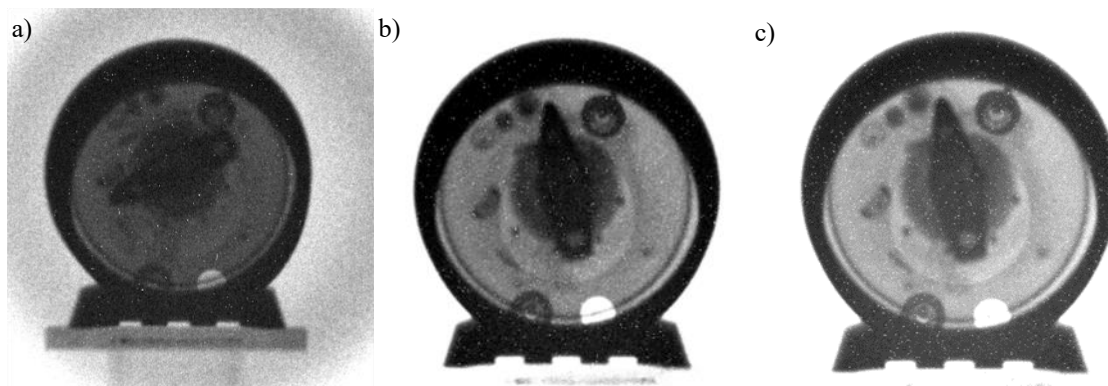


Figure 10. Timer neutrographies

a) $P = 200 \text{ kW}$, $t_e = 5 \text{ s}$; b) $P = 1 \text{ MW}$, $t_e = 5 \text{ s}$; c) $P = 1 \text{ MW}$, $t_e = 30 \text{ s}$.

3.2 Resolution Test Results

The neutrography obtained (Figure 11) was compared with the measurements of the piece and it was concluded that the resolution we obtained was good. Since the holes and smaller spaces with a diameter of 3.2 mm are well defined.

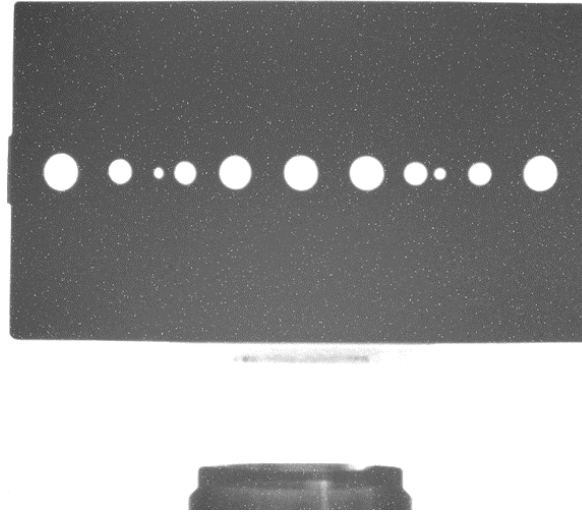


Figure 11. Neutrography of a device with resolution indicators
 $P = 500 \text{ kW}$, $t_e = 120 \text{ s}$.

3.3 Materials test results.

Figure 12 shows the neutrography of the electronic device with other materials, obtained with a power of 500 kW and an exposure time of 120 s, parameters turned out to be appropriate for this electronic device. There is an improvement in the sharpness and definition when approaching the neutrographed object to the detection system, so it was decided to place the electronic device as close as possible to the scintillation screen so that the closest semiconductor device were 2.5 cm away.

With low exposure times less contrast was observed, with high powers and longer exposure times the image had a greater amount of brightness that prevent the diferent components from being well seen. In addition, special care had to be taken to position the electronic device completely perpendicular to the neutron beam to avoid deformations in the image due to the tilt of the sample.

The left image shows the neutrography obtained without digital process. In this neutrography, the gamma component (white spots) is clearly observed; it also presents the electronic noise of the digital camera. The two elements do not allow the different components of the electronic device to be clearly identified.

In the image on the right, the neutrography is presented after the digital image processing stage, the electronic noise was substracted and the gamma spots were remove from the neutrography of the electronic device. Thus the image obtained allows us to specifically visualize the components of the electronic device.

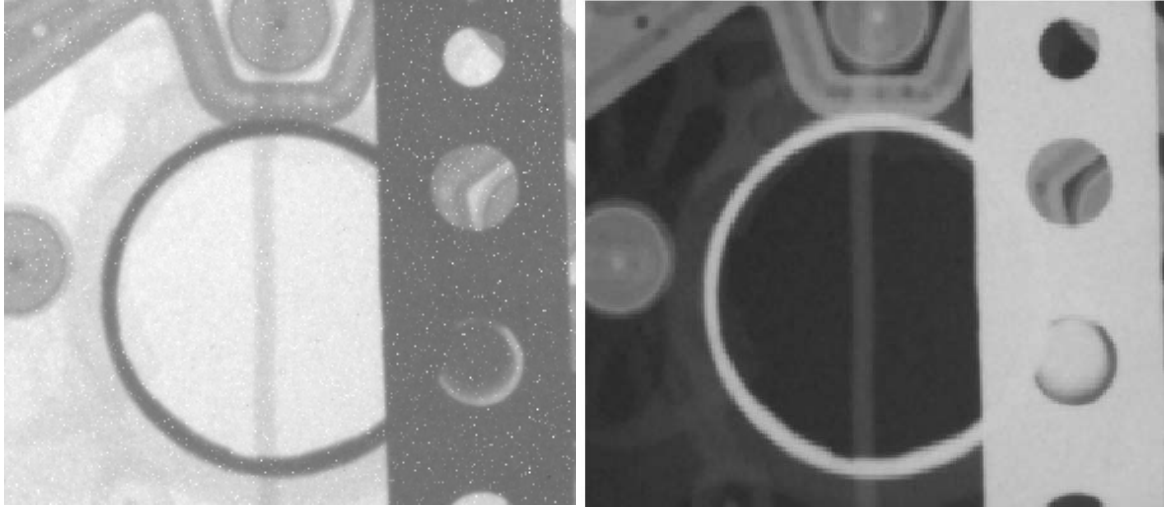


Figure 12. Neutrography of the electronic device with other materials, $P = 500 \text{ kW}$, $t_e = 120 \text{ s}$ (Left without digital process, right with digital process).

The neutrography presented after the processing stage allows us to identify the different components: isolating material, electrical connections, carcass, terminal connections and a semiconductor device. The transmission of neutrons through the electronic device was also observed: a high transmission for aluminum, for silicon and copper is lower.

The materials placed on the back of the sample show us the following information: the central copper wire located behind the electronic device can be fully appreciated, the tin solder wire is practically transparent like aluminum so it is not possible to observe it. On the other hand, the cadmium plate completely stops the neutrons, not allowing neutrons to pass through it.

4. CONCLUSIONS

The first neutrographies were obtained with a digital camera at the TRIGA Mark III Research Reactor. These neutrographs were obtained using the collimators that were available at the facility when film neutrographies were made. Different arrangements for the collimation system were sought to improve the neutrographies.

Very valuable relationships were found between the operating power and the exposure time to optimize the technique. The image becomes brighter with increasing power and the optimal value will depend on the sample material. The exposure time influences the roughness of the image and the longer the exposure time, the smoother the image will be. The distance between the sample and the scintillation screen should be reduced as much as possible to increase image definition. In combination, moving the sample closer to the scintillation screen and choosing the best irradiation parameters will result in clearer neutrographies.

It was possible to determine the specific parameters for obtaining the neutrography of the electronic device. Different components of the electronic device were observed. It was also possible to identify the different materials that make up the sample through the transmission of neutrons through it as well as observe different materials like copper, tin and cadmium placed behind the sample.

The system to obtain neutrographies still has many improvements to be made, such as the collimation system, shielding, resolution device and irradiation parameters for other materials.

ACKNOWLEDGEMENTS

We would like to express our appreciation to the National Institute for Nuclear Research for providing the necessary environment and resources to carry out this project. In addition, we would like to acknowledge our colleagues, Aguilar-Hernández F. from the Nuclear Technology Management, and from the Reactor Department, Alva-Escobar M., Enríquez-Cruz P., Herrera-Arriaga E., Ortega-Velázquez B., for their collaboration and constant support, which have been crucial for the realization of this project.

REFERENCES

1. Marin, J., Sanchez, F. A., & Blaumann, H., "Redesign, construction and characterization of the new neutron radiography facility of the RA-6", *XXXIX Annual meeting of the Argentine Association of Nuclear Technology*, Argentina (2012).
2. Berger H., Iddings F., *Neutron Radiography*, Nondestructive Testing Information Analysis Center, Austin, USA (1998).
3. ININ, "Reactor Safety Report," IFSR.UR-1 (2016).
4. H. S. Cruz-Galindo and R. Raya-Arredondo, "Study of Neutron Fluxes Before and After the Change of HEU to LEU Fuel of TRIGA MARK III Reactor of Mexico", *34th International Meeting on Reduced Enrichment for Research and test Reactors*, IAEA, October (2012).
5. Artemis Capture. Version 4.7.0.0., Atik Cameras (2011).
6. Delfin, A., Mazón, R., "Obtención de un haz de neutrones térmicos en tubos de haces del reactor para su aplicación en neutrografías", *Sociedad Nuclear Mexicana I Congreso Anual*, CDMX, Noviembre, Vol. 1, p.230-236 (1990).
7. Rafael C. Gonzalez, Richard E. Woods., "Digital Image Processing", *Global Edition. Pearson Editorial*, New York (2018).
8. Image J. Version 1.51q., National Institutes of Health, <https://imagej.net> (2015).

Investigating the relationship between soil properties and natural gamma emitter activity in Zacatecas using linear models and neural networks

Arreola-Ramírez Jesús Andrés, Ríos-Martínez Carlos and Escareño-Juárez Edmundo*
Unidad Académica de Estudios Nucleares, Universidad Autónoma de Zacatecas
Cipres 10, Peñuela, C.P. 98060, Zacatecas, Zacatecas, México.
36173045@uaz.edu.mx; crios@uaz.edu.mx; edmundoej@uaz.edu.mx

Hernández-Ramírez Daniel
Unidad Académica de Ciencias Químicas, Universidad Autónoma de Zacatecas
Carr. Zacatecas – Guadalajara km. 6, Col. “Ejido la Escondida”, C.P. 98160, Zacatecas,
Zacatecas, México.
dhernandez@uaz.edu.mx

Abstract

This study investigates the relationship between soil texture components and the specific activities of natural gamma emitters (Ra-226, Th-232, K-40) as well as the absorbed dose rate in soils from Zacatecas, Mexico. The research aims to develop predictive models using both linear regression and artificial neural networks (ANNs) to estimate radiological parameters based on soil texture composition. Soil samples were collected from 37 sites across Zacatecas, with additional samples from Coahuila and Durango. The soil texture was determined using the Bouyoucos hydrometer method, while specific activities of radionuclides were measured through high-resolution gamma spectrometry. Initial analysis revealed weak linear correlations between soil texture components (sand, silt, clay percentages) and radiological parameters. Linear regression models yielded low adjusted R^2 values (0.015 to 0.110), indicating poor predictive power. These results suggested the presence of complex, non-linear relationships between variables. To address this complexity, ANNs were employed as an alternative modeling approach. The ANN architecture consisted of an input layer with seven neurons, five hidden layers, and an output layer with a single neuron. The Resilient Backpropagation (RProp) algorithm with backtracking was used for optimization. The ANN models demonstrated significantly improved performance compared to linear regression. R^2 values for both training and leave-one-out cross-validation (LOOCV) exceeded 0.94 for all dependent variables, indicating excellent predictive capability and generalization. This study highlights the potential of ANNs in modeling complex relationships between soil properties and natural radioactivity. The developed models provide a valuable tool for estimating radionuclide activities and absorbed dose rates based on soil texture, which can aid in radiological risk assessment and environmental management in Zacatecas. Future research should focus on expanding the dataset, incorporating additional soil properties, and exploring other machine learning techniques to further enhance predictive accuracy and understand the underlying mechanisms governing radionuclide distribution in soils.

1. INTRODUCTION

Human exposure to natural sources of radiation is a continuous and unavoidable feature of life on Earth. This natural radiation comes mainly from two sources: cosmic radiation that passes through the Earth's atmosphere and terrestrial radiation from radioactive elements present in the Earth's crust since its formation [1]. These elements are known as radionuclides, which are ubiquitous in the environment, found in soil, water, air, food, building materials, and even in our own bodies. Most of these radionuclides emit gamma (γ) radiation, which can be directly determined by gamma spectrometry.

Gamma-ray spectrometry consists of obtaining the spectrum of gamma radiation emitted by radionuclides. It is based on the fact that the detector's response is proportional to the energy of the detected gamma ray, which allows obtaining its energy spectrum. This technique makes it possible to measure the number of atoms that disintegrate per unit of time, that is, the activity of the radionuclides presents in a sample [2]. The radiation dose due to natural sources, also known as background radiation or natural radiation, is variable and depends on various factors, with the radioactive content present in the soil being a prominent one.

Therefore, measuring radioactivity in the soil is essential to determine any changes in activity over time, as a result of the release of some radionuclides present in it. Controlling the release of radioactivity into the environment is crucial to ensure adequate radiological protection of the population [3]. It is necessary to study the relationship between the specific activities of radionuclides with respect to the textural components of the soil, in order to know if there is a correlation between them, and based on this, to develop models that allow us to predict the specific activity of natural radionuclides such as Radium-226, Thorium-232, and Potassium-40, as well as the absorbed dose rate, from the percentages of sand, silt, and clay in the soil.

The geospatial distribution of natural radionuclides in soils is a topic of great interest in the field of nuclear and environmental sciences. The state of Zacatecas, Mexico, presents particular geological and geochemical characteristics that can influence the concentration and distribution of Ra-226, Th-232, and K-40 radionuclides in its soils [4]. In addition, the granulometric composition of the soil, determined by the percentages of sand, silt, and clay, can have a significant impact on the retention and mobility of these radionuclides. Despite the importance of understanding the relationship between the physical properties of the soil and the distribution of natural radionuclides, there is currently a lack of studies that address this problem comprehensively in the state of Zacatecas. Most research has focused on determining the specific activities of radionuclides, without considering their relationship with the granulometric characteristics of the soil.

Studies that have taken into account the granulometric characteristics of the soil are mostly studies conducted abroad, the majority of them in Germany. Among these, the study by Dierke and Werban stands out, which demonstrated that, in a field site with homogeneous clay content, it is possible to use thorium (Th) concentrations for the indirect estimation of organic carbon (Corg) below pH 7. However, above this pH level, they found no relationship between Th and other soil properties [5]. Another study conducted in Germany is that of Heggemann et al., who found that linear regression models are not appropriate for satisfactory prediction of soil texture from gamma radiation data. Instead, prediction models calibrated with support vector machines (SVM) showed reliable performance for site-independent calibrations across a wide range of soils [6].

Both studies demonstrated the potential of proximal gamma-ray spectrometry for non-invasively mapping soil properties, especially texture.

Due to the few studies that focus on addressing this topic comprehensively, there is a need to develop models that allow predicting the specific activities of Ra-226, Th-232, and K-40, as well as estimating the effective dose received by the population due to exposure to these radionuclides as a function of the percentages of sand, silt, and clay present in the soil. These models will provide a valuable tool for radiological risk assessment and decision-making in radiological protection and environmental management in the state of Zacatecas.

The creation of these predictive models requires a broad database of soil samples, where both the texture and the specific activities of the radionuclides of interest have been determined. Using statistical techniques such as multiple linear regression, as well as neural network models, mathematical relationships that best explain the variability of specific activity and dose rate as a function of sand, silt, and clay percentages are sought. In this work, the main results obtained are analyzed and discussed to determine if it is possible to develop models that allow us to predict the specific activities of radionuclides (Ra-226, Th-232, and K-40) and the absorbed dose rate, based on the textural components of the soils.

2. MATERIALS AND METHODS

1.1. Soil Sampling

Thirty-seven sampling sites were selected throughout the state of Zacatecas, along with one sample from the state of Coahuila de Zaragoza and another from the state of Durango. The selection of sampling points was carried out using ad hoc sampling, choosing the locations based on convenience and accessibility. At each site, horizontal sampling was performed by collecting a sample from the top 15 cm of the soil surface.

2.2 Sample Preparation

Once obtained, the samples were sieved to remove impurities and rocks, thus obtaining a homogeneous and representative sample of the soil. Subsequently, they were stored in properly labeled airtight bags. The samples were oven-dried at 105°C for 24 hours to eliminate moisture. After drying, they were weighed and placed in Marinelli beakers, which were sealed with tape at the top and labeled for identification. Approximately 30 days were allowed to elapse for the sealed samples to reach secular radioactive equilibrium between the radionuclides of the natural series.

2.3 Soil Texture Determination

Soil texture was determined using the Bouyoucos hydrometer method [7]. Fifty grams of dry soil were weighed and placed in a 1000 mL graduated cylinder along with 10 mL of 5% sodium hexametaphosphate dispersing solution. Distilled water was added to reach a volume of 1000 mL. The mixture was vigorously stirred for 2 minutes using an electric stirrer. Immediately after

stirring, the hydrometer was inserted into the suspension, and two readings were taken, one to the 40 seconds and a second one after 2 hours. The temperature of the suspension was measured at each reading for corrections. The percentages of sand, silt, and clay were calculated from the hydrometer readings using standard formulas.

2.4 Gamma-ray Spectrometry

The specific activity of gamma-emitting radionuclides was determined by high-resolution gamma-ray spectrometry. An n-type high-purity germanium (HPGe) detector, model GeRe-3522, coupled to a Genie-2000 data acquisition system was used. The detector was operated with a negative voltage of 3950 V, a coarse gain of 10, a fine gain of 0.61, and a pulse shaping time of 4 μ s. Before the measurements, the laboratory background radiation was determined, and a multinuclide standard was measured to determine the detector efficiency for the gamma energies of interest. Each sample was measured for 80000 seconds.

The acquired gamma spectra were analyzed using the Genie-2000 software. The radionuclides present in each sample were identified, and their specific activities were determined from the net peak areas, detector efficiency, gamma emission intensity, sample mass, and measurement time. The energy calibration of the system was performed using the peaks of the background spectrum through a linear least-squares fit.

2.5 Linear and non-linear modeling

The linear and non-linear statistical models were performed using the R programming language version 4.4.1 [8]. For the fitting of linear models, the "leaps" and "GGally" packages were employed [9]. The "leaps" package provides functions for variable selection using the best subset method, while "GGally" offers tools for visualizing correlation matrices and scatter plots.

Regarding the non-linear models based on neural networks, the "neuralnet", "NeuralNetTools", and "caret" packages were utilized [10], [11], [12]. The "neuralnet" package allows for the construction and training of feedforward neural networks, while "NeuralNetTools" provides additional functions for visualizing and analyzing the trained neural networks. Finally, the "caret" package offers a wide range of tools for training and evaluating machine learning models, including neural networks.

The use of these specialized packages facilitates the implementation and evaluation of linear and non-linear statistical models in R, leveraging the specific capabilities and functionalities of each package to obtain robust and reliable results.

3. RESULTS

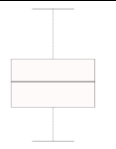
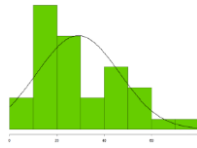
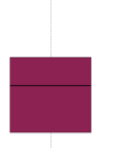
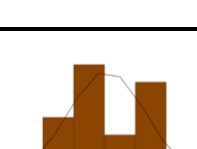
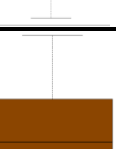
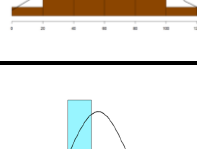
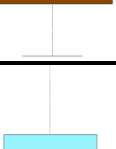
3.1 Specific activities of natural gamma emitters and percentages of textural components.

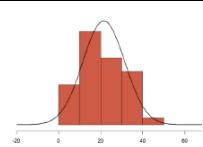
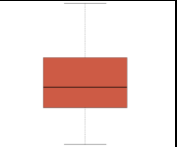
A descriptive analysis of the variables measured in the research was conducted, with the aim of understanding their characteristics and distribution before proceeding to the construction of predictive models. The statistical description of the generated variables provides a solid

foundation for understanding their behavior and relationships, which is fundamental for the development of robust and reliable predictive models.

Table I presents the descriptive statistics for the specific activities of radionuclides and the percentages of soil components. The table includes the mean, coefficient of variation (C.V.), minimum (Min), first quartile (Q1), median, third quartile (Q3), maximum (Max), p-value for the Shapiro-Wilk normality test (P-value S-W), and graphical representations (histogram and boxplot) for each variable.

Table I. Descriptive statistics of specific activities and percentages of soil components.

Variables	Mean	C.V	Min	Q1	Median	Q3	Max	P-value S-W	Histogram	Boxplot
As Ra-226, Bq/kg	29.52	0.45	2.12	17.72	29.37	39.70	62.92	0.57		
As Th-232, Bq/kg	29.01	0.59	1.88	17.11	29.01	42.34	74.40	0.05		
K-40, Bq/kg	723.7	0.38	199.7	475.2	750.7	913.7	1260.1	0.26		
Dose, nGy/h	61.53	0.41	10.50	41.64	56.56	82.36	120.34	0.20		
% Sand	62.88	0.19	39.33	55	59.33	71.67	90.67	0.21		
% Clay	21.46	0.46	2.52	13.44	19.61	28.11	44.19	0.69		

% Silt	15.66	0.51	3.59	9.96	14.87	19.72	34.87	0.12		
--------	-------	------	------	------	-------	-------	-------	------	---	---

The specific activity of Ra-226 has a mean of 29.52 Bq/kg, with a coefficient of variation of 0.45, indicating moderate variability in the data. The minimum and maximum values are 2.12 and 62.92 Bq/kg, respectively. The median (29.37 Bq/kg) is close to the mean, suggesting a relatively symmetric distribution, which is supported by the p-value of 0.57 for the Shapiro-Wilk normality test, indicating that the data do not significantly deviate from a normal distribution.

The specific activity of Th-232 has a mean of 29.01 Bq/kg and a higher coefficient of variation (0.59) compared to Ra-226, indicating greater variability in the data. The minimum and maximum values are 1.88 and 74.40 Bq/kg, respectively. The p-value for the Shapiro-Wilk test is 0.05, suggesting that the data may deviate from a normal distribution.

The specific activity of K-40 has a mean of 723.7 Bq/kg and a coefficient of variation of 0.38, indicating moderate variability. The minimum and maximum values are 199.7 and 1260.1 Bq/kg, respectively. The median (750.7 Bq/kg) is close to the mean, and the p-value for the Shapiro-Wilk test is 0.26, suggesting that the data do not significantly deviate from a normal distribution.

The absorbed dose rate has a mean of 61.53 nGy/h, and a coefficient of variation of 0.41, indicating moderate variability. The minimum and maximum values are 10.50 and 120.34 nGy/h respectively. The median of 56.56 nGy/h is close to the mean, and the p-value of the Shapiro-Wilk test is 0.20, suggesting that the data do not deviate significantly from a normal distribution.

The mean percentage of sand in the soil samples is 62.88%, with a coefficient of variation of 0.19, indicating relatively low variability. The minimum and 0 values are 39.33% and 90.67%, respectively. The p-value for the Shapiro-Wilk test is 0.21, suggesting that the data do not significantly deviate from a normal distribution.

The mean percentage of clay is 21.46%, with a coefficient of variation of 0.46, indicating moderate variability. The minimum and maximum values are 2.52% and 44.19%, respectively. The p-value for the Shapiro-Wilk test is 0.69, suggesting that the data do not significantly deviate from a normal distribution.

The mean percentage of silt is 15.66%, with a coefficient of variation of 0.51, indicating relatively high variability. The minimum and maximum values are 3.59% and 34.87%, respectively. The p-value for the Shapiro-Wilk test is 0.12, suggesting that the data do not significantly deviate from a normal distribution.

The histograms and boxplots provided in the table offer visual representations of the distribution and spread of the data for each variable, allowing for a more comprehensive understanding of the descriptive statistics presented.

3.1.1 Correlation between specific activities and percentages of textural components

The matrix plot in Figure 1 presents a comprehensive visualization of the relationships between the specific activities of radionuclides (Ra-226, Th-232, K-40), absorbed dose rate, and soil texture components (sand, clay, and silt percentages). The plot includes histograms, scatter plots, and Pearson correlation coefficients for all variable pairs.

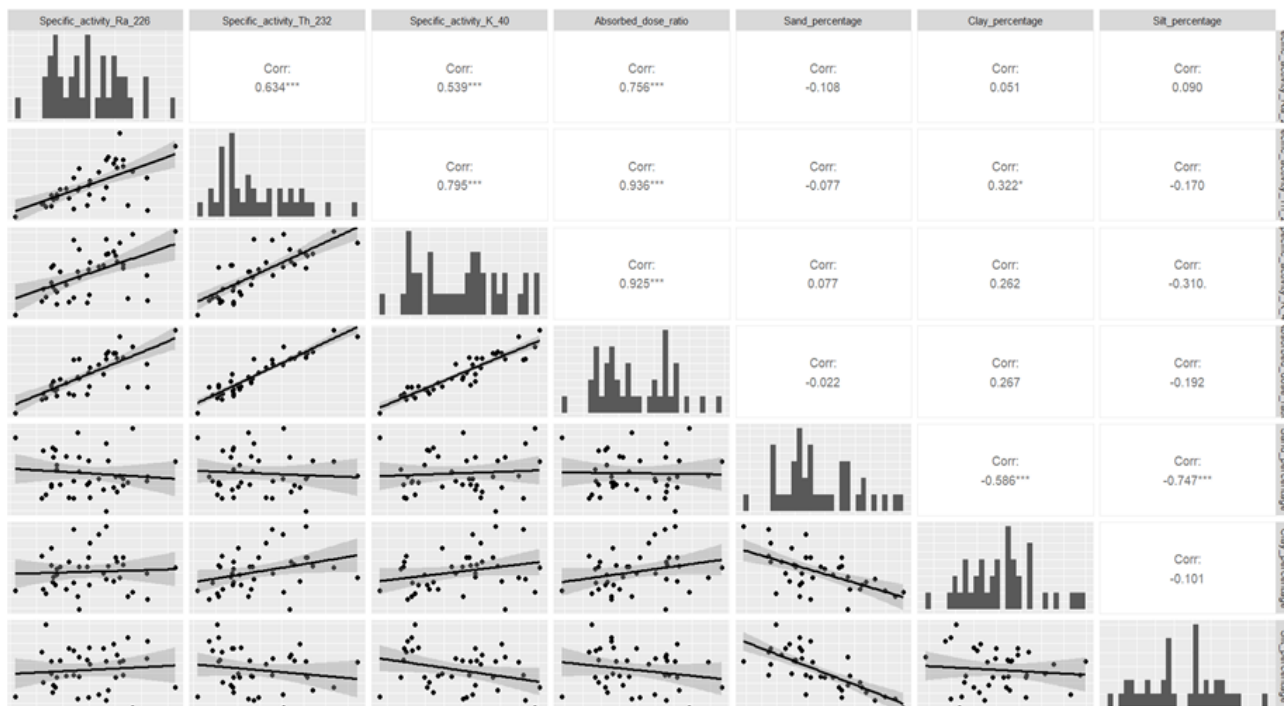


Figure 1. Matrix plot of scatter graphs, histograms and correlations of variables.

A key observation from this matrix plot is the notably low Pearson correlation coefficients between the independent variables (specific activities and absorbed dose rate) and the dependent variables (soil component percentages). Specifically:

- Specific activity of Ra-226 shows very weak correlations with sand (-0.108), clay (0.091), and silt (0.090) percentages.
- Specific activity of Th-232 exhibits weak correlations with sand (-0.077), clay (0.322), and silt (-0.170) percentages.
- Specific activity of K-40 displays weak correlations with sand (0.077), clay (0.262), and silt (-0.310) percentages.
- Absorbed dose rate shows very weak correlations with sand (-0.022), clay (0.297), and silt (-0.192) percentages.

These low correlation coefficients indicate that there are little to no linear relationship between the radiological parameters and the soil texture components. This suggests that predicting the specific activities of radionuclides or the absorbed dose rate based solely on the percentages of sand, clay, and silt in the soil may be challenging using simple linear models.

It's worth noting that while the correlations between the radiological parameters (Ra-226, Th-232, K-40, and absorbed dose rate) are relatively strong, ranging from 0.539 to 0.926, this does not directly contribute to predicting these parameters from soil texture components. The scatter plots in the matrix further visualize these weak relationships, showing dispersed patterns without clear linear trends between the radiological parameters and soil texture components.

These observations highlight the complexity of the relationship between soil texture and radionuclide activities, suggesting that more sophisticated, possibly non-linear models may be necessary to accurately predict radiological parameters based on soil texture composition.

3.2 Linear models

All possible models with one variable, two variables, three variables, and all possible interactions between independent variables (percentages of sand, silt, and clay) were fitted to predict each of the dependent variables (specific activities of Ra-226, Th-232, K-40, and absorbed dose rate). The adjusted coefficient of determination ($r^2_{Adjusted}$) was used to select the best models. Table II shows the best model for each dependent variable. The adjusted coefficient of determination ($r^2_{Adjusted}$) is a better method for selecting variables in a regression model because it penalizes the inclusion of non-significant variables, thus avoiding overfitting. Unlike the regular coefficient of determination (r^2), which always increases as more variables are added to the model, the adjusted r^2 only increases if the added variable significantly improves the model's predictive power. Table II shows the best model for each dependent variable.

Table II. Best regression models for predicting specific activities and absorbed dose rate.

Dependent Variable	Best Model	$r^2_{Adjusted}$
Ra-226 specific activity	$Ra-226 = 36.88 - 0.1171 * Sand_percentage$	0.01508
Th-232 specific activity	$Th-232 = 15.67 + 0.0144 * Sand_percentage * Clay_percentage$	0.09148
K-40 specific activity	$K-40 = 645.75 + 21.708 * Clay_percentage - 0.01419 * Sand_percentage * Clay_percentage * Silt_percentage$	0.1104
Absorbed dose rate	$ADR = 44.68 + 0.0183 * Sand_percentage * Clay_percentage$	0.06046

For the specific activity of Ra-226, the best model includes only the sand percentage as a predictor variable. The model suggests that the specific activity of Ra-226 decreases by 0.1171 units for each one-unit increase in the sand percentage. However, the adjusted r^2 of 0.01508 indicates that this model explains only 1.508% of the variability in the specific activity of Ra-226, suggesting that other factors not included in the model may have a more significant influence.

The best model for the specific activity of Th-232 includes the interaction between the sand and clay percentages. The model suggests that the specific activity of Th-232 increases by 0.0144 units for each one-unit increase in the product of the sand and clay percentages. The adjusted r^2 of 0.09148 indicates that this model explains 9.148% of the variability in the specific activity of Th-232.

For the specific activity of K-40, the best model includes the clay percentage and the interaction between the sand, clay, and silt percentages. The model suggests that the specific activity of K-40 increases by 21.708 units for each one-unit increase in the clay percentage but decreases by 0.01419 units for each one-unit increase in the product of the sand, clay, and silt percentages. The adjusted r^2 of 0.1104 indicates that this model explains 11.04% of the variability in the specific activity of K-40.

The best model for the absorbed dose rate includes the interaction between the sand and clay percentages. The model suggests that the absorbed dose rate increases by 0.0183 units for each one-unit increase in the product of the sand and clay percentages. The adjusted r^2 of 0.06046 indicates that this model explains 6.046% of the variability in the absorbed dose rate.

Overall, the relatively low adjusted r^2 values suggest that, although soil texture components contribute to the variability in radiological parameters, other factors not included in these models may have a more significant influence. These results highlight the complexity of predicting radionuclide-specific activities and the absorbed dose rate based on soil properties and suggest that further research is needed to identify other important predictors.

It is important to note that linear regression models, such as those used in this study, can only capture linear relationships between the independent variables (sand, silt, and clay percentages) and the dependent variables (specific activities of Ra-226, Th-232, K-40, and absorbed dose rate). However, there may be non-linear relationships between these variables that cannot be detected by linear models.

Non-linear relationships can take various forms, such as exponential, logarithmic, polynomial, or even more complex relationships. For example, the specific activity of a radionuclide might increase exponentially with an increase in the percentage of a soil texture component, or there might be a threshold in the percentage of a component above which the specific activity stabilizes or decreases.

Machine learning techniques, such as artificial neural networks, can also be useful for capturing complex and non-linear relationships between variables. These techniques do not require the form of the relationship to be specified in advance but can learn complex patterns from the data.

3.3 Artificial Neural networks

Artificial Neural Networks (ANNs) are a powerful machine learning tool that has gained significant popularity in recent years due to their ability to model complex and non-linear relationships in data [13]. Unlike traditional statistical models, such as linear regression, ANNs do not require strict adherence to theoretical assumptions about the data and are more flexible and robust.

In this section, we explore the use of neural networks as an alternative to linear models for analyzing a dataset where the Pearson correlations between the dependent variable and the independent variables were very low. Linear regression models, as used in the previous section, can only capture linear relationships between variables. However, the low adjusted r^2 values obtained from these models suggest that non-linear relationships may exist in the data that cannot be detected by linear models.

ANNs, on the other hand, are capable of learning and modeling complex patterns and non-linear relationships in data without requiring explicit specification of the form of the relationship. They achieve this through their architecture, which consists of interconnected nodes (neurons) organized in layers, resembling the structure of biological neural networks.

By applying ANNs to our dataset, we aim to uncover potential non-linear relationships between soil texture components (sand, silt, and clay percentages) and radiological parameters (specific activities of Ra-226, Th-232, K-40, and absorbed dose rate) that were not captured by the linear regression models. This approach may provide new insights into the complex interactions between soil properties and radionuclide activities, leading to improved predictions and a better understanding of the underlying mechanisms.

The proposed neural network structure consists of an input layer with seven neurons, one for each input variable (percentages of soil components and all their possible interactions). The hidden layer is composed of five sub-layers containing 15, 10, 7, 5, and 3 neurons, respectively, each with a sigmoid activation function. The output layer has a single neuron with a linear activation function. The optimization algorithm used is Resilient Backpropagation (RProp) with backtracking. Figure 2 shows the structure of the neural network.

This architecture allows for the capture of complex, non-linear relationships between the input variables and the target output. The multiple sub-layers in the hidden layer enable the network to learn hierarchical representations of the data, with each sub-layer capturing increasingly abstract features. The sigmoid activation function introduces non-linearity, allowing the network to model more complex patterns.

The choice of RProp as the optimization algorithm is well-suited for this task, as it adapts the learning rate for each weight based on the sign of the gradient, making it more robust to the choice of initial learning rate and improving convergence speed. The addition of backtracking further enhances the algorithm's ability to escape local minima and find a better solution.

By utilizing this neural network architecture and optimization algorithm, we aim to uncover the underlying non-linear relationships between soil composition and radiological parameters, potentially leading to more accurate predictions and a deeper understanding of the factors influencing radionuclide activities in soils.

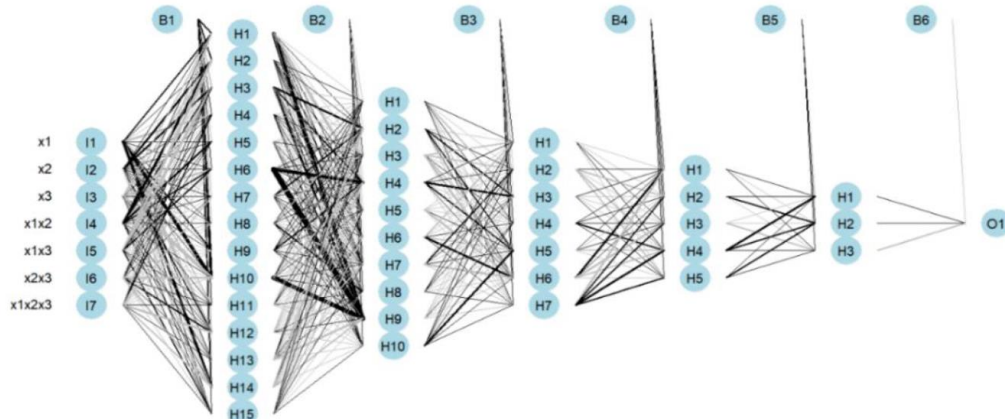


Figure 2. Structure of the neural network.

To validate the performance of the proposed neural networks, the "leave-one-out" cross-validation (LOOCV) technique was employed [10]. In this approach, the neural network is

trained using all the data except for one sample, which is reserved for validation. This process is iteratively repeated, leaving out each sample in turn, until all samples have been used for validation. The advantage of LOOCV is that it maximizes the use of available data for training while providing an unbiased estimate of the model's performance on unseen data. Moreover, LOOCV is particularly suitable for small datasets, where other cross-validation techniques, such as k-fold, might not be feasible. By using LOOCV, we can obtain a robust assessment of the generalization ability of the proposed neural networks and their capacity to accurately predict radionuclide-specific activities and the absorbed dose rate based on soil properties.

Table III presents the quality metrics for the neural networks. The r^2 value represents the fraction of variability explained during the training process using a seed of 123 for the optimization process. The table also includes the fraction of variance explained when applying the leave-one-out cross-validation (LOOCV) technique and the mean squared error (MSE).

The r^2 metric, also known as the coefficient of determination, measures the proportion of the variance in the dependent variable that is predictable from the independent variables. It provides an indication of how well the neural network model fits the training data when using a specific seed value (123) for the optimization process. A higher r^2 value suggests that the model explains a larger portion of the variability in the data.

The fraction of variance explained using LOOCV is a measure of the model's performance on unseen data. The fraction of variance explained using LOOCV provides an estimate of how well the model generalizes to new, unseen data.

Lastly, the mean squared error (MSE) is a commonly used metric to assess the performance of regression models. It measures the average squared difference between the predicted values and the actual values. A lower MSE indicates better model performance, as it suggests that the predictions are closer to the true values.

By presenting these quality metrics, Table III allows for a comprehensive evaluation of the neural network models' performance, considering both their ability to fit the training data using a specific optimization seed and their generalization capability when applied to unseen data through LOOCV.

Table III. Performance of Regression Models for Predicting Natural Radionuclide Activities and Absorbed Dose Rate.

Dependent Variable	r^2 with seed 123	r^2 LOOCV	MSE
Ra-226 specific activity	0.9429	0.9168	14.86
Th-232 specific activity	0.9997	0.9363	18.86
K-40 specific activity	0.9977	0.9501	3950.63
Absorbed dose rate	0.9996	0.9307	44.46

The results show excellent model performance for all dependent variables, with r^2 values above 0.94 for both the fixed seed fit and the LOOCV cross-validation. This indicates that the models explain a large proportion of the variability in the specific activities of Ra-226, Th-232, and K-

40, as well as in the absorbed dose rate. The MSE values vary among the dependent variables due to the different scales of the measurements. The specific activity of K-40 presents the highest MSE, which is expected given that it is typically found in higher concentrations compared to Ra-226 and Th-232.

Overall, these results suggest that the developed regression models are robust and have a high capacity to predict the radiological variables of interest. However, it is important to consider the study context and possible limitations, such as sample size and data representativeness, when interpreting these results and applying the models in future research or practical applications.

4. CONCLUSIONS

This study investigated the relationship between soil texture components and the specific activities of natural gamma emitters (Ra-226, Th-232, K-40) as well as the absorbed dose rate in soils from Zacatecas, Mexico. Linear regression models showed very weak correlations between soil texture components (sand, silt, and clay percentages) and radiological parameters. The adjusted r^2 values for these models were extremely low (ranging from 0.015 to 0.110), indicating that linear models are inadequate for predicting radionuclide activities based on soil texture alone. The poor performance of linear models suggested the presence of complex, non-linear relationships between soil texture and radiological parameters.

Artificial Neural Networks (ANNs) demonstrated significantly superior performance compared to linear regression models. The ANN models achieved r^2 values exceeding 0.94 for all dependent variables, both in training and leave-one-out cross-validation (LOOCV). The high r^2 values and low mean squared errors (MSE) of the ANN models indicate their robust predictive capability and excellent generalization to unseen data. The success of ANNs in modeling these relationships highlights the complex, non-linear nature of the interactions between soil texture components and radionuclide activities.

This study demonstrates the potential of machine learning techniques, particularly ANNs, in capturing and modeling intricate relationships in environmental radiological data that traditional linear models fail to detect. The developed ANN models provide a valuable tool for estimating radionuclide activities and absorbed dose rates based on soil texture in the Zacatecas region, which can aid in radiological risk assessment and environmental management. While the models show high predictive power, it's important to consider the study's limitations, such as sample size and regional specificity, when applying these models to other contexts.

Future research should focus on expanding the dataset, incorporating additional soil properties, and exploring other machine learning techniques to further enhance our understanding of the factors influencing natural radioactivity in soils. These findings contribute to our understanding of the complex relationships between soil properties and natural radioactivity, and demonstrate the value of advanced modeling techniques in environmental radiological studies.

REFERENCES

1. D. A. Atwood, *Radionuclides in the environment*. New York: Wiley, 2010.
2. Gilmore y Gordon, *Practical gamma-ray spectrometry*, 2^a ed. Chichester, England: Wiley, 2008.
3. Kurnaz, A., Kucukomeroglu, B., Damla, N., & Cevik, U. (2011). *Radiological maps for Trabzon, Turkey*. *Journal of Environmental Radioactivity*, 102(4), 393–399. <https://doi.org/10.1016/j.jenvrad.2011.02.2009>
4. Mireles, F., Dávila, J. I., Quirino, L. L., Lugo, J. F., Pinedo, J. L., & Ríos, C. (2003). NATURAL SOIL GAMMA RADIOACTIVITY LEVELS AND RESULTANT POPULATION DOSE IN THE CITIES OF ZACATECAS AND GUADALUPE, ZACATECAS, MEXICO. *Health Physics*, 84(3), 368-372. <https://doi.org/10.1097/00004032-200303000-00010>
5. Dierke, C., & Werban, U. (2013). Relationships between gamma-ray data and soil properties at an agricultural test site. *Geoderma*, 199, 90–98. <https://doi.org/10.1016/j.geoderma.2012.10.017>
6. Heggemann, T., Welp, G., Amelung, W., Angst, G., Franz, S. O., Koszinski, S., Schmidt, K., & Pätzold, S. (2017). Proximal gamma-ray spectrometry for site-independent in situ prediction of soil texture on ten heterogeneous fields in Germany using support vector machines. *Soil and Tillage Research*, 168, 99–109. <https://doi.org/10.1016/j.still.2016.10.008>
7. NORMA Oficial Mexicana NOM-021-RECNAT-2000, (2002). Que establece las especificaciones de fertilidad, salinidad y clasificación de suelos. Estudios, muestreo y análisis. p 7.1.9
8. R Core Team (2024). *_R_: A Language and Environment for Statistical Computing_*. R Foundation for Statistical Computing, Vienna, Austria. <https://www.R-project.org/>
9. Schloerke B, Cook D, Larmarange J, Briatte F, Marbach M, Thoen E, Elberg A, Crowley J (2024). R package version 2.2.1, <https://github.com/ggobi/ggally>, <https://ggobi.github.io/ggally/>.@Manual
10. Stefan Fritsch, Frauke Guenther, Marvin N. Wright, Marc Suling, Sebastian M. Muelle (2019) *Neuralnet: Training of neural networks*. 10.32614/CRAN.package.neuralnet
11. Beck MW. (2015). *NeuralNetTools: Visualization and Analysis Tools for Neural Networks*. Version 1.5.0. <https://cran.rstudio.com/package=NeuralNetTool>
12. Kuhn, M. (2008). Building Predictive Models in R Using the caret Package. *Journal of Statistical Software*, 28(5), 1–26. <https://doi.org/10.18637/jss.v028.i05>
13. Joaquín Amat Rodrigo. (2021). *Redes neuronales con R*. CC BY-NC-SA 4.0.

Track 7

Radiological Protection and Safety

Plan for the Decommissioning of Nuclear Facilities

Carolina Natalia Ayala and Laura Kniznik

CNEA- National Atomic Energy Commission

Buenos Aires, Argentina

Carolina.ayala@cab.cnea.gov.ar; laurakniznik@cnea.gob.ar

Sofia Elias Krizan

CNEA- National Atómico Energy Commission

Buenos Aires, Argentina

sofiaelias@cnea.gob.ar

Abstract

The goal of this work is to acquire capacities and develop specific techniques and technologies to initiate a comprehensive plan for the decommissioning of nuclear facilities in Argentina. To this end, a survey of the current situation will be carried out, strategies based on knowledge management will be planned to facilitate the transfer of information between the former and current professional and technical staff of each facility, and these strategies will be applied in specific case studies, in close collaboration with Nucleoeléctrica Argentina S.A. and in compliance with the requirements of the Nuclear Regulatory Authority

1. INTRODUCTION

The development of a comprehensive plan for the decommissioning of nuclear facilities is closely linked to the management of radioactive waste, spent fuel, and environmental remediation. This is crucial to address in a timely and sustainable manner, as it is a matter of interest for the current population and future generations, and a legal responsibility of CNEA.

Law 24804 on Nuclear Activity establishes, in Chapter I, article 2e, that CNEA is responsible for determining the manner of decommissioning relevant nuclear facilities in Argentina. Its regulatory decree 1390/88 stipulates that CNEA is responsible for the dismantling and decommissioning of Argentine nuclear power plants at the end of their operational life. However, after the existence of a Sub-Program for the decommissioning of nuclear facilities between 2000 and 2013, the area was discontinued and much of the involved personnel retired or changed roles. Therefore, it is vital to strengthen the relaunch of this area and the development of the mentioned comprehensive plan.

2. THE DECOMMISSIONING OF NUCLEAR FACILITIES

Argentina has a long history of collaborations with the International Atomic Energy Agency (IAEA) in the field of nuclear facility decommissioning. These collaborations can be divided into two time frames. The first time frame covers collaborations from 2000 to 2013, during which the Nuclear Facility Decommissioning Sub-Programme established collaborations with the IAEA, contributing valuable experience and knowledge to the National Atomic Energy Commission (CNEA). Specific projects during this period included a technical assistance project, a regional training course on decontamination and dismantling of nuclear facilities, and the provision of expert assistance by the IAEA.

The second time frame consists of more recent collaborations aimed at revitalising and reconstructing the nuclear decommissioning sector. Argentina's participation in technical meetings and conferences, such as the Technical Meeting on Financing Schemes for Radioactive Waste Disposal Programmes, reflects a renewed commitment to revitalising the sector and has helped raise awareness of essential issues for the CNEA.

2.1. Nuclear Technology - Technique/s that will be used

The decommissioning of nuclear facilities is a complex process that involves detailed studies, decontamination, dismantling, and management of waste and materials. In Argentina, the development of a comprehensive plan for decommissioning requires the expansion of infrastructure and acquisition of necessary equipment. Specific technologies, such as mechanical decontamination, concrete demolition, electrochemical decontamination, cutting, and robotization techniques, will be utilized.

These techniques have already been successfully used in various projects in Argentina, including the dismantling of the RA-2 Critical Facility, tank internals, and instrumentation in the RA-3 radioisotope production reactor, and the disassembly and repair of reactor internals at Atucha I Atomic Power Plant. The decontamination and dismantling of equipment in all CNEA laboratories and facilities associated with the nuclear fuel cycle and radioisotope development and production are also part of the process. Throughout the entire decommissioning process, utmost attention is given to the health and safety of operating personnel, the general public, and the environment.

2.2. Physical Infrastructure and Human Resources

The National Radioactive Waste Management Programme (PNGRR) of the CNEA has the necessary laboratories, facilities, and qualified personnel to be part of the project. Collaboration will also be sought from personnel within the CNEA and Nucleoeléctrica Argentina S.A., while adhering to the requirements of the Nuclear Regulatory Authority. The PNGRR has facilities for radioactive waste management and a characterisation laboratory at three different atomic centres. The Uranium Laboratory, which will directly participate in the project, is well-equipped with various tools and technologies.

The human resources division within the PNGRR dedicated to the project consists of professionals from various fields, including physics, chemical engineering, electronics, materials, and environmental management. These professionals have undergone specialized training in radiological and nuclear safety. Additionally, personnel from other areas of the PNGRR, as well as professionals from different departments within the CNEA and Nucleoeléctrica Argentina S.A., will contribute to the project. The team working on the project emphasises gender diversity and inclusion, consisting of three women and five men.

3. MAIN RESPONSIBILITIES AND POLICIES

The main responsibilities that the Radioactive Waste Management Programme currently supervises are:

- Management of radioactive waste and disused sealed sources.
- Management of spent fuel. Environmental remediation of closed Uranium mining and milling sites.
- Development of repositories and responsibility for long term institutional control.
- Research & Development activities.
- Elaboration of the Radioactive Waste Management Strategic Plan –PEGRR
- Establishment of waste acceptance criteria for the future repositories.
- Record keeping of the inventories of radioactive waste and other relevant documentation.
- Development of a public communication programme
- National Reports to the Congress and the JC.

National State, through PNGRR, is responsible for safe and secure waste management arising from nuclear energy applications, including waste from nuclear energy applications and waste from decommissioning of related facilities.

In addition, PNGRR must ensure safe management in order to protect present and future generations and environment.

The establishment of a Decommissioning Integral Plan is a challenge that involves multidisciplinary aspects and serve as a project to work with and to guide our actions. Case studies give the opportunity of testing capabilities and technical needs. This Plan includes a high degree of change, which requires flexibility to consider stages in an adaptive way, not as rigid steps.

4. CONCLUSIONS

- Being at an initial stage in the Decommissioning Integral Plan allows us to take advantage of the lessons learned in countries that are ahead of us in this matter.

- Meetings and Collaboration Projects which promote information sharing, knowledge and experiences related to nuclear decommissioning at international and regional level, are very valuable.
- In order to avoid starting from zero again, it is very important the Knowledge Management of previous steps in other decades and scenarios.
- During the entire process and from the start it is also necessary to emphasize Educational and Training aspects as well as Human Resources Development.

REFERENCES

1. Laura Kniznik Argentina IAEA Seventh Technical Meeting on the International Project on Decommissioning of Small Facilities (MIRDEC) Copenhagen, Denmark 9-13 October 2023
2. Lopez Cantón, F. (Nuclear Regulatory Authority). Presentation - International Conference on Nuclear Decommissioning, Vienna, 15-19 May 2023.
3. Puglia, G. Presentation in IAEA Technical Meeting on Knowledge Management for Decommissioning, Ispra, 11-15 September 2023

Qualitative Characterization of Uranium samples, oriented to investigation in nuclear forensics

Cintya Fabiola Herrera García¹, Graciela Zarazúa Ortega ², Ignacio Dávila Rangel¹
Universidad Autónoma de Zacatecas¹, Instituto Nacional de Investigaciones Nucleares²
cintyafhg77@hotmail.es; graciela.zarazua@inin.gob.mx; idavila@uaz.edu.mx

Nancy Lara Almazán
Instituto Nacional de Investigaciones Nucleares
nancy.lara@inin.gob.mx

Abstract

In this study, we analyze unknown uranium compounds using qualitative techniques to obtain an initial rapid characterization of the samples. The procedure consisted in the confirmation of the presence of radiation in the samples, follow by the identification of the nuclides found in the materials and their activities, using a portable detector. Subsequently a chemical characterization was performed on the samples by Fourier Transformed Infrared Spectroscopy. Finally, for comparison, a physical examination of the materials was made, by color classification and morphology observation in the Scanning Electron Microscope. This initial examination is crucial since the laboratory should be able to give a rapid answer to the authorities to help them develop a proper answer.

1.

INTRODUCTION

Nuclear forensics is the examination of nuclear, or other radioactive material, or of evidence that is contaminated with radionuclides, in the context of legal proceedings under international or national law related to nuclear security. The analysis of nuclear or other radioactive material is carried out using nuclear and conventional analytical techniques, with the objective of identifying the kind of materials, how, when and where the materials were made, and what their intended uses were[1]. The conduct of a nuclear forensic examination must be done both securely and safely to ensure the protection of the public, the environment and the evidence.

One of the main concerns of Nuclear Forensics is the generation of improvised nuclear devices or radiological dispersion devices known as RDDs, which use conventional explosives to spread radiological material with the intention of causing damage or injuries[2]. The materials of special interest to nuclear forensics are those that contain actinide elements, such as thorium (Th), uranium (U), plutonium (Pu), americium (Am), etc. and other radioactive nuclides like ^{60}Co , ^{90}Sr and ^{137}Cs , that can be used in RDDs. These materials can be found at different stages of the nuclear fuel cycle, from the mining, milling, extraction and purification, enrichment, fuel manufacturing, nuclear reactor, waste management, storage and use for medical and industrial applications[3].

The results obtained from the Nuclear Forensic analysis can be used by the states investigative authority to help in criminal investigations related to any event that involves nuclear or radioactive material, so that appropriated measures are implemented immediately. Additionally, they can be used to prevent and create proper safety measures in case of founding this type of materials out of regulatory control.

To identify the materials contained in the samples of interest, there has to be an specific protocol in the institute or laboratory that will make the examination, in order to assure the safety of the public, personal, the installations and the environment. Such protocol must follow both national an international laws and recommendations.

To comprehend the type of material that the investigation is dealing with, the very first analysis that should be performed is the confirmation of the presence of radiation in the sample, follow by the identification of the nuclide found in the material that is emitting such radiation and its activity. This initial examination is crucial since the laboratory should be able to give a rapid answer to the authorities to help them develop a proper answer, which can be vital in case of a high risk event.

In this work, non-destructive techniques were applied with the aim of characterizing uranium compounds, as part of the response program of the National Laboratory for Nuclear Forensics Research (LANAFONU), for its acronym in Spanish.

2.

MATERIALS AND METHODS

Five uranium samples where given to analyze, with unknown specifications. The samples where tagged with unique labels and the fist analysis was performed with precaution.

2.1. Radiometric characterization

To identify the nuclide found in the material and to measure the activity of the sample, a portable radionuclide identification device (identiFINDER[®]) was used. Once assured that most of the samples had a low activity, they were taken to an identification of chemicals device (Detective-DX-100T[®]) to confirm the obtained nuclide.

Since both devices gave a Dose Rate measurement, the activity was calculated using the formula (1) where the distance from the source and the Dose Rate Constant (Γ) were considered.

$$A = (\dot{D} * 4\pi d^2) / \Gamma \quad (1)$$

Where, A: Activity, \dot{D} : Dose rate measured, d: distance from the source, Γ : Dose rate constant.

2.2. Physical characterization

A physical analysis should be performed at every forensic sample, to identify the unique characteristics from every material in order to be able to differentiate it from similar material from a different source or to relate it to a certain common origin. The basis of this exam was to observe and record the precise color of the sample, the form, shape, size, and microscopic characteristics.

2.2.1. Color

To perform this exam, the samples were submitted to a visual exam to be classified as registered with a precise color, taking as reference a Pantone[®]. Photographical evidence was taken comparing every sample with the selected shade of the reference material.

2.2.2. Microscopy

A Jeol Scanning Electron Microscope (SEM) JSM-5900LV was used to observe the morphology of the samples from 100x to 3000x; in addition, a coupled energy-dispersive X-ray spectroscopy (EDS) detector was used for chemical analysis to determine the elements in the samples by their percentage in weight.

2.3. Chemical characterization

For the determination of the chemical compound where the nuclide is found, the samples were analyzed by Fourier Transform Infrared Spectroscopy (FTIR) using the ATR accessory model Carry 7600, Agilent Technologies. The analysis was performed in an interval from 4000 cm⁻¹ to 650 cm⁻¹, 64 scans and 4 cm⁻¹ resolution.

3. RESULTS

3.1. Radiometric characterization

The results (Table 1) were obtained from the identiFINDER[®] and the Detective-DX-100T[®] in a time of 60 seconds and 20 seconds per sample, respectively. This gave a total of 5 minutes for the first measurement and around 2 minutes for the second one.

Table I. Radiological characteristics of uranium samples

Sample	Dose rate (Mrem/h)	Nuclide	A (μCi)
9A	0.04	²³⁵ U/ ²³⁸ U	0.0085
9B	0.04	²³⁵ U/ ²³⁸ U	0.0085
10A	0.05	²³⁵ U/ ²³⁸ U	0.0107
10B	0.05	²³⁵ U/ ²³⁸ U	0.0107
11	0.02	²³⁵ U/ ²³⁸ U	0.0042

From these results we were able to identify that the isotopes in the samples were ²³⁸U and ²³⁵U, both present in each of the minerals. The obtained activity was determined to be accepted by the PR department ensuring that the procedures could be continued safely.



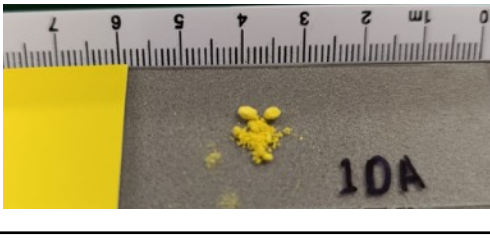

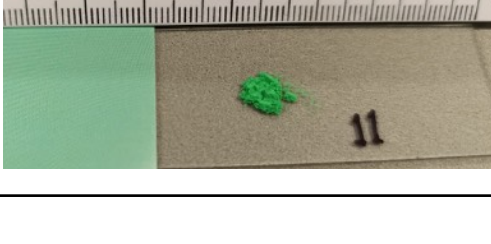
3.2. Physical characterization

3.2.1. Color

In this examination we observe the color of each sample compared and assigned from a Pantone[®], (Table 2).

Both, 9A and 9B presented the same type of yellow (Buttercup PANTONE 12-0752), which were the pair of samples that had showed physical similarities. Opposite to the expected, the samples 10A and 10B were found to be different shades of yellow with a subtle difference, and the sample 11 was observed to be a completely different color (Jade Cream PANTONE 15-6123), possibly indicating a fluoride compound.

Table 2. Uranium sample color

Sample	Color (Pantone reference)	Image
9A	Buttercup PANTONE 12-0752	
9B	Buttercup PANTONE 12-0752	
10A	Blazing Yellow PANTONE 12-0643	
10B	Buttercup PANTONE 12-0752	
11	Jade Cream PANTONE 15-6123	

3.2.2. Microscopy

The physical appearance of the samples was observed with a different morphology. The micrographs of the samples appear in the left and the X-ray spectrum at the right in the Figure 1.

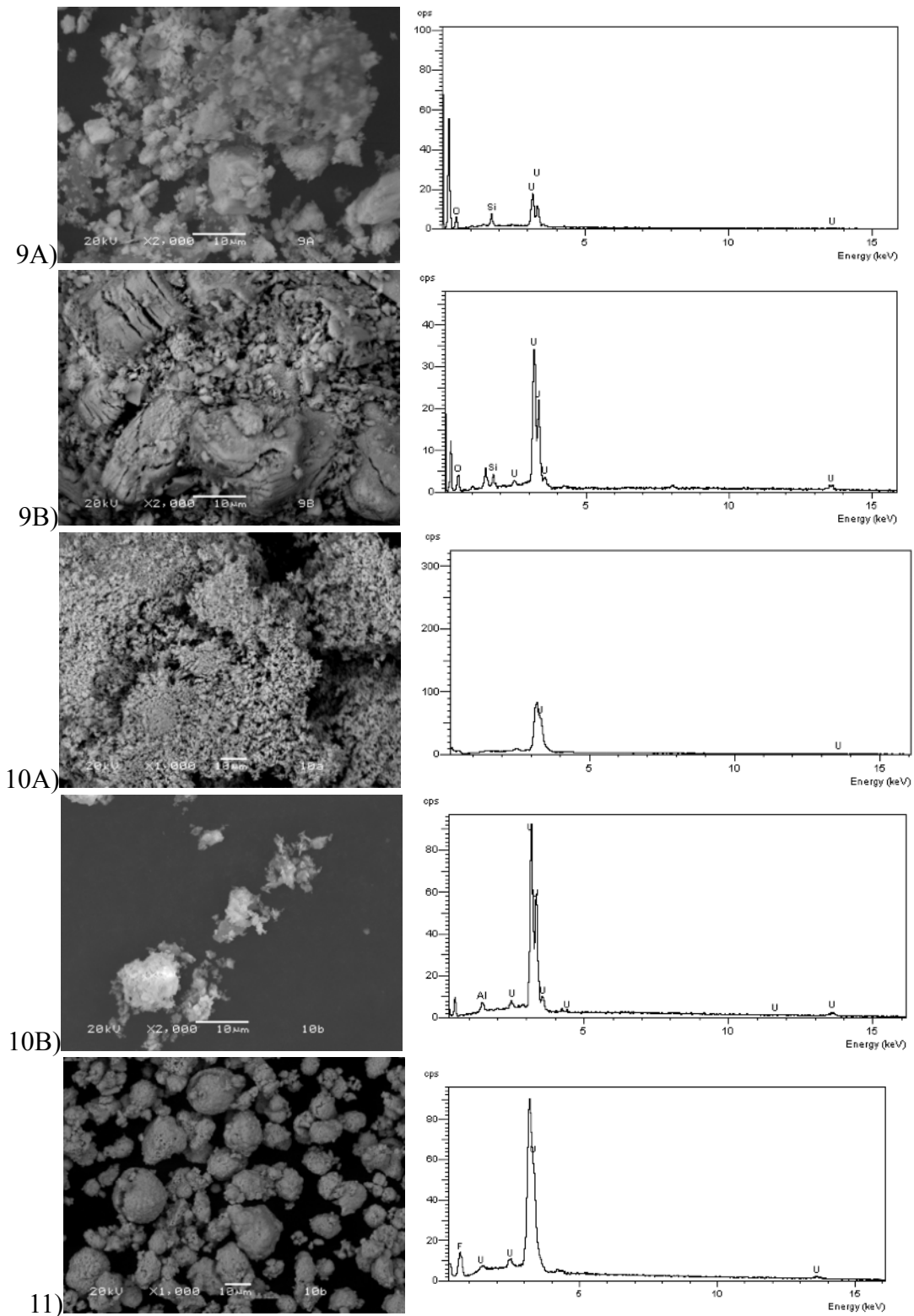


Figure 1. Scanning Electron Micrographs of irregular particles composed mainly of uranium.

Samples 9A and 9B were observed to have a different morphology. While the granules in sample 9A were irregular and rounded the ones of sample 9B were bigger and flatter. They both had different sizes granules with asymmetrical circumferences. The elemental composition of these samples was mainly U and the presence of Si was detected indicating that the nature of the material is primarily uranium silicates.

Sample 10A appears to be conformed by irregular crystals of approximately 70µm that agglomerate. Despite the different shade of color, sample 10B was observed to be very similar to 10A having a crystalline composition. In the elemental analysis, U was the most prevalent as well, indicating that this is the main composition of the matrix of the sample. Carbon was also detected but discarded because of the nature of the tape where the sample was placed in the aluminium holder.

On the other hand, sample 11 showed to be conformed by spherical particles formed around 10µm. The composition was observed to appear homogeneous through the area. The elements present in the sample were only F and U confirming the initial hypothesis from the color of the sample.

This examination was performed in a time of 60 seconds per sample, giving a total of 5 minutes for the analysis.

3.3. Chemical characterization

The main characteristic band was identified for U-O among 970(s) and 900(s) cm^{-1} [4]. With this, we were able to identify that the compounds of samples 9A, 9B, 10A and 10B were uranium oxides.

The analysis of 9A and 9B samples showed the presence of NaU_2O_7 by the identification of the functional group (νUO_2^{2+}) from sodium uranate at 900(s) cm^{-1} and the band of $\delta\text{H}_2\text{O}$ between 1615(m) and 1625(m) cm^{-1} indicating that the compound is in its hydrated form.

In the analysis of the samples 10A and 10B, ammonium uranyl carbonate was identified from the detection of the functional groups νUO_2 at 895(m) cm^{-1} , νNH bond at 3140(s, br) cm^{-1} , νOH in 3450(s, br) cm^{-1} and the presence of $\delta\text{H}_2\text{O}$ among 1615(m) and 1625(m) cm^{-1} .

Finally, the sample 11 didn't present significant signals at any area of the spectrum. As theorized, the compound in this material could be UF_4 , since the lack of presence of other bonds is confirmed in the analysis and the previous examination showed the characteristics of this molecule. Since this bond presents a different energy, it isn't observed in the range that the FTIR performs.

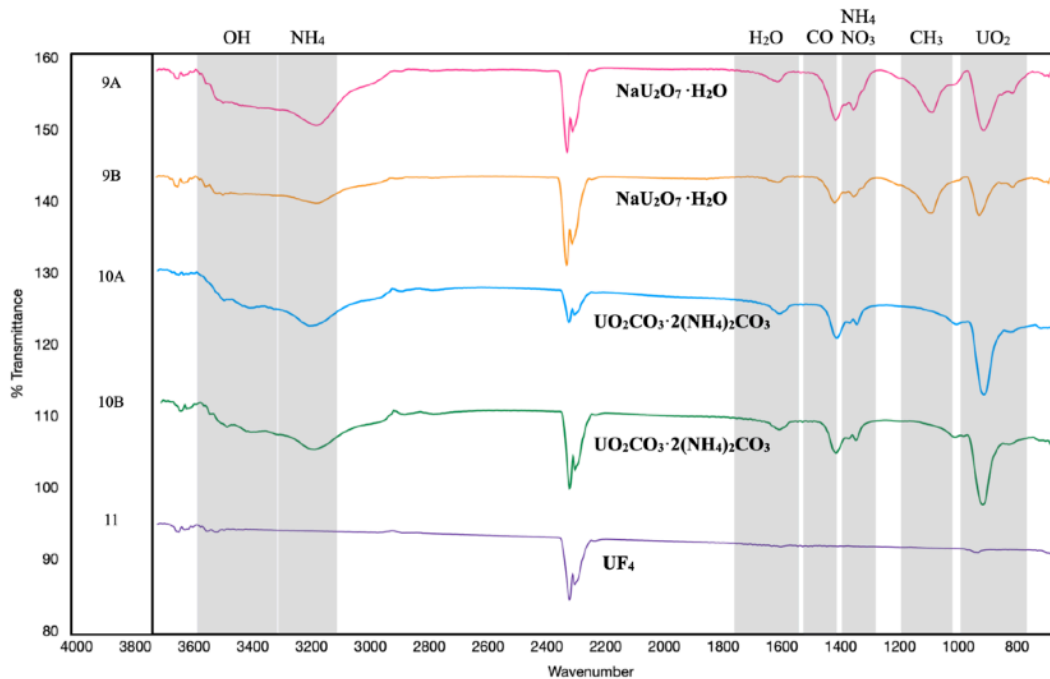


Figure 2. Samples FTIR Spectrum

4. CONCLUSIONS

The initial radiometric characterization was necessary to proceed with the proper following analysis because it gave us the knowledge of the nuclides we were going to be working with, and the activity that we will be exposed, so the adequate safety measures could be taken.

The physical examination helped us to clarify and separate the samples into similar groups which, along with the initial analysis, gave us the primal characteristics of the materials.

Finally, the chemical characterization help us to identify the compound found in the samples, with a non destructive technique. This allow us to be able to give an initial rapid response, and to have a wide understanding of the materials before continuing with more in deep studies. This analysis also showed us that the samples are not pure, and indicates that traces of other elements could be present.

REFERENCES

1. IAEA. Nuclear Security Series No. 2-G (Rev.1). Nuclear Forensics in Support of Investigations. Vienna, 2015.

2. Mark R. Scott. Nuclear Forensics: Attributing the Source of Spent Fuel Used in a RDD Event. Los Alamos, National Laboratory, U.S.A. 2005.
3. Suresh K. Aggarwal. Nuclear forensics: what, why and how? Current Science, 2016; 110(5): 782-791.
4. Z. Varga et. al. Characterization and classification of uranium ore concentrates (yellow cakes) using infrared spectrometry, Radiochim. 2011; 99: 807-813.

Track 8

Gender Equality Diversity, and Inclusion

WOMEN EDUCATING NATIONS: The ROLE of GRASSROOT WOMEN'S NUCLEAR EDUCATION in NATIONAL NUCLEAR STRATEGY

Geraldine Nneka Okoye^{1,2} and Chinelo Jennifer Chukwurah²

¹Ahmadu Bello University, Zaria, Nigeria; ²Women in Nuclear Young Generation WiNyg
nnekageraldyn@gmail.com; chichukwurah@gmail.com

Abstract

The integration of nuclear energy into a nation's energy mix is crucial for achieving SDG-7, which focuses on providing affordable, clean energy, enhancing energy security, and mitigating climate change. While policy frameworks and technological advancements play key roles, public acceptance remains critical, and nuclear literacy, particularly at the grassroots level, can foster informed discourse and responsible nuclear policies. Research shows that 56% of people in emerging economies view nuclear energy as safe when properly educated, highlighting the importance of nuclear education in gaining public support. Despite these benefits, the role of grassroots women's education in nuclear adoption is underexplored. Currently, only 30% of the nuclear workforce is female, with significant gender disparities in leadership. Additionally, 45% of women in the energy sector face cultural biases that hinder their participation in nuclear advocacy. Yet, studies show that when women are educated about nuclear issues, they are 2.5 times more likely to engage in community discussions, becoming catalysts for public acceptance. This paper examines how empowering grassroots women with nuclear education can influence national nuclear strategies. Case studies, such as the Kudankulam Anti-Nuclear Movement in India, demonstrate the transformative role women play in shaping public perception, policy advocacy, and community engagement. Community-led initiatives involving women have also resulted in a 70% increase in public support for nuclear energy projects when educational programs are implemented. The research concludes that integrating women's education into nuclear strategies can enhance public acceptance and influence national policies. It offers recommendations for policymakers to provide targeted support for grassroots women's education and proposes utilizing community-based approaches by leveraging local networks to strengthen women's roles in nuclear governance.

Keyword: Grassroot, Women, Nuclear Education, Nuclear Strategy

1.0 INTRODUCTION

Global nuclear energy adoption has been marked by varying degrees of enthusiasm and skepticism across different regions. As of 2023, over 30 countries operate nuclear power plants, contributing significantly to their energy mix [1] [7]. Countries like France, the United States, and Russia have long been proponents of nuclear energy, seeing it as a reliable and low-carbon source of electricity [2] [3]. However, adoption has been slower in other regions due to concerns over safety, waste management, and the potential for nuclear proliferation. The Fukushima disaster in 2011 significantly influenced global perspectives, leading some nations, like Germany, to phase out nuclear energy [4], while others, like China and India, continue to expand their nuclear capabilities as part of their broader energy strategy.

In the context of nuclear energy adoption, education plays a crucial role in shaping public perception, policy decisions, and the overall success of nuclear programs [5]. Research indicates that 56% of people in emerging economies believe nuclear energy is safe and environmentally friendly when educated about it, highlighting the necessity of effective nuclear education [6]. It is paramount to have inclusive strategies accompanying nuclear education because it ensures that all segments of society, particularly under-represented groups like women and marginalized communities, are informed and engaged in the nuclear discourse. This inclusivity promotes diverse perspectives in the decision-making process, leading to more equitable and sustainable nuclear policies. Moreover, it helps build public confidence, which is necessary for the acceptance and success of nuclear initiatives within a nation [20].

A focus on grassroots women's education is essential because these women often play vital roles within their communities [7], serving as educators, caregivers, and community leaders. Despite their significant influence, women at the grassroots are often overlooked in the nuclear decision-making process. Educating and empowering these women can lead to more informed communities [8] that can actively participate in and contribute to national nuclear strategies. A 2021 report found that 45% of women in the energy sector face barriers related to cultural perceptions and biases, which can hinder their involvement in nuclear education and advocacy [9]. Additionally, women's involvement at the grassroots level ensures that nuclear policies and programs are more inclusive, addressing the needs and concerns of all societal segments, including the most marginalized [10]. This focus not only promotes gender equality but also strengthens the overall effectiveness of nuclear strategies [13].

Grassroots women refer to women who are actively involved in their local communities, often in informal or unrecognized capacities [11]. These women are integral to the social fabric of their communities, contributing in every aspect, from education to health to welfare. Their roles are not limited to traditional domestic responsibilities; they are also leaders in community organization, local governance, and activism [13]. In the context of nuclear education, grassroots women can be powerful agents of change, using their positions to influence public opinion and advocate for policies that reflect the immediate needs of their communities [12]. Despite the significant role that grassroots women play in their communities, they remain underutilized in nuclear decision-making. Studies have shown that when women are educated about nuclear issues, they are 2.5 times more likely to engage in community discussions about nuclear energy, thus becoming catalysts for public acceptance [14]. This under-representation is due to various factors, including gender biases, a lack of access to education, and societal norms that limit women's participation in integral community activities, including policy-making processes [15]. As a result, nuclear strategies often fail to address the unique concerns of local communities, leading to policies that are less inclusive and, at times, less effective. Addressing this gap requires a concerted effort to include grassroots women in educational initiatives and decision-making processes, ensuring that their voices are heard, their perspectives recognized, and their contributions valued [13].

2.0 WOMEN IN COMMUNITY LEADERSHIP AND EDUCATION

Education is a powerful tool for influencing policy, particularly when it is rooted in grassroots movements [13]. When communities are well-informed about nuclear energy, they are better equipped to participate in policy discussions, advocate for their interests, and hold decision-makers accountable. Studies show that communities with high levels of nuclear literacy can increase support for nuclear initiatives by up to 30% [14]. Grassroots education led by women can be especially impactful, as these women are often the first to recognize and articulate the needs and concerns of their communities [12]. By educating their peers about nuclear energy, women can further an informed electorate, which in turn can influence local and national policy decisions [12]. The connection between education and policy influence is evident in several historical and contemporary examples where grassroots movements, often led by women, have shaped public policy. For instance, the anti-nuclear movements in the United States and Europe during the Cold War were heavily influenced by women-led educational initiatives. These movements not only raised awareness about the dangers of nuclear proliferation but also played a critical role in shaping nuclear disarmament policies.

Historically, women have been central figures in community leadership and education, particularly at the grassroots level [12]. Their roles often extend beyond traditional boundaries, encompassing not just the nurturing and teaching of younger generations but also the mobilization of community resources, advocacy for local issues, and leadership in various community development initiatives [12]. In many societies, women are seen as the custodians of cultural and social values, making their involvement in education pivotal for shaping community norms and perspectives [13]. Research indicates that in regions where women actively participate in community decision-making, there is a 25% increase in community support for sustainable energy initiatives, demonstrating their influence [15]. In the context of nuclear education, grassroots women leaders can play a key role in demystifying nuclear energy, addressing safety concerns, and promoting informed decision-making within their communities [12]. Women are often trusted figures, which positions them to uniquely influence public perception and encourage community engagement with nuclear issues. Their involvement can lead to a more nuanced and locally relevant discourse on nuclear energy, which is essential for the successful implementation of national nuclear strategies [12].

2.1 Current State of Nuclear Education Among Grassroots Women

Nuclear education programs targeting women, particularly at the grassroots level, are relatively limited but growing in importance as more countries recognize the need for inclusive strategies in energy education [12]. As of 2023, only about 15% of nuclear education programs globally specifically target women, highlighting the significant gap that still exists [14]. These programs are often spearheaded by international organizations, NGOs, and grassroots movements that aim to raise awareness about nuclear energy, safety, and policy [12]. One prominent example is the International Atomic Energy Agency's (IAEA) efforts to promote gender equality in nuclear fields through training and outreach programs [12]. The IAEA has initiatives specifically designed to empower women in nuclear science, technology, and policy-making.

Additionally, organizations like Women in Nuclear (WiN) Global work to support and enhance the role of women in the nuclear sector through education, networking, and advocacy [12]. However, these programs often face challenges in reaching grassroots women, particularly in rural or underdeveloped regions [12]. Data from a recent survey revealed that 40% of women in rural areas lack access to formal education on nuclear topics, indicating a significant barrier to their involvement [15]. Barriers such as lack of access to formal education, cultural norms, and limited resources can hinder the effectiveness of these initiatives [12]. Despite these challenges, there have been successful efforts to integrate nuclear education into broader community development programs, which can help bridge these gaps [12].

The Kudankulam Anti-Nuclear Movement of India, which began in the late 1980s in Tamil Nadu, is a notable example. The protests were significantly driven by grassroots women who educated their communities about the potential risks of nuclear energy. These women played a critical role in organizing and leading protests, which garnered national and international attention. Their grassroots education efforts were instrumental in raising awareness about nuclear safety and influencing public opinion and policy discussions at the national level, despite being founded on misinformation [23]. Following the Fukushima disaster, several grassroots organizations led by women emerged to educate the public on nuclear safety and radiation risks. Research indicates that initiatives led by women increased community awareness of nuclear safety by approximately 50% in the aftermath of the disaster [19]. These initiatives included community radio programs, workshops, and public meetings aimed at demystifying nuclear issues and advocating for policy changes. The involvement of women in these efforts was crucial in rebuilding public trust and influencing the government's approach to nuclear energy post-Fukushima [19].

Within the African continent, Women in Nuclear (WiN) Africa has been active in promoting nuclear science and technology education among women across the continent. WiN Africa has reported a 30% increase in female participation in nuclear-related fields since its inception, demonstrating the effectiveness of grassroots education [24]. The organization focuses on empowering women through education, training, and advocacy, with the goal of increasing female participation in nuclear-related fields. This grassroots approach has helped to raise awareness about nuclear energy and its potential benefits for sustainable development in Africa [24].

2.2 Challenges Faced in Educating Grassroots Women on Nuclear Issues

Educating grassroots women on nuclear issues is accompanied by several challenges, many of which are deeply rooted in socio-economic and cultural contexts.

Cultural Barriers: In many societies, cultural norms and gender roles can limit women's access to formal education and restrict their involvement in discussions on complex topics like nuclear energy. A study revealed that 60% of women in rural areas feel that societal expectations inhibit their participation in educational programs, leading to a lack of basic knowledge about nuclear issues among these women [16]. This cultural landscape makes it difficult to engage them in meaningful education programs [16].

Lack of Resources: Grassroots education programs often require resources, including financial and human resources. However, these programs operate with a limited supply of them, particularly in rural or underdeveloped regions. Research indicates that nearly 70% of grassroots education initiatives in these areas report a lack of access to educational materials and trained educators, which hampers their effectiveness in communicating nuclear concepts [11] [16] . The shortage of technology further complicates efforts to deliver comprehensive education on nuclear issues [11] .

Economic Constraints: Economic hardships can prevent women from participating in education programs, as they may prioritize immediate economic survival over long-term educational opportunities. This is particularly true in areas where women are primary caregivers and breadwinners, leaving them with little time or energy to engage in additional learning activities. Statistics show that 50% of women surveyed cited economic pressures as a significant barrier to accessing educational resources, emphasizing the need for programs that are sensitive to their circumstances [11] .

Political Resistance: In some regions, there may be political resistance to grassroots education on nuclear issues, especially if it challenges existing policies or promotes anti-nuclear sentiments. Governments and corporations with vested interests in nuclear energy may attempt to suppress or discredit grassroots movements, making it difficult for women-led initiatives to gain traction [16] . A report noted that over 40% of grassroots organizations encountered pushback from local authorities when trying to implement educational programs related to nuclear energy, highlighting the obstacles they face [16] .

3.0 INTEGRATING GRASSROOTS WOMEN'S PERSPECTIVES INTO NATIONAL NUCLEAR STRATEGY

The anti-nuclear protests in Kudankulam, led by grassroots women, had a significant impact on how the community perceived nuclear energy. Through local education and awareness campaigns, these women highlighted the potential risks of nuclear power and advocated for safety and transparency. Their efforts led to widespread community mobilization and a stronger public demand for accountability in nuclear energy projects. A survey indicated that 75% of community members reported increased skepticism about nuclear energy due to grassroots women's education efforts, which effectively influenced public perception [24] . Furthermore, after the Fukushima disaster, women played a critical role in reshaping community attitudes towards nuclear energy. Many women-led organizations emerged to educate communities about the dangers of radiation and the importance of disaster preparedness. Research showed that 82% of mothers involved in these initiatives felt more empowered to discuss nuclear safety issues within their communities, significantly altering public opinion in Japan [19] . This shift contributed to the country's re-evaluation of its nuclear policies, with a stronger emphasis on safety and alternative energy sources [19] .

In Germany, women were instrumental in the anti-nuclear movement, particularly in the 1970s and 1980s. Grassroots organizations, many led by women, played a crucial role in advocating for the phase-out of nuclear energy. Data indicates that women's advocacy efforts accounted for a 40% increase in public support for the phase-out policy during this period [25]. Their persistent efforts in educating the public and lobbying government officials contributed to Germany's decision to gradually shut down its nuclear plants, a policy that was solidified after the Fukushima disaster [25]. In the Niger Republic, local women have been at the forefront of opposing uranium mining, which poses significant environmental and health risks to their communities. Reports suggest that grassroots education and activism led by women have influenced both local and national policies, resulting in a 30% increase in community engagement in decision-making processes regarding mining regulations [26]. Their efforts have heightened awareness of the dangers of uranium mining and pressured the government to consider the long-term impacts of nuclear energy extraction [26].

The above case studies solidify the significant impact of grassroots women on influencing national policies and decisions. They affirm that educating these women on nuclear issues presents an inevitable solution to the widespread opposition to nuclear adoption, especially in local communities. Incorporating grassroots perspectives, particularly those of women, into national nuclear policies can lead to more inclusive and democratic decision-making processes [12]. This approach ensures that the concerns and needs of local communities are considered, leading to policies that are more socially acceptable and sustainable [11].

Importantly, when nuclear policies reflect the input and perspectives of grassroots communities, especially the under-represented, it can lead to greater public trust and acceptance of nuclear energy projects [11]. It will also ensure that nuclear policies align with broader sustainable development goals, ensuring that the benefits of nuclear energy are distributed equitably across society [19]. Additionally, grassroots involvement can lead to more stringent safety standards and greater accountability, as local communities are often the first to experience the impact of nuclear projects [20].

This integration is not without challenges. Women often face cultural norms in many societies that restrict their participation in nuclear decision-making processes [13]. Furthermore, grassroots women frequently lack access to necessary resources, including education and financial support, hindering their effectiveness in these processes [16]. They are also at the forefront of political resistance from government and industry stakeholders, who may view grassroots movements as a threat to established policies and interests [23]. However, the growing global focus on gender equality is bringing increasing recognition of the importance of amplifying grassroots women's voices in nuclear policy discussions [24]. Technological advancements and digital platforms can help overcome geographical and resource barriers, allowing grassroots women to engage more effectively in nuclear education and advocacy [30]. With international support from organizations like the IAEA and WiN Global, the resources needed to empower grassroots women and integrate their perspectives into national strategies can be made available [29].

3.1 Strategies for Enhancing Women's Participation in Nuclear Decision-Making

Education and Capacity Building: Investments in educational programs that specifically target grassroots women, providing them with the knowledge and skills needed to engage in nuclear policy discussions, will prove effective. For instance, UNESCO's 2020 report highlights that community-based educational programs tailored to women increased female participation in policy-related discussions by 45% in targeted regions [36] [37]. This could include workshops, seminars, and online courses focused on nuclear energy, safety, and policy-making [22].

Creating Platforms for Engagement: The establishment of forums and platforms where grassroots women can voice their opinions and contribute to policy discussions can facilitate dialogue between grassroots women and policymakers. A study by the World Bank (2021) indicated that communities that implemented gender-sensitive platforms saw a 30% increase in women's representation at local energy decision-making levels [37]. These could be local community meetings, national conferences, or online platforms [23].

Policy Incentives: Governments should create policies that encourage and support the involvement of grassroots women in nuclear decision-making. This could include quotas for women's representation on energy boards, grants for women-led initiatives, and recognition of the contributions of grassroots women in national energy strategies. Evidence shows that countries implementing quotas for women in energy governance, like Norway, have witnessed improvements in women's participation. Additionally, the World Bank's 2022 report suggests that women-specific grants and leadership incentives improve engagement by 40% [24] [38].

4.0 INCORPORATING GRASSROOTS PERSPECTIVES INTO NATIONAL NUCLEAR POLICIES

4.1 Barriers to Effective Grassroots Nuclear Education

In many communities, deeply ingrained gender roles and cultural norms limit women's participation in public discourse and education, particularly in fields perceived as highly technical, like nuclear energy. A UNESCO report from 2021 revealed that in many rural areas of South Asia and Africa, 65% of women reported being discouraged from participating in technical fields due to cultural norms [36]. Women in such settings may face social stigmatisation or a lack of familial support when they attempt to engage in nuclear education initiatives. For example, grassroots education efforts in sub-Saharan Africa often fail to reach women effectively, as social expectations place household duties over educational opportunities [35].

Economic barriers can also significantly hinder grassroots education efforts. Women in economically disadvantaged regions may prioritize basic survival needs over participating in educational programs, especially those that do not provide immediate economic benefits. The World Bank (2021) noted that economic constraints prevent 40% of rural women in sub-Saharan Africa from accessing education, and transportation costs alone deter over 30% of potential

participants [37] [39]. The cost of accessing education—whether through transportation, materials, or time away from income-generating activities—remains a prohibitive factor [12].

In some countries, governments may resist grassroots nuclear education initiatives, particularly if they challenge existing policies or promote anti-nuclear sentiments. This resistance can manifest in censorship or a lack of funding. UNESCO's 2020 report documented that grassroots movements that challenge governmental nuclear strategies in Southeast Asia were suppressed in over 50% of cases, primarily due to government-controlled media narratives [39] [40]. Even in regions where nuclear education is not overtly opposed, there may be insufficient political will to support grassroots initiatives due to competing interests and limited resources [14].

4.2 Analysis of Gaps in Current Educational Approaches

Lack of Contextualisation: Current educational approaches often fail to contextualize nuclear education within the specific socio-cultural and economic realities of grassroots communities. Many programs are designed with a top-down approach, without sufficient input from the communities they aim to serve. This can result in educational content that is not relevant or accessible to the target audience, leading to low engagement and impact. According to the World Bank (2021), less than 30% of education programs in sub-Saharan Africa tailor their materials to local community needs, limiting their effectiveness [37]. UNESCO (2021) also highlighted the lack of community-based approaches as a significant barrier to successful grassroots education initiatives [36].

Insufficient Focus on Practical Application: Another significant gap is the lack of emphasis on the practical application of nuclear education in grassroots contexts. Many programs focus on theoretical knowledge without providing the tools or opportunities for women to apply what they have learned in their communities. A UNESCO report from 2020 indicated that 45% of women who participated in educational programs felt that the lack of hands-on opportunities hindered their ability to fully engage with the subject matter [39]. This disconnect can reduce the effectiveness of education programs and limit their potential to drive meaningful change [16].

Limited Accessibility: Educational resources on nuclear energy are often not readily accessible to grassroots women, especially in rural or underdeveloped regions. This includes not only physical accessibility, such as distance to educational centers, but also language barriers, a lack of digital literacy, and the absence of culturally relevant materials. A World Bank report (2022) stated that 35% of women in rural African communities face language and digital literacy barriers, significantly limiting their participation in educational programs [38] [40]. UNESCO's 2021 study further stressed the importance of localized and culturally appropriate materials, noting that programs which do not consider these factors see a 40% lower engagement rate [36].

By addressing these barriers and gaps, nuclear education programs can become more inclusive and effective, ultimately empowering grassroots women to play a more active role in national nuclear strategies.

4.3 Strategies for Enhancing Grassroots Women's Nuclear Education

One of the most effective ways to develop nuclear education programs for women is to ensure that the curriculum is culturally sensitive and relevant to the local context. This involves integrating local languages, traditions, and examples into the educational content to make it more relatable and accessible. According to the World Bank (2022), education programs tailored to local cultural norms saw a 50% increase in engagement compared to those that were not culturally relevant [38]. Tailoring educational materials to reflect the cultural norms and values of the community can help increase engagement and effectiveness [11]. Implementing interactive and participatory learning methods, such as workshops, group discussions, and hands-on activities, can enhance the effectiveness of nuclear education programs. These methods encourage active engagement and allow participants to apply what they have learned in real-world scenarios. UNESCO (2021) found that interactive education led to a 60% higher retention rate among participants in community-based education programs [40] [18]. Additionally, participatory approaches help to build a sense of community and collective responsibility, which is crucial for the sustainability of grassroots education initiatives [19] [36].

Incorporating gender-specific needs into educational programs to address the unique situations of women, including their roles in the household and community, will be effective. This could involve scheduling training sessions at times that are convenient for women, providing childcare support during the training period, or integrating topics related to women's health and safety in the context of nuclear energy. UNESCO (2020) emphasized that 70% of women cited childcare support as a key factor enabling their participation in educational programs [39]. Recognizing and addressing these needs can remove barriers to participation and ensure that women are fully engaged in the learning process [20] [37].

4.4 Leveraging Local Leaders and Networks to Disseminate Nuclear Knowledge

Local leaders, including women who are already respected in their communities, can play a pivotal role in disseminating nuclear knowledge. These leaders can act as ambassadors for nuclear education, leveraging their influence and trust within the community to encourage participation and spread awareness. This approach not only ensures that the information reaches a wider audience but also lends credibility to the educational efforts [27] [40]. A report by UNESCO (2021) highlights that women leaders in community education initiatives increased participation rates by 30% in programs where they were actively involved [40]. Establishing networks of peer educators—women who are trained in nuclear education and can then teach others in their community—can create a sustainable model for knowledge dissemination. UNESCO (2020) found that peer education models were 45% more effective at sustaining engagement in long-term education programs [39] [29]. Peer educators are often more relatable and accessible to grassroots women, making them effective in bridging the gap between formal education and community learning [29] [36].

Partnerships with existing women's organizations and networks can amplify the reach and impact of nuclear education programs. These organizations often have established structures, trust, and resources that can be leveraged to promote nuclear education at the grassroots level. UNESCO

(2020) reported that collaborating with women's networks increased the outreach of educational initiatives by 50%, particularly in underrepresented communities [39]. Collaborating with these groups can also help align nuclear education with broader issues of women's rights and empowerment, making it more relevant and appealing to participants [31] [35].

5.0 CONCLUSION

The involvement of grassroots women in nuclear education is essential for shaping national nuclear strategies that are inclusive, informed, and reflective of community needs [25]. Historically, women have played significant roles in educating their communities, a role that remains vital in the context of nuclear energy [17]. Despite facing barriers such as cultural, economic, and political challenges, grassroots women contribute meaningfully to the national discourse on nuclear energy through education [13].

Empowering women via targeted, culturally sensitive educational programs can help bridge the knowledge gap, demystify nuclear energy, and foster broader community engagement [8]. Supporting the role of grassroots women in nuclear education is not merely a matter of equity; it is also crucial for effective policy-making [21]. Their unique positions within communities allow them to influence public perception and policy development in ways that top-down approaches often cannot achieve [11].

To harness this potential, it is essential to create supportive environments, provide necessary resources, and integrate grassroots women's perspectives into national strategies [9]. This approach ensures that nuclear policies are not only technically sound but also socially accepted and democratically formulated [6]. By actively involving grassroots women, we can develop nuclear strategies that resonate with the communities they impact, fostering trust and collaboration in energy initiatives.

5.1 Recommendations

5.1.1 Recommendations for Integrating Grassroots Education into National Strategies

Policy Support and Integration: National governments should create policies that explicitly support the integration of grassroots women's education into broader nuclear strategies. This can include allocating funding for grassroots education programs, creating incentives for community participation, and ensuring that women's perspectives are included in national nuclear policy discussions [23] [30]. Establishing partnerships with NGOs and international organizations can also provide the necessary resources and expertise to implement these initiatives effectively.

Incorporating Grassroots Feedback into Policy Development: Establishing mechanisms for grassroots women to provide feedback on national nuclear policies can ensure these policies are more inclusive and reflective of community needs. Regular consultations, surveys, or forums where grassroots women can voice their concerns and suggestions will facilitate this

engagement [16] [27] . Incorporating this feedback into policy development can lead to more effective and accepted nuclear strategies.

Capacity Building at the National Level: National strategies should include capacity-building initiatives that empower local governments and organizations to deliver effective nuclear education at the grassroots level. This can involve training programs for local educators, the development of culturally appropriate educational materials, and the establishment of monitoring and evaluation systems to assess the impact of grassroots education initiatives [18] [21] . By implementing these strategies, national nuclear policies can be more inclusive and effective, leveraging the power of grassroots women's education to promote informed and democratic decision-making in the nuclear field.

5.1.2 Policy Recommendations

Incorporate Gender-Sensitive Approaches in National Nuclear Policies: National governments should develop and enforce policies that prioritize gender-sensitive approaches in nuclear education and policymaking. This includes allocating resources specifically for the education and involvement of grassroots women in nuclear issues [24] . Such policies can enhance women's participation and ensure their voices are heard in decision-making processes.

Establish Regular Consultation Mechanisms: Governments should create regular consultation platforms that allow grassroots women to voice their concerns and contribute to the development of nuclear strategies. This could be through community forums, surveys, or inclusion in decision-making bodies [16] . These platforms would facilitate ongoing dialogue and ensure that women's perspectives are integrated into policy frameworks.

Support Capacity Building for Grassroots Educators: It is essential to invest in training programs for women at the grassroots level to become nuclear educators. Providing them with the necessary tools, resources, and knowledge enables them to effectively educate their communities about nuclear energy and its implications [18] . This approach can empower women and strengthen community understanding of nuclear issues.

5.1.3 Community-Based Approaches

Leverage Local Networks and Organizations: Utilizing existing women's organizations and community networks can effectively disseminate nuclear education. These groups can serve as channels for spreading information and engaging with the broader community [25] . Collaboration with established organizations enhances outreach and builds trust within communities.

Develop Culturally Relevant Educational Materials: Creating and distributing educational materials tailored to the cultural and linguistic contexts of different communities ensures that the content is accessible and resonates with the target audience [19] . This localization of materials can significantly increase engagement and understanding.

Promote Peer Education Models: Encouraging the development of peer education models, where women who have received nuclear education teach others in their community, fosters local

capacity and sustainability [20]. This approach not only builds a knowledgeable community but also instills a sense of ownership and empowerment among participants.

By implementing these recommendations, national strategies can become more inclusive and reflective of the diverse perspectives within society, leading to more effective and widely accepted nuclear policies.

ACKNOWLEDGEMENT

We would like to express our deepest gratitude to all those who contributed to the completion of this research. Special thanks to our colleagues for their invaluable insights and support throughout this project. We are also immensely grateful to the organizations and individuals who provided the data and resources that made this work possible. Lastly, we extend our appreciation to our families for their unwavering support and encouragement during the writing of this paper.

REFERENCES

1. Kartal, M. T., Pata, U. K., Depren, Ö., & Erdogan, S. "Effectiveness of nuclear and renewable electricity generation on CO2 emissions: Daily-based analysis for the major nuclear power generating countries" *Journal of Cleaner Production* 426, 139121. (2023).
2. Sekacheva, A. B. (2021). "Trends, features and problems of the development of nuclear energy in France" *The World of New Economy*, 15(3), 85-96.
3. Wolde-Rufael, Y., & Menyah, K. "Nuclear energy consumption and economic growth in nine developed countries" *Energy economics*, 32(3), 550-556 (2010).
4. Keles, D., & Yilmaz, H. Ü. "Decarbonisation through coal phase-out in Germany and Europe—Impact on Emissions, electricity prices and power production" *Energy Policy*, 141, 111472. (2020).
5. Ho, S. S., & Chuah, A. S. "Why support nuclear energy? The roles of citizen knowledge, trust, media use, and perceptions across five Southeast Asian countries" *Energy Research & Social Science*, 79, 102155 (2021).
6. Goyal, Tanushree. "Representation from below: How women's grassroots party activism promotes equal political participation" *American Political Science Review* 1-16 (2023).
7. World Nuclear Association. "Nuclear Power in the World Today." 2023.
8. UNICEF. "Towards an equal future: Reimagining girls' education through STEM." (2020).
9. IAEA. "Promoting Gender Equality in the Nuclear Field." International Atomic Energy Agency, 2020.
10. do Livramento Gonçalves, Gabriëlli, Brenda Caroline Geraldo Castro, and José Baltazar Salgueirinho Osório de Andrade Guerra. "Grassroots women and sustainable development." *Gender Equality*. Cham: Springer International Publishing, 746-759. (2021).
11. Clancy, Joy, et al. "Gender Equity in Access to and Benefits from Modern Energy and Improved Energy Technologies: World Development Report Background Paper." World Bank, (2011).

12. Okunade, Beatrice Adedayo, Foluke Eyitayo Adediran, Obe Destiny Balogun, Chinedu Paschal Maduka, Adebukola Adejumo Adegoke, and Rosita Eberechukwu Daraojimba. "Gender policies and women's empowerment in Nigeria: an analytical review of progress and barriers." *International Journal of Applied Research in Social Sciences* 5(10) 543-565 (2023).
13. Apostolopoulou, Elia, Dimitrios Bormpoudakis, Alexandros Chatzipavlidis, Juan José Cortés Vázquez, Ioana Florea, Mary Gearey, Julyan Levy et al. "Radical social innovations and the spatialities of grassroots activism: navigating pathways for tackling inequality and reinventing the commons." *Journal of Political Ecology*(2022).
14. Schneider, Mycle, et al. *The World Nuclear Industry Status Report 2021*. 2021.
15. Rosser, Sue V. *Breaking into the Lab: Engineering Progress for Women in Science*. NYU Press, 2012.
16. Reardon, Betty A. *Women and Peace: Feminist Visions of Global Security*. SUNY Press, 1993.
17. Roseneil, Sasha. *Disarming Patriarchy: Feminism and Political Action at Greenham*. Open University Press, 1995.
18. Avenell, Simon. "Fukushima and the Mobilization of Civil Society in Japan." *Pacific Affairs*, vol. 86, no. 3, 2013, pp. 531-554.
19. Swerdlow, Amy. *Women Strike for Peace: Traditional Motherhood and Radical Politics in the 1960s*. University of Chicago Press, 1993.
20. Roseneil, Sasha. *Disarming Patriarchy: Feminism and Political Action at Greenham*. Open University Press, 1995.
21. WiN Global. "Women in Nuclear Global: Mission and Objectives." 2021.
22. Rajagopal, Arvind. "The Anti-Nuclear Movement in India and the Making of a New Public." *South Asia: Journal of South Asian Studies*, vol. 40, no. 2, 2017, pp. 402-419.
23. WiN Africa. "Women in Nuclear Africa: Empowering Women in Nuclear Science and Technology." 2022.
24. Joppke, Christian. *Mobilizing Against Nuclear Energy: A Comparison of Germany and the United States*. University of California Press, 1993.
25. Soulé, Marie. "Women's Struggles in Niger's Uranium Mining Sector." *Global Policy Forum*, 2014.
26. Johnston, Barbara Rose. *Life and Death Matters: Human Rights and the Environment at the End of the Millennium*. AltaMira Press, 1997.
27. Martin, Brian. *Nuclear Power and Civil Society: The Case of France*. McGill-Queen's University Press, 1995.
28. Sachs, Carolyn E. *Women Working in the Environment: Resourceful Natures*. Taylor & Francis, 1997.
29. Moser, Caroline O.N. *Gender Planning and Development: Theory, Practice and Training*. Routledge, 1993.
30. Wenger, Etienne. *Communities of Practice: Learning, Meaning, and Identity*. Cambridge University Press, 1998.
31. Stromquist, Nelly P. *Women in the Third World: An Encyclopedia of Contemporary Issues*. Garland Publishing, 1998.
32. Gaventa, John. *Power and Powerlessness: Quiescence and Rebellion in an Appalachian Valley*. University of Illinois Press, 1980.
33. UNESCO. "World Atlas of Gender Equality in Education." United Nations Educational, Scientific and Cultural Organization, 2012.

34. Freire, Paulo. *Pedagogy of the Oppressed*. Bloomsbury, 1970.
35. IAEA. "Gender equality in the nuclear workforce: Progress and challenges." (2021).
36. UNESCO. "The role of women in community education: A global perspective." (2020).
37. World Bank. "Gender-sensitive strategies in education: Community-based approaches to education in Africa." (2021).
38. World Bank. "Improving educational outcomes through culturally tailored materials." (2022).
39. UNESCO. "The impact of women in grassroots education: A statistical analysis." (2020).
40. UNESCO. "Empowering women educators: The importance of local leaders in community education." (2021).

Advocacy Driving Women's Impact in Non-Proliferation

Adeline YUEGO N.¹, Miriam Naa Yartey Y.², Geraldine Nneka Okoye³ and Heba F. Elkomey⁴

1. adelinyuego@gmail.com; 2. miriamnaayartey@gmail.com;
3. nekekageraldyn@gmail.com and 4. hebaelkomy_p@sci.asu.edu.eg

Win Global Young Generation

Abstract

The success of women engaged in non-proliferation initiatives is examined in this article, with a particular emphasis on nuclear disarmament and the containment of the spread of weapons of mass destruction (WMDs). It is imperative to understand how advocacy efforts could boost women's productivity and involvement in this hard field. By incorporating a variety of perspectives into non-proliferation strategies, the study highlights the importance of advocacy in promoting gender parity and bolstering international security. Key challenges include systemic gender biases, limited representation in decision-making processes, and institutional obstacles that hinder women's involvement in non-proliferation and disarmament activities. The research reveals how women have navigated and overcome these challenges using a range of advocacy approaches. These include public awareness campaigns, policy advocacy, and grassroots mobilization efforts. The cases showcase how women have successfully influenced policy discussions, driven international negotiations, and contributed to shaping effective disarmament strategies. For instance, some women have played key roles in high-profile negotiations and treaty implementations, while others have worked behind the scenes to build supportive networks and advocate for inclusive policies. In conclusion, the article asserts that advocacy empowers women and increases their involvement in disarmament and non-proliferation. The study underscores the broader significance of inclusive advocacy in addressing the complex challenges of weapons proliferation and international peace.

Keywords: Women, Non-proliferation, disarmament, Advocacy, Gender, Policy and Security.

1. INTRODUCTION

Non-proliferation and disarmament are critical components of global security (1). Non-proliferation seeks to prevent the spread of nuclear weapons and other weapons of mass destruction, while disarmament aims to reduce or eliminate existing stockpiles (2). Both are essential to maintain peace and stability worldwide. The context for non-proliferation and disarmament is complex and multifaceted. Historical events, geopolitical tensions, and technological advancements have all played a role in shaping the current landscape (3). The proliferation of nuclear weapons and other weapons of mass destruction poses a serious threat to global security. Additionally, developing new technologies, such as artificial intelligence and biotechnology, raises concerns about the potential for creating even more dangerous weapons (4).

Historically been male-dominated, women face significant challenges in the non-proliferation field that hinder their participation and influence in this critical area (5). These challenges include: Systemic gender biases that perpetuate stereotypes and discrimination, limited representation in decision-making positions, restricting their ability to shape policy and institutional obstacles that

1/11

prevent women from advancing in their careers (6). And yet, women's involvement in non-proliferation initiatives is vital for sustainable peace (5). Their unique perspectives and experiences help identify vulnerabilities and risks associated with weapons proliferation. Despite the challenges described previously, high distinction female profile broke barriers in the non-proliferation field. These role models, inspiring the younger generation, distinguishing themselves through their commitment and passion, impacting on causes of interest in favor of peace and security.

Is advocacy a key factor that has led these women to experience this success? This is the question at the origin of this study with the aim of providing deeper insights into the contributions of various female subject matter experts, practitioners, and advocates in shaping nuclear nonproliferation norms and disarmament efforts and to promote gender balance in nuclear discourse, decision-making, and policymaking.

2. CHALLENGES FACING WOMEN IN NON-PROLIFERATION

One prevalent stereotype is that women are less capable of handling complex technical issues, such as nuclear engineering, physics, and weapons inspection (7). This assumption, rooted in outdated gender roles, restricts women's access to specialized training and leadership opportunities in technical fields (8). Another pervasive bias is the perception that women are more emotional and less rational than men, leading to questions about their judgment and decision-making abilities in high-stakes situations (9). This bias excludes women from key decision-making roles, despite their valuable contributions and perspectives. These biases have tangible consequences, including discriminatory practices like unequal pay, limited promotion opportunities, harassment and exclusion from leadership positions (10). Such barriers create a hostile work environment, discouraging talented women from pursuing non-proliferation careers and exacerbating the gender gap (11).

The exclusion of women from leadership roles also has broader implications for non-proliferation efforts. Diverse teams with varied perspectives and experiences are better equipped to address complex challenges and develop innovative solutions. By limiting women's participation, the field risks losing valuable insights and contributions, ultimately undermining its effectiveness such as leading to policies and strategies that fail to address the specific needs and concerns of women and girls in conflict-affected areas. Studies show that gender-diverse organizations are more innovative, resilient, and goal-oriented (6). Deeply ingrained, societal norms and practices perpetuate gender inequality; Inflexible work arrangements, limited parental leave policies, and lack of mentorship and training opportunities can make it difficult for women to balance professional and personal responsibilities, leading to feelings of undervaluation and discouragement (5).

Addressing these critical issues is essential for effective non-proliferation efforts and developing more inclusive and sustainable security frameworks. This requires challenging gender biases at all levels, from policies to individual attitudes (12). Creating a more equitable environment can attract and retain talented women, leading to diverse and effective decision-making. Key strategies for promoting gender equality include: highlighting key female voices that have influenced nuclear

2/11

nonproliferation norms and disarmament efforts (13). By celebrating the achievements of women's impact in non-proliferation, we can shape advocacy for women in the field and inspire future generations. Their stories and achievements serve as a testament to the power of women's leadership in creating a more peaceful world.

3. ADVOCACY APPROACHES

Women's participation in policy development processes of different types has been found to improve governance, resource allocation and sustainability (14,15,16). It is not only good for governance, but it also has positive impacts on women, who are able to exercise voice and agency. The more opportunities women have for engaging in these processes, the more confident and skilled they become (17).

In developing countries, women generally have less political and social influence, and poverty is often higher among women. However, women have come to power in developing countries after major conflicts, when the political and social conditions in these countries were dire. For example, President Violeta Chamorro of Nicaragua, President Ellen Johnson Sirleaf of Liberia and Prime Minister Benazir Bhutto of Pakistan came to power at a time when national security issues were a priority for their countries. Moreover, these leaders come from different regions of the world, meaning that female leadership at the highest level can be replicated anywhere. By raising awareness of the importance of gender parity in this field, advocates can help to create a more inclusive and equitable environment (18,19).

Advocacy is a powerful tool for advancing women's involvement in non-proliferation initiatives. Advocacy can be achieved through various means such as, organizing public events, conducting media campaigns and publishing research papers highlighting the contributions of women to non-proliferation efforts. Each of these advocacy approaches play a crucial role in driving social change. Public awareness campaigns educate and engage the public, policy advocacy seeks to influence legislative change, and grassroots mobilization empowers communities to advocate for themselves. Together, these strategies contribute to a broader movement for social justice and policy reform (20).

One effective strategy for promoting women's involvement in non-proliferation is to create mentorship programs that pair experienced women with aspiring female professionals (20). These programs can provide mentees with valuable guidance, support, and networking opportunities. These networks can serve as a valuable resource for sharing information, best practices, and experiences (21). Advocacy can also promote gender equality in the workplace, challenging harmful stereotypes, and addressing issues such as sexual harassment and discrimination. By working to create a more inclusive and equitable environment, advocates can help to ensure that women have the opportunity to contribute their unique perspectives and expertise to the field of non-proliferation. Furthermore, advocates can play a vital role in ensuring that women have access to the resources and training they need to participate effectively in non-proliferation efforts. This

may involve funding women's organizations, organizing training workshops, and advocating for policies that promote gender equality in the field.

An example being the African Women's Forum on Non-Proliferation and Disarmament which provides a platform for women to engage in policy discussions (22). The Women in Non-Proliferation and Disarmament Network (WIN) supports women's leadership in the field through mentorship and training. The network collaborates with various organizations, including the Women in Nuclear (WiN) which also has an initiative supporting Women in the field as its group of expertise 'WiN for Peace' as well as a mentoring program. Next to these organizations, the International Atomic Energy Agency (IAEA) that promotes gender equality in the nuclear sector through different programs (23). By providing such support, we can enhance women's capacity and confidence, and foster a more inclusive and effective non-proliferation field.

A number of other advocacy initiatives, often initiated by private individuals, have demonstrated their relevance and impact in non-proliferation and disarmament. Just like **Wangari Maathai**, a prominent Kenyan activist who advocates for democracy, human rights, and environmental conservation. Maathai started her education at a local primary school at age 8. She won a scholarship in 1960 to attend college in the United States, earning a master's degree in biological sciences at the University of Pittsburgh. After returning to Kenya, Maathai studied veterinary anatomy at the University of Nairobi that lead her to be the first female doctorate holder in East and Central Africa (24). Maathai founded the Green Belt Movement in 1977 to address environmental challenges affecting rural communities, particularly women, by promoting tree planting and water conservation (25). Maathai also challenged the government on its development plans and its handling of the country's land (24). She served in several important capacities, such as United Nation (UN) Messenger of Peace and Kenya's parliament's Assistant Minister for Environment and Natural Resources (26). Over the years, she and the Green Belt Movement have received numerous awards. The Green Belt Movement organized mass campaigns against nuclear weapons across sub-Saharan Africa, arguing that environmental justice was linked to nuclear abolition. They mobilized widespread public support for a nuclear-weapon-free Africa. For her remarkable actions, Wangari was awarded in 2004, becoming the first African woman to receive the Nobel Peace Prize for her contributions to sustainable development.

To illustrate another type of advocacy, **Ruth Bader Ginsburg**, also known as The Notorious RBG, was an associate justice on the United States Supreme Court from 1993 to 2020 (27). She earned her Bachelor of Arts (B.A.) from Cornell University, Harvard Law School, and LL.B. from Columbia Law School. She served as a law clerk to Judge Edmund L. Palmieri, a research associate and associate director of the Columbia Law School Project on International Procedure, and as a Professor of Law at Rutgers University School of Law. Ruth, she was the first Jewish woman and second woman to serve. Ruth advocated for gender equality and women's rights, inspiring the Lilly Ledbetter Fair Pay Act. Her notable quote is "Women will only have true equality when men share with them the responsibility of bringing up the next generation" (26).

In the other corner of the world, **Ela Bhatt**, an Indian gentle revolutionary who is a pioneer in women's empowerment and financial inclusion in India and abroad (28). Independent leader, Ela

4/11

is an organizer and activist who founded the Self-Employed Women's Association of India (SEWA) in 1972. She was also appointed by Nelson Mandela to the group of world leaders known as The Elders in 2007. Recognition: As part of the international labour, women, and microfinance movements, she won several national and international awards, including the Right Livelihood Award for "helping home-based producers to organize for their welfare and self-respect."

3. CASE STUDIES OF SUCCESSFUL WOMEN IN NON-PROLIFERATION

The noteworthy contributions of women in the field of nuclear non-proliferation and disarmament can be highlighted in several cases across the world. These examples illustrate how women are increasingly recognized as vital participants in shaping policies and practices in this traditionally male-dominated area (29) especially through advocacy.

Leading a group of women to form the Women Strike for Peace (WSP), a group that began the lobbying for nuclear non-proliferation in 1961, **Bella Abzug** left a significant legacy in the 1963 Limited Test Ban Treaty (LTBT) signed by the United States, Great Britain and the USSR. The treaty which banned the testing of nuclear weapons under water, in outer space and in the atmosphere was an incredibly momentous treaty amid Cold War tensions that were reified by the Cuban Missile Crisis of 1962. The WSP group continued with its nonproliferation advocacy after a successful support leading to LTBT, with a goal to get the "average woman" to engage in activism for peace and nuclear threat reduction, specifically by framing nuclear issues as impacting children, mothers and families (30). **Efua Theodora Sutherland**, renowned Ghanaian playwright, children's author and cultural activist, continued on the same pedestal. Efua was married to Bill Sutherland, an African-American civil rights and anti-war activist, member of the Sahara Team and a key figure in the Ghana Nuclear Disarmament Council (GNDC) initiative founded in 1959. At his side, they garnered significant support from notable public figures and organisations within Ghana, including the National Federation of Gold Coast Women. First Ghanaian national women's organisation led by Evelyn Mansa Amarteifio, a Ghanaian feminist activist, the Federation supported the Ghana Nuclear Disarmament Council and was instrumental in building grassroots support for nuclear disarmament in Ghana (31,32).

Also contributing immensely to the disarmament of the African continent was **Albertina Sisulu and Winnie Mandela** who were South African anti-apartheid activists and Political figures (32,33). These two friends were prominent voices against the apartheid government's nuclear weapons program, highlighting the disproportionate impact of nuclear testing on indigenous populations. There was also Namibia's born Ursula Ndamse who led Namibia's All-African Women's Freedom Movement (AAWFM) to launch demonstrations against South Africa's nuclear weapons programme, attracting over 5,000 women in 1982. Leaving her mark on the sand of time, is **Amb. Liberata Mulamula**, a Tanzanian diplomat (34), who participated in the United Nations - Organization of African Union joint group of experts to draft a treaty creating a nuclear-weapon-free zone (NWFZ) in Africa called the Pelindaba Treaty. Thereafter its creation, the Group met several times at various African venues to discuss implementing a convention or treaty for Africa's denuclearization; to address administrative aspects and the relationship of the Treaty to other

5/11

similar agreements (36); to produce a draft for comment and consideration by the African nations, with a view to the final adoption of the experts' report; to clarify and refine the elements for the treaty rather than negotiate the text of the treaty. Mrs. Liberata Mulamula was one of the only 3 national members who participated (32). Contributing to building consensus on key aspects of the treaty, including its administration and coverage. Her contribution, while working closely with representatives of other African states and international partners, was to address concerns, build consensus, and draft the treaty text. Liberata is a recognized local, regional and international leader with over 25 years of experience. In her 35 years as diplomat, she has transitioned from the Tanzanian Ministry of Foreign Affairs and Regional Cooperation to the United Nation as Tanzanian Ambassador. She is a founding member of Fem Wise-Africa - The Network of African Women in Conflict Resolution and Mediators.

Joining other women to further the course for nonproliferation in the African Continent is **Dr Nkosazana Dlamini-Zuma**, the first female chairperson of the African Union including its predecessor, the Organisation of African Unity has been in the trenches fighting for the liberation of South Africa. She was the founding chairperson of the Council of the African Union Foundation launch in 2015, which is aimed at mobilizing resources for the African Union and promoting its programmers, and an undisputed trailblazer in the upliftment and empowerment of women across the African continent. As the first female leader of the continental organization, elected in 2012, she committed herself to peace and development of the continent and signed the African Commission on Nuclear Energy (AFCONE), the Pelindaba Treaty, the African Nuclear-Weapon-Free Zone, an implementation agency (article 12), and a host agreement for the establishment of its headquarters. She worked providing visionary oversight and commitment to upholding the treaty's standards as the depositary and to have all states ratify and accede to the treaty and its protocols (33,34). Proving indispensable to reconciling competing strategic interests and achieving consensus on the landmark Pelindaba Treaty in 1994 is the renowned "Iron Lady of Africa" **Ambassador Joy Ogwu** of Nigeria. Amb. Joy was appointed diplomat as Nigeria's top envoy on nuclear nonproliferation. Ogwu was tasked with engaging heads of state across Africa to build support for a nuclear-weapons ban treaty. She Played a crucial role in overcoming initial resistance and achieving consensus on the Pelindaba Treaty.

Actively at the United Nation, **Izumi Nakamitsu**, the UN High Representative for Disarmament Affairs, has been a vocal advocate for women's inclusion in disarmament processes. She highlights the importance of creating supportive environments that enable women's participation and addresses systemic barriers that hinder their involvement. Her leadership exemplifies how women can influence disarmament diplomacy, and she encourages aspiring female leaders to pursue their goals and advocate for equality within the field. She has been a strong advocate for women's inclusion in disarmament discussions and has worked to elevate the role of women in nuclear policy-making. Nakamitsu emphasizes the importance of diverse perspectives in achieving effective disarmament and non-proliferation outcomes (35,36). In this same light, and also to pave the way for future generations of women in foreign policy and non-proliferation, the US first female Secretary of State, Madeleine Albright promoted diplomacy and democracy in the expansion of NATO eastward into the former Soviet bloc nations and in the non-proliferation of nuclear weapons from the former Soviet republics to rogue nations. During her tenure, she was involved in

6/11

diplomatic efforts to reduce nuclear threats, particularly in the context of the former Soviet Union and rogue states. She served as Ambassador to the United Nations in 1993 to 1996 before her appointment as Secretary of State (37).

Championing on the American continent among other women was **Condeleezza Rice** was the first woman to hold the position of the Head of the National Security Council of the United State. She greatly influenced the shaping of US foreign policy including nuclear nonproliferation strategies. Her expertise in security affairs contributed significantly to diplomatic initiatives aimed at reducing nuclear risks especially regarding Eastern Europe and the Soviet Union (37). Through a notable initiative, a symposium titled "Nuclear Nonproliferation and Security for Women in STEM in Latin America and the Caribbean" held in June 2023, women from various STEM fields were brought together to discuss nuclear non-proliferation and security policies. Participants, including **Camila Araujo**, a radiation protection officer from Brazil who first proposed the initiative, emphasized the importance of creating a supportive community and sharing best practices to inspire more women to engage in nuclear security efforts. Camila Araujo was instrumental in organizing the symposium which fostered an environment for women to express their ideas freely, share experiences, and build networks. This affirms her contributions to promoting women's participation in nuclear non-proliferation discussions (38).

4. DISCUSSION

Advocacy has fostered women's empowerment and significantly influenced non-proliferation efforts on a global scale. Through participation, advocacy has provided women with platforms to engage and actively involve in the decision-making process, especially those relating to disarmament and nonproliferation. By leveraging advocacy, women participation in policy discussions has enabled women to make their voices heard and opinions, recognized. In its own way, it has impacted positively to the careers of these women and strengthen the perspectives of women in non-proliferation and disarmament policies and their capacity to influence outcomes, enhanced the quality of discussions, and the unique impact of feminine perspectives is also recognized and accepted. For instance, initiatives aimed at increasing women's representation in international forums, like the Non-Proliferation Treaty (NPT) meetings, have highlighted the importance of diverse voices in shaping effective disarmament policies. Women's perspectives often bring attention to issues such as the humanitarian impacts of nuclear weapons, which can lead to more comprehensive policy frameworks.

In addition, advocacy efforts have facilitated the building of networks and coalitions among women in non-proliferation. These networks enhance collaboration, knowledge sharing, and mutual support, empowering women to take on leadership roles within their communities and internationally. By connecting women from various backgrounds and regions, advocacy fosters a sense of solidarity and collective action, which is essential for driving change in non-proliferation efforts. For example, campaigns that highlight the disproportionate impact of nuclear weapons on women and girls have helped to frame non-proliferation as a gender issue. These campaigns have effectively raised awareness about the importance of gender equality in non-proliferation and

7/11

disarmament processes. By addressing societal norms and stereotypes that hinder women's participation, advocacy has contributed to cultural shifts that support women's empowerment.

Furthermore, evidence-based advocacy which focus on generating and disseminating evidence about the links between gender and non-proliferation, have proven effective in influencing policy decisions. By providing data and case studies that illustrate the benefits of including women in these discussions, advocates make compelling arguments for gender-sensitive policies. This evidence-based approach counteracts gender-blind policies and promotes the integration of women's needs and perceptions into non-proliferation frameworks. Overall, advocacy has empowered women by facilitating their participation in non-proliferation and disarmament discussions, building supportive networks, raising awareness about gender issues in non-proliferation, and promoting evidence-based policy changes. These efforts not only enhance women's roles in shaping non-proliferation policies but also contribute to more effective and inclusive approaches to global security challenges.

It is worth appreciating that the integration of gender perspectives into non-proliferation and disarmament challenges traditional notions of security that often prioritize military strength and deterrence. By emphasizing human security and the impacts of armed conflict on civilians, particularly women, advocates shift the narrative towards a more holistic understanding of security. This transformation encourages policies that prioritize conflict prevention and resolution over military solutions, which can lead to more stable and peaceful societies This includes addressing issues such as gender bias, lack of access to decision-making spaces, and the need for supportive policies that promote gender equality in international security contexts. By advocating for these changes, the non-proliferation community can create a more equitable environment that fosters the contributions of all individuals, regardless of gender. These barriers must be addressed to ensure that women's perspectives and expertise are fully utilized in non-proliferation efforts.

5. CONCLUSION

Women play multifaceted roles in international disarmament initiatives, from grassroots activism to high-level policy advocacy. Their contributions are vital for creating inclusive and effective disarmament strategies that address the unique challenges faced by women and promote sustainable peace and security across the continent.

Advocacy has empowered women by facilitating their participation in disarmament discussions, building supportive networks, raising awareness about gender issues in non-proliferation, and promoting evidence-based policy changes. These efforts not only enhance women's roles in shaping disarmament policies but also contribute to more effective and inclusive approaches to global security challenges.

In addition, the implications for international security stemming from women's active efforts in disarmament and non-proliferation are significant. By broadening the scope of security to include human, environmental, and technological dimensions, the international community can develop

8/11

more effective strategies to address the complex challenges of the modern world. This holistic approach not only enhances global security but also promotes sustainable development and peace.

REFERENCES

1. Dewitt, D. B. (Ed.), *Nuclear non-proliferation and global security*, Routledge, Oxfordshire, United Kingdom (UK) (2020)
2. Lodgaard, S, *Nuclear disarmament and non-proliferation: towards a nuclear-weapon-free world?* Routledge, Oxfordshire, United Kingdom Page 288 (2010)
3. Wan, W, *Regional pathways to nuclear nonproliferation*, University of Georgia Press, Athens, United States of America, **3** (2018)
4. Surber, R. "Artificial intelligence: autonomous technology (AT), lethal autonomous weapons systems (LAWS) and peace time threats." *ICT4Peace Foundation and the Zurich Hub for Ethics and Technology (ZHET)* Page 21 (2018)
5. Alkış, M. A & Sinovets P, "Nuclear Security: Making Gender Equality a Working Reality." *International Journal of Nuclear Security*, **8.2**, Page 9 (2023)
6. Tabassum, N., & Nayak, B. S. "Gender stereotypes and their impact on women's career progressions from a managerial perspective." *IIM Kozhikode Society & Management Review*, **10.2**, Pages 192-208 (2021)
7. Cookmeyer D, Ozturk H, Wayne M, Barbercheck M & Wyer, *Women, science, and technology: A reader in feminist science studies*, Taylor and Francis, New York, USA Pages 88-98. (2001)
8. Ely, R. J., Ibarra, H., & Kolb, D. M. "Taking gender into account: Theory and design for women's leadership development programs." *Academy of management learning & education*, **10.3**, Pages 474-493. (2011)
9. Khurana, I., & Lee, D. J. "Gender bias in high stakes pitching: an NLP approach." *Small Business Economics*, **60.2**, Pages 485-502. (2023)
10. Strauss, S. "Implicit bias and employment discrimination." *Women and Management: Global Issues and Promising Solutions* **2** Pages 175. (2013)
11. Enloe, C. *Globalization and militarism: Feminists make the link*. Rowman & Littlefield, Maryland, USA (2016).
12. Heilman, Madeline E., and Suzette Caleo. "Combatting gender discrimination: A lack of fit framework." *Group Processes & Intergroup Relations* **21.5**: Pages 725-744. (2018)
13. Egeland, Kjøl, and Hebatalla Taha. "Experts, activists, and girl bosses of the nuclear apocalypse: feminisms in security discourse." *Zeitschrift für Friedens-und Konfliktforschung* **12.2** Pages 245-266 (2023).
14. Agarwal, Pawan, and G. Kamalakar. "Indian higher education: Envisioning the future." *The Indian Economic Journal* **61.1** Pages 151-155 (2013).

15. Krishna P, GP Acharya P, & Dahal G. D. "Advocacy campaign to improve governance in community forestry: a case from western Nepal." *Journal of Forest and Livelihoods* **6.1** Pages 59-69 (2007).
16. Wiliam-de Vries, D., and Sutarti N. "Gender equity: revealing the reality for the women of Jambi." (2006).
17. Gender in Agriculture Gender in Agriculture from Policy to Practice (2024)
18. Cornwall, A, & Althea-Maria R. "From 'gender equality and 'women's empowerment' to global justice: reclaiming a transformative agenda for gender and development." *Third world quarterly* **36.2** Pages 396-415 (2015).
19. DiMarco, N. "Female Leaders and Women's Empowerment"; 3 Case Studies." (2012).
20. Krook, Mona Lena, and Jacqui True. "Rethinking the life cycles of international norms: The United Nations and the global promotion of gender equality." *European journal of international relations* **18**(1) Pages 103-127 (2012).
21. Brown, Laura Rose, and Laura Considine. "Examining 'gender-sensitive' approaches to nuclear weapons policy: a study of the Non-Proliferation Treaty." *International Affairs* **98**(4) Pages 1249-1266 (2022).
22. Minor, E. "Addressing the political impact of inclusion and exclusion in multilateral disarmament forums." *Global activism and humanitarian disarmament* Pages 225-251 (2020).
23. International Atomic Energy Agency <https://www.iaea.org/services/key-programmes/together-for-more-women-in-nuclear> (2024)
24. Biography <https://www.biography.com/activist/wangari-maathai>, (2021)
25. Treefolks <https://www.treefolks.org/2024/02/19/wangari-maathai-the-grassroots-kenyan-heroine/> (2024)
26. International Training Website <https://www.itcilo.org/stories/5-women-who-changed-world-work> (2021)
27. United State Supreme Court <https://www.supremecourt.gov/about/biographyGinsburg.aspx>
28. Women's World Banking <https://www.womensworldbanking.org/insights/ela-ramesh-bhatt-a-gandian-revolutionary/>
29. Laura R B, Laura C, "Examining 'gender-sensitive' approaches to nuclear weapons policy: a study of the Non-Proliferation Treaty" *International Affairs*, **98**(4) Pages 1249–1266 (2022)
30. Center for Arms Control and Non-proliferation <https://armscontrolcenter.org/women-in-nuclear-history-bella-abzug/> (2019)
31. AMANDLA <https://amandlanews.com/ghanas-forgotten-hero-who-is-the-first-african-woman-to-hold-a-cabinet-portfolio/> (2019)
32. South Africa History Online <https://www.sahistory.org.za/article/albertina-sisulu-timeline-1918-2011>
33. African Union Foundation <https://www.africaunionfoundation.org/dr-nkosazana-dlamini-zuma>

34. SWOTAN LIVE <https://www.sowetanlive.co.za/news/south-africa/2019-09-16-nkosazana-dlamini-zuma-calls-for-tolerance-as-new-varsity-chancellor/> (2019)
35. Vienna Centre for Disarmament and Non-Proliferation <https://vcdnp.org/the-role-of-women-in-non-proliferation-and-disarmament-advocacy/> (2021)
36. European Leadership Network <https://europeanleadershipnetwork.org/commentary/women-in-disarmament-qa-with-high-representative-izumi-nakamitsu/> (2020)
37. U.S. Global Leadership Coalition <https://www.usglc.org/blog/5-women-trailblazers-in-foreign-policy/> (2022)
38. Middlebury Institute of International Studies at Monterey <https://nonproliferation.org/cns-women-in-stem-from-latin-america-and-the-caribbean-2023/> (2023)

Track 9

emPowering the Next Generation

The reactivation of the AJENM (A Mexican young association in nuclear).

Gálvez González Brian
Universidad Autónoma Metropolitana
Av. San Rafael Atlixco No. 186 Col. Vicentina Iztapalapa.
briangalvezgonzalez@hotmail.com

Ana Paulina León Aboyte
Instituto Tecnológico de Morelia
Avenida Tecnológico 1500, Col. Lomas de Santiaguito, Morelia, Michoacán México
paulina.imec@gmail.com

Abstract

When the nuclear era started in Mexico in 1955 from the hand of Miguel de la Madrid president, the country experienced some changes around how the industry had been generating the electricity, the idea of creating two nuclear power reactors with all the associations within this action, made possible the foundation of the Asociación de Jóvenes por la Energía Nuclear en México (AJENM), an Association that started in 2004 thanks to the enthusiasm of a young student named Armando Miguel Gómez Torres. AJENM is a young association that, since the first moment it was created, has focused on the divulgation and diffusion of nuclear technology, this idea of communicating all about nuclear science, brought with it the creation of articles, expos, etc. talking about energy, medicine, agriculture, and other nuclear applications. As a young association focusing on nuclear science and the transmission of knowledge around this, there were various works that could have maintained it relevant throughout the years, but it had been abandoned for many years until now. After all the years that AJENM disappeared, it has finally been reactivated thanks to the effort of many people. The next paper is made to show the actions, plans and ideas that the current members of the AJENM are preparing for the Association to become relevant national and internationally once again, all of these actions have a wide field of reach, this is because the members have different interests about the applications of the nuclear energy. There are many the ideas for the next months of work from the AJENM such as talks to the population about nuclear energy, the develop of webinars with nuclear energy experts, expositions in universities, high schools, and even elementary schools about the nuclear energy applications, the creation of content with other associations, societies, and institutes, etc., all of the ideas are created to make nuclear science more understandable for everyone.

1. INTRODUCTION

The Asociación de Jóvenes por la Energía Nuclear en México (AJENM, also known as Youth Association for Nuclear Energy in Mexico) formally started working on March 8 of 2003 just as [1] explained. When 2024 started, the Association had no members at all and the efforts that were

being made were focused on the resurgence of this, the Association had been paused for some years already; it was until a group of 7 enthusiastic students decided to restart the operations of the AJENM, the day was June 19 of 2024 when the beginning of a new era of nuclear divulgation in Mexico restarted from the hand of this group of young students and graduates from four different universities.

The mission of the AJENM was written in 2004 [1] and it said: To group young students who are interested in the nuclear field, and in their own professional growth, perhaps, the goal has changed but it is in the way that there are several goals that can be summarized as one: To become an Association known for the divulgation of nuclear energy to the public in Mexico and by other Associations, Societies and Centers. There are almost 60 Mexican students enrolled, nine of these actively doing an arduous work in divulgation and focused on make the AJENM a well-known Association again.

2. NUCLEAR FIELD IN MEXICO

Nuclear technology has various applications in general, as it was mentioned by the [2] nuclear energy can be applied in non-electric processes such as the desalination of sea water district and waste water, heating residences and commercial buildings, and on industrial process heat supply, but, these are not the only applications that this science has to offer, just as it is said by [3] that non-electric applications of nuclear technology are applied in medicine and health, food and agriculture and even on research for determining the age of substances.

Knowing all the applications that nuclear technology has to offer, besides nuclear power, now, it is important to show how these are applied in Mexico. There are several centers, schools, institutes that study this technology and do many science and engineering advances using nuclear energy.

2.1. Different Uses Of Nuclear Technology In Mexico.

Nuclear technology in Mexico has evolve throughout the years, speaking of nuclear power in Mexico, [4] mentioned that it all started in 1988 when the President Miguel de la Madrid authorized the loading of the first reactor unit at Laguna Verde, it was in this moment that all the nuclear power technology begin in Mexico, but it wasn't the beginning of the nuclear knowledge in Mexico, in 1955 the formation of a study group on nuclear energy bring the creation of the Comisión Nacional de Energía Nuclear (CNEN; also known as Nuclear Energy National Commission), the commission was created to have a governmental body responsible for nuclear activities in Mexico, this Commission will become later the Instituto Nacional de Investigaciones Nucleares (ININ; also known as Nuclear Investigation National Institute), the Comisión Nacional de Seguridad Nuclear y Salvaguardias (CNSNS; also known as National Commission for Nuclear Safety and Safeguards) and URAMEX.

It is in this context that nuclear energy in Mexico started, now, it has plenty study centers, schools and institutes that use this technology. The next commissions and institutes are the most important nuclear centers in Mexico.

2.1.1. The ININ

The ININ, located in La Marquesa, Toluca, Mexico is one of the most important institutions in nuclear research in the country. It offers services such as the Regional Center for Nuclear Training and Education (CRNE), where courses and training programs in safety and radiological protection, among others, are provided. Additionally, the ININ offers undergraduate, master's, and doctoral students the opportunity to conduct scientific research in the nuclear field. These projects are developed nationally in collaboration with universities, and internationally with the International Atomic Energy Agency (IAEA) [5]. The ININ focuses on eleven different nuclear research areas, including applications in sectors such as industry, health, agriculture, materials, nuclear sciences, nuclear technology, energy sources, and radioactive waste management, among others. Students can apply their knowledge on these projects or at the experimental reactor available at ININ: the Triga Mark-III reactor, which was designed for nuclear research development [6].

2.1.2. The CNSNS.

The CNSNS in Mexico is the regulatory body for nuclear matters. Its main responsibility is to ensure that all nuclear and radioactive facilities operate with the highest level of safety for the country's inhabitants. The CNSNS oversees the implementation of nuclear, radiological, and physical safety standards, as well as the necessary safeguards to ensure the safe and controlled use of nuclear energy. [7] The CNSNS regularly supervises and evaluates nuclear facilities to ensure compliance with safety regulations. It also implements safeguards to prevent the proliferation of nuclear weapons and collaborates with international organizations like the IAEA to meet global commitments. Additionally, it provides advice and training on nuclear safety, promoting a culture of protection in the use of nuclear technology in Mexico.

2.1.3. The Sociedad Nuclear Mexicana (SNM; also known as Mexican Nuclear Society).

The SNM is a non-profit civil association founded in 1988, composed of professionals, technicians, students, and institutions interested in promoting the peaceful use of nuclear energy. In Mexico, the SNM has positioned itself as an allied society of the American Nuclear Society and the Canadian Nuclear Society, among other national and international institutions. Since 1990, nuclear energy-related conferences have been organized in Mexico. These kinds of events have generated significant interest, as it coincided with the first operational cycle of the Central Nuclear Laguna Verde (CNLV; also known as Laguna Verde Nuclear Central), being the first in the world to reach this milestone [8].

In 2024, the SNM continues to fulfill its mission by providing opportunities for professionals to participate and share knowledge and interests related to nuclear energy in Mexico and around the world.

2.1.4. Schools with nuclear specialties.

By 2024, various Mexican universities and institutions offer programs in nuclear energy matter, these schools or institutes are the Universidad Nacional Autónoma de México (UNAM), Instituto Politécnico Nacional (IPN), Universidad Autónoma Metropolitana (UAM), Universidad Autónoma de Zacatecas (UAZ) and Universidad Autónoma de Nuevo León (UANL). Each of these universities have several plans on nuclear energy, technology, and applications.

3. AJENM PROJECTS AND PLANS

As it was said in the beginning of this paper, AJENM, as an Association of youth students, stopped activities for a period, the posts from Facebook were the only way that the Association was visible. In June of 2024, the activities restarted, all the ideas and plans that AJENM is developing now are summarized in this section.

There are several topics and actions that the AJENM wants to cover and do. Having a diverse variety of students from all the most important nuclear schools in Mexico, the need to talk about all the knowledge that each one has is an important goal to achieve. The plans are the making of infographic documents, webinars with important groups of specialists in the nuclear field either in Mexico or in another country, talks about nuclear energy and its applications in high schools and universities, etc.

3.1. North American Young Generation in Nuclear (NAYGN)

This is one of the major plans that AJENM has in its near objectives, as an Association that once was an important member of NAYGN, the team is looking forward to collaborating with this organization. Trying to become relevant again and well known in the nuclear field in North America, AJENM is preparing some topics to work side by side with NAYGN, the objective of this is to let the North American experts that Mexico is important and is developing knowledge on the nuclear field. It is known that Mexico has a Nuclear Central called Laguna Verde, the objective with these actions is to make clear all the knowledge and developments from Mexican associations, societies, and schools.

The first action is explained below:

- **Webinars:** As one of the easiest yet crucial ways to attract the people into this knowledge, AJENM is sure that collaborating with these simple actions surely help to make the nuclear science understandable and easy to get to know for everybody, furthermore, letting know other teams about the nuclear context and history in Mexico might help to assure that Mexico has different ways to be relevant in the nuclear field.

There are plenty of ideas around this collaboration, this is the most important of them and the first that AJENM is going to work with to make the Association visible worldwide.

3.2. SNM.

As one of the principal Societies in the Nuclear Field in Mexico, the SNM and AJENM are preparing several actions to collaborate. Seeking for the divulgation and future acceptance of the nuclear energy in Mexico, the plans to achieve with the SNM are:

- To reach the Mexican citizens from each state to talk about the nuclear energy and understand its viability in the energy transition for climate change: One of the main objectives that AJENM has is to tell all the Mexican people about the nuclear energy and its applications so they can have an informed decision about the benefits it has within.
- To create content in social media, schools, and other organizations about nuclear technology: This action is just the same as the NAYGN proposition, but it has the vision to be a detonator to have more people studying and supporting this technology.
- To do webinars with Mexican experts in nuclear topics: As many of other organizations and associations do, having talks with experts is a good way to generate interest in the people, from medicine to nuclear security topics, this huge variety of themes will show all the nuclear applications and will make it attractive to study or to be known to the people that has no idea about this science.

The objective with this collaboration is to prepare the first actions to become relevant in Mexico along this Society and to comment all the non-electric applications of the nuclear energy, we have special interest to transmit all this knowledge to the young people in Mexico.

3.3. General objectives from AJENM.

The last ideas and actions were focused on collaborating with important organizations with many years in the nuclear field. All the goals that AJENM has, are focused on becoming relevant national and internationally, the next actions that are listed are currently being done by the members of the AJENM some of them are planned to achieve through the next two years.

- Talk about the AJENM in an event from the United Nations Foundation: In the context of the summit of the future 2024, a social movement called Enseña por México (Teach for Mexico) along with the United Nations Foundation have prepared an event to gather some proposals and ideas to bring up in this summit that will be celebrated in Washington DC. AJENM was selected to talk about the challenges that the Association has had and the hopes about the future around the Association and the Nuclear Energy in Mexico.
- Talk in the IV Thematic Forum from SUTIN-URAMEX: In this Forum, AJENM will be presenting the vision about nuclear energy in the energy politics in Mexico, this is going to be focused on the actions that people and AJENM can do about it.
- Participation in forums about nuclear energy organized by the Deputies Camera: AJENM is planning to talk with some deputies about the possibility of being in forums or expos of energy presenting the importance of nuclear energy in the energetic transition.
- Developing of a plan to talk in schools: AJENM wants to generate talks and expos in universities and high schools, these ideas are focused on the need to have more people knowing about nuclear energy, it can be developed in specific days where the schools have

activities of divulgation or AJENM can propose a group of days where the main objective is to transmit, divulgate and teach about nuclear science.

- Presentation of expos from the team in a school from the UNAM: AJENM has the plan to be creating expos on the nuclear field in a school that has plenty engineering careers about mechanical and electrical science. Having these kind of topics and students learning all these themes, AJENM can show how it can be applied on the nuclear field.

As it was said on each plan, the main idea is to become known in Mexico and in the world, these ideas specifically are different and try to look for new horizons and new ways for the young people in nuclear energy to transmit and tell the ways that nuclear energy works and can be applied. It goes from schools in Mexico to activities or events from world associations.



Figure 1. Photograph taken on the official presentation of the AJENM along the AJENM's founder

4. CONCLUSIONS

Nuclear technology in Mexico has the potential to become more important throughout the next years thanks to all the institutes that teach all this technology. AJENM as a nuclear Association filled with young students and people divulgating this science is great to reach more people around the globe for them to be more informed about nuclear science for it to be more accepted. It is the work of the AJENM to try to reach even younger generations so they can be informed from early studies about nuclear energy and the applications it has within.

REFERENCES

1. A. T. Gómez and V. J. Xolocostli, “Nuclear Energy in Mexico, a Challenge for Youth”, *International Youth Nuclear Congress* (2004)
2. International Atomic Energy Agency, *Industrial Applications of Nuclear Energy*, IAEA, Vienna, Austria (2017)
3. M.A. Rosen, “Nuclear Energy: Non-Electric Applications”, *European Journal of Sustainable Development Research*, **Volume 4, no. 1** (2021)
4. D. Stevis and S.P. Mumme, “Nuclear Power Technological Autonomy, and the state in Mexico”, *Latin American Research Review*, **Vol. 26, no. 3**, p. 55-82 (1991)
5. Instituto Nacional de Investigaciones Nucleares, *Actividad Científica y Tecnológica en el Instituto Nacional de Investigaciones Nucleares*, Innovación editorial lugares de México, Mexico City, Mexico (2008)
6. F.H. Aguilar, “The Mexican TRIGA Mark-III Reactor with TRIGA Fuel Type 30/20” *Reduced Enrichment for Research and Test Reactors*, Warsaw, Poland, October 16th, Vol. 34, no. 8. (2012)
7. Secretaría de Energía, *Convención Conjunta sobre Seguridad en la Gestión del Combustible Gastado y sobre Seguridad en la Gestión de Desechos Radioactivos*, SENER, Mexico City, Mexico (2020)
8. Sociedad Nuclear Mexicana A.C., *Memorias*, Veracruz, Veracruz, November 17th Vol. 2 (1991).